ANALYTICAL CHEMISTRY
SEPTEMBER 15, 1995

Using CE to Investigate Protein Changes 3093

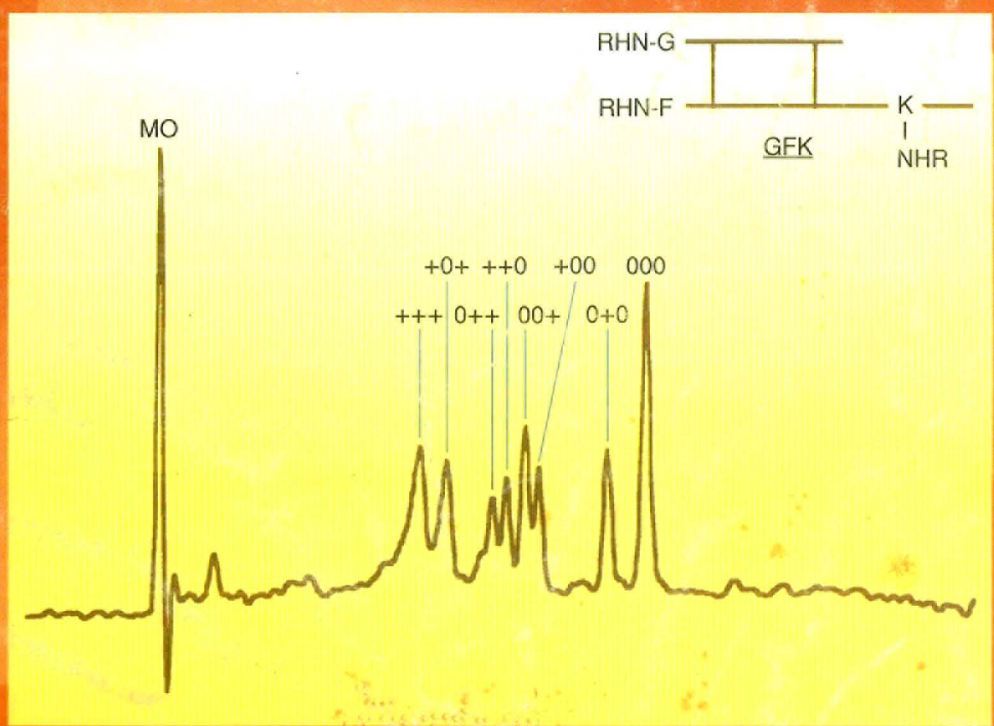

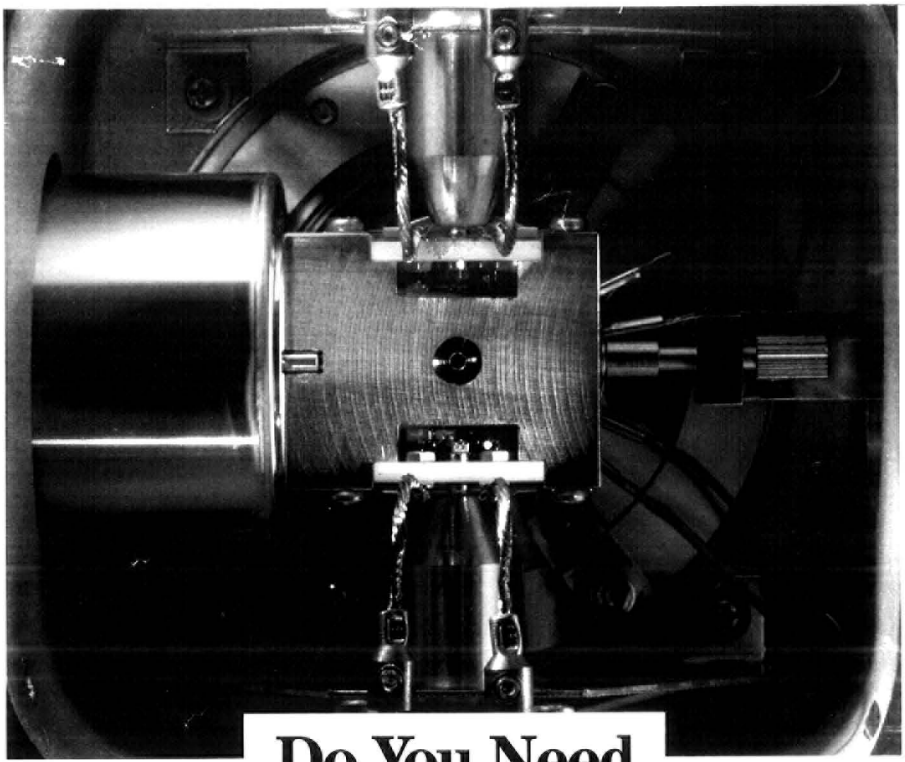

Do You Need A Comprehensive GC/MS Solution?

The Shimadzu GC/MS QP-5000. The new generation. Compact and complete.

Regardless of whether you work in water, air, or soil analysis, or whether you are looking for environmental analysis, additives in food, or forensics drug abuse, our new GC/MS QP-5000 is sure to exceed your expectations. Its mass spectrometer, covering the range 10 amu to 700 amu, is coupled to the proven performance of the GC-17A gas chromatograph, including AFC for setting carrier related flows and pressures. Our new GC/MS QP-5000 has been designed for the most stringent analytical methodology as well as routine analytical laboratory work. Its compactness and range of features are truly impressive. The overall width of the GC and MS is just 72.5 cm (28.5"). All system operations are controlled by Microsoft® Windows™-based software. The GC/MS QP-5000 is a highly sensitive bench-top GC/MS with computer-simulation-optimized ion optics and fully automated vacuum control. Available options include a jet-separator interface, a high capacity turbomolecular pump, chemical-ionization, and a direct inlet system for low volatiles. Call your nearest Shimadzu Representative today for more details on the GC/MS QP-5000. You can count on a prompt response from us.

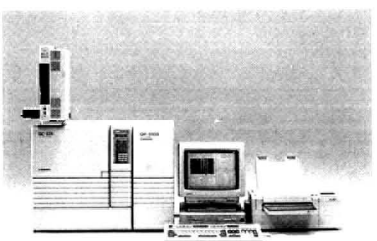

Microsoft® Windows™ is a registered trademark of Microsoft Corporation, Redmond, WA, USA.

For more information, please contact us.

SHIMADZU CORPORATION,
International Marketing Division
3, Kanda-Nishikicho 1-chome, Chiyoda-ku, Tokyo 101, Japan
Phone: 81(3)3219-5641 Fax.: 81(3)3219-5710

SHIMADZU SCIENTIFIC INSTRUMENTS, INC.
7102 Riverwood Drive, Columbia, Maryland 21046, U.S.A.
Phone: 1(410)381-1227 Fax.:1(410)381-1222

SHIMADZU EUROPA GmbH
Phone: 49(203)7687-0 Fax.: 49(203)766625 Germany.

SHIMADZU (ASIA PACIFIC) PTE LTD.
Phone: 65-778 6280 Fax.: 65-779 2935 Singapore.

SHIMADZU OCEANIA PTY. LTD.
Phone: 61(2)684-4200 Fax.: 61(2)684-4055 Australia.

SHIMADZU

Solutions for Science
since 1875

ANALYTICAL CHEMISTRY

EDITOR: ROYCE W. MURRAY
University of North Carolina

ASSOCIATE EDITORS: **Catherine C. Fenselau,** University of Maryland Baltimore County, **William S. Hancock,** Hewlett Packard, **James W. Jorgenson,** University of North Carolina, **Robert A. Osteryoung,** North Carolina State University, **Edward S. Yeung,** Iowa State University/Ames Laboratory

Editorial Headquarters, research section
Department of Chemistry
Venable and Kenan Laboratories
University of North Carolina
Chapel Hill, NC 27599-3290
Phone: 919-962-2541
Fax: 919-962-2542
E-mail: Murray@uncvx1.ori.unc.edu

Editorial Headquarters, A-page section
1155 Sixteenth St., N.W.
Washington, DC 20036
Phone: 202-872-4570
Fax: 202-872-4574
E-mail: acx96@acs.org

Managing Editor: Mary Warner

Associate Editor: Felicia Wach

Editorial Assistant: Deborah Noble

Contributing Editor: Marcia Vogel

Head, Graphics and Production: Leroy L. Corcoran

Division Art Director: Alan Kahan

Art Director: Michele Telschow

Manager, Copy Editing: Elizabeth Wood

Production Editor: Eric Sorensen

Electronic Composition: Wanda R. Gordon

Journals Dept., Columbus, Ohio

Editorial Office Manager: Mary E. Scanlan

Journals Editing Manager: Kathleen E. Duffy

Associate Editor: Lorraine Gibb

Assistant Editor: Stephanie L. Mallon

VOLUME 67, NUMBER 18

Analytical Chemistry (ISSN 0003-2700) is published semi-monthly by the American Chemical Society, 1155 16th St., NW, Washington, DC 20036. Second-class postage paid at Washington, DC, and at additional mailing offices. Postmaster: Send address changes to Member & Subscriber Services, P.O. Box 3337, Columbus, OH 43210 Canadian GST Reg. No. 127571347

1995 **subscription rates** include air delivery outside the U.S., Canada, and Mexico. Canadian subscriptions are subject to 7% GST.

	Members	Nonmembers (personal)	Nonmembers (institutional)
U.S.	$ 40	$ 85	$ 570
Canada and Mexico	77	122	607
Europe	123	168	653
Other countries	148	193	678

Members may share/donate their personal subscriptions with/to libraries and the like but only after 5 years from publication.

Nonmember rates in Japan: Rates above do not apply to nonmember subscribers in Japan, who must enter subscription orders with Maruzen Company Ltd., 3–10 Nihonbashi 2-chome, Chuo-ku, Tokyo 103, Japan. Tel: (03) 272-7211.

For multi-year and other rates, call toll free 800-227-5558 in the U.S. and Canada; in the Washington, DC, metropolitan area and outside the U.S., call 202-872-4363; fax 202 872 4615.

Single issues, current year, $24.00 except review issue, $50.00, and LabGuide, $50.00; **back issues and volumes and microform editions** available by single volume or back issue collection. For information or to order, call the number listed for subscription orders; or write the Microform & Back Issues Office at the Washington address.

Subscription orders by phone may be charged to VISA, MasterCard, or American Express. Call toll free 800-333-9511 in the continental U.S.; in the Washington, DC, metropolitan area and outside the continental U.S., call 202-872-8065. Mail orders for new and renewal subscriptions should be sent with payment to American Chemical Society, Department L-0011, Columbus, OH 43268-0011.

Changes of address must include both old and new addresses with ZIP code and a recent mailing label. Send all address changes to the ACS Columbus address. Please allow 6 weeks for change to become effective. **Claims for missing issues** will not be allowed if loss was due to failure of notice of change of address to be received in the time specified; if claim is dated (a) North America—more than 90 days beyond issue date, (b) all other foreign—more than 180 days beyond issue date. Hard copy claims are handled at the ACS Columbus address.

Instructions for authors of AC Research and guidelines for the Instrumentation, Report, Analytical Approach, and A/C Interface features are published in the Jan. 1 issue, p. 229, or can be obtained from our e-mail reflector "acinfo@acs.org" using the keyword phrases "ac research" or "ac apguide," respectively. Please consult these instructions prior to submitting a manuscript for consideration for publication.

Manuscripts for publication in AC Research (4 copies of text and illustrative material) should be submitted to the Editor at the University of North Carolina address. Please include a signed copyright status form; a copy of this document appears on p. 235 of the Jan. 1 issue. Manuscripts for publication in the A-page section should be submitted to the Washington editorial staff.

Supporting information is noted in the table of contents with a ■. It is available as photocopy ($12.00 for up to 3 pages and $1.50 per page for additional pages, plus $2.00 for foreign postage) or as 24× microfiche ($12.00, plus $1.00 for foreign postage). Canadian residents should add 7% GST. See supporting information notice at the end of journal article for number of pages. Orders must give complete title of article, names of authors, journal, issue date, and page numbers. Prepayment is required and prices are subject to change. In 1995, electronic supporting information is available to current journal subscribers via the Internet using either gopher or World Wide Web protocols. Most often, the material is available as PDF files, which may be viewed using Adobe's Acrobat Reader, a program that is freely available on the Internet. However, some articles may include computer programs, PostScript files, word-processing files, experimental data in a standard format (e.g., crystallographic parameters in CIF format), etc. In order to download the supplementary material files, users will need to enter their journal subscriber number, which can be found on the mailing label. Detailed instructions for using this service can be found on the Internet. With gopher, connect to pubs.acs.org, go to the "ACS Publications" selection, then to the "Supporting Information" selection. Read the README file in this directory for detailed instructions. When using a WWW client (e.g., Mosaic, Netscape), connect to the URL "http://pubs.acs.org/" and select the "Supporting Info. for Journals" link. For further information on electronic access, send electronic mail to gopher@acsinfo.acs.org, or phone (202) 872-4434. For information on microforms, contact Microforms & Back Issues at the ACS Washington address or phone (202) 872-4554. Supporting information, except structure factors, also appears in the microfiche edition.

The American Chemical Society and its editors assume no responsibility for the statements and opinions advanced by contributors. Views expressed in the editorials are those of the editors and do not necessarily represent the official position of the American Chemical Society.

Journals Department, American Chemical Society, 2540 Olentangy River Road, P.O. Box 3330, Columbus, OH 43210 (614-447-3600, Ext. 3171; TELEX 6842086; Fax 614-447-3745)

Member & Subscriber Services: American Chemical Society, P.O. Box 3337, Columbus, OH 43210 (614-447-3776; 800-333-9511)

Advertising Management: Centcom, Ltd., 1599 Post Rd. East, P.O. Box 231, Westport, CT 06881 (203-256-8211; fax 203-256-8175)

ANCHAM 67(18) 3093–3376 (1995)
ISSN 0003-2700

ANALYTICAL CHEMISTRY®

SEPTEMBER 15, 1995
Volume 67, Number 18

ACCELERATED ARTICLES

ARTICLES

CORRESPONDENCE

TECHNICAL NOTES

■ Supporting information for this paper is available separately (consult a current masthead page for ordering information). Supporting information is available to subscribers electronically via the Internet at http://pubs.acs.org (WWW) and pubs.acs.org (Gopher). All supporting information except for structure factor tables will also appear following the paper in the microfilm edition of the journal.

* In papers with more than one author, the asterisk indicates the name of the author to whom inquiries about the paper should be addressed.

Accelerated Articles

Anal. Chem. 1995, *67*, 3093–3100

Using Capillary Electrophoresis To Follow the Acetylation of the Amino Groups of Insulin and To Estimate Their Basicities

Jinming Gao, Milan Mrksich, Frank A. Gomez,† and George M. Whitesides*

Department of Chemistry, Harvard University, 12 Oxford Street, Cambridge, Massachusetts 02138

Capillary electrophoresis (CE) is an analytical method that is useful for investigating processes that modify the charge of proteins. This paper explores the ability of CE to rationalize charges and electrophoretic mobilities of a simple protein—insulin and its acylated derivatives—as a function of pH. Insulin is a peptide hormone (MW = 5700) that has two α-amino groups (G^{α} and F^{α}) and one ε-amino group (K^{ϵ}). Treatment of insulin with acetic anhydride affords seven derivatives that differ in the sites of acetylation of the three amino groups. Analysis of the pH dependence of the electrophoretic mobilities of these derivatives gives pK_a values for the two N-terminal ammonium groups: pK_a (G^{α}) = 8.4; pK_a (F^{α}) = 7.1. Values of the total charge of insulin estimated from electrophoretic mobility differ from those estimated from values of pK_a for its ionizable groups by less than 0.5 unit for both bovine and human insulins over the range of pH from 5.5 to 9.5. Analysis of the concentration dependence of the electrophoretic mobility of insulin yields a lower limit for the association constant for dimerization of insulin of $K_D \geq 6 \times 10^3$ M^{-1} (25 mM tris and 192 mM Gly, pH 8.4). Studies of electrophoretic mobility as a function of pH and extent of acetylation of amino groups rationalize the charge of insulin in detail. The sensitivity of CE to charge permits the quantitative study of electrostatic properties of proteins in solution. Insulin is a useful small-protein model with which to investigate phenomena in electrophoresis.

Capillary electrophoresis (CE) can analyze small quantities of proteins and peptides with high resolution under nondenaturing conditions.[1-6] CE has been used for peptide mapping,[7,8] measuring the total charge of a protein in solution,[9] and studying the binding affinities of ligands to proteins.[10-12] Here we describe the use of CE to characterize the products formed upon acetylation of the amino groups of insulin, to estimate the basicities of these amino groups, and to estimate the association constant for dimerization of insulin. These studies illustrate the value of variations in pH in deciphering complex CE data and suggest the accuracy of pK_a's derived from CE.

Basis for Separation in CE. The rate of migration of a protein in a capillary is characterized by its electrophoretic mobility, μ (cm^2 kV^{-1} s^{-1}), which is defined as the steady-state velocity per unit of electric field strength. It is calculated by comparing the migration time of the protein (t) to that of a neutral marker (t_{eo}, for mesityl oxide) using eq 1; L_{tot} is the total length of the capillary, L is the length of capillary separating the points of sample injection and detection, and V is the voltage applied across the capillary. Equation 2 is an approximate expression that

† Present address: Department of Chemistry and Biochemistry, California State University, Los Angeles, 5151 State University Drive, Los Angeles, CA 90032.

(1) *Capillary Electrophoresis: Theory and Practice*; Grossman, P. D., Colburn, J. C., Eds.; Academic Press: San Diego, CA, 1992.
(2) Engelhardt, H.; Beck, W.; Kohr, J.; Schmitt, T. *Angew. Chem., Int. Ed. Engl.* **1993**, *32*, 629–766.
(3) Kuhr, W. G.; Monnig, C. A. *Anal. Chem.* **1992**, *64*, 389–407.
(4) Novotny, M. V.; Cobb, K. A.; Liu, J. *Electrophoresis* **1990**, *11*, 735–749.
(5) Karger, B. L.; Cohen, A. S.; Guttman, A. *J. Chromatogr.* **1989**, *492*, 585–614.
(6) Gordon, M. J.; Huang, X.; Pentoney, S. L.; Zare, R. N. *Science* **1988**, *242*, 224–228.
(7) Mazzeo, J. R.; Martineau, J. A.; Krull, I. S. *Anal. Biochem.* **1993**, *208*, 323–329.
(8) Cobb, K. A.; Novotny, M. V. *Anal. Chem.* **1992**, *64*, 879–886.
(9) Gao, J.; Gomez, F. A.; Haerter, R.; Whitesides, G. M. *Proc. Natl. Acad. Sci. U.S.A.* **1994**, *91*, 12027–12030.
(10) Chu, Y.-H.; Avila, L. Z.; Biebuyck, H. A.; Whitesides, G. M. *J. Med. Chem.* **1992**, *35*, 2915–2917.
(11) Avila, L. Z.; Chu, Y.-H.; Blossey, E. C.; Whitesides, G. M. *J. Med. Chem.* **1993**, *36*, 126–133.
(12) Gomez, F. A.; Avila, L. Z.; Chu, Y.-H.; Whitesides, G. M. *Anal. Chem.* **1994**, *66*, 1785–1791.

0003-2700/95/0367-3093$9.00/0

$$\mu = \frac{LL_{to}}{V}\left(\frac{1}{t_{eo}} - \frac{1}{t}\right) \quad (1)$$

$$\mu \cong C_{eff}\frac{Z_{eff}}{M^{\alpha}} \cong C_P\frac{Z_P}{M^{\alpha}} \quad (2)$$

relates the electrophoretic mobility of a protein in an electrostatic field to its effective charge Z_{eff} or unperturbed charge Z_P and its mass M; C_{eff} and C_P are proportionality constants for Z_{eff} and Z_P, respectively. The mass of the protein is related to the hydrodynamic drag as it moves through the buffer by the term M^{α} (typically $M^{2/3}$ for globular proteins[13,14]). The *effective* charge is less than the *unperturbed* charge (Z_P) of a protein as modified (screened) by weak interactions with ions in solution.[15-18] The value of Z_P of a protein is determined by its charged components, including charged amino acid side chains, N-terminal amino and C-terminal carboxyl groups, bound metal ions or charged cofactors, ligands and prosthetic groups, and charged groups introduced by covalent modification (e.g., the sialic acid residues of glycosides). The charge of a protein can be *caiculated* (Z_{calc}) from values of pK_a of its ionizable residues; the value of Z_{calc} is equal to Z_P, provided that all ionization constants are known accurately.

We chose insulin for this study because of its structural simplicity and medicinal significance.[19-22] Insulin is a peptide hormone (MW = 5700) composed of two chains; these chains are linked by two disulfide bonds, and there is a third disulfide bond within the A chain. Insulin has only three primary amino groups (Figure 1): an α-amino group from the N-terminal glycine residue of the A chain (G^{α}), an α-amino group from the N-terminal phenylalanine residue of the B chain (F^{α}), and one ε-amino group from the lysine residue at position 29 of the B chain (K^{ε}). We used both bovine pancreatic and human recombinant insulins for the studies described here. Bovine and human insulins differ only in three residues; residue A8, Ala or Thr, respectively; residue A10, Val or Ile; residue B30, Ala or Thr (Figure 1).

Reactivity of Amino Groups. The α-amino groups of a protein are less basic than the ε-amino groups of Lys because they are closer to an amide group. Acylation of an ammonium group (RNH_3^+) occurs only by reaction of its deprotonated neutral form (RNH_2) with the acylating agent. Although neutral ε-amino groups are more basic and more reactive toward acylation than neutral N-terminal α-amino groups, the former have a smaller fraction in unionized form at physiological values of pH; eq 3

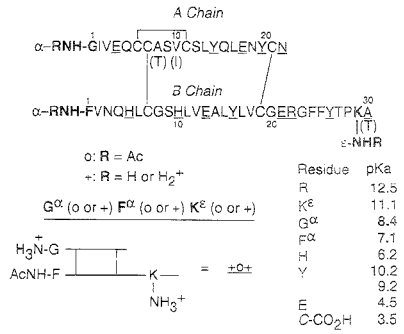

Figure 1. Primary sequences of bovine and human insulins. The three residues that differ in human insulin are listed in parentheses below the sequence of bovine insulin. The three disulfide bonds are indicated by lines. The two α-amino groups (G^{α} and F^{α}) and the ε-amino group (K^{ε}) are indicated in boldface type. Other charged residues (e.g., His (H), Glu (E), Arg (R), Tyr (Y), and C-terminal Asn (N) and Ala (A)) are underlined; pK_a values for these residues were either determined in this work (bold) or assigned reasonable values (bottom right). The symbols o and + are used to represent acetylated and unmodified amino groups, respectively. Insulin and its seve derivatives are characterized by three such symbols, each represent ing acetylation at one of the three residues: Gly, Phe, and Lys.

$$\theta = \frac{[RNH_2]}{[RNH_2] + [RNH_3^+]} = \frac{1}{10^{pK_a - pH} + 1} \quad (3)$$

$$\nu = \theta \log k = \frac{\varrho pK_a}{10^{pK_a - pH} + 1} \quad (4)$$

expresses this fraction, θ, as a function of the values of pK_a of the ammonium group and pH of solution. Manipulating θ makes it possible to control the relative rates of acylation (ν) of differe t amino groups (eq 4; ϱ is a parameter that correlates basicity with nucleophilicity and is assumed to be 0.8 in the simulation[24]). At a high pH, for example, both α- and ε-amino groups are predominantly in the neutral forms ($\theta \sim 1$), and the more nucleophilic ε-amino groups can be acylated more rapidly (Figure 2). At pH values between the pK_a values of the two ammonium groups, the fraction of α-amino groups in the neutral form is larger than that of ε-amino groups ($\theta_{\alpha} > \theta_{\varepsilon}$) and the α-amino groups can be acylated selectively. In this study, we used CE to follow the acylation of the three amino groups of insulin with acetic anhydride at different values of pH.

EXPERIMENTAL SECTION

CE Equipment. Isco Model 3140 and Beckman P/ACE system 5500 capillary electrophoresis systems were used in these studies. The capillary tubing (Polymicro Technologies, Inc., Phoenix, AZ) was of uncoated fused silica with an internal diameter of 50 μm. The conditions used for all CE experiments were as follows: voltage, 30 kV; current, 8–90 μA (depending on the ion composition and pH of the buffer); detection, 200 nm; temperature, 25 ± 2 °C. Samples (8 nL) were introduced into the capillary by vacuum injection. The capillary was flushed with 0.1 N sodium hydroxide for 5 min, water for 5 min, and buffer for 5 min before each experiment.

(13) Basak, S. K.; Ladisch, M. R. *Anal. Biochem.* **1995**, *226*, 51–58.
(14) Rickard, E. C.; Strohl, M. M.; Nielsen, R. G. *Anal. Biochem.* **1991**, *197*, 197–207.
(15) Atkins, P. W. In *Physical Chemistry*; Atkins, P. W., Ed.; W. H. Freeman & Co.: New York, 1986; pp 237–243.
(16) Grossman, P. D. In *Capillary Electrophoresis: Theory and Practice*; Grossman, P. D., Colburn, J. C., Eds.; Academic Press: San Diego, CA, 1992; pp 114–118.
(17) Abramson, H. A.; Moyer, L. S.; Gorin, M. H. In *Electrophoresis of Proteins and the Chemistry of Cell Surfaces*; Abramson, H. A., Moyer, L. S., Gorin, M. H., Eds.; Reinhold Publishing Corp.: New York, 1942; pp 105–172.
(18) For discussion of the relationship between charge and mobility, see: Compton, B. J.; O'Grady, E. A. *Anal. Chem.* **1991**, *63*, 2597–2602.
(19) Muller-Wieland, D.; Streicher, R.; Siemeister, G.; Krone, W. *Exp. Clin. Endocrinol.* **1993**, *101*, 17–29.
(20) Clauser, E.; Leconte, I.; Auzan, C. *Hormone Res.* **1992**, *38*, 5–12.
(21) Brange, J.; Owens, D. R.; Kang, S.; Volund, A. *Diabetes Care* **1990**, *13*, 923–954.
(22) Brange, J.; Langkjoer, L. *Pharm. Biotechnol.* **1993**, *5*, 315–350.
(23) Blundell, T.; Dodson, G.; Hodgkin, D.; Mercola, D. *Adv. Protein Chem.* **1972**, *26*, 279–402.
(24) Jencks, W. P.; Carriuolo, J. *J. Am. Chem. Soc.* **1960**, *82*, 1778–1786.

Correction

Anal. Chem. **1996**, *68*, 2287

Using Capillary Electrophoresis To Follow the Acetylation of the Amino Groups of Insulin and To Estimate Their Basicities

Jinming Gao, Milan Mrksich, Frank A. Gomez, and George M. Whitesides*

(Anal. Chem. 1995, *67,* 3093–3100).

The conditions for the acetylation of insulin at pH 6–7 in this paper used insulin as a *suspension* rather than as a *solution*. Insulin can be acetylated either as a suspension or as a solution. The distribution of acetylated products differs, and the intensities of the peaks in the electropherograms also differ. The course of the analysis that follows is not altered.

Page 3095, left column, lines 7–9 in the Experimental Section should read as follows: Stock suspensions of insulin (1.5 mg/mL, 250 μM) were prepared by mixing the lyophilized protein in distilled water. Stock solutions of insulin were prepared by adding 1 N NaOH to the above suspensions (pH 12).

On p 3095, left column, line 28, and on p 3095, left column, line 40, the word suspension should be used instead of solution.

AC9614001

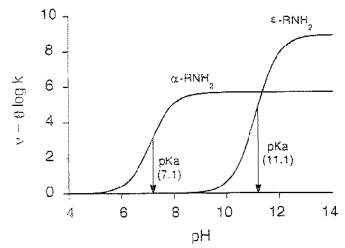

Figure 2. Rates of acylation of α- and ε-amino groups of insulin as a function of the value of pH of the reaction medium (simulated using eq 4). An α-ammonium group ($pK_a' = 7.1$, $\varrho = 0.8$) can be acylated selectively at pH 8, and an ε-ammonium group ($pK_a' = 11.1$, $\varrho = 0.8$) can be acylated selectively at pH 12.

Reagents. All chemicals were analytical grade and were used as received. Acetic anhydride and dioxane were purchased from Mallinckrodt. 1,2-Cyclohexanedinitrilotetraacetic acid (CDTA) and zinc sulfate heptahydrate were purchased from Fluka. Bovine pancreatic and human recombinant insulins were purchased from Sigma. Mesityl oxide was purchased from Eastman Organic Chemical (Rochester, NY). Stock solutions of insulin (1.5 mg/mL, 250 μM) were prepared by dissolving the lyophilized protein in distilled water.

Conditions for Studies of Zn(II)-Dependent Aggregation. Solutions of insulin (25 μM) were prepared in buffers containing tris (25 mM), Gly (192 mM), and either CDTA (20, 200, and 2000 μM) or $ZnSO_4$ (20, 50, 100, 200, 500, 1000, and 2000 μM) (pH 8.4). Mesityl oxide (MO; 18 mM) was added as a neutral marker, and soybean trypsin inhibitor (50 μM) was added as a protein marker. Each sample was analyzed using identical electrophoresis buffers.

Conditions for Estimation of Dimerization Constants. Electrophoresis buffers were prepared containing tris (25 mM), Gly (192 mM), and 0, 5, 10, or 20% dioxane (pH 8.4). Solutions of bovine pancreatic insulin (2, 5, 10, 20, 40, 80, 160, 300, and 400 μM) were prepared in these buffers with MO (18 mM) added as a neutral marker and soybean trypsin inhibitor (50 μM) added as a protein marker.

Conditions for Acetylation Reactions. Insulin was acetylated under three different sets of experimental conditions. In the first, 5, 10, and 20 equiv of acetic anhydride (10 mM in dioxane) were added separately to aliquots of a stock solution of insulin (0.5 mL, pH 6–7). After 30 min at room temperature, 10 μL of each sample was diluted with 100 μL of the electrophoresis buffer. MO was added (18 mM), and the samples were analyzed using CE.

In the second experimental protocol, the pH's of aliquots of a solution of insulin (0.5 mL) were adjusted to pH 12 with 1 N sodium hydroxide. Acetic anhydride (2, 5, or 10 equiv, 10 mM stock solution in dioxane) was added. After 5 min at room temperature, 10 μL of a sample was diluted with 100 μL of the electrophoresis buffer, MO was added (18 mM), and the samples were analyzed by CE.

In the third protocol, the pH of the solution of the products obtained using the first protocol (with 20 equiv of acetic anhydride) was adjusted to pH 12 using 1 N sodium hydroxide. Acetic anhydride (2, 4, 8, or 15 equiv) was added, and after five min, the samples were diluted with electrophoresis buffer. MO was added (18 mM), and the samples were analyzed by CE.

Conditions Used for the pH Titration of the Charge Ladder of Insulin. A solution of insulin and its seven acylated derivatives was prepared at a total concentration of 25 μM in electrophoresis buffer (pH 8.4) containing tris (25 mM), Gly (192 mM), and MO (18 mM) added as a neutral marker. Several electrophoresis buffers were prepared having different pH values (9.4, 9.0, 8.7, 8.0, 7.7, 7.4, 7.0, 6.7, 6.3, 6.0, and 5.6) by adding 2 N acetic acid or 1 N sodium hydroxide, as necessary, to the original tris–Gly buffer. The sample was analyzed in each electrophoresis buffer using CE.

RESULTS AND DISCUSSION

Nomenclature. Treatment of insulin with acetic anhydride affords a family of seven derivatives that differ in the site of acetylation of the three primary amino groups. The imidazole rings of the two histidine residues can also be acetylated under these conditions. The resulting *N*-acylimidazoles, however, are not stable under basic conditions and are not observed in these experiments.[25] We use the symbols + and o to represent unmodified and acetylated amino groups, respectively (Figure 1). The modified insulins are characterized by three such symbols, each representing acetylation at one of the three residues; G^a, F^a, and K^a. Using this nomenclature, for example, the native insulin is labeled +++, the fully modified insulin is labeled ooo, and the derivative with only F^a acetylated is labeled +o+ (Figure 1). We employed an electrophoresis buffer containing tris (25 mM) and Gly (192 mM) for all experiments described here: only the pH of the buffer differed.

Aggregation of the Insulin Monomer. Insulin dimerizes in aqueous solution, and the dimers can associate further to form tetrameric and hexameric aggregates.[22,23] The association constants for these processes in water depend on the pH, ionic composition and structure, and temperature of the solution: reported values for the dimerization constant ($K_D = [I_D]/[I_M]^2$; I_D and I_M are insulin dimer and monomer, respectively) are in the range of 10^5–10^6 M^{-1}; values of the association constants for formation of the tetramer from two dimers in the absence of Zn(II) are in the range of 20–100 M^{-1}; values for the association constant for formation of the hexamer from the dimer and the tetramer in the absence of Zn(II) are in the range of 200–1000 M^{-1}.[26–30] Because electrophoretic mobility scales linearly with charge and nonlinearly with mass, the mobilities of the aggregates *increase* with molecular weight (eq 2); we could therefore use CE to establish the relevant state of aggregation of insulin under the conditions of our experiments.

Aggregation Dependent on Zn(II). Formation of the tetramer and hexamer of insulin (but not dimer) is enhanced in the presence of Zn(II).[22,23] We measured the electrophoretic mobility of insulin with Zn(II) present in the sample and electrophoresis buffer ([Zn(II)] ranged between 20 μM and 2 mM). The electrophoretic mobility of insulin was constant over this range of concentrations of Zn(II); these data suggested that the state of aggregation of insulin did not change with increasing concentrations of Zn(II). Since bovine insulin obtained from Sigma contains

(25) Fife, T. H. *Acc. Chem. Res.* **1993**, *26*, 325–331.
(26) Roy, M.; Lee, R. W. K.; Brange, J.; Dunn, M. F. *J. Biol. Chem.* **1990**, *265*, 5448–5452.
(27) Sirazza, S.; Hunter, H.; Walker, E.; Darnall, D. W. *Arch. Biochem. Biophys.* **1985**, *238*, 30–42.
(28) Pocker, Y.; Biswas, S. B. *Biochemistry* **1981**, *20*, 4354–4361.
(29) Jeffrey, P. D. *Biochemistry* **1974**, *13*, 4441–4447.
(30) Carpenter, F. H.; Goldman, J. *Biochemistry* **1974**, *13*, 4566–4574.

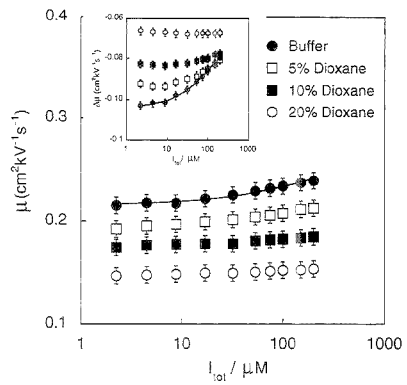

Figure 3. Electrophoretic mobility of bovine insulin as a function of the concentration of insulin, in several different buffers: (●) 25 mM tris−192 mM Gly, pH 8.4 (A); (□) 5% dioxane in buffer A; (■) 10% dioxane in buffer A; (○) 20% dioxane in buffer A. Soybean trypsin inhibitor was used as a protein marker to correct for changes in electroosmotic flow; the inset shows plots of corrected mobilities after subtracting the mobility of STI. A least-squares fit of the uncorrected [μ, I_{tot}] data to eq 6 gave a value of $K_D = 6(\pm 1) \times 10^3$ M^{-1} in buffer A.

0.5% Zn(II) by weight (0.5 equiv of Zn(II) per insulin monomer), there was the possibility that the insulin was present exclusively as the hexamer. We therefore examined the mobility of insulin using an electrophoresis buffer containing CDTA (20 μM to 2 mM); CDTA coordinates Zn(II) with an association constant of 10^{18} M^{-1}. The electrophoretic mobility of insulin did not change with the concentration of CDTA. Since the aggregation of insulin was not dependent on the concentration of Zn(II), and it is unlikely that insulin at a concentration of 25 μM was present exclusively as a tetramer or hexamer, we concluded that insulin was present as a monomer or dimer.

Dimerization of Insulin. We measured the electrophoretic mobility of insulin as a function of its concentration over the range from 2 μM to 400 μM. Soybean trypsin inhibitor (STI) was added to each sample as a marker to make it possible to correct for changes in electroosmotic flow. The electrophoretic mobility of insulin increased with the concentration of insulin in the sample (Figure 3), while the mobility of STI remained constant. If we assume that monomeric and dimeric forms of insulin exist at equilibrium and in rapid exchange in the migrating plug, the increase in mobility of insulin is consistent with a larger fraction of dimeric insulin in the migrating plug at higher concentrations of insulin. Fredericq reported that dioxane, when added to an aqueous solution of insulin, suppresses dimerization of the protein.[31] We repeated the experiment that measured the concentration dependence using electrophoresis buffers containing 5, 10, and 20% dioxane. With the buffer containing 20% dioxane, the electrophoretic mobility of insulin remained constant over the entire range of concentrations examined: the dimerization of insulin was completely inhibited in this buffer. The inhibition of dimer formation is consistent with the observation that solvents having low dielectric constants destabilize the hydrophobic interactions between the two monomers.[21,31] Buffers containing 5 and 10% dioxane were less effective at preventing the dimerization of insulin. These data, together with the observation that the electrophoretic mobility of the STI remained constant throughout all experiments, suggested that the changes in electrophoretic mobility of insulin with concentration were due to dimerization.

Measurement of the Dimerization Constant. We assume that the measured electrophoretic mobility of insulin (μ) is a weighted average of the electrophoretic mobilities of the monomer (μ_M) and dimer (μ_D) ($\mu = \mu_M(1 - \theta_D) + \mu_D\theta_D$), where θ_D is the mole fraction of dimer (eq 5). Equation 6 relates the measured

$$\theta_D = \frac{2[I_D]}{[I_{tot}]} = 1 + \frac{1 - \sqrt{8K_D[I_{tot}] + 1}}{4K_D[I_{tot}]} \quad (5)$$

$$\mu = (\mu_D - \mu_M)\left(1 + \frac{1 - \sqrt{8K_D[I_{tot}] + 1}}{4K_D[I_{tot}]}\right) + \mu_M \quad (6)$$

mobility, μ, to μ_M, to μ_D, to the dimerization constant (K_D), and to the concentration of insulin in the sample (I_{tot}). A least-squares fit of the [μ, I_{tot}] data to eq 6 using μ_D, μ_M, and K_D as adjustable parameters gave values of K_D of $6(\pm 1) \times 10^3$ and $4.7(\pm 0.5) \times 10^2$ M^{-1} at pH values of 8.4 and 10.0, respectively (25 mM tris, 192 mM Gly) (Figure 3). These dimerization constants are lower limits since the concentration of insulin in the capillary is reduced relative to that in the sample vial due to broadening of the analyte zone. The best-fit values of μ_D were a factor of 1.22 (at pH 8.4) and 1.14 (at pH 10) greater than μ_M, in good agreement with the expected value of 1.25 if the coefficient C_{eff} remains constant in eq 2 (where $\alpha = {}^2/_3$). We were unable to measure the dimerization constant at pH 6.0 because of the low solubility of insulin at this value of pH (the pI of insulin is ~5.5; see below). The dimerization constants for insulin in dioxane−water buffers were too low to be measured.

The CE experiments described in subsequent sections used solutions of insulin and its derivatives at a total concentration of 25 μM and analyzed in an aqueous electrophoresis buffer containing tris (25 mM) and Gly (192 mM). We believe insulin was present predominantly as a monomer at these conditions.

Selective Acetylation of α- and ε-Amino Groups of Insulin. CE of pure insulin, with MO as a neutral marker to establish the rate of electroosmotic flow, in electrophoresis buffer (pH 7.4) showed a single peak (Figure 4). This sample was divided and acetylated in buffers having two different pH values. In the first, the pH of aqueous solutions of insulin was adjusted to values between 6 and 7 with 1 N sodium hydroxide and different amounts of acetic anhydride (10 mM in dioxane) were added to aliquots of the insulin-containing solutions (no other salts were added). After 30 min, the samples were diluted with electrophoresis buffer and analyzed by CE. In the second set of experiments, the pH of insulin-containing solutions was adjusted to 12 with 1 N sodium hydroxide and different amounts of acetic anhydride were added to the samples. After 5 min, the solutions were diluted with electrophoresis buffer and analyzed by CE.

Identity of the Products of the Acetylation Reaction at Low pH. When acetylations were carried out at the lower pH, four peaks were observed in the electropherogram (buffer pH 7.4); these peaks indicated that at least three different derivatives of insulin had been formed (Figure 4). Electrophoresis of the same

(31) Fredericq, E. *J. Am. Chem. Soc.* **1957**, *79*, 599−601.

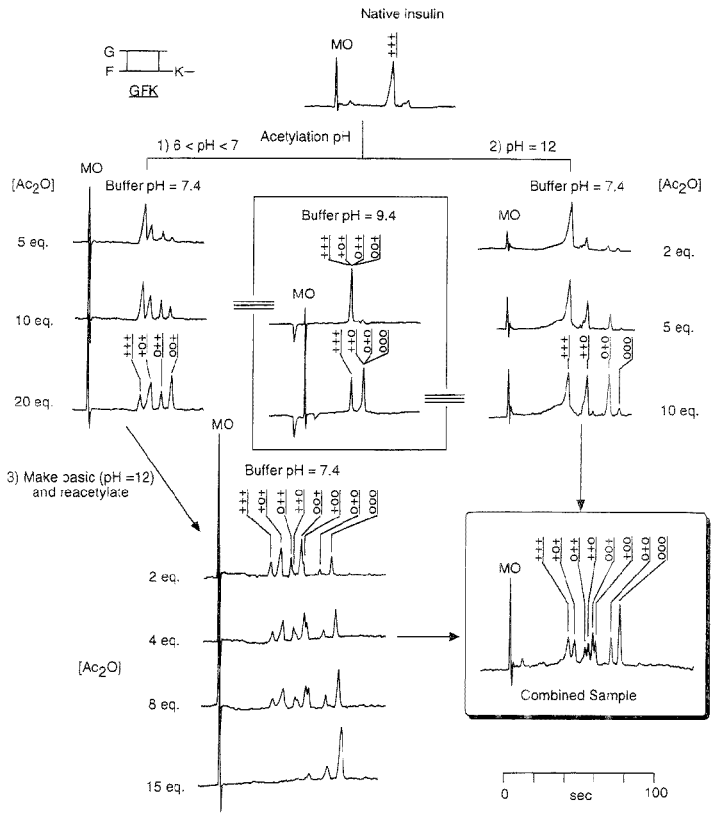

Figure 4. Selective acetylation of the three amino groups of bovine insulin. Electropherograms are shown for families of acetylated insulins that were generated using acetic anhydride (at three or four different concentrations) under three different sets of conditions: (1) selective acetylation of G^{α} and F^{α} at a pH between 6 and 7 (top left); (2) selective acetylation of K^{ε} and G^{α} at a pH of 12 (top right); and (3) basification of the solution resulting from reaction 1 to a pH of 12 and subsequent acetylation (bottom left). Analysis of the reaction products from conditions 1 and 2 using an electrophoresis buffer adjusted to a pH 9.4 identifies modified peptides that have K^{ε} acetylated (top middle). Combining the reaction products from conditions 2 and 3 affords a mixture containing insulin and its seven derivatives (bottom right). Samples were analyzed in 25 mM tris−192 mM Gly buffer (pH 7.4 or 9.4). MO was used as a neutral internal standard to establish the rate of electroosmotic flow: its migration time varies with pH and buffer but is typically in the range of 120−140 s. The time scale (lower right) applies to all electropherograms.

sample in a buffer at pH 9.4 showed a single peak. At this pH, the α-amino groups (G^{α} and F^{α}) were not protonated, and differences in charge, and hence, electrophoretic mobility, arose only from acetylation of K^{ε}. These four species (at pH 7.4) were thus native insulin (+++), two derivatives that were acetylated at either G^{α} or F^{α} (o++ or +o+), and one derivative that was acetylated at both α-amino groups (oo+). A co-injection experiment verified that the first peak was the native insulin; since the four species should migrate with mobilities proportional to their effective charge, the last peak was assigned as the oo+ derivative. Assignments of the peaks for the two singly modified derivatives were made on the basis of the fact that the value of the pK_a of G^{α} is higher than that of F^{α}.[32]

Identity of the Products of the Acetylation Reaction at High pH. Electrophoresis of the reaction products obtained from acetylation of insulin at a pH of 12 showed three major peaks and one minor peak (Figure 4). Electrophoresis of these four derivatives in a buffer at a pH of 9.4 showed two peaks: the mixture therefore comprised at least one derivative containing an unmodified K^{ε} group and at least one derivative containing an acetylated K^{ε} group. The four species were assigned as +++, ++o, o+o, and ooo. The identities of native insulin (+++) and the peracetylated derivative (ooo) were proved by co-injection experiments (for assignment of ooo, see the next paragraph). The assignments of the −−+o and o−−o derivatives were supported by co-injection experiments with a sample containing all of the acetylated derivatives of insulin (described in subsequent sections).

Preparation of a Sample Containing Insulin and its Seven Acetylated Derivatives. Solutions of products from the acetylation reaction at a pH of 6−7 were adjusted to pH 12 using 1 N sodium hydroxide and treated again with different amounts of acetic anhydride. After 5 min, an equal volume of a solution

(32) Hofford, M. A.; Oda, G.; Kaplan, H. *Biochem. J.* **1986**, *237*, 663−668.

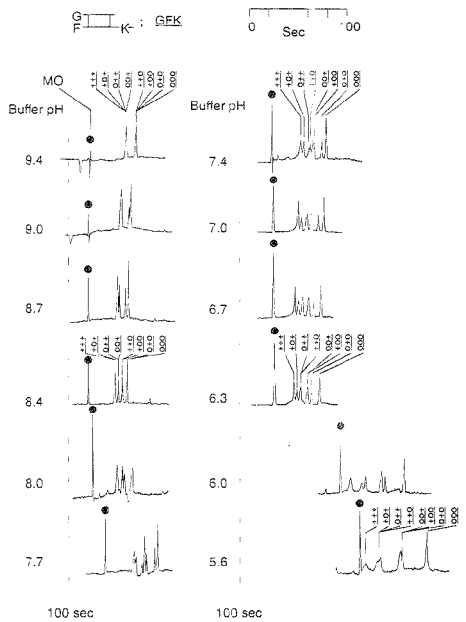

Figure 5. Electropherograms of a mixture of bovine insulin and its seven acetylated derivatives at several pH values of the electrophoresis buffer (25 mM tris and 192 mM Gly). The time scale applies to all experiments, and the vertical dashed lines provide a common reference point for direct comparison of absolute migration times. The peaks for the neutral marker (MO) are indicated by filled circles.

resulting from the acetylation reaction at the high pH value was added and the mixture was analyzed by CE. All eight derivatives were resolved using an electrophoresis buffer at a pH of 7.4 (Figure 4). The size of the peak with the slowest migration time increased with the amount of acetic anhydride in the reaction and was assigned as the peracetylated derivative (ooo). The identities of the other peaks were assigned by comparison with the mixtures prepared by the procedures described in previous sections: these assignments were further supported by pH titration experiments described in the next paragraph.

Electrophoretic Mobilities of Acetylated Derivatives of Insulin in Buffers with Different Values of pH. The electrophoretic mobilities of insulin and its acetylated derivatives depend on the pH of the buffer (Figure 5). Analysis of a mixture of the eight species in a buffer at pH 9.4 showed two peaks: each peak corresponds to the families of derivatives containing either an acetylated or unmodified (protonated) K^{ε} group. When the pH of the buffer was lowered to 8.7, two new peaks emerged from the two parent peaks: these peaks correspond to derivatives that contain an unmodified G^{α} and were resolved due to partial protonation of G^{α}. At pH's of 7.7 and 7.4, four additional peaks appeared in the electropherogram due to protonation of F^{α}; all eight derivatives of insulin were resolved by CE at this pH. Four groups of peaks were observed using a buffer at a pH of 5.6, where each group contained derivatives with an equal number of modified amino groups. At this low pH, acetylation of each amino group results in a change in the charge of the protein by ~ -1. A plot relating the electrophoretic mobility of each derivative to the

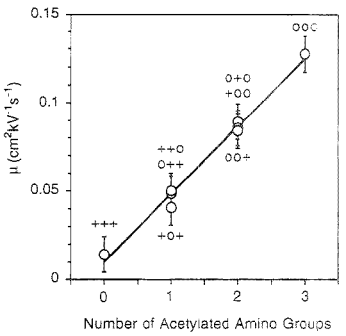

Figure 6. Relationship between electrophoretic mobility and the number of acetylated amino groups for insulin and its seven derivatives at a pH of 5.6. The electrophoretic mobilities of insulin and its acetylated derivatives are related linearly to the number of NH_3^+ groups.

number of modified amino groups gives a straight line: this correlation demonstrates that the differences in electrophoretic mobility of insulin and its acetylated derivatives depend only on differences in charge (Figure 6).

Determination of Values of pK_a of G^{α} and F^{α} of Insulin. We used CE to estimate the ionization constants of the α-ammonium groups of insulin.[33] The electrophoretic mobility (μ) of a protonated base (BH^+) containing no other acidic protons is related to the electrophoretic mobilities and mole fractions of the charged, protonated (μ_{BH^+}, θ_{BH^+}) and the neutral, unprotonated (μ_B, $1 - \theta_{BH^+}$) forms by eq 7. Rearrangement of eqs 3 and 7 gives

$$\mu = (1 - \theta_{BH^+})\mu_B + \theta_{BH^+}\mu_{BH^+} \quad (7)$$

$$\Delta\mu = \mu - \mu_B = (\mu_{BH^+} - \mu_B)\frac{1}{1 + 10^{pH - pK_a}} \quad (8)$$

eq 8, which relates the change in electrophoretic mobility of a species resulting from protonation of its basic residue to μ_{BH^+}, μ_B, the pH of the electrophoresis buffer, and the pK_a of the ionizable residue. The analysis based on eq 8, however, cannot be applied directly to the determination of pK_a of a unique ammonium group of insulin because ionization of several other residues also contributes to changes in the charge. We analyzed the electrophoretic mobilities of the +oo and o+o derivatives to determine the pK_a values of G^{α} and F^{α}, respectively; the two other amino groups in each species are acetylated and do not contribute to changes in total charge as the pH is changed. The effects of other ionizable residues (e.g., His) were eliminated by comparing the electrophoretic mobilities of the +oo and o+o derivatives *relative* to that of the peracetylated derivative ($\Delta\mu = \mu - \mu_{(ooo)}$): in this way, only the extent of protonation of either G^{α} or F^{α} contributed to changes in effective charge and, hence, to $\Delta\mu$. Plots of $\Delta\mu$ vs pH for insulin and its seven derivatives are shown in Figure 7. Equation 8 was fitted to the [$\Delta\mu$, pH] data for the +oo and o+o derivatives using values of ($\mu_{BH^+} - \mu_B$) and pK_a's of G^{α} and F^{α}, respectively, as adjustable parameters: the least-squares best-fit values of pK_a were 8.4(±0.1) for G^{α} and 7.1(±0.1) for F^{α}.

(33) For estimation of values of pK_a of simple organic acids, see: Smith, S. C.; Khaledi, M. G. *Anal. Chem.* **1993**, *65*, 193–198.

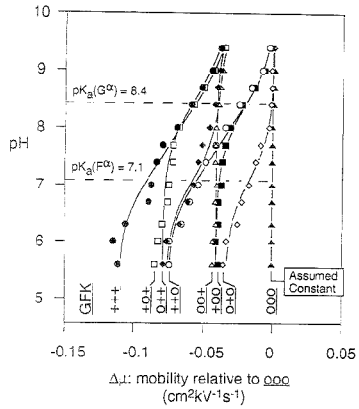

Figure 7. Dependence of $\Delta\mu$ on the pH of the electrophoresis buffer for insulin and its seven derivatives. Values of μ for each derivative were computed from the electropherograms in Figure 5 using eq 1. Values of $\Delta\mu$ were obtained by subtracting the value of μ(ooc) from the value of μ measured for each derivative: the mobility of ooo is *assumed* constant. The data are represented as follows: +++ (●), +o+ (□), o-+ (◆), ++o (○), oo+ (△), +oo (■), o+o (◇), and ooo (▲). Overlapping points are offset slightly for clarity. The curves superimposed on the data for the +oo and o+o derivatives were obtained by performing nonlinear least-squares fits using eq 8; these fits yielded pK_a values of 8.4(±0.1) for G^α and 7.1(±0.1) for F^α. The other curves were simulated on the basis of these values of pK_a and a value of 11.1 for K′ (see text).

Using these pK_a values, and a value of 11.1 for K′,[34] the dependence of $\Delta\mu$ on pH was simulated for insulin and its five other derivatives using eq 8. The contribution to $\Delta\mu$ from G^α, F^α, and K′ at each pH was determined by calculating the fractional protonation of each amino group using eq 3. The partial charges were summed and fitted to the experimental data using eq 8 and $(\mu_{BH^+} - \mu_B)$ as an adjustable parameter. These simulated curves agree well with the experimental data (Figure 7).

Influence of pH on the Total Charge of Insulin. We described previously a method to measure the total charge of a protein (Z_{exp}) using CE by analyzing a protein charge ladder—a series of derivatives of a protein that differ by known increments of charge but differ only minimally in hydrodynamic drag—generated by acylation of the ϵ-amino groups of Lys residues of the protein.[4,35] The method is based on the relationship between the electrophoretic mobilities of peaks in a charge ladder (μ_n) and their charges relative to the unmodified protein ($\Delta Z_P = Z_P(n) - Z_P(0)$, where n indicates the number of modified amino groups, eq 9). A plot of the electrophoretic mobilities of peaks

$$\mu_n - (C_P/M^\alpha)Z_P(0) = (C_P/M^\alpha)\Delta Z_P \qquad (9)$$

(μ_n) in the charge ladder vs the values of ΔZ_P gives a linear correlation where the intercept at the x-axis (where $\mu_n = 0$) is equal to the total charge of the native protein (eq 9). Using this analysis, we determined values of Z_{exp} of insulin at several values of pH of the buffer (Figure 8). The measured values of C_P/M^α (e.g., at pH 7.0, from the slope in Figure 8) were constant at different pH's in this experiment: $C_P/M^\alpha = 0.031 \pm 0.001$ cm^2 s^{-1} kV^{-1} charge^{-1}. Assuming $\alpha = {}^2/_3$, and using MW = 5700 for insulin, C_P is equal to 9.9 cm^2 s^{-1} kV^{-1} charge^{-1} $D^{2/3}$. We analyzed charge ladders generated from both bovine and human insulins using either an aqueous electrophoresis buffer or an aqueous buffer containing 10% dioxane.

(34) Bundi, A.; Wüthrich, K. *Biopolymers* **1979**, *18*, 285–297.
(35) For an early example of a charge ladder, see: Creighton, T. E. *Nature* **1980**, *284*, 487–489.

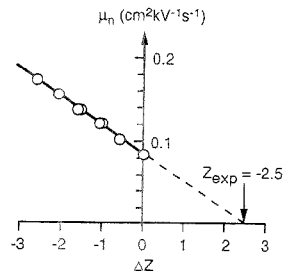

Figure 8. Determination of the total charge Z_{exp} of insulin at pH 7.0 using eq 9. The calculation of increments of charge (ΔZ_P) is described in the text. Extrapolation of the best-fit line to $\mu_n = 0$ gives a value of −2.5 for the charge of insulin at a pH of 7.0 (regression coefficient $r = 0.999$).

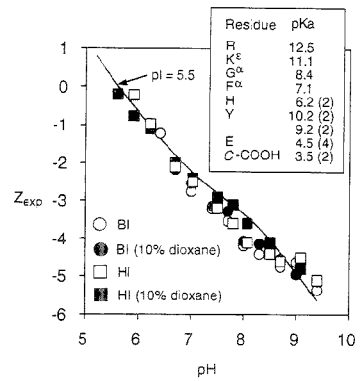

Figure 9. Influence of pH on the total charge of insulin. The measured charge of insulin (Z_{exp}) at each pH was determined by analyzing the charge ladder from bovine or human insulin using different electrophoresis buffers: bovine (○) and human (□) insulin in tris–Gly buffer, and bovine (●) and human (■) insulin in tris–Gly buffer containing 10% dioxane. The curve represents calculated values of charge of insulin (Z_{calc}) as a function of pH. The inset shows the values of pK_a of the ionizable residues of insulin used to calculate Z_{calc}.

Figure 9 shows plots of the measured total charge of insulin vs the pH of the buffer. The curve that is superimposed on the data was generated by *calculating* the charge of insulin as a function of pH. The charge carried by each ionizable residue was calculated using eq 3, the pH of the buffer, and its pK_a shown in Figure 9: these charges were added to yield the total charge of insulin (Z_{calc}). Extrapolation of the data from the four experiments to $Z_{exp} = 0$ provides an estimate of 5.5 ± 0.2 for the p*I* of insulin; this value is in good agreement with the literature value of 5.3.[36]

Although the experimental data agree well with the simulated curve, there remain slight differences in the range of pH from 7

(36) Tanford, C.; Epstein, J. *J. Am. Chem. Soc.* **1954**, *76*, 2163–2169.

to 9. In principle, the pK_a values for the ionizable residues used in the simulation may have been inaccurate or altered upon acetylation of amino groups. Nonetheless, this method to measure the electrostatic properties of insulin provides data that are well rationalized by its known structural characteristics.

CONCLUSIONS

Insulin is an excellent model system with which to study the influence of chemical modification of charged groups on the electrophoretic mobility of proteins. At pH 7.4, derivatives of insulin with 0.1 unit charge difference (o+− and ++o, oo+ and +oo) were well separated. For larger proteins, the resolution of partial charges will be much more difficult or impossible. Since the Lys ammonium groups of large proteins have similar, high values of pK_a, their selective modification[9] will only give derivatives that differ in full units of charge. Use of polycharged modifying agents to increase the increments in mobility in a protein charge ladder makes it easier to measure the charges of high molecular weight proteins using capillary electrophoresis, but the resolution in these systems will be less than that with insulin.

These studies demonstrate that CE is useful for the characterization of electrostatic properties of proteins in their native conformations. By analyzing a family of derivatives of a protein generated by acylation of its amino groups, partial charges of individual residues (and their pK_a values) and the total charge of the protein can be determined. The unique sensitivity of CE to the charge of a protein makes it appropriate for use in studies that involve protein electrostatics: for example, the influence of the charge of a protein on the binding of charged ligands to it.

ACKNOWLEDGMENT

This work was supported by the NIH (Grants GM 51559 and GM 30367). M.M. is grateful to the American Cancer Society for a postdoctoral fellowship and F.A.G. is grateful to the Damon Runyon–Walter Winchell Cancer Research Fund for a postdoctoral fellowship. We also thank Mathai Mammen for helpful discussions.

GLOSSARY

Frequently used abbreviations and symbols are listed in the order of appearance

CE	capillary electrophoresis
μ	electrophoretic mobility
t_{eo}	migration time of neutral marker
MO	mesityl oxide, as neutral marker
Z_{eff}	effective charge
Z_P	unperturbed charge
C_{eff} and C_P	proportionality constants for Z_{eff} and Z_P
Z_{calc}	calculated charge
G^{α}	α-amino group from N-terminal Gly of A chain
F^{α}	α-amino group from N-terminal Phe of B chain
K^{ϵ}	ε-amino group from Lys of B chain
θ	molar fraction
v	rate of acylation
K_D	dimerization constant
I_D	dimer of insulin
I_M	monomer of insulin
μ_D	electrophoretic mobility of dimer of insulin
μ_M	electrophoretic mobility of monomer of insulin
+++	native insulin
o++, +o+, ++o	monoacetylated insulin (see text for details)
+oo, o+o, oo+	diacetylated insulin (see text for details)
ooo	peracetylated insulin
Z_{exp}	charge determined by CE

Received for review May 30, 1995. Accepted July 17, 1995.[⊗]

AC9505177

[⊗] Abstract published in *Advance ACS Abstracts*, August 15, 1995.

Anal. Chem. 1995, *67*, 3101–3107

On-Line NMR Detection of Amino Acids and Peptides in Microbore LC

Nian Wu,† Andrew Webb, Timothy L. Peck, and Jonathan V. Sweedler*

Beckman Institute for Advanced Science and Technology, University of Illinois, Urbana, Illinois 61801

The combination of liquid chromatography (LC) and nuclear magnetic resonance (NMR) offers the potential of unparalleled chemical information from analytes separated from complex mixtures. However, the application of LC–NMR has been hindered by poor detection sensitivity. We develop a theoretical model for predicting signal-to-noise ratio (SNR) performance while scaling NMR detection cells for flowing experiments. The model includes the effects of separation parameters, coil geometry, and NMR acquisition parameters on SNR performance. Although the detector cell should be as large as possible to ensure adequate efficiency for a given separation, reducing the detector cell volume does not significantly degrade SNR. For example, our model predicts a 2-fold reduction in SNR for a 400-fold reduction in cell volume. The results of static NMR measurements of amino acids and peptides in a 50-nL-volume cell (~1 μg of each) demonstrate the performance of such a small-volume NMR microcell. Using this 50-nL detector cell with microbore LC, two-dimensional LC–NMR chromatograms are shown for amino acid and peptide separations.

Nuclear magnetic resonance (NMR) detection coupled with liquid chromatography (LC) offers great promise in combining the ability to separate complex mixtures into individual components with one of the most structurally rich detection schemes available. In 1978, Watanabe reported the coupling of LC effluent to NMR using a stopped-flow approach,[1] and within 1 year, an on-line system had been reported.[2] The major advantages of on-line as opposed to off-line NMR detection for LC are improved chromatographic resolution, consistent response, on-line data analysis, and rapid data acquisition. The drawbacks of continuous-flow NMR include poorer sensitivity due to the limited time available to measure each analyte and the flow rate dependence of the NMR line width. Over the past 15 years, numerous groups have reported improved LC–NMR hyphenation methods, improved NMR pulse sequences (e.g., to remove the effects of strong solvent resonances and hence alleviate the need for deuterated solvents), and increased chromatographic resolution.[3–13]

The principal drawback with these approaches has been the relatively poor mass sensitivity of the NMR detection system, especially when the observation time is limited for each analyte peak. Recent trends in LC separations have been toward smaller diameter columns, smaller injections, and faster separations, all of which make LC–NMR even more difficult. Previous flow cells for NMR detection were in the range of 25–200 μL,[1–13] with the smallest detector cells greater than 20 μL. Also problematic, the mass detection limits of previous on-line work appear to be greater than 10 μg. Thus, reductions in detector cell volume and improvements in mass sensitivity are needed for improved smaller volume LC columns.

Recently we reported the use of radio frequency (rf) microcoils for NMR spectroscopy to create 5 nL to 1-μL-volume detection cells.[14,15] The noise in an NMR experiment is predominantly thermal noise and originates primarily within the conducting sample and rf detection coil. When microcoils (i.e., rf coils less than ~1 mm in diameter) are used to examine small amounts of an aqueous or organic sample with high-field NMR spectrometers, the resistance of the coil dominates the resistance of the sample.[16,17] Furthermore, when solenoidal coils are used, the resistance is relatively independent of coil diameter.[17] Hence, as a coil is reduced in size, the mass sensitivity improves because of the increase in the strength of the rf field per unit current. Peck et al. studied this in detail, and found over 20-fold improvements in mass limits of detection (LODs) as the coil diameter is scaled from 1 mm to 50 μm.[18,19] This corresponds to a 400-fold increase in measurement time for the larger coil to obtain the same signal-to-noise ratio (SNR) as the smaller coil. Therefore, microcoils offer substantial advantages in NMR detectability for mass-limited samples such as the effluent from an LC column. Wrapping the microcoil directly around a section of capillary allows easy connection to the LC tubing and provides a high filling factor for enhanced NMR sensitivity.

† Present address: A. L. Pharma, Inc., Johns Hopkins Bayview Research Campus, Baltimore, MD 21224.

(1) Watanabe, N.; Niki, E. *Proc. Jpn. Acad.* **1978**, *54*, 194.
(2) Bayer, E.; Albert, K.; Nieder, M.; Grom, E.; Keller, T. *Adv. Chromatogr.* **1979**, *17*, 525.
(3) Haw, J. F.; Glass, T. E.; Hausler, D. W.; Motell, E.; Dorn, H. C. *J. Chromatogr.* **1979**, *186*, 497.
(4) Haw, J. F.; Glass, T. E.; Dorn, H. C. *Anal. Chem.* **1981**, *53*, 2237.
(5) Bayer, E.; Albert, K.; Nieder, M.; Grom, E.; Wolf, G.; Rindlisbacher, M. *Anal. Chem.* **1982**, *54*, 1747.
(6) Haw, J. F.; Glass, T. E.; Dorn, H. C. *Anal. Chem.* **1983**, *55*, 22.
(7) Buddrus, J.; Herzog, H. *Anal. Chem.* **1983**, *55*, 1611.
(8) Laude, D. A.; Lee, W.-K.; Wilkens, C. L. *Anal. Chem.* **1985**, *57*, 1464.
(9) Laude, D. A., Jr.; Wilkins, C. L. *Anal. Chem.* **1987**, *59*, 546.
(10) Albert, K.; Kunst, M.; Bayer, E. Spraul, M.; Besmel, W. *J. Chromatogr.* **1989**, *463*, 355.
(11) Dorn, H. C. *Anal. Chem.* **1984**, *56*, 747A.
(12) Grenier-Laustalot, M. F.; Grenier, F.; Beunoure, J.; Grall, M.; Panaras, R. *Analusis* **1990**, *18*, 200.
(13) Curran, S. A.; Williams, D. E. *Appl. Spectrosc.* **1987**, *8*, 1450.
(14) Wu, N; Peck, T. L.; Webb, A. G.; Magin,R. L.; Sweedler, J. V. *J. Am. Chem. Soc.* **1994**, *116*, 7929.
(15) Wu, N; Peck, T. L.; Webb, A. G.; Magin,R. L.; Sweedler, J. V. *Anal. Chem.* **1994**, *64*, 3864.
(16) Hoult, D. I.; Lauterbur, P. C. *J. Magn. Reson.* **1979**, *34*, 425.
(17) Cho, Z. H.; Ahn, C. B.; Juh, S. C.; Lee, H. K. *Med. Phys.* **1988**, *15*, 815.
(18) Peck, T. L.; Magin, R. L.; Lauterbur, P. C. *Proc. Soc. Magn. Reson.* **1990**, *1*, 207.
(19) Peck, T. L.; Magin, R. L.; Lauterbur, P. C. *J. Magn. Reson.*, in press.

0003-2700/95/0367-3101$9.00/0

Although we have demonstrated NMR detection for one of the smallest volume separation methods, capillary electrophoresis (CE),[11] these microcoils are even better suited for LC detection due to the larger sample size and longer available observation time for each analyte band. In designing an optimized cell for an LC experiment, the complex dependence of the NMR SNR on concentration, coil geometry, flow rate, NMR parameters such as number of acquisitions, pulse delay, and sample properties such as T_1 and T_2 should be considered. Here we develop a simplified model of the SNR of an LC–NMR experiment by assuming a given LC flow rate and sample volume and optimizing the microcoil size and NMR acquisition parameters. An important question that this model seeks to answer is, are higher sensitivity LC–NMR spectra obtained when the detector cell volume is approximately the same as the volume of the analyte peak and only relatively few NMR acquisitions are possible or with a much smaller volume detector cell so that the nuclei flow rapidly through the detector cell and many signal acquisitions are possible? Our model differs from previous LC–NMR work in that we include the performance of optimized NMR microcoils so that as the coil size is reduced, the mass sensitivity of the detection cell improves.

On the basis of the results of the theoretical treatment, as well as the goal of designing a detector cell useful for a variety of microbore LC separations, we have designed a solenoidal microcell out of a section of 250-μm-i.d., 360-μm-o.d., fused-silica capillary. This gives a filling factor of ~50%. By wrapping the microcoil over a 1-mm length of this capillary, a ~50-nL detector volume is created, thus reducing the detector cell volume *2 orders of magnitude* from previous on-line LC–NMR. The performance of this cell is demonstrated for amino acid and peptide detection for both static and LC separations.

THEORY

The goal of the following approach is to optimize the design of the flow cell for an on-line NMR measurement given a fixed flow rate and sample volume. In other words, for a given LC separation (flow rate and analyte peak volume), what is the optimum detector cell geometry? To simplify the theoretical treatment, we assume a rectangular sample profile, a 50% filling factor (i.e., the ratio of the inner diameter of the capillary to the diameter of the coil is 0.707), a 3:1 aspect ratio of coil length to diameter, and a homogeneous rf magnetic field over the active volume of the coil. The active volume is defined by the length of the coil and the inner diameter of the capillary (i.e., no edge effects).

We first calculate the SNR obtained for a given analyte band based on the residence time for each nucleus within the rf coil, the coil dimensions, and NMR data acquisition parameters. In this treatment, the total length of the analyte band can be subdivided into a number of separate sections, each of length L_{rep} (m), where the length of each section is equal to the distance that the analyte moves between successive rf pulses. Therefore,

$$L_{rep} = Ft_{rep}/\pi r^2 \tag{1}$$

where F (m³/s) is the flow rate, t_{rep} (s) is the delay between successive rf pulse sequences, and r (m) is the inner radius of the capillary. For our assumptions of 50% filling factor and 3:1 aspect ratio, $r = r_{coil}/2^{1/2}$, and $L_{coil} = 6r_{coil}$, where L_{coil} (m) is the length of the rf coil, and r_{coil} (m) is the radius of the rf coil. The residence time, τ (s), of any given analyte within the active volume of the coil is given by

$$\tau = \pi r^2 L_{coil}/F = 3\pi r_{coil}^3/F \tag{2}$$

The maximum allowed value of t_{rep} is τ, since any longer delay results in proton spins flowing though the coil that do not experience any rf pulses and therefore do not give rise to any signal intensity. The number of rf pulses that each individual section experiences as it flows through the rf coil is given by

$$N_{pulse} = L_{coil}/L_{rep} = 3\pi r_{coil}^3/Ft_{rep} \tag{3}$$

where N_{pulse} is the number of pulses. Generally, N_{pulse} will be a noninteger number. As an example, if $N_{pulse} = 4.8$, this implies that each nucleus in a section (L_{rep}) will experience four rf pulses, but 80% of the nuclei will experience the fifth rf pulse (and 20% will have passed through the detector cell).

To calculate the observable magnetization created by this repetitive pulsing, we use the Bloch equations with variable-tip angle α (degrees), t_{rep}, and spin–lattice relaxation time (T_1). We assume that the value of N_{pulse} is greater or equal to unity as the converse implies that the value of t_{rep} is greater than τ, leading to reduced sensitivity as discussed previously. Let N_{int} be the integer number of rf pulses experienced by all the spins in each sample plug (the integer part of N_{pulse}), and N_{fract} be the fraction of spins that experience the final rf pulse. The observable magnetization per unit volume, M, from each nucleus is expressed as a function of the total nuclear magnetization, M_o, (J s/m² C):[20]

$$M = M_o(\sin\alpha + N_{fract}(\sin\alpha)(1 + e_1\cos\alpha - e_1)^{N_{int}+1} + \sum_{n=1}^{N_{int}}(\sin\alpha)(1 + e_1\cos\alpha - e_1)^n) \tag{4}$$

where $e_1 = e^{(-t_{rep}/T_1)}$. The value of M_o is given by

$$M_0 = \frac{N\gamma^2 I(I+1)B_0}{3kT_s} \tag{5}$$

where N is the number of spins at resonance per unit volume, γ is the gyromagnetic ratio, $\hbar$ is Plank's constant divided by 2π, I is the spin angular momentum quantum number, B_0 is the strength of the static magnetic field, k is Boltzman's constant, and T_s is the temperature of the coil and sample. As we are interested in comparing various detector cell geometries and not absolute signal levels, we assume a fixed concentration of the eluted compound that is normalized to unity so that the total NMR signal from each section is proportional to the product of the total magnetization from each nucleus, the strength of the rf field B_1 per unit current, and the volume of each section. The peak voltage per unit volume (ξ) induced in the rf coil is given by[20]

$$\xi = \omega_o M B_1 \tag{6}$$

where ω_o is the Larmor frequency and the on-axis B_1 of a many-

(20) Hoult, D. I.; Richards, R. E. *J. Magn. Reson.* **1976**, *24*, 71.

turn solenoid is given by[19]

$$B_1 = \frac{\mu_0 n}{2} \frac{1}{\sqrt{r_{coil}^2 + (L_{coil}/2)^2}} = 0.158(\mu_0 n / r_{coil}) \quad (7)$$

where n is the number of wire turns in the solenoidal coil. As can be seen in eq 7, when the ratio of coil length to coil diameter and the number of turns are kept constant, the value of B_1 is inversely proportional to the radius of the rf coil. Consequently, the total *relative* signal intensity (in V) is given by the product of the total sample volume (V, in m^3), the magnetization per unit volume, and the B_1 per unit current:

$$\text{signal} \propto VMB_1 \propto nVM/r_{coil} \quad (8)$$

The experimental noise originates primarily in the windings of the coil and is proportional to the square root of the total number of signal acquisitions experienced by the sample. If data acquisition begins when the leading edge of a section first enters the coil and concludes when the trailing edge leaves the coil, then the number of pulses experienced by the entire analyte band is $(V + 3\pi r_{coil}^3)/Ft_{rep}$, so the noise is given by

$$\text{noise} = \sqrt{((V + 3\pi r_{coil}^3)/Ft_{rep})(4kT_s \Delta f R)} \quad (9)$$

where R is the resistance of the coil and Δf is the bandwidth used for data acquisition. The total time of the experiment is fixed by the volume of the analyte band, the flow rate, and the volume of the rf coil.

Therefore, the relative SNR for the flowing system is given by

$$\text{SNR} \propto \frac{VMB_1\sqrt{Ft_{rep}}}{\sqrt{(V + 3\pi r_{coil}^3)(4kT_s \Delta f R)}} \propto \frac{nVM\sqrt{Ft_{rep}}}{r_{coil}\sqrt{(V + 3\pi r_{coil}^3)T_s \Delta f R}} \quad (10)$$

This equation allows the SNR of the NMR detection cell to be calculated as a function of rf coil diameter. Figure 1 shows the relative SNR calculated for T_1 values between 2.5 and 10 s. This is the relevant range for organic and biomacromolecules. The parameters used in the simulation shown in Figure 1 are as follows: flow rate of 30 μL/min, analyte volume (at the detector cell) of 10 μL, coil length to diameter ratio of 3:1, and a constant filling factor of 50%. For each rf coil diameter, the values of α and t_{rep} are numerically optimized to give the maximum SNR.

The LC separation places practical constraints on observation times by eliminating larger volume detector cells. For example, the ~16-μL volume of the 1.2-mm-radius coil obtains the highest relative SNR in Figure 1 but degrades the separation efficiency so that a closely spaced series of bands would not be resolved. It may appear that the optimum detector cell volume is one in which the detector cell and peak volumes are matched; however, this is also problematic. The theoretical treatment assumes that a single optimum pulse occurs when the analyte band just fills the detector cell. Obviously, such prior knowledge of the analyte band position is not possible without an ancillary detector. As with other

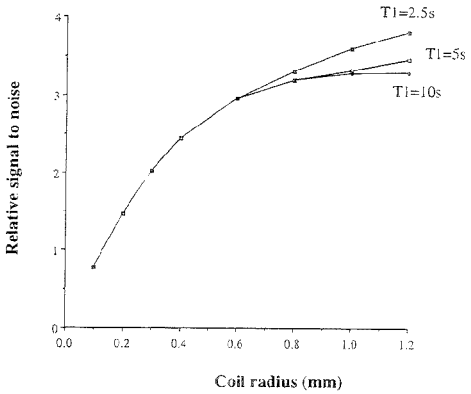

Figure 1. Relative SNR as a function of microcoil radius for three different values of analyte T_1 (2.5, 5, and 10 s). The model uses microcoils with a filling factor of 0.5, a 30 μL/min flow rate, a coil length to diameter ratio of 3:1, a rectangular sample profile, and a sample volume of 10 μL at the detector cell. See text for additional details about the model.

detection methods, a cell volume that allows the analyte band to be well defined by obtaining several spectra on every peak leads to better quantitative results with minimal reduction in detectability.

As shown in Figure 1, smaller rf coils show a decrease in SNR as the detector cell is reduced in size; however, the reduction is not severe over a relatively wide size range. This reduction occurs because there are fewer nuclei in the active volume of the coil. However, the smaller rf coil is inherently more sensitive than the larger coil at detecting these spins. In addition, much faster pulsing is possible as the flow continuously sweeps in new spins every residence time τ. Reducing the detector volume from ~16 μL (1.2 mm radius by 7.2 mm length) to ~50 nL (0.17 mm by 1.0 mm) reduces the relative SNR for a compound with a T_1 of 10 s by only a factor of 2. The 50-nL volume detector cell will not degrade the efficiency of the LC separation for microbore or even micropacked capillaries. In addition, when smaller columns are used, the flow rate and the analyte volume decrease over the 30 μL/min and 10 μL assumed here.

These results differ dramatically from those obtained by using a fixed size rf coil and simply reducing the sample cell size. Because the coil noise dominates the sample noise for diameters up to ~7 mm,[17] use of a fixed-diameter rf coil results in a 2-fold decrease in SNR for a 2-fold decrease in capillary radius. This is due to a 4-fold decrease in the SNR per NMR acquisition but the accumulation of 4-fold more NMR acquisitions due to the 4-fold smaller detector volume. The 2-fold reduction in SNR corresponds to a 4-fold increase in data acquisition time necessary to achieve the same SNR as the size-matched smaller coil. This is what happens for a conventional system using smaller diameter sample cells but using the same rf coil. Figure 2 shows the improvement in performance of a size-matched microcoil as a function of microcoil radius compared to a standard coil. In both cases, the same flow and detection parameters are used, with the performances of each approach normalized to the relative SNR obtained for a 5-mm rf coil.

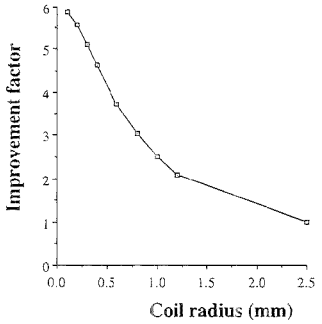

Figure 2. Improvement obtained using a size-matched microcoil as opposed to a fixed size microcoil as the detector cell volume is reduced. The performances of each are normalized to a 5-mm rf coil, and a 50% filling factor for the microcoil is assumed.

All of the preceding calculations have been for the total integrated NMR intensity from an analyte band. When calculating the SNR from an experimental separation, we use the conventional method of measuring the peak height and dividing by the *rms* baseline noise. For this definition of SNR, the spectral line-width affects the SNR. Up to now, the discussion has not considered the important effect of flow rate on line width. The observed NMR line width, $\Delta\omega_{flow}$, is affected by the residence time of the nuclei in the flow cell[11]

$$\Delta\omega_{flow} = \Delta\omega_{static} + 1/\tau \qquad (11)$$

As the detector cell is reduced in size, the residence time is decreased, increasing the minimum line width. This effect has been recognized before, and so many conventional LC systems use stop-flow techniques to provide both maximum SNR and minimum line width. However, in flowing systems, a tradeoff between sensitivity and line width exists for the smallest cells when faster flow rates are used. In all cases, the optimum SNR and minimum line width are obtained for the slowest flow rates. For the microcoils used here, the minimum line width is 7 Hz.[14,15] Thus, residence times of several hundred milliseconds may be used with minimal increases in observed line width.

EXPERIMENTAL SECTION

Chemicals. Deuterated acetonitrile (99.5% D), trifluoroacetic acid (TFA, 99.5% D), and deuterium oxide (99.9%D) are from Aldrich (Milwaukee, WI). The two larger peptides (Gly-His-Tyr-Ser-Tyr-Gly-Leu-Arg-Pro-Gly and Val-Phe-Gly-Thr-Gly-Thr-Lys-Val-Thr-Val-Leu-Gly-Gln-Pro-Lys-Ala) are from The Research Corp. Technologies (Tucson, AZ), and all other chemicals are of analytical grade from Sigma (St. Louis, MO). The samples are dissolved in a mobile phase consisting of 2% of TFA–D_2O and deuterated acetonitrile.

Apparatus. The experimental setup for the on-line ^1H NMR detection in LC is shown in Figure 3. The details of microcoil fabrication have been described previously.[15] Briefly, the microcoil is made by winding 42-gauge (63.1-μm diameter) varnished copper magnet wire directly onto fused-silica capillaries (355-μm o.d., 250-μm i.d.; Polymicro, Phoenix, AZ). We typically use 14–17 turns of wire for a total detection length of between 0.9 and 1.1 mm

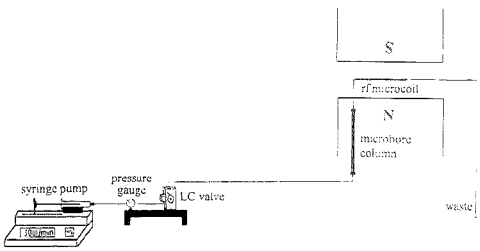

Figure 3. Experimental schematic of the ^1H NMR–LC system showing the placement of the rf microcoil, capillary cell, and LC column in the superconducting magnet.

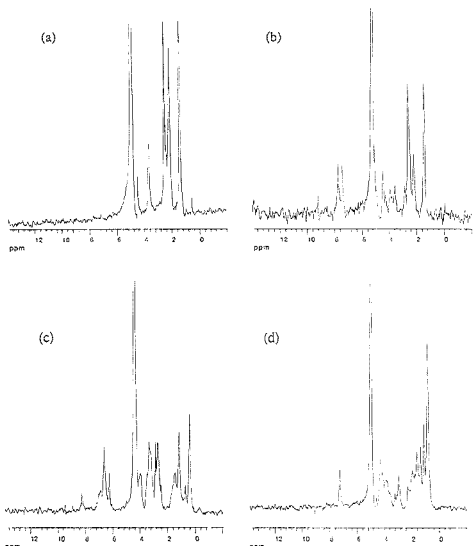

Figure 4. Static measurements for peptides in the 50-nL detection cell of (a) 1.4 μg (28 mM) of Leu-Arg (512 scans), (b) 0.78 μg (15.6 mM) of oxytocin fragment 6–9, Tyr-Pro-Leu-Gly-NH_2, (512 scans), (c) 1.2 μg (23 mM) of the 10-amino acid peptide Gly-His-Trp-Ser-Tyr-Gly-Leu-Arg-Pro-Gly (256 scans), and (d) 0.8 μg (16 mM) of the 16 amino acid peptide Val-Phe-Gly-Thr-Gly-Thr-Lys-Val-Thr-Val-Leu-Gly-Gln-Pro-Lys-Ala, (256 scans). Samples are dissolved in 25%CD_3-CN–D_2O with 0.2% of 0.25 N DCl added in (c) and (d) to aid in sample dissolution.

(creating a ~50-nL volume detector cell). The microcoil is contained within a custom NMR probe that allows the microcoil/capillary assembly to be positioned reproducibly in the bore of the NMR spectrometer.

NMR spectroscopy experiments (^1H) are performed using a GN-300 (7.05 T)/89 mm wide-bore NMR spectrometer (General Electric) and MacNMR software (Tecmag Corp., Houston, TX), available for the Apple Macintosh. All LC–NMR data files are imported to an IBM RS6000 workstation and manipulated and displayed using IBM Visualization Data Explorer. The two-dimensional chromatograms are 3 × 3 Gaussian filtered to reduce random noise and displayed using a nonlinear gray scale to emphasize minor features and baseline noise.

In the static experiments we use a tip angle of 50° and a pulse repetition time of 2 s or longer, based on the T_1 of each sample.

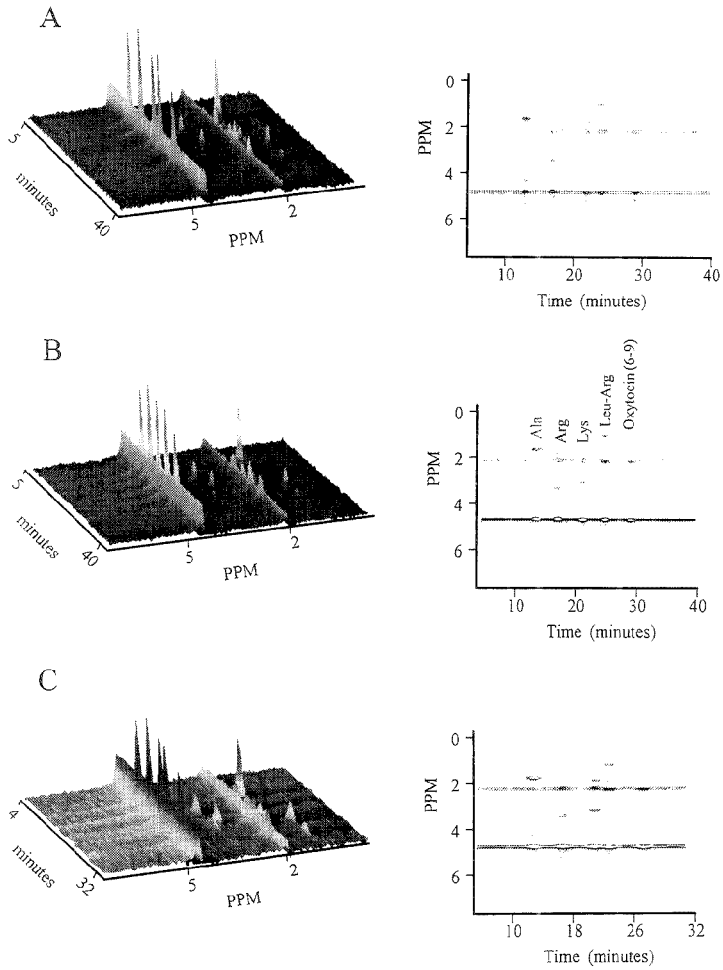

Figure 5. Two-dimensional chromatograms of (1) 67.3 mM alanine, (2) 32.8 mM arginine, (3) 34.5 mM lysine, (4) 17.3 mM Leu-Arg, and (5) 11.2 mM oxytocin (6–9) shown as both contour and surface plots. (A) Each NMR spectrum is 64 coadded scans with a 0.06-s pulse delay (9 s for each NMR spectrum); (B) 128 coadded scans with a 0.06-s pulse delay (18 s for each NMR spectrum); (C) 256 coadded scans with a 0.03-s pulse delay (36 s for each NMR spectrum).

For the LC experiments, new spins are introduced into the flow cell every 60–300 ms, and so much faster repetition rates can be used without saturation. In both cases, we acquire 512 point free induction decays (FIDs) over a ±4000-Hz spectral window.

For the static measurements, the capillary is flushed with the appropriate solution and placed within the bore of the magnet. The LC system consists of a Harvard Apparatus syringe pump (Model 55-2222, Harvard Apparatus, South Natick, MA) with a 1-mL Teflon Luer lock syringe (Hamilton, Reno, NV), a pressure gauge (0–3000 psig, Alltech, Deerfield, IL), and a Model 7125 sample injector with 10-μL injection loop (Reodyne, Cotati, CA). The LC column is located in the bore of the magnet and connected to the rf coil by a short (<10 cm) length of Teflon tubing. The syringe pump is separated from the column and the high field magnet by a 3-m length of Teflon tubing. The separations are optimized using a Spectra-100 UV–visible detector (Spectra Physics, San Jose, CA) set at 205 nm. The microbore HPLC column is a 5-μm Nucleosil C_{18} (1.0 × 150 mm) column (MetaChem Technologies, Torrance, CA)) or a 5-μm Vydac C18 (1.0 × 150 mm) column (201HS5115, Vydac, Hesperia, CA). Mobile phases are prepared by mixing appropriate amounts of 2% TFA in D_2O (pD = 2.4) and deuterated acetonitrile (74:26 v/v). Solutions are degassed by sonication for 10 min. Mobile phase flow rates between 10 and 50 μL/min are used.

RESULTS AND DISCUSSION

Preliminary studies on the suitability of the 50-nL microcell for obtaining NMR spectra have been performed under static conditions using a series of peptides containing from 2 to 16 amino acids. Figure 4 shows the resulting NMR spectra using 256–

512 scans for each peptide at concentrations between 16 and 28 mM (1–2 μg in the detection cell). Although these spectra represent acquisition times longer than possible for on-line NMR, they demonstrate the information obtainable from the microcell. As reported previously for this particular microcell,[14,15] the narrowest line widths that are obtained are between 7 and 15 Hz. However, even with this relatively large line width, a significant amount of information can be deduced from the NMR spectrum. For example, the presence of an aromatic group in Figure 4d (from a Phe residue in the peptide) can be deduced from the peak at 7.4 ppm.

For the on-line LC NMR experiments, the sample contains a mixture of three amino acids and two peptides. As discussed in the Theory section for a 360-μm-diameter rf coil, the optimum pulse repetition rate is the residence time of the analyte in the detection cell. The residence times (and hence optimum pulse rate) are on the order of 0.1 s at a flow rate of 30 μL/min and 0.06 s at 50 μL/min. The number of acquisitions to use should allow an NMR spectrum to be acquired at least every 10–20 s. As the NMR software used to acquire data requires multiple data transfers and stores each FID to disk as it is acquired, the actual data rate is much slower than the actual NMR acquisition times. Thus, the optimum pulse repetition rate determined experimentally is shorter than the predictions from our model as the model does not take into account these extra times. For the current system, acquiring 64, 128, or 256 scans takes 9, 18, and 36 s, respectively, with little difference in total acquisition time as the pulse repetition rate is changed from 0.03 to 0.06 s.

Figure 5 shows the resulting two-dimensional chromatograms (both as surface and contour plots) for a 30 μL/min flow rate, where each NMR spectrum is (A) 64 scans with a 0.06-s pulse delay, (B) 128 scans with a 0.06-s pulse delay, and (C) 256 scans with a 0.03-s pulse delay. Not surprisingly, the fewer the number of coadded scans, the better the separation efficiency. As shown in Figure 5A and B, increasing the number of scans from 64 to 128 (9–18-s spectral acquisition time) increases the SNR and only slightly reduces the efficiency. Acquiring additional scans as in (C) decreases the SNR because the additional scans are obtained after the analyte band has left the detection cell and dramatically reduces the separation efficiency. A slight increase in separation efficiency is observed by increasing the flow rate to 50 μL/min, although this is accompanied by a decrease in SNR due to the reduced analyte observation time. The number of theoretical plates is increased from ~1800 with a 30 μL/min (retention time of 11.7 min) flow rate to ~3000 at the flow rate of 50 μL/min (retention time of 6.9 min) for alanine.

In this study we have demonstrated the use of an rf microcoil for on-line NMR detection in LC. This technology makes possible effective NMR studies of ~1 μg of analyte using a 50-nL detector cell. The concentration limits of detection have been significantly improved as compared to the on-line detection in CE using a similar microcell.

The dependence of the relative SNR as a function of coil diameter differs significantly from previous theoretical calculations involving rf microcoils due to the flow rate dependence on detector cell geometry. Unlike static measurements, the higher mass sensitivity of the smaller coils is offset by the reduced residence time for a given flow rate. By properly size-matching the rf microcoil to the detector cell, significant gains in sensitivity and detectability are possible in on-line LC detection. Optimizing the

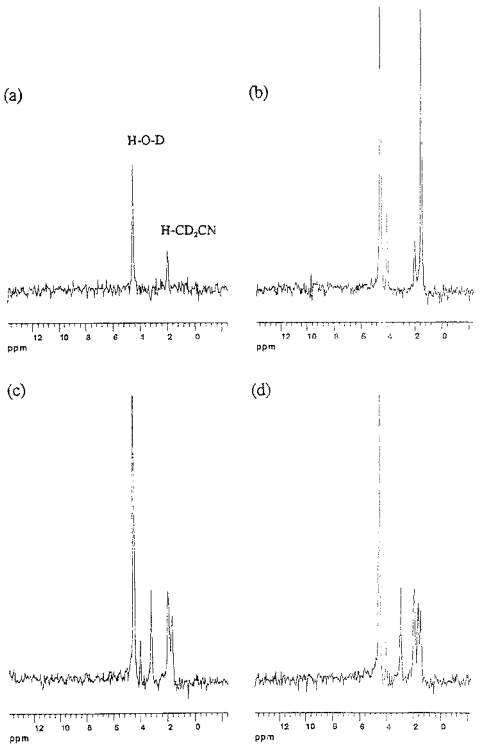

Figure 6. ^{1}H NMR spectra of (a) solvent, (b) alanine, (c) arginine, and (d) lysine. The spectra are taken from Figure 5A. Figure 4a and b show reference spectra of Leu-Arg and oxytocin (6–9).

system for maximum SNR and minimum line width requires that the detector cell be as large as possible compatible with maintaining adequate efficiency for a given separation. However, the reduction in SNR when smaller volume detector cells are used is not significant. Using the example parameters in the model developed earlier, a 400-fold reduction in cell volume is only accompanied by a 2-fold reduction in SNR. One of points of the present model is that the scaling laws for flow NMR favor miniaturization of NMR detector cells. Software optimized for rapid sequential acquisitions is required before complete experimental verification of the NMR SNR model is made. However, the ability to acquire high-quality NMR spectra with a detector cell two orders of magnitude smaller than the analyte band volume attests to the NMR detector cell scaling law developed with this model.

The most serious limitation to the present approach is the wide NMR spectral line widths. Preliminary results in static systems using an optimized solenoidal geometry and improved shimming techniques demonstrate a reduction of line width to less than 1 Hz.[21,22] Reducing the effective line width increases the SNR, increases the information content of the resulting NMR spectra, and makes possible the use of COSY, NOESY, and other two-dimensional NMR pulse sequences techniques. We fully expect that these nanoliter-volume detector cells will allow a variety of

microseparations methods to be interfaced to NMR spectrometers with greater sensitivity and flexibility than presently possible.

ACKNOWLEDGMENT

J.V.S. acknowledges the support of a NSF NYI Award (CHE-92 57024) and the David and Lucile Packard Foundation. The NMR facilities of the Biomedical Magnetic Resonance Laboratory and the NIH Biomedical Research Technology Grant (PHS 5P41RR05964) are acknowledged. The donation of an RS6000 workstation from the IBM SURS program is gratefully acknowledged.

(21) Olson, D. L.; Peck, T. L.; Webb, A. G.; Sweedler, J. V. On-line NMR Detection for Capillary Electrophoresis Applied to Peptide Analysis. In *Peptides: Chemistry, Structure, and Biology*; Kaumaya, P. T., Hodges, R. S., Eds.; ESCOM: Leiden, The Netherlands, in press.

(22) Olson, D. L.; Peck, T. L.; Webb, A. G.; Magin, R. M.; Sweedler, J. V. High Resolution Microcoil 1H-NMR for Mass Limited Nanoliter Samples, submitted.

Received for review April 19, 1995. Accepted July 26, 1995.[⊗]

AC9503825

[⊗] Abstract published in *Advance ACS Abstracts*, August 15, 1995.

Articles

Anal. Chem. 1995, *67*, 3108–3114

Thrombogenic Properties of Untreated and Poly(ethylene oxide)-Modified Polymeric Matrices Useful for Preparing Intraarterial Ion-Selective Electrodes

Cecilia Espadas-Torre and Mark E. Meyerhoff*

Department of Chemistry, The University of Michigan, Ann Arbor, Michigan 48109

In vitro platelet adhesion studies are used to compare the thrombogenic properties of various polymer matrices useful for preparing implantable ion-selective membrane electrodes. Conventional plasticized poly(vinyl chloride) and alternate polyurethane materials (Tecoflex, Pellethane) doped with proton- (tridodecylamine) and potassium-selective (valinomycin) ionophores are shown to be potentially thrombogenic. Incorporation of high molecular weight block copolymers of poly(ethylene oxide) and poly(propylene oxide) (e.g., Pluronic F108 and Tetronic 1508) within ion-selective membranes reduces platelet adhesion. A more marked decrease in platelet adhesion is, however, observed when the Tecoflex-based membranes are coated with a thin photo-cross-linked layer of poly(ethylene oxide). Such surface-modified membranes are shown to retain potentiometric ion response properties (i.e., selectivity, response times, response slopes, etc.) essentially equivalent to untreated membranes.

The availability of implantable sensors suitable for the continuous in vivo monitoring of clinically important analytes within flowing blood would clearly benefit the practice of modern medicine.[1,2] Indeed, the effective management of critically ill patients often requires the frequent measurement of blood gases (P_{O_2}, P_{CO_2}, pH) and electrolytes (Na^+, K^-, Ca^{2+}), and sensor-based technologies capable of providing such measurements in real-time are receiving increased interest.[3] Although research efforts in this area have been in progress for nearly two decades, the use of intraarterial devices based on miniaturized ion-selective electrode (ISE) technology, especially polymer membrane based potentiometric devices, is still mainly at the experimental stage.[4–13] This is somewhat surprising given the impact that this sensing technology has had on the routine measurement of blood electrolyte and gas levels within a wide range of laboratory as well as modern point-of-care instruments designed to measure these species in discrete samples in vitro.[3,14] However, in vivo, eventual fouling of the surfaces of miniaturized sensors via thrombus formation remains a major obstacle to overcome. Any potential improvement in sensor biocompatibility must be achieved without compromising the analytical performance which arises from the specific sensing chemistries employed within the implantable devices.

The events taking place upon blood/material interaction that eventually lead to thrombus formation have been described in detail elsewhere (see, for example, ref 15). Blood clots on a sensor's surface may affect its electroanalytical performance in vivo by a perturbed mass transfer of analyte to the surface. More importantly, thrombus deposition may be responsible for measurement errors due to the metabolic byproducts of the large number of cells (platelets and varying numbers of leukocytes and erythrocytes) entrapped within the clot layer. Indeed, local pH, P_{CO_2}, and P_{O_2} levels are generated that can differ significantly from the bulk blood. Consequently, while still functional, a thrombus-coated sensor can yield blood gas values quite different from those obtained by in vitro measurements on discrete blood samples collected from the same subject.

The surface properties of a material play a critical role in the events that eventually lead to thrombus formation. Historically, the matrix used most often to prepare polymer membrane-type

(1) Pickup, J. C.; Alcock, S. *Biosens. Bioelectron.* **1991**, *6*, 639.
(2) Espadas-Torre, C.; Telting-Diaz, M.; Meyerhoff, M. E. *Interface* **1995**, *4*, 41.
(3) Kost, G. J. *Crit. Rev. Clin. Lab. Sci.* **1993**, *30*, 153.
(4) Osswald, H. F.; Asper, K.; Dimai, W.; Simon, W. *Clin. Chem.* **1979**, *25*, 39.
(5) Fogt, E. J.; Eddy, A. R.; Clemens, A. H.; Fox, J.; Heath, H. *Clin. Chem.* **1980**, *26*, 1425.
(6) Lim, M.; Linton, R. A. F.; Band, O. M.; Chin, B. *Anesthesiology* **1982**, *57*, 272.
(7) Simon, W.; Amman, D.; Anker, P.; Oesch, U.; Band, D. M. *Ann. N.Y. Acad. Sci.* **1984**, *428*, 279.
(8) Ammann, D.; Anker, P.; Metzger, E.; Oesch, U.; Simon, W. In *Ion Measurements in Physiology and Medicine*; Kessler, M., et al., Eds.; Springer-Verlag: Berlin, 1985; p 102.
(9) Collison, M. E.; Aebli, G. V.; Petty, J.; Meyerhoff, M. E. *Anal. Chem.* **1989**, *61*, 2365.
(10) Telting-Diaz, M.; Collison, M. E.; Meyerhoff, M. E. *Anal. Chem.* **1994**, *66*, 576.
(11) Lindner, E.; Cosofret, V. V.; Ufer, S.; Johnson, T. A.; Ash, R. B.; Nagle, H. T.; Neuman, M. N.; Buck, R. P. *Fresenius J. Anal. Chem.* **1993**, *346*, 584.
(12) Lindner, E.; Cosofret, V. V.; Ufer, S.; Buck, R. P.; Kao, W. J.; Neuman, M. R.; Anderson, J. M. *J. Biomed. Mater. Res.* **1994**, *28*, 591.
(13) Cosofret, V. V.; Erdösy, M.; Buck, R. P.; Kao, W. J.; Anderson, J. M.; Lindner, E.; Neuman, M. R. *Analyst* **1994**, *119*, 2283.
(14) Meyerhoff, M. E. *Clin. Chem.* **1990**, *36*, 1567.
(15) Anderson, J. M.; Kottke-Marchant, K. *CRC Crit. Rev. Biocompat.* **1985**, *1*, 111.

0003-2700/95/0367-3108$9.00/0

Poly(vinyl chloride)

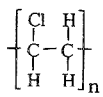

Pellethane Polyurethane

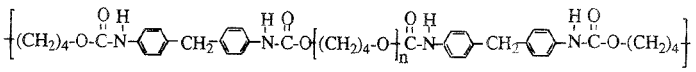

Tecoflex Polyurethane

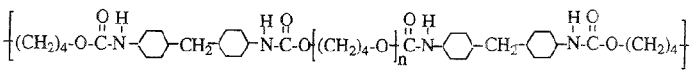

Pluronic F108

PEO_{129}-PPO_{56}-PEO_{129}

Tetronic 1508

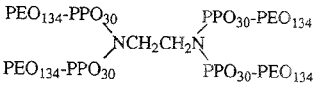

PEO -$(CH_2CH_2O)_n$-

PPO -$(CH_2CHO)_n$-

Figure 1. Polymers used as matrices for fabricating ion-selective membranes and commercial polymeric surfactants incorporated as membrane additives.

ISEs has been plasticized poly(vinyl chloride) (PVC). While used successfully in blood analyzers, lack of biocompatibility has prevented the adaptation of PVC-based devices for continuous in vivo measurements. Attempts to improve the blood compatibility of PVC membrane electrodes have included the use of conventional dialysis membranes or hydrogel layers as outer overlays,[16,17] but these efforts have generally resulted in sensors with longer response times and reduced sensitivities. The use of polyurethane as an alternate matrix to prepare ISEs was suggested more than two decades ago,[18] but its use did not become widespread. More recently, the reported enhanced blood compatibility of some commercial polyurethanes[19,20] has attracted renewed interest in the use of this class of materials for preparing ISEs. An aliphatic polyurethane (Tecoflex) (see Figure 1) was used previously to prepare membranes with potentiometric response characteristics essentially equivalent to PVC.[12,21] In addition, in at least one case,[22] the use of this new matrix resulted in the elimination of sample-induced asymmetry potentials after the sensor made contact with blood serum, presumably indicating that such membranes exhibit lower protein adhesiveness. Lindner et al.[12] observed recently that a decrease in plasticizer content of Tecoflex-based ISE membranes correlates with a reduction in the inflammatory response to subcutaneously implanted membranes.

We report herein on the use of in vitro platelet adhesion studies as a means to evaluate the relative thrombogenic properties of various ion-selective membranes formulated with classical PVC and alternate polyurethane-based compositions. The method, applied to both pH- and potassium-selective membranes, yields results that differ considerably depending on the type of polymeric matrix used. Further, in an attempt to produce ion-selective materials with improved blood compatibility, polyurethane-based membranes are modified by incorporating high molecular weight poly(ethylene oxide) (PEO) either as part of a nonionic amphiphilic additive blended with the polymer matrix, or as a thin outer cross-linked covalent surface coating. The potentiometric response properties and platelet adhesion characteristics of the modified and unmodified membranes are examined to determine whether any of the membranes yield the desired combination of improved blood compatibility and adequate electroanalytical performance for use in fabricating implantable ISE-type catheters.

EXPERIMENTAL SECTION

Materials and Reagents. High molecular weight poly(vinyl chloride) (PVC), valinomycin (VAL), dioctyl sebacate (DOS), dioctyl phthalate (DOP), and potassium tetrakis(*p*-chlorophenyl)-borate (Kt*p*ClPB) were purchased from Fluka (Ronkonkoma, NY), while tridodecylamine was a product of Eastman Kodak (Rochester, NY). Tecoflex SG-80A (Teco) was a gift from Thermedics, Inc. (Woburn, MA), Pellethane 2363-80AE (Pell) was a gift from DOW (Midland, MI), and the block copolymer surfactants Pluronic F108 (PLUR) and Tetronic 1508 (TETR) were gifts from BASF Corp. (Parsippany, NJ) (see Figure 1 for structures of various polymers). Poly(ethylene oxide) with average molecular weights of 18 500 (PEO 18.5K) and 200 000 (PEO 200K) were

(16) Fogh-Andersen, N.; Christiansen, T. F.; Komarmy, L.; Siggaard-Andersen, O. *Clin. Chem.* **1978**, *24*, 1545.
(17) Murphy, S. M.; Hamilton, C. J.; Davies, M. L.; Tighe, B. J. *Biomaterials* **1992**, *14*, 979.
(18) Fiedler, U.; Ruzicka, J. *Anal. Chim. Acta* **1973**, *67*, 179.
(19) Lelah, M. D.; Cooper, S. L. *Polyurethanes in Medicine*; CRC Press: Boca Raton, FL, 1986.
(20) Planck, H.; Egbers, G.; Syré, I. *Polyurethanes in Biomedical Engineering*; Elsevier: Amsterdam, The Netherlands, 1984.
(21) Cha, G. S.; Liu, D.; Meyerhoff, M. E.; Cantor, H. C.; Midgley, A. R.; Goldberg, H. D.; Brown, R. B. *Anal. Chem.* **1991**, *63*, 1666.
(22) D'Orazio, P.; Laios, I.; Bowers, G. N., Jr. In *Electrolytes, Blood Gases and other Critical Analytes: the Patient, the Measurement and the Government*; D'Orazio, P., Burrit, M. F., Sena, S. F., Eds.; Proceedings of an International Symposium. The Electrolyte/Blood Gas Division of the AACC, 1992; p 21.

Table 1. Compositions of Ion-Selective Membranes Studied

membrane	ion	composition	wt %
A	H^+	PVC/DOS/KtpClPB/TDDA	33.0/65.5/0.5/1.0
B	H^+	Teco/DOS/KtpClPB/TDDA	89.8/8.0/0.7/1.5
C	H^+	Teco/PLUR/DOS/KtpClPB/TDDA	79.8/10.0/8.0/0.7/1.5
D	H^+	Teco/TETR/DOS/KtpClPB/TDDA	79.8/10.0/8.0/0.7/1.5
E	H^+	Pell/DOP/KtpClPB/TDDA	92.8/5.0/0.7/1.5
F	K^+	PVC/DOS/KtpClPB/VAL	33.0/65.1/0.4/1.5
G	K^+	Teco/DOS/KtpClPB/VAL	90.1/8.0/0.4/1.5
H	K^+	Teco/PLUR/DOS/KtpClPB/VAL	80.1/10.0/8.0/0.4/1.5
I	K^+	Pell/DOP/KtpClPB/VAL	93.4/5.0/0.4/1.5

purchased from Polysciences, Inc. (Warrington, PA) and Scientific Polymer Products, Inc. (Ontario, NY), respectively. Glutaraldehyde (electron microscopy grade) was obtained from Ted Pella (Redding, CA) as an 8% (w/v) aqueous solution in sealed ampules. The organic solvents methanol, ethanol, tetrahydrofuran (THF), toluene, and dichloromethane were of the highest purity available. Hexamethyldisilazane was from Aldrich (Milwaukee, WI). Dicumyl peroxide (DCP) from Aldrich was used after repeated recrystallization from methanol. All other chemicals were analytical-reagent grade. All water used was reverse osmosis/deionized.

Preparation of Ion-Selective Membranes. The polyurethanes Tecoflex and Pellethane (see Figure 1) were used after being first extracted with methanol for at least 1 week and then thoroughly dried. Membrane cocktails with the compositions indicated in Table 1 were prepared by dissolving the components in the appropriate solvent. Dichloromethane (mixed with 20% THF for VAL-containing membranes) was used for Tecoflex-based membranes, and THF (freshly distilled) for Pellethane and PVC membranes. Membrane cocktail solutions containing 200 mg of membrane components in 3 mL of solvent were cast into 2.5 cm glass rings resting on clean glass plates. The solvent was allowed to evaporate at room temperature in a dust-free environment for 24–48 h. Membranes containing PLUR or TETR (C, D, and H in Table 1) were extensively rinsed and soaked in water for several days before further evaluation.

Coating of Tecoflex-based membranes with cross-linked PEO was accomplished in the following manner: a solution of 3% (w/w) PEO in toluene was prepared by vigorously stirring the PEO in toluene with slight warming until a clear liquid was obtained. The solution was filtered through a 0.45-μm GHP poly(propylene) filter (Gelman Sciences, Ann Arbor, MI), and after allowing the solution to reach room temperature, DCP was added to achieve a concentration of 0.15% (w/w). Membranes were dipped individually into this solution for 10–15 s, air-dried for a few minutes, vacuum-dried for 1 h, and then irradiated for 1 h under nitrogen with 254-nm UV light [Mineralight (San Gabriel, CA) lamp Model UVGL-58, 115 V, 0.16 A]. The side originally facing air during casting was exposed directly to the UV light. Pellethane-based membranes were coated in the same way, except that the PEO was dissolved in dichloromethane without prewarming. After irradiation, all membranes were extensively rinsed with flowing deionized water and then soaked in a large volume of water for 3 days (exchanging the water three times per day) to remove any noncovalently bound PEO.

Potentiometric Ion Response of Various Membranes. Disks were punched from the membranes and mounted into Philips IS-560 electrode bodies (Möller Glasbläserei, Zurich, Switzerland). The internal filling solution was 0.5 M HEPES buffer, pH 7.5, containing 0.05 M KCl and 0.05 M NaCl. Cell voltages were measured at 22.0 ± 1.0 °C vs a double-junction Ag/AgCl reference electrode from Fisher Scientific (Itasca, IL) with 1.0 M lithium acetate as salt bridge electrolyte. A Macintosh IIcx computer with an NB-MIO-16X analog/digital input/output board (National Instruments, Austin, TX) and a custom-built electrode interface module controlled by Lab-View 2 software (National Instruments) was used to obtained potentiometric ion response data as described elsewhere.[10]

Potentiometric measurements were made after conditioning the electrodes for at least 48 h in HEPES/saline [6 mM *N*-(2-hydroxyethyl)piperazine-*N*′-2-ethanesulfonic acid, 135 mM NaCl, 5 mM KCl, and 1.3 mM $CaCl_2$], pH 5.5. The pH of the solutions was monitored with an Ingold glass electrode. Response times were obtained by adding a small volume of 2 M NaOH to a rapidly stirred HEPES/saline solution (pH response) and by making an addition of 1 M KCl to a rapidly stirred 1.0 mM KCl solution containing 0.15 M NaCl (potassium response). Selectivity coefficients were determined by the fixed interferent method.[23] Liquid junction potentials were corrected according to the Henderson formalism, and activity coefficients were calculated according to ref 24. Other details are as specified in Table 2.

X-ray Photoelectron Spectroscopy (XPS) Surface Analysis. The surfaces of dry PEO(200K)-coated and uncoated Pellethane films (with no ionophore, plasticizer, or additives) were analyzed via XPS. Spectra were collected with a Perkin-Elmer PHI Model 5400 spectrometer using a 300-W Mg anode. A pass energy of 35.75 eV was used to obtain carbon 1s spectra at a 45° take-off angle. An electron gun was used to neutralize surface charging. Data were collected and stored on a Perkin-Elmer computer which also controlled the spectrometer. Software provided with the instrument was used to smooth and deconvolute the constituent peaks of the carbon 1s band.

Platelet Adhesion Studies. Blood was obtained from the jugular vein of a healthy Suffolk sheep at the University of Michigan Sheep Research Farm. Each pint of blood was drawn into a blood collection bag (Baxter Fenwal) containing 63 mL of CPDA-1 anticoagulant solution (2 g of dextrose, 1.66 g of sodium citrate dihydrate, 188 mg of citric acid, 140 mg of monobasic sodium phosphate monohydrate, and 17.3 mg of adenine). Within 30 min after collection, blood was centrifuged at 240*g* for 15 min. The supernatant was platelet-rich plasma (PRP) with a concentration of approximately 10^5 cells/μL as determined with a Coulter counter. The PRP was preincubated at 37 °C for 20 min. Polymer membranes previously conditioned in phosphate-buffered saline (PBS, containing 10 mM phosphate, 138 mM sodium chloride, and 2.7 mM potassium chloride, pH 7.4) for 3 days were immersed in PRP for 2 h at 37 °C. They were then rinsed in PBS and fixed in a PBS solution containing 2.0% (w/v) glutaraldehyde for 2 h at room temperature. Samples were dehydrated by immersion in serial dilutions of ethanol (30, 50, 70, 90, and 95% v/v), two immersions in absolute ethanol, and two in hexamethyldisilazane. After solvent evaporation within a desiccator, the membranes were coated with gold and examined using a Hitachi S-570 scanning electron microscope (SEM). Micrographs and results presented

(23) Bailey, P. L. *Analysis with Ion-Selective Electrodes*, 2nd ed.; Heyden: London, 1980.
(24) Meier, P. C. *Anal. Chim. Acta* **1982**, *136*, 363.

Table 2. Response Properties of Tecoflex-Based Ion-Selective Membranes

membrane	slope[a] (mV/decade)		detection limit (log a_i)		selectivity (log k_{ij}^{pot})				
					$i = H^+$			$i = K^+$	
	H^+ [b]	K^+ [c]	$i = H^+$ [d]	$i = K^+$ [e]	$j = Na^+$ [f]	$j = K^+$ [g]	$j = Ca^{2+}$ [h]	$j = Na^+$ [i]	$j = Ca^{2+}$ [j]
B	58.6 ± 1.0		−10.0		−9.1	−9.3	−9.1		
B-PEO (200K)	55.8 ± 1.9		−9.9		−9.0	−9.1	−9.1		
C	53.9 ± 0.7		−9.4		−8.5	−8.6	−8.9		
G		56.8 ± 0.2		−4.7				−3.8	−4.6
G-PEO (200K)		54.6 ± 0.6		−4.7				−3.8	−4.5
H		53.2 ± 0.6		−4.4				−3.5	−4.2

[a] Data are mean values ± SD for a minimum of four electrodes. [b] pH range, 6.5–8.0; by stepwise addition of HCl to a basic HEPES/saline solution (composition as in Experimental Section). [c] pK^+ range, 2.0–3.2; by additions of KCl standard solutions to HEPES/saline, pH 7.4, initially without KCl. [d] In HEPES/saline background. [e] In HEPES/saline background (initially without KCl), pH 7.4. [f] Determined in 10 mM Tris buffer with 130 mM NaCl and 10 mM NaOH, by addition of HCl. [g] Determined in 10 mM Tris buffer with 190 mM KCl and 10 mM KOH, by addition of HCl. [h] Determined in 10 mM Tris buffer with 90 mM $CaCl_2$ and 10 mM $Ca(OH)_2$, by addition of HCl. [i] A 150 mM NaCl background electrolyte. [j] A 100 mM $CaCl_2$ background electrolyte.

below are representative of various membrane materials subjected to this procedure on at least three different occasions.

RESULTS AND DISCUSSION

It should be stated from the outset that the final evaluation of any allegedly thromboresistant surface must take place in vivo, with in vitro tests lacking an absolute standard. However, platelets are central to blood/material interactions and in vitro studies of platelet adhesion are considered by many workers to be informative when different surfaces/materials are compared and helpful as an initial screen for selecting promising materials.[25-28] Sheep blood, which was used for these investigations, can be considered a conservative model for the human coagulation system.[29-31] Figure 1 illustrates the chemical structures of the polymer matrices (PVC, Tecoflex, Pellethane) examined in these studies. Also shown are the structures of two copolymers that were examined as membrane additives to potentially enhance biocompatibility. Preliminary experiments involved demonstrating that functional pH- and K^+-selective membranes could be prepared using plasticized films of these materials containing the appropriate ionophore (TDDA and VAL, respectively) and lipophilic anion site additive (KtpClPB). A low level of membrane plasticizer was desired since initial experiments showed that polyurethane membranes formulated with 50% (w/w) plasticizer resulted in substantially increased numbers of deposited platelets than those containing less than 10% (w/w) plasticizer. Moreover, a low plasticizer content was necessary to achieve a complete PEO surface coating in the subsequent surface modification of membranes (see below). Since complete elimination of plasticizer has been observed, in some instances, to degrade the selectivity of Tecoflex-based ISE membranes,[32] a plasticizer level of 8% (w/w) was utilized in the studies described herein. This level results in membranes with adequate sensitivity and selectivity for use in blood pH and potassium determinations[32] (see Table 2). The potentiometric response properties of Pellethane-based membranes were inferior in terms of reproducibility to those incorporating Tecoflex (probably due to inadequate compatibility between the polymer, plasticizer, and ionophore components), and potentiometric response data for such membranes are not presented here; however, they are included for comparisons of their surface properties and how these are affected by the PEO-coating procedure.

Results of the in vitro blood compatibility studies are presented via representative micrographs shown in Figure 2. These pictures show that the various ion-selective polymer materials examined differ significantly in their platelet adhesiveness under the conditions of the test. For every type of material investigated, the results were the same irrespective of the ionophore incorporated in the membrane (TDDA or VAL) and thus only one micrograph is shown as an example for each case. Conventional PVC-based pH- and potassium-selective membranes A and F (Table 1) consistently had the largest number of deposited platelets, an indication of the high thrombogenicity of these membranes, and were characterized by densely packed platelet aggregates (see Figure 2a for a micrograph of TDDA-doped membrane A; similar results for membrane F not shown). Proton- and potassium-selective membranes E and I prepared with the aromatic polyurethane Pellethane exhibited somewhat less platelet adhesion but were distinguished by an appreciable extension of pseudopodia and hyaloplasm spreading, a clear sign of substantial platelet activation (see Figure 2b, for micrograph of VAL-doped membrane I; similar results for E not shown). Membranes B and G, prepared with the aliphatic polyurethane Tecoflex, also appeared to have a significant number of platelets adhered to the respective surfaces (Figure 2c illustrates results for membrane type B); however, these were mostly round or incipiently dendritic single platelets or small loose clusters, an indication that such platelets are less strongly activated by contact with the Tecoflex surface.[33]

To determine whether it is possible to further decrease the degree of platelet adhesion onto the surface of functional pH and potassium ISE membranes prepared with the Tecoflex material,

(25) Goodman, S. L.; Lelah, M. D.; Lambrecht, L. K.; Cooper, S. L.; Albrecht, R. M. *Scanning Electron Microsc.* **1984**, *1*, 279.
(26) Chen, C. Y.; Su, Y. C.; Ishihara, K.; Nakabayashi, N.; Tamiya, E.; Karube, I. *Electroanalysis* **1993**, *5*, 269.
(27) Mathew, J.; Liu, S. Q.; Kodama, M. *Biomaterials* **1993**, *14*, 57.
(28) Haycox, C. L.; Ratner, B. *J. Biomed. Mater. Res.* **1993**, *27*, 1181.
(29) Gajewski, J.; Povar, M. L. *Am. J. Vet. Res.* **1971**, *32*, 405.
(30) Grabowski, E. F.; Didisheim, P.; Lewis, J. C.; Franta, J. T.; Stropp, J. Q. *Trans. Am. Soc. Artif. Intern. Organs* **1977**, *23*, 141.
(31) McIntire, L. V.; Addonizio, V. P.; Coleman, D. L.; Eskin, S. G.; Harker, L. A.; Kardos, J. L.; Ratner, B. D.; Schoen, F. J.; Sefton, M. V.; Fitlick, F. A. *Guidelines for Blood-Material Interactions*; National Heart, Lung and Blood Institute, NIH Publication No. 85-2185; U.S. Department of Health and Human Services, revised September 1985.
(32) Oesch, U.; Ammann, D.; Simon, W. *Clin. Chem.* **1986**, *32*, 1448.
(33) Park, K.; Mao, F. W.; Park, H. *Biomaterials* **1990**, *11*, 24.

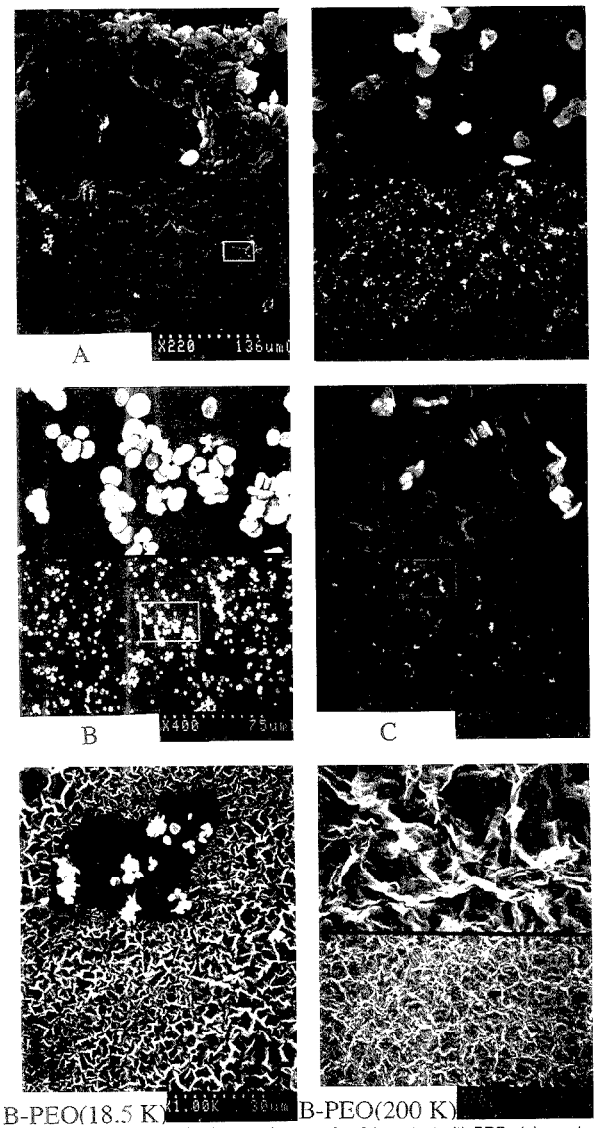

Figure 2. Scanning electron micrographs of ion-selective membranes after 2-h contact with PRP: (a) membrane type A (similar results for F); (b) type I (similar results for E); (c) type B (similar results for G); (d) type C (similar results for D and H); (e) type B, coated with PEO(18.5K) and (f) type B, coated with PEO(200K) [similar results for G-PEO(200K), E-PEO(200K), and I-PEO(200K)]. The upper half of each picture, except for (e), is a 10-fold magnification of the selected region in the bottom half. The indicated scale is that corresponding to the bottom half of each picture.

Pluronics F108 and Tetronics 1508, two commercial amphiphilic block copolymers of poly(ethylene oxide) and poly(propylene oxide) (Figure 1), were incorporated into the membrane formulations. It was found previously[34,35] that, when added in small quantities, these types of polymeric surfactants significantly change the surface properties of polyurethane matrices resulting in improved biocompatibility. This effect is apparently due to the rapid rearrangement of the chains of these copolymers upon contact with water to yield a highly hydrated poly(ethylene oxide)-rich surface that decreases the interactions with blood components. Test ISE membranes were therefore prepared with 10%

(34) Paulsson, M.; Kober, M.; Freij-Larsson, C.; Stollenwerk, B.; Wesslén, B.; Ljungh, A. *Biomaterials* **1993**, *14*, 845.
(35) Kober, M.; Wesslen, B. *J. Polym. Sci. A: Polym. Chem.* **1992**, *30*, 1061.

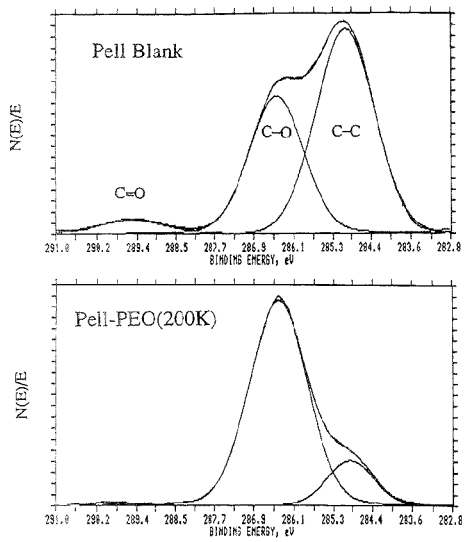

Figure 3. X-ray photoelectron spectra of polyurethane (Pellethane) surfaces, uncoated (blank) and coated with PEO(200K).

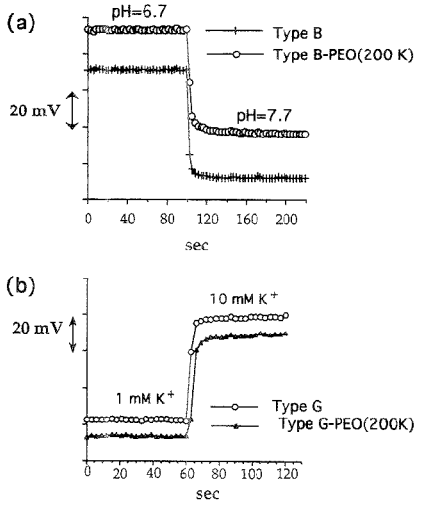

Figure 4. Dynamic potentiometric response of PEO(200K)-coated and uncoated proton (a) and potassium (b) ion-selective Tecoflex membranes.

(w/w) added surfactants (larger concentrations resulted in appreciable phase separation). Platelet adhesion results (as well as potentiometric properties, described below) of pH-selective membranes containing TDDA do not differ when either PLUR or TETR is present in the membrane. Only PLUR was used for doping VAL potassium-selective membranes. The micrograph shown in Figure 2d, obtained for membrane C (note: similar results observed for membrane D or H, not shown), illustrates that, compared to Tecoflex membranes without a surfactant additive, a decrease in platelet adhesion is indeed observed, although not completely eliminated when PLUR or TETR are present in the membrane, with the adherent platelets maintaining their discoid shape. This micrograph also shows that some apparent surface microporosity develops for the surfactant-doped membranes; however, continuous pores clearly do not form across the membrane even after prolonged soaking, as evidenced by the ability of the corresponding membrane electrodes to maintain their potentiometric ion-selective response for over 2 months.

A second approach examined for improving membrane blood compatibility of polyurethane ISE membranes involves coating membrane surfaces with a cross-linked PEO-based hydrogel layer. This was accomplished by adapting a procedure previously described for undoped polyurethane films[36] which leads to the formation of random cross-linked networks of PEO and the polyether segments of the membrane polyurethane. Figure 3 compares the XPS spectra of a PEO(200K)-coated and uncoated Pellethane membrane. The aliphatic C—C peak was referenced to 285 eV, with the ethereal C—O peak thus found at 286.5 eV. The band observed in the uncoated film's spectrum at 289 eV is assigned to the urethane C=O.[37] As expected, a dramatic increase in the C—O band relative to the C—C band results for the PEO-modified surface. It should be noted that XPS spectra from fully formulated ion-selective membranes (with plasticizer and ionophore) could not be obtained due to problems apparently arising from outgassing of the plasticizer-doped films. Nonetheless, on the basis of the XPS data, it appears that PEO can in fact be grafted to the polyurethane materials via the photo-cross-linking reaction.

After dehydration, PEO-coated blank polyurethane (Tecoflex or Pellethane) films, like the one analyzed above by XPS, exhibit a ruffled surface when examined under the scanning electron microscope. Similarly, PEO-coated fully functional ion-selective membranes (with plasticizer and ionophore) (see Figure 2f) show the same ruffled surface from the dehydration of the cross-linked PEO-hydrogel surface layer, suggesting that the PEO modification reaction on plasticized polyurethane membranes is just as effective as on the blank membranes, although not verifiable via XPS. From the SEM micrographs, the thickness of the outer cross-linked PEO layer (when dry) was estimated to be in the order of 3 μm.

The protein- and platelet-resistant character of PEO is widely recognized. Its unique properties in this respect have been reviewed (refs 38–40 and references therein) and will not be discussed here. Coating of Pellethane and Tecoflex membranes containing either TDDA or VAL with PEO(200K) produced, in every case, a drastic reduction in platelet adhesion after contact with PRP. As illustrated in Figure 2f, surfaces remained mostly clean, with only an occasional small platelet cluster present. It is important to note here that the ability to prepare functional membranes with a low plasticizer content (8% w/w for Tecoflex-based membranes) is extremely useful for the proposed surface modification procedure, as it was not possible to obtain a thorough coating of the surfaces with cross-linked PEO(200K) when the procedure was applied to membranes with higher amounts of

(36) Brinkman, E.; Poot, A.; van der Does, L.; Bantjes, A. *Biomaterials* **1990**, *11*, 200.
(37) Han, D. K.; Park, K. D.; Ahn, K. D.; Jeong, S. Y.; Kim, Y. H. *J. Biomed. Mater. Res.* **1989**, *23*, 87.
(38) Morra, M.; Occhiello, E.; Garbassi, F. *Clin. Mater.* **1993**, *14*, 255.
(39) Engbers, G. H.; Feijen, J. *Int. J. Artif. Org.* **1991**, *14*, 199.
(40) Amiji, M.; Park, K. *Biomaterials* **1992**, *13*, 682.

plasticizer (50%). A similar patchy, incompletely coated surface was obtained in initial experiments when PEO(18.5K) was used instead of the higher molecular weight PEO(200K). The SEM micrograph of such a surface is shown in Figure 2e and serves to illustrate the remarkable difference in platelet adhesiveness between the coated and uncoated areas. It has been found, however, that more uniform PEO coatings can be obtained even when the low molecular weight PEO (18.5K) is used if the membranes are also doped first with 10% (w/w) PLUR or TETR. It appears that the higher concentration of polyether segments within the membrane matrices (resulting from the presence of PLUR or TETR) enhances the cross-linking efficiency with PEO, facilitating a more complete PEO surface coating. As indicated above, the use of the TETR- or PLUR-doped matrices is made unnecessary, however, by using the higher molecular weight PEO-(200K) in the photo-cross-linking procedure.

Table 2 summarizes some potentiometric response properties of the various modified and unmodified Tecoflex-based ISE membranes. Surface treatment with PEO(200K) produced a slight decrease in the slope of both pH-selective and K^+-selective electrodes. The potentiometric selectivity coefficients of both ionophore membrane systems remained essentially unchanged after the PEO surface modification. Continuous 20-h monitoring of the potential of such electrodes in stirred HEPES saline solutions, pH 7.4, showed relatively low potential drift rates for these membranes (<2 mV over 24-h period). Figure 4 further illustrates that PEO-coated Tecoflex membranes maintained adequate response times, with t_{90} times (time required to achieve 90% of equilibrium potential change) of 10 s or less, only a small increase in response time compared to uncoated membranes. It should be noted that similar experiments performed in solutions containing 8% (w/v) bovine serum albumin indicated that the response times and slopes of such PEO-coated films are also not affected by the presence of protein. The fast response times are consistent with the presence of a very thin hydrogel surface layer with a high equilibrium water content. This is in sharp contrast to results previously reported for conventional PVC-based ISE membranes physically overlaid with 50-μm-thick layers of 2-hydroxyethyl methacrylate/methyl methacrylate copolymers, which displayed response times of about 15 min and decreased slopes compared to uncoated membranes.[17]

Table 2 also provides analytical response characteristics for PLUR-doped membranes (C, H), which, as mentioned above, exhibit a large decrease in response slope and selectivity compared to membranes not containing these copolymer additives (especially in the case of K^+-selective membranes). Obviously, such a loss in electroanalytical performance would compromise the application of such membranes in blood measurements. The observed increased cationic interference can likely be attributed to the known ability of flexible polyether chains to coordinate cations (ref 41 and references therein) and the overall increased polarity of the membrane.[42] This degradation in response characteristics coupled with the relatively modest improvement in platelet adhesion properties (compared to PEO-coated membranes) would make the PLUR- and TETR-doped membranes less attractive candidates for preparation of intraarterial ISE devices.

In summary, on the basis of the results presented above, it would appear that Tecoflex polyurethane-based ISE membranes coated with a thin layer of cross-linked high molecular weight PEO exhibit a unique combination of adequate electroanalytical performance and potentially good blood-contacting properties to be useful in preparing intraarterial ISE devices. Use of such a coated matrix to fabricate previously reported implantable polymer membrane ion- and combined ion/gas-sensing catheters, including a novel dual lumen pH/P_{CO_2} sensing design,[9,10] may result in sensing devices that will function reliably in vivo without systemic anticoagulation.

ACKNOWLEDGMENT

The scanning electron microscope used in this work was acquired under grant BSR-83-14092 from the National Science Foundation. We gratefully acknowledge financial support for this work from the National Institutes of Health (GM 28882-14).

Received for review March 28, 1995. Accepted June 15, 1995.[⊗]

AC950304H

(41) Adams, M. D.; Wade, P. W.; Hancock, R. D. *Talanta* **1990**, *37*, 875.
(42) Bakker, E.; Xu, A.; Pretsch, E. *Anal. Chim. Acta* **1994**, *295*, 253.

[⊗] Abstract published in *Advance ACS Abstracts,* July 15, 1995.

Anal. Chem. 1995, *67*, 3115–3122

Electron Transfer Kinetics at Modified Carbon Electrode Surfaces: The Role of Specific Surface Sites

Peihong Chen, Mark A. Fryling, and Richard L. McCreery*

Department of Chemistry, The Ohio State University, 120 West 18th Avenue, Columbus, Ohio 43210

The electron transfer (ET) kinetics of $Ru(NH_3)_6^{3+/2+}$, $IrCl_6^{2-/3-}$, $Fe(CN)_6^{3-/4-}$, $Fe_{aq}^{2+/3+}$, and $V_{aq}^{2+/3+}$ were examined on several modified glassy carbon surfaces. The kinetics of the aquated ions were very sensitive to the density of surface oxides, while those of the other redox systems were not. In particular, chemical derivatization of surface carbonyl groups decreased the rate of electron transfer with $Fe^{3-/2-}$ by 2–3 orders of magnitude but had little effect on $Ru(NH_3)_6^{3-/2-}$ or $IrCl_6^{2-/3-}$. The electron tranfer rates for $Fe^{3+/2-}$ correlated with surface C=O density determined by resonance Raman spectroscopy. Neutral, cationic, and anionic nonspecific adsorbers decreased the rates of ET with the aquated ions approximately equally but had little effect on $Ru(NH_3)_6^{2-/3-}$. The redox systems studied were classified into two groups: those which are catalyzed by surface carbonyl groups and those which are not. Possible catalytic mechanisms are considered.

A significant effort by many laboratories has been directed toward understanding the relationship between surface structure and electron transfer reactivity for carbon electrodes.[1-9] Complex surface chemistry and an often unknown level of surface impurities have made it difficult to determine the important structural variables controlling carbon electrode reactivity. At least three major phenomena affect electron transfer (ET) reactivity, and these vary in importance for different redox systems and solution conditions. First, many redox systems (e.g., $Fe(CN)_6^{3-/4-}$, ascorbic acid, dopamine) are very sensitive to surface cleanliness, and observed ET rates are strongly dependent on surface history.[4,10] Second, the microstructure of the carbon has a large effect on most redox systems, with the basal plane of highly ordered pyrolytic graphite (HOPG) exhibiting much slower ET than glassy carbon (GC).[10-12] Third, some redox systems are sensitive to the presence of surface oxides, which act as catalysts for electron transfer[13-15] or modify the surface charge.[16] Unfortunately, many common electrode surface preparation procedures affect more than one of these three variables. For example, electrochemical pretreatment (ECP) by anodization of the surface[7,8,17] changes the carbon microstructure, removes impurities, and forms surface oxides.[3] Thus it is difficult to determine which factor underlies the kinetic changes induced by ECP.

In several previous reports, we examined the effects of carbon microstructure,[10-12,18] cleanliness,[10,19] and surface oxidation[9,20] on a variety of redox systems, mostly transition metal complexes. Several conclusions which are relevant to the present work should be summarized here. First, 17 inorganic complexes and four organic redox systems exhibit much slower ET rates on HOPG compared to GC, a shortfall we attribute to the low density of electronic states in HOPG.[12] Second, disordering of HOPG by laser activation or ECP increases ET rates for most systems to values close to those observed on clean GC. Third, $Fe_{aq}^{2-/3-}$, $V_{aq}^{2+/3+}$, and $Eu_{aq}^{2-/3+}$ are further accelerated by the presence of surface oxides to ET rates well above the outer-sphere values predicted from homogeneous self-exchange rates via Marcus theory.[9] Fourth, this oxide catalysis is not consistent with mechanisms based on redox mediation, hydrophobic effects, or double layer effects.

Combined with the extensive literature on electrochemistry at carbon, these observations lead to a working hypothesis on the structural basis of ET reactivity at carbon.[4,21] Outer-sphere systems such as $Ru(NH_3)_6^{2+/3-}$, $IrCl_6^{2-/3-}$, etc. are sensitive to the electronic structure of the carbon (due to the electronic density of states, DOS) but are otherwise insensitive to surface functional groups or impurities. The effect of low DOS is nonspecific and applies to all 21 redox systems examined to date. In addition,

(1) McCreery, R. L. In *Electroanalytical Chemistry*; Bard, A. J., Ed.; Dekker: New York, 1991; Vol. 17, pp 221–374.
(2) Kinoshita, K. *Carbon: Electrochemical and Physicochemical Properties*; Wiley: New York, 1988.
(3) Sarangapani, S.; Akridge, J. R.; Schumm, B., Eds. *Proceedings of the Workshop on the Electrochemistry of Carbon*; The Electrochemical Society: Pennington, NJ, 1984.
(4) Hu, I. F.; Kuwana, T. *Anal. Chem.* **1986**, *58*, 3235.
(5) Wightman, R. M.; Deakin, M. R.; Kovach, P. M.; Kuhr, W. G.; Stutts, K. J. *J. Electrochem. Soc.* **1984**, *131*, 1578.
(6) Hu, I. F.; Karweik, D. H.; Kuwana, T. *J. Electroanal. Chem.* **1985**, *188*, 59.
(7) Engstrom, R. C. Strasser, V. A. *Anal. Chem.* **1984**, *56*, 136.
(8) Cabaniss, G. E.; Diamantis, A. A.; Murphy, W. R., Jr.; Linton R. W.; Meyer, T. J. *J. Am. Chem. Soc.* **1985**, *107*, 1845.
(9) McDermott, C. A.; Kneten, K. R.; McCreery, R. L. *J. Electrochem. Soc.* **1993**, *140*, 2593.
(10) Rice, R. J.; Pontikos, N. M.; McCreery, R. L. *J. Am. Chem. Soc.* **1990**, *112*, 4617.
(11) Kneten, R. K.; McCreery, R. L. *Anal. Chem.* **1992**, *64*, 2518.
(12) Cline, K. K.; McDermott, M. T.; McCreery, R. L. *J. Phys. Chem.* **1994**, *98*, 5314.
(13) Evans, J. F.; Kuwana, T. *Anal. Chem.* **1977**, *49*, 1632.
(14) Tse, D. C. S.; Kuwana, T. *Anal. Chem.* **1978**, *50*, 1315.
(15) Armstrong, F. A.; Bond, A. M.; Hill, H. A. O.; Olive, B. N.; Psalti, I. S. M. *J. Am. Chem. Soc.* **1989**, *111*, 9185.
(16) Deakin, M. R.; Stutts, K. J.; Wightman, R. M. *J. Electroanal. Chem.* **1985**, *182*, 113.
(17) Barbero, C.; Silber, J. J.; Sereno, L. *J. Electroanal. Chem.* **1988**, *248*, 321.
(18) Rice, R. J.; McCreery, R. L. *Anal. Chem.* **1989**, *61*, 1637.
(19) Poon, M.; McCreery, R. L.; Engstrom, R. *Anal. Chem.* **1988**, *60*, 1725.
(20) Allred, C. D.; McCreery, R. L. *Anal. Chem.* **1992**, *64*, 444.
(21) McCreery, R. L.; Cline, K. K.; McDermott, C. A.; McDermott, M. T. *Colloids Surf. A* **1994**, *93*, 211.

0003-2700/95/0367-3115$9.00/0

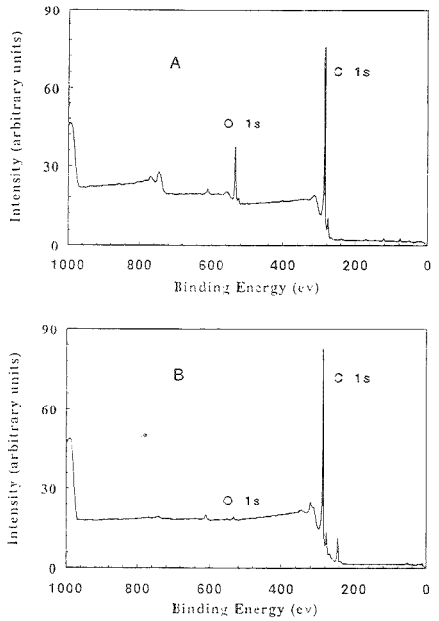

Figure 1. XPS survey spectra of (A) polished GC and (B) argon-sputtered GC.

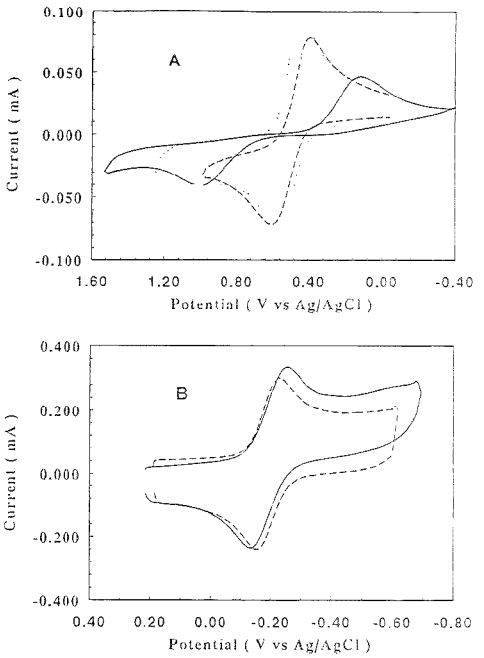

Figure 2. Voltammograms of (A) 5 mM $Fe^{3-/2-}$ in 0.2 M $HClO_4$ at polished (dashed line), argon-sputtered (solid line), and argon-sputtered/ECP (dotted line) GC electrodes (scan rate, 0.2 V/s; ECP procedure was seven cycles from 0 to 2.2 V in 1.2 M H_2SO_4 at 0.2 V/s) and (B) 1 mM $Ru(NH_3)_6^{3-/2-}$ in 1 M KCl at polished (dashed line) and argon-sputtered (solid line) GC electrodes (scan rate, 20 V/s).

there are many redox reactions, such as that of $Fe_{aq}^{2+/3-}$, which are catalyzed by specific interactions with surface oxides[9] and are therefore very sensitive to surface chemistry. The current experiments were designed to test this hypothesis in detail for several representative redox systems, including $Ru(NH_3)_6^{2+/3-}$ and $Fe_{aq}^{2+/3-}$. Various preparation techniques were used to vary the nature and density of surface functional groups before observing ET reactivity. By combining independent measures of oxide functional groups based on Raman spectroscopy and XPS with observations of kinetic behavior, the relationship between surface structure and ET rate was revealed.

EXPERIMENTAL SECTION

In all cases except in the study of argon-sputtered GC electrodes, the GC electrodes used were from Bioanalytical Systems Inc. (MF2070). In the case of argon sputtering pretreatment, Tokai GC-20 plates from Applied Industrial Material Co. were used. Polished GC electrodes were prepared by initial sanding with SiC paper when necessary and then polishing with successive slurries of 1, 0.3, and 0.05 μm alumina (Buehler) in Nanopure water on Microcloth polishing cloth (Buehler). Polished GC electrodes were sonicated in Nanopure water (Barnstead) for about 10 min before being placed into the electrochemical cell or further treatment. During transfers between each step, the surfaces of GC electrodes were kept wet to reduce contamination from air.

Argon sputtering treatment was carried out in the vacuum chamber of an XPS/Auger spectrometer (VG Scientific). The vacuum chamber was pumped to 10^{-9} Torr, then filled with argon gas to a pressure of 2×10^{-6} Torr. The GC surface was sputtered with an AG21 argon source (VG Scientific) at a focus energy of 3.6 kV and target current of 30 μA for 10 min. XPS survey spectra were obtained before and after argon sputtering with a VG Scientific XPS spectrometer (Mg X-ray radiation source). The GC pieces were transferred into 0.2 M $HClO_4$ solution immediately after they were taken from the vacuum system, and electrochemical measurements were carried out within 5 min.

2,4-DNPH derivatization of GC electrode surfaces and Raman measurement of the derivatized surfaces were performed as described previously.[22] Preceding electrochemical experiments on derivatized electrodes, the electrodes were rinsed thoroughly in 20 mL of Nanopure water twice before transfer into the electrochemical cell. To derivatize the electrode surface with 3,5-dinitrobenzoyl chloride, the electrode was polished and rinsed with pyridine, immersed in 0.1 M 3,5-dinitrobenzoyl chloride/pyridine solution, and heated on a hot plate for 1 min. After standing in the solution for 1 h, the electrode was thoroughly rinsed with pyridine followed by Nanopure water.

2,6-Anthraquinone disulfonate (AQDS) was adsorbed to GC electrodes by placing polished GC electrodes in 10 mM 2,6-AQDS aqueous solution for 10 min and rinsing in 30 mL of Nanopure water successively three times. The electrodes were then transferred into an electrochemical cell containing 0.1 M $HClO_4$ for voltammetry.

Methylene blue (MB) was adsorbed on GC electrodes by dipping polished GC in 0.1 mM MB in water for 10 min and rinsing

(22) Fryling, M. A.; Zhao, J.; McCreery, R. L. *Anal. Chem.* **1995**, *67*, 967.

Table 1. Electron Transfer Rate Constants (in cm/s) of Some Inner-Shere and Outer-Sphere Redox Systems at Modified GC Electrode

	polished GC	argon-sputtered GC	DNPH-treated GC	dinitrobenzoyl chloride-treated GC	2,6-AQDS-adsorbed GC	methylene blue-adsorbed GC	BMB-adsorbed GC
$Ru(NH_3)_6^{2+/3+}$	0.24 ± 0.07^a	0.039 ± 0.005	0.13 ± 0.01	0.15 ± 0.08	0.15 ± 0.02	$>0.093 \pm 0.005$	0.13 ± 0.02
$IrCl_6^{2-/3-}$	0.50 ± 0.06	0.11 ± 0.13	0.21 ± 0.04		0.25 ± 0.05	0.22 ± 0.03	0.20 ± 0.04
$Fe(CN)_6^{3-/4-}$	0.10 ± 0.02	0.037 ± 0.009	0.026 ± 0.006	0.084 ± 0.030	0.047 ± 0.008	0.078 ± 0.005	0.076 ± 0.004
$Fe_{aq}^{2+/3+}$	$(2.5 \pm 0.3) \times 10^{-3}$	$(2.1 \pm 1.3) \times 10^{-6}$	$(1.6 \pm 1.2) \times 10^{-5}$	$(1.1 \pm 0.5) \times 10^{-3}$	$(7.4 \pm 2.8) \times 10^{-4}$	$(3.8 \pm 0.3) \times 10^{-4}$	$(9.1 \pm 3.0) \times 10^{-5}$
$Eu_{aq}^{2-/3-}$	$(8.4 \pm 1.4) \times 10^{-4}$		$<6.0 \times 10^{-6}$				
$V_{aq}^{2+/3+}$	$(6.8 \pm 4.0) \times 10^{-4}$	$<2.0 \times 10^{-5}$	$<1.0 \times 10^{-6}$	$(7.8 \pm 2.4) \times 10^{-5}$	$(2.1 \pm 1.0) \times 10^{-2}$	$(2.9 \pm 1.3) \times 10^{-6}$	$<1.5 \times 10^{-6}$

[a] Standard derivatization, $N = 3$.

with 30 mL of Nanopure water three times. Raman spectra of MB were obtained with a spectrometer based on a single-stage spectrograph (Instruments SA, HR 640) with a 300/mm (1.0 μm blaze) grating coupled to a CCD (Photometric CH260 camera head/EEV 05-10 CCD with 296 × 1152 pixels, 0.66 cm × 2.59 cm active area).[23] Excitation was provided by a tunable Ti:sapphire laser (Coherent Model 890) operating at 691 nm, pumped by a 5 W argon ion laser (Coherent Model 90).

To adsorb 1,4-bis(2-methylstyryl)benzene (BMB) on GC electrodes, polished GC was first immersed in 1 mM BMB in acetone for 10 min and then rinsed twice with 10 mL of acetone, followed by two rinses with 30 mL of Nanopure water.

The redox systems studied were as follows: 1 and 5 mM Fe^{2+} in 0.2 M $HClO_4$ solutions made from $FeNH_4(SO_4)_2{\cdot}12H_2O$ (Mallinckrodt, Inc.) and 70% $HClO_4$ (GFS Chemicals); 3 mM V^{3+} in 0.2 M $HClO_4$ solution made from VCl_3 (Aldrich Chemical Co.); 5 mM Eu^{3+} in 0.2 M $HClO_4$ solution made from $Eu(NO_3)_3{\cdot}5H_2O$ (Aldrich); 1 mM $Ru(NH_3)_6^{3+}$ in 1 M KCl solution made from $Ru(NH_3)_6Cl_3$ (Strem Chemicals); 0.5 mM $IrCl_6^{2-}$ in 1 M KCl solution made from K_2IrCl_6 (Aldrich); 2 mM $Co(en)_3^{3+}$ in 1 M KCl solution made from $Co(en)_3Cl_3$ (J. T. Baker); $Fe(CN)_6^{3-/4-}$ in 1 M KCl made from $K_4Fe(CN)_6$ (J. T. Baker).

Other solutions included 10 mM 2,6-AQDS solution (Aldrich, recrystallized from water after being filtered through activated charcoal);[24] 0.1 mM methylene blue (Aldrich); 10 mM 2,4-DNPH (J. T. Baker) with 1% HCl (J. T. Baker) in dry ethanol (Quantum Chemical); 0.1% KOH (Jenneile Enterprises) in dry ethanol, 0.1 M 3,5-dinitrobenzoyl chloride (Aldrich) in pyridine (Mallinckrodt), and 1 M H_2SO_4 (Mallinckrodt). All solutions were prepared daily with distilled Nanopure water unless noted otherwise.

Cyclic voltammetry was performed with a computer triggered function generator (Tektronix) and Labmaster A/D converter. A Bioanalytical Systems Ag/AgCl (3 M NaCl) reference electrode and a platinum counter electrode were used. Electron transfer rate constants (k°, cm s^{-1}) were determined from voltammetric data using the commercial simulation program Digisim (Bioanalytical Systems). k° for the simulation was varied to match the ΔE_p values for experimental and simulated voltammograms. Although the value of the transfer coefficient (α) does not greatly affect ΔE_p, it was assumed to equal 0.5.

RESULTS

Several different manipulations of surface oxide density were carried out, and then the surface was characterized with XPS or Raman spectroscopy before kinetic evaluation with $Ru(NH_3)_6^{2+/3+}$, $Fe_{aq}^{2+/3+}$, $V_{aq}^{2+/3+}$, $Fe(CN)_6^{3-/4-}$, etc. Surface manipulations are separated into three groups: nonspecific removal of surface oxides by Ar^+ ion sputtering, chemical derivatization of specific surface oxides, and nonspecific adsorption of surface monolayers.

Ar^+ Sputtering. XPS survey spectra of polished GC-20 before and after Ar^+ sputtering in UHV are shown in Figure 1. Sputtering reduces the observed surface O/C ratio from 14% to less than 1%. After the GC specimen was quickly transferred (through air) to an electrochemical cell, the voltammograms of Figure 2 were obtained. Sputtering causes a 3 order of magnitude decrease in the ET rate for $Fe_{aq}^{2+/3+}$, while it has a relatively small effect (a factor of 6) on $Ru(NH_3)_6^{2+/3+}$. Electrochemical oxidation of the sputtered surface restores the observed $Fe_{aq}^{2+/3+}$ rate to a value somewhat higher than that on a polished surface. The observed rate constants are listed in Table 1, along with those for $IrCl_6^{2-/3-}$, $V_{aq}^{2+/3+}$, and $Fe(CN)_6^{3-/4-}$ following similar treatments. These results reveal that Ar^+ sputtering decreases the rate constants of $Fe_{aq}^{2+/3+}$ and $V_{aq}^{2+/3+}$ by a much larger factor than those of $IrCl_6^{2-/3-}$, $Ru(NH_3)_6^{2+/3+}$, or $Fe(CN)_6^{3-/4-}$. As is apparent from Figure 2A and several reports in the literature, electrochemical oxidation of GC dramatically increases k° for $Fe_{aq}^{2+/3+}$, $V_{aq}^{2+/3+}$, and $Eu_{aq}^{2-/3+}$. After ECP conditions similar to those used here, we observed k° values of 0.012, 0.009 and 0.004 cm/sec, for $Fe_{aq}^{2+/3+}$, $V_{aq}^{2-/3-}$ and $Eu_{aq}^{2-/3+}$, respectively.[9]

Specific Surface Derivatization. To examine the role of specific oxygen-containing functional groups on electrode kinetics, GC surfaces were treated with two organic reagents. Dinitrophenylhydrazine (DNPH) has been shown to specifically derivatize surface carbonyl groups, but not lactones, carboxylates, or alcohol groups.[22] DNPH forms a resonance Raman active adduct which may be observed quantitatively at 1–10% surface coverage by monitoring the peak area of the 1140 cm^{-1} N–N stretch. The voltammograms of Figure 3 and the fourth column of Table 1 indicate that DNPH treatment of a polished GC surface decreases the rates of $Ru(NH_3)_6^{3+/2+}$ and $IrCl_6^{2-/3-}$ by about 50%. However, the rates of $Fe_{aq}^{2+/3+}$, $Eu_{aq}^{2-/3-}$, and $V_{aq}^{2+/3+}$ decreased by factors of more than 100 following DNPH derivatization. We noted during control experiments that ethanol decreased the $Fe_{aq}^{2+/3+}$ rate by about a factor of 10 without DNPH treatment. The experiment was repeated with a DNPH reagent in 2 M HCl without ethanol. The rate following DNPH treatment with enthanol absent was 3.6 × 10^{-5}, while a control experiment with 2 M HCl yeilded $k^\circ = 1.8 \times 10^{-3}$. The 2M HCl treatment had no effect on the $Ru(NH_3)_6^{2-/3-}$ rate constant. Thus DNPH treatment consistently reduced the $Fe_{aq}^{2+/3+}$ by a factor of 70–100 whether or not ethanol was present.

(23) Frank, C. J.; Redd, D. C. B.; Gansler, T. S.; McCreery, R. L. *Anal. Chem.* **1994**, *66*, 319.

(24) He, P.; Crooks, R. M.; Faulkner, L. R. *J. Phys. Chem.* **1990**, *94*, 1135.

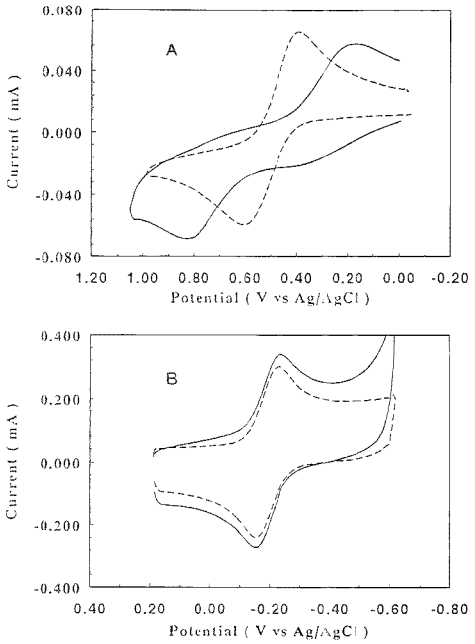

Figure 3. Voltammograms of (A) 5 mM $Fe^{3-/2+}$ in 0.2 M $HClO_4$ at polished (dashed line) and DNPH-treated (solid line) GC electrodes (ν = 0.2 V/s) and (B) 1 mM $Ru(NH_3)_6^{3+/2+}$ in 1 M KCl at polished (dashed line) and DNPH-treated (solid line) GC electrodes (ν V/s).

Table 2. Correlation between Raman Detected Carbonyl Density and the Electron Transfer Rate Constant of $Fe_{aq}^{2+/3+}$

surface treatment	area under DNPH–carbon adduct 1140 cm^{-1} Raman band (e^-)	electron transfer rate for $Fe_{aq}^{2+/3+}$ (cm/s)[a]
polished	270 ± 32[b]	2.5×10^{-3}
ECP 10 s, 2.2 V, 1 M NaOH	274 ± 63	2.0×10^{-3}
ECP 10 s, 1.5 V, 1.5 M H_2SO_4	525 ± 52	3.6×10^{-3}
ECP 10 s, 2.2 V, 1 M, HNO_3	575 ± 154	3.2×10^{-3}
ECP 10 s, 2.2 V, 1 M, $NaNO_2$	848 ± 174	3.6×10^{-2}
ECP 5 s, 1.8 V, 1 M H_2SO_4	1716 ± 351	7.1×10^{-3}
ECP 10 s, 2.2 V, 1 M H_2SO_4	3175 ± 416	1.0×10^{-2}

[a] Standard derivatization, $N \geq 3$. [b] Before DNPH derivatization. Two identical samples were electrochemically pretreated, and then one was used for $Fe^{2+/3-}$ voltammetry, the other for DNPH derivatization and Raman spectroscopy.

while neither DNPH nor ethanol affected the $Ru(NH_3)_6^{2+/3+}$ rate significantly.

In a previous report, we demonstrated that surface carbonyl density could be determined from the area of the 1140 cm^{-1} band of the resonance-enhanced, surface-bound DNPH.[22] The relationship between k° for $Fe_{aq}^{2+/3+}$ and DNPH coverage is shown in Table 2 and Figure 4. The carbonyl density was increased by ECP under various conditions (shown in Table 2), and then $Fe_{aq}^{2+/3-}$ voltammograms were obtained. An identically treated surface was subjected to DNPH derivatization, and then Raman spectra were obtained to evaluate C=O coverage. The 1140 cm^{-1} peak area indicates the density of surface C=O groups, with an

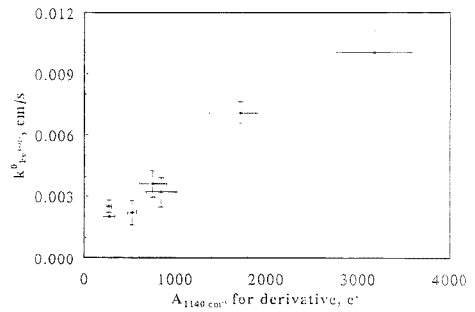

Figure 4. Correlation between the area of 1140 cm^{-1} DNPH–carbon adduct Raman band and rate constant of $Fe^{3+/2-}$ at carbon electrodes after ECP with various procedures. The ECP procedures are listed in Table 2. Rate constants were determined *before* DNPH derivatization. The 1140 cm^{-1} Raman band was observed *after* DNPH derivatization and indicates the surface carbonyl density.

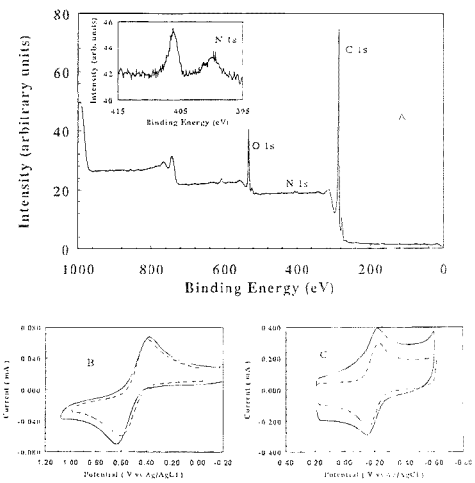

Figure 5. (A) XPS survey spectrum of DNBC-treated GC surface. Inset shows magnified nitrogen 1s region. (B) Voltammograms of 5 mM $Fe^{3+/2-}$ in 0.2 M $HClO_4$ on polished (dashed line) and DNBC-treated (solid line) GC electrodes (ν = 0.2 V/s). (C) Voltammograms of 1 mM $Ru(NH_3)_6^{3+/2+}$ in 1 M KCl on polished (dashed line) and DNBC-treated (solid line) GC electrodes (ν = 20 V/s).

area of 270 e corresponding to ~1% of a monolayer. As the surface C=O increases, k° for $Fe_{aq}^{2+/3+}$ also increases, monotonically and roughly linearly. The results establish a direct correlation between $Fe_{aq}^{2+/3+}$ ET rate and surface carbonyl density.

Although it was not studied in as much detail, dinitrobenzoyl chloride (DNBC) is a reagent which should react with surface OH groups to form a dinitrophenyl ester.[25] After reaction with DNBC, polished GC exhibited a nitrogen 1s peak from the surface-bound NO_2 group, with a surface coverage of ~1% (Figure 5). Voltammetry showed minor effects of DNBC on $Fe_{aq}^{2+/3+}$ and $Ru(NH_3)_6^{3+/2+}$ ET rates. The kinetic effects of DNBC derivatization are summarized in Table 1 for four redox systems.

(25) Siggia, S.; Hanna, J. G. *Quantitative Organic Analysis via Functional Group*; Wiley: New York, 1979; pp 31–40, 61–71.

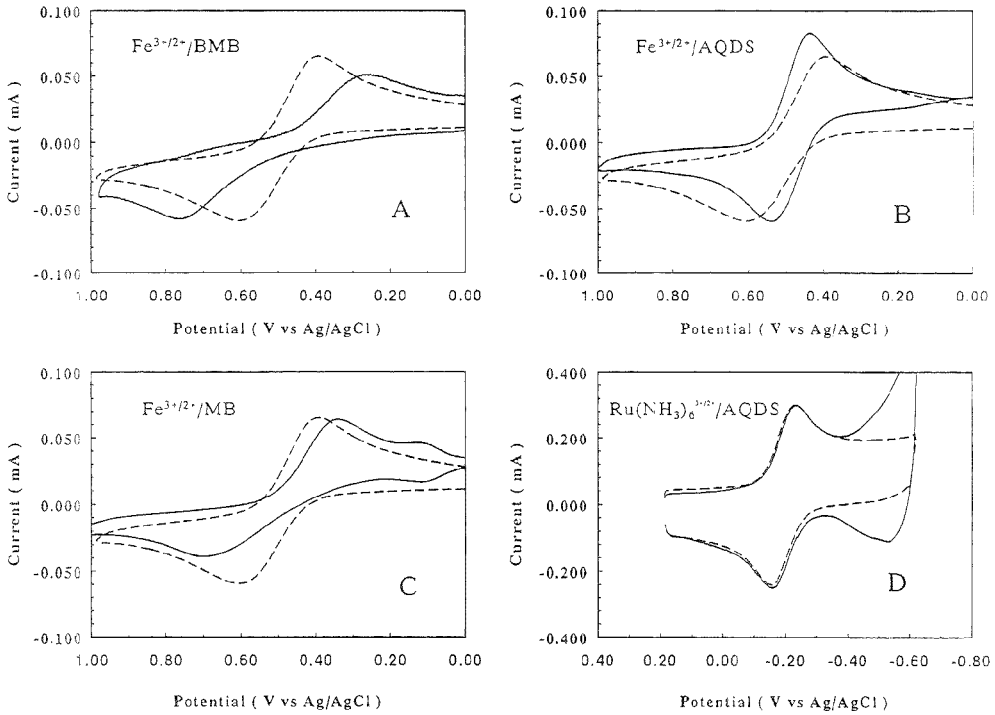

Figure 6. Voltammograms of (A) 5 mM $Fe^{3-/2+}$ in 0.2 M $HClO_4$ at polished (dashed line) and BMB treated (solid line) GC electrodes (ν = 0.2 V/s); (B) 5 mM $Fe^{3+/2+}$ in 0.2 M $HClO_4$ at polished (dashed line) and AQDS-treated (solid line) GC electrodes (ν = 0.2 V/s); (C) 5 mM $Fe^{3+/2-}$ in 0.2 M $HClO_4$ at polished (dashed line) and methylene blue-treated (solid line) GC electrodes (ν = 0.2 V/s); and (D) 1 mM $Ru(NH_3)_6^{3+/2+}$ in 1 M KCl at polished (dashed line) and AQDS-treated (solid line) GC electrodes (ν = 20 V/s). Conditions for adsorption of BMB, AQDS, and MB are indicated in the text.

Nonspecific Adsorption. The surface coverage of DNPH and DNBC on polished GC is on the order of the original oxide coverage, a few percent. We have demonstrated previously that anthraquinone 2,6-disulfonate (AQDS) and bis(4-methylstyryl)-benzene (BMB) physisorb on GC at monolayer levels.[26,27] AQDS forms a monolayer when adsorbed from dilute aqueous solution and can be detected voltammetrically. BMB forms a monolayer from acetone solution and is observable with Raman spectroscopy.[28] Figure 6 shows that methylene blue (MB) adsorbs strongly to polished GC from 0.1 mM aqueous solution, with the voltammogram of Figure 6A indicating a surface coverage of 190 pmol/cm^2. Resonance Raman spectra of adsorbed MB before (Figure 6B) and after (Figure 6C) voltammetry in $Fe_{aq}^{2+/3+}$ solution indicate that the MB is strongly adsorbed and does not desorb during voltammetry in a solution which does not contain MB.

The kinetic effects of these nonspecific adsorbers on $Fe_{aq}^{2-/3+}$ and $Ru(NH_3)_6^{3-/2+}$ are shown in Figure 7, and Table 1. BMB and MB have small negative effects on $Ru(NH_3)_6^{3+/2-}$ and $IrCl_6^{2-/3-}$ rate constants but decrease the $Fe_{aq}^{2+/3+}$ and $V_{aq}^{2-/3+}$ rates by about an order of magnitude. AQDS adsorption also decreases the $Ru(NH_3)_6^{2+/3-}$ and $IrCl_6^{2-/3-}$ rate constants slightly but *increases* the $Fe_{aq}^{2-/3+}$ and $V_{aq}^{2-/3-}$ rates.

Finally, adsorption of $Fe^{2+/3+}$ and $Ru(NH_3)_6^{3-/2+}$ was examined using the semiintegral approach described elsewhere.[29] The semiintegral of a $Ru(NH_3)_6^{3-/2-}$ voltammogram (Figure 8A) exhibits the ideal sigmoidal shape expected for a diffusion-controlled process. After ECP, a similar sigmoidal semiintegral was observed, with a slight peak on the plateau indicating weak adsorption of $Ru(NH_3)_6^{3+/2+}$ to the oxidized surface (Figure 8B). The semiintegral for the oxidation of Fe_{aq}^{2+} on a polished GC surface (Figure 8C) clearly indicates adsorption, which is increased significantly by ECP (Figure 8D). A rough estimate of the amount of adsorbed Fe^{2+} for the polished surface shown in Figure 8C yields ~40 pmol/cm^2.

DISCUSSION

The redox systems in Table 1 fall into two distinct groups, which differ in their sensitivity to surface chemistry. $Ru(NH_3)_6^{3+/2+}$, $IrCl_6^{2-/3-}$, and $Fe(CN)_6^{3-/4-}$ exhibit relatively small decreases in k° upon Ar^+ sputtering, derivatization of surface C=O or C—OH, and nonspecific adsorption. It is somewhat surprising that a

(26) McDermott, M. T.; Kneten, K.; McCreery, R. L. *J. Phys. Chem.* **1992**, *96*, 3124.
(27) McDermott, M. T.; McCreery, R. L. *Langmuir*, in press.
(28) Kagan, M. R.; McCreery, R. L. submitted for publication.
(29) Bowling, R.; McCreery, R. L. *Anal. Chem.* **1988**, *60*, 605.

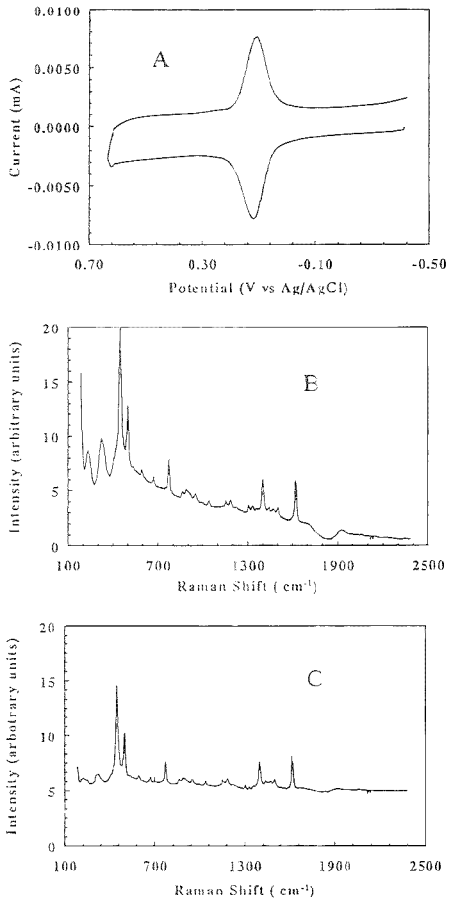

Figure 7. (A) Voltammogram of adsorbed methylene blue on GC obtained in 0.2 M $HClO_4$ after the electrode is immersed in 0.1 mM methylene blue solution for 10 min and washed three times in 30 mL of Nanopure water. (B) Raman spectrum of methylene blue-treated GC surface. (C) Raman spectrum of methylene blue-treated GC surface after six $Fe^{3-/2-}$ voltammograms had been acquired on the same surface.

monolayer of an organic adsorbate such as BMB or AQDS decreases the rate for these systems by factors of only about 2–5. The decrease is independent of the charge of the adsorbate (−2, 0, or +2), which rules out a major contribution from double layer effects.[16] It is probably an oversimplification to attribute the change solely to the increase in electron tunneling distance, but such an explanation is quantitatively reasonable. For a tunneling constant of about 1.0 $Å^{-1}$, a monolayer spacer between the electrode and the redox system would decrease the rate by less than an order of magnitude.[20]

Ar^+ sputtering should not deposit a monolayer of adsorbate (ignoring possible contamination during UHV to solution transfer) and should not inhibit ET. However, Raman spectroscopy reveals that Ar^+ sputtering disorders GC, with an undetermined effect on ET rates. We can conclude from the Ar^+ sputtering treament that reduction of surface oxide level and disordering reduce observed rates for $Ru(NH_3)_6^{3-/2+}$ and $IrCl_6^{2-/3-}$ by less than an order of magnitude. While $Fe(CN)_6^{3-/4-}$ behaves similarly, previous reports for both carbon and metallic surfaces indicate that the $Fe(CN)_6^{3-/4-}$ often behaves anomalously and should not be considered outer-sphere.[1,12,31] Therefore, we conclude that $IrCl_6^{2-/3-}$ and $Ru(NH_3)_6^{3+/2+}$ are behaving as outer-sphere systems, and $Fe(CN)_6^{3-/4-}$ will be set aside for now. Consistent with this conclusion is the observation that specific surface groups have small effects on $Ru(NH_3)_6^{3+/2+}$ or $IrCl_6^{2-/3-}$, at least for the conditions employed.

The aquated metal complexes $Fe_{aq}^{2+/3+}$, $V_{aq}^{2-/3-}$, and $Eu_{aq}^{2-/3-}$ behave much differently, exhibiting extreme sensitivity to surface chemistry. First, derivatization of carbonyl sites with DNPH decreases the rate for these systems by at least a factor of 100, even though the DNPH surface coverage is only ~1%. When DNPH was used to quantify C=O coverage rather than to block carbonyl groups, $Fe_{aq}^{2+/3+}$ rates tracked C=O density (Figure 4). Nonspecific adsorption of MB or BMB decreased the $Fe_{aq}^{2-/3-}$, $V_{aq}^{2+/3+}$, and $Eu_{aq}^{2+/3-}$ rates more than that of the outer-sphere systems, but not as much as DNPH. In addition, an OH specific reagent had a fairly small effect on $Fe_{aq}^{3+/2+}$ and $V_{aq}^{2-/3-}$. Collectively, these observations indicate the central role of surface C=O groups in accelerated ET to the aquated systems studied.

Unlike BMB and MB, AQDS adsorption *increases* the rate constants for $Fe_{aq}^{3+/2+}$ and $V_{aq}^{2+/3+}$. A similar increase was observed for 1,5-AQDS and for anthraquinone monosulfate. $Fe_{aq}^{2-/3+}$ and $V_{aq}^{2+/3+}$ have very different formal potentials in 1 M $HClO_4$ (+0.5 vs −0.4 vs SCE), so catalysis by anthraquinone is unlikely to involve redox mediation. Since the anthraquinones contain C=O groups, it is possible that they increase the $Fe_{aq}^{2+/3-}$ rate by increasing the "surface" C=O density. As an aside, it was observed that $Fe_{aq}^{2+/3+}$ catalysis occurred when the AQDS was adsorbed from a concentrated (10 mM) solution rather than a dilute solution (10^{-5} M), implying that catalysis is favored by the edge rather than flat orientation for the adsorbed AQDS. For the edge orientation, the carbonyl groups should be more accessible to the $Fe_{aq}^{2+/3+}$.

The correlation between surface carbonyl density and k° for the aquated systems is quite strong. At the limit of very low C=O coverages exhibited for the Ar^+-sputtered and the DNPH-treated surface, the rate for $Fe_{aq}^{2+/3+}$ is between 2×10^{-6} and 2×10^{-5} cm/s. This value is close to the outer-sphere rate observed on Pt and Au surfaces in the absence of chloride catalysis.[32] As noted previously, it is also less than the outer-sphere rates predicted from the homogeneous self-exchange rate by about an order of magnitude.[9] We proposed in a previous publication that surface oxides provided an inner-sphere route for $Fe_{aq}^{2+/3+}$, $Eu_{aq}^{2+/3+}$, and $V^{3+/2+}$, possibly involving a surface C=O and an adjacent OH group.[9] Based on this hypothesis, the nonspecific adsorbers BMB and MB decrease the $Fe_{aq}^{2+/3+}$ rate by blocking C=O sites but apparently not as effectively as covalent bonding to DNPH. In addition, ECP increases the C=O density, thereby increasing inner-sphere catalysis for these systems.

(30) Finklea, H. O.; Hanshew, D. D. *J. Am. Chem. Soc.* **1992**, *114*, 3173.

(31) Peter, L. M.; Durr, W.; Bindra, P.; Gerischer, H. *J. Electroanal. Chem.* **1976**, *71*, 31.

(32) Hung, N. C.; Nagy, Z. *J. Electrochem. Soc.* **1987**, *134*, 2215.

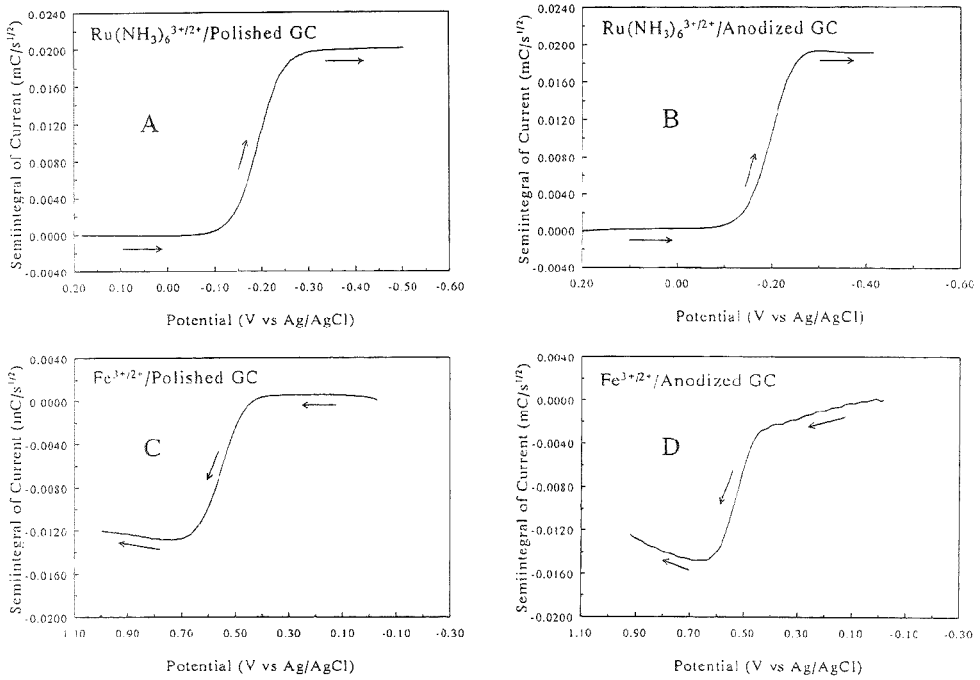

Figure 8. Semiintegrals of (A) 1 mM $Ru(NH_3)_6^{3+/2+}$ in 1 M KCl at polished GC electrode (ν = 20 V/s); (B) 1 mM $Ru(NH_3)_6^{3+/2+}$ in 1 M KCl at GC electrode after ECP (ECP procedure: three cycles from 0 to 2.2 V in 1 M H_2SO_4 at 0.2 V/s); (C) 1 mM $Fe^{3+/2+}$ in 0.2 M $HClO_4$ at polished GC electrode (ν = 2 V/s); and (D) 1 mM $Fe^{3+/2+}$ in 0.2 M $HClO_4$ at GC electrode after ECP (ν = 0.5 V/s).

Although the results strongly support the involvement of surface carbonyl groups in electrocatalysis of the aquated systems examined, there remain several possibilities for the mechanism of carbonyl catalysis. Redox mediation by C=O-containing surface groups is unlikely, given the redox potentials of the systems studied. Mediation by a surface group should yield voltammetric waves near the redox potential of the mediator. On the contrary, the $E_{1/2}$ values for $Fe_{aq}^{2+/3+}$, $Eu_{aq}^{2+/3+}$, and $V_{aq}^{2+/3+}$ occur near their expected values, not those of a mediator. A mechanism involving inner-sphere catalysis by adjacent C=O and OH groups proposed earlier is another possibility. The catalysis of $Fe_{aq}^{2+/3+}$ by chemisorbed Cl^- on Au noted by Nagy et al. provides a possibly useful analogy.[32] In that case, it was concluded that chemisorbed Cl^- provided a bridging group for inner-sphere catalysis, leading to large rate enhancement. For carbon electrodes, a C=O group could be a bridging ligand which is completely blocked by DNPH derivatization. We proposed previously that the carbonyl group could participate with a surface OH group to form a coordination site similar to that of acetoacetonate. However, the greater structural information available from the Raman results, combined with the small effect of surface OH derivatization, does not support OH involvement in catalysis. So, if an inner-sphere route is involved, it would require displacement of an H_2O ligand on the redox center by the surface C=O group. A precedent exists for such a mechanism, for $Cr^{2+/3+}$ binding to amide and ester C=O groups.[33]

A third possibility for surface C=O catalysis of aquated ions is "outer-sphere bridging", in which the inner coordination sphere of the redox center is not displaced during electron transfer.[34] The catalyst acts as a bridge between two reactants, leading to a transition state involving two redox centers and the bridge. Examples include K^+ catalysis of $Fe(CN)_6^{3-/4-}$ self-exchange and anion catalysis of Fe^{2+}, Cr^{2+}, and V^{2+} reduction of $Co(en)_3^{3+}$ and $Co(phen)_3^{3+}$. By analogy to this mechanism, the $M_{aq}^{2+/3+}$ ion would retain its hydration sphere, but the ion would interct with a surface C=O group to promote electron transfer. It is speculation at this point, but such an interaction could involve hydrogen bonding between a complexed water molecule and a surface C=O group. The observation of adsorption of Fe_{aq}^{2+} on GC implies that such an interaction may be quite strong.

In summary, $Ru(NH_3)_6^{2+/3+}$ and $IrCl_6$-3/-4 are examples of outer-sphere electron transfer reactions on carbon surfaces. The rates for these systems are insensitive to surface chemistry on disordered carbon electrodes such as glassy carbon, and the observed rates do not vary greatly with surface oxide coverage or the presence of monolayers of nonspecific adsorbers. In contrast, $Fe_{aq}^{2+/3+}$, $Eu_{aq}^{2+/3+}$, and $V_{aq}^{2+/3+}$ are very sensitive to the density of surface C=O groups, which provide a catalytic route to increase an inherently slow outer-sphere rate. Although the structural details of the catalytic mechanism are not yet known,

(33) Cannon, R. D. *Electron Transfer Reactions*; Butterworths: Boston, 1980; pp 156–161.
(34) Reference 33, p 166 ff.

rate enhancement depends on specific interactions with surface carbonyl groups. The strong effect of this specific interaction underlies the extreme sensitivity of $Fe_{aq}^{2+/3+}$, $Eu_{aq}^{2+/3+}$, and $V_{aq}^{2+/3+}$ electron transfer kinetics to surface chemistry on carbon electrodes.

ACKNOWLEDGMENT

This work was supported by the Surface and Analytical Chemistry Division of the National Science Foundation.

Received for review April 3, 1995. Accepted June 29, 1995.[⊗]

AC950325B

[⊗] Abstract published in *Advance ACS Abstracts*, August 1, 1995.

Anal. Chem. **1995**, *67*, 3123–3132

Carrier Mechanism of Acidic Ionophores in Solvent Polymeric Membrane Ion-Selective Electrodes

Ulrich Schaller,† Eric Bakker,‡ and Ernö Pretsch*

Department of Organic Chemistry, Swiss Federal Institute of Technology (ETH), Universitatstrasse 16, CH-8092 Zurich, Switzerland

The behavior of cation-selective solvent polymeric membrane electrodes based on acidic ionophores is investigated by studying the selectivity coefficients as a function of cationic or anionic additive concentration. This technique allows discrimination between neutral and charged carrier-related mechanisms, resulting in the following findings. Ionophores with a carboxylic acid group act as neutral carriers and sulfonic acid derivatives behave as charged carriers irrespective of the plasticizer used. The Ca^{2+}-selective organophosphate ionophore examined (bis-[4-(1,1,3,3-tetramethylbutyl)phenyl]phosphate) acts in low dielectric constant plasticizers in a mixed mode where the analyte ion forms two different complexes in the membrane phase—one with the charged form of the carrier and the other with the protonated form (neutral ionophore). From these results it can be seen that when developing novel ion-selective electrodes based on acidic ionophores, both cationic and anionic additives as well as plasticizers of high and low dielectric constant should be tested since completely different selectivity behavior could be obtained due to the charged and neutral forms of the carrier in the organic phase. The addition of potassium tetrakis[3,5-bis(trifluoromethyl)phenyl]borate to the calcium-selective membrane phase based on the organophosphate ligand mentioned above, the plasticizer dioctyl phenylphosphonate, and poly(vinyl chloride) improves the potentiometric properties of the electrodes with respect to membrane resistance and anion interference.

The ionophores used in ion-selective electrodes (ISEs) are normally divided into ion exchangers, neutral carriers, and electrically charged carriers.[1] The selectivities of ISEs based on ion exchangers are determined by the free energies of solvation of the ions and, for anions, correspond to the so-called Hofmeister series. ISEs based on neutral or charged carriers show a selectivity pattern different from ion exchanger electrodes due to the complexation properties of the ionophore. In the past, the distinction between ion exchangers and charged carriers was not made precisely. Therefore, charged carriers were often called ion exchangers and vice versa.[1]

Two decades ago, the addition of ionic sites was proposed for neutral carrier-based ion-selective liquid membrane electrodes in order to reduce the interference by lipophilic counterions[2] and to create permselectivity.[3] The presence of mobile ion exchange sites has proved to be beneficial in many other respects. The additive reduces the response time, lowers the electrical membrane resistance, and gives rise to significant changes in selectivity, e.g., improves the selectivity for divalent over monovalent ions.[4-6] Only very recently has the beneficial influence of ionic sites on the potentiometric properties of ISEs based on electrically charged carriers been demonstrated both theoretically and experimentally.[7] We were able to show that there is no fundamental difference between charged and neutral carriers with respect to the relationship of complex formation constants and selectivities of ISEs if appropriate ionic additivies are used, a result that stands in contradiction to earlier assumptions.[8] Since charged and neutral ionophores need lipophilic sites of opposite charge for optimum performance, it is possible to discriminate between neutral and charged carrier-related mechanisms as shown lately for anion-selective electrodes based on metalloporphyrins.[9]

The only relevant charged ionophores for cation-selective electrodes known so far are organophosphate derivatives. Since 1967, when Ross introduced the first calcium-selective electrode,[10] a variety of related compounds have been synthesized and used in ISEs.[11] In 1973, Ruzicka and co-workers stressed the possibility of organophosphate ionophores to form different complexes with Ca^{2+} in organic phases depending on the structure of the phosphate derivative, on the pH, and on the solvent used.[12] In the present work, calcium bis[4-(1,1,3,3-tetramethylbutyl)phenyl]-phosphate ($Ca(DTMBP\text{-}PO_4)_2$) was investigated as a representative of the organophosphate ionophores together with the antibiotic monensin (lipophilic carboxylic acid) and dinonylnaphthalenesulfonic acid.[13]

† Present address: Department of Chemistry, The University of Michigan, Ann Arbor, Michigan 48109.

‡ Present address: Department of Chemistry, Auburn University, Auburn, Alabama 36849.

(1) Umezawa, Y. *Handbook of Ion-Selective Electrodes: Selectivity Coefficients;* CRC Press: Boca Raton, FL, 1990.

(2) Morf, W. E.; Kahr, G.; Simon, W. *Anal. Lett.* **1974**, *7*, 9–22.

(3) Perry, M.; Läbel, E.; Bloch, R. *J. Membr. Sci.* **1976**, *1*, 223–235.

(4) Ammann, D.; Morf, W. E.; Anker, P.; Meier, P. C.; Pretsch, E.; Simon, W. *Ion-Sel. Electrode Rev.* **1983**, *5*, 3–92.

(5) Meier, P. C.; Morf, W. E.; Läubli, M.; Simon, W. *Anal. Chim. Acta* **1983**, *156*, 1–8.

(6) Eugster, R.; Gehrig, P. M.; Morf, W. E.; Spichiger, U. E.; Simon, W. *Anal. Chem.* **1991**, *63*, 2285–2289.

(7) Schaller, U.; Bakker, E.; Spichiger, U. E.; Pretsch, E. *Anal. Chem.* **1994**, *66*, 391–398.

(8) Morf, W. E. *The Principles of Ion-Selective Electrodes and of Membrane Transport;* Akadémiai Kiadó, Elsevier: Budapest, New York, 1981.

(9) Bakker, E.; Malinowska, E.; Schiller, R. D.; Meyerhoff, M. E. *Talanta* **1994**, *41*, 881–890.

(10) Ross, J. W. *Science* **1967**, *156*, 1378–1379.

(11) Moody, G. J.; Thomas, J. D. R. *Ion-Sel. Electrode Rev.* **1979**, *1*, 3–30.

(12) Ruzicka, J.; Hansen, E. H.; Tjell, J. C. *Anal. Chim. Acta* **1973**, *67*, 155–178.

(13) Harrell, J. B.; Jones, A. D.; Choppin, G. R. *Anal. Chem.* **1969**, *41*, 1459–1462.

0003-2700/95/0367-3123$9.00/0

Only a few studies on ion-pair formation and acid dissociation in PVC membranes have been published so far.[14-18] Salts are likely to be dissociated if 2-nitrophenyl octyl ether (*o*-NPOE) is used as a plasticizer because of its high dielectric constant of $\epsilon_{mem} = 14$.[18] In contrast, dissociation is hindered in membranes with 66% bis(2-ethylhexyl) sebacate (DOS) and 33% PVC ($\epsilon_{mem} = 4.8$).[14,15] DOS and *o*-NPOE are those two plasticizers commonly used in ISEs that differ most in their dielectric constants. Although the dielectric constant is definitely not the only factor governing the dissociation,[19,20] these two extreme plasticizers were used in this study.

Present models describing the effect of ionic additives on ISE responses predict that for a certain ligand only one charge type of additive is beneficial. If cation-selective neutral carriers are used, the presence of lipophilic anions R^- is mandatory. On the other hand, if charged carriers are used, lipophilic cations R^+ are beneficial in cation-selective electrodes. When we investigated the behavior of an organophosphate carrier, we found surprisingly that both cationic and anionic additives lead to a cationic emf response with selectivities deviating clearly from those induced by ion exchangers. To explain this behavior, which contradicted earlier findings and model predictions, we extended the theoretical description by including the protonation/deprotonation equilibrium of the carrier. Due to the increased complexity, number of parameters, and assumptions this description is only given to demonstrate the qualitative dependence of selectivity on additives.

EXPERIMENTAL SECTION

Reagents. For all experiments, doubly quartz-distilled water and chemicals of puriss or pa grade were used. Tridodecylmethylammonium chloride (TDMA-Cl; Polysciences Inc., Warrington, PA 18976) was recrystallized from ethyl acetate. Dinonylnaphthalenesulfonic acid (DNN-SO_3H) was obtained from Pfaltz and Bauer (Waterbury, CT) as a 50% solution in kerosene, which was removed by distillation and used without further purification. Bis[4-(1,1,3,3-tetramethylbutyl)phenyl]phosphate calcium salt ($Ca(DTMBP\text{-}PO_4)_2$), monensin, potassium tetrakis[3,5-bis(trifluoromethyl)phenyl]borate (K-TFPB), potassium tetrakis(4-chlorophenyl)borate (K-TpClPB), dioctyl phenylphosphonate (DOPP), bis(2-ethylhexyl) sebacate (DOS), 2-nitrophenyl octyl ether (*o*-NPOE, all Selectophore), and poly(vinyl chloride) (PVC, high molecular) were from Fluka AG (Buchs, Switzerland).

Bis[4-(1,1,3,3-tetramethylbutyl)phenyl]phosphoric acid ($DTMBP\text{-}PO_4H$) was prepared by dissolving the salt $Ca(DTMBP\text{-}PO_4)_2$ in methylene chloride, shaking it against 1 M HCl, and evaporating the organic phase. Tridodecylmethylammonium bis[4-(1,1,3,3-tetramethylbutyl)phenyl]phosphate (TDMA $DTMBP\text{-}PO_4$) was obtained after dissolving $Ca(DTMBP\text{-}PO_4)_2$ and TDMA-Cl (molar ratio 1:2) in methylene chloride, shaking this solution against water, and evaporating the organic phase. Both constitutions were confirmed by ^1H NMR ($CDCl_3$).

Membranes. The solvent polymeric membranes were prepared according to ref 21 by using 0.1−1 wt % carrier, 64−66 wt % plasticizer, 33 wt % PVC, and 0−2 wt % additive. For conditioning (overnight) and as internal filling solution, 0.1 M $CaCl_2$ and 0.1 M NaCl were used for calcium- and sodium-selective electrodes, respectively. The electrodes were stored in the same solutions when no measurements were performed.

emf Measurements. Measurements of emf were carried out at 22 ± 1 °C with cells of the following type:

Hg | Hg_2Cl_2 | KCl(satd) | 3 M KCl || sample solution || liquid membrane || internal filling solution | AgCl | Ag

The external half cell was a calomel reference electrode of the free-flowing free-diffusion liquid junction type.[22] The equipment used for the potentiometric measurements was as specified earlier.[21] The measured emf values were corrected for changes in the liquid junction potential by applying the Henderson formula.[23] The activity coefficients used are described in detail earlier.[24] Membrane resistances were determined by the voltage divider method[25] and selectivity coefficients by the separate solution method (SSM)[26] in 0.1 M aqueous solutions of metal chlorides.

^{31}P NMR Experiments. Spectra were recorded on an AM 300 or an AMX 500 NMR spectrometer (Bruker/Spectrospin, Fällanden, Switzerland), and the phosphorus atom of the plasticizer DOPP (−19.2 ppm relative to H_3PO_4) was used as internal reference. The composition of the solutions were 2 wt % ionophore ($Ca(DTMBP\text{-}PO_4)_2$ or $DTMBP\text{-}PO_4H$) in 96−98 wt % DOPP and a varying amount of TDMA-Cl or K-TpClPB (0 − 2 wt %).

Calculations. Excel 4.0 was used to calculate the curves of the figures in the theoretical part.

THEORY

Differentiation of Cation Exchanger and Charged and Electrically Neutral Ligands. On the basis of the assumption that only the external phase boundary potential is variable, the effect of ionic additives on the selectivity of ISEs was described with a simple theoretical model for neutral[5,8] and for charged carriers.[7] In the following, selectivity coefficients calculated using these models are given for cation-selective membranes containing a cation exchanger or a charged or an electrically neutral ionophore with and without ionic additives considering only monovalent primary (I^+) and interfering ions (J^+). For a *cation exchanger*, provided the cationic additive (R^+) is not in excess.[27]

(14) Armstrong, R. D.; Todd, M. *Electrochim. Acta* **1987**, *32*, 155−157.
(15) Armstrong, R. D.; Covington, A. K.; Proud, W. G. *J. Electroanal. Chem.* **1988**, *257*, 155−160.
(16) Verpoorte, E. M. J.; Chan, A. D. C.; Harrison, D. J. *Electroanalysis* **1993**, *5*, 845−854.
(17) Kuratli, M.; Baderischer, M.; Rusterholz, B.; Simon, W. *Anal. Chem.* **1993**, *65*, 3473−3479.
(18) Armstrong, R. D.; Horvai, G. *Electrochim. Acta* **1990**, *35*, 1−7.
(19) Eugster, R.; Rosatzin, T.; Rusterholz, B.; Aebersold, B.; Pedrazza, U.; Rüegg, D.; Schmid, A.; Spichiger, U. E.; Simon, W. *Anal. Chim. Acta* **1994**, *289*, 1−13.
(20) Bakker, E.; Xu, A.; Pretsch, E. *Anal. Chim. Acta* **1994**, *295*, 253−262.
(21) Behringer, Ch.; Lehmann, B.; Haug, J.-P.; Seiler, K.; Morf, W. E.; Hartmann, K.; Simon, W. *Anal. Chim. Acta* **1990**, *233*, 41−47.
(22) Dohner, R. E.; Wegmann, D.; Morf, W. E.; Simon, W. *Anal. Chem.* **1986**, *58*, 2585−2589.
(23) Meier, P. C.; Ammann, D.; Morf, W. E.; Simon, W. In *Medical and Biological Applications of Electrochemical Devices*; Koryta, J., Ed.; Chichester and Wiley: New York, 1980; pp 13−91.
(24) Meier, P. C. *Anal. Chim. Acta* **1982**, *136*, 363−368.
(25) Oesch, U.; Simon, W. *Anal. Chem.* **1980**, *52*, 692−700.
(26) Guilbault, G. G.; Durst, R. A.; Frant, M. S.; Freiser, K.; Hansen, E. H.; Light, T. S.; Pungor, E.; Rechnitz, G.; Rice, N. M.; Rohm, T. J.; Simon, W.; Thomas, J. D. R. *Pure Appl. Chem.* **1976**, *48*, 127−132.
(27) Pretsch, E.; Wegmann, D.; Ammann, D.; Bezegh, A.; Dinten, O.; Läubli, M. W.; Morf, W. E.; Oesch, U.; Sugahara, K.; Weiss, H.; Simon, W. In *Ion Measurements in Physiology and Medicine*; Kessler, M., et al., Eds.; Springer: Berlin, 1985; pp 11−16.

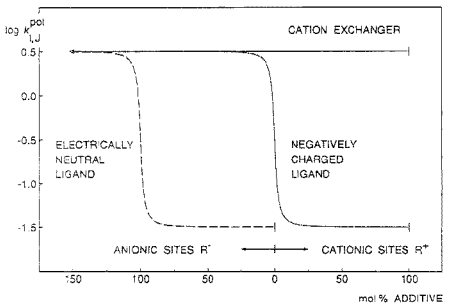

Figure 1. Comparison of cation exchanger and charged and electrically neutral ionophores in cation-selective membranes. Selectivity coefficients for I^- over J^+ were calculated as a function of anionic (R^-) or cationic additive (R^+) concentration according to eqs 1–3 with the following assumptions: $L_T = 5 \times 10^{-3}$ mol·kg^{-1}, log K_{IJ} = log k_J/k_I = 0.5. $\beta_{IL} = 10^7$ kg·mol^{-1}, and $\beta_{JL} = 10^5$ kg·mol1^{-1}.

the following term for $k^{pot}_{I,J}$ is obtained:[28]

$$k^{pot}_{I,J} = k_J/k_I = K_{IJ} \tag{1}$$

with

$$k_i = \exp(\{\mu_i^0(\text{aq}) - \mu_i^0(\text{org})\}/RT)$$

where k_I (k_J) is the so-called single ion distribution coefficient of I^+ (J^+) between the aqueous and the organic phase, K_{IJ} the ion exchange equilibrium constant for I^+ and J^+, and μ_i^0 the chemical standard potential of the ion i in the respective solvent ("aq" denotes species in the aqueous phase, "org" species in the organic phase).

In analogy to eq 10 in ref 7 and eq 2 in ref 9, the formalism for a *negatively charged* and an *electrically neutral carrier* both forming 1:1 complexes with I^+ and J^+ is described by

$$k^{pot}_{I,J} = K_{IJ}\frac{\beta_{JL}}{\beta_{IL}}\frac{[R^+]\beta_{IL} - 1 - \sqrt{([R^+]\beta_{IL}+1)^2 + 4\beta_{IL}(L_T - [R^+])}}{[R^+]\beta_{JL} - 1 - \sqrt{([R^+]\beta_{JL}+1)^2 + 4\beta_{JL}(L_T - [R^+])}} \tag{2}$$

and

$$k^{pot}_{I,J} = K_{IJ}\frac{\beta_{JL}}{\beta_{IL}}\frac{([R^-] - L_T)\beta_{IL} + \sqrt{\beta_{IL}^2(L_T - [R^-])^2 + 4\beta_{IL}[R^-]}}{([R^-] - L_T)\beta_{JL} + \sqrt{\beta_{JL}^2(L_T - [R^-])^2 + 4\beta_{JL}[R^-]}} \tag{3}$$

respectively. L_T, $[R^+]$, and $[R^-]$ are the total concentrations of the ligand and the cationic and the anionic additives in the organic phase and β_{IL} and β_{JL} the complex formation constants. Figure 1 shows the calculated logarithmic selectivity coefficients as a function of charge and concentration of the additive for the three cases: cation exchanger (eq 1) and charged (eq 2) and electrically neutral carriers (eq 3).

(28) Sandblom, J.; Eisenman, G.; Walker, J. L., Jr. *J. Phys. Chem.* **1967**, *71*, 3862–3870.

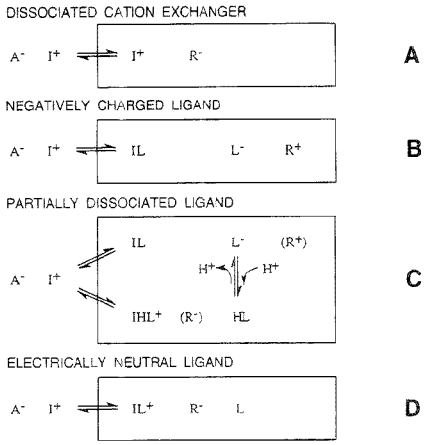

Figure 2. Schematic diagram of four different membrane types containing a (A) dissociated ion exchanger, (B) negatively charged (L^-), (C) partially dissociated (HL and L^-), or (D) electrically neutral ligand (L). I^+, analyte ion; A^-, counterion; R^- and R^+, lipophilic anionic and cationic sites (ion exchanger), respectively.

The selectivity of membranes with a *cation exchanger* cannot be influenced by additives and is always determined by the lipophilicity of the cations. When an *uncharged ionophore* is used, lipophilic anions R^- have to be added to the membrane to obtain a cationic response function, while cationic sites R^+ result in an anionic slope. On the other hand, cationic additives R^- (up to 100 mol % relative to the ionophore) are beneficial to the selectivities of a *negatively charged carrier.* Higher concentrations (>100 mol %) result in anionic emf responses. But when anionic sites R^- are applied to a membrane containing such a ligand, ISEs with selectivities of a cation exchanger are obtained.

Thus, a distinct difference in the potentiometric properties is obtained for charged and for electrically neutral carriers when the sites are changed from anionic to cationic or vice versa.

Partially Dissociated Ligand (Mixed Mode). Here we extend the two models mentioned above by allowing the following dissociation equilibrium for acidic ionophores:

$$HL \overset{K_a}{\rightleftharpoons} L^- + H^+$$

where L^- is the charged form and HL is the neutral form of the ionophore and K_a the acidity constant. Both forms may build complexes with ions in the membrane phase leading to a neutral (IL) and a positively charged (IHL^+) complex, as shown in Figure 2 (mechanism C, partially dissociated ligand). In the same figure the schemes for a cation exchanger, a charged ligand, and a neutral ligand are given as well and show the similarities of mechanism C to B and D. The neutral form of the partially dissociated ionophore (HL in scheme C) corresponds to the neutral ligand L in scheme D. It is obvious that the neutral and charged carrier mechanisms (D and B, Figure 2) correspond to the limiting cases of the present model (C, Figure 2)). By adding a defined amount of cationic (R^-) and anionic (R^-) sites, the

concentrations of the free ligand L^- (cf. B and C, Figure 2) and of the positively charged complexes IHL^+ and IL^+ (cf. C and D, Figure 2) are increased due to electroneutrality.

Earlier theories considered liquid ion exchangers being completely dissociated or strongly associated.[8,29,30] But so far, the existence of two complexes with different charge and the influence of ionic additives on the selectivity behavior of the corresponding ISEs has not yet been taken into account.

The theoretical description is given for cation-selective electrodes and is based on the following assumptions:

(1) Only the phase boundary potential at the sample/membrane interface is considered. The inner phase boundary potential is constant due to the fixed internal electrolyte solution. The diffusion potential within the membrane phase is usually much smaller than the boundary potentials and is therefore neglected.

(2) The organic phase boundary in contact with the sample is in chemical equilibrium with the aqueous sample solution.

(3) The electroneutrality condition is fulfilled in both phases.

(4) Ion pairs in the membrane phase are neglected; i.e., the association constants are assumed to be invariant for a specific ion.

(5) The description is given for singly charged primary ion I^- and interfering ion J^+ forming 1:1 complexes either with the charged form of the ionophore (L^-) or with the neutral form (HL).

(6) The relevant species in the membrane phase are the two forms of the ionophore (L^- and HL), the ionic additives R^- or R^+, the hydrogen ion H^+, and the primary (I^+) or the interfering ion (J^+) and their complexes with both the charged and neutral forms of the ionophore (IL, JL, IHL^+, JHL^+).

The following general formalism for the Nicolsky selectivity coefficient, k_{IJ}^{pot}, is used for the calculations:[5,7,9]

$$k_{I,J}^{pot} = K_{IJ}[I^-]/[J^-] \quad (4)$$

According to SSM determinations of selectivity coefficients, the concentrations $[I^-]$ and $[J^+]$ refer to two different measurements. Brackets indicate generally concentrations in the organic phase, which are used instead of activities for all species in the membrane by assuming that the corresponding activity coefficients are constant.

In the following the concentration of the primary ion in the membrane phase is described as a function of the complex stability constants of the primary ion with both forms of the carrier (β_{IL} (eq 5) and β_{IHL} (eq 6)), the protonation equilibrium (eq 7), the electroneutrality condition for membranes with negative sites R^- (eq 8), and the mass balance of the ligand (eq 9):

$$\beta_{IL} = [IL]/([I^+][L^-]) \quad (5)$$

$$\beta_{IHL} = [IHL^+]/([I^+][HL]) \quad (6)$$

$$K_a = [H^+][L^-]/[HL] \quad (7)$$

$$[L^-] + [R^-] = [I^+] + [IHL^+] + [H^+] \quad (8)$$

$$L_T = [L^-] + [HL] + [IL] + [IHL^+] \quad (9)$$

with L_T being the total concentration of the ligand.

The concentration of H^+ in the membrane phase is assumed to be much smaller than that of the other positively charged species ($[H^+] \ll [I^+] + [IHL^+]$). Therefore, the combination of eqs 5–9, by omitting $[H^+]$ in eq 8, leads to the following quadratic expression for $[I^+]$:

$$(\beta_{IL} + \beta_{IHL}K_a^{-1}[H^+])[I^+]^2 + (1 + K_a^{-1}[H^+] + \beta_{IHL}K_a^{-1}[H^+]L_T - \beta_{IL}[R^-] - \beta_{IHL}K_a^{-1}[H^+][R^-])[I^+] - (L_T + [R^-] + K_a^{-1}[H^+][R^-]) = 0 \quad (10)$$

$[J^+]$ is obtained in complete analogy:

$$(\beta_{JL} + \beta_{JHL}K_a^{-1}[H^+])[J^+]^2 + (1 + K_a^{-1}[H^+] + \beta_{JHL}K_a^{-1}[H^+]L_T - \beta_{JL}[R^-] - \beta_{JHL}K_a^{-1}[H^+][R^-])[J^+] - (L_T + [R^-] + K_a^{-1}[H^+][R^-]) = 0 \quad (11)$$

The solutions of eqs 10 and 11 are inserted into eq 4 to give

$$k_{I,J}^{pot} = K_{IJ}\frac{\beta_{JL} + \beta_{JHL}K_a^{-1}[H^+]}{\beta_{IL} + \beta_{IHL}K_a^{-1}[H^+]} \times \frac{-A + \sqrt{A^2 + 4(\beta_{IL} + \beta_{IHL}K_a^{-1}[H^+])(L_T + [R^-](1 + K_a^{-1}[H^+]))}}{-B + \sqrt{B^2 + 4(\beta_{JL} + \beta_{JHL}K_a^{-1}[H^+])(L_T + [R^-](1 + K_a^{-1}[H^+]))}} \quad (12)$$

with

$$A = 1 + K_a^{-1}[H^+] + \beta_{IHL}K_a^{-1}[H^+]L_T - \beta_{IL}[R^-] - \beta_{IHL}K_a^{-1}[H^+][R^-]$$

and

$$B = 1 + K_a^{-1}[H^+] + \beta_{JHL}K_a^{-1}[H^+]L_T - \beta_{JL}[R^-] - \beta_{JHL}K_a^{-1}[H^+][R^-]$$

The same formalism is valid for cationic additives R^- if $[R^-]$ is replaced by $-[R^+]$ (different electroneutrality condition, see eq 8).

Two limiting cases will be discussed in the following. For a very small acidity constant (i.e., $K_a^{-1}[H^+]$, $\beta_{IHL}K_a^{-1}[H^+]$, and $\beta_{JHL}K_a^{-1}[H^+] \gg 1$), eq 12 is simplified to give

$$k_{I,J}^{pot} = K_{IJ}\frac{\beta_{JHL}}{\beta_{IHL}}\frac{\beta_{IHL}([R^-] - L_T) + \sqrt{\beta_{IHL}^2(L_T - [R^-])^2 + 4\beta_{IHL}[R^-]}}{\beta_{JHL}([R^-] - L_T) + \sqrt{\beta_{JHL}^2(L_T - [R^-])^2 + 4\beta_{JHL}[R^-]}} \quad (13)$$

This corresponds to the description for neutral carriers in cation-selective electrodes (eq 3).

The second case is obtained when K_a is very large (i.e., $K_a^{-1}[H^+]$, $\beta_{IHL}K_a^{-1}[H^+]$, and $\beta_{JHL}K_a^{-1}[H^+] \ll 1$) resulting in eq 2,

(29) Eisenman, G. In *Ion-Selective Electrodes*; Durst, R. A., Ed.; National Bureau of Standards Special Publication 314; Government Printing Office: Washington, DC, 1969; pp 1–56.
(30) Eisenman, G. *Anal. Chem.* **1968**, *40*, 310–320.

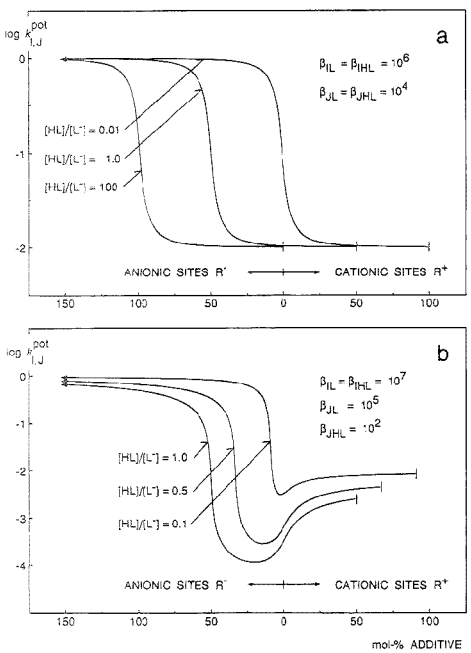

Figure 3. Calculated selectivity coefficients for I^{n+} over J^+ as a function of anionic and cationic additive concentration for cation-selective electrodes based on acidic carriers. To calculate the selectivity coefficient according to eq 12, the following assumptions were made: $L_T = 10^{-2}$ mol·kg^{-1}, $K_{IJ} = 1$, and the indicated stability constants in kg·mol^{-1}. For each picture, three different values were chosen for the ratio [HL]/[L$^-$] as denoted.

which is the formalism for negatively charged carriers in cation-selective electrodes. Thus eq 12 includes the description for neutral and charged carriers as the borderline cases of the present model.

To show that the present model can account for the unusual behavior of the organophosphate-based electrodes, selectivity coefficients were calculated as a function of the charge type and concentration of ionic sites by assuming that the ratio [HL]/[L$^-$] and thus [H$^+$] is constant. Only two simple cases are simulated and presented in Figure 3 because six parameters (β_{IL}, β_{IHL}, β_{JL}, β_{JHL}, K_a, [H$^+$]) are not known and only L_T and [R$^-$] or [R$^+$] can be controlled by weighing.

In Figure 3a, the same stability constants for complexes of the measuring or the interfering ions with both forms of the ligand were chosen ($\beta_{IL} = \beta_{IHL} = 10^6$ and $\beta_{JL} = \beta_{JHL} = 10^4$) to calculate selectivity coefficients for three different cases according to eq 12. While identical stability constants are rather improbable, this case is of theoretical interest since it helps in understanding the main mechanistic concepts. While the right curve ([HL]/[L$^-$] = 0.01) approximates the behavior of a charged carrier[7] (cf. Figure 1), the left curve ([HL]/[L$^-$] = 100) resembles that of a neutral ligand[9] (cf. Figure 1). For [HL]/[L$^-$] = 1 (middle curve), the same concentrations of the charged and of the neutral form of the ligand are present in the membrane phase. In the last case, maximum selectivity ($k^{pot}_{I,J} = -2$) is achieved between 50 mol % R$^-$ and 50 mol % R$^+$; i.e., similar responses and properties are expected by using cationic *or* anionic additives. Such behavior cannot be explained by other models presently used. For R$^+$ > 50 mol %, an anionic emf response is obtained and thus the selectivity coefficient $k^{pot}_{I,J}$ is no longer defined. The addition of more than 50 mol % R$^-$ results in cation-selective electrodes with selectivities dominated by the free energy of hydration of the ions. For given values of the stability constants, the ratio [HL]/[L$^-$] (given by the acidity of the ligand in the membrane phase and by the sample pH) determines the turning point of the curve and defines the range where a cationic emf response is obtained.

Figure 3b shows the case in which the neutral ligand is more selective than the charged one ($\beta_{IHL}/\beta_{JHL} > \beta_{IL}/\beta_{JL}$) for three values of [HL]/[L$^-$]. The best selectivity is obtained if only a small amount of anionic additives is used, but cationic sites as well give selectivities deviating clearly from those of cation exchanger electrodes.

The description for other stoichiometries or divalent cations was omitted since no new qualitative information is expected and the calculations would be less reliable due to an increasing number of parameters and assumptions.

RESULTS AND DISCUSSION

Three ionophores with different acidity constants were studied to investigate their complexation behavior in ISEs with the plasticizers *o*-NPOE, DOS and, in one case, DOPP. Ion-selective membranes with different concentration ratios of additive to ionophore were prepared, and their potentiometric properties were used to classify the carriers as follows. Neutral carriers need R$^-$ and charged carriers R$^+$ for optimal performance (see Figure 1). A third case including the protonation equilibrium of the ionophore was introduced in the theoretical part. The partially dissociated ligand is able to form a neutral and a charged complex with the analyte ion in the membrane phase. This mixed mode is characterized by (highly) selective electrodes with both R$^-$ or R$^+$ (Figure 3a, middle curve). The possibility of carriers operating in a mixed mode was not considered in the classification system for ionophores.[1]

Sulfonic Acids. Recently we showed that the ligand DNN-SO_3H acts as a charged carrier in an ISE membrane plasticized with *o*-NPOE.[7] For this membrane system, the incorporation of cationic sites (TDMA-Cl) leads to Nernstian emf functions, decreased electrode resistance, and enhanced selectivity, which is in perfect agreement with the theoretical description given in that paper.

Table 1 and Figure 4 demonstrate that cationic sites improve the potentiometric properties of the ISEs based on DNN-SO_3H even when the less polar plasticizer DOS is used. Even a small amount of lipophilic borate (1C) deteriorates the calcium selectivity enormously. The selectivities of the alkaline earth ions were omitted in Figure 4 because no change could be seen and they were similar to those in *o*-NPOE.[7] The electrodes 1B–1F show nearly Nernstian emf response functions for Ca^{2+} and only the slope of the ion exchanger electrode (1A) is smaller (Table 1). All these findings prove that DNN-SO_3H is a charged carrier in the more apolar plasticizer DOS. This means that mechanism B in Figure 2 is valid where the free ligand L$^-$ corresponds to the DNN-SO_3^- species. A minor disagreement with the theoretical description (Figure 2 or Figure 3a, right curve) is found because electrode 1E (9.5 mol % TDMA-Cl) is less selective than 1D (no additives) but 1F (48 mol % TDMA-Cl) is again in accord.

Table 1. Composition of Membranes Based on the Ca^{2+}-Selective Ionophore DNN-SO_3H in DOS/PVC (2:1) and Their Potentiometric Properties in Macroelectrodes at 22 °C[a]

mem-brane	composition[b] (wt %) DNN-SO_3H	K-TFPB	TDMA-Cl	resistance[c] (MΩ)	slope[c,d] (mV)
1A		1.0		0.7 ± 0.2	22.7 ± 0.4
1B	1.1	1.0 (48.7)		0.5 ± 0.4	27.8 ± 0.1
1C	1.1	0.2 (9.1)		1.4 ± 0.4	30.0 ± 0.2
1D	1.1			30.6 ± 0.9	29.4 ± 0.5
1E	1.0		0.12 (9.5)	9.7 ± 2.0	29.1 ± 0.6
1F	1.0		0.62 (47.9)	4.3 ± 0.5	29.2 ± 0.3

[a] Average from three electrodes; standard deviation given. [b] Mole percents relative to DNN-SO_3H are given in parentheses. [c] One day after preparation of the ISEs. [d] For 10^{-4}–10^{-1} M $CaCl_2$ ($N = 4$); $s_{theor} = 29.3$ mV.

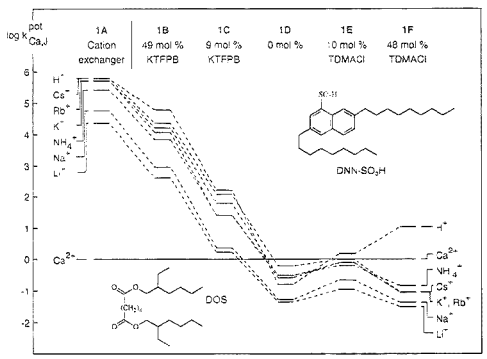

Figure 4. Experimental potentiometric selectivity coefficients, log $k^{pot}_{Ca,J}$, of calcium-selective electrodes based on DNN-SO_3H in the plasticizer DOS 1 day after preparation. For compositions of membranes 1A–1F, see Table 1.

Table 2. Composition of Membranes Based on the Na^+-Selective Ionophore Monensin in *o*-NPOE/PVC (2:1) and Their Potentiometric Properties in Macroelectrodes at 22 °C[a]

mem-brane	composition[b] (wt %) monensin	K-TFPB	TDMA-Cl	resistance[c] (MΩ)	slope[c,d] (mV)
2A	1.0	0.65 (49.8)		0.3 ± 0.1	53.6 ± 0.2
2B	1.0	0.13 (10.1)		0.4 ± 0.1	59.6 ± 0.9
2C	1.1			10.1 ± 4.7	28.5 ± 2.0
2D	1.0		0.13 (15.7)	1.2 ± 0.3	−28.5 ± 7.9
2E	1.1		0.44 (47.8)	0.3 ± 0.1	−41.9 ± 0.6

[a] Average from three electrodes; standard deviation given. [b] Mole percents relative to monensin are given in parentheses. [c] One day after preparation of the ISEs. [d] For 10^{-4}–10^{-1} M NaCl ($N = 4$); $s_{theor} = 58.6$ mV.

Carboxylic Acids. The Na^+-selective antibiotic monensin carrying a carboxyl group had been believed to be a charged ionophore.[8,31,32] Table 2 and Figure 5 show the potentiometric properties of ISEs based on this ligand in the plasticizer *o*-NPOE. A small amount of the cationic additive TDMA-Cl relative to monensin gives a negative slope for the emf response (2D, 2E).

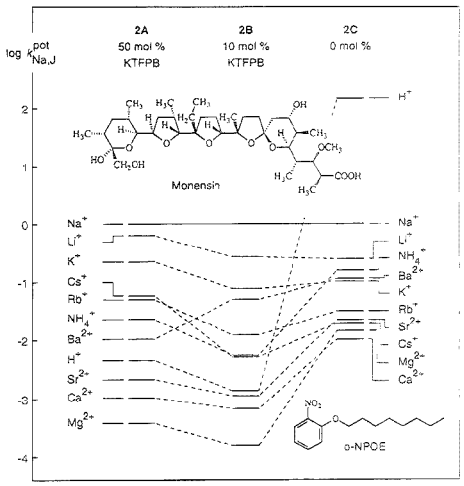

Figure 5. Experimental potentiometric selectivity coefficients, log $k^{pot}_{Na,J}$, of sodium-selective electrodes based on the antibiotic monensin in the plasticizer *o*-NPOE 1 day after preparation. For compositions of membranes 2A–2C, see Table 2.

The anionic additive K-TFPB (2A, 2B) on the other hand improves the slope (Table 2) and the selectivity (Figure 5), as it should be for neutral ligands. Very similar results were obtained with monensin in the plasticizer DOS and with the potassium-selective antibiotic nigericin (in DOS), which is also a carboxylic acid. It was therefore concluded that ionophores with carboxylic groups act as neutral ligands in ion-selective electrode membranes plasticized with DOS or *o*-NPOE. This case is shown in Figure 2 as mechanism D, and the uncomplexed ligand L corresponds to monensin-COOH. These findings are in accord with those for carboxylated PVC, where only a small portion of the carboxyl groups is ionized.[33] Earlier results with electrodes based on monensin, *o*-NPOE, and PVC are very similar to those presented here. Their potentiometric properties are between those of electrodes 2B (10 mol % K-TFPB) and 2C (0 mol % K-TFPB), indicating that a significant amount of inherent anionic sites was present.[31,32] Moreover, it was reported that the neutral ionophore monensin methyl ester has selectivities similar to its carboxyl analog,[32] showing that no negatively charged COO^- group takes part in the complexation process.

Organophosphates. The organophosphate ionophore DTMBP-PO_4^- with an estimated acidity constant K_a of the corresponding acid between that of carboxylates and sulfonates was investigated in *o*-NPOE and DOS. Unfortunately, the solubility of this ligand is very low in both plasticizers (<0.2 wt %).

The slopes of the emf response function in Table 3 and the selectivity behavior in Figure 6 of membranes containing Ca-(DTMBP-PO_4)$_2$, *o*-NPOE, and PVC indicate a charged carrier-related mechanism (B in Figure 2 with L^- corresponding to DTMBP-PO_4^-). While membrane 3F (37 mol % TDMA-Cl) demonstrates the best slope and selectivity, 3D (without additives) has sub-Nernstian slopes so that without additives no reliable

(31) Kraig, R. B.; Nicholson, C. *Science* **1976**, *194*, 725–726.
(32) Schindler, J. G.; Schindler, M. M. *Biomed. Tech.* **1987**, *32*, 22–24.
(33) Lindner, E.; Gráf, E.; Niegreisz, Z.; Tóth, K.; Pungor, E.; Buck, R. P. *Anal. Chem.* **1988**, *60*, 295–301.

Table 3. Composition of Membranes Based on Ca(DTMBP-PO_4)$_2$ in *o*-NPOE/PVC (2:1) and Their Potentiometric Properties in Macroelectrodes at 22 °C[a]

membrane	composition[b] (wt %) Ca(DTMBP-PO_4)$_2$	K-TFPB	TDMA-Cl	resistance[c] (MΩ)	slope[c,d] (mV)
3A	0.20	0.25 (70.9)		0.3 ± 0.1	24.8 ± 0.9
3B	0.21	0.11 (29.6)		0.4 ± 0.2	25.3 ± 0.3
3C	0.14	0.03 (10.5)		2.2 ± 0.4	11.2 ± 2.4
3D	0.18			8.8 ± 0.6	13.4 ± 0.3
3E	0.10		0.02 (16.3)	1.9 ± 0.2	23.2 ± 0.4
3F	0.21		0.09 (37.3)	0.6 ± 0.1	26.8 ± 0.1
3G	0.20		0.18 (79.0)	0.5 ± 0.1	24.6 ± 0.2
3H	0.20		0.37 (158.1)	0.2 ± 0.1)	−54.1 ± 3.6

[a] Average from three electrodes; standard deviation given. [b] Mole percents relative to anionic moiety (DTMBP-PO_4^-) are given in parentheses. [c] One day after preparation of the ISEs. [d] For 10^{-4}–10^{-1} M $CaCl_2$ (N = 4); s_{theor} = 29.3 mV.

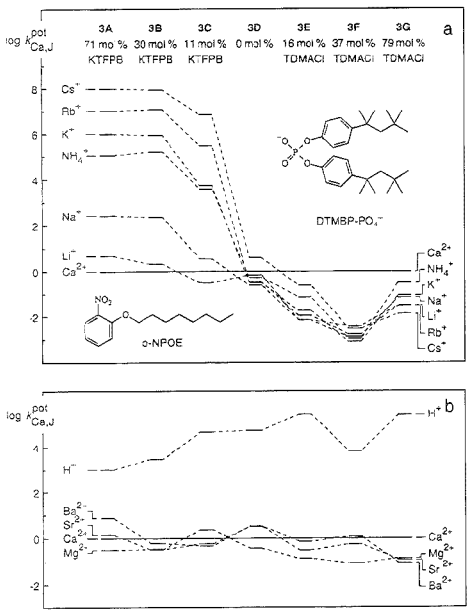

Figure 6. Experimental potentiometric selectivity coefficients, log $k^{pot}_{Ca,J}$, of calcium-selective electrodes based on Ca(DTMBP-PO_4)$_2$ in the plasticizer *o*-NPOE 1 day after preparation. For compositions of membranes 3A–3G, see Table 3. (a) shows the selectivity of alkaline cations and (b) those of alkaline earth cations and of the hydrogen ion relative to Ca^{2+}.

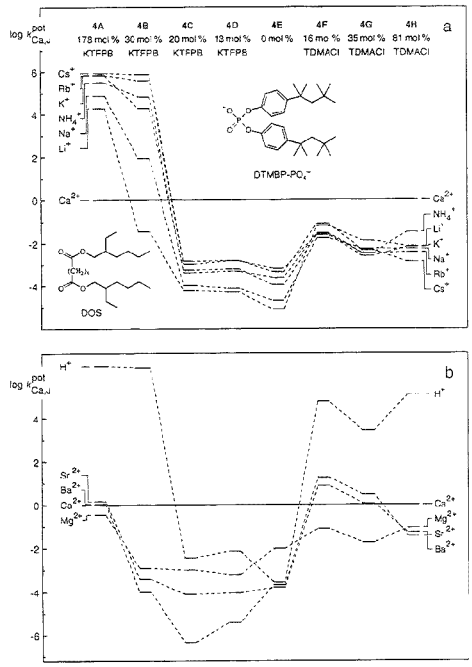

Figure 7. Experimental potentiometric selectivity coefficients, log $k^{pot}_{Ca,J}$, of calcium-selective electrodes based on Ca(DTMBP-PO_4)$_2$ in the plasticizer DOS 1 day after preparation. For compositions of membranes 4A–4H, see Table 4. (a) shows the selectivity of alkaline cations and (b) those of alkaline earth cations and of the hydrogen ion relative to Ca^{2+}.

electrode can be prepared. The incorporation of lipophilic anionic sites (3A–3C) leads to selectivities similar to those of cation exchanger electrodes. An excess of cationic sites (3H, 158 mol %) results, as expected, in a negative slope. The behavior of the selectivity in Figure 6a clearly resembles the theoretical description for charged carriers.[7] The selectivities over alkaline earth cations, as shown in Figure 6b, are constant and are very similar to those of electrodes with DNN-SO_3H in *o*-NPOE/PVC.[7]

When Ca(DTMBP-PO_4)$_2$ in DOS was used, the influence of ionic additives on the selectivities was in striking contrast to the expectation for charged or neutral carriers (Figure 7). The addition of both anionic (4C, 4D) or cationic sites (4F–4H) lead to highly selective ISEs with selectivities deviating clearly from those of ion exchanger electrodes (1A, Figure 4). Table 4 shows that membranes 4B–4D incorporating anionic sites and 4F–4H incorporating cationic sites have slightly super- and sub-Nernstian slopes, respectively. More than 100 mol % TDMA-Cl leads to an anionic response, as expected. Based on the model given in the theoretical section, Figure 3b was calculated according to eq 12 by assuming that the neutral form of the ionophore is more selective than the charged. The selectivity behavior of alkaline cations (Figure 7a), alkaline earth cations, and hydrogen ion (Figure 7b) follows essentially the trend shown in Figure 3b. Taking into account that anionic sites (e.g., tetraphenylborate)

Table 4. Composition of Membranes Based on Ca(DTMBP-PO_4)$_2$ in DOS/PVC (2:1) and Their Potentiometric Properties in Macroelectrodes at 22 °C[a]

membrane	composition[b] (wt %) Ca(DTMBP-PO_4)$_2$	K-TFPB	TDMA-Cl	resistance[c] (MΩ)	slope[c,d] (mV)
4A	0.11	0.36 (177.8)		0.9 ± 0.1	23.0 ± 1.3
4B	0.16	0.09 (30.3)		4.8 ± 1.2	33.8 ± 1.7
4C	0.10	0.04 (20.3)		9.9 ± 1.0	31.9 ± 2.3
4D	0.09	0.02 (12.9)		6.6 ± 1.7	36.5 ± 0.2
4E	0.19			66 ± 11	34.1 ± 0.2
4F	0.10		0.02 (15.9)	19.9 ± 1.5	25.3 ± 0.2
4G	0.20		0.08 (35.2)	9.3 ± 0.5	24.7 ± 0.2
4H	0.10		0.09 (81.3)	5.8 ± 0.4	26.7 ± 0.2
4J	0.09		0.17 (162.9)	3.6 ± 0.5	−53.4 ± 1.8

[a] Average from three electrodes; standard deviation given. [b] Mole percents relative to anionic moiety (DTMBP-PO_4^-) are given in parentheses. [c] One day after preparation of the ISEs. [d] For 10^{-4}–10^{-1} M $CaCl_2$ (N = 4); s_{theor} = 29.3 mV.

Table 5. Composition of Membranes Based on the Ca(DTMBP-PO_4)$_2$ in DOPP/PVC (2:1) and Their Potentiometric Properties in Macroelectrodes at 22 °C[a]

membrane	composition[b] (wt %) Ca(DTMBP-PO_4)$_2$	K-TFPB	TDMA-Cl	resistance[c] (MΩ)	slope[c,d] (mV)
5A		1.0		0.2 ± 0.1	28.7 ± 0.4
5B	1.0	2.23 (122.1)		0.2 ± 0.1	28.7 ± 0.4
5C	1.0	1.29 (70.6)		0.3 ± 0.1	29.1 ± 0.4
5D	0.9	0.65 (38.2)		0.6 ± 0.1	29.2 ± 0.6
5E	1.0	0.37 (19.9)		0.8 ± 0.1	29.5 ± 0.1
5F	1.0	0.22 (11.7)		0.9 ± 0.1	29.5 ± 0.2
5G	1.0			2.8 ± 0.3	29.4 ± 0.1
5H	1.0		0.12 (10.5)	1.4 ± 0.2	29.0 ± 0.4
5J	1.0		0.38 (32.2)	1.0 ± 0.1	27.2 ± 0.1
5K	1.0		0.71 (60.8)	0.6 ± 0.1	28.0 ± 0.2
5L	1.0		1.03 (87.2)	0.5 ± 0.1	23.7 ± 1.0
5M	1.1		1.99 (153.2)	0.3 ± 0.1	−57.6 ± 4.8

[a] Average from three electrodes; standard deviation given. [b] Mole percents relative to anionic moiety (DTMBP-PO_4^-) are given in parentheses. [c] One day after preparation of the ISEs. [d] For 10^{-4}–10^{-1} M $CaCl_2$ (N = 4); s_{theor} = 29.3 mV.

are essential for neutral carriers and that membrane 4E (without additives) has a small amount of anionic impurities which have the same effect as K-TFPB, the selectivity of membranes 4C (20 mol % K-TFPB)–4E must be dominated by the neutral form of the ionophore (DTMBP-PO_4H). This is also supported by the very good selectivity over H^+ for 4C–4E as compared to the other membranes. Therefore, it was concluded that the organophosphate derivative studied acts as a partially dissociated carrier in ISE membranes based on DOS and PVC. This is represented in Figure 2 as mechanism C, where the two forms of the uncomplexed ligand, L^- and HL, correspond to DTMBP-PO_4^- and DTMBP-PO_4H, respectively.

The classical plasticizer for calcium-selective electrodes based on organophosphates is DOPP, in which the solubility of Ca(DTMBP-PO_4)$_2$ is much better than in *o*-NPOE or DOS. A series of membranes based on this plasticizer was prepared and a theoretical slope of the emf response function is obtained for must compositions investigated (Table 5). Only an excess of TDMA-Cl (membrane 5M, 153 mol % TDMA-Cl) results in an anionic response function. Figure 8 shows the selectivity coefficients as a function of ionic additive concentration. A robust behavior from membrane 5E (20 mol % anionic additives)–5K (61 mol % cationic additives) is obtained except for H^+. This can be explained by a mixed mechanism where the neutral form of the ionophore displays slightly better selectivities than the charged form (mechanism C in Figure 2 with L^- = DTMBP-PO_4^- and HL = DTMBP-PO_4H). The behavior found with DOPP can be easily simulated using eq 12 (not shown). Membrane 5L is near the borderline case so that the potentiometric properties are worse. The selectivity pattern of the electrode incorporating ion exchanger (1 wt % K-TFPB) but no ligand (5A) deviates clearly from the usual sequence, showing that the plasticizer DOPP is a ligand for Li^+, Ca^{2+}, and other cations as was described earlier.[34] Therefore, the complexation of Ca^{2+} cannot be ascribed to the ionophore DTMBP-PO_4^-/DTMBP-PO_4H alone, since DOPP also has an effect.

Three different behaviors of selectivity as a function of ionic site concentration were obtained for ISE membranes with the same organophosphate ionophore but different plasticizers (Figures 6–8). They can be qualitatively described by the model of the partially dissociated ligand: The trends of the experimental data in Figures 6–8 correspond to the theoretical curves in Figure 3a, right curve and Figure 3b and Figure 3a middle curves, respectively. When the plasticizer was changed from DOS or DOPP to the polar *o*-NPOE, the carrier mechanism changed from the mixed mode to the charged carrier type.

^{31}P NMR. To provide information about the species present in the membrane phase, ^{31}P NMR studies of the organophosphate ionophore were performed in DOPP as a solvent. The solubility

(34) Hiratani, K.; Okada, T.; Sugihara, H. *Bull. Chem. Soc. Jpn.* **1986**, *59*, 2015–2016.

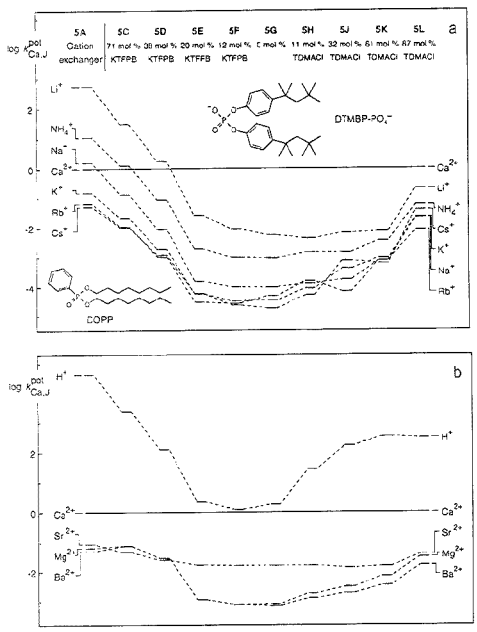

Figure 8. Experimental potentiometric selectivity coefficients, log $k^{pot}_{Ca,J}$, of calcium-selective electrodes based on $Ca(DTMBP\text{-}PO_4)_2$ in the plasticizer DOPP 1 day after preparation. For compositions of membranes 5A–5L, see Table 5. (a) shows the selectivity of alkaline cations and (b) those of alkaline earth cations and of the hydrogen ion relative to Ca^{2+}.

of $Ca(DTMBP\text{-}PO_4)_2$ in DOS and *o*-NPOE is too low to obtain reliable spectra.

The phosphorus chemical shift of the ionophore DTMBP-PO_4H is −10.2 ppm in DOPP. The spectrum of the calcium salt $Ca(DTMBP\text{-}PO_4)_2$ exhibited, surprisingly, two broad signals at −15.6 and −12.1 ppm. The former has been assigned to the calcium complex of the charged ligand. Since $Ca(DTMBP\text{-}PO_4)_2$ is hygroscopic and corresponding protons were also found in the ^{1}H NMR spectrum at 2.2 ppm, the second signal has been assumed to originate from the complexed protonated ligand DTMBP-PO_4H, which is a product of the hydrolysis of the calcium salt.

The DOPP solutions of DTMBP-PO_4H and of $Ca(DTMBP\text{-}PO_4)_2$ were twice equilibrated with an excess of a 0.1 M $CaCl_2$ solution by several vigorous shakings. This process mimics the conditioning of the ISE overnight in the identical solution. After equilibration, virtually the same signal positions of −12.3 and −12.4 ppm were obtained. The results indicate that regardless of the initially added form of the ionophore ($Ca(DTMBP\text{-}PO_4)_2$ or DTMBP-PO_4H), the same membrane composition is present after equilibration. The chemical shift lies between those of $Ca(DTMBP\text{-}PO_4)_2$ (−15.6 ppm) and DTMBP-PO_4H (−10.2 ppm). It can be concluded that after equilibration part of the ionophore is protonated and part is in the Ca^{2+} salt form and that both species are in rapid exchange. Thus, during conditioning, Ca^{2+} in the membrane is partly exchanged by H^+ for $Ca(DTMBP\text{-}PO_4)_2$ as initially applied ionophore and H^+ in the membrane is partly replaced by Ca^{2+} when DTMBP-PO_4H is used.

In further experiments, the lipophilic ammonium chloride TDMA-Cl was added to the DOPP solution of $Ca(DTMBP\text{-}PO_4)_2$ in a molar fraction of 25 and 90% (relative to DTMBP-PO_4^-). The chemical shifts were −11.9 and −10.8 ppm after equilibration of the solutions with aqueous $CaCl_2$. These values are between the one obtained without TDMA-Cl (−12.4 ppm) and the one measured for TDMA DTMBP-PO_4 (−10.1 ppm), which was prepared for a separate measurement. This monotonous change of the chemical shift indicates that the concentration of the charged ionophore (DTMBP-PO_4^-) is increasing with the increase in the added amount of TDMA-Cl. The same holds if 90 mol % TDMA-Cl is added to DTMBP-PO_4H. Upon equilibration, exactly the same chemical shift (−10.8 ppm) is observed as for the corresponding $Ca(DTMBP\text{-}PO_4)_2$/TDMA-Cl (90 mol %) solution. During the equilibration process, $CaCl_2$ or HCl leaves the organic phase and there is an exchange of Ca^{2+} and H^+ between organic and aqueous phases or vice versa.

A more complicated situation is obtained with the addition of K-TpClPB, where a very broad or more than one signal were present after equilibration. The tetraphenylborate derivative increases the concentration of the positively charged complexed species in the organic phase but due to different unknown complexes, where not only the ionophore but also the plasticizer DOPP may be involved, no interpretation could be made.

Ohmic Electrode Resistance. Tables 1–5 also show the electrode resistance for all ISEs discussed above. The incorporation of cationic or anionic additives into the membrane always reduces the resistance, this agrees with the findings for charged and neutral carrier-based electrodes. Thus, miniaturization is facilitated so that mini- and microelectrodes might be developed more easily.

Anion Interference. The interference by lipophilic counter ions was tested for electrodes based on $Ca(DTMBP\text{-}PO_4)_2$ and DNN-SO_3H by studying the emf response function in $Ca(ClO_4)_2$ solutions (data not shown). As expected, the addition of tetraphenylborate salts or the use of an apolar plasticizer (DOS) reduces the anion interference, while an increasing amount of tetraalkylammonium salts or a polar plasticizer does the opposite. This might be an advantage for carriers displaying a mixed mode when the neutral form of the ionophore is more selective than the charged because the incorporation of tetraphenylborate salts improves not only the selectivity but also reduces the anion interference. For charged carriers, a trade-off between anion interference versus selectivity enhancement must be found when sites of opposite charge are added to the ionophore.

So far, electrodes based on $Ca(DTMBP\text{-}PO_4)_2$, DOPP, and PVC have been prepared without ionic additives.[11,12,35] As shown in this work, they may be improved by the incorporation of lipophilic tetraphenylborate derivatives into the membrane phase with respect to electrode resistance and anion interference.

CONCLUSIONS

In ion-selective electrodes, ionophores with a carboxylic acid group (i.e., monensin and nigericin) and with a sulfonate group (i.e., dinonylnaphthalenesulfonic acid) act independently of the plasticizer as neutral and charged carriers, respectively. On the other hand, the organophosphate ligand used shows, in membranes with the plasticizer DOS or DOPP, a mixed mechanism

(35) Egorov, V. V.; Lisbchik, Ya. F.; Pavlovskaya, E. A. *J. Anal. Chem.* **1992**, *47*, 388–392.

where not only the charged but also the neutral form of the ionophore (DTMBP-PO_4^-/DTMBP-PO_4H) contributes to the complexation of the ions, resulting in two different complexes in the membrane phase—charged and electrically neutral. Only in the very polar plasticizer *o*-NPOE is a charged carrier-related mechanism obtained with DTMBP-PO_4^-. Up to now, the organophosphate is the only ionophore showing two different complexation mechanisms, depending on the plasticizer used. Due to these findings, the classification of the ion-selective ionophores should be expanded by a group of ionophores acting in a mixed mode (partially dissociated ligand).

An extended theory including the protonation equilibrium of the ionophore can account for the experimental findings. The theoretical descriptions for neutral and for charged carrier mechanisms proved to be the borderline cases of this model. The addition of ionic sites to the membrane is nearly in all cases advantageous for the selectivity, but there might be only a small amount necessary. Sometimes the inherent impurities in the membrane give a sufficient site concentration for optimum selectivity (cf. membrane 4E), but also here additional K-TFPB reduces the electrode resistance and the anion interference while slope and selectivity are hardly affected (cf. membranes 4C and 4D). Electrodes based on charged carriers may suffer from counterion interference, especially when plasticizers of high dielectric constant are used. The concentration of the appropriate sites has to be chosen carefully since it enlarges the counterion interference but improves the selectivity.

Phosphorus NMR experiments of solutions of ionophore in plasticizer show that the ionophore is partly charged and partly neutral after conditioning with 0.1 M $CaCl_2$. In addition, it could be shown that after equilibration the same chemical shift of the carrier was obtained independently of the initial hydrophilic counterion of the organophosphate ionophore used to prepare the membrane, indicating that complete ion exchange is taking place during the conditioning period.

Since acidic carriers could act as classical charged, neutral, or mixed-mode carriers, as shown in this work, the optimum selectivity of the corresponding ion-selective electrodes should be evaluated by incorporating both anionic and cationic sites into the membrane. Thus, different potentiometric properties might be obtained with the identical ionophore.

The explanation of the unexpected pH dependence, the so-called potential dip,[11,36] of the response of ISEs based on organophosphate ionophores with the model presented in this work will be topic of a further paper.

ACKNOWLEDGMENT

The authors are grateful to Mr. F. Bangerter and Dr. P. Skrabal, Swiss Federal Institute of Technology, Zürich, for recording the ^{31}P NMR spectra. This work was partly supported by the Swiss National Science Foundation.

Received for review July 19, 1994. Accepted June 21, 1995.[⊗]

AC940729O

(36) Bagg, J.; Vinen, R. *Anal. Chem.* **1972**, *44*, 1773.

[⊗] Abstract published in *Advance ACS Abstracts*, August 1, 1995.

Anal. Chem. 1995, *67*, 3133–3139

Doubly Crowned Calix[4]arenes in the 1,3-Alternate Conformation as Cesium-Selective Carriers in Supported Liquid Membranes

Zouhair Asfari,*,† Christophe Bressot,† Jacques Vicens,*,† Clément Hill,*,† Jean-François Dozol,*,‡ Hélène Rouquette,‡ S. Eymard,‡ Véronique Lamare,‡ and B. Tournois‡

EHICS, URA 405 du CNRS, 1 rue Blaise Pascal, F-67008, Strasbourg, France, and SEP/SEATN Centre d'Etudes de Cadarache, Commissariat à l'Energie Atomique, 13108 Saint-Paul-lez-Durance, France

Calix[4]biscrowns 9–15 in the 1,3-alternate conformation are prepared by a one-step procedure in ~50-80% yields, which are sufficiently high enough to allow their use as selective cesium carriers in supported liquid membranes (SLMs). The application of the Danesi diffusional model allows the transport isotherms of trace level ^{137}Cs through SLMs (containing calix[4]biscrowns) to be determined as a function of the ionic concentration of the aqueous feed solutions. Compound 13 appeared to be much more efficient than mixtures of crown ethers and acidic exchangers, especially in very acidic media. Decontamination factors greater than 20 are obtained in the treatment of synthetic acidic radioactive wastes. Permeability coefficient measurements are conducted for repetitive transport experiments in order to qualify the SLMs' stability with time. Very good results (over 50 days of stability) and high decontamination yields are observed with 1,3-calix[4]biscrowns 13 and 14. The 1,3-calix[4]biscrowns are shown to be a new family of selective carriers for cesium removal from radioactive liquid wastes.

The chemistry of calixarenes is well documented. Several accounts[1] and three books[2] have appeared which give an overview of the development and chemistry of these compounds. *p-tert*-Butylcalix[4]arene, which is the cyclic tetramer of the series, has been shown to be the most important building block because (a) it can be produced selectively in large amounts from inexpensive starting materials,[3] (b) it can easily be chemically transformed at the phenolic oxygens (lower rim) and at the para positions (upper rim), and (c) the chemical modification associated with the conformational properties lead to a large variety of tailor-made receptors.[2]

Since Alfieri et al.[4] reported the synthesis of the first member of a new class of macropolycyclic crown compounds with two opposite OH groups in *p-tert*-butylcalix[4]arene bridged by a pentaethylene glycol chain, attention has been paid to the design, synthesis, and metal cation complexation properties of so-called "calixcrown" compounds. The 1,3-capping of calix[4]arenes at the lower rim has been achieved with poly(oxyethylene) chains leading to calixcrown ethers,[5] doubly crowned calixes,[5c,6] and a double calix crown.[7]

Due to the presence of a glycol chain in their framework, calixcrowns have been used as complexing agents of alkali and alkaline-earth metal cations.[2] The selectivities of complexation were shown to depend on the conformation (cone, partial cone, 1,2-alternate, 1,3-alternate) adopted by the rigidified calix[4]arene unit.[1d] For example the partial-cone isomer of 1,3-dimethoxy-*p-tert*-butylcalix[4]crown-5 exhibited the highest free energy for complexation of potassium cation[5b] and was used as selective carrier of this cation in supported liquid membranes (SLMs).[5c] The K^+ selectivities of three different conformers of 1,3-diethoxy-

CNRS.

‡ Centre d'Etudes de Cadarache.

(1) (a) Gutsche C. D. *Acc. Chem. Res.* **1983**,*16*, 161. (b) Gutsche C. D. *Top. Curr. Chem.* **1984**, *123*, 1. (c) Ungaro, R.; Pochini, A. In *Frontiers in Supramolecular Organic Chemistry and Photochemistry*; Schneider, H. J., Dürr, H., Eds.; VCH Verlagsgesellschaft: Weinheim, 1990; pp 57–81. (d) Arduini, A.; Casnati, A.; Fabbi, M.; Minari, P.; Pochini, A.; Sicuri A. R.; Ungaro, R. In *Supramolecular Chemistry*; Balzani, V., De Cola L., Eds.; Kluwer Academic Publishers: Dordrecht, The Netherlands, 1992; pp 31–50. (e) Asfari Z.; Weiss, J.; Vicens, J. *Synlett* **1993**, 719. (f) Shinkai, S. *Tetrahedron* **1993**, *49*, 8933. (g) Asfari, Z.; Weiss, J.; Pappalardo, S.; Vicens, J. *Pure Appl. Chem.* **1993**, *65*, 585. (h) Böhmer, V. *Angew. Chem., Int. Ed. Engl.* **1995**, *34*, 713.

(2) (a) Gutsche, C. D. *Calixarenes*, Royal Society of Chemistry, Cambridge, England, 1989. (b) Vicens, J.; Böhmer V. *Calixarenes, a Versatile Class of Macrocyclic Compounds*; Kluwer Academic Publishers: Dordrecht, Holland, 1991. (c) Vicens, J.; Asfari, Z.; Harrowfield, J. McB. *Calixarenes 50th Anniversary: Commemorative Volume*; Kluwer Academic Publishers: Dordrecht, Holland, 1994.

(3) Gutsche, C. D.; Iqbal M. *Org. Synth.* **1989**, *68*, 234.

(4) Alfieri, C.; Dradi, E.; Pochini, A.; Ungaro, R.; Andreetti, G. D. *J. Chem. Soc., Chem. Commun.* **1983**, 1075.

(5) (a) Dijkstra, P. J.; Brunink, J. A.; Bugge, K.-E.; Reinhoudt, D. N.; Harkema, S.; Ungaro, R.; Ugozzoli, F.; Ghidini, E. *J. Am. Chem. Soc.* **1989**, *111*, 7567. (b) Ghidini, E.; Ugozzoli, F. Ungaro, R.; Harkema, S.; El-Fadl, A. A.; Reinhoudt, D. N. *J. Am. Chem. Soc.* **1990**, *112*, 6979. (c) Nijenhuis, W. F.; Buitenhuis, E. G., De Jong, F.; Sudhölter, E. J. R.; Reinhoudt, D. N. *J. Am. Chem. Soc.* **1991**, *113*, 7963. (d) Brzozka, Z.; Lammerink, B.; Reinhoudt, D. N.; Ghidini, E.; Ungaro, R. *J. Chem. Soc., Perkin Trans. 2* **1993**, 1037. (e) Ungaro, R.; Casnati, A.; Ugozzoli F.; Pochini, A.; Dozol, J. F.; Hill, C.; Rouquette, H. *Angew. Chem., Int. Ed. Engl.* **1994**, *33*, 1506. (f) Cacciapaglia, R.; Casnati, A.; Mandolini, L.; Ungaro, R. *J. Chem. Soc., Chem. Commun.* **1992**, 1291. (g) Cacciapaglia, R.; Casnati, A.; Mandolini, L.; Ungaro, R. *J. Am. Chem. Soc.* **1992**, *114*, 10959. (h) Cacciapaglia, R.; Casnati, A.; Mandolini, L.; Schiavone, S.; Ungaro, R. *J. Chem. Soc., Perkin Trans. 2* **1993**, 369. (i) Cacciapaglia, R.; Mandolini, L. *Chem. Soc. Rev.* **1993**, 221. (j) King, A. M.; Moore, C. P.; Scandanayake, K. R. A. S.; Sutherland, I. O. *J. Chem. Soc., Chem. Commun.* **1992**, 582. (k) Reinhoudt D. N.; Engbersen, J. F.; Brzozka, Z.; Van den Viekkert, H. H.; Honig, G. W. N.; Holterman, A. J.; Verker, U. H. *Anal. Chem.* **1994**, *66*, 3618. (l) Kraft, D.; Arnecke, R.; Böhmer, V.; Vogt, W. *Tetrahedron* **1993**, *49*, 9019.

(6) (a) Arduini, A.; Casnati, A.; Dodi, L.; Pochini, A.; Ungaro, R. *J. Chem. Soc., Chem. Commun.* **1990**, 1597. (b) Asfari, Z.; Pappalardo, S.; Vicens, J. *J. Inclusion Phenom.* **1992**, *14*, 189. (c) Masci, B.; Saccheo, S. *Tetrahedron* **1993**, *49*, 10739. (d) Iasi, G. D.; Masci, B. *Tetrahedron Lett.* **1993**, 6635. (e) Asfari, Z.; Harrowfield, J. M.; Sobolev, A. N.; Vicens, J. *Aust. J. Chem.* **1994**, *47*, 757.

(7) Asfari, Z.; Abidi, R.; Arnaud, F.; Vicens, J. *J. Inclusion Phenom.* **1992**, *13*, 163.

0003-2700/95/0367-3133$9.00/0

Chart 1. 1,3-Calix[4]biscrowns 9–15

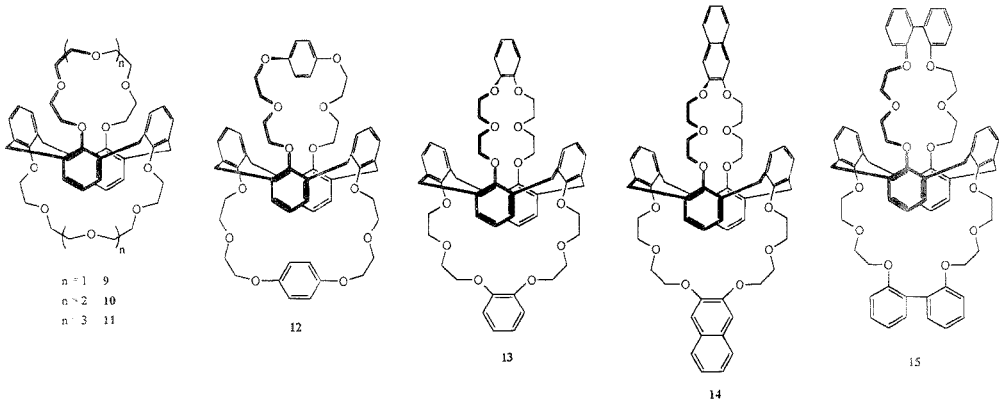

Scheme 1. Synthesis of 9–15

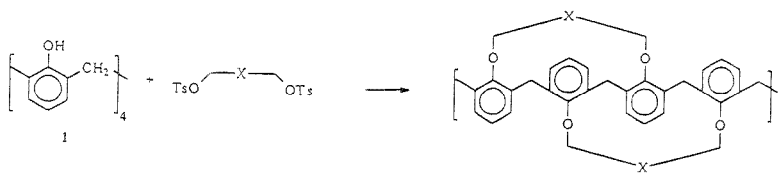

	X	
2	$-CH_2CH_2(OCH_2CH_2)_3-$	9
3	$-CH_2CH_2(OCH_2CH_2)_4-$	10
4	$-CH_2CH_2(OCH_2CH_2)_5-$	11
5	$-(CH_2CH_2O)_2-C_6H_4-(OCH_2CH_2)_2-$	12
6	$-(CH_2CH_2O)_2$, $-(CH_2CH_2O)_2$	13
7	$-(CH_2CH_2O)_2$, $-(CH_2CH_2O)_2$	14
8	$-(CH_2CH_2O)_2$, $-(CH_2CH_2O)_2$	15

p-tert-butylcalix[4]crown-5 have been measured for chemically modified field effect transistors (CHEMFETs)[5k] and membrane ion-selective electrodes (ISEs).[5d] The ionophores showed decreasing K^+/Na^+ selectivities in the order partial cone > 1,3-alternate > cone. The 1,3-Dialkoxycalix[4]crown-6 compounds in the 1,3-alternate conformation presented binding preference for cesium ion.[5c] The X-ray crystal structure of the 1:1 complex of 1,3-dimethoxycalix[4]crown-6 with the cesium picrate indicated the presence of cation/π-electron interactions.[5e]

In this paper we report the synthesis and complexing properties of macrotricyclic 1,3-calix[4]biscrowns **9–15** in the 1,3-alternate conformation (see Chart 1). Their use as selective cesium carriers in supported liquid membranes is described.

RESULTS AND DISCUSSION

Syntheses. 1,3-Calix[4]biscrowns **9–15** were prepared according to Scheme 1. Thus calix[4]arene **1** was reacted with 2–4 equivs of ditosylates **2–8** in refluxing acetonitrile in the presence of an excess of potassium carbonate for times that ranged from 6 to 14 days. The ditosylate and potassium carbonate were added in two portions (see Experimental Section). 1,3-Calix[4]biscrowns **9–15** were obtained pure as white precipitates of the crude

Table 1. Liquid–Liquid Extraction Experiments: Selectivity Determination[a]

no.	extracting agents used	D_{Na}	D_{Cs}	$\alpha_{(Cs/Na)}$
9	1,3-calix[4]biscrown-5	2×10^{-3}	0.4	
10	1,3-calix[4]biscrown-6	1.3×10^{-2}	19.5	1500
11	1,3-calix[4]biscrown-7	$<10^{-3}$	0.3	
12	1,3-calix[4]bis-*p*-benzo-crown-6	$<10^{-3}$	2×10^{-2}	
13	1,3-calix[4]bis-*o*-benzo-crown-6	1.7×10^{-3}	32.5	19000
14	1,3-calix[4]bisnaphthyl-crown-6	$<10^{-3}$	29.5	29000
15	1,3-calix[4]bisdiphenyl-crown-6	$<10^{-3}$	7×10^{-2}	
16	*n*-decylbenzo-21-crown-7	1.2×10^{-3}	0.3	250
17	*tert*-butylbenzo-21-crown-7	1.2×10^{-3}	0.3	250

[a] Aqueous feed solution, 5.0×10^{-3} M $M^+(NO_3^-)$ in 1 M HNO_3; organic solution, 10^{-2} M extracting agent in 1,2-nitrophenyl hexyl ether.

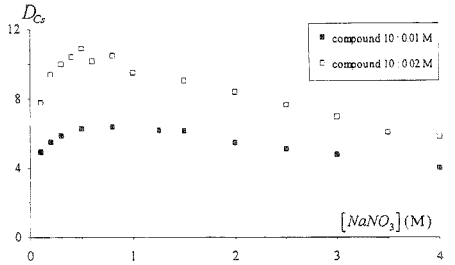

Figure 1. Extraction isotherms for ^{137}Cs in sodium nitrate solutions by 1,3-calix[4]biscrown-6 in 1,2-NPOE: aqueous solution, $NaNO_3$ at various concentrations (pH 2); organic solution, 1,3-calix[4]biscrown-6 in 1,2-nitrophenyl octyl ether.

products from appropriate solvents. The yields ranged from 48 to 79%. Doubly crowned calix[4]arenes **9**–**15** were fully characterized by ^1H NMR, FAB positive mass spectrometry, and elemental analysis. They were deduced to be in 1,3-alternate conformation from their ^1H NMR spectra, which showed singlets at 3.88, 3.87, 3.76, 3.68, and 3.76 ppm, respectively, for the Ar–CH_2–Ar methylene protons in the macrorings of **9**–**15**. In this conformation, 1,3-calix[4]arene-biscrowns **9**–**15** present a special arrangement: one glycolic chain connects two opposite oxygen atoms while the second enforces the calix[4]arene to adopt the 1,3-alternate conformation by linking the two remaining oxygen atoms. This globular arrangement is verified in the X-ray structure of *p-tert*-butylcalix[4]biscrown-5.[6c]

Sodium–Cesium Extractions. The removal of cesium from medium-level radioactive wastes involves extraction of cesium from aqueous solutions that are 1 M in HNO_3 and 4 M in $NaNO_3$.[8] In a preliminary study, extraction experiments with ligands **9**–**15** were performed by mixing equal volumes (5–7 mL) of aqueous and organic solutions (calixarene, 10^{-2} M in 1,2-nitrophenyl hexyl ether) in sealed polypropylene tubes for 1 h at room temperature (25 ± 1 °C). The aqueous solutions contained either $NaNO_3$ or $CsNO_3$ (5.0×10^{-4} M) in HNO_3 (1 M) to assess the selectivity toward cesium in the hypothetical presence of sodium. A measure for the selectivity was assumed to be the ratio of the distribution coefficients obtained separately for both cations:

$$\alpha_{(Cs/Na)} = D_{Cs}/D_{Na} \quad \text{with } D_M = \sum[\bar{M}]/\sum[M]$$

where $\sum[\bar{M}]$ denotes the total concentration of the metal cation (complexed and uncomplexed) in the organic phase at equilibrium and $\sum[M]$ denotes its total concentration in the aqueous phase at equilibrium. $\sum[\bar{M}]$ and $\sum[M]$ were determined experimentally by analyzing aliquots (2 or 5 mL) of each phase by γ spectrometry after centrifugation.

From the data in Table 1, it is seen that ligands **10**, **13**, and **14** with six oxygen atoms in the glycol chain are much more selective toward cesium over sodium than **9** and **11**, with five or seven oxygen atoms in their rings, and **12** and **15**, in which the polyether chains are sterically constrained by the presence of phenyl units. We have previously noted that the glycolic chains containing five oxygens in *p-tert*-butylcalix[4]biscrown-5, related to **9**, are suitable for potassium and sodium cations but too small for large cesium.[6c] In comparison, **10**, **13**, and **14** show 100 times higher selectivities toward cesium than do crown ethers **16** and **17**, which are well-known for their abilities to complex and extract large alkali cations from acidic media.[8] One explanation is that the complexes with calixarene derivatives are best formed because they are stabilized by the π-bonding interactions with the phenyl rings present in the basket frame of 1,3-calix[4]biscrowns **10**, **13**, and **14**.[5c,9]

Although ligands **9**–**15** present two potential complexation sites, the complex stoichiometry was found to be 1:1 (calixarene:cesium cation).[10] This behavior may be explained by a negative allosteric effect, which has been found in complexing systems containing two conformationally related crown ether subunits.[11] These systems are only able to complex cations in one of their two subunits at a time because when one complex is formed, the other subunit has an unsuitable conformation to bind any species.[11]

As shown in Figures 1 and 2, which display cesium extraction isotherms for **10** as a function of aqueous salt concentrations ($0 < [NaNO_3] < 4$ M, $0 < [HNO_3] < 7$ M and cesium at trace level), back-extraction of cesium was usually allowed and favored in deionized water (where D_{Cs} is very small). This remarkable property allowed the use of **9**–**15** as cesium-selective carriers in supported liquid membranes. Since cesium extraction was strongly enhanced in concentrated acidic media for **9**–**15** as compared to mixtures of a crown ether such as *tert*-butylbenzo-21C7 (**17**)[12] and an acidic exchanger ligand, **9**–**15** might be used to treat medium-level radioactive wastes. The decrease of D_{Cs} for sodium nitrate concentrations greater than 0.5 M (see Figure 1) or for nitric acid concentrations greater than 2 M (see Figure 2) reveals both the competitive extraction of HNO_3 or $NaNO_3$ by the tested calixarenes and the decrease of the mean activity coefficient of trace-level cesium in a concentrated aqueous media.

(8) (a) Gerow, H.; Davis, M. W., Jr. *Sep. Sci. Technol.* **1979**, *14*, 395. (b) Gerow, H.; Smith, J. E., Jr.; Davis, M. W., Jr. *Sep. Sci. Technol.* **1981**, *16*, 519. (b) Blasius, E.; Nilles, K.-H. *Radiochim. Acta* **1984**, *35*, 173. (c) Dozol, J. F. In *Future Industrial Prospects of Membrane Processes*; Cécille, J., Toussaint, J. C., Eds; Elsevier Applied Science: New York, 1989.

(9) For π–cation interactions, see also, for example: (a) Ikeda, A.; Tsuzuki, H.; Shinkai, S. *Tetrahedron Lett.* **1994**, 8417. (b) Ikeda, A.; Shinkai, S. *J. Am. Chem. Soc.* **1994**, *116*, 3102. (c) Ikeda, A.; Shinkai, S. *Tetrahedron Lett.* **1992**, 7385. (d) Iwamoto, K.; Shinkai, S. *J. Org. Chem.* **1992**, *57*, 7066. (e) Fujimoto, F.; Nishiyama, N.; Tsuzuki, H.; Shinkai, S. *J. Chem. Soc., Perkin Trans. 2* **1992**, 643. (f) Araki, K.; Shimizu, H.; Shinkai, S. *Chem. Lett.* **1993**, 205.

(10) Thermodynamic studies by UV and NMR from this laboratory have also shown 1:1 stoechiometry for alkali metal **9**–**15** complexes. These results will be published in due course.

(11) (a) Costero, A. M.; Rodriguez, S. *Tetrahedron Lett.* **1992**, 623. (b) Costero, A. M.; Rodriguez, S. *Tetrahedron* **1992**, *48*, 6265. (c) Costero, A. M.; Pitarch, M. *J. Org. Chem.* **1994**, *59*, 2939.

(12) Mc Dowell, W. J.; Case, G. N. *Anal. Chem.* **1992**, *64*, 3013.

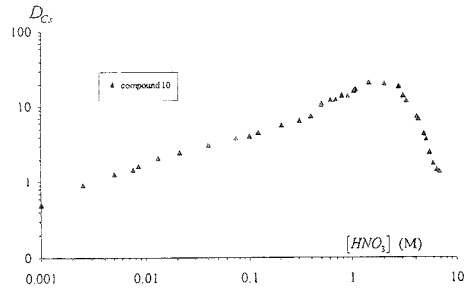

Figure 2. Extraction isotherm for ^{137}Cs in nitric acid solutions by 1,3-calix[4]biscrown-6 (10^{-2} M) in 1,2-NPOE: aqueous solution, HNO_3 at various concentrations; organic solution, 1,3-biscalix[4]-crown-6 (10-2 M) in 1,2-nitrophenyl octyl ether.

Cesium Transport through Supported Liquid Membranes (SLMs). Selective alkali cation permeation through liquid membranes has been intensively studied to mimic natural antibiotics, to transduce chemical information into electronic signals, or to treat radioactive wastes.[13] For instance, taking advantage of the phenolic ionization of parent calixarenes (*p-tert*-butyl- and *p-tert*-pentylcalix[*n*]arenes) under basic conditions, Izatt et al. achieved quantitative cesium transport through bulk liquid membranes (25% v/v CH_2Cl_2–CCl_4) from aqueous feed solutions of CsOH (pH >12) to water.[14] However, no cesium permeation was observed in the case of neutral metal nitrate salts in the feed solutions during similar experiments.[14] Polyether-bridged calix[4]arenes were first applied to SLMs in order to study potassium/sodium permeation selectivities as compared to those of valinomycin.[13a] We therefore decided to determine the selective ionophoric properties of calix-[4]biscrowns **9**–**15** by measuring under similar experimental conditions (stirring rates, concentration gradients) the permeability coefficients of cesium as described in the Danesi model of trace-level cation permeation through SLMs.[15] Although the Danesi model was applied to ion-pair extraction in apolar solvents, constant permeability coefficients have also been observed on long-term transport experiments (over 10 h) using a more polar organic solvent such as nitrophenyl octyl ether.[16]

The use of **9**–**15** as carriers in SLMs led to coupled cotransport of cesium and nitrate ions from aqueous feed solutions of 4 M in $NaNO_3$ and 1 M in HNO_3—simulating concentrated medium-level radioactive wastes—to deionized water (the receiving solution) because of the NO_3^- concentration gradient. The decrease of ^{137}Cs radioactivity in the feed solutions was followed by regular measurements with γ spectrometry analysis (1500 kBq·L^{-1} < ^{137}Cs initial aqueous activity < 2500 kBq·L^{-1}).

Permeability coefficients P_M (cm·h^{-1}) for cesium permeation through the SLMs were graphically determined by plotting the logarithm of the ratio C/C° vs time:[15]

$$\ln (C/C^\circ) = (\theta S/V)P_M t \qquad (1)$$

where C is the concentration of the cation in the feed solution at time t (M); C° is the initial concentration of the cation in the feed solution (M); θ is the volumic porosity of the SLM (%); S is the membrane surface area (cm^2) depending on the device; V is the volume of feed and stripping solutions (cm^3) depending on the device; and t = time (h).

The data summarized in Table 2 confirm the results obtained previously in sodium–cesium extraction studies (see Table 1) although the organic solvent used in these experiments (1,2-nitrophenyl octyl ether) is a slightly more polar and more viscous diluent than 1,2-nitrophenyl hexyl ether. Carriers **10**, **13**, and **14** with six oxygen atoms in the glycol chain are much more efficient to transport cesium through SLMs than **9** and **11**, with five or seven oxygen atoms in their rings, and **12** and **15**, in which the polyether chains are sterically constrained.

Certain assumptions of the Danesi model[15] (transport being only controlled and limited by diffusion) allow the permeability coefficients P_M to be evaluated by

$$P_M \approx D_M/\Delta_c \qquad (2)$$

where D_M is the distribution coefficient of the permeating cation

Table 2. ^{137}Cs Transport Experiments through Flat Sheet-Supported Liquid Membranes: Permeability Determination after 6 h of Permeation[a]

no.	carriers used	P_{Cs} (cm·h^{-1})
9	1,3-calix[4]biscrown-5	9×10^{-2}
10	1,3-calix[4]biscrown-6	1.3
11	1,3-calix[4]biscrown-7	4×10^{-2}
12	1,3-calix[4]bis-*p*-benzo-crown-6	3×10^{-3}
13	1,3-calix[4]bis-*o*-benzo-crown-6	2.8
14	1,3-calix[4]bisnaphthyl-crown-6	2.7
15	1,3-calix[4]bisdiphenyl-crown-6	0.1
16	n-decylbenzo-21-crown-7	9×10^{-2}

[a] Aqueous feed solution, $NaNO_3$ (4 M) and HNO_3 (1 M); aqueous strip solution, deionized water; organic solution, 10^{-2} M carrier in 1,2-nitrophenyl octyl ether.

Table 3. Transport Yields (after 24 h) of Sr, Rb, Y, Zr, Ru, Rh, Cs, Ba, La, Ce, and Eu Permeation from Simulated High-Active Wastes to Deionized Water by 1,3-Calix[4]biscrown-6, by 1,3-Calix[4]bis-*o*-benzo-crown-6, and by 1,3-Calix[4]bisnaphthyl-crown-6 (10^{-2} M) in 1,2-NPOE[a]

element	init concn in feed soln (mg·L^{-1})	M concn in receiving soln after 24 h (mg·L^{-1}) 10	13	14
Sr	87.6	$<5 \times 10^{-2}$	$<5 \times 10^{-2}$	$<5 \times 10^{-2}$
Rb	85.5	34	63	47
Y	88.9	$<5 \times 10^{-3}$	$<5 \times 10^{-3}$	$<5 \times 10^{-3}$
Zr	91.2	$<5 \times 10^{-2}$	$<5 \times 10^{-2}$	$<5 \times 10^{-2}$
Ru	101.0	$<5 \times 10^{-3}$	$<5 \times 10^{-3}$	$<5 \times 10^{-3}$
Rh	102.9	$<5 \times 10^{-3}$	$<5 \times 10^{-3}$	$<5 \times 10^{-3}$
Cs	132.9	92	125	105
Ba	137.3	$<5 \times 10^{-2}$	$<5 \times 10^{-2}$	$<5 \times 10^{-2}$
La	138.5	$<5 \times 10^{-3}$	$<5 \times 10^{-3}$	$<5 \times 10^{-3}$
Ce	140.1	$<5 \times 10^{-3}$	$<5 \times 10^{-3}$	$<5 \times 10^{-3}$
Eu	151.9	$<5 \times 10^{-3}$	$<5 \times 10^{-3}$	$<5 \times 10^{-3}$

[a] Aqueous feed solution, 3 M HNO_3 and 10^{-3} M element; aqueous stripping solution, deionized water; SLM, **10**, **13**, or **14** (10^{-2} M) in 1,2-nitrophenyl octyl ether.

(13) (a) Nijenhuis, W. F.; van Door, A. R.; Reichwein, A. M.; de Jong, F.; Reinhoudt, D. N. *J. Am. Chem. Soc.* **1991**, *113*, 3607. (b) Visser, H. C.; Reinhoudt, D. N.; De Jong, F. *Chem Soc. Rev.* **1994**, 76. (c) Verboom, W.; Rudkevich, D. M.; Reinhoudt, D. N. *Pure Appl. Chem.* **1994**, *66*, 697. (d) Von Straten-Nijenhuis, W. F.; De Jong, F.; Reinhoudt, D. N. *Recl. Trav. Chim. Pays-Bas* **1993**, *112*, 317. (e) Brown, P. R.; Hallman, J. L.; Whaley, L. W.; Desai, D. H.; Pugia, M. J.; Bartsch, R. A. *J. Membr. Sci.* **1991**, *56*, 195.
(14) (a) Izatt, R. M.; Lamb, J. D.; Hawkins, R. T.; Brown, P. R.; Izatt, S. R.; Christensen, J. J. *J. Am. Chem. Soc.* **1983**, *105*, 1782. (b) Izatt, S. R.; Hawkins, R. T.; Christensen, J. J.; Izatt, R. M. *J. Am. Chem. Soc.* **1985**, *107*, 63–66.
(15) Danesi, P. R. *Sep. Sci. Technol.* **1984**, *19*, 857.
(16) Hill, C. Ph.D. Thesis, University of Strasbourg, 1994.

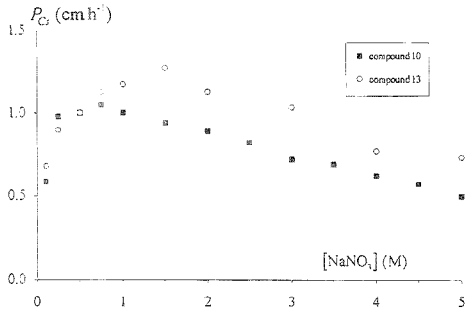

Figure 3. Transport isotherms for ^{137}Cs from sodium nitrate solutions to deionized water by 1,3-calix[4]biscrown-6 and by 1,3-calix[4]bis-*o*-benzocrown-6 (10^{-2} M) in 1,2-NPOE: aqueous feed solution, $NaNO_3$ in various concentrations (pH, 1.4); aqueous stripping solution, deionized water; SLM, **10** or **13** (10^{-2} M) in 1,2-nitrophenyl octyl ether.

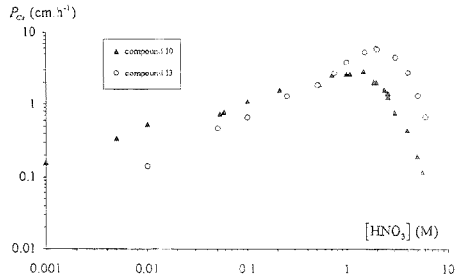

Figure 4. Transport isotherms of ^{137}Cs from nitric acid solutions to deionized water for 1,3-calix[4]biscrown-6 and for 1,3-calix[4]bis-*o*-benzo-crown-6 (10^{-2} M) in 1,2-NPOE: aqueous feed solution, HNO_3 in various concentrations; aqueous stripping solution, deionized water; SLM, **10** or **13** (10^{-2} M) in 1,2-nitrophenyl octyl ether.

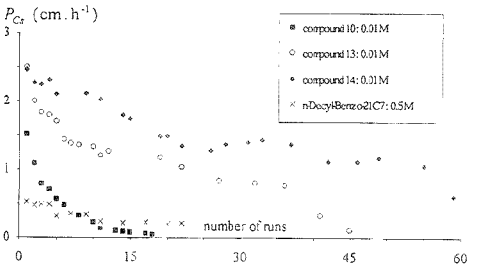

Figure 5. Repetitive transport experiments of ^{137}Cs from simulated medium-active liquid wastes for 1,3-calix[4]biscrown-6, for 1,3-calix-[4]bis-*o*-benzocrown-6 and for 1,3-calix[4]bis-1,2-naphthylcrown-6 (10^{-2} M) in 1,2-NPOE: aqueous feed solution, $NaNO_3$ (4 M) and HNO_3 (1 M); aqueous stripping solution, deionized water; SLM, **10**, **13** or **14** (10^{-2} M) in 1,2-nitrophenyl octyl ether.

and Δ_o, the ratio of the organic path length (thickness of the membrane × tortuosity) to the organic diffusion coefficient, $(\delta\tau)/D_O$.

Equation 2 shows that P_M is proportional to D_M, which directly depends on the organic carrier concentration in the SLM. That is why the cesium transport isotherms shown in Figures 3 and 4 for **10** reproduced the same trends as those found previously in extraction isotherms (Figures 1 and 2): (1) an increase of cesium permeability coefficient for $[NaNO_3] < 1$ M in the feed solution (Figure 3) and for $[HNO_3] < 2$ M in the feed solution (Figure 4) as D_{Cs} previously increased with salt concentration in the feed solution (Figures 1 and 2); (2) a maximum of transport kinetics due to the maximum of D_{Cs}; (3) a decrease of P_{Cs} for $[NaNO_3] > 1$ M or $[HNO_3] > 2$M, revealing three different phenomena, namely, (a) a decrease of D_{Cs} due to sodium nitrate or nitric acid competitive extraction and transport of sodium nitrate or nitric acid; (b) a decrease of trace-level cesium mean activity coefficient with the increase of salt concentration in the aqueous feed solutions; and (c) leaching of the SLMs by the feed and the receiving solutions favored by the partitioning of the carrier, especially in the case of **10**, which shows very poor lipophilicity.

The higher selectivity and efficiency of **13** compared to **10** can easily be noticed by comparing both transport isotherms shown in Figures 3 and 4.

Time stability of the most efficiently prepared SLMs was estimated by repeating transport experiments in which both aqueous feed and stripping solutions were renewed every day while the SLMs remained the same. Consequently, daily partitioning of the carrier from the membrane phase to the renewed aqueous solutions caused a decrease of the carrier concentration in the SLMs, thus a decrease of D_M and, proportionally, of P_M. The evolution of the permeability coefficients vs the number of runs was therefore a way to describe the leaching of the membrane by the aqueous solutions and characterized the SLMs' stability with time.

As shown in Figure 5, repeated cesium transport experiments showed that **10** rapidly leached out of the SLMs ($P_{Cs} < 0.1$ cm·h^{-1} after 15 runs), because of its low partition constants between 1,2-nitrophenyl octyl ether and the aqueous solutions. Very good stability and efficiency were observed with the more lipophilic compounds **13** and **14**, for which the cesium permeability coefficients were 5 times higher than those of the crown ether **16** even when the concentration of the crown ether was 50 times higher in 1,2-nitrophenyl octyl ether.

1,3-Calix[4]biscrowns **13** and **14** allowed selective removal of ^{137}Cs from sodium-containing solutions. Less than 100 mg of the ~100 g of sodium (initially present in the feed solution) was transported in 24 h by **14**, whereas more than 95% of trace level ^{137}Cs was concentrated in the stripping solution. Nitric acid transport, due to the basicity of both the organic diluent and the calixarene, could not be limited to less than 5% (0.05 M) in 24 h leading to concentration factors (ratio of initial waste concentration to final waste concentration) greater than 100 for a single-step process.

To summarize, 1,3-calix[4]biscrowns containing six oxygen atoms appeared to be a promising family of carriers for the selective removal of cesium from high-salinity media, such as medium-level radioactive liquid wastes, with SLMs. By choosing a highly hydrophobic organic diluent, 1,2-nitrophenyl octyl ether, and a very lipophilic calix[4]biscrown in the 1,3-alternate conformation suitable for cesium complexation over that of sodium, very selective and stable SLM can be obtained (over a period of 50 days).

Transport of Cesium from Simulated Fission Product Solutions. Application of calix[4]biscrowns **10**, **13**, and **14** to decontaminate medium- or high-level radioactive wastes, such as fission product solutions, was also investigated. Figure 6 shows

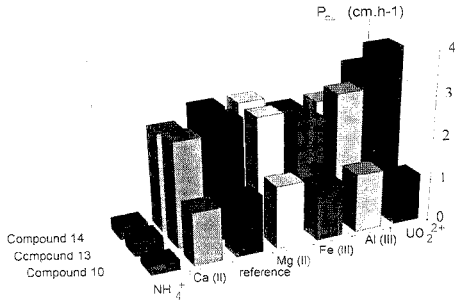

Figure 6. Influence of the presence of nitrate salts on the permeation of ^{137}Cs from simulated medium-active liquid wastes to deionized water by 1,3-calix[4]biscrown-6, by 1,3-calix[4]bis-*o*-benzocrown-6 and by 1,3-calix[4]bisnaphthylcrown-6 (10^{-2} M) in 1,2-NPOE: aqueous feed solution $NaNO_3$ (4 M), HNO_3 (1 M), and nitrate species (NH_4^+, Ca^{2+}, Mg^{2+}, Fe^{3+}, Al^{3+}, or UO_2^{2+} at 0.1 M); aqueous stripping solution deionized water; SLM, **10**, **13**, or **14** (10^{-2} M) in 1,2-nitrophenyl octyl ether.

the effect of the presence of six different nitrate salts (NH_4^+, Ca^{2+}, Mg^{2+}, Fe^{3+}, Al^{3+}, UO_2^{2+}) on cesium permeation from aqueous feed solutions simulating medium-active concentrates (4 M in $NaNO_3$ and 1 M in HNO_3) to receiving solutions of deionized water. Except for ammonium nitrate salts, which usually behave like alkali cations and drastically hinder cesium separation in classical industrial decontamination processes (coprecipitation, ion exchange, etc.), none of the other five added species (Ca^{2+}, Mg^{2+}, Fe^{3+}, Al^{3+}, UO_2^{2+}) potentially present in medium-active wastes disfavored trace level cesium permeation through the SLMs.

Table 2 records the transport yields of 11 main elements (out of 34 present in very high-level radioactive liquid wastes, such as fission products solutions) from nitric acid feed solutions (3 M in HNO_3 and 10^{-3} M in element) to deionized water. Metal cation concentrations were determined by atomic absorption spectrometry of aliquots sampled in the receiving solutions after 24 h of permeation. Except for rubidium, whose chemical behavior is similar to that of cesium among other alkali cations, the high selectivity of the tested 1,3-calix[4]biscrowns toward cesium is maintained in the presence of the other nine elements.

CONCLUSION

The preparation of calix[4]biscrowns **9**–**15** in the 1,3-alternate conformation by one-step procedures has been achieved in yields sufficiently high for their use as Cs carriers in supported liquid membranes. Application of the Danesi diffusional model allowed the transport isotherms of trace-level ^{137}Cs through SLMs (containing calix[4]biscrowns) to be determined as a function of the ionic concentration of the aqueous feed solutions. Compound **13** appeared to be much more efficient than a combination of crown ether and an acidic exchanger, especially in very acidic media. This allowed a one-step treatment of synthetic acidic radioactive wastes with decontamination factors greater than 100. Permeability coefficient measurements were also conducted in repetitive transport experiments in order to characterize SML stability with time. Very good results (over 50 days of stability) and high decontamination yields were observed with 1,3-calix[4]biscrowns **13** and **14**. The 1,3-calix[4]biscrowns are shown to be a new family of selective carriers for cesium removal from radioactive liquid wastes leading to 1:1 stoichiometry complexes (1,3-calix[4]biscrown–Cs).

Future work is directed in two directions: (i) determination of the stoichiometry and stability constants of the complexes of ligands **9**–**15** with alkali cations by spectrophotometric studies and NMR experiments and (ii) determination of the X-ray crystal structure of these complexes.

EXPERIMENTAL SECTION

Starting Materials for Syntheses. The solvents and all compounds were commercial reagents and were used without further purification.

Analytical Procedures. The melting points (mp) were taken on a Büchi 500 apparatus in capillaries sealed under nitrogen. Silica gel columns were prepared with Kiesielgel Merck (No.11567). Elemental analyses were performed at the Service de Microanalyse of the Institut de Chimie de Strasbourg. The ^1H NMR spectra were recorded at 200 MHz on a Bruker SY200 spectrometer. The FAB mass spectra were obtained on a VG-Analytical ZAB HF apparatus.

Syntheses. Preparation of 9. According to a procedure described by us,[17] a 1-L round-bottomed flask was equipped with a condenser and charged with acetonitrile (700 mL), calix[4]arene **1** (6.00 g, 14.2 mmol), and potassium carbonate (19.62 g, 142 mmol). The reaction mixture was stirred at room temperature for 30 min. Tetraethylene glycol ditosylate **2** (7.14 g, 14.2 mmol) was added, and the mixture was refluxed for 7 days. The same quantities of potassium carbonate and tetraethylene glycol ditosylate **2** were added, and the reflux was continued for 7 additional days. After cooling to room temperature, the solvents were removed in vacuo (45 °C bath). Dichloromethane (600 mL) was added and the suspension was neutralized by 1 N HCl. The organic layer was dried over sodium sulfate. The filtered solution was concentrated and precipitated with methanol–diethyl ether to yield pure **9** as a white solid: mp 117–118 °C; yield 53%; ^1H NMR ($CDCl_3$) γ 7.09 (d, 8H, J_{H-H} = 7.5 Hz, meta Ar*H*), 6.89 (t, 4H, J_{H-H} = 7.5 Hz, para Ar*H*), 3.88 (s, 8H, ArCH_2Ar), 3.59–3.06 (m, 32H, OCH_2CH_2O); FAB positive, 740.3. Elemental analysis calcd for $C_{44}H_{52}O_{10}.CH_3OH$: C, 70.02; H, 7.18. Found: C, 70.23; H, 6.92.

Preparation of 10. Same as for **9**; calix[4]arene **1** (0.85 g, 2 mmol), potassium carbonate (5.52 g, 40 mmol), pentaethylene glycol ditosylate **3** (2.28 g, 4 mmol), and acetonitrile (100 mL); 14 days; yield 48%; white solid from methanol–diethyl ether: mp 145–146 °C; ^1H NMR ($CDCl_3$) δ 7.10 (d, 8H, J_{H-H} = 8.0 Hz, meta Ar*H*), 6.87 (t, 4H, J_{H-H} = 8.0 Hz, para Ar*H*), 3.87 (s, 8H, ArCH_2Ar), 3.70–3.28 (m, 40H, OCH_2CH_2O). FAB positive, 828.4. Elemental analysis calcd for $C_{48}H_{60}O_{12}.CH_3OH$: C, 70.02; H, 7.18. Found: C, 70.23; H, 6.92%.

Preparation of 11. Same as for **9**; calix[4]arene **1** (1.70 g, 4 mmol), potassium carbonate (5.52 g, 40 mmol), hexaethylene glycol ditosylate **4** (2.36 g, 4 mmol); acetonitrile (200 mL). The same quantities of potassium carbonate and hexaethylene glycol ditosylate were added after 10 days: total reflux time 14 days; white solid from methanol–diethyl ether: mp 120–121° C; yield 62%; ^1H NMR ($CDCl_3$) δ 7.14 (d, 8H, J_{H-H} = 7.5 Hz, meta Ar*H*), 6.80 (t, 4H, J_{H-H} = 7.5 Hz, para Ar*H*), 3.79–3.42 (m, 48H, OCH_2CH_2O), 3.57 (s, 8H, ArCH_2Ar). FAB positive, 916.4. El-

(17) Wenger, S. Asfari, Z. Vicens, J. *Tetrahedron Lett.* **1994**, *35*, 8369.

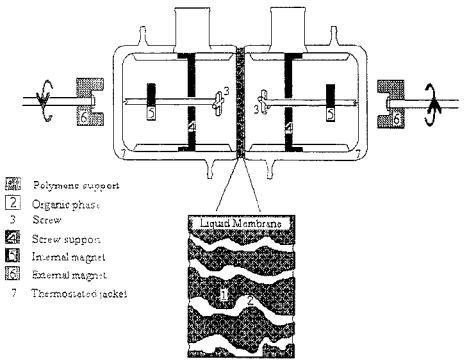

Figure 7. Flat-sheet supported liquid membrane device for transport experiments.

emental analysis calcd for $C_{56}H_{76}O_{16}$: C, 68.10, H 7.47. Found: C, 68.30, H, 7.27.

Preparation of 12. Same as for **9**; calix[4]arene **1** (0.64 g, 1.5 mmol), potassium carbonate (0.83 g, 40 mmol), ditosylate **5** (0.89 g, 1.5 mmol), and acetonitrile (60 mL). The same quantities of potassium carbonate and ditosylate were added after 4 days. Total reflux time, 8 days: white solid from methanol–diethyl ether: mp 81–82 °C; yield 54%; ^{1}H NMR ($CDCl_3$) δ 7.07 (d, 8H, J_{H-H} = 7.5 Hz, meta Ar*H*), 7.03 (s, 8H, Ar′*H*), 6.83 (t, 4H, J_{H-H} = 7.5 Hz, para Ar*H*), 3.82–3.67 (m, 32H, OCH_2CH_2O), 3.76 (s, 8H, $ArCH_2Ar$). FAB positive, 924.4. Elemental analysis calcd for $C_{56}H_{68}O_{12}$: C, 72.70; H, 6.54. Found: C, 72.48; H, 6.44.

Preparation of 13. Same as for **9**; calix[4]arene **1** (1.14 g, 2.69 mmol), potassium carbonate (3.72 g, 26.9 mmol), ditosylate **6** (1.60 g, 2.69 mmol), and acetonitrile (130 mL). The same quantities of potassium carbonate and ditosylate were added after 7 days: total reflux time 14 days; yield 54%; white solid from methanol–diethyl ether; mp 188–189 °C. ^{1}H NMR ($CDCl_3$) δ 7.07 (d, 8H, J_{H-H} = 7.5 Hz, meta Ar*H*), 6.99 (s, 8H, Ar′*H*), 6.80 (t, 4H, J_{H-H} = 7.5 Hz, para Ar*H*), 3.72–3.64 (m, 32H, OCH_2CH_2O), 3.68 (s, 8H, $ArCH_2Ar$); FAB positive, 925.6. Elemental analysis calcd for $C_{56}H_{68}O_{12}$: C, 72.70, H, 6.54. Found: C, 72.42; H, 6.41.

Preparation of 14. Same as for **9**; calix[4]arene **1** (2.13 g, 5 mmol), potassium carbonate (6.91 g, 50 mmol), ditosylate **7** (3.15 g, 5 mmol), and acetonitrile (250 mL). The same quantities of potassium carbonate and ditosylate were added after 3 days: total reflux time 6 days; yield 78%; white solid from acetone : mp 108–109 °C; ^{1}H NMR ($CDCl_3$) δ 7.75–7.24 (m, 12H, naphthyl *H*), 7.09 (d, 8H, J_{H-H} = 8.0 Hz, meta Ar*H*), 6.67 (t, 4H, J_{H-H} = 8.0 Hz, para Ar*H*), 4.28 (t, 8H, J_{H-H} = 5.0 Hz, OCH_2CH_2OAr), 3.86 (t, 8H, J_{H-H} = 5.0 Hz, OCH_2CH_2OAr), 3.76 (s, 8H, $ArCH_2Ar$), 3.65 (t, 16H, J_{H-H} = 5.0 Hz, naphthyl-OCH_2CH_2O), 3.45–3.29 (m, 8H, naphthyl-OCH_2CH_2O); FAB positive 1025.2. Elemental analysis calcd for $C_{64}H_{64}O_{12}$: C, 74.97, H, 6.30. Found: C, 74.90; H, 6.35.

Preparation of 15. Same as for **9**; calix[4]arene **1** (2.13 g, 5 mmol), potassium carbonate (6.91 g, 50 mmol), ditosylate **8** (3.36 g, 5 mmol), and acetonitrile (250 mL). The same quantities of potassium carbonate and ditosylate were added after 4 days: total reflux time 8 days: yield 79%; white solid from acetone; mp 82–83 °C. ^{1}H NMR ($CDCl_3$) δ 7.41–7.04 (m, 16H, diph-*H*), 7.21 (d, 8H, J_{H-H} = 8.0 Hz, meta Ar*H*), 6.78 (t, 4H, J_{H-H} = 8.0 Hz, para Ar*H*), 4.03 (t, 8H, J_{H-H} = 5.0 Hz, OCH_2CH_2OAr), 3.86 (t, 8H, J_{H-H} = 5.0 Hz, OCH_2CH_2OAr), 3.72 (s, 8H, $ArCH_2Ar$), 3.62–3.50 (m, 8H, diphenyl-OCH_2CH_2O), 3.45–3.29 (m, 8H, diphenyl-OCH_2CH_2O); FAB positive, 1077.03. Elemental analysis calcd for $C_{68}H_{68}O_{12}$: C, 75.82%; H, 6.36. Found: C, 75.80; H, 6.44.

Starting Materials for Extraction and SLMs Transports. The inorganic salts used to prepare the synthetic aqueous feed solutions for extraction and transport experiments ($NaNO_3$, $CsNO_3$, etc.) were analytical grade products from Prolabo and Aldrich. Radioactive ^{22}Na and ^{137}Cs used to spike the aqueous solutions (1500 kBq·L^{-1} < initial aqueous activity < 2500 kBq·L^{-1}) were provided by the Amersham Co. The ^{22}Na and ^{137}Cs γ spectra were obtained on a detection chain from Interchnique, an EGSP-2000-20R γ spectrometer equipped with germanium detectors. The counting was always sufficiently long to ensure a relative error in activity measurement of less than 5%. The organic diluents, 1,2-nitrophenyl hexyl ether (1,2-NPHE) and 1,2-nitrophenyl octyl ether (1,2-NPOE) used to dissolve **9**–**15** were synthesized by Chimie Plus and used without further purification.

Transport Measurements. The same flat-sheet supported liquid membrane device described by Stolwijk et al.[18] and shown in Figure 7 was used for the transport experiments. The volume of both aqueous solutions (feed and stripping) was ranging from 45 to 55 mL, depending on the glass devices manufactured by Prodilab and Verre & Science Co. The aereas of circular membranes were about 15–16 cm^2 made of polypropylene Celgard 2500 microporous support (of 25 μm thickness and 45% internal volumic porosity) soaked with a 10^{-2} M solution of **9**–**15** in 1,2-nitrophenyl octyl ether. The measurements were performed at a constant temperature of 25 °C.

Received for review February 10, 1995. Accepted June 21, 1995.[⊗]

AC950153I

(18) Stolwijk, T. B.; Sudhölter, E. J. R.; Reinhoudt, D. N. *J. Am. Chem. Soc.* **1987**, *109*, 7042.

[⊗] Abstract published in *Advance ACS Abstracts*, August 1, 1995.

Anal. Chem. **1995**, *67*, 3140–3147

Electrogenerated Chemiluminescence. 57. Emission from Sodium 9,10-Diphenylanthracene-2-sulfonate, Thianthrenecarboxylic Acids, and Chlorpromazine in Aqueous Media

Thomas C. Richards and Allen J. Bard*

Department of Chemistry and Biochemistry, The University of Texas at Austin, Austin, Texas 78712

The anodic oxidation of aqueous sodium 9,10-diphenylanthracene-2-sulfonate (DPAS) and 1- and 2-thianthrenecarboxylic acid (1- and 2-THCOOH) in the presence of tri-*n*-propylamine as a coreactant in aqueous solution produces electrogenerated chemiluminescence (ECL). In addition, the cathodic reduction of DPAS in the presence of peroxydisulfate as a coreactant also produces ECL in an acetonitrile–water solution (1:1 v/v). For DPAS, both the oxidative and the reductive ECL spectra are characteristic of DPAS fluorescence, with peak intensities at 430 nm. In contrast, the ECL spectra for 1- and 2-THCOOH are significantly red-shifted from the fluorescence spectra, indicating that the emission arises from a product of THCOOH rather than the excited state of the intact acid. The oxidation of chlorpromazine produces an ECL emission in the absence of an added coreactant following an unprecedented "self-annihilation" mechanism. These new aqueous ECL reactions should be useful in the design of new labels for ECL analysis of biomolecules (i.e., immunoassays, DNA probes).

Electrogenerated chemiluminescence (ECL)[1] arises from an energetic electron-transfer reaction between electrogenerated redox species represented by A^- and D^+, typically radical ions, to form an excited state (A^* or D^*) that emits in the visible region:

$$A + e^- \rightarrow A^- \qquad E_A \tag{1}$$

$$D - e^- \rightarrow D^+ \qquad E_D \tag{2}$$

$$A^- + D^+ \rightarrow A + D^* \quad (\text{or } A^* + D) \tag{3}$$

$$D^* \rightarrow D + h\nu \tag{4}$$

More recently, it was discovered that ECL precursors can also be generated in aqueous solution despite the limited potential range imposed by the oxidation and reduction of water.[2] Here, ECL is achieved by the simultaneous oxidation of tris(2,2′-bipyridinyl)ruthenium(II) [$Ru(bpy)_3^{2+}$] and a coreactant (e.g., $C_2O_4^{2-}$[3] or tri-*n*-propylamine (TPrA)[4]) capable of generating a suitable reductant upon oxidation (i.e., an oxidative-reduction mechanism):

$$Ru(bpy)_3^{2+} - e^- \rightarrow Ru(bpy)_3^{3+} \tag{5}$$

$$C_2O_4^{2-} - e^- \rightarrow C_2O_4^{\bullet-} \tag{6}$$

$$Ru(bpy)_3^{3+} + C_2O_4^{2-} \rightarrow Ru(bpy)_3^{2+} + C_2O_4^{\bullet-} \tag{6a}$$

$$C_2O_4^{\bullet-} \rightarrow CO_2 + CO_2^{\bullet-} \tag{7}$$

$$Ru(bpy)_3^{3+} + CO_2^{\bullet-} \rightarrow Ru(bpy)_3^{2+*} + CO_2 \tag{8}$$

$$Ru(bpy)_3^{2+*} \rightarrow Ru(bpy)_3^{2+} + h\nu \tag{9}$$

In these ECL schemes, the coreactant can be oxidized either at the electrode via eq 6 or in solution by the emitter via eq 6a.[3,4a] The excited state can also be generated by the sequence of eqs 10 and 11, as previously discussed for oxalate[3] and TPrA.[4a] In

$$Ru(bpy)_3^{2+} + CO_2^{\bullet-} \rightarrow Ru(bpy)_3^{+} + CO_2 \tag{10}$$

$$Ru(bpy)_3^{+} + Ru(bpy)_3^{3+} \rightarrow Ru(bpy)_3^{2+*} + Ru(bpy)_3^{2+} \tag{11}$$

the parallel reaction sequence for TPrA, the bond-breaking step (eq 7) involves the loss of a proton from the α-carbon of the radical cation. These ECL reactions have been used for the determination of both $Ru(bpy)_3^{2+}$[3c] and oxalate.[3b] To complement these oxidative-reduction examples, peroxydisulfate ($S_2O_8^{2-}$)[3c,5] and $Ru(bpy)_3^{2+}$ undergo an analogous inversion of this scheme (a reductive-oxidation mechanism, eqs 12–14 followed by eq 9) when the initial reactants are reduced rather than oxidized. In this case, the reduction of $S_2O_8^{2-}$ results in the formation of the strong oxidizing agent $SO_4^{\bullet-}$.

(1) Faulkner, L. R.; Bard, A. J. In *Electroanalytical Chemistry*; Bard, A. J., Ed.; Marcel Dekker: New York, 1977; Vol. 10, p 1.
(2) Knight, A. W.; Greenway, G. M. *Analyst* **1994**, *119*, 879.
(3) (a) Rubinstein, I.; Bard, A. J. *J. Am. Chem. Soc.* **1981**, *103*, 512. (b) Rubinstein, I.; Martin, C. R.; Bard, A. J. *Anal. Chem.* **1983**, *55*, 1580. (c) Ege, D.; Becker, W. G.; Bard, A. J. *Anal. Chem.* **1984**, *56*, 2413.
(4) (a) Leland, J. K.; Powell, M. J. *J. Electrochem. Soc.* **1990**, *137*, 3127. (b) McCord, P.; Bard, A. J. *J. Electroanal. Chem.* **1991**, *318*, 91.
(5) White, H. S.; Bard, A. J. *J. Am. Chem. Soc.* **1982**, *104*, 6891.

0003-2700/95/0367-3140$9.00/0

$$Ru(bpy)_3^{2+} + e^- \rightarrow Ru(bpy)_3^{+} \quad (12)$$

$$S_2O_8^{2-} + e^- \rightarrow SO_4^{\bullet-} + SO_4^{2-} \quad (13)$$

$$Ru(bpy)_3^{+} + S_2O_8^{2-} \rightarrow Ru(bpy)_3^{2+*} + SO_4^{\bullet-} + SO_4^{2-} \quad (13a)$$

$$Ru(bpy)_3^{+} + SO_4^{\bullet-} \rightarrow Ru(bpy)_3^{2+*} + SO_4^{2-} \quad (14)$$

By analogy with eqs 10 and 11 for oxalate and TPrA, an alternative to eq 14 for generation of the excited state with $S_2O_8^{2-}$ is eq 15 followed by eq 11.

$$Ru(bpy)_3^{2+} + SO_4^{\bullet-} \rightarrow Ru(bpy)_3^{3+*} + SO_4^{2-} \quad (15)$$

The sensitivity and selectivity of these coreactant analyses has led to the recent adaptation of the $Ru(bpy)_3^{2+}$/TPrA system for commercial analytical applications utilizing $Ru(bpy)_3^{2+}$ as a label (IGEN, Inc., Gaithersburg, MD, and Perkin-Elmer Corp., Norwalk, CT). Such applications and the need for novel labels to allow simultaneous analyses and internal referencing has prompted us to consider emitters other than $Ru(bpy)_3^{2+*}$ as ECL labels in aqueous solutions. The successful development of new labels is subject to several constraints, including the following: (1) the emitter must be soluble in aqueous solution, (2) the emission wavelength must be distinct from that of $Ru(bpy)_3^{2+*}$, (3) the oxidative or reductive electrochemistry must proceed within the relatively narrow potential range imposed by the oxidation and reduction of water, and (4) the oxidized or reduced intermediate must react with the electrogenerated coreactant intermediate, allowing formation of the excited state.

Sodium 9,10-diphenylanthracene-2-sulfonate (DPAS) has a strongly fluorescent excited state and is an energy acceptor from singlet ketones in aqueous media.[6]

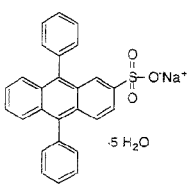

DPAS

DPAS was of particular interest for ECL studies, given its high fluorescence efficiency and short wavelength emission ($\Phi_F = 0.87$, peak emission at 428 nm[6]) compared to those of $Ru(bpy)_3^{2+}$ ($\Phi_F \approx 0.05$,[7] peak emission at 620 nm[7a]). We show here that DPAS does produce ECL, and we report the blue emission resulting from an oxidative-reduction scheme involving DPAS as the emitter and TPrA as the coreactant in aqueous media. We also report the ECL of DPAS in a reductive-oxidation scheme using $S_2O_8^{2-}$ as a coreactant in an MeCN–water solution (1:1 v/v).

With an interest in additional blue emitters, we have also studied the aqueous ECL of two carboxylic acid derivatives of thianthrene (TH), namely 1- and 2-thianthrenecarboxylic acid (1- and 2-THCOOH). We were attracted to the THCOOH derivatives

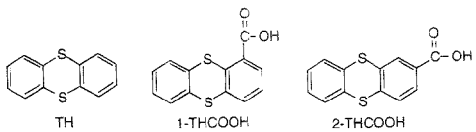

given the known blue ECL emission for TH (peak intensity at 434 nm[8]) in MeCN following the ion annihilation scheme of eqs 1–4. Derivatization of TH to its carboxylic acid derivative afforded the necessary solubility in aqueous solution, and these derivatives do produce ECL emissions in an oxidative-reduction scheme with TPrA as a coreactant. However, for these compounds, the ECL spectra are significantly red-shifted from the fluorescence spectra.

Finally, we have considered the aqueous ECL of the tranquilizer chlorpromazine (CPZ),[9] which is structurally related to TH.

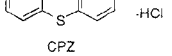

CPZ

Although we are unaware of reports of ECL for CPZ, the fluorescence, chemiluminescence, and electrochemistry of this pharmaceutical are well documented, including analytical applications. McCreery et al. studied the oxidation of CPZ and various reactions of the cation radical[10] and, more recently, extended the work to consider the reaction of the CPZ cation radical with dopamine,[11,12] methoxypromazine,[12] and hydroquinone.[12] In addition, the fluorescence[13–16] (including analytical applications[17,18]) and chemiluminescence[19,20] of CPZ have been investigated. CPZ also emits when oxidized in the absence of an added coreactant, presumably because the tertiary amine on the CPZ side chain acts as an internal coreactant. Related work (without the covalent binding of the coreactant to the emitter) is cited in a recent paper by Holeman and Danielson[21] on the chemiluminescence reactions of thiazide compounds with $Ru(bpy)_3^{3+}$. Here they discuss the

(6) Catalani, L. H.; Wilson, T.; Bechara, E. J. H. *Photochem. Photobiol.* **1987**, *45*, 273.
(7) Juris, A.; Balzani, V.; Barigelletti, F.; Campagna, S.; Belser, P.; von Zelewsky, A. *Coord. Chem. Rev.* **1988**, *84*, 85.
(8) Keszthelyi, C. P.; Tachikawa, H.; Bard, A. J. *J. Am. Chem. Soc.* **1972**, *94*, 1522.
(9) Siegel, G. J.; Albers, R. W.; Katzman, R.; Agranoff, B. W. *Basic Neurochemistry*, 3rd ed.; Little, Brown and Co.: Boston, 1981.
(10) Cheng, H. Y.; Sackett, P. H.; McCreery, R. L. *J. Am. Chem. Soc.* **1978**, *100*, 962.
(11) Deputy, A.; Wu, H. P.; McCreery, R. L. *J. Phys. Chem.* **1990**, *94*, 3620.
(12) Deputy, A. L.; McCreery, R. L. *J. Electroanal. Chem.* **1989**, *285*, 1.
(13) Mellinger, T. J.; Keeler, C. E. *Anal. Chem.* **1964**, *36*, 1840.
(14) Mellinger, T. J.; Keeler, C. E. *Anal. Chem.* **1963**, *35*, 554.
(15) Ragland, J. B.; Kinross-Wright, V. J. *Anal. Chem.* **1964**, *36*, 1356.
(16) Udenfriend, S.; Duggan, D. E.; Vasta, B. M.; Brodie, B. B. *J. Pharmacol. Exp. Ther.* **1957**, *120*, 26.
(17) Takahashi, D. M. *J. Pharm. Sci.* **1980**, *69*, 184.
(18) Clark, B. J.; Fell, A. F.; Milne, K. T.; Pattie, D. M. G.; Williams, M. H. *Anal. Chim. Acta* **1985**, *170*, 35.
(19) Nakano, M.; Sugioka, K.; Nakano, H.; Takyu, C.; Inaba, H. *Biochem. Biophys. Res. Commun.* **1985**, *130*, 952.
(20) Trush, M. A.; Reasor, M. J.; Wilson, M. E.; Van Dyke, K. *Chem.-Biol. Interact.* **1979**, *28*, 71.
(21) Holeman, J. A.; Danielson, N. D. *Anal. Chim. Acta* **1993**, *277*, 55.

utilization of tertiary amines present in the structures of erythromycin[22] and clindomycin[23] to assay these antibiotics via reactions with $Ru(bpy)_3^{2+}$ using flow injection and liquid chromatographic analyses.

EXPERIMENTAL SECTION

Chemicals. MeCN (Burdick and Jackson, Baxter Health Care Corp., Muskegon, MI) was transferred unopened into a glovebox (Vacuum Atmospheres Corp., Los Angeles, CA) under helium atmosphere and was used as received. For experiments run in MeCN, a sealed cell was loaded in the glovebox prior to each experiment. Tetrabutylammonium tetrafluoroborate ($TBABF_4$, electrometric grade; SACHEM, Inc., Austin, TX) was purified by recrystallization from either ethyl acetate–pentane (2 times; 1:1 v/v) or ethyl acetate–diethyl ether (3 times; 9:1 v/v), followed by drying under vacuum at 100 °C. Tetraethylammonium perchlorate (TEAP, electrometric grade wet with 8% water; SACHEM, Inc.), tri-*n*-propylamine (TPrA, 98%; Aldrich, Milwaukee, WI), thianthrene (97%, Aldrich), chlorpromazine hydrochloride (98%, Aldrich), sodium phosphate, monobasic monohydrate ($NaH_2PO_4 \cdot H_2O$, 99%; Baker, Phillipsburg, NJ), sodium phosphate, dibasic heptahydrate ($Na_2HPO_4 \cdot 7H_2O$, 99%; Mallinckrodt, Paris, KY), and ammonium peroxydisulfate ($(NH_4)_2S_2O_8$, 99%; Fischer Scientific, Fair Lawn, NJ) were used as received.

Sodium phosphate buffer solutions, 0.15 M, prepared with Milli-Q water (Millipore Corp., Bedford, WA) were 0.10 M in $Na_2HPO_4 \cdot 7H_2O$ and 0.05 M in $NaH_2PO_4 \cdot H_2O$. Buffer solutions containing TPrA were prepared similarly except that 0.15 M $NaH_2PO_4 \cdot H_2O$ was used to offset the basicity of TPrA. The pH of these buffer solutions was adjusted with either concentrated phosphoric acid (H_3PO_4) or 4 M NaOH.

DPAS was synthesized according to a variation on the procedure of Catalani and co-workers.[5] Thus, the initial reaction mixture consisted of 1 g of 9,10-diphenylanthracene (DPA, 98%; Aldrich) suspended in 7 mL of nitrobenzene (99%; Kodak), to which 0.25 mL of fuming sulfuric acid (27–33% free SO_3; Aldrich) was added. The final product was purified by ion-exchange column chromatography using Dowex 1 × 2–100 resin (50–100 dry mesh; Aldrich). Aqueous solutions of DPAS·$5H_2O$ were prepared by dissolving the required amount of solid in a few drops of methanol prior to transfer to the aqueous solution.

1- and 2-THCOOH were synthesized according to procedures of Gilman and Swayampati[24] with the exception that 1.6 M *n*-butyllithium in hexane (Aldrich) was substituted for their ethereal solutions of *n*-butyllithium.

Instrumentation. Cyclic voltammetry experiments without photon detection utilized either a BAS 100A electrochemical analyzer (Bioanalytical Systems, West Lafayette, IN) or a Princeton Applied Research Model 173/175 potentiostat/universal programmer (PAR, Princeton, NJ) and an Omnigraphic 2000 *X*–*Y* recorder (Bausch and Lomb–Houston Instrument Division, Austin, TX). Cyclic voltammograms with simultaneous photon detection were recorded using the PAR 173/175 in conjunction with a Hamamatsu C1230 photon counter (Bridgewater, NJ) equipped with a Hamamatsu R928-P photomultiplier tube. The photomultiplier tube was housed in a water-jacketed Products For Research, Inc. Model TE308TSRF refrigerated chamber maintained at −10 °C. Primary cooling of the water jacket to 10 °C was accomplished using an MGW Lauda Model RMS6 refrigeration unit (Brinkmann Instruments Co., Westbury, NY). For plots of ECL intensity versus potential, the output from the photon counter was fed into the *y*-axis of the *X*–*Y* recorder during potential scans.

Fluorescence and ECL spectra were recorded using a charge-coupled device (CCD) camera and spectrometer (1 mm entrance slit) interfaced to a Dell System 200 personal computer (Austin, TX) as previously described.[25] The same procedures (spectral calibration, etc.) were followed except that different pulse sequences were used and the CCD detector was maintained at −110 °C for the TPrA/THCOOH and TPrA/DPAS experiments and at −100 °C for the $S_2O_8^{2-}$/DPAS experiments. Excitation for the fluorescence spectra was achieved by holding a longwave (366 nm) UV lamp (Model UVGL-25; UVP, Inc., San Gabriel, CA; sold by Fisher Scientific, Pittsburgh, PA) next to the cell and at right angles to the entrance slit of the spectrometer.

Cells and Electrodes. Except where noted, all electrochemical and ECL experiments utilized Pt disk working electrodes (sealed in glass) in a conventional three-electrode cell configuration. These working electrodes were polished on a felt pad (Buehler, Ltd., Lake Bluff, IL) before each experiment with 0.05 μm alumina (Buehler, Ltd.) suspended in water.

For ECL experiments employing a Pt gauze working electrode, the electrode consisted of a 6 × 9 mm gauze flag (52 mesh; Aldrich). The electrode was cleaned prior to each experiment by immersion in concentrated nitric acid, followed by rinsing in distilled water and heating in a Bunsen burner flame. The CPZ experiments utilized a highly oriented pyrolytic graphite (HOPG; Union Carbide, Cleveland, OH) working electrode (with freshly exposed material for each experiment) in a recently described configuration.[26] This same arrangement was used with a Pt electrode for the 2-THCOOH ECL emission versus potential experiments.

Nonaqueous potential referencing to ferrocene was accomplished by adding the standard directly to the solutions. Potential referencing of aqueous solutions to the saturated calomel electrode (SCE) was accomplished by acquiring data versus a Ag quasi-reference electrode for which the potential versus SCE was known. For qualitative comparison purposes, the ferrocene $E^{0\prime}$ vs SCE varies (due primarily to differences in liquid junction potentials) from +0.307 to +0.56 V, depending upon the solvent/supporting electrolyte system.[27,28]

RESULTS AND DISCUSSION

Sodium 9,10-Diphenylanthracene-2-sulfonate. The maximum solubility of aqueous DPAS in 0.15 M sodium phosphate buffer (pH 7.5) is $\approx 1 \times 10^{-5}$ M. At this low concentration, no anodic current is observed for DPAS above the background oxidation of water. However, if 1×10^{-5} M DPAS is oxidized in

(22) Danielson, N. D.; He, L.; Noffsinger, J. B.; Trulli, L. *Pharm. Biomed. Anal.* **1989**, *7*, 1281.
(23) Targrove, M. A.; Danielson, N. D. *J. Chromatogr. Sci.* **1990**, *28*, 505.
(24) Gilman, H.; Swayampati, D. R. *J. Am. Chem. Soc.* **1957**, *79*, 208.
(25) The setup for spectral acquisition utilized a hybridization of schemes a and b shown in Figure 1 of ref 4b. Thus, instead of removing the 100 mm Pentax camera lens, the spectrometer was placed about 15 in. from the camera, with the lens focused on the spectrometer exit port. This allowed recording of broader spectra than was possible with the setup shown in Figure 1b.
(26) Xu, X.; Bard, A. J. *Langmuir* **1994**, *10*, 2409.
(27) Bard, A. J.; Faulkner, L. R. *Electrochemical Methods: Fundamentals and Applications*; Wiley: New York, 1980; p 701.
(28) Geiger, W. E. In Journal of Organometallic Chemistry Library 22: *Organometallic Radical Processes*; Trogler, W. C., Ed.; Elsevier: Amsterdam, 1990; p 144.

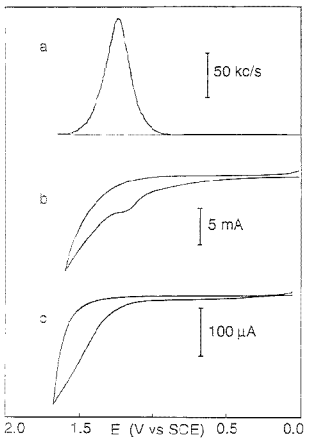

Figure 1. Emission (a) during cyclic voltammetry (b) of 1×10^{-5} M DPAS and 0.15 M TPrA in pH 7.5 sodium phosphate buffer at 6 × 9 mm Pt gauze (52 mesh) electrode. Scan rate, 100 mV/s. (c) Cyclic voltammogram of 0.05 M TPrA in pH 7.5 sodium phosphate buffer at a 1.5 mm diameter Pt electrode. Scan rate, 200 mV/s.

the presence of 0.15 M TPrA, an emission is observed that coincides with an oxidation wave that is superimposed on the TPrA oxidation and background oxidation of water, as shown in Figure 1, parts a and b. For comparison, the oxidation of 0.05 M TPrA in the absence of DPAS is shown in Figure 1c. The fact that an oxidation current is observed for 1×10^{-5} M DPAS only in the presence of TPrA suggests a catalytic current enhancement due to the regeneration of DPAS via reduction of $DPAS^{-}$ by TPrA or an intermediate. Presumably, ECL results from a sequence of reactions analogous to eqs 5–8 (or eqs 10 and 11) and eq 9, where $Ru(bpy)_3^{3+/2+}$ is replaced by $DPAS^{-/0/+}$, $C_2O_4^{2-}$ by TPrA, $CO_2^{\bullet-}$ by $Pr_2NCHEt^{\bullet}$ and CO_2 by H^{+}. Despite the low DPAS concentration (1×10^{-5} M), this emission is visible when viewed in a dark room, and no emission is observed in the absence of either TPrA or DPAS. For the DPAS/TPrA system, electrode passivation occurs after one scan and prevents observation of subsequent emissions without electrode cleaning. This behavior suggests that products of chemical reactions following the oxidation of DPAS passivate the electrode. The electrode can be cleaned mechanically or by pulsing into the background reduction of water (−1.4 V vs SCE) for a few seconds, after which ECL can again be observed upon oxidation. In an effort to understand the passivation process, we undertook cyclic voltammetric experiments in MeCN; a typical voltammogram is shown in Figure 2. Clearly, the oxidation of DPAS is complicated by subsequent chemical reactions, as evidenced by the lack of chemical reversibility. This behavior, which persists at scan rates as high as 10 V/s, could be due to reaction of $DPAS^{-}$ with water or OH^{-} (supplied by the five waters of hydration) to form products. The addition of neutral alumina to these solutions in an attempt to remove water did not result in profound changes in the electrochemistry. Attempts to increase the ECL emission intensity by stabilization of $DPAS^{+}$ using surfactant or by polysulfonation of DPA were unsuccessful. For the DPAS/TPrA system, ECL emissions can be detected (using the photon counter) at a concentration as low as 2×10^{-8} M. For comparison, $Ru(bpy)_3^{2+}$ can be detected at concentrations

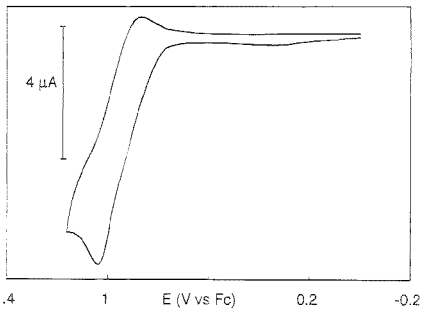

Figure 2. Cyclic voltammogram of 0.92 mM DPAS in MeCN at a 1.5 mm diameter Pt electrode. Supporting electrolyte, 0.1 M $TBABF_4$; scan rate, 200 mV/s.

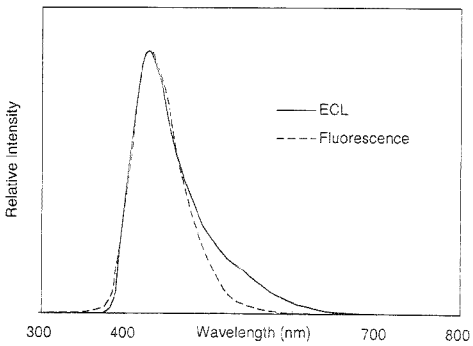

Figure 3. Scaled fluorescence and ECL spectra for a solution of 1×10^{-5} M DPAS and 0.15 M TPrA in pH 7.5 sodium phosphate buffer. The ECL emission was generated by repetitively pulsing a 6 × 9 mm Pt gauze (52 mesh) electrode from 0.0 V (vs SCE, 8 s) to +1.2 V (2 s) to −1.4 V (2 s) and back to 0.0 V. Light was generated on the positive pulse in this sequence (the negative pulse was for electrode cleaning purposes) and was integrated for 2 min to produce the spectrum. Both peak intensities are at 430 nm.

about 60 times more dilute at similar emission intensities. At higher concentrations of 5×10^{-6} M and using the CCD camera (and correcting for the detector sensitivity), the $Ru(bpy)_3^{2+}$ emission is ~100 times more intense than the DPAS emission. Figure 3 shows the ECL and fluorescence spectra of 1×10^{-5} M DPAS. The similarity between the fluorescence and ECL spectra (despite the discrepancy on the long wavelength side) suggests that the ECL emission is from $DPAS^{*}$.

Details concerning the electrochemistry and ECL of the $Ru(bpy)_3^{2+}/S_2O_8^{2-}$ system in MeCN–water have been considered previously[5] and the reductive cyclic voltammogram of $S_2O_8^{2-}$ is shown in Figure 4a. Here, the irreversibility is due to the process outlined in eq 13. Under these conditions, the onset of the background reduction of water (not shown) producing gaseous H_2 occurs at about −1.0 V. The reduction of DPAS in MeCN is shown in Figure 4b, and the reversibility of this couple ($DPAS^{0/-}$) compared to the oxidation of DPAS shown in Figure 2 indicates that $DPAS^{-}$ is significantly more stable in MeCN than $DPAS^{+}$. The small prewave in Figure 4b appears to be due to adsorbed DPAS, since the current for this wave increases linearly with scan rate (ν), whereas that for the more negative couple increases with

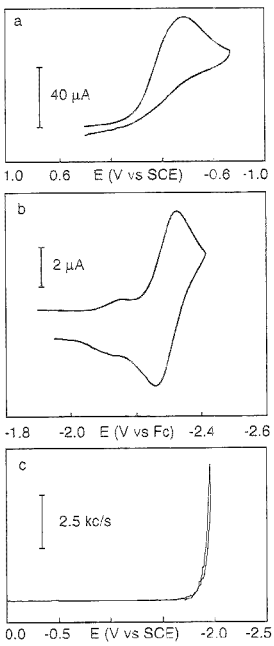

Figure 4. (a) Cyclic voltammogram of 11 mM $(NH_4)_2S_2O_8$ in an MeCN–water solution (1:1 v/v) at a 1.5 mm diameter Pt electrode. Supporting electrolyte, 0.2 M TEAP; scan rate, 100 mV/s. (b) Cyclic voltammogram of 0.93 mM DPAS in MeCN at a 1.5 mm diameter Pt electrode. Supporting electrolyte, 0.1 M $TBABF_4$; scan rate, 200 mV/s. (c) ECL emission for the reduction of 1.1 mM DPAS and 25 mM $(NH_4)_2S_2O_8$ in MeCN–water solution (1:1 v/v) at a 2.0 mm diameter Pt electrode. Supporting electrolyte, 0.2 M TEAP; scan rate, 100 mV/s.

$v^{1/2}$ over a range of 0.1–10 V/s. Because this reduction occurs well into the background reduction of water, no cathodic current above background is evident in MeCN–water (1:1 v/v) solutions. However, if the potential is scanned into the background reduction of water in the presence of $S_2O_8^{2-}$, an emission is observed at a potential corresponding to the reduction of DPAS (after making the approximate conversion from ferrocene to SCE potentials using the values given in the Experimental Section), as shown in Figure 4c. No emission is observed in the absence of either $S_2O_8^{2-}$ or DPAS. This result is consistent with previous results with the $Ru(bpy)_3^{2+}/S_2O_8^{2-}$ system,[5] in which no emission is seen until the potential is scanned sufficiently negative to reduce $Ru(bpy)_3^{2+}$ and allow generation of the excited state via the sequence of reactions 12–15. This scheme can be modified to describe the ECL reactions for DPAS by substituting $DPAS^{+/0/-}$ respectively for $Ru(bpy)_3^{3+/2+/+}$. As shown in Figure 5, the blue ECL spectrum for the DPAS emission matches the fluorescence spectrum and also matches the ECL and fluorescence spectra for the oxidative-reduction of DPAS with TPrA shown in Figure 3.

In considering the energetics of an ECL system, one notes the standard potentials of the relevant half-reactions (yielding the free energy of the electron-transfer reaction) and the energy of the emitting state. For the oxidation of DPAS and TPrA, these

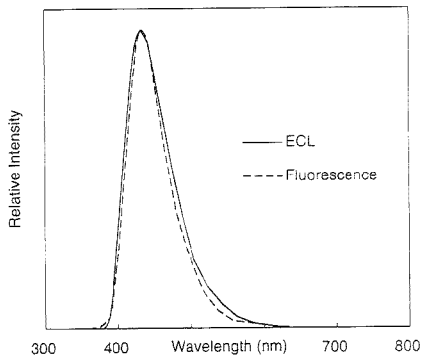

Figure 5. Fluorescence and ECL spectra for the same solution as in Figure 4c. The ECL emission was generated by pulsing a 2.0 mm diameter Pt electrode to −2.2 V (vs SCE) and integrating the emission for 5 s. Both peak intensities are at 430 nm.

are

$$DPAS^{\bullet+} + E^- \rightarrow DPAS \qquad E^\circ \approx +1.3 \text{ V vs SCE}$$

$$Pr_2NC^+HEt + e^- \rightarrow Pr_2N\dot{C}HEt \qquad E^\circ \approx -1.1 \text{ V vs SCE}^{29}$$

$$DPAS^* \text{ (singlet)} \rightarrow DPAS - h\nu \qquad E_s = 2.9 \text{ eV}$$

The enthalpy of the electron-transfer reaction between $DPAS^{\bullet-}$ and $Pr_2N\dot{C}HEt$, correcting for an entropy of about 0.1 eV, is −2.3 eV, clearly well below that needed to produce singlet DPAS*, so that this would be classified as an "energy-deficient" reaction. As with other reactions of this type, the excited singlet probably forms via triplet-triplet annihilation (a T-route).[1] Although the oxidative DPAS/oxalate system would be "energy-sufficient", no emission was observed for experiments with oxalate as the coreactant.

The reductive path energetics corresponds to the following half-reactions:

$$DPAS + e^- \rightarrow DPAS^{\bullet-} \qquad E^\circ \approx -1.9 \text{ V vs SCE}$$

$$SO_4^{\bullet-} + e^- \rightarrow SO_4^{2-} \qquad E^\circ \approx +3.2 \text{ V vs SCE}^{30}$$

In this case, the electron-transfer reaction between $DPAS^{\bullet-}$ and $SO_4^{\bullet-}$ is sufficient to produce singlet DPAS* directly (an S-route). Despite these favorable energetics, the emission intensity for 1×10^{-5} M DPAS is about the same for the DPAS/TPrA oxidation as it is for the DPAS/$S_2O_8^{2-}$ reduction.

Thianthrenecarboxylic Acids. The oxidation of 2-THCOOH in aqueous solution occurs near +1.0 V, as shown in Figure 6a. The broad anodic process between 0.0 and +0.5 V and the more prominent cathodic process at −0.2 V are characteristic of oxide formation and reduction at a Pt electrode in aqueous solution at this pH and appear in scans in the absence of 2-THCOOH. These processes can be eliminated if the potential is cycled no further negative than +0.15 V, as shown in Figure 6b. The chemical

(29) The reduction potential for a similar species, $Et_2NC^{\bullet}HMe$, is reported as −1.12 V vs SCE: Wayner, D. D. M.; McPhee, D. J.; Griller, D. *J. Am. Chem. Soc.* **1988**, *110*, 132.

(30) Memming, R. *J. Electrochem. Soc.* **1969**, *116*, 785.

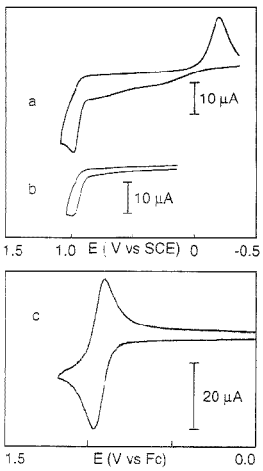

Figure 6. (a) Cyclic voltammogram of 2.0 mM 2-THCOOH in pH 8.5 sodium phosphate buffer at a 1.5 mm diameter Pt electrode at a scan rate of 200 mV/s. (b) Cyclic voltammogram of 1.4 mM 2-THCOOH under the same conditions as for part a, except that the scan cycled from −0.15 V instead of from −0.35 V. (c) Cyclic voltammogram of 2.0 mM 2-THCOOH at a 1.5 mm diameter Pt electrode in MeCN, 0.1 M $TBABF_4$ at a scan rate of 200 mV/s. Aqueous scans a and b are referenced to SCE. Nonaqueous scan c is referenced to ferrocene.

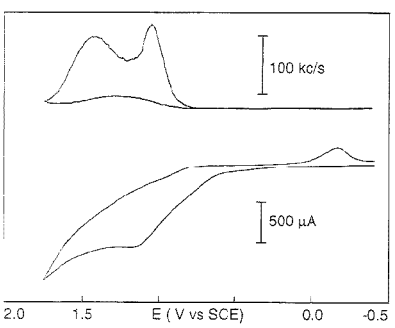

Figure 7. Cyclic voltammogram (bottom) and simultaneous emission (top) of 5.2 mM 2-THCOOH and 0.15 M TPrA in pH 7.5 sodium phosphate buffer at a 6 mm diameter Pt electrode at a scan rate of 100 mV/s.

irreversibility shown in parts a and b of Figure 6 (and observed in similar experiments scanning up to 50 V/s) indicates the instability of oxidized 2-THCOOH in aqueous solution and its rapid conversion to some product. In contrast to this, similar experiments run in dry MeCN (Figure 6c) show the oxidized product to be stable. This suggests that the decomposition of the oxidized acid is due to reaction with water as opposed to other possibilities, such as decarboxylation with loss of CO_2.

Both 1- and 2-THCOOH produce ECL emission when oxidized in aqueous sodium phosphate buffer solution in the presence of TPrA as a coreactant, as shown in Figures 7 and 8 for 2-THCOOH. (The behavior of 1-THCOOH is similar except that the peak emission intensity is 6−7 times less intense than that of 2-THCOOH.) If these same experiments are run in the absence of

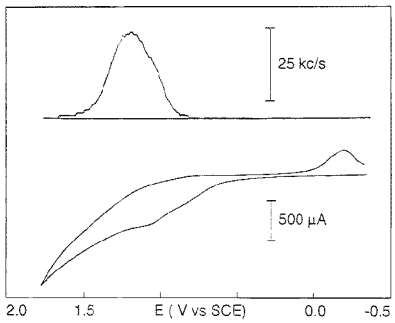

Figure 8. Cyclic voltammogram (bottom) and simultaneous emission (top) of 0.26 mM 2-THCOOH and 0.15 M TPrA under the same conditions as in Figure 7.

TPrA or the acid, no emission is observed. Although the anodic current is dominated by the oxidation of the deprotonated acid, the electrochemistry is complicated by the coincidence of this process with both the onset of the broad, irreversible oxidation wave for TPrA (Figure 1c) and the background oxidation of water. The two distinct emission peaks as a function of potential in Figure 7 suggest contributions from two different electrode processes. It is possible that the first peak is due to reactions associated with the homogeneous oxidation of TPrA following reaction 6a (with $2\text{-TH}^{-}\text{COO}^{-}$ replacing $Ru(bpy)_3^{2+}$) and that the second peak results from the direct heterogeneous oxidation of TPrA at the electrode following reaction 6. This hypothesis is supported by the results of Figure 8 recorded at a lower 2-THCOOH concentration, where the second-order reaction 6a will be slower and less important. Under the conditions of Figure 8, the first emission appears as a small shoulder in the dominant second emission.

The fluorescence and ECL spectra of 1- and 2-THCOOH are shown in Figure 9. The fluorescence maxima for 1- and 2-THCOOH are at 505 and 480 nm, respectively. For comparison, the emission maximum for thianthrene fluorescence in MeCN is at 434 nm.[8] The ECL maxima for each acid are at 570 nm, showing a strong shift toward longer wavelength compared to the respective fluorescence spectra. Under these optimized conditions, the 2-THCOOH emission is just visible to the dark-adapted eye. The differences between the fluorescence and ECL spectra for the THCOOH acids suggest that at least part of the ECL emission is from some species other than an excited state of the intact acid.

Chlorpromazine. McCreery and co-workers[10] previously investigated reactions associated with the oxidation of CPZ, and the voltammetric curves found in our laboratory (Figure 10) agree with their results. Under acidic aqueous conditions, the oxidation proceeds as two discrete processes (Figure 10a), the first of which is quasi-reversible and the second irreversible. The abnormally sharp peak on the first anodic wave seen in parts a and b of Figure 10 has been attributed[10] to adsorption of CPZ. Likewise, the shoulder on the cathodic return wave in Figure 10b can be attributed to an adsorption process. When the scan is reversed after the first oxidation, as shown in Figure 10b, the increased reversibility (compared to Figure 10a) suggests that a product from the second oxidation reacts with the oxidized form of CPZ.

If CPZ is oxidized at higher pH in sodium phosphate buffer solution, the electrochemistry changes to that shown in the bottom

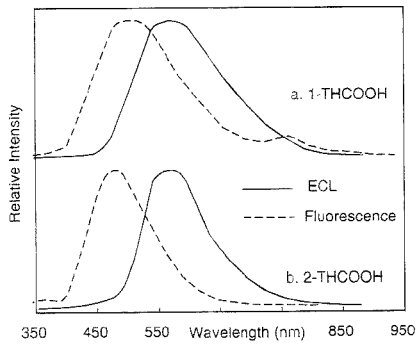

Figure 9. Fluorescence and ECL spectra of 9.1 mM 1-THCOOH (a) and 20 mM 2-THCOOH (b) taken in pH 8.5 sodium phosphate buffer containing 0.15 M TPrA. ECL emissions were generated by alternately pulsing a 6 × 9 mm Pt gauze (52 mesh) electrode between +1.4 (0.5 s) and −0.5 V (2 s) vs SCE for a duration of 40 min for 1-THCOOH and 20 min for 2-THCOOH with a stirred solution. The peak fluorescence intensity is at 480 nm for 2-THCOOH and 505 nm for 1-THCOOH. The peak ECL intensities are at 570 nm for both isomers. The intensities have been scaled for comparison purposes. At equal THCOOH concentrations (20 mM) and acquisition times, the intensities of the 2-THCOOH emissions are ~6–7 times those of 1-THCOOH.

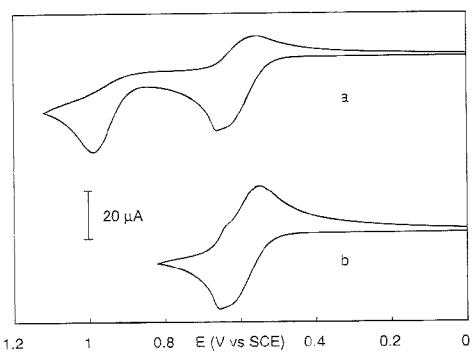

Figure 10. (a) Cyclic voltammogram of 0.98 mM CPZ in 0.01 M HCl, 0.2 M NaCl at a 6 mm diameter HOPG electrode at a scan rate of 50 mV/s. (b) Cyclic voltammogram for the same system and conditions as in part a with scan reversal after the first oxidation.

of Figure 11. The first oxidation is now irreversible, and the electrochemistry is in general more complex than that of Figure 10, as evidenced by a shoulder on the first oxidation wave, increased current, and a broadening of the second wave. As with the TPrA oxidation, analysis of the second oxidation process is complicated by its coincidence with the background oxidation of water. A more important observation under these conditions is ECL emission associated with the second oxidation process (in the absence of an added coreactant), as shown in Figure 11. Attempts to acquire the ECL spectrum for this process for comparison to the photoluminescence spectrum were unsuccessful due to low emission intensities and electrode fouling. Also unsuccessful were attempts to determine the wavelength of the peak emission using interference filters for specific, narrow wavelength ranges between 450 and 600 nm. No emission is

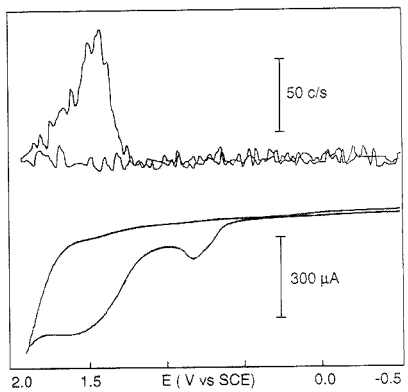

Figure 11. Cyclic voltammogram (bottom) and simultaneous emission (top) for 1.0 mM CPZ taken at a 6 mm diameter HOPG electrode in pH 7.5 sodium phosphate buffer at a scan rate of 200 mV/s.

observed under the conditions of Figure 10 (with or without 50 mM TPrA added), where the electrochemistry is less complex and electrode fouling does not occur.

Earlier mechanistic work by McCreery and co-workers[10] has shown that monooxidized forms of CPZ are converted to sulfoxides in aqueous solution via nucleophilic attack by water at the sulfur position. That work, in conjunction with our results, suggests that the first oxidation of CPZ is associated with the tricyclic ring system and that the second oxidation involves the tertiary amine on the side chain (analogous to the oxidation of THCOOH and TPrA). Presumably, the amine then undergoes reactions similar to those seen with TPrA,[4a] eqs 6 and 7, to produce a strong reducing agent that reacts with the ring system to generate a luminescent excited state. Thus, it is likely that this "self-annihilation" ECL process proceeds as shown in eqs 5–8, where the tricyclic portion of CPZ replaces $Ru(bpy)_3^{2+}$ and is covalently bonded to the coreactant X (the tertiary amine on the side chain). The self-annihilation could proceed via an intramolecular or an intermolecular process.

CONCLUSIONS

New ECL reactions of modified hydrocarbons and aromatic heterocyclic compounds that occur in aqueous solutions with the coreactants TPrA and $S_2O_8^{2-}$ have been found. These can be useful as ECL-active labels for analysis of biomolecules (immunoassay, DNA probes) and complement $Ru(bpy)_3^{2+}$ which is used in such studies.

When DPAS is oxidized in the presence of TPrA or reduced with $S_2O_8^{2-}$, a blue ECL emission results which is characteristic of DPAS fluorescence. The spectral separation between this emission and that for $Ru(bpy)_3^{2+}$ makes DPAS a good choice for use as a complementary label to $Ru(bpy)_3^{2+}$ in bioanalytical applications.

Oxidation of thianthrenecarboxylic acid in the presence of TPrA results in an ECL emission from a product that is different from the intact acid. Oxidation of chlorpromazine without added

coreactant (TPrA) produces an ECL emission via an unprecedented self-annihilation reaction.

ACKNOWLEDGMENT

This work was generously supported by grants from the Texas Advanced Research Program and IGEN, Inc. We thank Fu-Ren (Frank) Fan, Paul McCord, Mark Richter, and Xiaohong Xu for discussions throughout this work. We also gratefully acknowledge Union Carbide Corp. for the donation of HOPG and IGEN, Inc. and Perkin-Elmer Corp. for their donations of prototype ECL instruments and reagents.

Received for review November 23, 1994. Accepted June 29, 1995.[⊗]

AC941125N

[⊗] Abstract published in *Advance ACS Abstracts,* August 15, 1995.

Anal. Chem. 1995, *67*, 3148–3153

Determination of Ca, Cu, Fe, K, Na, and Si in Polyimides for Microelectronics by Electrothermal Atomic Absorption Spectrometry Involving Sample Dissolution in Organic Solvents

Viliam Krivan* and Bernhard Koch

Sektion Analytik und Hochstreinigung, Universität Ulm, D-89069 Ulm, Germany

A method for the direct determination of the problem trace impurities of Ca, Cu, Fe, K, and Na as well as of Si in solutions of polyimides in organic solvents by electrothermal atomic absorption spectrometry is described. The suitability of different solvents and the influence of matrix residues accumulating in the atomizer on the characteristic mass and the tube lifetime were examined. For all elements excluding Si, no chemical modification was necessary, and depending on the applied sample size, the tube lifetime varied between 400 and 800 atomization cycles. For the elements Ca, Cu, Fe, K, Na, and Si, detection limits of 0.5, 2, 5, 2, and 25 ng·g^{-1}, respectively, were obtained, these being by a factor of 5 (for Fe)–1200 (for Ca) lower than those obtained by the digestion method. Comparison of the results by the proposed method with neutron activation analysis and four other methods proved that satisfactory accuracy was achieved.

Polyimides are employed as permanent coatings in manufacturing of advanced integrated circuits. Highly viscous solutions of these organic polymers are usually applied on silicon wafers as layers of 1–10 μm. The most detrimental impurities include the natural radioactive elements Th and U, causing the so-called soft errors. The metals K, Na, Ca, Fe, Cr, and Cu as well as the anionic species Cl^- and SO_4^{2-} may lead to corrosion and degradation of the devices.[1,2] Because of their high mobility, the alkali metal ions are of extraordinary importance.[3] Typically, a maximum sum concentration of 0.5–1 μg·g^{-1} for all metallic impurities is specified;[2] thus powerful, reliable, and rapid analytical methods are required for routine analysis of these materials.

Of the direct methods that employ solid samples, instrumental neutron activation analysis (INAA) and laser ablation ion trap mass spectrometry (LAITMS) has been applied to analysis of polyimides to date. Applying INAA to this kind of matrix, difficulties occur with formation of gaseous products during the irradiation, and its instrumental performance is considerable limited also by high Compton background due to ^{82}Br.[4,5] Therefore, the required limits of detection can often be achieved only by using radiochemical separations. LAITMS allows a three-dimensional analysis of the analyte distribution;[6] however, the calibration is difficult, and this highly specialized method is not suitable for routine analysis. Total reflection X-ray fluorescence spectroscopy (TXRFS) has proved to be a useful method, not only for the determination of metallic impurities in and on the oxide layer of silicon wafers[7] but also for the direct determination in insulating polyimide layers on the chip as well.[8] Electrothermal atomic absorption spectrometry (ETAAS) with direct solid sampling has been applied to the analysis of some polymers,[9–12] but not yet to the analysis of polyimides. Due to only minimized sample handling, this technique can largely overcome the contamination problems; however, the introduction of solid samples into the graphite furnace is not yet satisfactorily developed, especially with respect to automation. In the analysis of powdered polymer samples by ETAAS using slurry sampling, problems occur with the preparation of homogeneous suspensions.[13]

Solution techniques require time-consuming digestion procedures (microwave digestion, plasma ashing), which represent a considerable source of contamination; therefore, their application for the determination of the elements posing contamination risk, such as alkali and alkali-earth metals in the prescribed concentration range, is extremely difficult. So far, digestion of polyimides has been used in connection with inductively coupled plasma mass spectrometry (ICPMS).[14]

The dissolution of polymers in organic solvents has proved to be more advantageous than their digestion with mineral acids.[10,15,16] Scheubeck and Quella[16] reported the analysis of solutions of polyimide in *N*-methylpyrrolidone (NMP) by ETAAS; however, the detection limits achieved are too poor for the analysis attempted here (0.5 μg·g^{-1} for K and 1 μg·g^{-1} for Fe and Cu). Much lower detection limits were reported by Fitzgerald and

(1) Casper, L. A., Ed. *Microelectronics Processing*; American Chemical Society: Washington, DC, 1986.
(2) Gercken, B.; Pavel, J.; Reus, G. Presented at the 12th International Symposium on Microchemical Techniques, Cordoba, Spain, 1992.
(3) Sacher, E. *IEEE Trans. Electr. Insul.* **1983**, *EI-18*, 369–373.
(4) Franek, M.; Krivan, V. *Anal. Chim. Acta* **1993**, *274*, 317–325.
(5) Kobayashi, K.; Kudo, K. *Isotopenpraxis* **1982**, *18*, 47–50.
(6) Gill, C. G.; Blades, M. W. *J. Anal. At. Spectrom.* **1993**, *8*, 261–267.
(7) Eichinger, P.; Rath, H. J.; Schwenke, H. *ASTM Spec. Tech. Publ.* **1989**, *990*, 305–313.
(8) Reus, U.; Freitag, K.; Fleischhauer, J.; Haase, A.; Prange, A.; Pavel, J. Presented at Denver X-Ray Conference, Colorado Springs, CO, 1992.
(9) Girgis-Takla, P.; Chroneos, I. *Analyst* **1978**, *103*, 122–127.
(10) Henn, E. L. *Anal. Chim. Acta* **1974**, *73*, 273–281.
(11) Rühl, W. J. *Fresenius Z. Anal. Chem.* **1985**, *322*, 710–712.
(12) Janssen, A.; Brückner, B.; Grobecker, K.-H.; Kurfürst, U. *Fresenius Z. Anal. Chem.* **1985**, *322*, 713–716.
(13) Chiricosta, S.; Gum, G.; Gallo, R.; Spadaro, A.; Vitarelli, P. *At. Spectrosc.* **1982**, *3*, 185–187.
(14) Gercken, B.; Pavel, J.; Suter, O. *Spec. Publ. R. Soc. Chem.* **1993**, *124*, 12–21.
(15) Bellara, M. A.; Anzano, J. M.; Castillo, J. R. *Analyst* **1990**, *115*, 955–957.
(16) Scheubeck, E.; Quella, F. *Siemens Forsch. EntwicklungsBer.* **1987**, *16* (3), 122–126.

0003-2700/95/0367-3148$9.00/0

Table 1. Instrumental Parameters and Experimental Conditions

experimental conditions	element					
	Ca	Cu	Fe	K	Na	Si
wavelength (nm)	422.7	324.8	248.3	766.5	589.0	251.6
spectral band width (nm)	0.7	0.7	0.2	0.7	0.2	0.2
current (mA) of HCL light source	15	15	30	12	12	40
drying temp (°C)	130 (dioxane)/240 (NMP and cyclohexanone)					
	ramp time 5 s, hold time 30 s, for all elements					
pyrolysis temp (°C)	1400	1200	1200	1000	900	1200
	ramp time 10 s, hold time 20 s, for all elements					
atomization temp (°C)	2200	2300	2300	2000	1800	2600
	max power heating, hold time 5 s, for all elements (except Ca in dioxane: hold 7 s)					
int gas flow ($mL \cdot min^{-1}$ Ar)	250	0	0	250	250	0
cleaning	2600 °C, hold 3 s, for all elements					
modifier						30 μg Pd/20 μg $Mg(NO_3)_2$

Almeida[17] for Ca, Cu, and Fe by ICP-AES (5, 7, and 15 $ng \cdot g^{-1}$, respectively) and for Na by ETAAS (10 $ng \cdot g^{-1}$).

In this paper, an ETAAS technique for determination of Ca, Cu, Fe, K, Na, and Si at concentrations to lower nanogram per gram level in polyimides that involves their dissolution in organic solvent is described.

EXPERIMENTAL SECTION

Apparatus. All measurements were carried out with a Perkin-Elmer 4100ZL atomic absorption spectrometer (Perkin-Elmer, Überlingen, Germany) equipped with a transversely heated graphite atomizer (THGA) and tubes with integrated platforms (Part No. 504 033), a solvent-resistant valve set, and an AS 70 autosampler. Hollow cathode lamps (HCL) were used as light sources. An ultrasonic probe Sonoplus HD 70 (Bandelin Electronic, Berlin, Germany) was used for pretreatment of the sample solutions for the determination of iron. Background correction was performed by the longitudinal Zeeman effect.

A pressure microwave decomposition system PMD (H. Kürner, Rosenheim, Germany) equipped with quartz bombs was used for digestion of the samples.

Samples and Reagents. Samples PI-1–PI-3 were supplied as powders and samples PI-4–PI-6 as highly viscous liquids by Ciba Geigy (Basel, Switzerland). The solvents *N*-methylpyrrolidone (NMP, for synthesis quality), dioxane (pro analysi quality), cyclohexanone (extra pure quality), nitric acid (65%, pro analysi quality), and hydrochloric acid (32%, pro analysi quality) were obtained from Merck (Darmstadt, Germany) and purified by subboiling distillation using a quartz apparatus. Prior to subboiling distillation, about 10 g of solid potassium hydroxide (pro analysi quality) was added to 1 L of dioxane, and the mixture was left to stand overnight in order to decompose peroxides. Calibration standards were prepared by the dilution of stock standard solutions (Merck) of 1 $g \cdot L^{-1}$ for each analyte. Magnesium nitrate and calcium nitrate were of Suprapur quality, and palladium chloride was of pro analysi quality (Merck). For the preparation of standards and modifier solutions, doubly distilled water was used.

Procedure. For the preparation of the sample solutions, 0.01–1.5 g of polyimide powder was added to a cleaned 20-mL PE vessel with 10 mL of subboiled organic solvent, previously checked for contamination, and then shaken vigorously. Dioxane could be used only for the solid samples PI-1, PI-2, and PI-3, whereas NMP was a suitable solvent for all samples examined. Tests with cyclohexanone were only made with PI-4. For complete dissolution, samples PI-2 and PI-3 had to be treated for about 1 h with NMP. To avoid analyte adsorption on the walls of the PE vessels, the sample solutions were acidified by the addition of 7 M HNO_3 to a final concentration of 0.5% (v/v) HNO_3, except for iron, which required a final HNO_3 concentration of 2% (v/v). Aliquots (20 μL) of the sample solutions were dispensed into the graphite tube by the autosampler. Dioxane was used to rinse the sampling capillary. For the determination of iron, the dioxane sample solutions were homogenized for 30 s at 4 W using the utrasonic probe Sonoplus HD 70.

The instrumental parameters and the temperature programs are summarized in Table 1. Quantification was performed by both the standard addition method with 1 $\mu g \cdot g^{-1}$ aqueous standards and the calibration graphs recorded by the use of organic solutions of the standards prepared by diluting 1 $\mu g \cdot g^{-1}$ aqueous standards with the organic solvent by 10–100-fold. For the determination of silicon, 30 μg of Pd and 20 μg of $Mg(NO_3)_2$ per atomization were used as chemical modifiers. Using dioxane as a solvent, the matrix residues on the platform were removed after approximately 150 cycles by 10–20 atomizations of 300 μg of $Ca(NO_3)_2$ in 20 μL of water.

For the dissolution method, about 140 mg of sample was digested with 2 mL of HNO_3 and 0.5 mL of HCl (both subboiled) at a microwave power of 600 W for 17 min. The sample solutions were transferred into 10-mL quartz flasks and filled with doubly distilled water. Aliquots (20 μL) of these solutions were taken for analyses by ETAAS using the Perkin-Elmer standard temperature programs.

RESULTS AND DISCUSSION

Dissolution of samples. Insufficient dissolution was achieved with cyclohexanone, in addition to contamination by Ca, K, and Na. For this reason, this solvent was applied only to the determination of Fe and Cu.

With the use of subboiled dioxane as a solvent, no significant contamination was observed for all analyte elements under

(17) Fitzgerald, E. A.; Almeida, R. F. *J. Electrochem. Soc.* **1992**, *139*, 1413–1414.

(18) Lythgoe, D. J. *Analyst* **1981**, *106*, 743–750.

(19) Gitelman, H. J.; Alderman, F. R. *J. Anal. At. Spectrom.* **1990**, *5*, 687–689.

(20) Thompson, K. C.; Godden, R. G.; Thomerson, D. R. *Anal. Chim. Acta* **1975**, *74*, 289–297.

(21) Rawa, J. A.; Henn, E. L. *Anal. Chem.* **1979**, *51*, 452–455.

(22) Welz, B.; Schlemmer, G.; Mudakavi, J. R. *J. Anal. At. Spectrom.* **1992**, *7*, 1257–1271.

(23) Perkin Elmer Benutzerdokumentation, B3110.06 Release 1.4.

investigation. This was also true for potassium in spite of the potassium hydroxide used for the destruction of peroxides prior to the subboiling distillation. An additional advantage of dioxane is its good miscibility with water and nitric acid, which enables both a problem-free spiking of the sample solutions with aqueous standard solutions and the addition of nitric acid to prevent analyte adsorption on the walls of the vessels. Furthermore, in order to prevent reprecipitation of the polymer, dioxane was used to rinse the sampling capillary during the measurements instead of water. The dioxane waste can be easily recycled by treatment with KOH with subsequent distillation. However, this solvent can be applied only to solid polyimide samples. Further disadvantageous aspects include the deleterious effects of the matrix residues on the platforms described below and the necessity of destruction of peroxides in the purification stage.

All solid polyimides were soluble in NMP. The addition of dioxane to the liquid samples led to the precipitation of an amorphous mass, but dilution with NMP was well applicable. However, when high polymer concentrations are necessary, spiking with aqueous standards is limited to volumes of about 20 μL, after which precipitation of the polymer occurs. Another disadvantage of the use of NMP as the solvent is the formation of soot residues in both the distillation apparatus used for purification and the graphite furnace that is difficult to remove. On the other hand, matrix residues on the platform had no appreciable effects on the absorption signals and analytical results, and tube regeneration was unnecessary. Also, with this solvent, no significant contamination problems occurred.

Optimization of the Procedure. After several dozens of heating cycles of about 0.5 mg of polyimide, considerable residues of pyrocarbonaceous matter were observed on the platform. However, using NMP as solvent, it was possible to carry out 400–500 atomizations with polyimide NMP solutions with about 250 standards and blanks processed in between. In spite of the considerable amount of residue, no significant effects on the areas and shapes of the peaks were observed. For instance, for about 10 ng of Fe mL^{-1} sample solution in NMP, within 400 atomizations, a peak area of 0.0524 ± 0.007 $A{\cdot}s$ was obtained. As can be seen from Figure 1, even up to 420 runs with polyimide solutions and 250 additional runs with sample-free solutions, the absorbance signal of potassium shows an excellent form (see Figure 1a); after the same number of runs, the shape of the sodium signal is slightly worse (Figure 1b), but still acceptable. Similar behavior was observed for all other analyte elements investigated, excluding silicon.

With dioxane as the solvent, a highly reflective platform surface produced by the matrix residues was observed after a certain number of runs. For example, after about 150 atomizations for iron with about 0.8 mg of polyimide, a sudden drop of the background signal occurred (see Figure 2). A regeneration of the atomizer could be achieved by performing 10–20 atomization cycles with the introduction of 300 μg of $Ca(NO_3)_2$ as matrix modifier, which led to a substantial reduction of the residues. The same regeneration effect could be achieved with magnesium nitrate. After the regeneration, the tube could be used for at least 100 more atomizations with polyimide solutions before applying another cleaning step. Thus, the total tube lifetime could be increased from 150 atomizations of polyimide solutions (0.8 mg of sample) without regeneration to approximately 400 cycles with the addition of two cleaning steps. In order to elucidate the

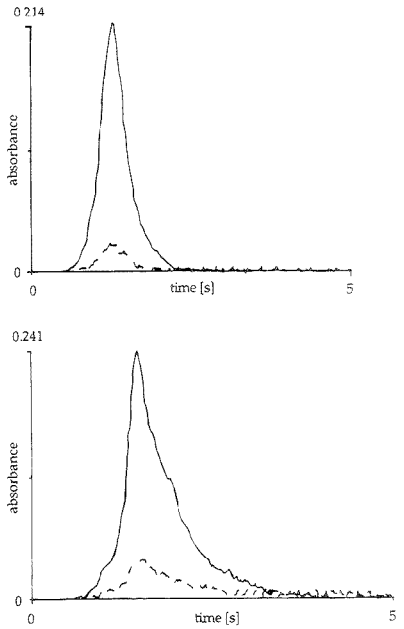

Figure 1. Absorbance signal of (a, top) potassium and (b, bottom) sodium obtained after 420 atomizations with a solution of polyimide in NMP (1.22 g/10 mL) and 250 additional atomizations with sample-free solutions. Solid line, Zeeman-background-corrected analyte signal; dotted line, background. For instrumental parameters, see Table 1.

dependence of the tube lifetime on the concentration of the polymer in the solution, additional experiments were performed with very dilute and very concentrated solutions. For example, the tube lifetime could be prolonged up to 800 atomizations for the determination of calcium that employed highly diluted sample solutions (1 mg·mL^{-1}). The formation of a slight residue can even act as a permanent recoating of the graphite surface, sealing tears and crevices in the pyrolayer.

On the other hand, applying very concentrated sample solutions (150 mg·mL^{-1}), as required in the determination of silicon due to its low content, huge amounts of matrix were deposited in the atomizer that produced an uneven platform surface with steadily changing topography, ultimately leading to poor reproducibility. Calcium nitrate has been proposed as a modifier for silicon by several researchers,[18–21] however, in our instance (organic matrix and organic solvent), the absorbance signals obtained with the use of this modifier were of very poor quality, as can be seen in Figure 3a.

Using the Pd/Mg modifier (30 μg/20 μg per run),[22] an enhanced signal quality and reproducibility could be obtained (for experimental conditions see Table 1). A typical absorbance signal of silicon is shown in Figure 3b. Difficulties associated with this modifier began to appear after 80–90 atomizations and consisted of the accumulation of matrix residue. The residue accumulated predominantly in the center of the platform, with extremely uneven topography, and caused poor reproducibility and even screening of the light beam. The alternate determinations of silicon with this modifier and of other elements without modifiers led to worse

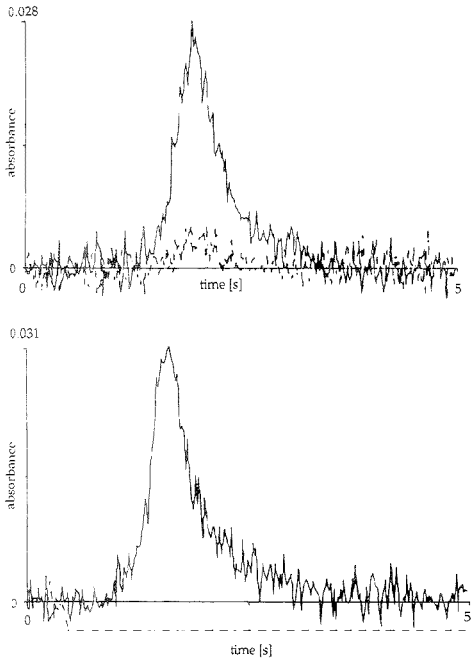

Figure 2. Iron signals (solid lines) and background (dotted lines) recorded (a, top) after 20 atomizations and (b, bottom) after 150 atomizations of 0.8 mg of polyimide (sample PI-1) in each case.

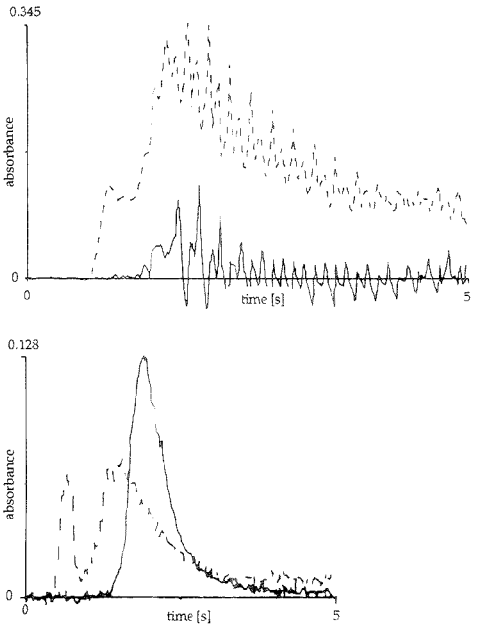

Figure 3. Absorbance signal of silicon obtained in processing of 2.0 mg of polyimide dissolved in NMP using (a, top) 300 μg of Ca-$(NO_3)_2$ and (b, bottom) 30 μg of Pd/20 μg of $Mg(NO_3)_2$ as modifier. Solid line, Zeeman-background-corrected analyte signal; dotted line, background.

silicon signal profiles; therefore, it is advisable to reserve a separate tube for silicon determinations.

For the determination of all other elements, it was not necessary to use a modifier. This is a favorable circumstance especially in the determination of Ca, Fe, K, and Na, which are prone to contamination; it is obvious that the use of a modifier would lead to considerable blank problems and, consequently, to an increase of the limits of detection.

The optimized temperatures for thermal pretreatment and atomization using organic solvents are listed in Table 1. They are, in many instances, significantly higher than those recommended for aqueous solutions.[23]

Calibration and Analysis of Samples. In order to test the performance of the standard addition and standard calibration curve methods, in the sample PI-1, the elements Ca, Cu, Fe, K, and Na were determined by both methods. The results obtained did not show any significant difference with respect to both the accuracy and the precision, which were well within the total standard deviations of the analytical results given in Table 2. The agreement of the characteristic masses obtained for the elements Cu and Fe by using the calibration curve method with the values referred by PE (see Table 3) is additional evidence for the accuracy of the calibration method. As no systematic deviation trend and no significant signal depression due to the matrix effect was observable, the more convenient calibration curve method was used for the analysis of the samples.

In Table 3, the characteristic masses (m_0) obtained by ETAAS of solutions of polyimides in organic solvents for Cu, Fe, and Si are compared with PE values based on aqueous standard solutions obtained with the same spectrometer system (PE 4100ZL).[23] For Fe and Cu, the agreement can be considered as excellent, whereas for Si, a somewhat lower characteristic mass was obtained with solution of polyimides in organic solvents. The m_0 values of Ca, K, and Na were measured at an internal gas flow of 250 mL·min^{-1} during atomization that was used for the determination of these elements in all samples in order to obtain a reduced sensitivity. Thus, a direct comparison with the PE values given for "gas stop" is not possible.

In Table 2, the results obtained by ETAAS of the solutions of polyimides, dissolved in dioxane and NMP, are compared with those obtained in our laboratory by INAA and in other laboratories by ICPMS, ICP-AES, and TXRFS.[24] From the comparison of the concentrations of Ca, Cu, Fe, K, and Na in PI-1 with dioxane and NMP, and of Cu and Fe in the sample PI−4 dissolved in NMP and cyclohexanone, no significant influence of the type of the organic solvent on the analytical results could be observed. The results of this technique for Ca, Fe, K, and Na in PI-2 and PI-3 could be compared with those obtained by INAA, and excluding the content of Na in sample PI-3, the results of both methods were in good agreement.

For the concentrations of Cu and Fe determined in all samples by this method, the agreement with results obtained by ICPMS and ICP-AES can be considered as satisfactory, whereas two of three results of TXRFS seem to be too low. For Ca, in the sample PI-3, the results of all methods are in excellent agreement, and in the sample PI-6, in acceptable agreement; however, for the other

Table 2. Contents of Elements Ca, Cu, Fe, K, Na, and Si Determined by ETAAS in Polyimides Using Organic Solvents and Comparison with Results of Other Methods and Laboratories (in *Italics*)

		concentrations ($\mu g \cdot g^{-1}$)					
sample	method	Ca	Cu	Fe	K	Na	Si
solid samples							
PI-1	ETAAS[a]	2.4 ± 0.2	0.016 ± 0.002	0.09 ± 0.02	0.034 ± 0.008	0.057 ± 0.019	0.35 ± 0.09
	ETAAS[b]	2.4 ± 0.4	0.014 ± 0.004	0.11 ± 0.02	0.038 ± 0.008	0.051 ± 0.006	
	ETAAS[d]			0.11 ± 0.01			
	ICPMS[c]	1.5	<0.1	0.2	<0.4	<0.1	<6
PI-2	ETAAS[b]	2.5 ± 0.6	0.17 ± 0.01	4.5 ± 0.6	1.0 ± 0.1	1.1 ± 0.1	
	ETAAS[d]			4.1 ± 1.3			
	ICPMS[c]	1.3/2.5	0.22/–	5.0/6.9	2.2/2.1	1.5/0.5	
	ICP-OES[f]	0.9	0.1	3.9	0.6	0.8	
	TXRFS[g]	0.5	0.15	2.0	1.5		
	INAA[h]	<6	–	4.2 ± 0.4	1.4 ± 0.13	1.3 ± 0.04	
PI-3	ETAAS[b]	0.6 ± 0.1	0.09 ± 0.01	3.7 ± 0.3	0.60 ± 0.1	0.10 ± 0.02	
	ETAAS[d]			4.2 ± 0.8			
	ICPMS[c]	0.5/<1	0.05/–	4.8/5.5	0.7/0.5	<1/<0.5	
	ICP-OES[f]	0.6	0.1	4.2	<0.2	0.2	
	TXRFS[g]	0.6	0.086	1.6	3.0	0.23	
	INAA[h]	<4	–	4.1 ± 0.7	0.56 ± 0.1	0.25 ± 0.1	
liquid samples							
PI-4	ETAAS[b]	0.96 ± 0.08	0.007 ± 0.001	0.079 ± 0.007	0.093 ± 0.012	0.19 ± 0.01	200 ± 10[i]
	ETAAS[c]		0.006 ± 0.001	0.078 ± 0.014			
	ICPMS[c]	<0.10	<0.010	0.13/0.10	<0.10	0.10/0.17	210[i]
PI-6	ETAAS[b]	0.07 ± 0.01	0.015 ± 0.002	0.08 ± 0.01	0.02 ± 0.01	0.16 ± 0.01	
	ICPMS[c]	0.1/<0.8	–/–	0.1/<2	<0.5/<0.3	0.4/<0.5	
	TXRFS[g]	0.19		0.09	0.11		

[a] ETAAS of a solution of polyimide in dioxane ($n = 6$). [b] ETAAS of a solution of polyimide in NMP ($n = 6$). [c] ETAAS of a solution of polyimide in cyclohexanone ($n = 6$). [d] ETAAS of microwave-digested polyimide samples ($n = 4$). [e] Ciba-Geigy Basel (first number) and Ciba-Geigy Monthey (second number). [f] Merck, Darmstadt. [g] Seifert, Ahrensberg. Sample preparation, cold plasma ashing. [h] Sektion Analytik und Höchstreinigung, Universität Ulm ($n = 3$). [i] Sample PI-5 instead of PI-4.

Table 3. Characteristic Masses Achieved in Analysis of Polyimides in Organic Solutions by ETAAS (Solvent NMP or Dioxane) and Their Comparison with Referred Values for Aqueous Solutions According to Ref 23

	characteristic masses (pg)	
element	org sol, this work	aq sol, Perkin-Elmer[23]
Ca	4[a]	1[a]
Cu	19[a]	17[a]
Fe	13[a]	12[a]
K	4[b]	2[a]
Na	4[b]	1.2[a]
Si	90[a]	120[a]

[a] Gas stop. [b] Internal gas flow of 250 mL·min^{-1}.

Table 4. Detection Limits Achieved in Analysis of Polyimides in Organic Solutions by ETAAS (Solvent NMP or Dioxane) and Their Comparison with Other Methods

	detection limites ($ng \cdot g^{-1}$)				
	ETAAS, this work[a]		other methods		
element	org sol[b]	microwave dig[c]	ICP-AES[23]	ICPMS[14,d]	INAA
Ca	0.5	600	5	20	
Cu	2	80	7	1	
Fe	5	25	15	10	200
K	3	250		10	30
Na	3	300	10[e]	5	1
Si	25				

[a] The detection limits are based on three times the standard deviation of the blank ($n = 6$). [b] ETAAS of polyimide solutions in NMP or dioxane. [c] ETAAS of microwave-digested polyimide samples. [d] ICPMS after cold plasma ashing. [e] ETAAS.

three samples, higher results were obtained by ETAAS. For silicon, the result of an independent method was available only for one sample which was in agreement with the result obtained with our method. Unfortunately, the results of the independent methods were available only without the corresponding data on uncertainties, and thus, more exact conclusions on the comparison of the results cannot be made.

The first results we obtained for Fe in samples with high Fe contents were much lower (1.2 ± 0.1 $\mu g \cdot g^{-1}$ in PI-2, and 0.7 ± 0.1 $\mu g \cdot g^{-1}$ in PI-3) than those of INAA, ICPMS, ICP-AES, and TXRFS. The results obtained by ETAAS after microwave digestion with nitric acid agreed well with results of the other methods. A more detailed investigation showed that the poorer results were due to the adsorption of iron, present in the solution probably in colloidal form, on the walls of the PE vessels. The adsorption could be eliminated by an increase in the concentration of nitric acid followed by pretreatment of the sample solution with ultrasound (30 s, 4W). An acceptable nitric acid concentration was found to be 2% (v/v). However, using NMP as solvent, this nitric acid concentration caused precipitation of the polymer. Therefore, when the modified procedure needs to be applied to the determination of Fe, the use of dioxane as solvent is advisable. Under these conditions, the shapes of the signals of iron and of the other elements were of good quality.

Limits of Detection. The limits of detection achievable in analysis of polyimides dissolved in dioxane or NMP (the effect of the solvent is negligible) and of solutions resulting from microwave digestion by ETAAS are listed in Table 4 and compared with those of other potential methods. For both ETAAS techniques, the limits of detection are expressed as 3 standard deviations of the blank. For all elements investigated excluding Si, the limits

of detection of the ETAAS technique involving sample dissolution in organic solvents were at the lower nanogram per gram range or below. Because of inevitable contamination and low applicable sample portions in the technique involving microwave digestion with acids, the detection limits of ETAAS using solutions of polyimides in organic solvents were enhanced by factors of 5, 30, 80, 100, and 1200 for Fe, Cu, K, Na, and Ca, respectively. In fact, in the samples under investigation, only Fe could be determined by the digestion method. In this context, it is worth mentioning that the solution resulting from the digestion, which contained 2.8 M nitric acid, caused a severe destruction of the platform surface. For the elements Ca, Fe, K, and Si, the limits of detection obtained by the method developed here are the lowest that have been achieved so far. The improvement is extraordinarily significant for Ca. Only for Na does INAA provide slightly lower limits of detection. The limits of detection of ICPMS involving sample digestion were determined by the blank and are much higher than the instrumental limits of detection of this method. In ICP-AES, the blank determined the limit of detection only for Na. The determination of silicon at ultratrace levels represents still an extremely difficult analytical task: the solution methods are limited by contamination and also by volatilization losses when HF is used for digestion. NAA requires a specific separation of the indicator radionuclide ^{31}Si, which is almost a pure β emitter. The direct MS methods are applicable only to conducting materials and suffer from calibration problems. Therefore, the possibility of detecting silicon in polyimides at the 10 $ng \cdot g^{-1}$ level by this method seems to be of considerable significance.

(24) Pavel, J. Central Analytical Department, Ciba, CH-4002 Basel, Switzerland, private communication on Analytical Round-Robin Testing on PROBIMIDE 200, 1989.

CONCLUSION

The simple method developed is very well suited for the routine determination of the relevant trace impurities of Ca, Cu, Fe, K, and Na in polyimides for microelectronic applications at the lower nanogram per gram level and of Si at the 10 $ng \cdot g^{-1}$ level. The risk of contamination and the analysis time are essentially lower compared with techniques involving sample digestion with mineral acids. For the elements Ca, Fe, K, and Si, this method provides the best limits of detection of all methods that have been applied to analysis of polyimides. For Cu only ICPMS and for Na only INAA provides slightly lower limits of detection than this method.

Received for review February 3, 1995. Accepted June 20, 1995.[⊗]

AC950126S

[⊗] Abstract published in *Advance ACS Abstracts*, August 1, 1995.

Anal. Chem. **1995**, *67*, 3154–3159

Selective Surface-Enhanced Raman Spectroscopy Using a Polymer-Coated Substrate

Anjali Pal, David L. Stokes, Jean Pierre Alarie, and Tuan Vo-Dinh*

Advanced Monitoring Development Group, Health Sciences Research Division, Oak Ridge National Laboratory, Oak Ridge, Tennessee 37831-6101

The polymer, poly(vinylpyrrolidone), is investigated as a potential coating for alumina-based surface-enhanced Raman scattering (SERS) substrates. Description for dip-coating alumina substrates with a 5% (w/v) methanolic solution of the polymer is included. Using these polymer-coated substrates, various compounds, including monocyclic aromatic compounds with hydroxyl, carboxyl, and various nitrogen-based functional groups, are detected. Intensity of SERS signals from the polymer-coated substrates in comparison to that of SERS signals from uncoated substrates is demonstrated to be a function of the analyte permeability to the polymer coating. Different enhancement factors are reported for various compounds, such as benzoic acid, isonicotinic acid, and 2,4-dinitrophenol, thus indicating some enhancement selectivity of the polymer coating to various analytes. Using benzoic acid as a test compound, various coating procedures (horizontal and vertical dipping procedures) have been evaluated. The poly(vinylpyrrolidone)-coated substrate is shown to yield a relative standard deviation in SERS signal intensity of ~20%. The potential of the polymer-coated substrate as a selective detection probe is illustrated using the analyses of binary mixtures. Finally, the advantages of the polymer coating for protecting the SERS-active layer are also discussed.

Raman spectroscopy has always been viewed as a valuable analytical technique. Because of the very narrow, highly resolved bands associated with the process, Raman spectroscopy offers the advantage of providing structural information for analyte molecules and is in several ways considered a complementary technique to infrared absorption spectroscopy. Also, the highly resolved bands offer the potential of multicomponent mixture analysis without time-consuming sample treatment. In the past, the development of Raman-based technologies has been hindered by the extremely low cross section of the Raman scattering process. In recent years, however, increased interest has been focused on Raman spectroscopy as a practical analytical technique due to the discovery of a Raman enhancement factor of up to 10^7 by Fleischmann et al.[1] and Jeanmaire and Van Duyne.[2] The enhancement is observed when samples are excited in close proximity to roughened metal surfaces (particularly silver), thus the term surface-enhanced Raman scattering (SERS). There are several theories explaining the enhancement mechanism, and some general models have been adopted, including chemical models of the complexation of the analyte with the atom of the metal surface[3] and the formation of an "adatom" via adsorption of the analyte with the silver surface.[4,5] An electromagnetic model attributes the enhancement to the generation of intense local electric fields resulting from the excitation of the collective oscillations of conduction electrons (surface plasmons) in the metal surface.[6–8] While the short-range chemical effect has been described as being dependent on surface roughness at the atomic scale,[4,5] the long-range electromagnetic effect has likewise been described as being dependent on large-scale surface roughness.[9–11]

Since the SERS discovery, exhaustive efforts have been devoted in this and other laboratories toward the development of practical substrates to investigate and utilize the SERS effect. Results of these efforts have included works with silver particles on quartz posts,[12] metal island films,[13] silver island films,[14] and metal-coated microsphere-based substrates.[15,16] The microsphere-based substrates, particularly the silver-coated alumina-based substrate,[16] offer the advantages of simplicity, reproducibility, and low cost of production. These substrates have been successfully used for the analysis of polycyclic aromatic compounds,[15] organophosphorus chemical agents,[17] chlorinated pesticides,[18] and fungicides.[19] They have also been incorporated into an optical fiber probe design for remote sensing.[20] Electrochemical probes have been the basis for SERS sensors.[21,22] Other studies have

(1) Fleischmann, M. J.; Hendra, P. J.; MacQuillan, A. J. *Chem. Phys. Lett.* **1974**, *26*, 163–166.
(2) Jeanmaire, D. J.; Van Duyne, R. P. *J. Electroanal. Chem. Interfacial Electrochem.* **1977**, *84*, 1–20.
(3) Furtak, T. E. *J. Electroanal. Chem. Interfacial Electrochem.* **1983**, *150*, 375–382.
(4) Otto, A.; Mrozek, I.; Grabhorn, H.; Akemann, W. J. *J. Phys. Condens. Matter* **1992**, *4*, 1143–1212.
(5) Otto, A. *J. Raman Spectrosc.* **1991**, *22*, 743–752.
(6) Gertsen, J.; Nitzan, A. *J. Chem. Phys.* **1980**, *73*, 3023–3037.
(7) Kerker, M.; Wang, D. S.; Chew, H. *Appl. Opt.* **1980**, *19*, 4159–4174.
(8) Ferrell, T. L. *Phys. Rev. B: Condens. Matter* **1982**, *25*, 2930–2932.
(9) Schatz, G. C. *Acc. Chem. Res.* **1984**, *17*, 370–376.
(10) Zeman, E. J.; Schatz, G. C. In *Dynamics on Surfaces: The Jerusalem Symposia on Quantum Chemistry and Biochemistry*; Pullman, B., Jortner, J., Gerber, B., Nitzan, A., Eds.; D. Reidel Publishing Co.: Dordrecht, Holland, 1984; Vol. 17, pp 413–424.
(11) Zeman, E. J.; Schatz, G. C. *J. Phys. Chem.* **1987**, *91*, 634–643.
(12) Vo-Dinh, T.; Meier, M.; Wokaun, A. *Anal. Chim. Acta* **1986**, *181*, 139–148.
(13) Jennings, C.; Avcca, R.; Hor, A.; Loufyt, R. O. *Anal. Chem.* **1984**, *56*, 2033–2035.
(14) Berthod, A.; Laserna, J. J.; Winefordner, J. D. *Appl. Spectrosc.* **1987**, *41*, 1137–1141.
(15) Vo-Dinh, T.; Hiromoto, M. Y. K.; Begun, G. M.; Moody, R. L. *Anal. Chem.* **1984**, *56*, 1667–1670.
(16) Bello, J. M.; Stokes, D. L.; Vo-Dinh, T. *Appl. Spectrosc.* **1989**, *43*, 1325–1330.
(17) Alak, A. M.; Vo-Dinh, T. *Anal. Chem.* **1987**, *59*, 2149–2153.
(18) Alak, A. M.; Vo-Dinh, T. *Anal. Chim. Acta* **1988**, *206*, 333–337.
(19) Narayana, V. A.; Begun, G. M.; Stokes, D. L.; Sutherland, W. S.; Vo-Dinh, T. *J. Raman Spectrosc.* **1992**, *23*, 281–286.
(20) Bello, J. M.; Vo-Dinh, T. *Appl. Spectrosc.* **1990**, *44*, 63–69.

0003-2700/95/0367-3154$9.00/0

enhanced the usefulness of the SERS technique. The use of indicators for selective metal ion and pH detection have been reported.[23,24] Selective adsorption of metal ions and aromatic compounds by thiol-modified metal surface has also been demonstrated.[25,26] A reversed-phase liquid chromatography (RPLC) stationary phase applied to silver surfaces for the study of nonpolar analyte interaction with the stationary phase via Raman spectroscopy has been reported.[27] Clearly, the potential for the practical use of SERS in environmental analysis has been demonstrated in recent years.

In spite of these advances, serious limitations still exist. Important factors of the microstructured SERS substrates developed in our laboratory are durability and longevity. The metal coating of the SERS substrate is vulnerable to mechanical disturbance and is also subject to air oxidation, which could affect the SERS effect. Therefore, there has been increased effort in developing protective coatings for the SERS substrate in the form of polymer layers. Such layers may hinder the interaction of the analyte with the metal surface, which is imperative for the SERS effect. In this work, a polymer, viz., poly(vinylpyrrolidone) (PVPL), was investigated as a potential protective coating for SERS substrates. Previous studies have demonstrated its permeability to compounds having hydrogen-bonding properties.[28] Because of this permeability, the PVPL coating could be applied in relatively thick layers while still enabling the detection of monocyclic aromatic compounds, including alcohol, carboxylic acid, and various nitrogen-based functional groups, with varying signal enhancement. The results of this study demonstrate PVPL as a potential durable, effective coating for SERS substrates.

EXPERIMENTAL SECTION

SERS Substrates. Alumina-based substrates, which were used in this study, have been described in detail in a previous report.[16] They consisted of a glass base plate (1 cm × 2.5 cm), coated with an even layer of alumina microparticles (Baikowski International, Charlotte, NC), followed by 1000 Å of silver. The alumina microparticles had a nominal diameter of 0.1 μm, and the silver layer was deposited via thermal evaporation.

For polymer-coated substrates, a simple dipping procedure was employed. A 5% (w/v) solution of poly(vinylpyrrolidone) (Aldrich) was first prepared in reagent-grade methanol (J. T. Baker). A fresh solution of the polymer was required daily, so no more than 5–10-mL volumes were prepared at a time in 20-mL glass vials. The alumina-based substrates described above were individually dipped rapidly in the solution and immediately placed on a level surface and allowed to cure for at least 30 min at room temperature (300 K) prior to use. The angle of dipping was varied for evaluation.

Instrumentation. SERS spectra were acquired with an Instruments SA, Inc. HR-320 spectrograph equipped with a Princeton Instruments red-enhanced intensified charge-coupled device (RE-ICCD) (Model RE/ICCD-576S). The spectrograph was equipped with a 600 grooves/mm grating, yielding a reciprocal linear dispersion of 50 nm/mm. All measurements were performed with a 30-μm entrance slit; the resolution was ~3.3 cm^{-1} at 675 nm. After calibration, the spectral accuracy of the spectrograph was ±1.5 cm^{-1}. The RE-ICCD was thermoelectrically cooled to −34 °C. All data acquisition and processing steps were carried out with a software package supplied by Princeton Instruments (CSMA, v.2.0). In a previous study, this instrument had been demonstrated to combine the advantages of low noise, high sensitivity, and time-saving multichannel detection for remote SERS measurements using a high-powered argon ion laser.[29]

For these studies, the excitation radiation was the 632.8-nm line of a helium–neon laser (Spectra Physics, Model 106-1). A bandpass filter (Corion, Model P3-633-A-X516) was placed in the laser beam prior to the sample. The full-width at half maximum (fwhm) value for the filter was 3.0 ± 0.5 nm, and the resulting beam intensity was ~3 mW at the sample. The beam was focused down to a diameter of ~100 μm at the sample, and the Raman-scattered radiation was collected at 180° with respect to the excitation beam using a two-lens system. A holographic notch filter (Physical Optics Corp.) was placed in the collected beam to reject the unwanted Rayleigh scattering. The Raman radiation was focused onto a 600-μm diameter optical fiber (General Fiber Optics), which transmitted the collected signal to the spectrograph.

A 5-mm path length quartz cell was used to contain the aqueous sample solutions. SERS substrates were cut to fit the cell (0.6 cm × 1 cm) and placed in the bottom of the cell with the SERS-active (silver) side up. Sample solutions were then added to the sample cell, completely submerging the substrate. For volatile samples, a glass microscope slide cover was placed over the cell to retain the sample during the measurement. Vertical and horizontal translation stages were used to position the sample cell in the laser beam, which was focused through the back (glass) side of the SERS substrate to the front (silver) surface.

Chemicals. All chemicals were purchased at the highest commercially available purity and used without further treatment. Test compounds included *p*-aminobenzoic acid (99% pure, Aldrich), 4-aminopyrimidine (98% pure, Aldrich), benzoic acid (reagent grade, Mallinckrodt), 2,4-dinitrophenol (90–95% pure, Sigma), isonicotinamide (99% pure, Aldrich), isonicotinic acid (99% pure, Aldrich), and 4-picoline (98% pure, Aldrich). All samples were prepared in water which was purified with a Waters Milli-Q$^+$ filtration system, at various concentrations (10^{-3}–10^{-1} M).

RESULTS AND DISCUSSIONS

Use of a polymer coating for substrates is important because it can provide a protective coating to the SERS substrate. The polymer can make the SERS substrate more resistant to scratching, thereby making it more rugged for field work. This feature was illustrated when both polymer-coated and uncoated substrates were scraped with a brush. While the uncoated substrate was severely damaged, no visible surface change was observed for the polymer-coated substrate. In addition, the coating could minimize air oxidation of the silver surface and thereby extend its useful shelf life. We have been able to observe SERS signals

(21) Angel, S.; Archibald, D. *Appl. Spectrosc.* **1989**, *43*, 1097–2102.
(22) Carrabba, M.; Edmonds, R.; Rauh, R. *Anal. Chem.* **1987**, *59*, 2559–2563.
(23) Mullen, K.; Wang, D.; Crane, L.; Carron, K. *Anal. Chem.* **1992**, *64*, 930–936.
(24) Carron, K.; Mullen, K.; Lanouette, M.; Angersbach, H. *Appl. Spectrosc.* **1990**, *44*, 63–69.
(25) Heyns, J. B. B.; Sears, L. M.; Corcoran, R. C.; Carron, K. T. *Anal. Chem.* **1994**, *66*, 1572–1574.
(26) Carron, K.; Peterson, L.; Lewis, M. *Environ. Sci. Technol.* **1992**, *26*, 1950–1954.
(27) Thompson, W. R.; Pemberton, J. E. *Anal. Chem.* **1994**, *20*, 3362–3370.
(28) Mourey, T.; Carpenter, A. P.; Siggia, S.; Lane, A. *Anal. Chem.* **1976**, *48*, 1592–1597.
(29) Alarie, J. P.; Stokes, D. L.; Sutherland, W. S.; Edwards, A. C.; Vo-Dinh, T. *Appl. Spectrosc.* **1992**, *46*, 1608–1612.

Table 1. Compounds of Interest

compound	structure
p-aminobenzoic acid (PABA)	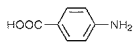
4-aminopyrimidine	
benzoic acid	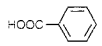
DIMP	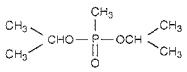
2,4-dinitrophenol	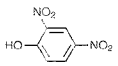
isonicotinamide	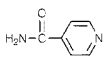
isonicotinic acid	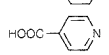
4-picoline	

from poly(vinylpyrrolidone)-coated substrates after 120 days of storage in an ordinary laboratory environment. For comparison, a similar uncoated substrate was observed to drastically lose its SERS activity within 25 days. This improved durability and enhanced longevity could be attributed to the polymer coating. The thickness of a typical polymer coating was determined to be ~7 μm using a confocal microscope.

In general, the SERS effect is strong for analyte compounds adsorbed onto or close to the metal surface. A distance of 7 μm is large even for the SERS long-range effect, which rapidly decreases beyond molecular distances. For this reason, we believe the analyte molecules need to permeate through the polymer coating and get close to the silver surface. The relatively thick layers of PVPL have permitted the detection of various compounds for which the polymer coating exhibits permeability. Some of the compounds that we have investigated are listed in Table 1, along with their structures. Generally, we have been able to detect monocyclic aromatic compounds with carboxylic acid or alcohol functional groups, as would be expected from permeability data in the literature.[28] Our results have also included detection of monocyclic aromatic compounds with nitrogen-based functional groups, including amino, amide, nitro, and azo groups. The PVPL coating has produced a signal enhancement in addition to the SERS effect for several compounds. We refer to this feature as an "additional enhancement" (AE) due to the polymer coating. Figures 1–3 illustrate compounds that were detected when exposed to the polymer-coated SERS substrate. In all cases, the bottom (B) spectra were obtained with bare uncoated substrates, while the top (A) spectra were obtained with polymer-coated substrates. For each PVPL-coated substrate, the polymer was applied by dipping the untreated SERS substrate horizontally into the 5% poly(vinylpyrrolidone) solution. For each pair of spectra, all conditions of measurement were held constant. Figure 1 illustrates the comparison of the SERS spectra of a 3.4×10^{-3} M solution of benzoic acid. In this case, an AE factor of ~6.7 (using the 1010 cm^{-1} peak as reference) is observed for the polymer-coated substrate. Figure 2 illustrates

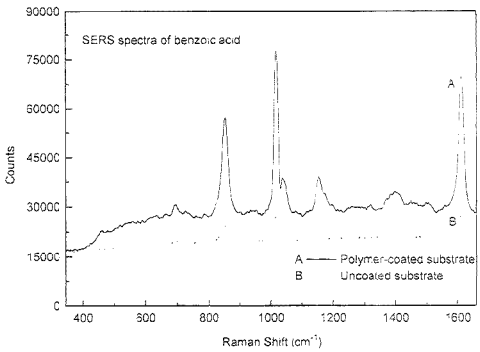

Figure 1. SERS spectra of benzoic acid on (A) polymer-coated substrate and (B) uncoated substrate.

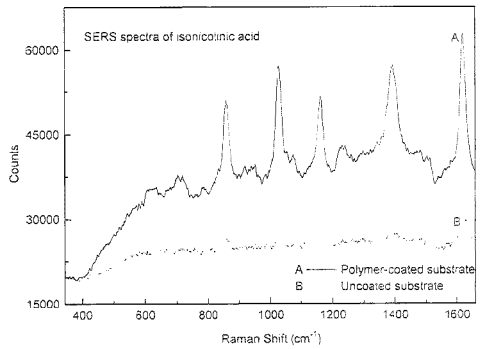

Figure 2. SERS spectra of isonicotinic acid on (A) polymer-coated substrate and (B) uncoated substrate.

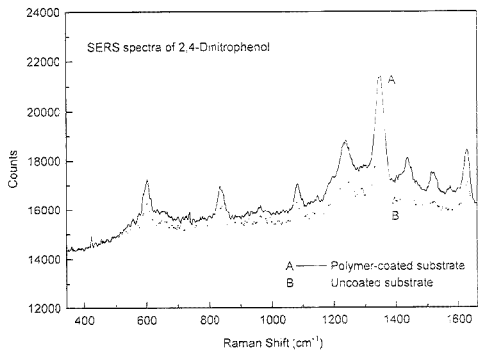

Figure 3. SERS spectra of 2,4-dinitrophenol on (A) polymer-coated substrate and (B) uncoated substrate.

the corresponding comparison for a 2.2×10^{-3} M solution of isonicotinic acid. Based on the peak at 1020 cm^{-1}, an improved AE factor of ~9.6 is clearly demonstrated. Figure 3 shows the spectra of a 2.5×10^{-3} M solution of 2,4-dinitrophenol. In this case, the AE factor is ~1.3, based on the peak at 1346 cm^{-1}. The differences in the AE factor for different compounds may be used as a selectivity parameter for the analysis of mixtures. Therefore, this study demonstrates the potential of polymer-coated SERS

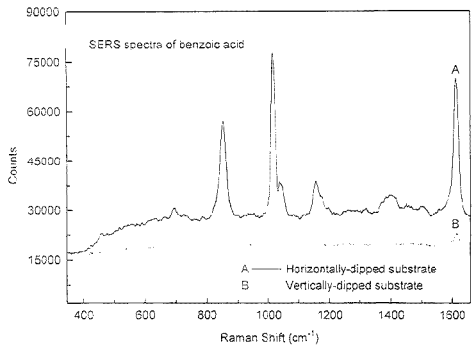

Figure 4. SERS spctra of benzoic acid on (A) horizontally and (B) vertically coated substrate.

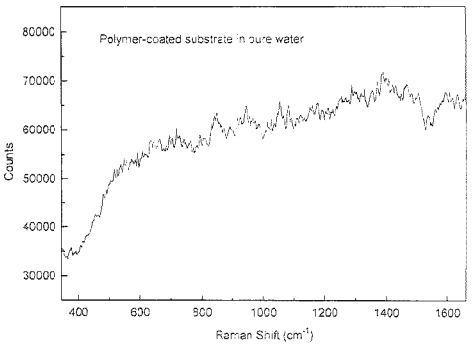

Figure 5. SERS spectrum of poly(vinylpyrrolidone)-coated alumina-based substrate in pure water.

substrates as selective detection probes, while also improving the durability due to the protective coating.

Coating Procedure Evaluation. The structure of the analyte compound appears to be the primary factor in the various enhancement effects for SERS signal. Other parameters which could affect the thickness and density of the polymer layer were also investigated to optimize the enhancement. Such parameters included polymer solution concentration, dipping time, and the angle of dipping. A 5% methanolic solution of poly(vinylpyrrolidone) was selected for this study. The dipping time was kept constant at 1 s. Measurements were performed to evaluate the effect of the angle of dipping. Data acquired with a substrate which was coated via horizontal dipping (0° with respect to the polymer solution surface) is represented in Figure 4A. Figure 4B illustrates the result of vertical (90° with respect to the polymer solution surface) dipping. All other measurement parameters were held constant for both spectra. The horizontal dipping procedure appeared to be most effective, yielding a SERS signal at 1010 cm^{-1} which was ~13 times more intense than that yielded by the vertically dipped substrate. The horizontal dipping procedure was used in all subsequent experiments.

Reproducibility Study and Background Measurement. A relatively high degree of reproducibility in an isonicotinic acid spectrum from substrate to substrate was observed. In performing the reproducibility study, a 2.2×10^{-3} M aqueous solution of isonicotinic acid was added to the sample cell. Upon addition of a polymer-coated substrate to the solution, intensity growth of the SERS signal was observed to taper off and stabilize after ~10 min of exposure. Five trials were performed, each with a fresh polymer-coated substrate and fresh sample test solution. The relative standard deviation for these measurements was determined to be ~20%. This result is encouraging since one usually expects a relative standard deviation of ~15% from the uncoated substrate itself.[16]

A useful feature of the polymer coating is the low background SERS signal from for the coating itself. Figure 5 illustrates a blank spectrum for the polymer-coated substrate submerged in pure water. No significant SERS or Raman bands from the polymer layer coating are observed for the spectral region of interest.

Selectivity Study with Binary Mixtures. The polymer coating exhibits different AE factors for different compounds. We further investigated this selectivity feature by the analysis of binary mixtures having compounds with varying affinity for the PVPL-coated substrate. In the first test, a mixture of 4-picoline and benzoic acid was tested with the anticipation that the benzoic acid detection would be favored due to the carboxylic acid functional group (see Table 1). The concentration of benzoic acid was 1.73×10^{-3} M, while the concentration of 4-picoline was 2.55×10^{-3} M. Parts A and B of Figure 6 show the SERS spectra obtained with use of a polymer-coated and an uncoated SERS substrate submerged in the sample solution, respectively. Parts C and D of Figure 6 respectively illustrate the individual spectra of benzoic acid (3.4×10^{-3} M) and 4-picoline (5.1×10^{-3} M) acquired with uncoated substrates. Different conditions were used for each measurement (e.g., detector gain and duty time). The results of this figure indicate that the dominant compound detected with the uncoated substrate was 4-picoline, with two bands (1248 and 1472 cm^{-1}) uniquely attributable to 4-picoline. Unfortunately, the bands at 1026, 1405, and 1626 cm^{-1} are common to both compounds, so their assignment was uncertain. Review of Figure 6A reveals the presence of bands characteristic for both benzoic acid (864 and 1174 cm^{-1}) and 4-picoline (1248 and 1472 cm^{-1}). This demonstrates permeability of the polymer to both compounds. However, the fact that the relative intensities of two bands common to both compounds (1026 and 1626 cm^{-1}) are dramatically increased, along with the fact that additional unique benzoic acid bands appear in Figure 6A, indicates that the PVPL coating preferentially favors the detection of benzoic acid in this binary mixture, as was anticipated.

A second test was performed for 4-aminopyrimidine (1.73×10^{-3} M) and isonicotinic acid (1.1×10^{-3} M), with the anticipation that the isonicotinic acid detection would be favored by the polymer-coated substrate due to its carboxylic acid functional group (see Table 1). Figure 7, parts A and B, represents SERS spectra of the mixture acquired with coated and uncoated substrates, respectively. The individual SERS spectra for 4-aminopyrimidine (3.5×10^{-3} M) and isonicotinic acid (2.2×10^{-3} M) generated with uncoated substrates are shown in Figure 7, parts C and D, respectively. Each of the spectra were acquired with varying detector gain and duty times. For the uncoated substrate (Figure 7B), the bands characteristic to both isonicotinic acid (868, 1036, 1402, and 1630 cm^{-1}) and 4-aminopyrimidine (898, 1216, 1330, and 1504 cm^{-1}) were present. In addition, the Raman bands occurring at 1090 and 1170 cm^{-1} could be attributed to either compound. In this case, both compounds are practically equally represented by the spectrum obtained with the uncoated

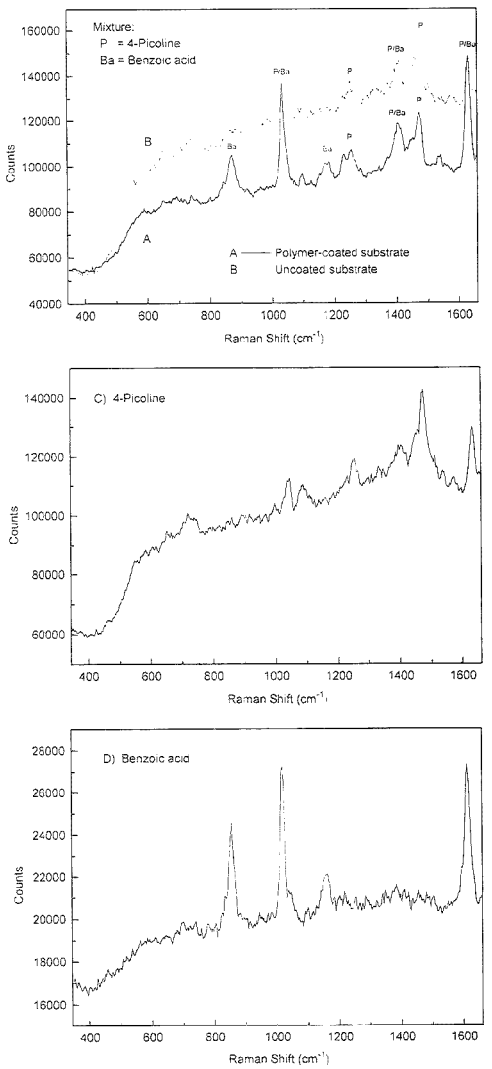

Figure 6. SERS spectra of a binary mixture of 4-picoline and benzoic acid on (A) polymer-coated substrate and (B) uncoated substrate. Individual spectra of (C) 4-picoline on bare substrate and (D) benzoic acid on uncoated substrate.

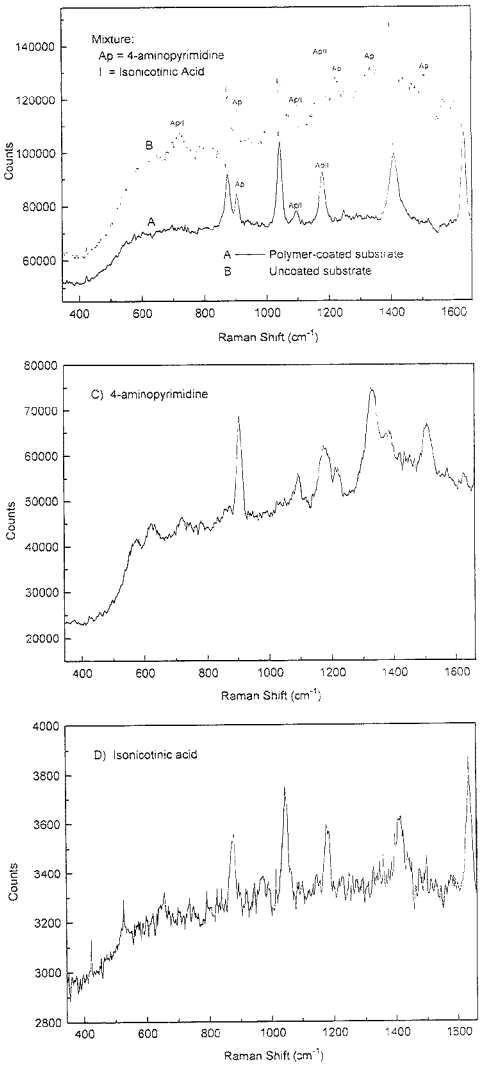

Figure 7. SERS spectra of a binary mixture of 4-aminopyrimidine and isonicotinic acid on (A) polymer-coated substrate and (B) uncoated substrate. Individual spectra of (C) 4-aminopyrimidine on bare substrate and (D) isonicotinic acid on uncoated substrate.

SERS substrate. On the other hand, the spectrum in Figure 7B, obtained with the polymer-coated substrate, is clearly dominated by the SERS bands belonging to isonicotinic acid. For example, four major bands occurring at 868, 1036, 1402, and 1630 cm^{-1} are unique to isonicotinic acid. One major peak and one minor peak at 1172 and 1090 cm^{-1}, respectively, can be attributed to either compound, but the change in relative intensity of these bands along with the major bands unique to isonicotinic acid suggests that isonicotinic acid is the major contributor to these common bands as well. For this example, the results show that the PVPL-coated substrate favored the detection of isonicotinic acid, as anticipated. In fact, the spectrum in Figure 7A is almost entirely composed of bands that can be assigned to isonicotinic acid, with one sole exception—the medium band occurring at 897 cm^{-1}.

CONCLUSION

This work has demonstrated the SERS detection of various compounds by using a polymer-coated substrate. A useful feature of the poly(vinylpyrrolidone) coating is that it can provide a protective barrier to mechanical disturbance and air oxidation of the SERS-active (metal) substrate layer, thereby making the underlying alumina-based substrate more durable for field work.

The relatively good reproducibility exhibited by the polymer coating and the absence of background structure are also very useful characteristics. The fact that the coating is insoluble in water and exhibits variable permeability to different compounds further demonstrates the potential of a selective SERS detection probe for chemical and biological analysis. Current efforts are being devoted toward extending the usefulness and applicability of this polymer.

ACKNOWLEDGMENT

This work was jointly sponsored by the U.S. Department of Defense BMDO (DGAM4-0238) and the U.S. Department of Energy (DOE) Office of Health and Environmental Research under Contract DE-AC05-84OR21400 with Martin Marietta Energy Systems, Inc. The authors acknowledge the assistance of Dr. Robert J. Palmer of the Center for Environmental Biotechnology in the measurement of the coating thickness.

Received for review January 9, 1995. Accepted June 20, 1995.[⊗]

AC950031Q

[⊗] Abstract published in *Advance ACS Abstracts,* August 1, 1995.

Anal. Chem. **1995**, *67*, 3160–3166

Oxygen-Sensitive Luminescent Materials Based on Silicone-Soluble Ruthenium Diimine Complexes

Ingo Klimant and Otto S. Wolfbeis*

Institute for Organic Chemistry, Karl-Franzens University, Heinrichstrasse 28, A-8010 Graz, Austria

New oxygen-sensitive luminescent materials were obtained by physically immobilizing luminescent ruthenium(II) diimine complexes in silicone rubber. The dyes were made silicone-soluble by converting them into the respective ion pairs with organic anions. Acetic acid-releasing one-component RTV silicones were found to provide the best matrix for sensor membranes. The dyed silicone prepolymers were spread onto planar solid supports, cured, and characterized in terms of quenching by oxygen, response time, interferences, storage stability, and photostability. Strong evidence is presented from quenching experiments that the luminescent ion pairs are present in both a monomolecular and an aggregated form, the respective quenching constants being highly different. This results in nonlinear Stern–Volmer graphs. The new oxygen-sensitive materials are considered to present a major improvement over existing sensor materials in terms of response time, luminescence intensity, and long-term stability. They not only may be applied as planar films but also as very thin coatings on various kinds of waveguides. We also describe several novel materials for use as light-tight optical isolations. They are spread onto the oxygen-sensitive films in order to minimize interferences by (a) ambient light and (b) potentially interfering sample properties such as color, turbidity, fluorescence, and varying refractive index.

The most common type of optical oxygen sensors are those based on the quenching of the luminescence of suitable indicators.[1] Usually, such indicators are dissolved in a polymer matrix which not only acts as a "solvent" for the dye but also provides a means to improve sensor selectivity in being impermeable to other quenchers, notably heavy metal cations and certain anions such as iodide. In addition, it is known that the properties of the matrix material strongly affect the efficiency of quenching by oxygen, response time, and rate at which the indicator leaches out.[1] Desirable matrix properties include high permeability for oxygen, adequate mechanical and chemical stability, and high solubility for the indicator.

Silicone rubber has been described as the material of choice for use in oxygen optrodes, and various polycyclic aromatic hydrocarbons (PAHs) were dissolved in silicones in the early 1980s to give useful oxygen sensors.[1–5] The attractive features of silicone rubber include an extraordinarily high permeability for oxygen (being 2 orders of magnitude greater than for any other organic polymers[6] and resulting in high quenching efficiencies), as well as excellent chemical and mechanical stability. Because of its hydrophobic character, ionic species cannot penetrate silicone rubber.

Although dynamic quenching of luminescence by oxygen has been known for decades, the number of useful dyes is limited due to the particular requirements for indicator dyes to be useful for optical sensing. These include photostability, high luminescence quantum yields, efficient quenching, long lifetime, compatibility with solid-state light sources, high molar absorbance, and adequate solubility in the polymer employed. Unfortunately, most indicators display poor solubility in silicones. To overcome this problem, PAHs such as benzo[*ghi*]perylene and decacyclene have been made silicone-soluble by introducing *tert*-butyl groups.[7] Another frequently used class of oxygen indicators comprises the highly luminescent metalloorganic ruthenium complexes having diimine ligands such as 2,2′-bipyridyl, 1,10-phenanthroline, or 4,7-diphenyl-1,10-phenanthroline.[8–11] Being ionic, they display poor solubility in silicone rubber. In order to overcome this problem, the dyes were adsorbed onto silica gel first and then embedded into silicones.[8,12] In an alternative approach, Bacon and Demas[9] as well as Carraway et al.[10] have soaked silica gel-filled silicones with dichloromethane solutions of ruthenium complexes, while MacCraith et al.[11] incorporated ruthenium–tris(bipyridyl) into sol–gels. The luminescence of either of the resulting sensing materials is efficiently quenched by molecular oxygen but suffers from nonlinear Stern–Volmer calibration graphs. In addition, the preparation and dispersion of silica gel adsorbates is tedious.

Another way of immobilizing indicators in silicone materials involves covalent binding of the dye to the matrix. Holloway and Kiang[13] immobilized ruthenium complexes by introducing cross-linking functions which react with the silicone prepolymer during copolymerization, while Hsu and Heitzmann[14] covalently linked PAHs to silicone rubber using the same method. However, the

(1) Wolfbeis, O. S. Ed. *Fiber Optic Chemical Sensors and Biosensors*; CRC Press: Boca Raton, FL, 1991; Vol. 1, Chapters 7 and 12.
(2) Kroneis, H.; Marsoner, H. J., *Sens. Actuators* **1983**, *4*, 587–592.
(3) Cox, M. E.; Dunn, B. *Appl. Opt.* **1985**, *24*, 2114–2120.
(4) Gehrich, J. L.; Lübbers, D. W.; Opitz, N.; Hansmann, D. R.; Miller, W. W.; Tusa, J. K.; Yafuso, M. *IEEE Trans. Biomed. Eng.* **1986**, *33*, 117–132.
(5) Sharma, A.; Wolfbeis, O. S. *Appl. Spectrosc.* **1988**, *42*, 1009–1014.
(6) Brandrup, J., Immergut, E. H., Eds. *The Polymer Handbook*, 3rd ed.; Wiley: New York, 1989; pp VI/435–VI449.
(7) Wolfbeis, O. S.; Posch, H. E.; Kroneis, H. *Anal. Chem.* **1985**, *57*, 2556–2561.
(8) Wolfbeis, O. S.; Leiner, M. J. P.; Posch, H. E. *Mikrochim. Acta* **1986**, *3*, 359–366.
(9) Bacon, J. R.; Demas, J. N. *Anal. Chem.* **1987**, *59*, 2780–2785.
(10) Carraway, E. R.; Demas, J. N.; DeGraff, B. A.; Bacon, J. R. *Anal. Chem.* **1991**, *63*, 337–342, and references therein to previous work.
(11) MacGraith, B. D.; McDonagh, C. M.; O'Keefe, G.; Keyes, E. T.; Vos, J. G.; O'Kelly, B.; McGilp, J. F. *Analyst* **1993**, *118*, 385–388.
(12) Moreno Bondi, M. C.; Wolfbeis, O. S.; Leiner, M. J. P.; Schaffar, B. P. H. *Anal. Chem.* **1990**, *62*, 2377–2381.
(13) Holloway, R. R.; Kiang, T. T. U.S. Patent 5,070,158, 1991.
(14) Hsu, L.; Heitzmann, H. U.S. Patent 4,712,865, 1987.

0003-2700/95/0367-3160$9.00/0

resulting materials have not been described in terms of quenchability and signal intensity, so they are hard to assess. Sensors with covalently immobilized indicators have the unique advantage of not suffering from indicator leaching, but are difficult to make and cannot easily be used in thin-film sensors where classical spreading methods and prepolymers of defined composition are applied. Thin-film sensors result in very fast response times as they are required in respiratory gas analysis. We present an attractive alternative to either adsorptive or covalent immobilization of ruthenium complexes by making use of novel, highly silicone-soluble ion pairs, resulting in sensor films with high indicator concentrations, and also describe, in more detail, methods on how to blind the resulting sensors against environmental disturbances by applying an optical isolation.

EXPERIMENTAL SECTION

Reagents. Ruthenium (III) chloride trihydrate, and 4,7-diphenyl-1,10-phenanthroline (dpp) were obtained from Alpha Products (Karlsruhe, Germany). Ruthenium(II)–tris(1,10-phenanthroline)dichloride ($Ru(phen)_3Cl_2$), sodium dodecyl sulfate (Na-DS), sodium trimethylsilylpropansulfonate (Na-TSPS), and titanium dioxide were obtained from Aldrich (Steinheim, Germany). One-component silicone prepolymers E-4 (transparent, acetic acid releasing), E-41 (transparent, acetic acid releasing), N-199 (transparent, oxime releasing), N-10 (transparent, oxime releasing), N-189 (black, oxime releasing), and A-07 (transparent, amine releasing) were from Wacker (Burghausen, Germany). The transparent two-component silicone prepolymers PS 1055 and PELD 15, and the one-component prepolymer PS 252 (transparent, acetic acid releasing), were from ABCR GmbH (Karlsruhe, Germany) and of technical grade. The polyester support (Mylar, type GA 10, 175 μm) was from Dupont (Vienna). The black tetrafluoroethylene foil (12 μm) was from General Electric (Schenectady, NY). Acetone, chloroform, 2-butanone, and diethyl ether were of analytical grade. Double distilled water was used throughout.

Syntheses of Silicone-Soluble Ruthenium Complexes. *$Ru(dpp)_3(DS)_2$* (**1a**). Ruthenium trichloride trihydrate (225.9 mg) was dissolved in a mixture of 5 mL of ethylene glycol and 0.5 mL of water at 120 °C. Then, 862.6 mg of dpp was added. The mixture was heated to 165 °C under reflux for 45 min. After cooling, the solution was dissolved in 50 mL of acetone, filtered, and diluted with acetone. The filtrate contains the crude $Ru(dpp)_3Cl_2$. A total of 100 mL of a 10 mM aqueous solution of Na-DS was added to 100 mL of the filtrate. Finally, 100 mL of 1 M sodium chloride solution was added. The orange precipitate was filtered and washed four times with distilled water. Further purification was accomplished by recrystallization from an acetone/water mixture (80:20, v/v). Finally, the precipitate was washed with diethyl ether and dried under vacuum at 40 °C. The dye was obtained as an orange powder in 75–85% yield. Elemental analysis (calc/found) for the tetrahydrate ($C_{96}H_{102}N_6O_{16}S_2Ru$; MM 1669.0): C, 69.01/68.90; H, 6.15/5.98; N, 5.03/5.02.

$Ru(dpp)_3(TSPS)_2$ (**1b**). This indicator was prepared in the same way as described for **1a** by replacing the aqueous Na-DS solution by a solution of Na-TSPS. The dye was obtained as an orange powder in 70–80% yield. Elemental analysis (calc/found) for the dihydrate ($C_{84}H_{82}N_6O_8S_2Si_2Ru$; MM 1525.0): C, 66.10/66.19; H, 5.37/5.35; N, 5.37/5.34.

$Ru(phen)_3(DS)_2$ (**2a**). A 200-mg sample of $Ru(phen)_3Cl_2$ was dissolved in 100 mL of distilled water. After addition of 50 mL of a 10 mM aqueous solution of Na-DS, a finely dispersed precipitate was obtained. Then, 20 mL of a 1 M sodium chloride solution wass added and the precipitate filtered after 3 h. The resulting complex was washed with distilled water and diethyl ether and dried under vacuum at 30 °C for 24 h. The indicator was obtained as an orange powder in 80–85% yield. Elemental analysis (calc/found) for the tetrahydrate ($C_{90}H_{74}N_6O_8S_2Ru$; MM 1212.5): C, 59.43/59.83; H, 6.81/6.49; N, 6.93/7.01.

$Ru(phen)_3(TSPS)_2$ (**2b**). A 200-mg sample of $Ru(phen)_3Cl_2$ was dissolved in 100 mL of distilled water, and 70 mL of a 10 mM aqueous solution of Na-TSPS was added. The ion pair (**2b**) was extracted into 50 mL of chloroform. The chloroform phase was washed with distilled water and evaporated and the residue dried under vacuum at 30 °C for 24 h. An orange powder of **2b** was obtained in 70% yield. Elemental analysis (calc/found) for the dihydrate ($C_{48}H_{58}N_6O_8S_2Si_2Ru$; MM 1068.4): C, 53.02/52.89; H, 5.52/5.50; N, 7.73/7.66.

Table 1. Composition of Oxygen-Sensitive Materials Used in This Study

membrane	indicator[a]	silicone
M-1	$Ru(phen)_3(DS)_2$	E-4
M-2	$Ru(phen)_3(TSPS)_2$	E-4
M-3	$Ru(dpp)_3(DS)_2$	E-4
M-4	$Ru(dpp)_3(TSPS)_2$	E-4
M-5	$Ru(dpp)_3(DS)_2$	E-41
M-6	$Ru(dpp)_3(DS)_2$	PS 252
M-7	$Ru(dpp)_3(DS)_2$	A-07
M-8	$Ru(dpp)_3(DS)_2$	N-99
M-9	$Ru(dpp)_3(DS)_2$	N-10
M-10	$Ru(dpp)_3(DS)_2$	PS 1055
M-11	$Ru(dpp)_3(DS)_2$	PELD 15
M-12	$Ru(dpp)_3(DS)_2$	E-4 + TiO_2

[a] The concentration of the fluorescent dye was 4 mM throughout.

Preparation of Oxygen-Sensitive Membranes. The new materials were investigated with respect to luminescence properties and quenching by oxygen by casting them onto a polyester support. Membranes were obtained by first dissolving the respective ruthenium complexes (**1a,b**; **2a,b**) in dry chloroform (or ethyl acetate) to form 2 mM solutions. A 2-g sample of the respective prepolymer (see Table 1) was dissolved in 4 mL of the indicator solution (in chloroform or ethyl acetate). This "cocktail" was spread onto a polyester foil in a thickness of 20 μm by either spin coating or by placing ~0.2 mL of the cocktail on a 2 × 5 cm polyester foil and spreading the viscous material in defined thickness using a metal blade. Excess cocktail was removed. After the chloroform had evaporated, the resulting membranes were dried in ambient air for, typically, 4 h and cured at 90 °C in an oven for 12 h. We calculate the thickness of the sensing layer after solvent evaporation and curing to be 4–5 μm. However, membranes as thin as 1 μm have been prepared by this method as well. In case of membrane type M-3, a second layer (20 μm of black silicone N-189, or 12-μm black Teflon) acting as an optical isolation was spread onto this sensing layer.

Membrane M-12 was prepared in a modified procedure in that 2 g of silicone prepolymer E-4 was dissolved in 4 mL of the indicator solution. Then, 0.7 g of titanium dioxide, dispersed in 4 mL of chloroform, was added. After homogenizing, the mixture was spread onto the polyester foil in a thickness of 50 μm. The curing process was carried out at 90 °C for 24 h. Table 1

summarizes the composition of the sensing membranes described here in more detail.

Instrumentation and Characterization of Materials. Luminescence spectra and response curves were acquired on an Aminco SPF 500 spectrofluorometer equipped with a 250-W tungsten halogen lamp as a light source and an R 928 red-sensitive photomultiplier (Hamamatsu). The sensing membranes were fixed inside a home-machined flow-through cell to form one of its four walls. A 530-nm cutoff filter was inserted as an secondary filter to remove scattered blue excitation light. Absorption measurements were carried out with a UV 2101 PC photometer (Shimadzu). All measurements were carried out at room temperature. The luminescence of the sensing films was excited at 465 nm and emission measured at 610 nm.

Oxygen/nitrogen mixtures were obtained fom cylinders of pure oxygen and nitrogen using a Digimix gas mixing device (Wösthoff, Dortmund, Germany). Humidified gas mixtures were obtained by bubbling gases through water-filled washing bottles, while oxygen-equilibrated water solutions were obtained by tonometry of water or buffer contained in reservoirs.

Fluorescence lifetimes were measured with an pulse lifetime instrument (FL 900, Edinburgh Instruments, Edinburgh, Scotland) calibrated with a deaerated solution of $Ru(dpp)Cl_2$ in 2-butanone (τ_0 6.22 μs at 23 °C). Quantum yields were determined using $Ru(bipy)Cl_2$ in deaerated water as a standard (ϕ = 0.042 at 23 °C).[15]

RESULTS

Selection of Ruthenium(II) Diimines and Counterions. At present, Ru(dpp) appears to be the luminescent oxygen indicator of choice in the ruthenium diimine series. Unfortunately, Ru(dpp) ion is insoluble in silicone rubbers when present as the chloride, perchlorate, or sulfate, a fact that prevents the design of silicone-based sensing films containing such indicator dyes in homogeneous distribution. On the other side, silicone rubber is the material of choice in the case of oxygen sensing because of its high permeability for oxygen, ease of handling, good adhesion to glass fibers, inertness to biological samples, and optical transparency.

It was conceived that replacement of the inorganic counteranion (chloride) by an organic counteranion would result in a distinctly improved solubility of the Ru(dpp) complex in organic polymeric solvents, in particular in silicones. Two types of commercially available organic anions were selected to replace the inorganic counterions. The first included several aliphatic carboxylates and sulfates which—because of their hydrophobicity—were expected to render ruthenium complexes soluble in silicone. Among those, the dodecyl sulfate counteranion was found to be most viable and resulted in indicators **1a** and **2a**. The second group comprised anions containing silicone-like structures such as the trimethylsilylpropanesulfonate anion, and this resulted in ruthenium complexes **1b** and **2b**. The ion pairs were synthesized as described in the Experimental Section, and their chemical structures are summarized in Table 2. In addition to the Ru(dpp) complexes, and for comparison purposes, we also have prepared ion pairs of Ru(phen), where phen stands for 1,-10-phenanthroline. The respective chloride is commercially available and a frequently used oxygen probe.

(15) Juris, A.; Balzani, V.; Barigelletti, F.; Campagna, S.; Belser, P.; von Zelevsky, A. *Coord. Chem. Rev.* **1988**, *84*, 85–132.

Table 2. Chemical Structures of the New Silicone-Soluble Ion Pairs $Ru(dpp)_3X_2$[a] and $Ru(phen)_3X_2$[b]

ion pair	Ru(diimine)	anion (X)
1a	$Ru(dpp)_3$	n-$C_{12}H_{25}SO_3^-$ (DS)
1b	$Ru(dpp)_3$	$(CH_3)_3SiCH_2CH_2CH_2SO_3^-$ (TSPS)
2a	$Ru(phen)_3$	n-$C_{12}H_{25}SO_3^-$ (DS)
2b	$Ru(phen)_3$	$(CH_3)_3SiCH_2CH_2CH_2SO_3^-$ (TSPS)

[a] dpp, 4,7-diphenyl-1,10-phenanthroline. [b] phen, 1,10-phenanthroline.

Synthesis of the new probes follows a widely applicable scheme, and all were obtained in sufficient purity. They showed one single spot on TLC (silica gel, dichloromethane/acetone, 1:1) and gave satisfactory elemental data (taking into account that they crystallize with two or four crystal water molecules). The UV and luminescence spectra of the DS and TSPS salts (**1a**,**b**; **2a**,**b**) are virtually identical to those of the respective chlorides. Most impressive, though, is the tremendous effect of the anion on the solubility of the dyes (see below) and the mobility of the dyes on a TLC plate: The R_f value of $Ru(dpp)Cl_2$ on silica gel plates developed with pure dichloromethane is 0.0, while that of dye **1a** is 0.7.

Spectral and Photophysical Properties. The effect of counterions on the spectral and photophysical properties of ruthenium complexes was studied in 2-butanone solvent. In addition to **1a** and **1b**, the respective chlorides and perchlorates were tested as well. Not unexpectedly, the new counterions do not cause a measurable change in the absorption and emission spectra. Quantum yields were determined to be 0.35 ± 0.04 for both **1a** and **1b** and 0.08 ± 0.02 for both **2a** and **2b**. Within experimental error, they are identical with the respective chlorides and perchlorates. The natural lifetimes, determined relative to $Ru(bipy)^{3+}$ in deaerated water, are 6.3 ± 0.39 μs for **1a**,**b** and 0.74 ± 0.1 μs for **2a**,**b**. Evidently, the spectral and photophysical properties of the probes are mainly determined by the cationic chromophore, while the anionic counterion governs solubility.

The luminescence intensity of the sensing membranes is more than 10 times higher than those of membranes based on silica gel-adsorbed ruthenium probes having the same film thickness. It is lower, though, by at least a factor of 2 than that of sensing films based on plasticized pvc or polystyrene and having the same indicator concentration.[17,18] Unlike in silica gel-adsorbed Ru(dpp), the concentration of dyes 1 and 2 in silicone can be largely increased (and, hence, luminescence intensity adjusted to an optimum) by increasing the dye concentration. Ru(dpp) deposited on silica gel tends to undergo self-quenching of luminescence when its concentration exceeds a certain critical value, which strongly depends on the loading capacity of the kind of silica gel used. This is explained in in terms of a high local concentration of dye on the surface of the silica gel, while in the material presented here the dye is rather evenly distributed in the membrane, so that it cannot accumulate at the filler/silicone interface.

Solubility. The solubility of ion pairs **1a**,**b** and **2a**,**b** in several solvents was investigated in order to identify a common solvent

(16) Draxler, S.; Lippitsch, M. E.; Klimant, I.; Kraus, H.; Wolfbeis, O. S. *J. Phys. Chem.* **1995**, *99*, 3162–3167.
(17) Li, X. M.; Ruan, F. C.; Wong, K. Y. *Anal. Chim. Acta* **1992**, *262*, 27–32.
(18) Gruber, W. R.; Klimant, I.; Wolfbeis, O. S. *Proc. SPIE (Soc. Photoinstrum. Eng.)* **1993**, *1885* (Adv. Fluoresc. Sensing Technol.), 448–457.

Table 3. Solubility of the New Ruthenium Ion Pairs in Various Solvents[a]

solvent	$Ru(dpp)_3(DS)_2$ (1a)	$Ru(dpp)_3(TSPS)_2$ (1b)	$Ru(phen)_3(DS)_2$ (2a)	$Ru(phen)_3(TSPS)_2$ (2b)	$Ru(phen)_3Cl_2$
water	−	−	+	+	+++
ethanol	++	++	++	++	++
2-butanone	+++	+++	+++	+++	+
chloroform	+++	+++	+++	+++	+
toluene	+++	+	++	+	−
ethyl acetate	+++	++	++	++	−
diethyl ether	++	+	+	−	−
n-hexane	+	−	+	−	−

[a] Key: −, solubility below 1 μM; +, solubility between 1 and 10 μM; ++, solubility between 0.01 and 1.0 mM; +++, solubility better than 1 mM.

Table 4. Effect of the Type of Silicone Matrix on Curing, Luminescence Intensity, and Quenching by Oxygen of Indicator 1a in 4 mM Concentration

membrane	silicone	curing time	luminescence intensity	quenching[a]	remarks
M-3	E-4	3 days	high	60	clear
M-5	E-41	3 days	high	61	clear
M-6	PS 252	1 day	high	59	slightly turbid
M-7	A-07	3 h	low	15	turbid
M-8	N-199	1 day	low	16	turbid
M-9	N-10	1 day	low	15	turbid
M-10	PS 1055	*b*	high		slightly turbid
M-11	PELD 15	*b*	medium		clear

[a] Decrease in signal (%) on changing from nitrogen to air. [b] No curing observed.

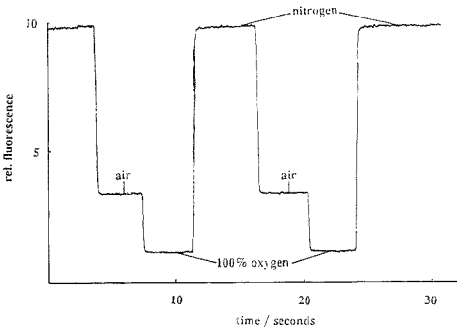

Figure 1. Response time, relative signal change, and reversibility of oxygen sensor membrane M-3 on exposure to nitrogen, air, and 100% oxygen at 23 °C.

for both the silicone prepolymer and the indicator (Table 3). Chloroform appeared to be the solvent of choice for membrane preparation. The resulting films are of intense yellow color, display strong luminescence, and are efficiently quenched by molecular oxygen. Since, however, chloroform is toxic and its use is restricted, a replacement was sought. It was found that most ion pairs are soluble in ethyl acetate as well (Table 3), so that sensing membranes may be prepared from this solvent rather than from chloroform. For indicators having dodecyl sulfate as a counterion, toluene is another good choice for making sensor membranes.

Variation of the Silicone Matrix. Various silicones were evaluated for use as a sensor matrix and with respect to their effect on signal intensity, oxygen quenching, and curing rate. Prepolymers of one-component and two-component silicones were dissolved in a 2 mM solution of **1a** in chloroform or ethyl acetate, spread on polyester foil, and cured at room temperature. Despite the chemical similarity of the silicones, the properties of the sensing films strongly depend on the prepolymer as shown in Table 4. Membranes based on one-component RTV silicones (M-3−M-9) form stable sensing films within 3 days. In contrast to the acetic acid-releasing silicones E-4, E-41, and PS 252, membranes based on amine-releasing or oxime-releasing silicones (N-10, N-199, A-07) remain turbid and are weakly luminescent only. Additionally, the quenching efficiency by oxygen is strongly reduced. The microscope shows fractions of **1a** to be present in the crystalline (i.e., nonquenchable) form.

Two-component RTV silicones (PS 1055, PELD 15) were assumed to be an attractive alternative to one-component silicones because no byproducts such as acetic acid are being formed during the curing process. However, curing in the presence of the ruthenium complexes turned out to proceed extremely slowly (or did not occur at all), probably because of deactivation of the catalyst. When the indicator concentration was lowered by a factor of 10, curing occurred within several days, but this compromises luminescence intensity and leads to the formation of rather soft membranes, probably due to weak cross-linking.

From these findings we conclude that acetic acid-releasing one-component silicones represent the most suitable silicone for this kind of indicators. The resulting sensing films are fully transparent, intensely yellow, and highly luminescent. Quenching by molecular oxygen is highly efficient: Exposure to air, for example, causes luminescence intensity to be quenched by ~60%. Because of the high quenching efficiency observed in this matrix, the E-4 silicone has been used in all further studies.

Response to Oxygen. The response time to gaseous oxygen is much faster (t_{95} < 1 s) than to oxygen dissolved in water (t_{95} ~ 50 s), as can be seen in Figures 1 and 2. A reasonable interpretation of the difference in the response times is the poor solubility of oxygen in water: Air-saturated water contains ~8 ppm oxygen. This requires a substantial volume of water to pass the silicone membrane (with its high solubility for oxygen) until it is equilibrated with oxygen and a steady-state response is obtained. The 50-s response time in water is faster by a factor of 5−10 than that of sensors based on ruthenium diimines adsorbed on silica gel as described earlier. All signal changes are fully reversible, and no hysteresis is found.

Quenching Constants. Stern−Volmer plots are given in Figure 3 for sensor materials M-1−M-4. They are nonlinear, which is in contrast to what may be expected for a quasi-homogeneous dye-in-polymer solution. However, nonlinear quenching along with the existence of several decay profiles and of

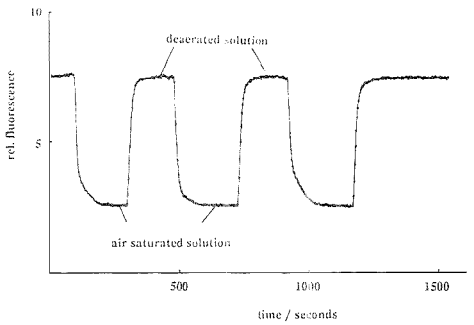

Figure 2. Response time, relative signal change, and reversibility of oxygen sensor membrane M-3 on cycling from air-saturated water to nitrogen-purged water.

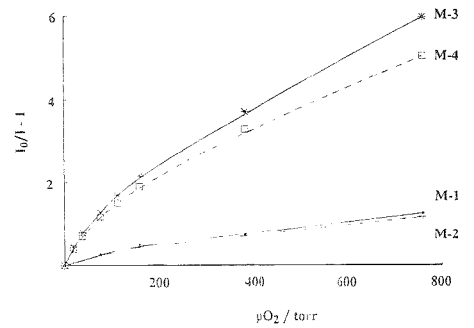

Figure 3. Nonlinearity of the Stern–Volmer plots of the quenching of the luminescence of membranes M-1–M-4 by oxygen.

species with different quenchabilities has been observed in numerous other cases as well,[11] and strictly linear Stern–Volmer behavior seems to be the exception rather than the usual case even in seemingly homogeneous (i.e., filler-free) materials.

The quenching curves were analyzed for two components, namely, the freely dissolved (homogeneously distributed) and the aggregated forms, using the equation of Carraway et al.[10]

$$I/I_0 = f_1/(1 + K_{SV1}pO_2) + f_2/(1 + K_{SV2}pO_2) \qquad (1)$$

where I and I_0 are the quenched and unquenched luminescence intensities of the respective sensor membrane, K_{SV1} and K_{SV2} are the Stern–Volmer constants of the two quenching processes, and f_1 and f_2 are the relative contributions (weighing factors). pO_2 is the oxygen partial pressure that causes the luminescence to drop from I_0 to I. The results are summarized in Table 5 and clearly show that the efficiency of the quenching attributed to the aggregates is smaller by a fairly constant factor (K_{SV12}) of 23–28 than that of the dissolved species. The ratios of the weighing factors (f_{12}), in contrast, vary substantially (from 0.30 to 3.35). The regression coefficients are excellent. Data also were analyzed according to another recently proposed method,[17] but this gave less satisfactory results.

Effects of Storage. When membranes of type M-3 were stored in water for 2 months, the quenching constant decreased by 10%, and when stored at room temperature in a plastic bag for 1 year, the quenching efficiency (K_{SV1}) decreased by 20–30%. In contrast to membranes M-3 and M-4, membranes M-1 and M-2 when stored in water for 2 weeks show little leaching, only detectable by the very weak luminescence of the water solution. This leaching occurs during the first few hours of storage, and it is assumed that it is the surface-bound fraction of the dye that is dissolved by water. Indicator leaching is also negligable when membranes are stored in water containing 1 mM concentrations of either sodium dodecyl sulfate or cetyltrimetylammonium bromide. The silicone sensing layers have excellent adhesion to the polyester support membrane. When, for example, plain water was passed over membrane M-3 for 2 weeks, no delamination occured.

Table 5. Quenching Constants (Torr^{-1}) and Weighing Factors of the Quenching of the Luminescence of Sensor Membranes M-1–M-4 as Analyzed via Eq 1

membrane	K_{SV1}	K_{SV2}	K_{SV12}	f_1	f_2	f_{12}	regression
M-1	0.0275	0.0010	27.5	0.23	0.77	0.30	0.9993
M-2	0.0239	0.0009	26.5	0.25	0.75	0.33	0.9997
M-3	0.0322	0.0014	23.0	0.76	0.24	3.17	0.9999
M-4	0.0276	0.0010	27.6	0.77	0.23	3.35	0.9998

Photostability. Daylight illumination of membrane M-3 for 1 year caused no measurable photodecomposition. When illuminated in the flow-through cell of the Aminco fluorometer with its 200-W halogen lamp at an excitation wavelength of 450 nm and a bandpass of 5 nm, the signal loss was smaller than 1% in 5 h. Since the light intensity is even smaller when exciting Ru(dpp) with a blue LED, which is the preferred source for excitation,[18] the photostability obviously is more than adequate for most applications. The 450-nm light of a 200-W xenon lamp, in contrast, caused a 5% signal loss per hour in the presence of nitrogen. In pure oxygen, the rate of indicator decomposition is higher than in nitrogen by a factor of 4. This observation is in agreement with results of Carraway et al.[10] and can be explained in terms of oxidation by reactive singlet oxygen.

Interferences. Interference tests were performed with membrane M-3, which is considered to be the most suitable for many applications. When dry gases were replaced by gases of 100% humidity, a 2% decrease in I_0 (the luminescence intensity under nitrogen) and a 2% reduction in the quenching efficiency (K_{SV}) was observed. The effect is fully reversible. Results of studies on the cross-sensitivities toward potential chemical interferents are summarized in Table 6. The lack of interference by ionic quenchers such as heavy metals obviously is due to exclusion by the hydrophobic silicone material. Luminescence also is independent of pH and ionic strength of the sample. Surfactants did not interfere, as tested for sodium dodecyl sulfate and cetyltrimethylammonium bromide. Sulfur dioxide, hydrogen peroxide, and chlorine act as reversible quencher in low concentrations. At higher levels, chlorine seems to oxidize the indicator in the presence of light, as tested for a 10 mM solution of sodium hypochlorite. As a result, the membrane turns brown and luminescence strongly decreases over time.

Optical Isolation. In order to eliminate any interferences caused by ambient light as well as effects of sample fluorescence, turbidity, coloration, and refractive index (which affects the numerical aperture of an optical waveguide), an optical isolation

Table 6. Effect of Potential Interferents on the Luminescence of Membrane M-3 in Nitrogen-Purged Water[a]

interferent	concentration	signal change (%)
Cu^{2+}	0.1 mM	<1
Fe^{3+}	1.0 mM	<1
HCl (pH 1)	0.1 M	<1
NaOH (pH 13)	0.1 M	<1
NaCl	3% water solution	<1
lauryl sulfate	1.0 mM	<1
CTAB[b]	1.0 mM	<1
CO_2	pure gas	<1
Cl_2	~1% in nitrogen	−25
SO_2	~1% in nitrogen	−28
H_2O_2	3% water solution	−6

[a] Unless otherwise stated. [b] Cetyltrimethylammonium bromide.

(OI) was spread on top of the actual sensing layer. A typical cross section through the resulting sensor layer can be found in Figure 1 in a related paper.[19] An OI is expected to be light-impermeable but analyte-permeable and to possess good adhesion to the sensing layer. Three types of potentially useful materials were tested. The first was black silicone deposited as a 10-μm top layer. It has the advantages of excellent adhesion and oxygen permeability. The second was a black 12-μm Teflon membrane, uniformly spread onto the sensing layer. When compared to silicone, it shows distinctly lower oxygen permeability. The third was white titanium dioxide powder, which was dispersed into the silicone matrix. It turned out that the particles not only act as an OI but also as scattering centers, thereby tremendously improving the excitation efficiency and, hence, the signal obtained. The efficiencies of the three kinds of materials are summarized in Table 7.

The 10-μm layer of black silicone (N 189) was used previously[7] and seems to work best. It had no effect on the sensitivity, while the signal intensity decreased by 15%, and the response time remained unchanged. The OI did not delaminate after 3 months of storage in water. A colored sample (bromothymol blue in water) as well as a turbid sample (titanium dioxide suspended in water) did not at all affect the luminescence intensity of M-3.

When M-3 was covered with a 12-μm black Teflon foil, the sensitivity to oxygen did not change either, but I_0 dropped by 10%. Unfortunately, the Teflon coating increased the response time to gaseous oxygen by a factor of 10, which probably is the result of its poor permeability for oxygen. The adhesion of Teflon to silicone is adequate, but uniform layers are difficult to make by hand. Sample coloration and turbidity again cause no change in signal intensity.

The use of a white titanium pigment incorporated into the sensing layer is an interesting alternative to black OIs and also may simplify sensor preparation. It results in white, translucent sensor membranes (M-12) with an oxygen sensitivity similar to sensing membranes without pigment. To achieve an efficient OI, membranes had to be 20 μm thick, or more. Notwithstanding this relatively large thickness, the OI is not as good as with black silicone or black Teflon. A 3% increase in signal intensity was measured on changing from pure water to a strongly scattering sample solution, and a 2% signal decrease was observed when sensor M-12 was exposed to a deeply yellow sample solution, indicating that the OI is not perfect. On the other side, M-12 exhibits a luminescence intensity higher by 1 order of magnitude when compared to homogeneous membranes based on transparent silicones (e.g., M-3). This can be attributed to both a very efficient absorption of excitation light because of multiple scattering and an efficient backscattering of luminescence.

DISCUSSION

Among the ruthenium diimine oxygen probes, Ru(dpp) appears to be the indicator of choice. The use of its chloride, sulfate, or perchlorate was hampered, so far, by their insolubility in silicone rubber, which is the preferred material in the case of oxygen sensing. This work demonstrates that the problem can be overcome by making use of ion pairs **1** and **2**, thus enabling the design of silicone-based sensing films containing homogeneously distributed dyes. Because of their excellent solubility, indicators now can be applied in high concentrations, so that very thin (1−4 μm) but highly luminescent sensing layers can be prepared. As a result, response times become very short. Unlike sensors based on silica gel-adsorbed Ru(dpp), luminescence intensity is linear with dye concentration over a wide range, and no self-quenching is observed even at rather high dye concentrations. Silica gel adsorbates, in contrast, have an upper limit of surface loading, above which quenching of the luminescence of ruthenium adsorbates becomes inefficient even though luminescence intensity may still increase.

We think the nonlinear Stern−Volmer plots observed with the new materials result from the fact that indicator ions pairs are present in two forms, viz. (a) a molecular and evenly distributed form and (b) a kind of micellar (aggregated) form, the latter however not being crystalline. The two forms are assumed to have different quenching constants, weighing factors, and decay times, and this—obviously—results in a nonlinear Stern−Volmer plot. The decrease in sensitivity (in terms of K_{SV}) is attributed to the effect of a slow transition from the homogeneous to the aggregated (less quenchable) form.

There is no evidence for dye crystallization even after a 12-month storage of sensing membranes M-1−M-4 on air. In fact, crystal formation was observed under the microscope only with membranes made from Ru(dpp) *perchlorate* (which is sparingly soluble in silicone) after evaporation of the solvent in the same types of silicone. Luminescence intensities and quenching efficiencies are much smaller in this case. Quenching constants

Table 7. Properties of Membranes of Type M-3 with Different Kinds of Optical Isolation

optical isolation	adhesion	quenching by air[a]	rel signal intens	response time ($t_{0.5}$) in gas (s)	effect of turbidity[b]	effect of color[c] (%)
without	na[d]	60	1.0	<1	+50	−15
black silicone, 10 μm	sufficient	61	0.85	~1	<1	<1
black Teflon, 12 μm	sufficient	59	0.80	~5	<1	<1
TiO_2 (dispersed)	na[d]	59	20.0	~2	+2	−2

[a] Decrease in signal (%) on changing from nitrogen to air. [b] Signal change (%) on exposure to an aqueous solution containing suspended (10 g/L) TiO_2 particles. [c] Signal change (%) on exposure to a yellow solution of bromothymol blue (absorbance at 460 nm). [d] No adhesion.

are similar for sensor membranes based on silicones containing either hydrophobic silica gel as filler (e.g., M-4) or no filler (e.g., M-6).

Stern–Volmer plots show strong deviations from linearity although dyes seems to be homogeneously dissolved in the silicone and no inhomogeneities are visible under the microscope. In addition, the quenching efficiencies are distinctly lower than those reported for the perchlorate and chloride salts of Ru(dpp) which were *adsorptively* immobilized on a silica filler inside a rather similar silicone (RTV-118).[19] Both findings clearly indicate that different quenching mechanisms are operative in the present type of material, and in the adsorption (filler) type sensor materials, i.e., where the dye is localized on the surface of the silica gel filler.

The ion pairs used in this work can be excited with blue LED light sources, and luminescence can be detected with photodiode light detectors as was shown before for other ruthenium-based sensors.[18] Aside from measurement of oxygen partial pressure via luminescence intensity, the long lifetime of ruthenium diimines also lends them to oxygen sensing via luminescence lifetime.[20] In fact, the counterion is known to exert almost no effect on the lifetime of the cation, while a viscous or solid solvent may increase the lifetime even further.[15] While shown for planar sensing films only in this work, the new materials may also be deposited as a clad or tip coating on optical fibers or on integrated optical waveguides. Because the materials do not contain filler particles (of typical 1 μm diameter) anymore, they can be deposited in thicknesses as thin as 50–100 nm, which is in contrast to the rather thick (>10 μm) membranes we and others have used so far. This results in very fast response times and allows the materials to be deposited on the core of an optical fiber or on an integrated optical waveguide. The short response times and negligible cross-sensitivity to humidity make the sensing materials useful for respiratory gas analysis. The excellent operational and storage stability along with the high quenching constants, in turn, make such sensors most useful for continuous monitoring applications in the clinical laboratory and performance of long-term environmental analyses.

(19) Preininger, C.; Klimant I.; Wolfbeis, O. S. *Anal. Chem.* **1994**, *66*, 1841–1846.

(20) Lippitsch, M. E.; Pusterhofer, J.; Leiner, M. J. P.; Wolfbeis, O. S. *Anal. Chim. Acta* **1988**, *205*, 1–6.

ACKNOWLEDGMENT

This work was supported by the Austrian Science Foundation (FWF) within Project S5702-PHY, which is gratefully acknowledged.

Received for review March 9, 1995. Accepted June 28, 1995.[⊗]

AC9502460

[⊗] Abstract published in *Advance ACS Abstracts*, August 1, 1995.

Anal. Chem. 1995, *67*, 3167–3171

Spatial Distribution of Atoms in a dc Glow Discharge

K. Hoppstock† and W. W. Harrison*

Department of Chemistry, University of Florida, P.O. Box 117200, Gainesville, Florida 32611-7200

An argon glow discharge acts as a reactive chemical cell involving sputtered analyte and argon atoms and ions. The spatial distribution of atoms from several samples has been monitored by an atomic absorption and emission arrangement simultaneously with mass spectrometric monitoring of the discharge. We have examined the effect of varying the sample to exit orifice distance on resultant atom profiles. Copper was studied by atomic absorption and iron by atomic emission, revealing complementary population shifts near the cathode surface. Argon metastable species were also monitored and correlated with the analyte response. Movement of the sample insertion probe by 90° allowed a vertical perspective to be obtained for the discharge atom population. The effect of different discharge voltages was also examined to show sputter variations. Atom populations are defined by many factors, including sputter rate, diffusion rates, chemical reactivity, and discharge pressure.

In recent years the importance of rapid and reliable trace analytical characterization of environmental samples, high-purity materials, and advanced ceramics has steadily increased. Glow discharge (GD) techniques, particularly glow discharge mass spectrometry (GDMS), have gained popularity especially for the direct trace elemental analysis of solid materials. To improve further the capabilities of GDMS and related GD atomic spectrometric techniques, it is beneficial to enhance the understanding of glow discharge fundamental processes that can significantly affect analytical results.

The GD is usually operated at a pressure of a few millibars, and for analytical applications, the most common gas used is argon. At a discharge pressure of about 1 Torr, the argon mean free path is in the order of 50 μm, and therefore, the sputtered analyte originating from the cathode will experience many collisions (e.g., with discharge gas species, contaminants, or analyte species) before reaching the exit orifice 1 cm or more away from the cathode. In this study, the diffusion characteristics of the sputtered atoms were evaluated by the examination of plasma properties in different parts of the plasma. Mass spectrometry is a sensitive tool for the study of gas discharges, but it is not conducive to spatially resolved studies, as it samples only a plasma volume adjacent to the exit orifice. Optical methods such as emission, absorption, or fluorescence spectrometry are proven techniques for probing various parts of the plasma without disturbing its shape and composition. By use of both optical and mass spectrometry, complementary measurements can be made to explore signal relationships among the many prominent species in the GD.

Early works by H. Hörmann in 1935[1] and J. Friedrich in 1959[2] investigated high-pressure arc discharges, focusing on temperature distributions, electron densities, and luminescence density distributions rather than atom or ion distributions. Stirling and Westwood[3] used atomic absorption techniques to examine atom profiles in a glow discharge, in particular the sputtering processes of aluminum in Ar. Using dye laser fluorescence spectroscopy, Elbern[4] measured axial atom density profiles of a dc GD with Fe disk electrodes. Fereira, et.al.[5] determined by AAS the distribution of metastable argon atoms in a modified Grimm-type discharge, and Loving[6] employed AAS and MS to study an Ar GD with a Fe cathode. Recently, Djurovic et al. reported a study of spatially and temporally resolved OES measurements of a rf-GD.[7]

To study the glow discharge under conditions optimized for mass spectrometry, we designed around the discharge chamber of our GDMS unit an optical system for atomic absorption and emission spectrometry, permitting careful and detailed profiling of the discharge, simultaneously with mass spectrometric measurements.

EXPERIMENTAL SECTION

The glow discharge quadrupole mass spectrometer has been described previously.[8] A schematic diagram is shown in Figure 1a of the GD ion source, constructed from a six-way cross featuring 2.75-in. flanges with quartz glass windows for the optical path at right angles to the ion beam extraction. The source features a cryogenic cooling coil[9] coaxial about the direct insertion probe in-line with the mass spectrometer axis, which will be referred to as the *x*-axis in this paper. Figure 1b shows that a second port on the six-way cross allows the insertion perpendicular to the *x*-axis, where the cryogenic cooling coil with the bellow assembly and ball valve was replaced by a blank flange.

Figure 2 shows the schematic diagram of the optical arrangement. The movable arm is mounted to a translation stage, permitting precise positioning along the *x*-axis with a millimeter screw. A Spex 340E monochromator (Spex Industries, Inc., Edison, NY) with a focal length of 0.34 m, equipped with a

† Present address: Research Center Jülich GmbH, Zentralabteilung für Chemische Analysen, P.O. Box 1916, D-52425 Jülich, Germany.

(1) Hörmann, H. *Z. Phys.* **1935**, *97*, 539–560.
(2) Friedrich, J. *Ann. Phys.* **1959**, *3*, 327–333.
(3) Stirling, A. J.; Westwood, W. D. *J. Appl. Phys.* **1970**, *41*, 742–748.
(4) Elbern, A. *J. Vac. Sci. Technol.* **1979**, *16*, 1564–1568.
(5) Ferreira, N. P.; Strauss, J. A.; Humar, H. G. C. *Spectrochim. Acta* **1982**, *37B*, 273–279.
(6) Loving, T. J.; Harrison, W. W. *Anal. Chem.* **1983**, *55*, 1523–1526.
(7) Djurovic, S.; Roberts, J. R.; Sobolewski, M. A.; Olthoff, J. K. *J. Res. Natl. Inst. Stand. Technol.* **1993**, *98*, 159–180.
(8) Bruhn, C. G.; Bentz, B. C.; Harrison, W. W. *Anal. Chem.* **1978**, *50*, 373–375.
(9) Ohorodnik, S. K.; Harrison, W. W. *Anal. Chem.* **1993**, *65*, 2542–2544.

0003-2700/95/0367-3167$9.00/0

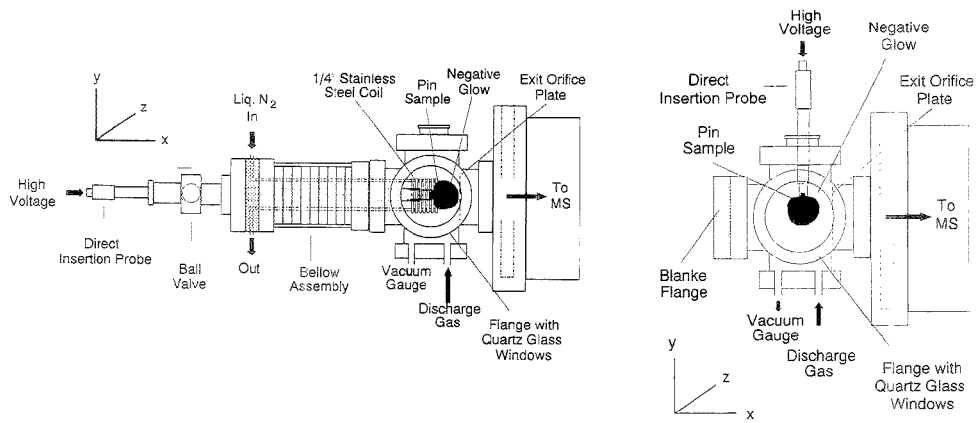

Figure 1. Glow discharge source and direct insertion probe for GD mass spectrometry and GD optical spectrometry: (a, left) axial insertion of sample; (b, right) 90° variation to permit alternative profile measurements.

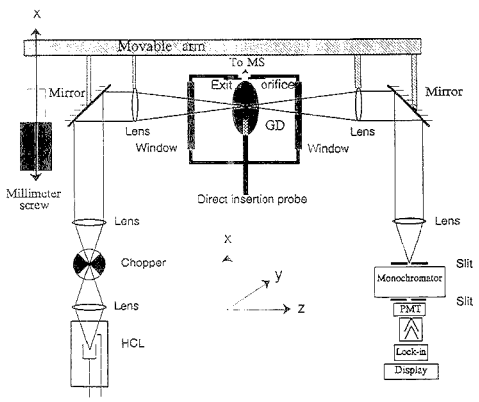

Figure 2. Schematic arrangement for spatially resolved optical measurements in the glow discharge source.

Hamatsu R1547 PMT tube and a Pacific Instruments photometer Model 110, was used for all the optical measurements. For emission studies, the photometer signal was registered on a strip chart recorder (Houston Instruments, Austin, TX). Atomic absorption measurements with hollow cathode source lamps were performed using a mechanical chopper (Scitec Instruments) with a Model 5207 lock-in amplifier (EG&G Princeton Applied Instruments, Princeton, NY) to discriminate against emission. In order to obtain a high spatial resolution, an entrance slit width of 0.2 mm and a slit height of 0.167 mm were used. The exit slit of the monochromator was set to 0.2 mm.

Ultra-high-purity-grade argon (Liquid Air Corp., San Francisco, CA) was used with an operating pressure of 1 Torr (~1.3 mbar). The pin cathodes used in these experiments were electrolytic iron [National Institute of Standards and Technology (NIST) (Gaithersburg, MD) SRM 1265a], 99.999% puratronic grade Ag and Cu wire, 2-mm diameter (Johnson Matthey Chemicals, Ward Hill, MA) and 99.97% Ti wire, 2-mm diameter (Aldrich Chemical Co., Inc., Milwaukee, WI). The iron samples were machined into 2 mm diameter pins from bulk disk samples. A 4–5-mm segment of the pins was exposed to the discharge. The experiments were performed with constant dc discharge current of 4 mA, if not otherwise stated. Before the measurements were taken, the cathode was presputtered for 20 min to get a clean surface and to remove as many impurities from the system as possible. The discharge chamber was also periodically baked for several hours, after which the plasma was monitored for contaminants by mass spectrometry. Cryogenic cooling was used for all measurements.

RESULTS AND DISCUSSION

The glow discharge is a ready source of sputtered atoms from the sample cathode. Atoms ablated from the sample surface are subjected to a high collision rate in the 1-Torr discharge, with many atoms being returned to the sample surface, while others diffuse into the plasma. In addition to diffusion effects, atom distribution may be influenced by discharge gas flow patterns and by electric fields in the case of ions. As a result of these processes, heterogeneous steady-state concentration profiles are established across the glow discharge.

Measurements along the *x*-Axis. To gain a better understanding of the plasma processes, it is useful to monitor various discharge species, such as ground-state and excited-state atoms, ions, and metastable (Ar_m^*) species in various parts of the plasma. Our first interest was directed toward the distribution of the sputtered analyte, the ground-state atom population, which was studied by atomic absorption spectrometry. Four different settings of cathode to exit orifice distance were studied (Figure 3). For a copper cathode, the absorbance profiles for each of those distance settings are shown, reflecting the changing shape of the glow discharge plasma as the cathode is moved closer to the exit orifice. The measurements are quite reproducible, with variations generally falling within the data symbols shown. For all cathode materials used in this study (Ag, Cu, Fe, Ti), the profile exhibits this same general shape, although the measured absorbances differed significantly. It should be noted that the maximum absorbance is not observed immediately adjacent to the cathode surface, but instead about 0.75–1 mm in front of the surface. This phenomenon, previously noted by other investigators,[3,5] is somewhat surprising, as all the copper atoms present in the plasma

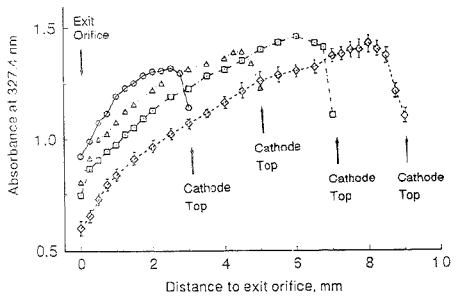

Figure 3. Absorbance profiles of copper (327.4 nm) along the *x*-axis (see Figure 2) in an Ar plasma with a Cu cathode (4 mA, 1 Torr, and ~1000 V). Distance between sample and exit orifice: (○) 3, (△) 5, (□) 7, and (◇) 9 mm.

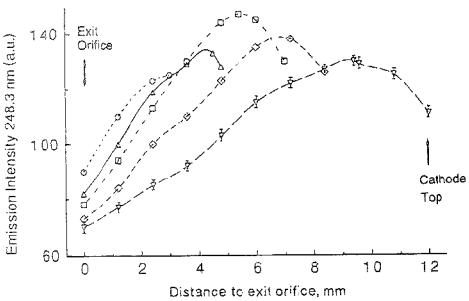

Figure 4. Emission profiles of Fe (I) at 248.3 nm along the *x*-axis for different distances between cathode and exit orifice in an Ar GD at 1 Torr and 4 mA (discharge voltage ~1000 V). Distance between sample and exit orifice: (○) 3, (△) 5, (□) 7, (◇) 9, and (▽) 12 mm.

originate from the cathode surface. This could suggest that not all the cathode material is sputtered in the form of single ground-state atoms. Possibly some multiatom species are ejected in the form of dimers, trimers, and other cluster forms. Some significant amount of sputtered material may also be released as excited-state species or as ions. None of these species could be detected by our atomic absorption measurements, so whether such factors could account for the drop of absorbance near the cathode is not clear. The production of molecules or related species by the sputtering process had been reported earlier.[3,10,11] Winefordner, et al. reported diatomic lead in a GD as measured by laser-excited fluorescence.[12]

As a comparison to the measured absorbance profiles of ground-state atoms, emission measurements of the excited-state populations were also made using the same experimental conditions. Figure 4 shows spatially resolved emission profiles of Fe (I) at 248.3 nm in an argon discharge using an iron cathode. The general shapes of these curves are similar to those seen in Figure 3; a steady increase of signal intensity is found as the measurement site is moved from the anode (exit orifice) toward the cathode. Again, a drop in signal intensity is seen near the cathode surface. The decrease near the cathode is less abrupt than in the case of

(10) Stirling, A. J.; Westwood, W. D. *J. Phys. D: Appl. Phys.* **1971**, *4*, 246–252.
(11) Gough, D. S. *Anal. Chem.* **1976**, *48*, 1926–1931.
(12) Patel, B. M.; Smith, B.; Winefordner, J. D. *Spectrochim. Acta* **1985**, *40B*, 1195–1204.

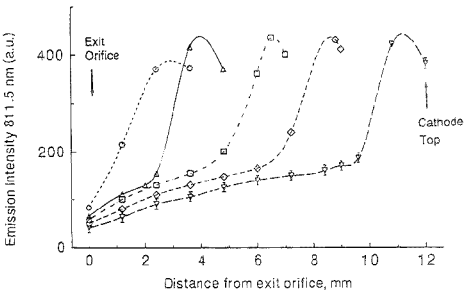

Figure 5. Emission profiles of argon metastable species (811.5 nm) along the *x*-axis. Distance between sample and exit orifice: (○) 3, (△) 5, (□) 7, (◇) 9, and (▽) 12 mm.

the ground-state atoms but clearly indicates the reduced population in this area. The data in Figures 3 and 4 show that both ground-state and excited-state populations are diminished near the cathode.

Metastable argon atoms have been implicated as key energy transfer species in glow discharges. Therefore, their axial distribution was determined in order to provide some additional insight into the profile shapes of sputtered species. Figure 5 shows emission profiles of argon metastables (Ar_m^*) taken at five different sample to exit orifice distances. These plots have some general similarities to the sputtered species plots, but also significant differences. Indeed, factors affecting the respective populations should be quite different. There is an overall decrease in metastable population moving from the cathode to the exit orifice, but the changes are more abrupt. A sharp transition occurs for each distance plot, occurring each time just into the negative glow. At that location in the plasma, about $^2/_3$ of the signal decrease occurs within ~1–2 mm of distance in the plasma. Most likely this is related to optimum electron energy distributions affecting metastable formation. A small, but distinctive drop in metastable population also occurs just inside the dark space of the glow discharge, similar to that observed for sputtered species. While this could be some factor in the decreased analyte emission, it does not follow that the larger abrupt metastable reduction in the negative glow necessarily has any relationship to the corresponding decrease of the sample atoms. As seen in Figure 3, a much smoother decline in intensity occurs. Profiles for the various species show that formation and loss mechanisms do not affect all the critical species uniformly.

Perpendicular Probe Insertion. Radial Measurements. The optical configuration shown in Figure 2 allows measurements along one axis only. To study the plasma along other axes would have required major reorientation of the optical system. Instead, we took advantage of the symmetry of the six-way cross to move the direct insertion probe 90° from the conventional measurement mode. In this manner, the pin sample is perpendicular to the *x*-axis through the top port, as shown in the inset of Figure 6. With this configuration, driving the movable arm along the *x* axis probes the plasma radially at varying distances from the cathode center. The distance away from the cathode tip is varied by moving the direct insertion probe up or down along the *y*-axis (Figure 6).

The data collected by this process permit construction of the absorbance profile shown in Figure 6. A copper pin was used as

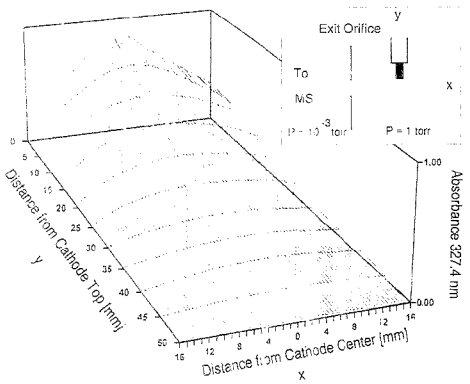

Figure 6. Absorbance profile of copper (327.4 nm) in an argon glow discharge; probe inserted perpendicular to the *x*-axis. Distance of cathode center to exit orifice, 16 mm.

the cathode in a 1-Torr argon glow discharge. The ground-state copper atom population decreases (as expected) with increasing distance from the cathode. Of more interest, when the probing beam (0.17 mm × 0.20 mm) passes just beneath the cathode top, we observed a drop in absorbance in the cathode center region, corresponding to the results previously shown (Figure 3), where the absorbance also decreased in front of the cathode. (This center region will be discussed in more detail when Figure 7 is considered.)

Comparing the radial decrease in absorbance on either side of the cathode, the slope on the exit orifice side (left side in Figure 6) becomes significantly steeper than that observed on the opposite side away from the exit orifice. The GDMS system requires an intense differential pumping system to maintain the high vacuum on the mass spectrometer side simultaneously with the much greater pressure (~1 Torr) in the discharge chamber. The resulting pressure differential creates a jet expansion of the argon/sputtered-atom plasma mixture through the exit orifice. This effect enhances the diffusion-based material transport and also dilutes the plasma mixture by introducing discharge gas from outer plasma regions. These results indicate that the plasma in this particular setup is not as symmetrical as might be expected. The asymmetry may explain why our attempts to employ Abel conversion computations[13,14] of the data did not create reliable results. It also indicates that atom distribution profiles obtained in this radial direction may differ slightly in configuration from those taken axially as a result of the differential pumping effect.

The drop in absorbance near the cathode was detailed more completely as shown by the data in Figure 7. Measurements were taken at 0.5-mm intervals and at four different discharge voltages. Increasing voltages increases the current and the sputter rate, and consequently, the absorbance. The contrast between the maximum absorbance (~1 mm from the pin center) and the minimum absorbance at the cathode center remains generally constant within the precision of these measurements. It seems unlikely that reduced sputtering is occurring at the center. The results do indicate, however, the presence of fewer sputtered ground-state atoms, for reasons that may involve excited states, polyatomics, clusters, or some other unknown effect.

(13) Sacks, R. D.; Walters, J. P. *Anal. Chem.* **1970**, *42*, 61–84.
(14) Cremers, C. J.; Birkeland, R. C. *Appl. Opt.* **1966**, *5*, 1057–1063.

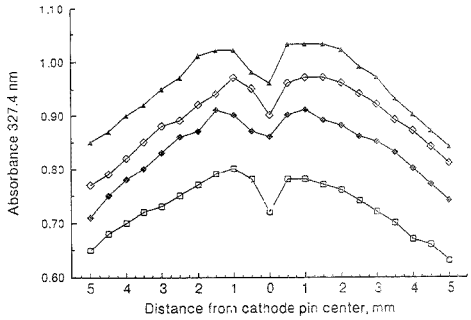

Figure 7. Absorbance profiles directly in front of the cathode surface using an Ar glow discharge with a Cu cathode (inserted along the *y*-axis); operated with different discharge voltages. Applied voltages: (▲) 1000, (◇) 1250, (■) 1500, and (□) 1750 V.

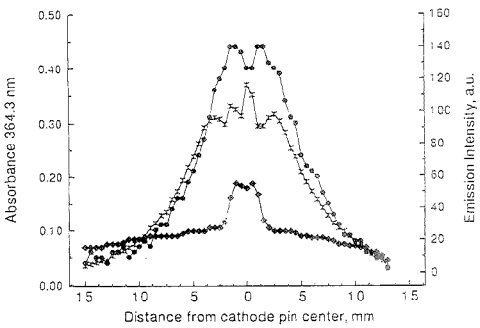

Figure 8. Profiles of absorbance (364.3 nm) and emission (Ti (II) at 300 nm, and Ar_m^* at 811.5 nm) taken directly in front of the cathode surface of an Ar glow discharge with a Ti pin (inserted along the *y*-axis): (●) OES Ar_m^* 811.5 nm, (×) OES Ti (II) 323.4 nm, and (◆) AAS Ti 364.3 nm.

Another possible cause for the absorbance drop could involve the formation of ions in this central cathode region. By mass spectrometry, we can only sample ions that form near the ion exit orifice, but by monitoring optical emission from some suitable element, spatial measurements of the ion populations can be determined. Ti was selected as the test element due to its strong ion lines. In this way, sputtered titanium atoms could be measured by atomic absorption and titanium ions by atomic emission. Figure 8 shows a comparison of ground-state and ion distributions obtained in an Ar GD with a Ti pin as the cathode. In addition, argon metastable atoms were monitored by their atomic emission.

The profile of Ti atoms is quite similar to that of Cu (Figure 3), with the same type of characteristic dip in front center of the cathode. The shape observed for the Ar_m^* emission generally tracks the ground-state metal atom population, suggesting that the forces affecting the sputtered atom population may also influence metastable formation. The Ti ion emission profile presents an interesting contrast, as highest emission intensity is observed at the cathode center. In fact, the sharp increase of ions coincides with the drop in atom population. That implies that a fraction of Ti could be sputtered in ionic form or ionized within the first few micrometers (which cannot be resolved with the present system). Sputtered ions should be returned to the cathode by the dark space field adjacent to the cathode, but ions

formed in plasma interactions beyond that field would be in a generally field-free region. The multiple peaks observed with the ion profile are surprisingly reproducible. An ion source design that samples cathodically through a center ion orifice might be worth reconsidering. The hollow cathode ion source[15] that provided the impetus in our laboratory for initial GDMS work featured this mode of sampling. High-intensity ion beams of sputtered analytes were obtained, although the ion energy spread was too large to be suitable for a quadrupole system. We are currently considering the possibility of revisiting this type of ion source.

CONCLUSIONS

Sputtered atom populations in a glow discharge are influenced by a number of factors. Diffusion of atoms away from the cathode sample causes significant concentration gradients toward the source extremities. The ion exit port of a GDMS source contributes its own effect as a result of the large differential pressure across the ion exit orifice, and this is at the very site where ions are produced for GDMS. A small, but well-defined reduction in sputtered atom density occurs near the center of the cathode face, possibly due to ionization processes. The atom distribution plots show that mass spectral sensitivity may be unduly reduced by the present source designs. A GDMS source that sampled ions nearer the cathode may be worth further consideration.

ACKNOWLEDGMENT

This research was supported by the Department of Energy, Division of Basic Energy Sciences. In addition, K.H. was supported by the Deutsche Forschungsgemeinschaft.

Received for review January 3, 1995. Accepted June 20, 1995.[⊗]

AC950009X

(15) Harrison, W. W.; Magee, C. W. *Anal. Chem.* **1973**, *46*, 461–464.

[⊗] Abstract published in *Advance ACS Abstracts*, August 1, 1995.

Anal. Chem. **1995**, *67*, 3172–3180

Oxygen Sensors Based on Luminescence Quenching: Interactions of Pyrene with the Polymer Supports

Wenying Xu,[†] Robert Schmidt,[†] M. Whaley,[†] J. N. Demas,*[,†] B. A. DeGraff,*[,‡] E. K. Karikari,[§] and B. L. Farmer*[,§]

Department of Chemistry, and Department of Material Science, SEAS, University of Virginia, Charlottesville, Virginia 22901, and Department of Chemistry, James Madison University, Harrisonburg, Virginia 22807

Oxygen quenching of pyrene has been studied in a diverse series of polymers. Most measurements were made using homo- or copolymers containing a poly(dimethylsiloxane) region. Systematic variations in the polymer properties have been made in order to delineate the structural features important for satisfactory use as supports for oxygen sensors. In particular, quenching behavior was examined as a function of the type and amount of copolymer cross-linkers; these were added to produce domains of different polarity and rigidity that would segregate the sensor molecule. A domain model (Xu, W.; et al. *Anal. Chem.* 1994, *66*, 4133–4141) was used to explain the variations in oxygen-quenching properties as a function of additives and cross-linkers. The relative affinity of the different domains for the pyrene and the efficacy of the domains for oxygen quenching controls the overall behavior of the sensing response.

Virtually all materials used as sensors are on a polymer support. In some cases the support is a passive anchor while in others it has an active role. Indeed, the support may have quite stringent criteria for suitable performance. For example, in oxygen sensors, a high diffusion coefficient is necessary for rapid response; a high locally effective quenching constant around the sensor molecule is necessary for good sensitivity; and, because of the considerable interest in physiological monitoring, a high degree of biocompatibility is necessary.

Unfortunately, unlike solution properties of sensors, the understanding of the detailed role of the polymer support in controlling photophysical behavior is still very much in its infancy. This is true not only for metal complexes[1-5] but also for analogous systems based on luminescent organic molecules.[4,5] Our goals were to systematically explore the interplay of polymer structure and design on oxygen sensor performance. In an earlier paper[3] we focused on the interactions of the support with metal complexes using $[Ru(Ph_2phen)_3]Cl_2$ (Ph_2phen = 4,7-diphenyl-1,10-phenanthroline) as a model system. A polar–hydrophobic domain model was developed to explain the quenching properties of the complex in a variety of polymers and in polymers with silica filler.

The current work was undertaken to determine whether the domain model would also be of predictive value in explaining the behavior of nonpolar sensors in homo- and heteropolymer systems. For a probe we chose the much more hydrophobic pyrene sensor molecule because it has a long excited state lifetime (400 ns), is heavily oxygen quenched, and has a vibronic intensity ratio that is highly sensitive to solvent polarity[6] and, thus, supplies us with another potential tool for assessing the local environment of the probe in the polymers. For example, pyrene was used with great success to study the binding regions and solvent interactions with C-18 reverse phase chromatographic surfaces.[7]

In fluid solutions, where every molecule experiences the same average environment, the normal Stern–Volmer intensity and lifetime quenching equations including static and dynamic quenching are

$$\tau_0/\tau = 1 + K_{SV}[Q] \tag{1a}$$

$$K_{SV} = k_2\tau_0 \tag{1b}$$

$$I_0/I = 1 + (K_{SV} + K_{eq})[Q] + K_{eq}K_{SV}[Q]^2 \tag{1c}$$

where I's are emission intensities, τ's are lifetimes, k_2 is the bimolecular quenching constant, K_{SV} is the Stern–Volmer intensity quenching constant, and K_{eq} is the equilibrium constant for formation of a nonluminescent complex between the luminescent species and the quencher. The subscript 0 denotes the value of the quantity in the absence of quencher. Static quenching will always yield an upward-curved Stern–Volmer intensity plot. If only dynamic quenching is present in solution, one normally finds that the intensity and lifetime Stern–Volmer curves match.

$$\tau_0/\tau = I_0/I \tag{2}$$

In solid supports, however, the probe can frequently exist in a variety of different environments that persist throughout the

[†] Chemistry Department, University of Virginia.
[‡] James Madison University.
[§] Department of Material Science, University of Virginia.
[∥] Current address: HiPPAC Center, Clark Atlanta University, 223 James P. Brawley Dr., SW, Atlanta, GA 30314.

(1) Kaneko, M.; Takekawa, T.; Asakura, T. *Makromol. Chem., Macromol. Symp.* **1992**, *59*, 183–197.
(2) Kaneko, M.; Iwahata S.; Asakura, T. *Photochem. Photobiol.* **1992**, *55*, 505–509.
(3) Xu, W.; McDonough, R. C., III; Langsdorf, B.; Demas, J. N.; DeGraff, B. A *Anal. Chem.* **1994**, *66*, 4133–4141.
(4) Charlesworth, J. M. *Sens. Actuators* **1994**, *22*, 1–5.
(5) Wong, A. L.; Hunnicutt, M. L.; Harris, J. M. *Anal. Chem.* **1991**, *63*, 1081–1090.
(6) Kalyanasundarum, K.; Thomas, J. K. *J. Am. Chem. Soc.* **1977**, *99*, 2039–2044.
(7) Carr, J. W.; Harris, J. M. *Anal. Chem.* **1987**, *59*, 2546–2550.

0003-2700/95/0367-3172$9.00/0

decay process (persistent microheterogeneity).[8] This means that molecules in spectroscopically distinguishable sites will remain distinguishable during their decay and show different lifetimes and possibly spectral changes. If different sites have different degrees of quenching, then the intensity Stern–Volmer equation becomes

$$I_0/I = \left[\sum \frac{f_{0j}}{1 + K_{SVj}[Q]}\right]^{-1} \quad (3)$$

where the summation is over all of the different sites present and f_{0j} is the contribution of the jth site to the unquenched emission intensity.

An even more complex problem arises in the decay time measurements where nonexponential decays are observed because sites with different lifetimes and degrees of quenching contribute to the decay. The sample impulse response $i(t)$ becomes

$$i(t) = \sum_{j=1}^{N} \alpha_j \exp(-t/\tau_j) \quad (4)$$

where the α's are the fractional contribution to the initial intensity at $t = 0$ of the different species. In principle, each component will conform to a lifetime Stern–Volmer equation, and one should be able to extract details of the decay kinetics. In practice, fitting such multiexponential decay data is an ill-defined problem, and it has proved difficult to extract meaningful single-site decay times.[9] Indeed, even verifying that there is no static quenching has proved difficult. Recently, we reported a preexponential factor weighted lifetime measurement that allowed direct comparison of lifetime and intensity data even in highly microheterogeneous systems.[10] One fits the data to the sum of lifetimes and then computes a τ_M given by

$$\tau_M = \sum_{j=1}^{N} \alpha_j \tau_j / \sum_{j=1}^{N} \alpha_j \quad (5)$$

It is unnecessary for the α's to represent fundamental quantities. They are, in general, only parameters required to fit the data. If only dynamic quenching is present, a modified Stern–Volmer equation using τ_{M0}/τ_M will match the intensity Stern–Volmer equation.

$$\tau_{M0}/\tau_M = I_0/I \quad (6)$$

τ_{M0}/τ_M data that fall below the I_0/I data may be indicative of static quenching.

EXPERIMENTAL SECTION

Our previous paper[3] describes the experimental method and sample preparation. Decay time measurements were made using the system described in the previous paper except that all of the measurements were made on the Tektronix TDS-540 digital oscilloscope. The pyrene was purified as described earlier.[11] Our observed instrument impulse response is about 10 ns (FWHM), which allowed direct measurements of decays with lifetimes of ≥15 ns.

In emission experiments, we always checked to ensure that there was no significant excimer emission in the 500 nm region. Only in the cases of the liquid PDMS did we see excimer emission if the pyrene concentration was raised too high. In lifetime measurements, we also looked for pyrene excimer emission in the same region. Excimer emission was characterized by a slow rise time relative to that from the laser and oscilloscope. All reported data were done under conditions where there was no detectable excimer. Stern–Volmer intensity data were examined at different wavelengths to assess heterogeneity. In particular, we focused on the first and third vibronic bands, which are the most sensitive to perturbation by solvent environment.

Polymers. The prepolymers and the cross-linking agents are shown in Figure 1. The preparation of the different polymers, including the ring siloxane polymer, was described earlier.[3] Since the ring polymer results proved uninteresting (vide infra), their structures are omitted, although they are given earlier.[3]

Sensor Preparation. Films were prepared as described earlier.[3] The pyrene was dissolved in CH_2Cl_2. The films were immersed in the solution for 15–30 min to give transparent clear films with, generally, intense blue emissions. Sensor films were kept dry and in the dark until used. Because pyrene does exhibit photochemistry, exposure to excitation was limited, and the data were discarded where there were discernible changes in emission properties with time.

X-ray. Room-temperature X-ray diffraction patterns were obtained using an evacuated Wahrus camera and nickel filtered Cu Kα radiation from a conventional sealed X-ray tube. Nominal sample to film distances of 5, 17, and 29 cm were used. Exposures of 24–48 h were required.

RESULTS

X-ray. X-ray diffraction patterns of mixed acrylate (Gp-163 and -851) with varying amounts of MMA showed only broad, fairly diffuse features. Observed intensity maxima corresponded to periodicities of about 7–8 and 17–18 Å. The reflection at the smaller spacing was sharpest and diminished in intensity as the MMA content increased. Cerius (Molecular Simulations, Inc.) was used to examine the diffraction to be expected from a randomly oriented siloxane segment in a gauche conformation. The models suggested that the 7–8 Å spacing could be attributed to the siloxane backbone.

Consistent with the clarity of the films, there was no evidence of phase segregation in the diffraction patterns from any of the materials examined. Domains that may have formed must therefore be of a size outside the limits of our diffraction measurements or of such nonuniform size distribution as to make their presence unobservable.

Pure Poly(dimethylsiloxane) (PDMS). In order to establish how quenching varied with macroscopic viscosity and how this correlated with polymer structure, we examined oxygen quenching of pyrene in different viscosity PDMS oils, a structurally similar solid polymer, and a normal alkane solvent. Figure 2 shows the quenching of pyrene in PDMS of different viscosities. For

(8) Demas, J. N.; DeGraff, B. A. *Makromol. Chem.* **1992**, *59*, 35–51.
(9) Demas, J. N.; DeGraff, B. A *Sens. Actuators B* **1992**, *11*, 35–41.
(10) Carraway, E. R.; Demas, J. N.; DeGraff, B. A. *Anal. Chem.* **1991**, *63*, 332–336.
(11) Xu, Wenying; Demas, J. N.; DeGraff, B. A.; Whaley, M. *J. Phys. Chem.* **1993**, *97*, 6546–6554.

Polymers

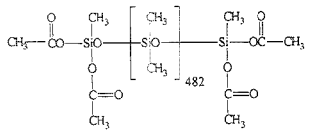

PDMS, methyldiacetoxy terminated
PS 368.5

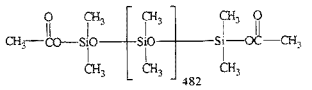

PDMS, dimethylacetoxy terminated
PS 363.5

Crosslinking Agents

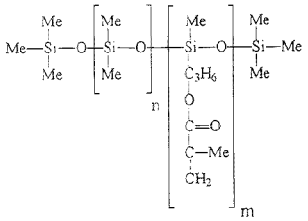

Gp-163 (n=710, m=30)
851 (n=710, m=15)

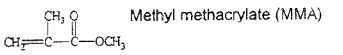

Methyl methacrylate (MMA)

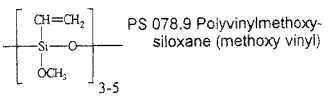

PS 078.9 Polyvinylmethoxy-siloxane (methoxy vinyl)

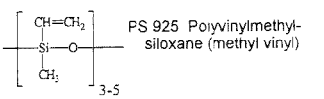

PS 925 Polyvinylmethyl-siloxane (methyl vinyl)

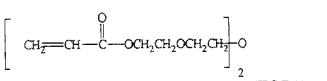

Tetraethylene glycol diacrylate (TGDA)

Figure 1. Prepolymers and cross-linkers.

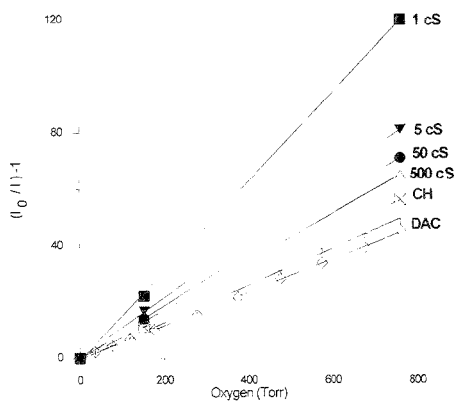

Figure 2. Oxygen quenching of pyrene in PDMS of different viscosities, in cyclohexane and in the diacetoxy-terminated PDMS polymer.

comparison we also show the results for cyclohexane and the diacetoxy-terminated polymer. These are modified Stern–Volmer plots where the independent variable is oxygen partial pressure. The Stern–Volmer quenching constants are given in Table 1. The solubility of oxygen in 1 and 5 cs PDMS at 38 °C is 0.0134 and 0.011 M, respectively.[12] The actual solubility at our measurement temperature would be somewhat higher. These numbers are within experimental error of each other, and the solubility is likely

Table 1. Stern–Volmer and Bimolecular Quenching Constants for Pyrene in Different Solvents

solvent	K_{SV} (Torr^{-1})	$k_2 \times 10^{-9}$ (M^{-1} s^{-1})
PDMS, 1 cs	0.157	21[a]
PDMS, 5 cs	0.107	15[a]
PDMS, 50 cs	0.0933	13[a]
PDMS, 500 cs	0.0855	12[a]
cyclohexane	0.0736	11

[a] Based on an assumed solubility of oxygen the same as average for the 1 and 5 cs PDMS.

nearly the same in both 1 and 5 cs oils as one might expect based on the very similar solvent structure. In cyclohexane, oxygen solubility at 1 atm was at 0.0116 M.[13] These numbers yield the bimolecular quenching constants shown in Table 1. For the higher viscosity oils where we have no solubilities, we assume the solubility is the same as the average for the 1 and 5 cs oils. The result shows that the quenching constants in PDMS have only a weak viscosity dependence. Also, the greater degree of quenching in 1 cs PDMS versus cyclohexane is probably predominantly due to the higher bimolecular quenching constant in PDMS rather than to a higher solubility. While our estimated rate constants will be too high in the PDMS because of the higher

(12) *Solubilities, Inorganic and Metal-Organic Compounds. K–Z*; Linke, W. F., Ed.; American Chemical Society: Washington, DC, 1965; Vol. 2, p 1236.
(13) *Solubility Data Series, Volume 7, Oxygen and Ozone*; Battino, R., Ed.; Pergammon Press: New York, 1981; p 242.

Table 2. *R*'s for Pyrene in Miscellaneous Solvents and Polymers

solvent	R (I_{III}/I_I)
100% PDMS, 5 cs	1.88
hexane	1.86
100% MMA	1.0
100% PMMA	0.90
50% MMA + 50% PDMS	1.2
ethyl acetate	0.82

oxygen solubility at room temperature, the factor of 2 difference between cyclohexane and 1 cs PDMS appears to be too great to arise only from oxygen solubility. Even for the solid diacetoxy-terminated polymer, the degree of quenching is only slightly smaller than for the 500 cs PDMS at the same oxygen pressure. Exceptionally high diffusion coefficients in high-viscosity PDMS are also known for pyrene excimer formation.[14]

Solvent Sensitivity of *R*. Many sensor molecules provide no direct evidence as to the nature of the local environment around the sensor; this also means that the sensor molecule provides no direct evidence for heterogeneity in the sensor binding environments. Pyrene provides a unique structure for assessing the extent and nature of heterogeneous binding. The vibrational bands on pyrene show a strong dependence on solvent. The marker that proves most sensitive for probing different solvent environments is the ratio of vibronic peak III to vibronic peak I. This ratio is denoted by R and is given by

$$R = I_{III}/I_I \tag{7}$$

where I_{III} and I_I are the intensities of the third and first vibronic peak, respectively. For cyclohexane $R = 1.8$ and for water $R = 0.6$. Table 2 summarizes some of our measured R's in different solvents, polymers, and mixtures.

In order to interpret the observed variations in R in polymers, we also examined the variation of R in mixtures of a polar and a nonpolar solvent, which is a homogeneous system. Figure 3 shows the variation of R with volume percent of ethyl acetate in 5 cs PDMS. This mixture was chosen since PDMS represents a major component of our polymers, and ethyl acetate has a structure and polarity similar to PMMA, which is one of our cross-linkers. Note that even a relatively small amount of ethyl acetate produces a dramatic decrease in R. The decrease is monotonic over the whole range.

Acrylate Siloxane Polymers. We wished to examine sensor responses as the polymer polarity was varied in a systematic fashion. Addition of MMA to the acrylate macromonomer Gp-163 is a convenient way to vary the polarity of the polymer. Earlier we used this approach to increase the compatibility of the polymer with our relatively polar Ru(II) complex. Figure 4 shows Stern–Volmer quenching plots for pyrene in the 6% (Gp-163) homoacrylate polymer with varying degrees of MMA cross-linker. Predominantly, intensity data are shown, but one representative lifetime data set is shown for 3.6% added MMA. The pure 6% homopolymer was not very consistent in the degree of quenching for different preparations. However, for systems with added MMA, reproducibility was much better. This may be due to the difficulty of dissolving the initiator in the pure homopolymer with a resultant variability in the products.

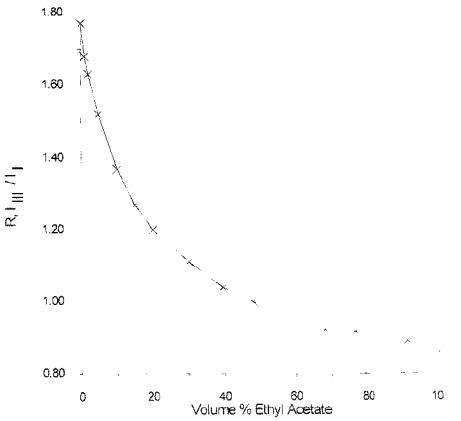

Figure 3. Dependence of R for pyrene in mixed PDMS (5 cs) and ethyl acetate.

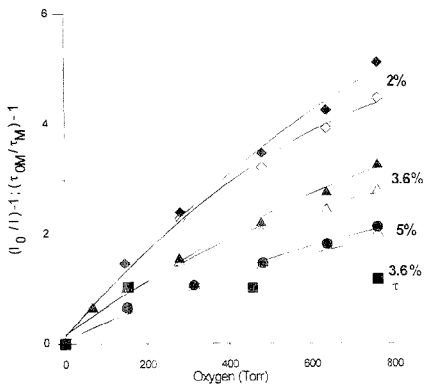

Figure 4. Lifetime and intensity oxygen quenching of pyrene in the 6% (Gp-163) acrylate-terminated homopolymer as a function of MMA.

Because the different vibronic peaks are characteristic of the polarity of the environment, examination of the variation in quenching at the different peaks is a way of determining heterogeneity of the binding sites. Differences in quenching behavior of the different peaks unequivocally demonstrate that molecules in different polarity sites are quenched differently. Quenching data in Figure 4 are shown for two different monitoring wavelengths (372 and 384 nm) that correspond to the first and third vibronic transitions. Clearly, there is heterogeneity since quenching at the two wavelengths differs.

The τ_M lifetime data in Figure 4 are typical. The reason for comparing lifetime and intensity data is to assess the degree of static and dynamic quenching in these systems (eq 6). The lifetime data agree well with the intensity data at low oxygen pressures but fall below it at higher oxygen concentrations. This was typical of all systems exhibiting a high degree of heterogeneity as evidenced by curved Stern–Volmer intensity plots. We attribute this to the need in calculating τ_M of using all of the decay components present. However, at the higher oxygen pressures,

(14) Chu, D. Y.; Thomas, J. K. *Macromolecules* **1990**, *23*, 2217–2222.

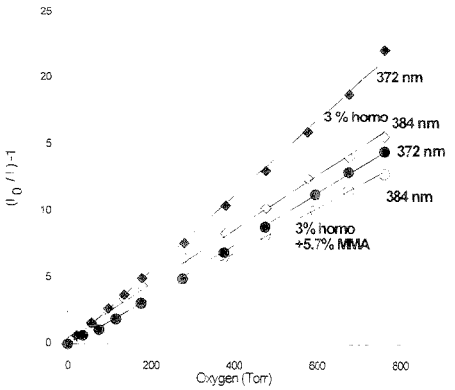

Figure 5. Lifetime and intensity oxygen quenching of pyrene in 3% (851) homoacrylate siloxane polymers and with 5.7% cross-linking MMA polymer.

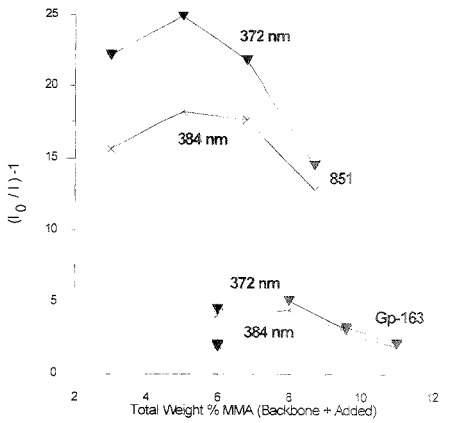

Figure 6. I_o/I_{oxygen} for pyrene in 3 (851) and 6% (Gp-163) acrylate polymer with varying amounts of MMA. The plot is versus the total weight percent of MMA regardless of whether the source is from the homopolymer or the added MMA. The upper curve for each polymer is at 372 nm while the lower curve is at 384 nm.

these systems were heavily quenched and apparently some components were too short to measure and were covered by the scatter curve. The omission of these components causes overestimation of τ_M and so τ_{M0}/τ_M falls below the intensity data. We consistently find that at an atmosphere of air the lifetime data match the intensity data at increasingly higher concentrations they dip below the intensity data and then tend to plateau. In a few cases where there was very little heterogeneity, as shown by nearly linear Stern–Volmer intensity plots, the lifetime and intensity data coincided up to nearly 1 atm of oxygen.

In order to assess the changes in behavior with source of the MMA in the polymer, we also looked at 851, which has 3% MMA on the polymer backbone versus 6% for the GP-163. Figure 5 shows the intensity quenching of pyrene in the 3% homoacrylate polymer (851) and the 3% homoacrylate with 5.7% added MMA. The data are nearly linear, suggesting little heterogeneity, but both show significant differences for the two monitoring wavelengths. This discrepancy at the two wavelengths unequivocally demonstrates heterogeneity in the quenching of different sites with different emission characteristics.

We reasoned that the differences in quenching behavior in the acrylate composites might be only a function of the total weight percentage of the polar MMA present relative to the nonpolar PDMS. That is, a 6% (Gp-163) homopolymer might be equivalent to a 3% (851) homopolymer with 3% added MMA. To test this hypothesis we measured mixtures of the 3 and 6% acrylate polymers with varying amounts of MMA. The range of MMA in the two copolymers overlapped. Figure 6 shows quenching behavior for different mixtures as a function of the total weight percent of MMA. Only I_o/I_{oxygen} is shown rather than complete Stern–Volmer plots. Heterogeneity again reveals itself as differences between data taken at the two wavelengths. The irreproducibility of the 6% homopolymer is shown by the different values.

We have also examined other polar cross-linkers to see what effect differences in the cross-linker would have on sensor behavior and as alternative tests of the domain model. Figure 7 shows quenching curves for the 6% (Gp-163) homopolymer with varying amounts of TGDA cross-linker, a very polar molecule. The heterogeneity at the two monitoring wavelengths is greatest for the 1% TGDA-containing polymer.

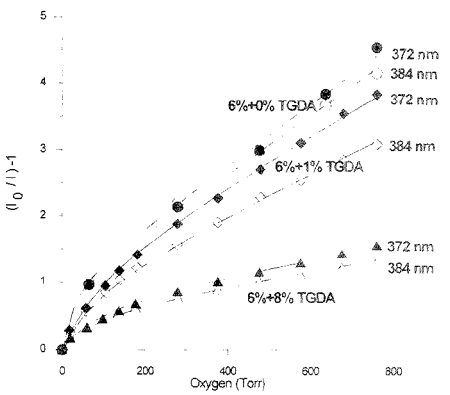

Figure 7. Stern–Volmer quenching plots for pyrene in 6% acrylate Gp-163 polymer with varying amounts of TDGA. The wavelength of each measurement is indicated by the number next to each curve. The pure 6% homopolymer result with highest degree of quenching has been shown.

In Figure 8, we summarized the I_o/I_{oxygen} data for Gp-163 with TGDA, MMA, and vinyl methoxy cross-linkers. Not shown is the vinyl methyl polymers, which exhibited a good response as judged by I_o/I_{oxygen}. However, the response time was extremely slow (about 10 min) compared to the other polymers. Thus, from a practical standpoint, even though the terminal response is comparable to the other additives, the poor response time made this copolymer unacceptably slow and no further studies were conducted with it. The vinyl methoxy copolymer responds much more rapidly even though it has a similar degree of quenching.

Ring Polymers. We were unable to do ring polymer work with pyrene. After impregnation, pumping with a vacuum always reduced the emission intensity. This may have been due to poor binding of the pyrene and subsequent evaporation under vacuum. Due to the limited amount of polymer available, no further studies were attempted.

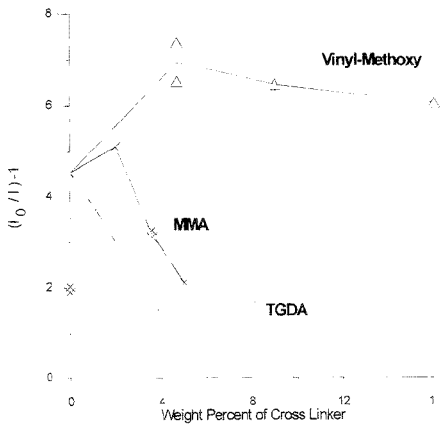

Figure 8. I_0/I_{oxygen} for pyrene in 6% acrylate Gp-163 polymer with varying amount of TDGA, MMA, and vinyl methoxy cross-linkers.

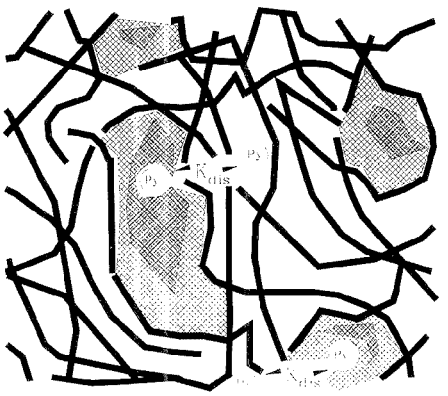

Figure 9. Schematic representation of domain model for pyrene in a heteropolymer. The solid lines represent the PDMS regions with the cross-hatched regions representing domains with polar cross-linkers. The heavier the cross-hatching, the more polar the domain.

Photochemistry. Most of the pyrene systems suffered from severe photochemical instability. Therefore, it was necessary to minimize photon dose during quenching experiments to prevent irreproducibility. This was done by using minimum excitation slits, keeping the sample in the dark except during emission scanning, and limiting emission scans to 360–390 nm (the information-rich first through third vibronic bands). As a check, after completing a quenching series the sample was returned to its original air conditions. If the intensities had changed significantly, the results were discarded. The photochemistry was exacerbated in the presence of oxygen but was not absent even in evacuated cells. The increased sensitivity suggests a self-sensitized singlet oxygen attack, but the photochemistry even in the absence of oxygen suggests that other modes are probably present.

DISCUSSION

Polymer Characteristics. The polymers and their characteristics are described elsewhere.[3] The PDMS backbone of all the polymers represented the most hydrophobic region. MMA and TGDA provided much more polar contributions to the polymers. However, the two siloxane cross-linkers did reduce the overall hydrophobicity of the Gp-163 polymer. The X-ray data demonstrated that the mixed MMA/PDMS polymers were not crystalline and there were no large regular domains. There also appeared to be a decrease in helical PDMS structure with increasing amounts of MMA either on the backbone or as added cross-linker.

Domain Model. The major variation in the polymers was the extent and nature of the polar functionality and rigidity. Our results can be explained on the basis of a microscopic irregular domain model where there is a tendency for polar groups to cluster and nonpolar regions to separate from the polar regions. Specifically, our systems are characterized by three types of regions or domains. First, we have a largely hydrophobic domain where the major constituent is PDMS. Second, we can have a more polar region contributed by the cross-linker. Finally, we can have interfacial regions, which are admixtures of the polar and nonpolar components. Figure 9 is a schematic representation of this model showing the different binding environments for the pyrene probe. We will now show that this model is adequate for explaining the main features of all of our systems.

The domain model explains qualitatively the primary features of the quenching curves. It can, however, be quantitated. We will give a qualitative description of our different results within this framework and then explore a more quantitative analysis of the quenching.

PDMS Results. PDMS has substantial void or free volume. These void volumes, and the opening and closing of them, provide the very high rates of diffusion of oxygen through the PDMS polymer. This is clearly seen in the pure PDMS fluids, which above about 5 cs show little dependence of oxygen quenching on macroscopic viscosity. Indeed, the solid diacetoxy polymer has quenching that is only slightly less than that of the 500 cs oils or even the very fluid cyclohexane. In contrast, the rigid glassier polymer regions provided by the MMA and TGDA allow little opportunity for oxygen diffusion and, therefore, quenching. We see no oxygen quenching of pyrene in PMMA.

Copolymer Results. There is the suggestion of a slight increase of quenching response on the addition of small amounts of MMA to the 3% (851) and 6% (Gp-163) homoacrylate polymers, but larger amounts of MMA or TGDA substantially degrade oxygen-quenching sensitivity. However, the vinyl cross-linkers improve the degree of quenching significantly. The initial falloff in quenching is not so rapid for the MMA as was observed for the Ru(II) complex reported earlier,[3] but otherwise the general effects are similar.

We explain the TGDA and MMA copolymer results with the domain model of Figure 9. The polar domains grow with increasing amount of polar cross-linkers. While the pyrene is preferentially soluble in the PDMS regions, there will still be some tendency for it to dissolve in, or associate with, the more polar components; this is especially true in the interfacial regions. Since MMA and TGDA are stiff homopolymers with poor oxygen quenching, any pyrene that segregates into these regions of the copolymer will experience reduced quenching. Thus, increasing amounts of polar cross-linkers will tend to partition increasing

amounts of the pyrene in this poor quenching environment, and the degree of quenching will fall. Alternatively, increasing the polar component will increase the partially polar interfacial region at the expense of the remaining pure PDMS regions. This stiffer interfacial region will exhibit decreased pyrene-quenching efficiency. Another way of looking at this interfacial region is indicated by the X-ray data, which suggest that MMA disrupts the helical structure of the PDMS backbone. The disruption at interfacial regions may lower the ability of the PDMS to provide void volumes for efficient transport of oxygen. We cannot differentiate between these interpretations and, in reality, a mixture of the mechanisms may be at work in reducing the quenching. Alternatively, there are variations in the local solubility of oxygen that affect the degree of quenching. In view of the relatively small differences in oxygen solubilities in different organic solvents, we favor changes in diffusional properties.

The enhanced quenching observed for the vinyl siloxane cross-linkers can be ascribed to two factors. First, one is adding a siloxane polymer itself, which could have better quenching properties than the starting polymer. Second, the vinyl polymer may be disrupting the existing structure, making it more porous, and increasing oxygen permeability. However, we have been unable to examine the pure vinyl siloxane polymers, since we have been unable to polymerize the pure prepolymer. Finally, one should note from the differences between the vinyl methyl and the vinyl methoxy results that good terminal response does not necessarily correspond with rapid equilibration. Both polymers give comparable final responses, but the rate of oxygen equilibration is much slower with the vinyl methyl. Thus, pyrene must exist in sites that are comparable in quenching character, but the bulk oxygen diffusion properties of the polymers are quite different.

Diacetoxy Polymer. This cross-linked polymer made from PS 368.5 is nearly pure PDMS. The extremely high degree of quenching is consistent with the known superb oxygen diffusion properties of pure PDMS.

This polymer does have some polarity, apparently associated with unterminated SiOH's.[6] Since the more PDMS-like a polymer is the greater the degree of quenching, we sought to increase the percentage of PDMS in the system by making copolymers with the monoacetoxy prepolymer (PS 363.5). The monoacetoxy-terminated prepolymer can only yield a linear polymer; it never achieves more than a very viscous liquid state, unlike the rubbery polymer from the diacetoxy prepolymer.

We examined a series of mixed diacetoxy monoacetoxy-terminated polymers. The compositions varied from pure diacetoxy to 33 wt % diacetoxy. All polymer films were of reasonable quality except the 33% polymer, which was very difficult to cross-link, and even after extensive heating in a humid atmosphere was still rather sticky and oily with a very poor optical surface. This may account for its deviations from the other systems. All plots were nearly linear and the lifetime data matched the intensity quenching data well except at the highest oxygen concentrations where we could not make accurate measurements. Table 3 shows the quenching results and the R values for the different systems. Thus, the quenching does not change greatly with increasing levels of PDMS in this system. This result probably just reflects the minimal amount of cross-linking relative to the PDMS regions in all cases. Thus, for a very hydrophobic sensor molecule like pyrene, increasing the amount of PDMS region over that already present in the pure diacetoxy-terminated polymer gains little or nothing in quenching and degrades the mechanical properties of the polymer.

Table 3. Quenching Data for Pyrene in Mixed Diacetoxy–Monoacetoxy-Terminated Polymers

	I_0/I_{oxygen}		
diacetoxy (%)	372 nm	382 nm	$R([O_2] = 0), R([O_2] = 760$ Torr)
100	50	46	1.33, 1.44
66	59	52	1.34, 1.52
50	57	51	1.35, 1.48
33	33	31	1.34, 1.41

Lifetimes. We did not do exhaustive lifetime measurements on all of the polymers. However, for those studies where the data could be trusted, there was no evidence for any static quenching. Where there was substantial heterogeneity as indicated by complex decay curves, τ_M at low oxygen pressures varied in a fashion consistent with dynamic quenching. The deviations from the intensity data at higher oxygen pressure precluded a definitive resolution of this question, although at this time we have no compelling evidence to suggest that there is any static quenching in the pyrene system.

Intensity Quenching Model. We now turn to a quantitative model for explaining the intensity-quenching data. The simplest model that can account for the curved Stern–Volmer plots is the two-site model that we have used earlier.[7] This model treats the probe as existing in two distinguishable sites. In the earlier work, where the emission spectra were insensitive to quenching, we assumed that the only differentiation was by the quenching at each of the two sites.

In our current pyrene work, the pyrene shows both differential quenching at different sites and different emission spectra at the different sites. This results in the Stern–Volmer quenching curves being different when monitored at different wavelengths. Our two-site model assumes that each of two sites has its own characteristic R and quenching constant K_{SV}. The modified Stern–Volmer equations measured at each of the two vibronic lines is then given by

$$\left(\frac{I_o}{I}\right)_I = 1/\left(\frac{f_{01}}{1 + K_{SV1}[O_2]} + \frac{f_{02}}{1 + K_{SV2}[O_2]}\right) \quad (8a)$$

$$\left(\frac{I_o}{I}\right)_{III} = rf_{01} + f_{02}/\left(\frac{rf_{01}}{1 + K_{SV1}[O_2]} + \frac{f30_2}{1 + K_{SV2}[O_2]}\right) \quad (8b)$$

$$r = (I_{III}/I_I)_{site1}/(I_{III}/I_I)_{site2} = R_{site1}/R_{site2} \quad (8c)$$

I_0 and I are the measured emission intensities in the absence and presence of oxygen, respectively. K_{SV}'s are apparent Stern–Volmer quenching constants given in units of the reciprocal external pressure of the oxygen, f_{0i}'s are the fractional contributions of the ith site to the unquenched emission intensity for peak I. The subscripts I and III correspond to data taken at peaks I and III, respectively, and are the directly measured values. R_{site1} and R_{site2} correspond to the peak ratios of sites 1 and 2, respectively, and are not directly measurable quantities. A similar expression was used earlier for studies of pyrene in C-18 chromatographic material.[7] The variable r, given by eq 8c, is the

Table 4. Two-Site Fitting Parameters for Quenching of Pyrene in Different PDMS Polymers

polym comp[a]	f_{01}	K_{SV1} (Torr^{-1})	K_{SV2} (Torr^{-1})	$r = R_1/R_2$	R_1, R_2	R_0^{obs}
Diacetoxy Polymer						
DAC						
100% (4)	0.380	0.0465	0.0847	2[b]	1.92, 0.96	1.33
851 Copolymer with MMA Cross-Linker						
MMA (wt %)						
0 (4)	0.23	0.0101	0.0513	2[b]	1.61, 0.81	0.99
5.7 (4)	0.29	0.0129	0.0230	2[b]	1.58, 0.79	1.02
0[c] (3)	0.40	0.0133	0.0847	2[b]	1.41, 0.71	0.99
5.7[c] (3)	0.80	0.0155	0.0847	2[b]	1.13, 0.57	1.02
Gp-163 Copolymers with MMA Cross-Linker						
MMA (wt %)						
0 (4)	0.47	0.00221	0.0838	1.08	0.97, 0.90	0.94
2 (4)	0.32	0.001755	0.0265	1.18	1.11, 1.95	1.00
3.6 (4)	0.48	0.001506	0.0365	1.21	1.05, 0.86	0.95
5 (4)	0.61	0.001351	0.0222	1.19	1.09, 0.91	1.02
2[c] (3)	0.47	0.00258	0.0847	1.12	1.05, 0.95	1.00
3.6[c] (3)	0.56	0.00186	0.0847	1.23	1.03, 0.84	0.95
5[c] (3)	0.71	0.00165	0.0847	1.22	1.07, 0.88	1.02
Gp-163 Copolymers with TGDA Cross-Linker						
MMA (wt %)						
0 (4)	0.47	0.00221	0.0838	1.08	0.97, 0.90	0.94
1 (4)	0.47	0.001424	0.0236	1.39	1.22, 0.88	1.04
8 (4)	0.55	0.000644	0.0207	1.24	1.18, 0.95	1.08
1[c] (3)	0.55	0.00228	0.0847	1.43	1.20, 0.84	1.04
8[c] (3)	0.68	0.00101	0.0847	1.28	1.16, 0.91	1.08

[a] Values in parentheses are the number fitting parameters. [b] Best fits were obtained with even larger values, but this is probably the largest chemically reasonable value. Further, the differences in the quality of the fits is negligible for larger r values. [c] K_{SV1} was fixed at 0.0817, and the remaining parameters were adjusted. The standard deviation was 0.3% higher for the fixed versus fully floating fits.

ratio of R's for the two sites and can be derived from fitting quenching data. Quenching data were simultaneously fit at peaks I and III. We have chosen to analyze the data in two ways.

In Table 4, we list the polymer systems that were fit to this model. The polymers are arranged from top to bottom in decreasing hydrophobicity of the parent polymer. The diacetoxy-terminated polymer is first, followed by the 851 (3% acrylate on a PDMS backbone) and its MMA-enriched version, Gp-163 (6% acrylate on a PDMS backbone) with added MMA, and finally Gp-163 with added TGDA. For ease of visualization, we show the 0% MMA entry for both Gp-163 sets.

In the first fitting method, we used a two-site model with four free floating parameters: r, f_{01}, K_{SV1}, and K_{SV2}. f_{02} is determined by $f_{02} = 1 - f_{01}$. These are the results that give the fits shown in the figures. These parameters are given in Table 4. One of the oddities that arises from this fitting procedure is the sometimes physically unreasonable variation of a parameter, particularly f_{01} with changes in polymer structure. Note, for example, Gp-163 with added MMA, where f_{01} does not increase monotonically with the amount of polar MMA. Indeed, f_{01} drops and then increases with increasing percentage of MMA, which seems chemically unreasonable.

One fitting problem that we encountered for the DAC and 851 polymers is in the fitting of r. For these systems, r tended to increase to physically impossible values of 10 or more. A physically realistic maximum for r is probably 2, and we fixed this parameter at 2 when fitting these systems. In general, the differences in the quality of the fit with $r = 2$ or free floating were negligible (less than 0.5% in the standard deviation of the fit) so this is not an unreasonable procedure.

The second fitting method of treating the data was based on the striking similarity of the K_{SV2}'s for DAC, pure 851, and pure Gp-163, as well as the excellent agreement of these K_{SV}'s with that for the 500 cs viscosity PDMS. In the framework of our domain model, it seems plausible that the largest quenching constant might be associated with a largely PDMS region and that the K_{SV} associated with this domain might be essentially constant over all the polymer mixtures examined. We thus fixed K_{SV2} at 0.0847 Torr^{-1}, the value for pure DAC, and refit the data by varying only K_{SV1}, f_{01}, and r. These fits were generally very good, although some small systematic deviations were observed; the resulting parameters are shown in Table 4 (denoted as a three-parameter fit). The effect of this change is to give f_{01}'s that monotonically increase with increasing amounts of the polar polymer component in the mixtures, which is chemically more reasonable.

While in all cases the four parameter fits were essentially quantitative, we wish to state a caveat. These are complex kinetic systems, and a good fit is not a guarantee of physical significance. Very different models with completely different physical assumptions can quantitatively fit the same data. For example, while we assumed two sites, any number of sites or distribution of sites can give equally good fits. Indeed, given the complexity of our data, we suggest that our modeling should be taken only as a suggestion of the underlying physical reality.

In keeping with our domain model, note the results for the pure DAC, pure 851, and pure Gp-163. All exhibit heterogeneity. Further, all are fit with a single highly quenched component and a more poorly quenched component. For DAC, the poorly quenched component still has an excellent quenching constant (only a factor of 2 smaller than K_{SV} for the highly quenched one) and, thus, the excellent linearity on the Stern–Volmer quenching curve. However, on going to pure 851 (3% acrylate) and Gp-163 (6% acrylate), the K_{SV} for the poorly quenched component plunges to 0.01 Torr^{-1} and finally 0.002 Torr^{-1}. Also, on going from pure 851 to pure Gp-163, the fraction of poorly quenched component increases from about 0.2 to 0.5. This result is consistent with a domain model where an increase in the amount of acrylate on the PDMS backbone increased both the percentage of poorly quenched component and the stiffness of these domains with a resultant reduction in its K_{SV}. These stiff domains have poor diffusion coefficients and also probably reduced segmental motion in the adjacent PDMS regions. Reduced motion in the PDMS region lowers the rate of opening and closing of void volumes with a concomitant reduction in diffusion and quenching.

We turn now to the polymers with added cross-linker. Again, in keeping with the domain model, increasing the fraction of a stiff polar cross-linker dramatically decreases overall quenching. Our quantitative fits with a fixed $K_{SV1} = 0.0857$ Torr^{-1} show an increase of the poorly quenched fraction with increasing polar component. For example, for Gp-163 with MMA it goes from 0.47 to 0.71 as the weight percent of added MMA increases from 0 to 5%. Similarly, for Gp-163 + TGDA, the fraction increases from 0.47 to 0.68.

The behavior of the R's, however, is surprising and we have seen no precedent in the literature. Even in DAC, the most readily quenched component has the smallest R or the highest polarity. This is true in all of the other systems, although the disparity

between the R's is less for the other cross-linkers. Indeed, the best quenched component usually has a polarity equivalent to that of MMA or PMMA rather than PDMS.

That very readily quenched molecules can exist in what appear to be rather polar environments can be, in part, a quirk of the dependence of R, which is a complex function of polarity and organization in microheterogeneous systems.[6,11] R is not a linear function of average solvent polarity in these cases. For example,[11] in water solutions pyrene that is double capped by β-CD senses a polarity equivalent to that of cyclohexane; it is completely shielded from water and sees only the hydrophobic CD core. Singly capped pyrene, even though roughly 50% of the pyrene is shielded from water, has an emission similar to that of pyrene in pure water. In the case of double capping of pyrene by the smaller α-CD, encapsulation is incomplete. The two ends are capped, and a narrow annular ring of the pyrene is exposed to the water. Even though a relatively small percentage of the pyrene surface is exposed, R of this encapsulated pyrene is equivalent to that observed for pure water. Thus, exposure of even a relatively small portion of pyrene to a polar environment can dramatically affect R. The complexity of this behavior is well illustrated by Figure 3. A small amount of ethyl acetate dramatically reduces R. Thus, our assumption is that the well-quenched sites are indeed essentially pure PDMS with intermixing of enough acrylate to depress R but without disrupting the efficient transport of oxygen and quenching.

The presence of a more polar site in DAC is consistent with our results for quenching of $[Ru(Ph_2phen)_3]^{2+}$.[3] This ionic complex has reasonable solubility in DAC, which demonstrates the existence of polar regions. We attributed this to unterminated SiOH's.

This still leaves the question of the apparent low polarity of the most poorly quenched sites even in the polymers with the most polar cross-linker (e.g., TGDA). While in these more polar systems the R's are only somewhat larger for the quenched than the unquenched sites, the effect is still there. At present, we have no plausible explanation for this effect other than to suggest that use of R for explaining local polarity in microheterogeneous systems may not be as clearcut as has been believed.

Regardless of the quantitative details, however, there is no doubt about the presence of persistent heterogeneity in the binding environment of pyrene in any of these polymers. By "persistent" we mean that the different sites persist on a time scale that is long with respect to the excited state lifetime. The nonlinear intensity quenching curves establish that the pyrene exists in a minimum of two sites for all polymers. Even DAC shows a substantial heterogeneity with two sites although the quenching constants are within a factor of 2 of each other. For DAC versus pure 851 versus pure Gp-163, there is a monotonic decrease in the degree of quenching. This decrease in quenching is largely the result of a decrease in quenching constant for site 1, the more poorly quenched site, rather than an overall decrease in quenching of both sites.

Finally we wish to make several points about polymer organization. It is very clear that even small changes in the composition or even the organization of a polymer can have a dramatic effect on quenching behavior. Compare DAC, pure 851, and pure Gp-163. Addition of 3% and then 6% acrylate to the system dramatically alters the quenching properties. Also, the source of the MMA component can have a huge effect. Even 851 with added MMA up to a total of 8 wt % acrylates is a far better support for good quenching than the 6% Gp-163 without additional MMA. Thus, shortening the runs of PDMS by increasing the backbone component of acrylate is far more deleterious to quenching than cross-linking acrylates. This feature could be used to improve mechanical properties without adversely affecting photophysics.

CONCLUSIONS

Our results suggest certain rules of design that should be kept in mind when selecting polymeric probe supports for oxygen sensors. Typically, the more PDMS in the support the better the quenching. Even relatively small amounts of polar or stiff components can substantially degrade performance.

Just because a polymer is a good solvent for the sensor does not preclude severe heterogeneity, as shown by a nonlinear Stern–Volmer response.

The two-site model is a very good quantitative one for a wide variety of quite different structural polymers. However, one should not use good fits as an unequivocal demonstration of the accuracy of the two-site model for the underlying physical reality. Such complex systems can be fit equally well by a wide variety of models involving more than two sites or by complex distributions. Only by means of very good lifetime measurements will one be able to fully unravel the complexity of these systems. Finally, our results do not prove a specific mechanism for the nonlinear quenching. It could arise from variations in local oxygen concentrations, local coefficients, and local shielding by polymer conformation around the sensor. Unraveling some of these complexities will be the subject of future investigations.

ACKNOWLEDGMENT

We gratefully acknowledge support by the National Science Foundation (Grants CHE 88-17809, 91-18034, and 94-19704) and an NIH Biomedical Research Support Grant BRS-5-36187.

Received for review February 15, 1995. Accepted July 3, 1995.[8]

AC9501654

[8] Abstract published in *Advance ACS Abstracts*, August 1, 1995.

Anal. Chem. 1995, *67*, 3181–3186

Single-Molecule Electrophoresis

Alonso Castro* and E. Brooks Shera

Biophysics Group, Mail Stop D434, Los Alamos National Laboratory, Los Alamos, New Mexico 87545

A novel method for the detection and identification of single molecules in solution has been devised, computer simulated, and experimentally achieved. The technique involves the determination of electrophoretic velocities by measuring the time required for individual molecules to travel a fixed distance between two laser beams. Computer simulations of the process were performed beforehand in order to estimate the experimental feasibility of the method and to determine the optimum values for the various experimental parameters. Examples of the use of the technique for the ultrasensitive detection and identification of rhodamine-6G, a mixture of DNA restriction fragments, and a mixture of proteins in aqueous solution are presented.

The rapid and efficient detection and separation of minute quantities of biologically important molecules plays a central role in a variety of fields, including molecular biology, biotechnology, immunology, medical diagnosis, and forensic analysis. It has proven difficult to identify and separate biomolecules at such low concentrations by existing means. Therefore, it is important to develop methods that are capable of probing samples at such low concentrations with adequate sensitivity, resolution, quantitation, and ease. Here, we describe a new method for the ultrasensitive detection and identification of fluorescent compounds in solution. The technique involves the measurement of electrophoretic velocities of individual molecules in a mixture and identification by comparison with the electrophoretic velocity known to be characteristic of a particular molecular species. In our experiments, the sample solution is contained in a capillary cell at a concentration in the femtomolar range. An external voltage is applied between the ends of the capillary, which causes the molecules to migrate toward the cathode or anode, depending on their charge. The migration velocity of each molecule, which is the vector sum of the electrophoretic velocity and the electroosmotic flow velocity, is calculated from the time required to travel a fixed distance between two laser beams. The passage of individual molecules through each of the laser beams was detected by using a modified version of our recently developed technique of single-fluorescent-molecule detection.[1-3] A Monte Carlo computer simulation of the electrophoretic separation and single-molecule detection processes was performed in order to demonstrate the feasibility of the method and to find the optimum parameters for the experimental execution. The experimental application of the method to the ultrasensitive detection and identification of a mixture of TOTO-stained λ DNA restriction fragments, a mixture of phycobiliproteins, and the single-fluorophore rhodamine-6G has been demonstrated in this work. Although we have focused on the detection and identification of biologically important molecules, we believe that the technique will also find applications in many areas of ultrasensitive organic and inorganic chemical analysis.

EXPERIMENTAL SECTION

Single-Molecule Electrophoresis (SME). A Spectra-Physics 3800 frequency-doubled mode-locked Nd:YAG laser producing 70-ps pulses at 532-nm wavelength and 82-MHz repetition rate was used as the excitation source. The laser output was attenuated by a variable neutral density filter and then split into two parallel beams by a beamsplitter–mirror combination. The resulting 1–5-mW laser beams were focused into the sample capillary cell by an achromatic lens to yield two 10-μm spots ($1/e^2$ value). The ends of the 2-cm-long, 100- × 100-μm square cross-section glass capillary were connected to two sample reservoirs by means of plastic tubing (Figure 1). This arrangement, combined with a 10- × 10-μm detection area (see below) translates to a 1% sampling of the total number of molecules flowing through the capillary. The reservoirs, capillary, and tubing were filled with the sample solution. The total sample volume required to fill the sample compartment is ~3 mL. For the purpose of accommodating samples present in minuscule amounts, the sample compartment of our apparatus could be reconstructed, if necessary, to have a volume as small as 1 μL. The output of a high-voltage power supply was connected to the sample reservoirs by means of platinum electrodes. Typical applied voltages were in the 100–200 V/cm range. The applied electric field causes the ultradilute solute molecules to migrate to the cathode or anode, depending on their charge. As the individual molecules move through each laser beam due to the electrophoretic effect, repeated excitation–emission cycles produce a fluorescence photon burst. This fluorescence light from each beam is collected by a 40×, 0.75 NA microscope objective and spatially filtered by a 0.4- × 0.4-mm square slit, which defines a 10- × 10-μm detection area for each laser beam. The light is then spectrally filtered by 30-nm-bandwidth, eight-cavity interference filters centered at the wavelength of emission maximum and detected by two EG&G single-photon avalanche photodiodes. Each detector output signal is analyzed by independent time-correlated single-photon-counting electronics under computer control. The detection electronics reject Raman and Rayleigh scattering by using a time-gate window set such that only delayed fluorescence photons are detected, thus increasing the signal-to-noise ratio of single-molecule detection.[1] Fluorescence data were collected in 1-ms intervals. Every burst produced at the second beam by a given molecule will be delayed with respect to the burst produced at the first beam by a time equal to the interbeam distance divided by the molecule's migration velocity. Therefore, a histogram of these times will

(1) Shera, E. B.; Seitzinger, N. K.; Davis, L. M.; Keller, R. A.; Soper, S. A. *Chem. Phys. Lett.* **1990**, *174*, 553–557.
(2) Soper, S. A.; Davis, L. M.; Shera, E. B. *J. Opt. Soc. Am. B* **1992**, *9*, 1761–1769.
(3) Castro, A.; Fairfield, F. R.; Shera, E. B. *Anal. Chem.* **1993**, *65*, 849–852.

0003-2700/95/0367-3181$9.00/0

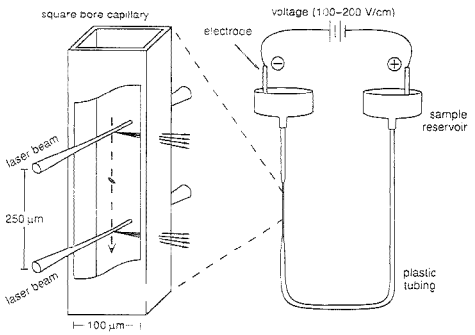

Figure 1. Single-molecule electrophoresis setup. An expanded view of the square-bore capillary cell is depicted at left, showing the two parallel laser beams focused through the cell. Fluorescence light, represented by two sets of arrows, is collected at right angles.

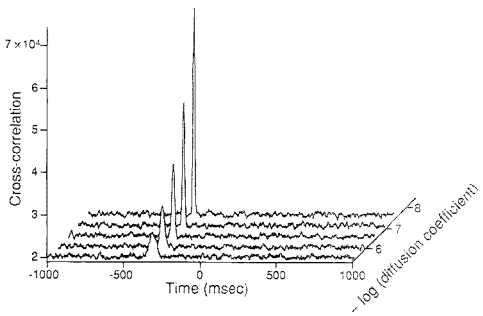

Figure 2. Cross-correlation traces between the simulated signals from the two detection channels for various diffusion coefficient values. The peak's *x*-axis center position represents the most probable time taken by a molecule to travel the distance between the laser beams. Diffusion coefficient units are cm^2/s.

produce a series of peaks, one for each molecular species present, since different species generally exhibit different electrophoretic mobilities. A sample run time of 819.2 s was used in the present measurements.

Sample Preparation. λ DNA (full-length, *Apa*I and *Xba*I digests) and TOTO-1 were purchased from New England Biolabs (Beverly, MA), and Molecular Probes (Eugene, OR), respectively. Nucleic acid solutions were prepared by dilution in TBE buffer (10 mM Tris, 9 mM boric acid, 0.1 mM EDTA, pH 8.0) to the desired concentration. TOTO-1 was added to the DNA samples at a final base pair to dye ratio of 5:1. B-Phycoerythrin and B-phycoerythrin–streptavidin conjugate were purchased from Molecular Probes. Protein solutions were prepared by dilution in 10 mM potassium hydrogen phthalate (KHP) buffer solution, pH 4.8. Rhodamine-6G was purchased from Exciton (Dayton, OH) and diluted in water. Water was deionized and doubly distilled prior to use. All solutions were prepared immediately before each experiment.

COMPUTER SIMULATIONS

A Monte Carlo modeling computer program for the simulation of the single-molecule electrophoresis process was developed on the basis of the above description. This computer simulation has proven to be an invaluable tool for predicting the feasibility of the single-molecule electrophoresis experiments, as well as for understanding the various factors affecting the molecular migration and low-level fluorescence detection processes. The algorithm consists of generation of individual molecules at random positions and times at the top of the capillary cell, translation of molecules due to both electrophoretic–electroosmotic migration and random diffusion, excitation of molecules when they interact with the Gaussian laser beams, fluorescence emission, photon collection and detection, and random generation of background noise. The simulation of the electrophoretic migration consisted of adding a measured constant velocity to each generated molecule in the direction of the capillary axis. The simulation of the single-molecule detection process employed the common fluorophore rhodamine-6G as model system and considered such parameters as laser power, extinction coefficient, photodegradation quantum efficiency,[4] fluorescence quantum yield, and overall photon detection efficiency. Simulations were carried out on a Cray Y-MP computer. Results were output as the cross-correlation between the raw signals from the two detection channels, such that a peak is obtained for each molecular species present in the sample. Alternatively, the results were output as a histogram of travel times, where again, each species is represented by a peak. In this case, the time position of each fluorescence burst that exceeded a set threshold was determined by least-squares fitting to a Gaussian curve. The travel time for a given molecule was then calculated by subtracting the time positions of the fluorescence bursts for that molecule originating at each of the two laser beams. This latter data analysis method allows for greater histogram peak resolution at the expense of decreased histogram peak amplitudes. Some of the simulation parameters, such as laser power, electrophoretic velocity (proportional to the applied voltage), and distance between laser beams, were varied until the best signal-to-noise ratio was obtained and were later used experimentally.

In order to investigate the effect of molecular diffusion on the efficiency of electrophoretic velocity determination, a set of simulations was performed where the aqueous solution diffusion coefficient was varied from that corresponding to a small common fluorophore, such as rhodamine-6G ($\sim 3 \times 10^{-6}$ cm^2/s),[5] to that of a large biomolecule, such as a 6.6 kbp nucleic acid ($\sim 3 \times 10^{-8}$ cm^2/s).[6] Figure 2 shows the results. As expected, the cross-correlation width increases as the diffusion coefficient value is increased, because diffusion causes a broadening in the distribution of total molecular velocities. A decrease in peak amplitude (and peak area) is also observed, because diffusion causes a deviation of the molecular trajectories from a straight path between the two laser beams.

The dynamic range of the technique was investigated by performing another set of computer simulations. The sample concentration was varied over 4 orders of magnitude, from 62.5 aM to 1.02 pM. The net peak amplitude (and area) was found to increase linearly with concentration over the whole range ($r = 0.9999$). The signal-to-noise ratio increased by only 1300 times over the same concentration range, indicating that the baseline

(4) Soper, S. A.; Nutter, H. L.; Keller, R. A.; Davis, L. M.; Shera, E. B. *Photochem. Photobiol.* **1993**, *57*, 972–977.
(5) Tamai, N.; Yamazaki, T.; Yamazaki, I.; Mataga, N. *Chem. Phys. Lett.* **1985**, *120*, 24–28.
(6) Madelung, O., Ed. *Landolt-Börnstein—Numerical Data and Functional Relationships in Science and Technology, New Series*; Springer-Verlag: Berlin, 1990; Vol. 1c, p 272.

noise increased somewhat with concentration. At high concentrations, the probability that two or more molecules migrate very close to each other increases. Since there is no way to tell which molecule produced which fluorescence burst, it is possible that a "false" migration time originating from two different molecules will be counted, along with the "true" migration times originating from each individual molecule. These "false" migration times are randomly distributed and are the cause of the observed increase in baseline noise at high concentrations. If necessary, this slight decrease in signal-to-noise ratio at high concentrations could be overcome by adding a third laser beam and detector, which would allow the use of algorithms that would effectively discard such "false" migration times.

RESULTS

Once the feasibility of the single-molecule electrophoresis technique was successfully predicted, the experimental demonstration was then accomplished. It is important to note that the computer simulations were performed employing molecular parameters corresponding to a single fluorophore, which represents the ultimate level of detection difficulty. Therefore, the detection of biological molecules, which often contain multiple fluorophores, is expected to proceed with even greater efficiency.

In one series of experiments, a mixture of DNA restriction fragments was chosen for the experimental demonstration of the technique. Since the fluorescence quantum yield of DNA is very small, we intercalated the fluorescent dye TOTO-1 (a dimer of thiazole orange) into DNA.[3,7] Figure 3 shows the fluorescence bursts observed from the two detection channels for a 10 fM solution of λ DNA (48 502 bp) in TBE buffer to which TOTO-1 was added at a base pair to dye ratio of 5:1. Every burst on the first detector appears shifted on the second detector by the time taken for an individual molecule to travel the distance between the two laser beams. To investigate the identification of DNA fragments according to size, we used a mixture of DNA fragments of three different sizes: 38, 24 and 10 kbp. It is a well-known fact that DNA fragments of different sizes experience essentially the same drag force per unit charge in free solution, which makes their separation impossible.[8] However, capillary electrophoresis separations of DNA fragments have been successfully demonstrated with use of a semidilute, low-viscosity, entangled polymer solution as sieving media.[9,10] We therefore added hydroxypropylmethyl cellulose at a concentration of 0.25% to that effect. The time required for each molecule in the mixture to travel the 250-μm distance between laser beams was recorded. As expected, larger fragments are retarded by the sieving media, whereas smaller fragments travel faster. Figure 4 shows a histogram of these times for ~1000 DNA molecules. Three peaks are observed, corresponding to each one of the DNA fragment sizes. The peak assignment was verified by running each DNA digest independently under identical experimental conditions.

In another series of experiments, a mixture of two fluorescent proteins was analyzed. Phycoerythrin (PE) and streptavidin-conjugated phycoerythrin (SPE) were mixed at an individual concentration of 20 fM in KHP buffer. These proteins were chosen because they fluoresce in the visible region and because of the importance of phycobiliprotein conjugates in flow cytometry and immunofluorescence.[11] Separation of the two components was enhanced by taking advantage of the difference in their isoelectric points, which were determined by standard agarose gel isoelectric focusing techniques. The isoelectric point values obtained were 4.43 ± 0.03 for PE[12] and 4.57 ± 0.03 for SPE. The

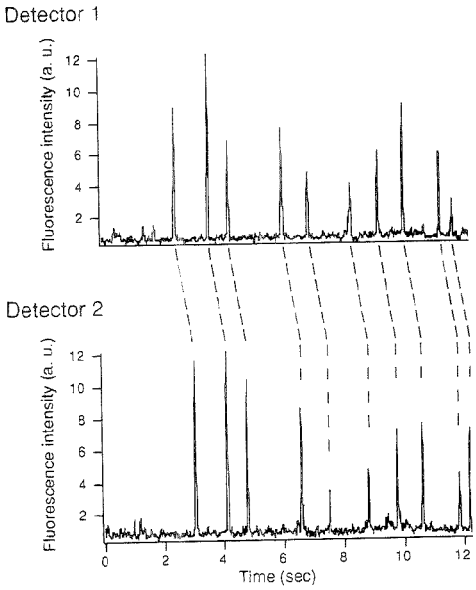

Figure 3. Fluorescence signals for a 10 fM λ DNA solution in TBE buffer. Each fluorescence burst represents the passage of a molecule through the laser beam. The bursts generated at the second laser beam are delayed by a fixed amount of time, about 600 ms in this particular case. Applied voltage, 120 V/cm.

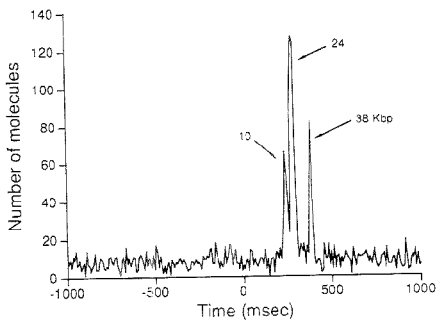

Figure 4. Histogram of travel times for a mixture of three different DNA fragments in TBE/HPMC buffer (10 fM each). Applied voltage, 150 V/cm.

(7) Rye, H. S.; Yue, S.; Wemmer, D. E.; Quesada, M. A.; Haugland, R. P.; Mathies, R. A.; Glazer, A. N. *Nucleic Acids Res.* **1992**, *20*, 2803–2812.
(8) De Gennes, P. G. *J. Chem. Phys.* **1971**, *55*, 572.
(9) Yoshinobu, B.; Sumita, C.; Hice, K.; Ishimaru, N.; Samata, K.; Tanaka, A.; Tsuhako, M. *J. Liq. Chromatogr.* **1993**, *16*, 955–965.
(10) Zhu, M.; Hansen, D. L.; Burd, S.; Gannon, F. *J. Chromatogr.* **1989**, *480*, 311–319.
(11) Haugland, R. P. *Handbook of Fluorescent Probes and Research Chemicals*; Molecular Probes, Inc.: Eugene, OR, 1992.
(12) In agreement with the literature value of 4.38. Glazer, A. N.; Hixson, C. S. *J. Biol. Chem.* **1977**, *252*, 32–42.

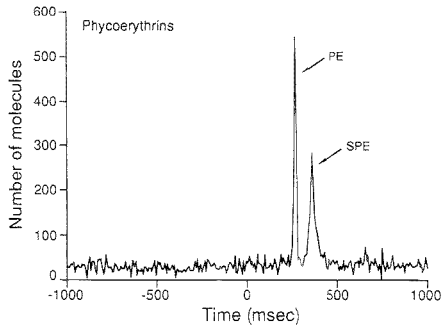

Figure 5. Histogram of travel times for a mixture of 20 fM phycoerythrin and 20 fM streptavidin–phycoerythrin in KHP buffer. Applied voltage, 100 V/cm.

pH of the buffer solution was adjusted to 4.8, where PE acquires a more negative character compared to SPE. Under these experimental conditions, both proteins will migrate toward the cathode, but SPE will migrate at a lower rate, because of both a less negative character and its larger size. Figure 5 shows a histogram of travel times for ~2500 protein molecules, where a peak is observed for each component. Again, peak identities were determined by running each component independently.

Our computer simulations indicated that our technique is sensitive enough to detect and analyze a small, single-fluorophore molecule, as well as fluorescently labeled DNA and the phycoerythrins, which are multifluorophore-bearing macromolecules. To verify this hypothesis, we analyzed a sample consisting of 20 fM rhodamine-6G in water. Figure 6 shows the raw data corresponding to single-molecule fluorescence bursts observed at the two detection channels. Fluorescence bursts corresponding to the same molecule are labeled by the same number. Bursts at detector 1 are delayed by a constant amount of time with respect to the bursts at detector 2 (about 420 ms in the case illustrated). The molecule in detector 2 marked by an X either drifted away so that it missed the detector 1 laser beam or photodegraded while in the first beam. Water blanks for each detector are also shown, where single-molecule fluorescence bursts are not present. A histogram of the migration times is shown in Figure 7. These results show the applicability of the technique to the analysis of single-fluorophore molecules.

DISCUSSION

One of the most commonly used techniques for DNA restriction fragment sizing and for protein separations is gel–slab electrophoresis. Despite its popularity, gel electrophoresis suffers from some limitations, mainly because it involves a series of manually intensive procedures that cannot be run unattended and cannot be readily automated; casting gels, applying samples, and running and subsequently staining the gels are time-consuming tasks susceptible to poor quantitative accuracy and poor reproducibility. In some cases, in order to improve sensitivity, a radioisotope needs to be incorporated into the sample, which brings up a set of safety and environmental concerns. An additional advantage over conventional gel electrophoresis is that the identification process is continuous, rather than batch oriented, and the process is therefore suitable for applications that require

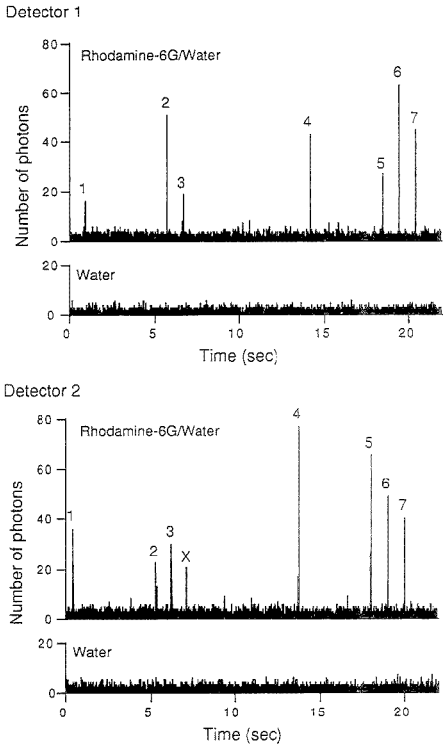

Figure 6. Fluorescence signal versus time for detector 1 (top) and detector 2 (bottom) for a 20 fM rhodamine-6G aqueous solution. In this case, molecules travel toward the cathode, such that they are observed first in detector 2 and then in detector 1. Fluorescence bursts corresponding to the same molecule are labeled by the same number. The molecule in detector 2 marked by an X either drifted away so that it missed the detector 1 laser beam or photodegraded while in the first beam. Water blanks for each detector are also shown. Applied voltage, 100 V/cm.

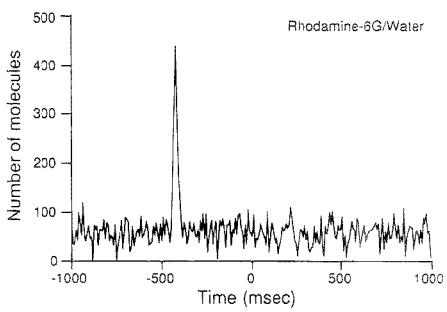

Figure 7. Histogram of travel times extracted from Figure 6. The distribution peak appears at negative times because our sign convention considers that positive times correspond to migration toward the anode.

rapid, continuous on-line analysis. Capillary zone electrophoresis (CZE) alleviates some of these problems, offering rapid, automated analysis, improved reproducibility, and better quantification. Our

technique shares with CZE the basic idea of measuring migration times for performing the analysis. In CZE, all molecules are simultaneously injected at one end of the capillary, and the sample components separate into bands according to electrophoretic velocities. The detector at the end of the capillary records the arrival of the various bands. In SME, the migration times are recorded for each molecule arriving at the laser beams in a continuous way, as opposed to the batch mode of operation of CZE. Thus, SME is also suitable for applications that require continuous, real-time analysis, such as those processes where the sample composition and concentration change with time. SME, however, does not currently achieve the separation efficiency of gel–slab or capillary electrophoresis (~0.2%). The present separation efficiency limit of the technique can be determined from the widths of the peaks shown in Figure 2. For smaller diffusion coefficients, such as those associated with biomolecules, the separation efficiency values (expressed as peak fwhm divided by peak center position) lie in the range 2%–3%, which is satisfactory for most laboratory separations. In principle, increasing the interbeam separation would cause an increase in the technique's separation efficiency. Since the root-mean-square molecular displacement due to diffusion scales as the square-root of time, increasing the total distance will cause a decrease in the electrophoretic velocity distribution width. We have estimated that increasing the interbeam distance to, for example, 2500 μm, theoretical separation efficiencies of 1% and 0.2% could be obtained for rhodamine-6G and DNA in water, respectively. With use of high-viscosity sieving media, the diffusion-induced distribution width should be negligible. We are presently in the process of further investigating this matter.

It is conventional to quote detection sensitivity in terms of a limit of detection parameter (LOD) equal to the number of molecules required to produce a signal equivalent to three times the standard deviation of the baseline (background) of the measurement. In the present measurements, we detect individual molecules as they pass through the laser beams. Therefore, the LOD is clearly <1 molecule. Still, it is useful to present LOD values as a measure of signal and background levels and for comparison with other published results. For the three solutions discussed in the Experimental Section, LOD values computed from the raw detector data streams are as follows: nucleic acids, 0.047 molecules; proteins, 0.052 molecules; and rhodamine-6G, 0.28 molecules. This latter value can be compared with the recent result of Chen et al.,[13] who obtained an LOD of six molecules[14] for sulforhodamine-101 using laser-induced fluorescence capillary zone electrophoresis coupled with a sheath flow system.[15]

Although the present technique has a smaller LOD than CZE, a more important property not revealed by the LOD values is the ability to analyze extremely dilute solutions. By its nature, CZE is a batch-oriented technique and is limited by the small volumes that can be loaded onto the capillary. A number of molecules equal to or greater than the LOD must be present in this small sample volume, or the technique fails. SME, on the other hand, is a continuous analysis process in which arbitrarily large volumes of solution can be analyzed if necessary to identify a rare or extremely dilute component or to obtain statistical accuracy in determining the concentration of such a component. The ultimate dilution that can be analyzed is limited only by the running time available.

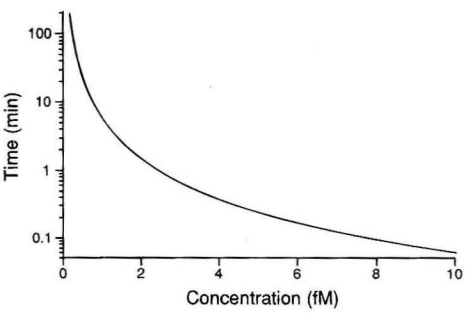

Figure 8. Estimated running time required to achieve a S/N = 3 versus concentration for the single-fluorophore rhodamine-6G.

In the present experiments, we have not attempted to optimize the efficiency with which the sample solution volume is used. Thus, the capillary tube is much larger than the small laser beam spots, and therefore most sample molecules pass by undetected. A smaller capillary, larger beam spots, or a sheath flow focusing system would make more efficient use of the sample. Nevertheless, it is useful to explore the limits of the present SME system for the analysis of dilute solutions. For this purpose, we assume that the data from the detectors are analyzed using the cross-correlation technique, which is convenient for long runs and large data sets. For the present experimental conditions, we estimate that with a 1 fM solution run for 35 min, ~80 molecules will pass through the detection regions. For rhodamine-6G, 80 molecules yield a cross-correlation signal amplitude of about 2232, or 27.9/molecule. This signal is linearly proportional to the concentration. The cross-correlation background is ~41.6 times the run time in seconds. These values lead to the following relationship:

$$\text{S/N ratio} = 0.16 \times \text{run time (s)} \times \text{concentration (fM)}$$

Thus, for a given concentration, the S/N ratio will improve as the square-root of the time the sample is run. Figure 8 shows a plot of the run time required to obtain S/N = 3 as a function of solution concentration. Note that concentrations below 1 fM can be analyzed in a few minutes, and concentrations above 5 fM can be analyzed in only a few seconds. A concentration limit of 1 fM is >100 times smaller than that required for state-of-the-art CZE.[13]

Although the single-molecule electrophoresis technique relies on measuring molecular fluorescence, nonfluorescent molecules may be detected by attaching a fluorescent tagging molecule to them. In addition, some of the experimental conditions, such as buffer composition, pH, viscosity, inner-surface capillary coating, excitation and emission wavelengths, among others, can be optimized to achieve the best separation of the particular sample components being analyzed. In fact, many of the analytical protocols specially developed for capillary electrophoresis separations are directly applicable to the present technique. For many

(13) Chen, D. Y.; Adelhelm, K.; Cheng, X. L.; Dovichi, N. J. *Analyst* **1994**, *119*, 349–352.

(14) This value of six molecules is based on an estimated injected sample amount of 17 molecules. If some of these molecules randomly diffused away after exiting the capillary and never reached the laser beam in the sheath flow cuvette, the actual LOD values obtained by Chen et al.[13] may be lower.

(15) Pinkel, D.; Stovel, R. In *Flow Cytometry: Instrumentation and Data Analysis*; Van Dilla, M. A., Dean, P. N., Laerum, O. D., Melamed, M. R., Eds.; Academic Press, Inc.: London, 1985; Chapter 3, pp 77–128.

years, researchers have optimized various capillary electrophoresis methods for the separation of a large variety of chemical species ranging from small organic and inorganic ions to various kinds of pharmaceutical drugs and natural products.

The new method described here promises to combine the advantages of free-solution capillary electrophoresis (system automation, speed, reproducibility) with the unsurpassed sensitivity of single-molecule detection. The sensitivity and versatility of the method may open the way to develop fluorescence immunoassay, hybridization, and DNA fingerprinting techniques that do not require extensive DNA amplification using the polymerase chain reaction (PCR)[16,17] or other methods. Although PCR is a highly effective amplification mechanism, the use of many PCR cycles may introduce ambiguities arising from contamination and by mechanisms not yet fully understood.[17-20] Besides the demonstrated ability for the analysis of single fluorophores, mixtures of nucleic acids, and proteins, the technique may find applications in many other fields that require the ultrasensitive analysis of sample components.

(16) Scharf, S. J.; Horn, G. T.; Erlich, H. A. *Science* **1986**, *233*, 1076–1078.
(17) Boj, A. K.; Mahbubani, M. H.; Alias, R. M. *Crit. Rev. Biochem. Biophys.* **1991**, *26*, 301–334.
(18) Reiss, J.; Krawczak, M.; Schloesser, M.; Wagner, M.; Cooper, D. *Nucleic Acids Res.* **1990**, *18*, 973–978.
(19) Dunning, A. M.; Talmud, P.; Humphries, S. E. *Nucleic Acids Res.* **1988**, *16*, 10393.
(20) Kwoh, S.; Higuchi, R. *Nature* **1989**, *339*, 237.

ACKNOWLEDGMENT

We thank Lloyd Davis for helpful discussions and Mark Peters for technical assistance.

Received for review May 10, 1995. Accepted July 11, 1995.[⊗]

AC950470P

[⊗] Abstract published in *Advance ACS Abstracts*, August 15, 1995.

Anal. Chem. 1995, *67*, 3187–3192

Detection of Aromatics in Aqueous Solution by Surface-Enhanced Raman Scattering by Substrates Chemically Modified with *p-tert*-Butylcalix[4]arenetetrathiol

Wieland Hill,*,† Bernhard Wehling,† Charles G. Gibbs,‡ C. David Gutsche,‡ and Dieter Klockow†

Institut für Spektrochemie und Angewandte Spektroskopie (ISAS), P.O. Box 101352, 44013 Dortmund, Germany, and Texas Christian University, P.O. Box 32908, Fort Worth, Texas 76129

Chemical modification of rough silver surfaces by *p-tert*-butylcalix[4]arenetetrathiol (BCAT) has been demonstrated to produce substrates for surface-enhanced Raman scattering (SERS) that form reversibly complexes with aromatics from aqueous solutions. Due to this complexation, the detection limits for aromatics without groups that attach to silver are clearly decreased in comparison to mere adsorption at the bare metal surface and were found to be 100 μM for benzene, 50 μM for chlorobenzene, and 5 μM for 1,2-dichlorobenzene in water. The SERS bands of the surface-bound BCAT have been used as an internal standard for the surface concentration of aromatics. The intensity ratio of bands of adsorbed aromatics and surface-bound BCAT has given a measure for the solution concentration of the aromatics with a dynamic range of about 2 orders of magnitude. Characteristic shifts of aromatics bands due to substitution have permitted the identification of benzene derivatives as well as mixture analyses. An adsorption enthalpy of −6.7 kJ/mol has been determined for the adsorption of chlorobenzene by measuring its temperature dependence.

Recent improvements of instrumentation clearly extend the fields of application of Raman spectroscopy using compact, sensitive, and portable spectrometers. The surface-enhanced Raman scattering (SERS) at rough metal films or particles is a rather promising tool for chemical sensors because of its ability to easily detect submonomolecular layers of organic substances adsorbed at metal surfaces. A major problem in the application of SERS to chemical sensing arises from the necessity for adsorption at a metal surface. Metals exhibit rather unspecific adsorption properties and are chemically reactive. Therefore, analytes may not be adsorbed or adsorption centers may be poisoned by concomitant substances. Such problems can be avoided by organic modification of SERS active metal substrates.[1]

By chemical modification, selectively adsorbing centers can be generated. However, at a modified surface, analytes interact with the organic adsorption centers and not directly with the metal surface. Therefore, the chemical contribution to the SERS enhancement due to bonding to the metal[2] may be suppressed for the analyte. Chemically enhanced SERS bands of the modified layer might superpose the weaker analyte bands. We will show that this effect does not dominate for the investigated system. Furthermore, iodide ions that were shown in a previous paper[3] to exhibit selective enhancement proved to be useful for a selective enlargement of analyte bands in comparison with those of the modified layer.

Thioorganics such as thiols or disulfides are known to be useful agents for the organic modification of metal surfaces, since the sulfur functions react chemically with the metal, yielding stable surface compounds.[4] Adsorption of chlorinated ethylenes and of aromatics at SERS substrates hydrophobized with octadecanethiol has been demonstrated in recent papers.[5,6] Lipophilic interaction resulted in a concentration of the investigated organics within the SERS active layer and lowered the SERS detection limits.

A first example of stoichiometric adsorption at thioorganically modified SERS substrates was the complexation of alkali metal ions with immobilized thiol-derivatized dibenzo-18-crown-6.[7] Recently, SERS was used to detect complexation of methyl orange at colloidal silver coated with thiol-derivatized cyclodextrin.[8]

In the present paper, evidence for reversible complexation of organic molecules with organically modified SERS substrates is reported. Since organic analytes in general exhibit characteristic SERS bands, a double selectivity can be achieved by this detection principle: selective complexation combined with specific detection.

EXPERIMENTAL SECTION

Raman Spectroscopy. Raman measurements were carried out with a 0.5 m triple monochromator with subtractive dispersion of the first two stages (DILOR XY). The dispersion of the spectrometer was 1.1 nm/mm. The excitation source was a cw Ti:sapphire laser (Coherent 890) operating at a wavelength of 702 nm. The laser radiation was filtered by a grating monochromator

† ISAS.
‡ Texas Christian University.

(1) McGlashen, M. L.; Davis, K. L.; Morris, M. D. *Anal. Chem.* **1990**, *62*, 846–849.
(2) Otto, A.; Mrozek, I.; Grabhorn, H.; Akemann, W. *J. Phys.: Condens. Matter* **1992**, *4*, 1143–1212.
(3) Wehling, B.; Hill, W.; Klockow, D. *J. Mol. Struct.* **1995**, *349*, 117–120.
(4) Ulman, A. *An Introduction to Ultrathin Organic Films. From Langmuir–Blodgett to Self-Assembly*; Academic Press: Boston, 1991.
(5) Mullen, K.; Carron, K. *Anal. Chem.* **1994**, *66*, 478–483.
(6) Carron, K.; Peitersen, L.; Lewis, M. *Environ. Sci. Technol.* **1992**, *26*, 1950–1954.
(7) Heyns, J. B.; Sears, L. M.; Corcoran R. C.; Carron, K. T. *Anal. Chem.* **1994**, *66*, 1572–1574.
(8) Maeda, Y.; Kitano, H. *J. Phys. Chem.* **1995**, *99*, 487–488.

0003-2700/95/0367-3187$9.00/0

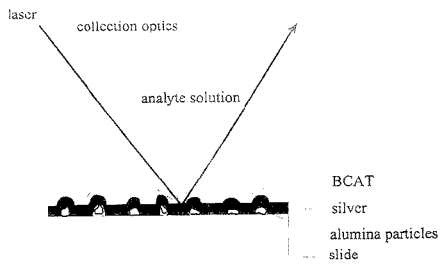

Figure 1. Schematic of a SERS substrate.

to remove low-intensity sidebands and the spontaneous emission background. Laser light with a power of ~10 mW was focused to the sample on a spot with a diameter of 30 μm. An $f/1.0$ collection optics produced a 5-fold enlarged intermediate image of the laser spot in the plane of the entrance slit of the spectrometer. Slit widths were 300 μm. A nitrogen-cooled CCD camera (Wright Instruments) with a 298 × 1152 chip (EEV 88131) served as the detector. Integration times were 5 min, unless otherwise stated. SERS spectra were taken in backscattering geometry from substrates (Figure 1) immersed in aqueous solutions of aromatics contained in a conventional 1 cm quartz cuvette for fluorescence measurements. The cuvettes were closed to prevent evaporation of volatile analytes during the measurements. The analyte solution was thermostated by a water thermostat connected to a home-made cuvette holder within a temperature range from 274 to 343 K.

Peak heights of SERS bands of the analytes were determined using difference spectra of substrates immersed in analyte solution and in pure water. The given detection limits are based on measurements with analyte peak heights of minimum 3 times the standard deviation of the difference spectra background.

Materials. Rough metal films of a thickness of 75 nm were prepared by vacuum evaporation of 99.99% silver onto glass slides previously spin-coated with 150 μL of aqueous suspensions of 0.3 μm alumina particles according to a method described by Bello et al.[9] Scanning electron microscopy showed that the substrates exhibit submicrometer roughness due to separate alumina particles as well as larger structures of aggregates.

p-tert-Butylcalix[4]areneteträthiol (BCAT) was prepared from *p-tert*-butylcalix[4]arene (BCA) as described elsewhere.[10] Silver SERS substrates were coated with BCAT by immersion of the substrates for 90 min in 100 μM BCAT solutions in toluene. The dependence of SERS intensities on the immersion time indicated practically completed adsorption of BCAT after 90 min. In the standard procedure, BCAT-coated substrates were immersed for 5 min in 1 mM aqueous KI solutions and rinsed with high-purity water before the adsorption experiments with aromatics. Adsorption of iodide ions is known to enhance the SERS intensities by chemical effects.[11,12] The iodide was not applied for measurements of the subsection "complexation".

Benzene (Merck, >99.5% GC), chlorobenzene (Merck, >99.5% GC), 1,2-dichlorobenzene (Fluka, >99% GC), hexachlorobenzene (Schuchardt, >98%), and toluene (Merck, >99.7% uvasol) were used as delivered for the preparation of aqueous and toluenic solutions. High-purity water with an electrical conductivity below 0.07 μS was produced by a commercial water purification system (Millipore Milli-Q) equipped with an additional filter for organics.

Concentrated aqueous solutions of the analytes (20 mM benzene, 2 mM chlorobenzene, and 0.5 mM 1,2-dichlorobenzene, respectively) were produced by pipetting with a newly calibrated pipet the desired amount of analyte and mixing it with the solvent within a closed, calibrated glass bulb. Complete dissolution of chlorobenzenes was achieved by ultrasonic treatment. Diluted solutions were obtained by pipetting from the concentrated original solutions immediately before the SERS measurements. The saturated aqueous solution of hexachlorobenzene was produced by lasting treatment of a mixture of the analyte with water in an ultrasonic bath.

Safety Considerations. The analytes used here are toxic and/or carcinogenic. Swallowing, skin contact, and breathing in of these chemicals should be strictly avoided. Intense collimated laser light can cause skin irritation. Observation of collimated or scattered laser light with unprotected eyes can lead to serious eye damage.

RESULTS AND DISCUSSION

Immobilization. Basket-shaped calixarenes are known as complex-forming agents for various compounds.[13,14] Replacement of the hydroxyl groups of the lower rim of BCA by thiol groups[10] produces an agent that can be easily immobilized at metal surfaces by the procedure described above. However, the strong intramolecular hydrogen bonding among the OH groups is assumed to contribute essentially to the formation of the cone conformation (Figure 2, structure **1**), in which BCA exists almost exclusively in solution and in the solid state.[10] The thiol groups exhibit weaker hydrogen bonding, and the BCAT was found to exist in the 1,3-alternate conformation (Figure 2, structure 2) in both the solid and the solution state.[10]

Complexing capabilities of immobilized BCAT should strongly depend on its conformation. Therefore, the question arises whether the cone conformation can be restored by bonding to the surface or the alternate conformation predominates there also. A comparison of the SERS spectrum of the immobilized BCAT with the Raman spectrum of the same substance in the solid form before immobilization (Figure 3) shows a complete disappearance of the S–H stretching bands around 2540 cm^{-1} after bonding to the surface. Thus, it can be assumed that at least the major part of the surface-bound molecules has formed four S–Ag bonds with the surface. Since this 4-fold bonding is hardly imaginable for the alternate conformation, one should assume that the conformation of the BCAT changed to conelike (Figure 2, structure 3) due to the bonding to the surface. This assumption is further supported by the complexing capabilities of the immobilized BCAT described below. Further differences between the spectra of the immobilized BCAT and the solid reagent may also be caused by the change of conformation. However, a detailed analysis of the

(9) Bello, J. M.; Stokes, D. L.; Vo-Dinh, T. *Appl. Spectrosc.* **1989**, *43*, 1325–1330.
(10) Gibbs, C. G.; Gutsche, C. D. *J. Am. Chem. Soc.* **1993**, *115*, 5338–5339.
(11) Jeanmaire, D. L.; Van Duyne, R. P. *J. Electroanal. Chem.* **1977**, *84*, 1–20.
(12) Pettinger, B.; Wetzel, H. In *Surface Enhanced Raman Scattering*; Chang, R. K., Furtak, T. E., Eds.; Plenum Press: New York and London, 1982; pp 293–314.
(13) Gutsche, C. D. Calixarenes. In *Monographs in Supramolecular Chemistry*; Stoddart, J. F., Ed.; Royal Society of Chemistry: London, 1989.
(14) Böhmer, V., Vicens, J., Eds. *Calixarenes: A Versatile Class of Macrocyclic Compounds*; Kluwer Academic Publishers: Dordrecht, 1991.

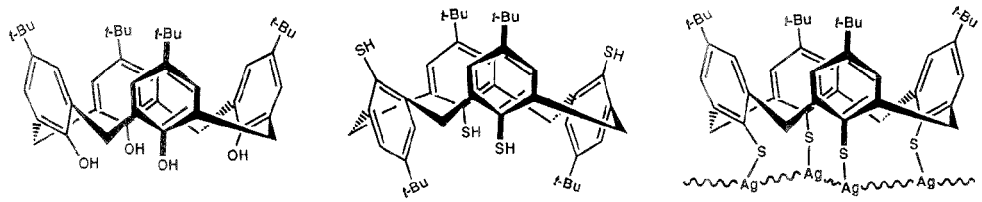

1 2 3

Figure 2. Conformation of calix[4]arene (1), its thio derivative BCAT (2), and the surface-bound molecule 2 (3).

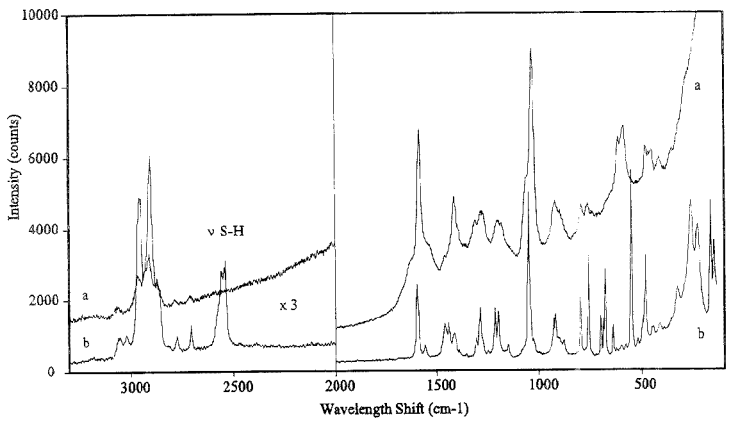

Figure 3. SERS spectrum of *p-tert*-butylcalix[4]arenetetrathiol after bonding to a silver substrate (a) and Raman spectrum of the same calix[4]arene in the solid state (b). (Bands in spectrum a are stronger than those in the following figures due to the use of a stronger enhancing SERS substrate charge.)

vibration modes of this comparatively large molecule cannot be given at present.

Complexation. Benzene is lacking functional groups that can interact with the silver surface. Therefore, SERS signals of benzene at silver substrates could be observed only at comparatively high benzene concentrations. For a bare metallic substrate immersed in a 10 mM benzene solution, the strongest benzene SERS band at 992 cm^{-1} had a height of about 10% of the continuous background of the SERS substrate itself. The continuous inelastic background is generally observed together with SERS,[15] and it limits the detection of weak adsorbate bands rather than their scattering intensity.

For a BCAT-coated SERS substrate, the same ratio of the intensity of the 992 cm^{-1} band and the background was obtained with 1 mM solution. Unfortunately, a simple comparison of band intensities does not provide a proper measure of surface coverages with and without BCAT, because SERS enhancement strongly depends on the distance and chemical interaction between molecule and metal. Definitely, the BCAT-complexed benzene is positioned a certain distance from the metal, and thus, the enhancement should be weaker than that for molecules that are in direct contact with the bare metal surface.

The SERS spectrum of a BCAT-coated substrate immersed in benzene solution (Figure 4a) is apparently a superposition of the SERS spectrum of the BCAT-coated substrate (Figure 4b) and the Raman spectrum of benzene (Figure 4c). No indications for spectral changes due to the interactions between BCAT and benzene can be observed.

Chlorobenzene and 1,2-dichlorobenzene have also been complexed with the BCAT-coated substrates, giving SERS spectra with high signal to noise ratio even for substrates immersed into micromolar solutions. At bare metal substrates, 1,2-dichlorobenzene was not observable even in nearly saturated solution, and the strongest SERS band of chlorobenzene could be distinguished from the background only in 2 mM solution. As with benzene, the SERS spectra of BCAT-coated substrates immersed in chlorobenzene (Figure 5) and 1,2-dichlorobenzene solutions (Figure 6) are merely superpositions of the spectra of the substrate with that of the adsorbates without any indication of spectral changes due to complex formation.

Alternate immersion of BCAT-coated substrates into solutions of the aromatics and pure water showed that the adsorption of all three investigated compounds is completely reversible. With solutions of higher concentrations, measurements with integration times of 10 s showed that the adsorption is practically complete after about 10 s.

SERS Enhancement by Iodide. Iodide is known to give a substance-specific additional enhancement of SERS intensities.[2] For the BCAT-coated substrates, it only slightly affected the BCAT intensities, but the intensities of aromatics adsorbed at BCAT-coated substrates were increased 2–3-fold. Furthermore, the

(15) Akemann, W.; Otto, A. *Surf. Sci.* **1994**, *307–309*, 1071–1075.

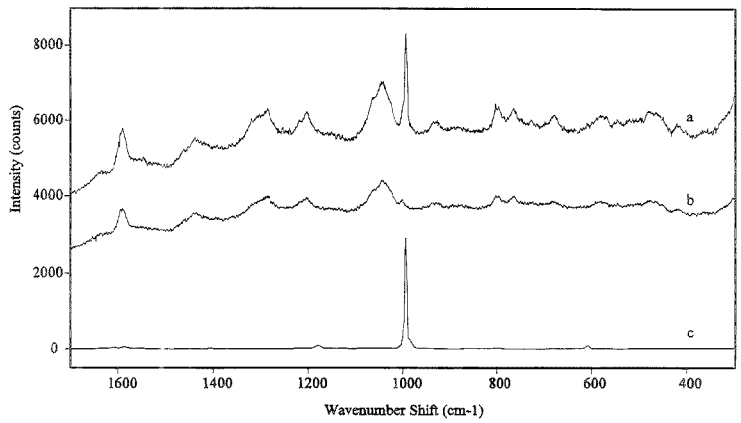

Figure 4. SERS spectra of a BCAT-coated substrate within a 5 mM aqueous benzene solution (a) and within pure water (b). The Raman spectrum of benzene (c) is given for comparison. The SERS spectra are shifted upward.

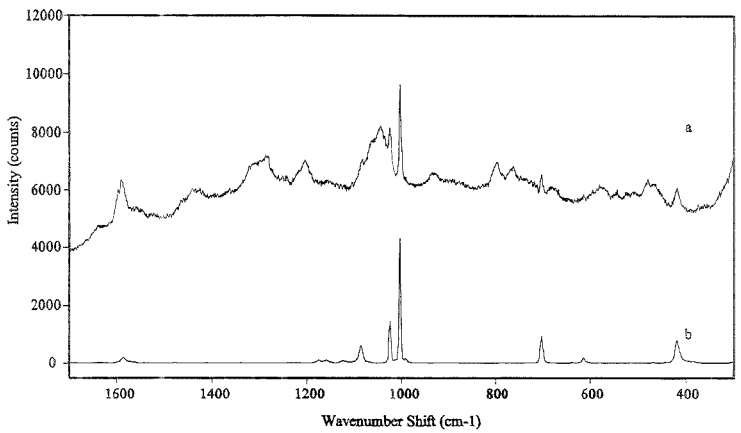

Figure 5. SERS spectrum of a BCAT-coated substrate within a 0.5 mM aqueous chlorobenzene solution (a). The Raman spectrum of chlorobenzene (b) is given for comparison. Spectrum a is shifted upward.

broadband background signal was reduced by the iodide. Altogether, the signal to noise ratio in the detection of aromatics was clearly improved. Therefore, iodide addition was included in the standard procedure for the measurements discussed further below.

Concentration Dependence. The concentration dependencies of the analyte to BCAT peak height ratios are given in Figure 7. The detection limits derived were 100 μM for benzene, 50 μM for chlorobenzene, and 5 μM for 1,2-dichlorobenzene in water. Further lowering of these values should be straightforward by use of a holographic filter with high throughput instead of the two subtractively coupled monochromators for stray light reduction, by reduction of the dispersion of the spectrometer, and by evaluation of peak areas instead of heights.

The calibration functions are roughly linear, as is expected for the low-concentration part of Langmuir isotherms. Complexation of single analyte molecules within BCAT cages should strongly suppress interactions between the adsorbed analyte molecules. Therefore, the observed Langmuir isotherm should necessarily appear for this type of adsorption. No saturation of the surfaces was observed up to solution concentrations near saturation. The dynamic range of the observable concentration dependencies was about 2 orders of magnitude. It was limited at higher concentrations by the solubility of the aromatic compounds in water and at lower concentrations by the broadband background signal from the substrate.

The absolute intensities of the SERS bands scatter by some 10% for different substrate positions. Apparently this is caused by a somewhat inhomogeneous distribution of alumina particles on the glass slides and, therefore, a position dependence of the SERS enhancement. The use of the BCAT band intensities as an internal standard clearly reduces the dependence of aromatic intensities on the substrate properties and gives the reasonably linear calibration functions shown in Figure 7. This good linearity indicates that the adsorption at the coated substrate might include a stoichiometric complexation of the aromatics with the surface-bound BCAT.

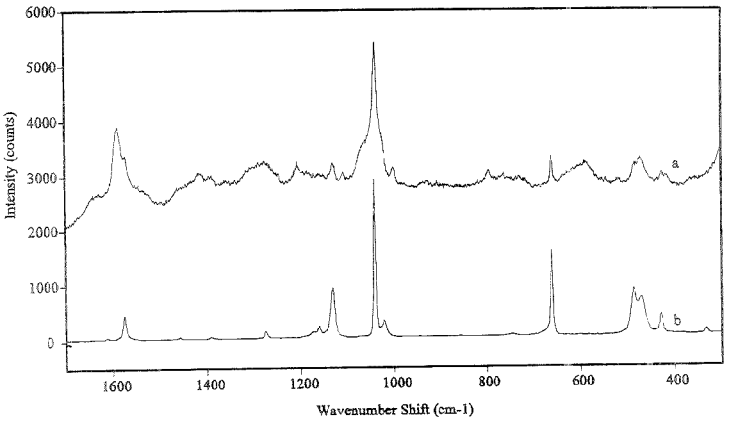

Figure 6. SERS spectrum of a BCAT-coated substrate within a 0.25 mM aqueous 1,2-dichlorobenzene solution (a). The Raman spectrum of 1,2-dichlorobenzene (b) is given for comparison. Spectrum a is shifted upward.

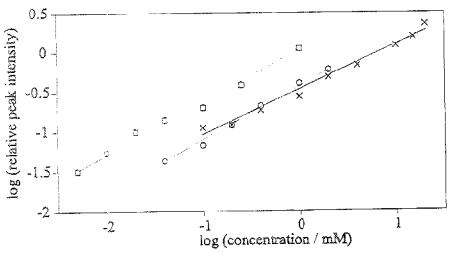

Figure 7. Concentration dependence of the SERS band height ratios of aromatic bands to the BCAT band at 1043 cm^{-1}. For benzene (×) and chlorobenzene (○), the strongest bands, at 992 and 1002 cm^{-1}, respectively, were used. For 1,2-dichlorobenzene (□), the band at 661 cm^{-1} was chosen because of the overlap of the strongest band, at 1039 cm^{-1}, with a BCAT band.

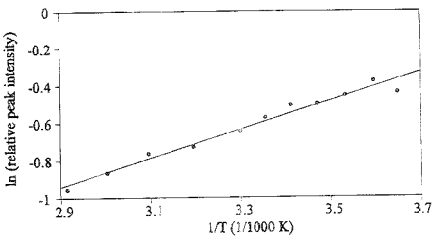

Figure 8. Temperature dependence of the band height ratio of the chlorobenzene band at 1001 cm^{-1} and the BCAT band at 1043 cm^{-1} observed for a BCAT-coated substrate immersed in a 1 mM aqueous chlorobenzene solution.

The slope of the concentration curves in the double logarithmic plot is somewhat smaller than the value of 1 expected for the surface coverage from Langmuir adsorption and slightly dependent on the adsorbed substance. A possible explanation for this effect may be that the plotted peak height ratios were not exactly proportional to the surface coverages with the analytes. For instance, the BCAT band height used as a reference may be somewhat enlarged by the adsorption of aromatics by an influence of the guest molecule on the structure, orientation, or polarizability of the host BCAT molecule.

The lowering of the detection limits with increasing number of chloro substituents from 0 to 2 seems to point either to an interaction between BCAT and these substituents or to an inverse relationship between adsorption and solubility, as was observed for chlorinated ethylenes at octadecanethiol-coated substrates.[6] However, a direct comparison of surface concentrations of the different compounds cannot be given, since the band intensities depend on the polarizabilities of the considered molecules, and the peak intensity ratios give, therefore, only a relative measure for the surface coverage.

Attempts to detect hexachlorobenzene at modified substrates immersed in a saturated aqueous solution of this analyte failed because analyte bands were completely missing in the SERS spectra. This shows that the adsorption at the BCAT-coated substrate is neither exclusively an inverse function of solubility, which is clearly lower for hexachlorobenzene than for the other investigated analytes, nor related only to an affinity between the chloro substituent and the BCAT cage. The missing hexachlorobenzene adsorption rather indicates that adsorption within the BCAT cage is a shape- or size-selective process.

Temperature Dependence. Absolute surface coverages are not directly measurable by SERS, since the Raman scattering intensities at the surface strongly depend on the unknown orientation of the adsorbed molecules. Therefore, the adsorption equilibrium constants for the analytes cannot be derived from our measurements. However, adsorption enthalpies can be obtained from changes of relative surface coverages due to temperature variation.

An investigation of the dependence of the chlorobenzene to BCAT peak height ratio on the temperature was carried out in the temperature range between 2 and 70 °C. By always employing peak height ratios for quantification of the analytes, temperature influences on the SERS effect should be largely excluded, and the ratios should be good estimates for relative surface coverages with chlorobenzene. In the logarithmic plot of the peak height ratio versus $1/T$ (Figure 8), a linear relationship was obtained, as expected for Langmuir adsorption far from saturation. The slope of the curve gives an adsorption enthalpy of −6.7 kJ/mol for

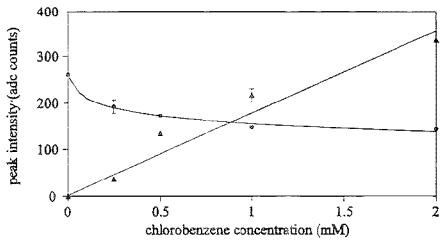

Figure 9. Dependence of SERS band height ratios of the benzene band at 992 cm^{-1} (●) and the chlorobenzene band at 1002 cm^{-1} (▲) to the BCAT band at 1043 cm^{-1} on the chlorobenzene concentration. The benzene concentration is fixed to 1 mM. Error bars represent the standard deviation of repeated measurements on the same substrate with repeated filling of the cell.

chlorobenzene at immobilized BCAT. This low enthalpy indicates merely van der Waals interaction and may be due to the comparatively small size of the BCAT cone, not forming an optimum "recipient" for the aromatic guest molecules.

The enthalpy is somewhat below the typical mean value of van der Waals interaction, which is −20 kJ/mol. It should be mentioned, however, that the measured value represents the difference between complexation and solvation enthalpies of the molecules.

Adsorption from Mixtures. Since the SERS bands of the adsorbed compounds clearly depend on the substituents, the adsorbed aromatics can be identified and mixtures of the aromatics can be analyzed using BCAT-coated substrates. For quantitative analysis, however, it is necessary to know the mutual influence of coadsorbed species. Figure 9 shows the benzene and chlorobenzene band intensities as a function of the chlorobenzene concentration at a fixed benzene content. The relative peak height of the selected band of chlorobenzene, which is supposed to interact more strongly with BCAT, depends linearly on its concentration regardless of the presence of benzene. This corresponds to the expected behavior for low benzene coverage of the surface.

In contrast, the benzene band intensity is clearly diminished with increasing chlorobenzene concentration, which points to a replacement of benzene by its chloro derivative. However, the stronger decrease of the benzene band intensity at lower chlorobenzene concentrations in comparison to higher concentrations cannot be explained by the simple model of a merely competitive adsorption.

CONCLUSIONS

Coating of rough silver films with BCAT has produced SERS substrates that form reversibly complexes with benzene and two of its chloro derivatives. The detection limits of SERS for these compounds have been lowered considerably by this complexation and by the additional enhancement effect caused by iodide. The reversibility of the surface complexation opens the possibility to determine the aromatic compounds considered via adsorption from aqueous solution with a dynamic concentration range of about 2 orders of magnitude. The comparatively small adsorption enthalpy resulting for chlorobenzene indicates the predominant effectiveness of van der Waals forces.

Concerning possible applications for chemical sensors, substance-specific SERS sensing could exhibit selectivity and multisubstance capabilities superior to those of most other sensor principles, in which selective adsorption is used in connection with detection of less specific parameters such as refractive index, layer thickness, mass, light absorption, or fluorescence.

ACKNOWLEDGMENT

This work was financially supported by the Ministerium für Wissenschaft und Forschung des Landes Nordrhein–Westfalen, the Bundesministerium für Forschung und Technologie, Germany, the National Science Foundation, and the Robert A. Welch Foundation.

Received for review April 3, 1995. Accepted June 20, 1995.[a]

AC950335C

[a] Abstract published in *Advance ACS Abstracts*, August 1, 1995.

Anal. Chem. 1995, *67*, 3193–3201

Development of High-Accuracy ICP Mass Spectrometric Procedures for the Quantification of Pt, Pd, Rh, and Pb in Used Auto Catalysts

E. S. Beary* and P. J. Paulsen

NIST, Gaithersburg, Maryland 20899

Inductively coupled plasma mass spectrometric procedures have been developed for the high-accuracy determination of three platinum group elements (Pt, Pd, and Rh) and Pb in two used automobile catalysts. Isotope dilution quantification was applied for the certification of Pb, Pt, and Pd. The mononuclidic Rh was quantified using an internal standard after careful assessement of potential systematic errors from incomplete dissolution and instrumental interferences. The Pb concentrations are certified at 6228 ± 49 mg/kg in SRM 2556 (Used Auto Catalyst—Pellets) and 13931 ± 97 mg/kg in SRM 2557 (Used Auto Catalyst—Monolith). The certified concentrations for the platinum group elements in SRM 2556 and SRM 2557, respectively, are, for Pt, 697.4 ± 2.3 and 1131 ± 11 mg/kg; for Pd, 326.0 ± 1.6 and 233.2 ± 1.9 mg/kg; and for Rh, 51.2 ± 0.5 and 135.1 ± 1.9 mg/kg.

Motor vehicle exhaust is considered a major source of air pollution. Since the mid-1960s, when the state of California passed legislation aimed at restricting environmental pollutants including automobile emissions, car manufacturers have focused attention on methods that reduce exhaust pollutants. The Federal Clean Air Acts of 1975 and 1991 scheduled increasing environmental restrictions extending to the turn of the century. By the 1970s, all car manufacturers had modified their exhaust systems to include the catalytic converter. Although more sophisticated versions of these converters are used today, they remain the principal device used to reduce hazardous emissions by converting CO and hydrocarbons to CO_2 and NO_x to H_2O and N_2.

The active components of automotive catalytic converters are platinum, palladium, and rhodium (platinum group elements, or PGEs), which are finely dispersed on an inert substrate such as alumina using a solution "washcoat". Per year, approximately $500 million worth of PGEs are used in the automobile industry alone. Therefore, this industry is actively studying ways to increase the efficiency of catalytic converters and reduce their cost. The economic value of PGEs from used catalytic converters has created a significant recycling industry, with the value of the recycled catalyst dependent upon accurate chemical assay of the PGEs. These analyses are notoriously difficult since PGE recoveries by most analytical procedures are nonquantitative and variable. Differences in assay can represent significant differences in the assigned value for these materials.

Geologists were among the first to apply inductively coupled plasma mass spectrometry (ICPMS) to PGE determinations in the mid-1980s.[1,2] The improved detection limits over graphite furnace atomic absoption spectroscopy (GFAAS) and neutron activation analysis (NAA) permitted their determination in low-abundance crustal rocks[2] and waters.[3] The methods of quantification used were adapted from conventional optical spectroscopic procedures. In 1993, Hall et al. reported isotope dilution (ID) ICPMS procedures for the determination of platinum and palladium in freshwater samples.[4]

A variety of other analytical methods have been routinely applied to the determination of the PGEs in automobile catalysts. Some industrial methods include wavelength dispersive X-ray fluorescence (WDXRF) and inductively coupled plasma atomic emission spectroscopy (ICP-AES) with mixed acid digestion or fire assay.[5] However, in round robin analyses, it was demonstrated that agreement among laboratories was poor, and technique-based biases were indicated.[5] Dissolution of these materials, particularly the spent catalyst, was difficult and presented a possible source of systematic bias. Brown et al. investigated the use of microwave-assisted dissolution followed by ICPMS analyses quantified by internal standardization.[6] The ICPMS results for Pd and Rh compared favorably with interlaboratory WDXRF results.

Instrumental neutron activation analysis (INAA) provides a method of direct solid analysis but is not routinely applied.[7] Glow discharge atomization atomic absorption spectroscopy (GDA-AAS) offers an alternative through direct atomization from the solid state after mixing with a suitable conductive host matrix.[8] However, the relative errors associated with these techniques approach 5% for these materials.

The need for highly accurate assay standards led to the production of two used auto catalysts standard reference materials (SRMs) by the International Precious Metals Institute (IPMI) and the National Institute of Standards and Technology (NIST).[9]

This paper describes the development of methods for the ICPMS certification of Pt, Pd, Rh, and Pb in the two used auto catalysts. For this work, all of the elements except for mononuclidic Rh were quantified by ID. Of the PGEs, only Pd has been

(1) Date, A. R.; Davis, A. E.; Cheung, Y. Y. *Analyst* **1987**, *112*, 1217.
(2) Liche, F. E.; Meier, A. L.; Crock, J. G. *Anal. Chem* **1987**, *59*, 1150.
(3) Hall, G. E. M.; Pelchat, J. C. *Geol. Newsl.* **1990**, *14*, 197.
(4) Hall, G. E. M.; Pelchat, J. C. *J. Anal. At. Spectrom.* **1993**, *8*, 1059.
(5) Bozic, J.; Maggs, S.; Glabb, A.; Kane, J. Presented at the Seminar of the International Precious Metals Institute, New Orleans, LA, March 1991.
(6) Brown, J. A., Jr.; Kuntz, F. W.; Belitz, R. K. *J. Anal. At. Spectrom.* **1991**, *6*, 33.
(7) Brunfelt, A. O., Steinnes, E., Eds.; *Activation Analysis in Geochemistry and Cosmochemistry*; Proceedings of the NATO Advanced Study Institute; Scandanavian University Books: Oslo, Norway, 1971; p 339.
(8) Winchester, M. R.; Hayes, S. M.; Marcus, R. K. *Spectrochim. Acta* **1991**, *46B*, 615.

previously determined by isotope dilution mass spectrometry (IDMS) at NIST using spark source mass spectrometry (SSMS),[9] while Pb is routinely determined using both thermal ionization mass spectrometry (TIMS) and ICPMS. ID-ICPMS has been used at NIST for the certification of reference materials since the mid-1980s[10-12] and is now the instrument of choice for IDMS. However, the ICPMS is also capable of quantitative measurement without isotope dilution, and the analytical procedures used to obtain the Rh (mononuclidic) concentration at the required accuracy are detailed.

EXPERIMENTAL SECTION

Materials and Reagents. All of the high-purity mineral acids and water used in this work were prepared and analyzed at NIST.[13] All chemical preparation experiments were performed in a Class 10 clean laboratory.[14] A Class 100 clean air hood is suspended above the sample introduction system of the ICPMS.

Description of Autocatalyst SRMs. The two used auto catalyst SRMs, 2556 and 2557, are pulverized and sieved powders of the recycled pellets and monolith material, respectively. The material was supplied by Inco Ltd., the major recycler of used auto catalysts in North America, according the following procedure. As individual batches of automotive catalysts were recycled, 2–3 kg samples were set aside until ~150 kg of each of the two materials was accumulated. Each material was pulverized and sieved (about 200 mesh), and the bulk supply was shipped to NIST and bottled in 70 g units.

The catalytic converters being recycled utilized either alumina pellets or a ceramic "honeycomb" (monolith) substrate since a large surface area is required to successfully reduce hydrocarbon emissions. A washcoat typically containing Zr, Ce, La, Ba, Ca, Fe, and Ni was used to incorporate the PGEs onto the substrate. The high level of lead present in the used catalyst is a contaminant from the use of leaded gasoline. In an ICPMS survey analysis, it was determined that the Zr, Ni, and Ba content of this recycled monolith is up to 2 orders of magnitude higher than that in the recycled pellet SRM. The residual Cd, As, and Pb content is slightly higher in the monolith SRM.[15]

Instrumentation. The ICPMS used for this work was a PQ II Turbo Plus mass spectrometer from Fisons Instruments. The operating parameters were as follows: rf power, 1.3 kW; coolant argon flow, 15 L/min; auxiliary argon flow, 0.95 L/min; nebulizer argon flow, 0.85 L/min. A peristaltic pump fitted with poly(vinyl chloride) (PVC) tubing provided a constant sample flow rate of 0.3 mL/min into a concentric nebulizer and a water cooled spray chamber at 2 °C. The lens voltages were adjusted to provide maximum signal for elements in the mass range of interest.

Note: Certain commercial equipment, instruments, or materials are identified in this report to specify adequately the experimental procedure. Such identification does not imply recommendation or endorsement by the National Institute of Standards and Technology, nor does it imply that the materials or equipment identified are necessarily the best available for this purpose.

Isotope Dilution Method for the Quantification of Pt, Pd, and Pb. The Pt, Pd and Pb were quantified using isotope dilution. The ^{104}Pd (isotope adundance, 94.00%) and ^{198}Pt (isotope abundance, 95.31%) were purchased from Oak Ridge National Laboratory as metal powders, dissolved in aqua regia, and stored as 2 mol/L HCl solutions. The ^{206}Pb wire is NIST SRM 983, radiogenic Pb (92.15% ^{206}Pb), which was dissolved and stored in dilute HNO_3.

The concentrations of each enriched isotope, ^{198}Pt, ^{104}Pd, and ^{205}Pb, were determined versus gravimetrically prepared natural solutions of the respective elements using isotope dilution analysis. This process is sometimes referred to as reverse isotope dilution or spike calibration.

Lead isotopic ratios are variable in nature since Pb from the radiogenic decay of U and Th is mixed with primeval Pb. Therefore, the isotopic composition of the lead calibrant as well as the isotopic composition of the Pb in each auto catalyst was determined versus a solution of NIST SRM 981, common Pb isotopic standard.

Internal Standard Method for Rhodium Quantification. Three possible internal standards were selected for the mononuclidic Rh determination and were carried throughout the experiment: the ^{104}Pd, which is one mass unit removed and chemically similar to the Rh; ^{198}Pt, which is chemically similar but has a large mass difference; and ^{115}In, which is chemically different but close in mass and naturally absent in the auto catalyst material. The assayed enriched isotope spikes, ^{104}Pd and ^{198}Pt, were the major sources of the respective standard isotopes in the spiked samples and required only a small correction for the natural contribution. The In was purchased from Indium Corp. of America as the high-purity metal, dissolved and stored in dilute HNO_3.

The internal standard method required that the relative sensitivity factor (RSF) of Rh versus the internal standard(s) be determined, since the relative transmission and ionization efficiency vary among elements. For this RSF determination, Rh was added, along with the natural Pt and Pd, to the spike calibration mixes.

Three different Rh assay standards were used since its accurate assay can be difficult. Two of the three Rh standards used for the RSF determination were prepared from a spectrometric standard rhodium solution, NIST SRM 3144, which is now available to commercial users.[16] A third standard was prepared using high-purity Rh metal from an independent source. Dissolution of this metal was accomplished using a Carius tube heated to 240 °C for 72 h using HCl and HNO_3.[17,18] (***Caution***: Glass tubes under high pressure should be handled with care. The safety considerations of such procedures are discussed in detail by Paulsen and Kelly.[19])

In summary, each spike calibration mix contained ^{104}Pd, ^{198}Pt, and In, as well as the high-purity natural Pt, Pd, and Rh assay standards. The final selection of the internal standard for the Rh quantification was made after the analytical data were collected on the basis of the isotope pair with the least uncertainty in ratio measurement during the analysis.

Chemical Procedures. *Dissolution and Isotope Equilibration.* Samples of each auto catalyst material, weighing about 0.1 g,

(9) Alvarez, R.; Paulsen, P. J.; Kelleher, D. E. *Anal. Chem.* **1969**, *41*, 955.
(10) Moody, J. R.; Epstein, M. S. *Spectrochim. Acta* **1991**, *46B*, 1571.
(11) Beary, E. S.; Paulsen P. J.; Fassett, J. D. *J. Anal. At. Spectrom.* **1994**, *9*, 1363.
(12) Fassett, J. D.; Paulsen, P. J. *Anal. Chem.* **1989**, *61*, 643A.
(13) Paulsen, P. J.; Beary, E. S.; Bushee, D. S.; Moody, J. R. *Anal. Chem.* **1988**, *60*, 971.
(14) Moody, J. R. *Anal. Chem.* **1982**, *54*, 1358A.
(15) NIST Certificates of Analysis for SRMs 2556 and 2557, issued August 1993.
(16) Beck, C. M., III; Salit, M. L.; Watters, R. L., Jr.; Butler, T. A.; Wood, L. J. *Anal. Chem.* **1993**, *65*, 2899.
(17) Gordon, C. L. *J. Res. Nat. Bur. Stand. (U. S.)* **1943**, *30*, 107.
(18) Wichers, E.; Schlecht, W. G.; Gordon, C. L. *J. Res. Nat. Bur. Stand. (U. S.)* **1944**, *33*, 363.
(19) Paulsen, P. J.; Kelly, W. R. *Anal. Chem.* **1984**, *56*, 708.

were dissolved using a combination of HNO_3 and HF and either $HClO_4$ or HCl, depending on the analyte and dissolution technique. (***Caution***: These mineral acids are irritants to eyes, skin, and mucous membranes. HF is particularly corrosive and a contact and inhalation hazard.[20] In addition, perchorates can form explosive mixtures in combination with carbonaceous material.[21])

Two analytical sample sets were prepared. Only lead was determined in the first sample set to avoid complicating the determination of Rh and Pd, which suffered from a minor Pb^{2+} interference at masses 103 and 104. These samples were spiked with ^{206}Pb and dissolved using a mixture of HNO_3, HCl, HF, and $HClO_4$ in Teflon beakers on a hotplate. This hotplate procedure is sufficiently agressive to solubilize the Pb in the sample and to promote its equilibration with the Pb spike.

A two-step dissolution procedure was applied to the second sample set, since the PGEs can be difficult to dissolve. Analytical samples were spiked with a solution of ^{198}Pt and a solution mix containing ^{104}Pd and In. The first step was an aggressive Carius tube dissolution,[17] using HCl as a chlorine source and HNO_3 as an oxidizing agent. For the second step, the sample solutions and any SiO_2 residue were rinsed into Teflon beakers and treated with HF. While it is unlikely that this residue contained any chemically bound Pt, Pd, or Rh, physical inclusion of these elements in the precipitate was of concern. A weight correction was made on the basis of a third sample set, which was calcined (roasted) for 2 h at 500 °C.[15]

ICPMS Procedures. *Mass Bias Correction and Drift Correction.* The measured isotopic ratio of an element differs from the true ratio because the transmission and detection efficiencies of the mass spectrometer have a mass dependence. Mass bias corrections for the Pt and Pd were referenced to primary standards prepared from high-purity natural metals. The reference values for natural isotope abundances for the Pt and Pd were taken from the IUPAC reference tabulation.[22] SRMs 981 and 982, with certified isotopic compositions, were used as the Pb isotopic standards for the mass bias correction.

The mass bias correction can drift with time in ICPMS. The drift corrections for the isotope dilution analyses were made using working isotopic standards at the same concentration and with approximately the same isotope ratios as the samples to minimize any memory effect between the sample and the standard. The working isotopic standard was run after every second sample (approximately half-hour intervals), and the drift correction was made assuming a linear drift with time. For the isotope dilution determinations of the Pt, Pd, and Pb, one spike calibration sample (previously described) was used as the working isotopic standard since these sample/standard isotopic mixes are similar by design. Since this spike calibration sample is referenced to primary standards, all results are normalized to "absolute", bias-free ratios.

The relative transmission of two different elements with the potential for matrix-dependent changes was a much larger concern. For the quantification of Rh versus the internal standard, accurate measurement of both the relative transmission and its drift were required. Therefore, the working control standard was matrix-matched; the Pt/Pd/Rh/In spike calibration sample was mixed with the synthetic matrix sample. The synthetic matrix sample for each SRM was prepared on the basis of ICPMS semiquantitative data and contained percent levels of Al, Si, and Mg, as well as Ce and La. The proportional addition of the matrix elements had no effect on the isotope ratios for the isotope dilution determination of the Pt and Pd. Therefore, the same solution (a matrix laden spike calibration sample) could be used as the working isotopic standard for all the isotope/element pairs. Since the relative concentrations of the analytes in the two SRMs were significantly different, a working isotopic standard was prepared for each SRM.

Data Collection. All analytical data were collected in the peak jump mode. In a well-calibrated system, the peak jump mode provides higher sensitivity as well as better precision and accuracy than the scan mode over an extended mass region (>10 amu), since more data/collection time can be accumulated on just the masses of interest.[11]

The PGEs were determined simultaneously by peak hopping across peaks of interest; that is, from mass 103 (Rh) to mass 104 then 106 (Pd), to mass 115 (In), to mass 195 then 198 (Pt). The Pb was determined by measuring the 206/208 ratio in a separate sample set. For each sample set, the mass scale was adjusted to be centered on the peak tops being measured. The centering was tested using multiple points per peak. When correctly centered, there will be <1% decrease in signal intensity per 0.02 Da on each side of center. All isotope ratio data were collected using one point per peak to maximize the number of sweeps per unit time, resulting in improved signal averaging.

Sample solutions were introduced into the ICPMS in 0.02 mol/L HNO_3 and diluted so that the major peak gave $\leq 200-300 \times 10^3$ counts/s. This is the maximum practical count rate used for ICPMS without causing errors due to loss of ion multiplier gain and uncertainty in the deadtime correction.[11] In multielement analyses, the dilution factors are controlled by the most concentrated isotope measured. For these samples, the ^{198}Pt was diluted to 10 ppb in solution (giving 250×10^3 counts/s); all other peaks were measured at lower concentrations and, therefore, lower count rates.

RESULTS AND DISCUSSION

The determination of Pt, Pd, and Pb in the NIST automobile catalysts relied on the known high accuracy of isotope dilution analysis. The internal standard method of quantification of mononuclidic Rh required careful assessment of potential systematic errors. These potential errors could result from instrumental interferences, which could not be detected using methods routinely used for multiisotope analytes. The methods investigated for the Rh determination included chemical separations designed to quantitatively or reproducibly isolate the PGEs, as well as the use of synthetic matrix sample to assess the status of molecular or doubly charged ion interferences.

Assessment of Matrix Interferences. The ICP mass spectrometer is a nonspecific ionization source, and as such matrix interferences were of concern in the analysis of these auto catalysts SRMs. Three types of interferences are possible in ICPMS which affect isotope dilution quantification. Elemental isobaric interferences and doubly charged ion interferences are usually readily identified. Molecular ion interferences, however,

(20) Sam, N. I. *Dangerous Properties of Industrial Materials*; Van Nostrand Reinhold Co.: New York, 1979.
(21) Schilt, A. A. *Perchloric Acid and Perchlorates*; The G. Frederick Smith Chemical Co.: Columbus, OH, 1979.
(22) Peiser, H. S.; Holden, N. E.; DeBievre, P.; Barnes, I. L.; Hagemann, R.; DeLaeter, J. R.; Murphy, T. J.; Roth, E.; Shima, M.; Thode, H. G. *Element Review of Their Atomic Weights*; IUPAC Publication; Pergamon Press Ltd.: Great Britain, 1984.

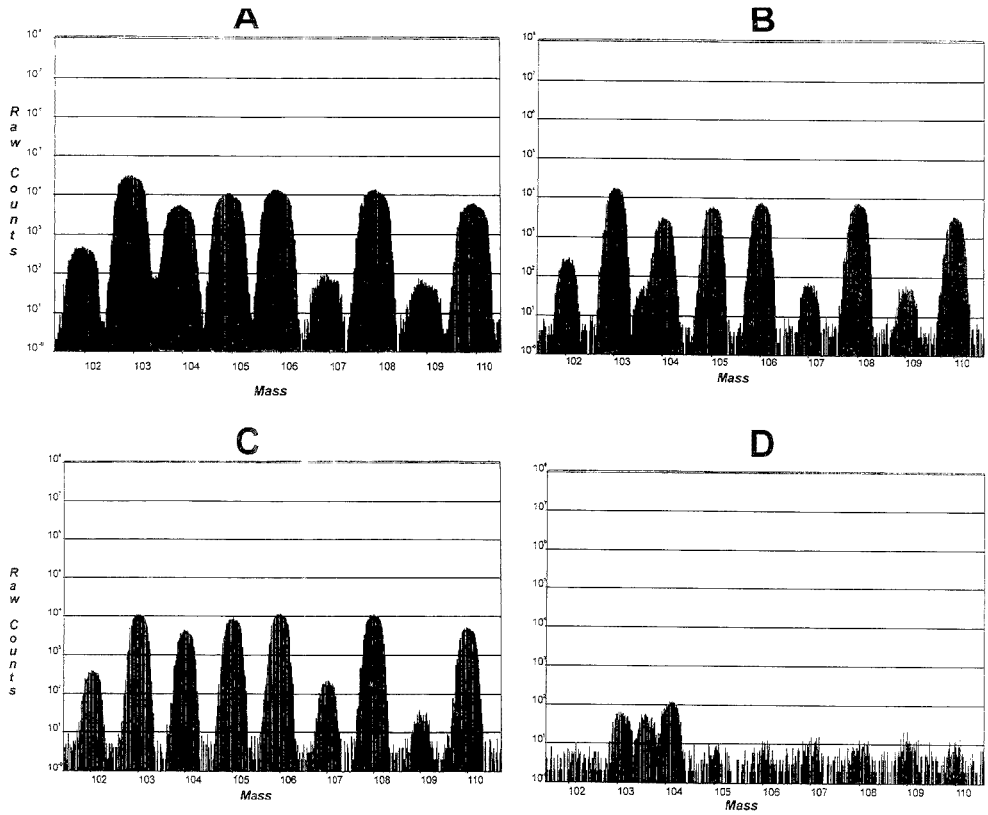

Figure 1. Mass scans of a limited mass region, where the mass is plotted versus the log of the signal. (A) Scan of the monolith auto catalyst at normal scan resolution; (B) the same sample scanned at higher resolution. (C) Scan of a monolith auto catalyst with the Pb removed. (D) Scan of a solution of pure Pb.

plague midmass measurements and are often difficult to identify.[23] An analyte is considered interference-free when its measured isotope ratio in the sample matches, within experimental error, the isotope ratio of the element in a pure standard solution under the same experimental conditions. This procedure was used to assess the accuracy of the measurement system for Pt and Pd. For these samples, there was no interference for Pt since the isotopic composition of the Pt in an unseparated, dissolved sample of each SRM matched the natural Pt, within experimental error, in consecutive mass spectrometric runs. Since the isotope composition of the Pt in the sample matches that of the pure Pt standard, it is clear that the presence of the matrix does not interfere with the accurate measurement of Pt.

The Pb isotopic composition varies in nature. Thus, this procedure of detecting interferences is not appropriate. Variations in natural composition are normal and do not necessarily imply interferences. However, interferences at high mass are unlikely, and their absence in these SRMs was easily confirmed by examination of the mass spectrum. Since both the auto catalysts have a much higher Pb concentration than those elements immediately downmass, the probability of forming polyatomic interferences at Pb is extremely low.

(23) Beary, E. S.; Paulsen, P. J. *Anal. Chem.* **1993**, *65*, 1602.

Interference in the Pd and Rh Mass Region Due to Pb^{2+}. The Pd isotopes in the samples were measured versus a natural standard. The 106/108 ratio agreed within experimental error; however, the 106/104 ratio in the sample was low relative to that ratio in the natural standard, due to excess counts at mass 104. Doubly charged ions from the percent level Pb in the sample produced an interference at m/z 104 ($^{208}Pb^{2+}$). This implied a similar interference for Rh at m/z 103 from $^{206}Pb^{2+}$. This Pb^{2+} interference is depicted in Figure 1. In all four mass scans, the log of the signal intensity is plotted versus mass. Figure 1A is a scan of the auto catalyst sample showing the limited mass region of interest. The elevated background at m/z 103.5 in comparison to m/z 104.5 and 105.5 is a clear indication of an interference. Figure 1B is a mass scan taken at higher resolution, showing the shoulder on the low mass side of m/z 104 from $^{207}Pb^{2+}$ at m/z 103.5. However, hidden in these mass spectra are the interferences at m/z 103 and 104 from $^{206}Pb^{2+}$ and $^{208}Pb^{2+}$, respectively. These are more clearly shown in Figure 1D, which is a mass scan of pure Pb at a concentration comparable to that in the auto catalyst sample. For these samples, the detected Pb^{2+} at the ^{104}Pd and ^{103}Rh interference was about 0.5%. Figure 1C is a high-resolution scan of an auto catalyst sample with Pb selectively removed. The distinct valleys between masses indicate the

absence of interferences due to Pb^{2+}. The absence of other interferences for Pd was confirmed by comparing the isotope ratio of Pd in the separated sample to natural Pd.

Validation of the ^{103}Rh Procedures. *Investigation of Chemical Separations.* Other interferences due to the formation of (low-probability) matrix molecular ions would be extremely difficult to detect for mononuclidic ^{103}Rh, with no confirming isotope available. Therefore, chemical separations to isolate the PGEs in these samples were vigorously pursued to check for Rh interferences. However, only the selective, quantitative removal of the Rh from the autocatalyst sample and the subsequent absence of a peak at mass 103 would provide confirmation of the absence of interferences for Rh.

Two different precipitation techniques as well as ion exchange chromatography were investigated. A summary of results from these separations and the relative recoveries of the Pt, Pd, and Rh are discussed below. Since Pb was a known interference, its concentration in each fraction was tracked, along with the PGEs. Both isolation of the Pd and Rh and their separation from Pb was of interest. All of the separations data were obtained in an ICPMS semiquantitative scan using internal standards to correct for instrumental drift.

Hypophosphorous acid precipitation in ~5 mol/L HCl reduced about 95% of the complex chloro ion of Pt, Pd, and Rh to the respective metals. Theoretically, the Pb is not reduced and remains in the filtrate. Experimentally, 97% of the Pb was found in the filtrate, although further washing of the precipitate may have improved this separation. However, the filtrate, with the residual Pt, Pd, and Rh, was extremely unstable and prone to sudden explosive reaction. Therefore, this method of separation was abandoned.

A suitable separation using a specialty resin from EIChroM industries was then investigated. Sr Spec resin, a crown ether on an inert substrate, was designed to isolate Sr quantitatively. However, Pb is also strongly bound by the crown ether, so its removal from the auto catalyst matrix while the PGEs were being recovered was examined. ICPMS, in a semiquantitative survey mode, is a useful method to provide relative concentrations for elements of interest in chromatographic fractions. For this separation, the eluent containing the PGEs and most of the matrix elements, as well as the resin digest, was analyzed. The results for two independent sample separations of identical sample aliquots were as follows: 99.9% and 98.6% of the Pt was eluted; 99.9% and 96.8% of the Pd was eluted; and, 99.8% and 99.7% of the Rh was eluted. These procedures did not have the required reproducibility for these elements. A survey analysis confirmed, as expected, that >99.9% of the Pb had remained on the resin.

Precipitation of the PGEs with $SnCl_2$ was carefully investigated since it is a classic technique to quantitatively reduce complex ions of the PGEs to the respective metals. This procedure was recently applied to the recovery of PGEs from geological samples using Se as a carrier.[21] In this work, the efficiency of the precipitation using both Se and As as carriers was examined, as well as precipitation without a carrier. The matrix elements were contained in the filtrate for all three $SnCl_2$ precipitations studied. However, <5% of the Pt and Rh was found in the precipitate when no carrier was used, compared to 99.4% of the Pd. With the As carrier, 99% of the Pd was recovered, while only 49% of the Pt and 20% of the Rh was recovered. Precipitation using the Se carrier was the most efficient technique, recovering >98% of both the Pt and Pd and 91% of the Rh. While our experiments may not have been optimized, none were reproducible to 1% or better, as was required for the accurate and precise determination of Rh in this analysis. In addition, the recovery of Rh did not track with the recovery of Pt or Pd, whose spikes might serve as an internal standard. Therefore, separation of the PGEs from the matrix elements was not pursued further for the Rh determination.

The separations results did provide important information. With the Pb removed from the sample, the isotopic composition for Pd matched the isotopic composition of the natural under the same instrumental conditions, thus confirming that there was no interference other than the $^{208}Pb^{2+}$ at m/z 104. However, the above separations could not confirm that Pb was the only interference for Rh at m/z 103, where simutaneous determination with the Pt and Pd was desired. Therefore, additional experiments using a synthetic matrix sample were performed to further assess Rh interferences in these SRMs.

Preparation of the Matrix-Matched Synthetic Samples. An ICPMS semiquantitative survey was performed on each dissolved SRM, and the concentrations of 70 elements were estimated versus an internal standard. Synthetic samples were prepared on the basis of this semiquantitative data so that each auto catalyst matrix could be artificially duplicated. About 15 elements were selected for the synthetic samples on the basis of their potential of forming molecular ions which add up to 103, as well as their concentration relative to Rh. The synthetic samples contained Na, Mg, Al, Si, P, Ca, Ti, Cr, Fe, Mn, Ni, Zn, Cu, Ce, and La. The elements of most concern were matrix elements below mass 87. The concentrations of elements of interest in the synthetic sample were adjusted to match each SRM by comparing signal levels in alternate samples run in rapid sequence and altering the synthetic standard accordingly. These synthetic standards had no deliberately added Rh or Pb (but did contain Pd to serve as a reference), and no peak at m/z 103 was observed. Figure 2 shows the mass region of interest for synthetic SRM 2556, in which the total counts per second are plotted versus mass. The plot for synthetic SRM 2557 is similar, with 34 counts/s at m/z 103, which is comparable to background. Therefore, the absence of interferences from molecular ions in these SRMs is established.

In summary, the Pt and Pb were free from interferences and could be determined directly in a dissolved, spiked sample using IDMS quantification. Both the Pd and Rh suffered from a Pb^{2+} interference of ~0.5%. With Pb removed from the dissolved sample, a comparison to natural Pd verified that the $^{208}Pb^{2+}$ was the only Pd interference. The absence of interferences other than $^{206}Pb^{2+}$ for the Rh was verified using a synthetic standard. If only Pd were of interest, separations to remove the Pb would have been the method of choice, since nonquantitative recoveries would not compromise the IDMS results. However, quantititative or reproducible recoveries for both mononuclidic Rh and the selected internal standard (^{105}Pd, ^{198}Pt, or ^{115}In) would be required for accurate quantification of the Rh. Therefore, for both the Pd and Rh determinations, the Pb correction was made instrumentally, using the following technique: (a) isotopic abundances of the Pb in the sample were measured; (b) the signals at m/z 104, 106 and 108 were measured in pure Pd and in the unspiked sample; (c) the 108/106 Pd ratio in the sample was the same as that in the natural standard and, therefore, free from interference; (d)

(21) Porto da Silveira, C.; Bastos, M. Presented at the 1992 Winter Conference on Plasma Spectrochemistry, San Diego, CA, Jan 6–11, 1992.

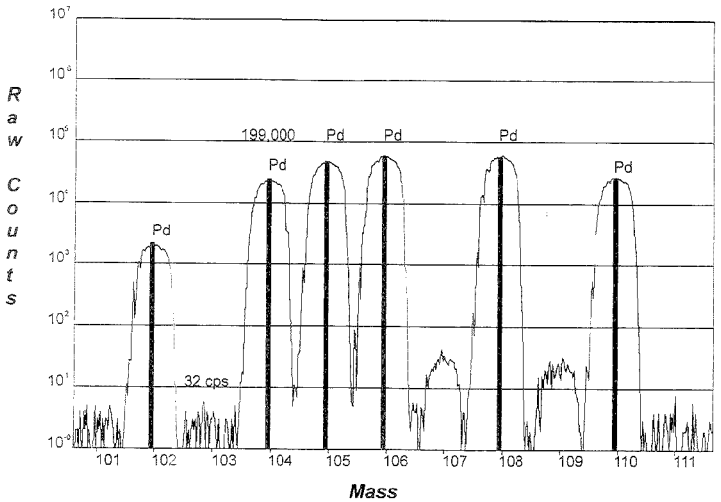

Figure 2. Limited mass region of a full mass scan of a synthetic catalyst sample, SRM, 2556. Rh in SRM 2556 > ^{110}Pd; 103 bkg ≈ 29 counts/s; ^{104}Pd = 199 000 counts/s.

Table 1. Selected Molecular Ions at Nominal Mass 103

element	anion	actual/calcd mass	difference from ^{103}Rh
^{103}Rh		102.905 50	
^{87}Rb	^{16}O (oxides)	102.904 098	1/73399
^{87}Sr	^{16}O	102.903 805	1/60711
^{71}Ga	$^{16}O_2$ (double oxides)	102.914 530	1/11396
^{66}Zn	^{37}Cl (chlorides)	102.891 94	1/7589
^{68}Zn	^{35}Cl	102.893 70	1/8721
^{63}Cu	^{40}Ar (argides)	102.891 82	1/7612
$^{206}Pb^{2+}$		102.897 228	1/1259

Table 2. Calibration of Enriched Isotopes

	^{104}Pd	^{198}Pt	^{206}Pb
av (μmol/g)	0.9611	1.6453	32.872
n	15	15	4
rsd (%)	0.30	0.20	0.11

the 104/106 alteration from natural was due to $^{208}Pb^{2+}$ at *m/z* 104, and its contribution could be calculated; and (e) in the same manner, the ^{206}Pb correction at ^{103}Rh could be calculated.

Double-focusing ICP mass spectrometers can operate at higher resolution than the quadrupole and have the potential of resolving an element from a molecular ion interference falling at the same nominal mass. Currently available high-resolution instruments operate at a maximum resolution of 5000–10 000. Table 1 lists the mass for Rh, the calculated masses for several molecular ions, and their differences from Rh. These hypothetical molecular ions could form in the ICP from the support gas (Ar), water (O), and matrix elements (such as Cl). It is problematic that 10 000 resolution would resolve a 1% molecular ion interference with a 1 part in 8000 (chloride and argide) mass difference from Rh. The oxide is well beyond the resolution capabilities of the current instruments. The Pb^{2+}, as previously discussed, would be resolved. The $^{206}Pb^{2+}$ requires only about 1300 resolution; however, only 250 resolution is required to measure the $^{207}Pb^{2+}$ and to calculate the 206 contribution at ^{103}Rh. From the mass differences calculated, it is clear that a high-resolution ICPMS could not assure the absence of interferences at ^{103}Rh, and alternate approaches, as previously described, would be required.

Analytical Results. *Calibrations of Enriched Isotopes.* The accuracy of IDMS analyses is directly tied to the accuracy and precision of spike calibration, that is, how well the concentration of each of the enriched isotopes (^{104}Pd, ^{198}Pt and ^{205}Pb) is known. Errors in these critical analyses will bias the analytical result. Calibration samples are chemically simple, contain known amounts of each isotope of the analyte, and can be easily optimized for instrumental procedures. The sets of seven ratio measurements for each calibration mix had precisions better than 0.2% rsd.

Fifteen spike calibrations are reported for this work. This number of calibrations was unusually large for the following reasons: (i) three different Rh standards were compared, and the Pt and Pd were done at the same time; (ii) spikes were calibrated at two different times, 1 month apart, to assess solution stability; and (iii) two different solutions were prepared to serve as mass bias calibrants (one for SRM 2556 and a second for SRM 2557) due to the vastly different relative concentration of the analytes. The average concentration of each spike (in μmol/g) and the precision (expressed as % rsd) are shown in Table 2. Precisions of better than 0.3% rsd were achieved for each enriched isotope calibrations. The Pb spike was calibrated in a single element determination, with a precision of 0.1% rsd. The Pt and Pd were determined simultaneously, along with the Rh. A slight degradation of precision was observed for the Pd calibration, possibly due to the fact that its concentration in the calibration standard was lower than the Pt, and thus the signal was not optimized.

Determination of RSF for Rh Quantification. The relative sensitivity factor (RSF) is unique to each element combination based on masses, ionization potentials, and other chemical properties peculiar to the conditions of the ICP torch at 6000–8000 °C. Since the amounts of ^{104}Pd and ^{198}Pt spikes added to the samples were accurately known, the analysis was designed

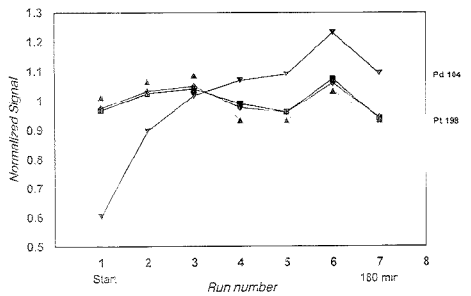

Figure 3. Change in signal intensity versus time (run number) for (▲) ^{198}Pt, (▼) ^{104}Pd, (■) ^{103}Rh, and (◆) ^{115}In in an auto catalyst sample.

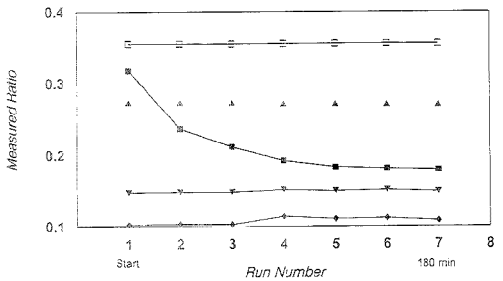

Figure 4. Stability of the measured ratio versus time (run number). (■) 103/104, (▼) 103/115, (◆) 103/198, (▲) 106/104, and (□) 195/198.

to use these spikes, and the quantitatively added In, as internal standards for the Rh determination. Figure 3 shows the changes in the Pt, Pd, Rh, and In signals versus time. The signal from the individual sample runs normalized to the average signal from all the runs is plotted versus run number, with ~30 min between each run. When the actual analysis measurements were initiated, the Pd signal changed in an uncharacteristically rapid fashion, perhaps due to selective (ad)absorption on the walls of the sample introduction system. The drift in signal is typical for Pt, In, and Rh. The Pd isotopic ratio calculated from these data, however, was very constant, as shown in Figure 4, and suitable for isotope dilution quantification. The Pt ratios, as well as the ^{103}Rh versus ^{104}Pd, ^{115}In, and ^{198}Pt are also plotted. These plots show that Pd could not be used as the internal standard for Rh. The use of In and ^{198}Pt was continued.

Twelve different calibration mixes were compared for the RSF determination, using three different Rh standards and two different In/Pd/Pt standards. The average precision of the ^{198}Pt/^{103}Rh ratio measurements during the analysis was 0.8% rsd, as compared to 0.6% rsd for the ^{115}In/^{103}Rh. Therefore, the results were calculated using only the Rh/In pair. The overall precision of <0.5% rsd of the calculated Rh/In RSF regardless of the Rh standard used is a good indication that their concentrations (and assays) are accurate to at least the same degree. These calibration results are listed in the Table 3. The 0.5% rsd reflects the fact that internal standard quantification, even when optimized, is less precise than isotope dilution.

Examination of Analytical Procedures. The precision of the calibration results were within the expected analytical uncertainty for the procedures described. However, the analytical goal

Table 3. Determination of RSF of ^{103}Rh/^{115}In

Rh std ID	RSF
1	1.1001
metal A	1.0993
	1.0959
	1.0981
2	1.0995
salt	1.0936
3	1.1083
metal B	1.0936
1	1.1086
metal A	1.1069
	1.1037
av	1.1007
s	±0.0055
rsd	±0.50%

is the accurate and precise determination of the analytes in the complex catalyst material. Three aspects of sample analysis and the associated uncertainty are provided in the following paragraphs. The discussion is limited to sampling, dissolutions, and mass bias drift corrections.

Sampling. Sampling and spike additions were accomplished gravimetrically using calibrated analytical balances. It is generally accepted that these weights are reproducible to better than 0.05% for weights in the 0.1–1 g range. However, establishing the analytical basis weight involves more than weighing uncertainties and is critical to accurate analyses. For the auto catalyst material, the most reproducible weight basis was obtained by calcining at 500 °C and is specified as the drying procedure on the certificate of analysis for these SRMs.[15] This drying protocol was adopted when lower temperatures failed to provide a reproducible basis weight. Residual hydrocarbons in the used catalyst material was the likely cause of the problem.

Even under optimum conditions, the uncertainty of the calcining process can contribute to the overall uncertainty. Sample was taken from each of eight bottles and weighed into tared crucibles. Following calcining, the crucibles were cooled in a desiccator over $Mg(ClO_4)_2$ and weighed at 2.5 and then 3.5 h after removal from the furnace. For these samples, rapid weighing is desirable since the catalyst material is hygroscopic after heating to 500 °C. After 2.5 h of cooling, the calcined samples of SRM 2556 lost an average of 4.39%, with a range of 4.54%–4.21%. Duplicate samples were reproducible to better than 1% relative or 0.03% absolute. All tare weights were reproducible to better than 0.003% relative. At 3.5 h, also a reasonable "cooling" time, the weight loss was an average of 4.08% for the calcined sample set, a difference of 0.11% absolute from the first average. In addition, calcined samples from the same bottles dried 1 month later had an average weight loss of 4.78% after cooling for 2.5 h. If the earlier average of 4.39% was used for the weight correction, a bias of 0.4% absolute would have been introduced. For these samples, a weight correction based on a single bottle can introduce biases greater than 0.3% absolute. The drying of SRM 2557 was similarly studied. The average weight loss of the calcined samples was 0.99%, ranging from 1.04% to 0.92% for eight sample bottles. These values were reproducible to 0.04% absolute.

Dissolution. Carius tube dissolution was used in the certification procedure for these SRMs. However, as a comparison, SRM 2556, the recycled pellet material, and a new (unused) monolith material were analyzed using a hotplate dissolution. The hotplate dissolution utilized HNO_3, $HClO_4$, and HF, and samples were

heated to about 200 °C. The dissolution was as aggressive as practical when Teflon containers were used on a hotplate. After the dissolution was "complete", the solutions were visually clear. However, biases were found when comparing the average concentration values for each of the elements.

For SRM 2556, the Pt, Pd, and Rh concentrations were lower by 0.16%, 0.43%, and 1.00%, respectively, in the samples dissolved on the hotplate. In general, the among sample precision was also poorer for the samples dissolved on the hotplate. There was some evidence of incomplete dissolution (low values for all PGEs) and/or precipitation of the PGEs after isotope equilibration (relatively large Rh bias). However, limited sampling and homogeneity issues, as well as analytical uncertainty, make any explanation speculative for this used catalyst SRM.

The results from the hotplate dissolution of the new catalyst (monolith) material were more conclusive. For Pt, two of the four samples prepared had concentrations 2% lower than the average value obtained from Carius tube dissolution. The results obtained for the other two samples were about 0.7% lower than the Carius tube average. The analytical precision, expressed as rsd for n = 4, was nearly 1% for the hotplate samples but the rsd was <0.5% for the samples dissolved in the Carius tube (n = 7). For Pd and Rh, each concentration calculated was lower than each Carius tube result, and the average was 1.87% and 1.72% lower for Pd and Rh, respectively. The precision was about 0.5% rsd for both elements for both dissolution procedures.

The PGEs were finely dispersed on the new catalyst material from a homogeneous solution containing the three elements; therefore, the ratios of their concentrations were compared. For the Carius tube dissolution of this new catalyst material, the ratios of the Pt concentration to the Pd concentration had a precision of <0.1% rsd for seven separate samples, an indication of the analytical precision. Since the precision obtained for the individual element concentrations for the same seven samples was about 0.5% rsd, the increased imprecision is ascribed to the homogeneity of the new catalyst material for the PGEs. For the four samples dissolved on the hotplate, the Pt/Pd concentration ratios had a precision of 0.50% rsd. These results show the loss of analytical precision and accuracy (due to incomplete and variable dissolution) relative to the Carius tube procedure.

Mass Bias and Mass Bias Drift Corrections. The theoretical versus experimentally measured isotopic ratios will exhibit a difference depending on the element and instrumental conditions. Mass bias corrections of ~4.5% for $^{195}Pt/^{198}Pt$ and $^{104}Pd/^{106}Pd$ and ~0.5% for $^{206}Pb/^{208}Pb$ isotope ratio were observed for these experiments. These corrections vary among instruments and with instrument setup. As an example of long-term reproducibility of mass bias (several years), the range in mass bias corrections observed for Pb under optimal instrumental conditions in a variety of materials was about 1% relative. For low-mass elements, such as Mg, the range is >5%. In addition, there are short-term drifts in mass bias that are observed with no changes to instrument parameters, such as gas flow, refocusing etc. This short-term drift might be caused by physical changes such as deposition of solids on the sampling/skimmer cones or by voltage drifts of the ion optics. The precision, expressed as rsd, of samples with correction for drift during this time period was 0.81% for Pt and 0.67% for Pd, while without the drift correction, it would be 1.2% and 0.93% for Pt and Pd, respectively.

Table 4. Concentration of Pt, Pd, Pb, and Rh in SRM 2556 (μg/g)

	Pt	Pd	Pb	Rh
	700.6	326.1	6223.7	51.31
	696.7	326.8	6253.1	50.42
	696.6	326.9	6229.0	51.02
	695.5	327.8	6312.6	50.91
	696.0	325.1	6203.6	51.37
	698.5	324.0	6200.8	51.29
	697.8	326.9	6203.3	51.30
	697.3	324.7	6194.4	51.79
av	697.375	326.04	6227.6	51.18
s	1.618	1.31	39.4	0.40
rsd (%)	0.23	0.40	0.63	0.78
certified values[a]	697.4 ± 2.3	326.0 ± 1.6	6228 ± 49	51.2 ± 0.5

[a] The expanded uncertainties are 99% confidence intervals of the single method means and include both type A and type B errors.[25]

Table 5. Concentration of Pt, Pd, Pb, and Rh in SRM 2557 (μg/g)

	Pt	Pd	Pb	Rh
	1135.9	231.7	13933	136.33
	1142.9	232.4	13919	133.72
	1141.2	231.8	13990	136.82
	1134.4	231.9	13858	136.02
	1124.4	233.7	13893	136.06
	1117.8	234.9	14014	132.09
	1122.5	233.0	13806	135.27
	1126.8	235.9	14033	134.69
av	1130.74	233.2	13931	135.13
s	9.17	1.56	79	1.58
rsd (%)	0.81	0.67	0.56	1.17
certified values[a]	1131 ± 11	233.2 ± 1.9	13931 ± 97	135.1 ± 1.9

[a] The expanded uncertainties are 99% confidence intervals of the single method means and include both type A and type B errors.[25]

Analytical Results for SRM Certification of Pt, Pd, Rh, and Pb. Individual ICPMS results as well as the certified values for Pt, Pd, Rh, and Pb in SRM 2556 and SRM 2557 are given in Tables 4 and 5, respectively. The average blank values for four independent samples were <20 ng for Pt and Pd, <5 ng for Pb, and <0.4 ng for Rh. Their contributions were insignificant for these elements at near milligram per gram levels and higher in the catalyst material. The high-accuracy analytical procedures developed for the PGE determinations in the auto catalysts directly resulted in accurate concentration data. In addition, the level of homogeneity of the materials could be assessed using the analytical precision.

Matrix effects do not degrade analytical precision for the IDMS measurements. This fact is routinely demonstrated (and was demonstrated for these materials) since the measured ratio of the analyte in the sample agrees with the measured ratio of a pure analtye standard when no isobaric interferences exist. In addition, the RSF of Rh/In was determined with and without the synthetic matrix sample, and the results agreed within experimental error. This implies that the relative transmission of the Rh/In was not affected by the matrix under the instrumental conditions used. Therefore, the relatively large analytical sample precision (expressed as rsd), compared to the precision achieved for the calibration samples, can be ascribed to the material's inhomogeneity. The rsds found in these analyses demonstrate that the pellet material, SRM 2556, has a higher degree of homogeneity for the

PGEs than the monolith material, SRM 2557. In both cases, however, this level of material homogenity for a 100 mg sample is considered excellent.

The certified values listed are based on the ICPMS certification analyses. Their uncertainties are the 99% confidence interval of the single method means and include both type A and type B uncertainties.[25] Confirmatory analyses were performed at NIST and cooperating laboratories using instrumental neutron activation, XRF, and ICP-AES.

CONCLUSION

Methodologies which enhance the precision of ICPMS procedures have been described. Analytical sampling uncertainty was minimized by optimizing the drying procedures and using gravimetric sample preparation procedures. Carius tube procedures ensured that the PGEs were solubilized. In addition to proper instrument calibration, the mass bias and its drift were measured and appropriate corrections made.

IDMS procedures were used for Pt, Pd, and Pb in each of the two SRMs. Isotope dilution quantification procedures utilize the strength of the ICPMS instrument, that is, the capability of high-precision ratio measurements in complex materials. It is inherently more precise and accurate than other internal standard techniques and, therefore, the method of choice for high-accuracy analyses. While the initial investment for enriched isotopes could be significant (the cost of the Pt and Pd spikes were approximately $30/mg in 1992), the cost of each spike per sample for this certification analysis was less than $3.00.

The quantification of mononuclidic Rh using a conventional internal standard technique required additional attention to sources of bias to obtain accuracy comparable to that of IDMS procedures. For these materials, the preparation of synthetic samples was required to identify possible Rh interferences. Other than the Pb^{2+} interference, none were found. In addition, the working Rh/In control standard was prepared by mixing the synthetic sample with the Rh/In standard. With the procedures described, both IDMS and internal standard quantitation met the analytical goals for the determination of Pt, Pd, Rh, and Pb in the auto catalyst material to 1% or better.

ACKNOWLEDGMENT

The authors thank Jack Fassett for his scientific input and JoAnne Brooks and Terri Hamilton for their help in preparing the figures and tables.

Received for review March 17, 1995. Accepted June 8, 1995.[⊗]

AC950272Y

[⊗] Abstract published in *Advance ACS Abstracts,* July 15, 1995.

(25) Taylor, B. N.; Kuyatt, C. E. Guidelines for Evaluating and Expressing the Uncertainty of NIST Measurement Results. NIST Technical Note 1297; U.S. Government Printing Office: Washington, DC, 1994.

Anal. Chem. **1995**, *67*, 3202–3210

Mining Genomes: Correlating Tandem Mass Spectra of Modified and Unmodified Peptides to Sequences in Nucleotide Databases

John R. Yates, III,* Jimmy K. Eng, and Ashley L. McCormack

Department of Molecular Biotechnology, Box 357730, University of Washington, Seattle, Washington 98195-7730

The correlation of uninterpreted tandem mass spectra of modified and unmodified peptides, produced under low-energy (10–50 eV) collision conditions, with nucleotide sequences is demonstrated. In this method nucleotide databases are translated in six reading frames, and the resulting amino acid sequences are searched "on the fly" to identify and fit linear sequences to the fragmentation patterns observed in the tandem mass spectra of peptides. A cross-correlation function is then used to provide a measurement of similarity between the mass-to-charge ratios for the fragment ions predicted by amino acid sequences translated from the nucleotide database and the fragment ions observed in the tandem mass spectrum. In general, a difference greater than 0.1 between the normalized cross-correlation functions for the first- and second-ranked search results indicates a successful match between sequence and spectrum. Measurements of the deviation from maximum similarity employing the spectral reconstruction method are made. The search method employing nucleotide databases is also demonstrated on the spectra of phosphorylated peptides. Specific sites of modification are identified even though no specific information relevant to sites of modification is contained in the character-based sequence information of nucleotide databases.

Large-scale nucleotide sequence projects are beginning to produce long stretches of contiguous sequence from the *Caenorhabditis elegans*, *Saccharomyces cerevisiae*, and *Escherichia coli* genomes.[1-6] Complete sequence information has been obtained for chromosomes II (840 kb), III (315 kb), and IX (666 kb) of the *S. cerevisiae* genome.[3-5] The genome projects will produce complete sequence information for model experimental organisms for the study of prokaryotic and eukaryotic cell biology, development, differentiation, and behavior. The mouse genome sequence will serve to contrast that obtained from the human genome as well as to provide a closely related experimental system.[7,8] Most importantly, the genome projects will provide a sequence infrastructure that will accelerate the pace and increase the depth of understanding of genetic, biochemical, and physiological studies in these organisms.

While only a small proportion of the human genome (0.6%) has been sequenced,[9] considerable attention has recently been focused on the nucleotide sequence data generated by random sequencing of reverse transcribed messenger RNA (cDNA) from human tissues.[10-14] The principle advantage of cDNA sequencing is direct sequence analysis of DNA which codes for genes.[12] Functionally unique tissues, however, express different sets of genes, necessitating the isolation of mRNA from a variety of types of cells to obtain sequences from as many genes as possible.[12] This sequence information represents genetic elements actively transcribed in a cell and consequently will not contain the sequences of transiently expressed genes, such as those involved in differentiation or development.[12] The emphasis of this approach is high-throughput sequence analysis by using single sequencing "runs" with minimal effort expended on verification or extension of the sequence tracts.[15] This high-throughput, low-redundancy approach will produce partial nucleotide sequence information for much of the ~100 000–200 000 genes of the human genome in only a few years. Furthermore, cDNA sequencing is rapidly becoming an important technique for gene expression studies of specific cell types and is well suited for integration with biochemical studies.[16]

A powerful approach for utilizing the sequence infrastructure created by the genome projects is through the data produced by mass spectrometry.[17-22] One compatible method, microcolumn

* Phone: (206) 685-7388. FAX: (206) 685-7301. E-mail: jyates@u.washington.edu.

(1) Waterston, R.; Ainscough, R.; Anderson, K.; Berks, M.; Blair, D.; Connell, M.; Cooper, J.; Coulson, A.; Craxton, M. Dear, S.; et al. *Cold Spring Harbor Symp. Quant. Biol.* **1993**, *58*, 367–376.
(2) Olson, M. *Curr. Opin. Biol.* **1992**, *2*, 221–225.
(3) Feldmann, H.; Aigle, M.; Aljinovic, G.; André, B.; Baclet, M. C.; Barthe, C.; Baur, A.; Becam, A. M.; Biteau, N.; Boles, E.; et al. *EMBO J.* **1994**, *13*, 5795–5809.
(4) Dujon, B.; Alexandraki, D.; André, B.; Ansorge, W.; Baladron, V.; Ballesta, J. P.; Banrevi, A.; Bolle, P. A.; Bolotin-Fukuhara, M.; Bossier, P.; et al. *Nature* **1994**, *369*, 371–378.
(5) Oliver, S. G.; van der Aart, Q. J.; Agostoni-Carbone, M. L.; Aigle, M.; Alberghina, L.; Alexandraki, D.; Antoine, G.; Anwar, R.; Ballesta, J. P.; Benit, P.; et al. *Nature* **1992**, *357*, 38–46.
(6) Sofia, H. J.; Burland, V.; Daniels, D. L.; Plunkett, G.; Blattner, F. R. Analysis of the Escherichia coli genome. V. *Nucleic Acids Res.* **1994**, *22*, 2576–2586.
(7) Olson, M. *Proc. Natl. Acad. Sci. U.S.A.* **1993**, *90*, 4338–4344.
(8) Kocp, B. F.; Hood, L. *Nat. Genet.* **1994**, *7*, 48–53.
(9) Bork, P., Ouzounis, Christos, and Sander, C. *Curr. Opin. Struct. Biol.* **1994**, *4*, 393–403.
(10) Marshall, E. *Science* **1994**, *266*, 1800–1802.
(11) Marshall, E. *Science* **1994**, *266*, 25.
(12) Adams, M. D.; Kelley, J. M.; Gocayne, J. D.; Dubnick, M.; Polymeropoulos, M. H.; Xiao, H.; Merril, C. R.; Wu, A.; Olde, B.; Moreno, R. F.; Kerlavage, A. R.; McCombie, W. R.; Venter, J. C. *Science* **1991**, *252*, 1651–1656.
(13) Adams, M. D.; Soares, M. B.; Kerlavage, A. R.; Fields, C.; Venter, J. C. *Nat. Genet.* **1993**, *4*, 373–380.
(14) Adams, M. D.; Kerlavage, A. R.; Fields, C.; Venter, J. C. *Nat. Genet.* **1993**, *4*, 256–267.
(15) Boguski, M. S.; Lowe, T. M. J.; Tolstoshev, C. M. *Nat. Genet.* **1993**, *4*, 332–333.
(16) Orr, S. L.; Hughes, T. P.; Sawyers, C. L.; Kato, R. M.; Quan, S. G.; Williams, S. P.; Witte, O. N.; Hood, L. *Proc. Natl. Acad. Sci. U.S.A.* **1994**, *91*, 11869–11873.

0003-2700/95/0367-3202$9.00/0

reverse-phase high-performance liquid chromatography (HPLC) electrospray ionization tandem mass spectrometry (ESI-MS/MS), provides a rapid and sensitive method for the mass and sequence analysis of complex mixtures of peptides.[23] Furthermore, automated approaches to the data-dependent acquisition of tandem mass spectra during LC analysis have greatly increased both the volume of data that can be obtained and the efficiency of data acquisition.[24-26] To effectively analyze this large volume of collision-induced dissociation (CID) data, we have developed an automated approach to correlate tandem mass spectrometry data to the character-based amino acid sequences contained in protein databases.[26,27] This procedure takes the form of a reverse pseudospectral library search and employs a correlation function to compare a "predicted" tandem mass spectrum to the experimentally derived spectrum. This approach is effective for matching sequences contained in the protein database to their corresponding tandem mass spectra of both covalently modified and unmodified peptides.[27] An exact match to an amino acid sequence can serve to both interpret the spectrum and identify the protein sequence from which it was derived.

The ability to search nucleotide sequence data directly with tandem mass spectra would allow facile integration of biochemical studies with nucleotide sequencing, in particular cDNA sequencing. In addition, it would be advantageous to search nucleotide databases when a spectrum fails to match a sequence in the protein database. Increasingly, the protein sequences deposited in the database are derived by translation of the nucleotide sequence. A nonmatch to a protein sequence could result from one of several possibilities. First is the possibility that the sequence has not been determined and is not contained in a database. Additionally, the appearance of a translated sequence in the protein database may lag behind submission of the nucleotide sequence. Finally, errors or base ambiguities in a nucleotide sequence as is common in "one-pass" sequencing of cDNA (EST) sequences may result in an incorrect translation of the protein sequence being placed in a database.[15]

In this paper we demonstrate the ability to directly search nucleotide sequence information with uninterpretated tandem mass spectra of peptides. To consider all possible interpretations of the nucleotide sequence data, a six-reading-frame translation is used. The large amount of nucleotide sequence data, coupled with a translation in all reading frames, creates an even larger set of amino acid sequences that must be considered. As the genome projects proceed, the amount of nucleotide sequence will increase dramatically. Consideration of the data in all possible translations will increase the number of amino acid sequences approximately ~6-fold. Thus, a decrease in the signal-to-noise ratio of the search result may occur. In other mass spectrometry-based database search strategies, additional information is combined with peptide molecular weight information to decrease ambiguity in the search result.[28,29] For example, amino acid sequence information derived from chemical derivatization experiments[28] or partial sequence information obtained from manual interpretation of the tandem mass spectrum can improve search results.[29] In the method presented in this paper, no information beyond the mass of the peptide and the *m/z* values contained in the tandem mass spectrum is utilized to search the nucleotide databases. Results are presented for searches of nucleotide databases by using six-frame translation and for searches employing spectra of covalently modified peptides.

EXPERIMENTAL SECTION

Peptide and Protein Sources. Peptides and proteins of known sequence were obtained from the following commercial sources. Bovine α-casein, (Catalog No. C-6780, lot no. 78F-9555), bovine α-lactalbumin (Catalog No. L-4379, lot no. 75C-8110), and bovine serum albumin (Catalog No. A-4503, lot no. 98F-0047) were obtained from Sigma Chemical Co. (St. Louis, MO). Sequencing grade trypsin (Catalog No. 1047-841, lot no. 12676220-10) was obtained from Boehringer Mannheim (Indianapolis, IN). Peptides were generated from intact proteins by digestion with the enzyme trypsin in 50 mM Tris-HCl, pH 8.6, or 50 mM ammonium bicarbonate, pH 8.6, for 4–8 h at 37 °C. The heavy chain of glycoasparaginase (N^4-(β-*N*-acetylglucosaminyl)-L-asparaginase, EC 3.5.1.26) was obtained as previously described.[27] *E. coli* and *S. cerevisiae* proteins were treated as previously described.[27] Peptides isolated from the binding groove of class II major histocompatibility proteins were obtained as previously described.[30]

Microcolumn High-Performance Liquid Chromatography Electrospray Ionization Tandem Mass Spectrometry. Peptides were analyzed as mixtures by using microcolumn high-performance liquid chromatography as previously described.[26,27,30] Mass spectra were recorded on a Finnigan MAT (San Jose, CA) TSQ700 equipped with an electrospray ionization source.[31] Electrospray ionization was performed using the following conditions. The needle voltage was set at 4.6 kV. The sheath and auxiliary gases consisted of nitrogen gas (99.999%) and were set at 20 psi and 5 u, respectively. The heated capillary temperature was set at 150 °C.

Product ion tandem mass spectra were acquired "on the fly" during an LC/MS analysis by using a computer program written in the TSQ 700's instrument control language (ICL). At the start

(17) Yates, J. *News Intelligenet.* **1988**, *4*, 1–4. The concept of using mass spectrometry data and protein databases is described in this application note.
(18) Henzel, W.; Billeci, T.; Stults, J.; Wond, S.; Grimley, C.; Watanabe, C. *Proc. Natl. Acad. Sci. U.S.A.* **1993**, *90*, 5011–5015.
(19) Yates, J. R.; Speicher, S.; Griffin, P. R.; Hunkapiller, T. *Anal. Biochem.* **1993**, *214*, 397–408.
(20) Pappin, D.; Hojrup, P.; Bleasby, A. *Curr. Biol.* **1993**, *3*, 327–332.
(21) James, P.; Qaudroni, M.; Carafoli, E.; Gonnet, G. *Biochem. Biophys. Res. Commun.* **1993**, *195*, 58–64.
(22) Mann, M.; Hojrup, P.; Roepstorff, P. *Biol. Mass Spectrom.* **1993**, *22*, 338–345.
(23) Arnott, D.; Shabanowitz, J.; Hunt, D. F. *Clin. Chem.* **1993**, *39*, 2005–2010.
(24) Stahl, D. C.; Martino, P. A.; Swiderek, K. M.; Davis, M. T.; Lee, T. D. Proceedings of the 40th ASMS Conference on Mass Spectrometry and Allied Topics, Washington, DC, 1992; pp 1801–1802.
(25) Yates, J. R.; McCormack, A. L.; Eng, J. Identification of Individual Proteins in Mixtures using Micro-Column HPLC Tandem Mass Spectrometry and Automated Database Analysis. Presented at the Methods in Protein Structure Analysis Meeting, Snowbird, UT, Sept 9–13, 1994.
(26) Yates, J. R., III; Eng, J.; McCormack, A. L. *Anal. Chem.* **1995**, *67*, 1426–1436.
(27) Eng, J.; McCormack, A. L.; Yates, J. R., III. *J. Am. Soc. Mass Spectrom.* **1994**, *5*, 976–989.
(28) Pappin, D. J. C.; Rahman, D.; Hansen, H. F.; Bartlet-Jones, M.; Jeffery, W. A.; Bleasby, A. J. Chemistry, mass spectrometry and peptide-mass databases: Evolution of methods for the rapid identification and mapping of cellular proteins. In *Mass Spectrometry in Health and Life Sciences*; Burlingame, A. L., Carr, S. A., Eds.; Elsevier, New York, 1995 (in press).
(29) Mann, M.; Wilm, W. Anal Chem. **1994**, *66*, 4390–4399.
(30) Yates, J. R., III; McCormack, A. L.; Hayden, J. B.; Davey, M. P. In *Cell Biology: A Laboratory Handbook*; Celis, J. E., Ed.; Academic Press, San Diego, 1994, pp 380–388.
(31) Griffin, P. R.; Coffman, J. A.; Hood, L. E.; Yates, J. R., III. *Int. J. Mass Spectrom. Ion Processes* **1991**, *111*, 131–149.

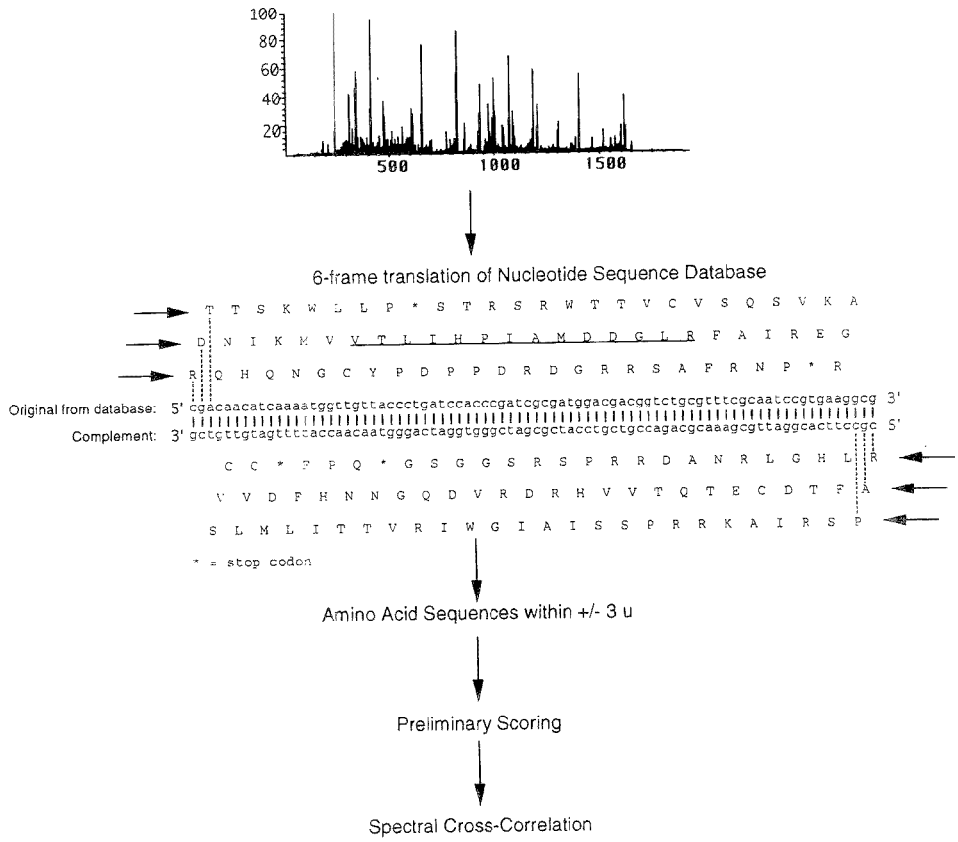

Figure 1. Schematic of the approach used by the computer algorithm to translate nucleotide sequences in six reading frames and to match product ion tandem mass spectra to the translated amino acid sequences.

of the program, the instrument was configured to scan the second mass analyzer (Q_3) from an m/z of 400 to 1400 at 1.5 s/scan. When the ion current for a particular m/z value was above a preset threshold value of 250 000 counts, the program switched the instrument to scan in the product ion MS/MS configuration. The m/z value measured in the main beam mode was used to set the precursor ion m/z value in the first mass analyzer. The mass range was set at 50 u to 2 times the precursor ion m/z value, with a scan time of 1.5 s during acquisition of product ion tandem mass spectra. Five scans were acquired, and the instrument was returned to the main beam mode of scanning. All analyses were performed with the collision cell filled with argon to a pressure of 3.5 mTorr. The collision energy for product ion scans was set by dividing the m/z value of the precursor ion by a constant (−35). This process was repeated throughout the LC analysis.

Computer Analysis of MS/MS Data. All computer algorithms were written in the C-programming language under the UNIX operating system. The European Molecular Biology Laboratory (EMBL) Nucleotide Sequence Database (Release 41, December 1994) was obtained by anonymous ftp from the European Bioinformatics Institute (ftp.ebi.ac.uk). Nucleotide sequence databases were divided by taxonomic classification and used without further subdivision. Spectra of peptides from bovine, *E. coli*, *S. cerevisiae*, and *Homo sapiens* proteins were searched through the "other mammals" (mam.dat, 5965 entries), "prokaryote" (pro.dat, 20 167 entries), "fungi" (fun.dat, 7892 entries), and "primate" (pri.dat, 32 551 entries) nucleotide databases, respectively. To create the "combined" nucleotide database (131 687 entries), the above databases were added to the EST database (65 112 entries) (EMBL).

The OWL database version 24.0 (88 823 entries) was obtained as an ASCII text file in the FASTA format from the National Center for Biotechnology Information (Washington, DC) and has been previously described.[26] Species-specific databases were constructed by selecting protein sequences derived from *H. sapiens* (14 191 entries), bovine (2005 entries), *E. coli* (3856 entries), and *S. cerevisiae* (3870 entries) from the OWL database. The sequence of bovine trypsin was added to each database to screen for autolysis products. Searches were performed on a DecStation 3000/900 Alpha workstation (Maynard, MA). Methods for data reduction, preliminary scoring, and cross-correlation analysis used in the computer algorithm have been described elsewhere.[25,27] Search times ranged according to the following: taxonomic nucleotide database, 40 s to 5 min, combined nucleotide database,

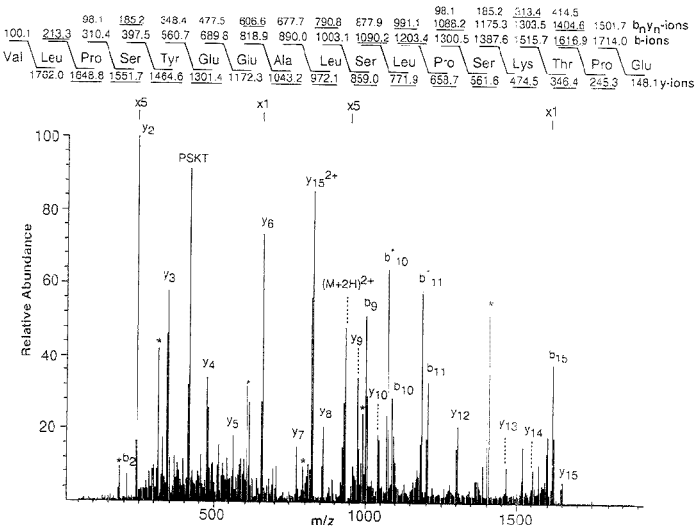

Figure 2. Collision-induced dissociation mass spectrum recorded on the $(M+2H)^{2+}$ ions at *m/z* 931 of a peptide presented by class II major histocompatibility molecules on the surface of EBV cells homozygous for HLA-DRB*0401. Fragments of type b- and y-ions having the general formulas $H(NHCHRCO)_n^-$ and $H_2(NHCHRCO)_nOH^+$, respectively, are shown above and below the amino acid sequence at the top of the Figure. Fragment ions of the type $b_n y_n$ are labeled with an asterisk. Neutral losses of water or ammonia from fragment ions are designated by the ion type and an asterisk, e.g., b_n^*. Ions observed in the spectrum are underlined. Leu and Ile were assigned by correspondence to the sequence derived from the database. The blow up factors in the spectrum refer to regions just to the right of the tick mark and extend to the next tick mark.

8–12 min, combined nucleotide database search with spectra of modified peptides, 40 min to 5 h, and species-specific protein database, 13–25 s.

RESULTS AND DISCUSSION

The objectives of this research were to develop and demonstrate the efficacy of directly searching nucleotide databases with uninterpreted tandem mass spectra of peptides and covalently modified peptides. The intent was to translate nucleotide sequence data in all six reading frames during the course of the search and to consider all translated amino acid sequences within a specified mass tolerance of the search "on the fly". No information on the specificity of enzymatic proteolysis was to be used in the search. In this manner, spectra obtained from incompletely digested peptides or from peptides generated by the use of less specific enzymes, such as chymotrypsin or pepsin, can be used. Additionally, peptides presented by class I and II major histocompatibility molecules or isolated from subcellular vesicles involved in antigen processing pathways can yield peptides produced by proteases of unknown specificity. These studies were designed to evaluate the potential and limitations for directly searching nucleotide databases by using the method of Yates et al.[26] and Eng et al.[27]

The strategy employed in the search is depicted in Figure 1. Spectra are preprocessed for the search and cross-correlation analysis as described previously by Yates et al. and Eng et al.[26,27] Each entry in the database is then read into the program and evaluated in a similar fashion. The nucleotide sequence information is converted to amino acid sequence by translating from the first base of each entry using the standard genetic code.[32] The mass of the corresponding amino acid sequence is summed, and if a sequence is within the mass tolerance of the search (±3 u), this sequence is directed to a preliminary scoring routine and is evaluated as previously described.[25,27] The algorithm then returns to the second nucleotide and repeats the translation and mass calculation. In this manner, a three-frame translation is performed. The complementary strand of the sequence is then predicted and analyzed 5′→3′ in a similar manner to complete the six-frame translation. An obvious result of this process is a large increase in the number of protein sequences that must be evaluated. This in turn results in a significant increase in the number of peptides falling within the mass tolerance of the search and the potential for a decreased signal-to-noise ratio (S/N) in the results.

Shown in Figure 2 is the tandem mass spectrum of the doubly charged ion for the peptide VLPSYEEALSLPSKTPE ($(M + 2H)^{2+}$, *m/z* 931) that is presented by the class II major histocompatibility molecule HLA-DRB*0401. This mass spectrum was used to search the OWL protein database, and no amino acid sequence which fit the spectrum with a ΔC_n value greater than 0.1 was found. A search of a nucleotide database containing primate sequences (32 551 entries) was then performed. A total of 1 931 059 different amino acid sequences were identified to be within the mass tolerance of the search (±3 u) in a process requiring ~3 min of computer time on a DecStation 3000/900. Note that translation of the 32 551 entries into each of the six reading frames increases the total number of entries evaluated to ~195 000. In this case, the exact specificity of the protease used to create the peptide was not known. Thus, all possible linear combinations were evaluated and ranked during the search. The

(32) Watson, J. D.; Tooze, J.; Kurtz, D. T. *Recombinant DNA: A Short Course*; W. H. Freeman and Co.: New York, 1983.

Table 1. Results of Searches of Nucleotide Databases Using the Collision-Induced Dissociation Mass Spectra of Peptides Obtained by Proteolytic Digestion of Proteins[a]

			combined nucleotide			taxonomic nucleotide			species-specific protein		
mass	sequence	description	corr	Sp	ΔC_n	corr	Sp	ΔC_n	corr	Sp	ΔC_n
1480.7	LGEYGFQNALIVR	bovine serum albumin	1	1	0.3452	1	1	0.3452	1	1	0.5211
1267.5	YLGYLEQLLR	bovine α-s1 casein	1	1	0.1695	1	1	0.2682	1	1	0.4359
1957.1	DAIPENLPPLTADFAEDK	bovine serum albumin	1	72	0.1140	1	3	0.1140	1	1	0.4004
1306.5	HLVDEPQNLIK	bovine serum albumin	1	5	0.0831	1	1	0.2553	1	1	0.3177
1551.8	VTLIHPIAMDDGLR, +3	*E. coli* elongation factor TU	1	1	0.0295	1	1	0.1162	1	1	0.1982
1172.4	VGEEVEIVGIK	*E. coli* elongation factor TU	2[b]	14	0.0705	2[b]	3	0.0705	1	1	0.1765
1351.5	LTDDDMTHEGK	*E. coli* hypothetical 8.3 kDa protein in DINF-QOR intergenic region	1	1	0.0462	1	1	0.0916	1	1	0.2003
1993.2	VVTLSGFVESQAQAEEAVK	*E. coli* osmotically inducible protein OSMY precursor	1	1	0.2580	1	1	0.3397	1	1	0.4734
1189.4	RNVIPDPSKY	human asparaginase precursor	1	9	0.1242	1	2	0.1628	1	1	0.2264
1695.5	KIHGRVGDSPIPGAGAY	human asparaginase precursor	1	2	0.2563	1	1	0.3655	1	1	0.4181
1476.6	WELLQQVDTSTR	human keratin	1	1	0.2356	1	1	0.2086	1	1	0.2808
1278.5	LALDIEIATYR	human keratin	1	2	0.2390	1	1	0.2960	1	1	0.3050
1572.8	IDDLIHEIITVGPH	yeast ribosomal protein	1	1	0.3218	1	1	0.4720	1	1	0.4844
1014.2	ANELLINVK	yeast alcohol dehydrogenase	1	22	0.0398	1	6	0.0917	1	3	0.2156
1313.5	SIGGEVFIDFTK	yeast alcohol dehydrogenase	1	1	0.1052	1	1	0.1052	1	1	0.3102
1232.4	TGGGASLELLEGK	yeast phosphoglycerate kinase	1	1	0.1036	1	1	0.2750	1	1	0.2990
1861.1	VLPSYEEALSLPSKTPE	human mRNA for ORF	1	1	0.1163	1	1	0.1163			
1762.0	LPSYEEALSLPSKTPE	human mRNA for ORF	1	5	0.1477	1	1	0.1428			
1632.8	LPSYEEALSLPSKTP	human mRNA for ORF	1	1	0.1659	1	1	0.1666			

[a] All spectra were acquired under electrospray ionization conditions. Charge state of the ion used in the MS/MS experiment is listed along with the protein description if it was other than +2. The designation C_n refers to rankings of the correct amino acid sequences by normalized correlation parameters. These rankings are provided for searches of a combined nucleotide database, a taxonomic nucleotide sequence database, and through a species-specific protein sequence database. The mass tolerance used in the searches was ±3 u. Fragment ion mass tolerance was ±1 u. [b] VGQEVEIVG(I/L)K ranked 1st.

sequence of the peptide represented in the tandem mass spectrum displayed in Figure 2 was found to be from a human mRNA for an open reading frame (ORF). A similarity search of this sequence with others in the database was performed using the program BLAST.[33] This program aligns the query sequence to others in the database to identify similar amino acid sequences in an attempt to identify similarity to a protein with a known function. Sequence similarity was observed to an immunoglobulin heavy chain from *Xenopus laevis*. Two other tandem mass spectra obtained from the same LC/MS/MS analysis were also matched from the same region of the human mRNA ORF (Table 1, last two entries). The ability to search the nucleotide database directly provided interpretation of these spectra without the necessity of having to perform manual analysis. The translation of this ORF eventually appeared in a later version of the genpept protein sequence database (version 87.0, 2/17/95), but the ability to search the nucleotide database provided analysis of the MS/MS data before the translated sequence appeared in a protein database.

The results for additional searches of the nucleotide database are shown in Table 1. Under the column heading "combined" are the results obtained for searches using the combined nucleotide database of 131 687 entries. Upon translation, an approximate total of 790 000 entries are evaluated. All but one of the searches displayed in Table 1 identified the correct amino acid sequence. The one false positive, VGQEVENGI/LK, resulted in the identification of an amino acid sequence with a one amino acid change in the third position of the correct sequence. In this position, Gln is substituted for Glu, an amino acid change which is consistent with the mass tolerance used for the search. For comparative purposes, the results of searches through taxonomic nucleotide databases and species-specific subsets of the OWL database (protein sequences) are also shown. The ranks of the correct amino acid sequences of the peptides represented by their tandem mass spectra are shown in the Table. In addition, the ΔC_n values for each search are shown along with the rank of the sequence as determined by the preliminary scoring routine.

The analysis of cDNA sequences has become an important component of genome research and gene expression studies. These sequences are generally obtained by automated single pass sequencing and result in higher average error rates (~3%). A detailed study of the type of errors observed in automated single pass sequencing has been performed by Koop et al.[34] Over the first 350–400 nucleotides, errors are less than 1% and then begin to increase from 400 to 650 nucleotides. For 0–400 nucleotides, the most common error is ambiguity in the nucleotide identification. Beyond 400 nucleotides, errors caused by deletions and insertions predominate. The presence of these types of errors in sequences submitted to databases depends on the confidence of the investigators in the late sequence calls and ultimately where the submitted sequence is terminated. The matching of a tandem mass spectrum to a sequence depends on matches to a correct local sequence rather than to a correct contiguous translation. Only one or two exact matches are necessary to make an identification (certainty increases with the number of matches). The nucleotide sequence of bovine serum albumin was utilized to test the ability to match tandem mass spectra to the translated sequence when nucleotide ambiguities of 1% are randomly placed in the nucleotide sequence. Figure 3A shows partial nucleotide sequence of bovine serum albumin and the six-reading-frame

(33) Altschul, S. F.; Gish, W.; Miller, W.; Myers, E. W.; Lipman, D. J. *J. Mol. Biol.* **1990**, *215*, 403–410.

(34) Koop, B. F.; Rowan, L.; Chen, W.-Q.; Deshpande, P.; Lee, H.; Hood, L. *Biotechniques* **1993**, *14*, 442–447.

A.

```
...aaagtccacaaggaatgctgccatggtgacctacttgaatgcgcagatgacagggcagatcttgccaagtacatatgtga
taatcaagatacaatctccagtaaactgaaggaatgctgtgataagcctttgttggaaaaatcccactgcattgctgaggtag
aaaaagatgccatacctgaaaacctgccccattaactgctgactttgctgaagataaggatgtttgcaaaaactat...
```

Results of Translation of the Above Nucleotide Sequence in 6 reading frames:

```
f 0:  ...KVHKECCHGDLLECADDRADLAKYICDNQDTISSKLKECCDKPLLEKSHCIAEVEKDAIPENLPPLTADFAEDKDVCKNY...
f 1:  ...KSTRNAAMVTYLNAQMTGQILPSTYVIIKIQSPVN*RNAVISLCWKNPTALLR*KKMPYLKTCPH*LLTLLKIRMFAKT...
f 2:  ...SPQGMLPW*PT*MRR*QGRSCQVHM**SRYNLQ*TEGML**AFVGKIPLHC*GRKRCHT*KPAPINC*LC*R*GCLQKL...
r 0:  ...IVFANILIFSKVSS*WGQVFRYGIFFYLSNAVGFFQQRLITAFLQFTGDCILIITYVLGKICPVICAFK*VTMAAFLVDF...
r 1:  ...*FLQTSLSSAKSAVNGGRFSGMASFSTSAMQWDFSNKGLSQHSFSLLEIVS*LSHMYLARSALSSAHSSRSPWQHSLWT...
r 2:  ...SFCKHPYLQQSQQLMGAGFQVWHLFLPQQCSGIFPTKAYHSIPSVYWRLYLDYHICTWQDLPCHLRIQVGHHGSIPCGL...

* = stop codon or unrecognized base pair
```

B.

```
...aaagtccacanggaatgctgccatggngacctacttgaatgcgcagatgacagggcagatcntgccaagtacatatgtga
taatcaagatacaatctccagtaaactgaaggaatgctgtgataagcctttgttggaaaaatcccactgcattgctgaggtag
aaaangatgccatacctgaaaacctgcccccatnaactgctgactttgctgaagataaggatntttgcaaaaacnat...
```

Results of Translation of the Above Nucleotide Sequence in 6 reading frames:

```
f 0:  ...KVH*ECCHGDLLECADDRAD*AKYICDNQDTISSKLKECCDKPLLEKSHCIAEVE*DAIPENLPP*TADFAEDKD*CKN*...
f 1:  ...KST*NAAM*TYLNAQMTGQI*PSTYVIIKIQSPVN*RNAVISLCWKNPTALLR*K*MPYLKTCPH*LLTLLKIR*FAKT...
f 2:  ...SP*GMLPW*PT*MRR*QGRSCQVHM**SRYNLQ*TEGML**AFVGKIPLHC*GRK*CHT*KPAP*NC*LC*R*G*LQK*...
f 0:  ...*VFA*ILIFSKVSS*WGQVFRYGI*FYLSNAVGFFQQRLITAFLQFTGDCILIITYVLG*ICPVICAFK*V*MAAF*VDF...
f 1:  ...*FLQ*SLSSAKSAV*GGRFSGMASFSTSAMQWDFSNKGLSQHSFSLLEIVS*LSHMYLA*SALSSAHSSRSPWQHS*WT...
f 2:  ...*FCK*PYLQQSQQ*MGAGFQVWH*FLPQQCSGIFPTKAYHSIPSVYWRLYLDYHICTW*DLPCHLRIQVG*HGSIPCGL...

* = stop codon or unrecognized base pair
```

Figure 3. (A) The partial nucleotide sequence for bovine serum albumin and the six-reading-frame translation to the protein sequence. The amino acid sequences underlined were matched by tandem mass spectra in a single reading frame. An asterisk indicates the presence of a stop codon. (B) The partial nucleotide sequence for bovine serum albumin with errors introduced and the six-reading-frame translation. The amino acid sequences underlined were matched by tandem mass spectra. The letters f and r indicate the translation is in the forward or reverse (complementary strand) 5′ → 3′ direction, and the number indicates the reading frame. An asterisk indicates the presence of a stop codon, and an n represents an ambiguous nucleotide identification.

translation of the sequence. A total of 26 tandem mass spectra were used to search this sequence, and all were placed within the correct reading frame (data not shown). The placement of three spectra is shown in Figure 3A. Figure 3B shows the partial nucleotide sequence after the random introduction of nucleotide ambiguities, signified by the letter n, at a level of 1%. The amino acid sequences for which tandem mass spectra were matched in this region are underlined. A total of 19 of the 26 (~75%) tandem mass spectra were placed within the sequence (data not shown). The same level of success is observed when all types of errors are randomly placed in the sequence at the same rate. Insertion and deletion errors change the amino acid sequence in the correct reading frame (f 0), but spectra are matched to correct translations that appear in the other reading frames. By using multiple spectra in the search, the probability of matching spectra to the translated sequence of nucleotide sequences containing errors increases. If the entire sequence is correct, all spectra should be placed within the same reading frame; consequently, this may be a useful technique for identifying errors in nucleotide sequences.

We had observed previously that the magnitude of the difference in the normalized correlation values, ΔC_n, for the first and second answers provided a general indication of a correct answer.[27] In Figure 4, a plot of the ΔC_n values obtained for each spectrum used to search the combined, taxonomic, and protein (species-specific OWL) databases is presented. As the number of entries and the number of sequences considered increases, the ΔC_n values decrease. For example, the mass of the first entry in Table 1 matches 6 543 609, 442 872, and 27 291 amino acid sequences through the combined, taxonomic, and species-specific (protein) databases, respectively. Intuitively, a general decrease in the ΔC_n value is to be expected, since an increase in the number of sequences evaluated raises the likelihood of identifying amino acid sequences that produce similar fragmentation patterns. The general trend observed by Eng et al., that a difference in value between the first and second answers of 0.1 or greater is indicative of a correct answer, is generally true for searches through the nucleotide databases.[27] This trend does not hold when two highly similar sequences appear in the first two positions (sixth entry,

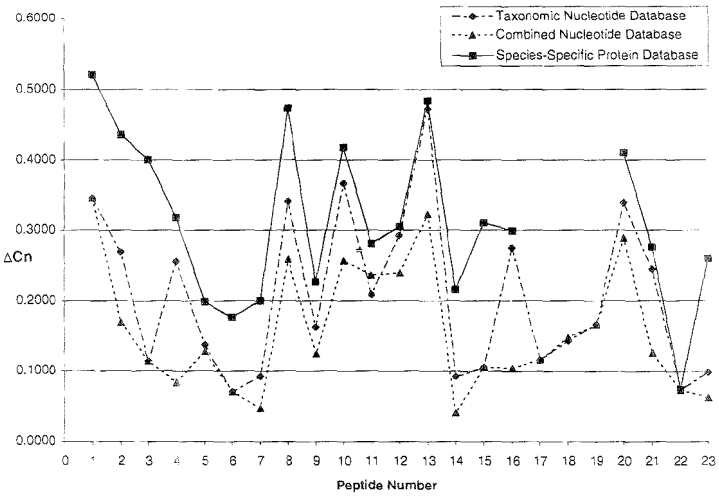

Figure 4. Plot of ΔC_n values obtained for each of the spectra used in searches of the combined and taxonomic nucleotide databases and the species-specific protein database. The peptide numbers refer to the order of appearance of the spectra in Tables 1 and 2.

Table 2. Results of Searches of Nucleotide Databases Using the Collision-Induced Dissociation Mass Spectra of Modified Peptides Obtained by Proteolytic Digestion of Proteins of Known Sequence

			combined nucleotide			taxonomic nucleotide			species-specific protein		
mass	sequence	description	corr	Sp	ΔC_n	corr	Sp	ΔC_n	corr	Sp	ΔC_n
1701.9	FLDDDLTDDIM**C**VK	bovine α-lactalbumin	1	1	0.2881	1	1	0.3382	1	1	0.4100
1445.5	Y**I**C**D**NQDTISSK	bovine serum albumin	1	1	0.1251	1	1	0.2441	1	1	0.2761
1928.8	D**T**G**S**E**S**TEDQAMEDIK	bovine α-s1 casein	1	4	0.0725	1	4	0.0725	1	1	0.0725
1660.8	VPQ**L**E**T**VPN**S**AEER	bovine α-s1 casein	1	28	0.0628	1	2	0.0981	1	1	0.2604

[a] In the course of the search, each putative site of modification is considered as modified and unmodified. The top two sequences were considered as having a single site of modification at Cys. The bottom two sequences were considered as being phosphorylated; consequently, each potential phosphorylation site (Ser, Thr, Tyr) is evaluated. All spectra were acquired under electrospray ionization conditions. Charge state of the ion used in the MS/MS experiment is listed along with the protein description if it was other than +2. The designation C_n refers to rankings of the correct amino acid sequences by normalized correlation parameters. These rankings are provided for searches of a combined nucleotide database (131 687 entries), a taxonomic nucleotide sequence database (other mammals, 5965 entries), and through a species-specific protein sequence database (bovine, 2005 proteins). The mass tolerance used in the searches was ±3 u. Fragment ion mass tolerance was ±1 u. Modification sites localized to particular residues are in bold and underscored typeface to indicate the site.

Table 1). Nor does it hold when searches using spectra of modified peptides containing multiple potential sites of modification are performed (third entry, Table 2).[26] In this case, variations in the site of modification can appear in the top answers. The ΔC_n values for the top answer and the first unrelated sequence generally exhibit the 0.1 difference.

A unique feature of this search method is a scoring technique that uses a comparison of the similarity of a theoretical tandem mass spectrum reconstructed from the amino acid sequences retrieved from the database and the query spectrum. In efforts to study the effectiveness of this method of evaluation, and to identify areas for improvement, the cross-correlation values obtained in searches using experimental spectra were compared with those from searches with theoretical "spectra" created by using the reconstruction method. The reconstructed tandem mass spectra would serve as theoretically perfect spectra and should result in the highest possible spectral similarity. Reconstructed spectra were prepared for each sequence shown in Tables 1 and 2. The ΔC_n and cross-correlation values for each spectral search through the taxonomic nucleotide and protein-species databases were plotted as shown in Figures 5 and 6, respectively. Both comparisons illustrate that scoring is significantly improved by using a spectrum for the cross-correlation comparison that more closely matches the query spectrum. Thus, the development of theoretical models which allow prediction of fragment ion abundance for a given sequence would result in an improved reconstruction method and better absolute and normalized scores.

Searches of Nucleotide Databases with Spectra of Modified Peptides. Recent work has shown the ability to match the tandem mass spectra of covalently modified peptides and to identify the site of modification of sequences in protein databases even though information about modification sites is not contained in the sequences.[26] This method uses mass values of both the modified and the unmodified amino acid. Rather than consider universal modification of specific amino acids and the resulting mass changes that occur at every occurrence of the amino acid, the method of Yates et al. considers the possibility at each occurrence of the amino acid, modified or not.[26] Thus, a sequence containing one putative modification site is considered as modified and unmodified, for a total of two different sequences considered.

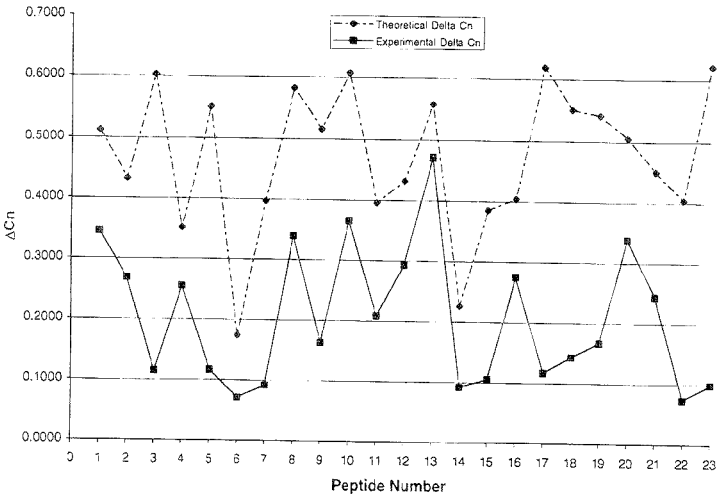

Figure 5. Plot of the differences of the normalized cross-correlation values between the first and second results obtained for searches using experimental and theoretical CID spectra. The theoretical CID spectra produce a maximum cross-correlation value for a given amino acid sequence. The peptide numbers refer to the order of appearance of the spectra in Tables 1 and 2.

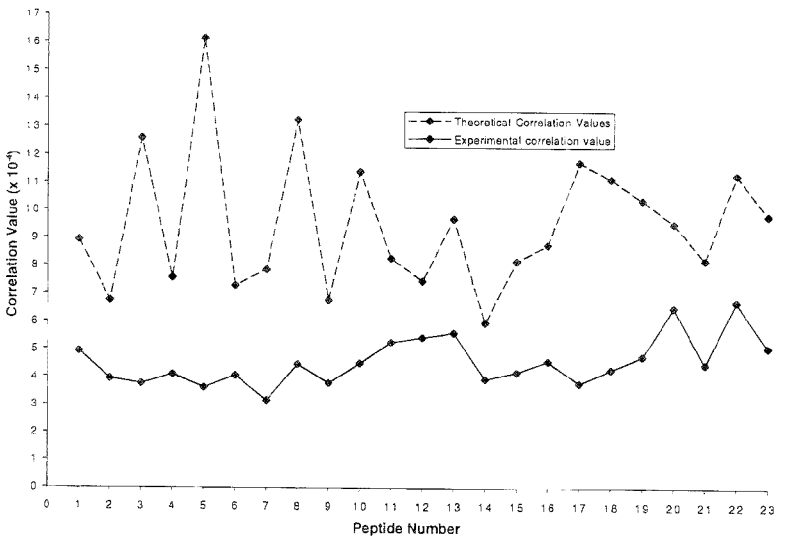

Figure 6. Plot of the absolute cross-correlation values obtained for searches using experimental and theoretical CID spectra. The theoretical CID spectra produce a maximum absolute correlation value for a given amino acid sequence since it is primarily correlated with itself. The peptide numbers refer to the order of appearance of the spectra in Tables 1 and 2.

The number of different sequences to examine varies by 2^n, where n is the number of potential modification sites in each peptide. By employing a mass tolerance, only those modified or unmodified sequences which fall within that range are considered further, and the total number of sequences that must be considered is limited. These studies are meant to examine the sensitivity and the corresponding time constraints when searching nucleotide databases with spectra of modified peptides.

Shown in Table 2 are the results for searches of singly modified peptides. To illustrate the analysis, S-carboxymethylated Cys-containing peptides are used as models. The search considers only a single type of modification. In the course of the search, 10 613 705 amino acid sequences were found to be within ±3 u of the mass 1703 u. The correct result, FLDDDLTDDIMCVK, is identified with a ΔC_n value of 0.2881. This search required slightly over 30 min of computer time through the combined nucleotide database.

Shown in Table 2 are the results of searches using spectra of phosphorylated peptides. The search considers potential phosphorylation at each occurrence of Ser, Thr, and Tyr, as well as

the possibility of multiple phosphorylation sites. No information such as the number of modifications to expect in the sequence is given to the program. Searches using spectra from two different phosphorylated peptides are shown. The correct answer is found in both searches. The first contains three potential sites of phosphorylation and two actual sites of modification. The ΔC_n value for the search is well below the acceptable cutoff of 0.1. The top three results, however, are for the same sequence with different sites of modification. This result is consistent with that observed in searches of protein databases.[26] The search of the combined nucleotide database requires a large amount of computer time, approximately 5 h, as opposed to a search of the taxonomic database (~20 min). The method involving translation in all six reading frames and considering all possible variations of phosphorylation generates a large number of sequences to evaluate. During the search, 102 012 392 different amino acid sequences within the ±3 u mass tolerance of the search were considered. Thus, the search correctly identifies to 1 in 100 million the right sequence and the sites of modification. Even though a molecular weight mass tolerance of ±3 u is used in the course of the search, the accuracy is remarkably good. By decreasing the mass tolerance, the number of amino acid sequences considered is decreased, thereby shortening search times, but not greatly so. The accuracy, however, is not significantly improved.

CONCLUSION

The objective of this research was to develop and test methods to match the tandem mass spectra of modified and unmodified peptides to their corresponding translated nucleotide sequences in the database. The results presented demonstrate that a direct search is possible and is quite accurate even though there is a large increase in the number of amino acid sequences considered in the course of the search. By increasing the number of amino acid sequences considered, the S/N of the search result decreases, but not to a level where results are unreliable. As the database grows in size, the S/N is likely to decrease further, thus additional study to improve the scoring procedure is warranted. The studies of the search method using theoretical query spectra suggest approaches that can be used to improve scoring methods. By developing more effective methods to accurately reconstruct a tandem mass spectrum for a given amino acid sequence, such as better methods to predict the likely abundances of fragment ions, a stronger correlation between experimental and reconstructed spectra could be obtained. At present, the scoring routine is very effective in finding the correct answer and in providing a parameter (ΔC_n) to determine if the answer is correct or a false positive.

The approach described in this paper is ideal for automation of data analysis since no preanalysis of the spectra is required of the investigator. As currently implemented, all tandem mass spectra placed in the analysis directory are batch processed by the program. A search with a spectrum of an unmodified peptide is sufficiently fast through a large nucleotide database as to limit concern about efficiency and throughput. A batch search to identify phosphorylated peptides of all the spectra obtained during an LC/MS/MS analysis through a large nucleotide database would not be practical at this point in time. A more efficient strategy would be to perform a search for nonmodified sequences to identify a likely gene sequence and then to perform modification searches on the nucleotide sequence for that gene.

Incorporating this approach with those of Eng et al.[27] and Yates et al.[26] permits the creation of automated methods to match spectra of peptides directly to protein and nucleotide sequences. Such a strategy has applications in the automated identification of proteins separated by two-dimensional gel electrophoresis. This separation technique allows the parallel isolation of 1–3000 proteins in a single analysis. By utilizing autosampling techniques in conjunction with HPLC and data-dependent acquisition of tandem mass spectra, large numbers of samples could be automatically processed. The methods described in this paper and others present a powerful strategy to automate data analysis of the large numbers of spectra acquired.[26,27] This will provide an important tool to integrate data obtained from cDNA and genomic sequencing projects with biochemical studies.

ACKNOWLEDGMENT

This work was supported by the University of Washington's Research Royalty Fund. Partial support was received from the National Science Foundation, Science and Technology Center (DIR 8809710), NIH (GM52095), and Digital Equipment Corp.

Received for review April 17, 1995. Accepted June 27, 1995.[⊗]

AC950371B

[⊗] Abstract published in *Advance ACS Abstracts*, August 1, 1995.

Anal. Chem. 1995, *67*, 3211–3218

Capillary Electrophoretic Enzyme Immunoassay for Digoxin in Human Serum

Xuhui Liu and Yan Xu*

Department of Chemistry, Cleveland State University, Cleveland, Ohio 44115

Michael P. C. Ip

Department of Pathology, MetroHealth Medical Center, Cleveland, Ohio 44109

The combined use of capillary electrophoretic (CE) separation and homogeneous enzyme immunoassay for analyzing drugs in hemolyzed, lipemic, or icteric serum samples was investigated. An FDA-approved EMIT assay kit for digoxin in human serum was used. After the enzyme immunoassay, the enzymatic reaction product (NADH) and remaining substrate (NAD^+), together with internal standard (*p*-nitrophenol, NP), were electrokinetically injected into a polyacrylamide-coated electrophoresis capillary and separated under applied potential. Detection was made by monitoring the UV adsorption at wavelength of 260 nm. The digoxin level in human serum was determined by comparing the peak area ratio of NADH and NP to the ratios established by the known digoxin standards. In this study, the factors that influence the CE separation were also investigated. Under the optimum conditions, NADH, NAD^+, and NP were separated at electric field strength of 438 V/cm in the coated capillary (100 μm × 57 cm) with 200 mM Tris–borate buffer (pH 7.9) containing 0.2% hydroxypropyl methylcellulose. CE analyses of serum samples spiked with NADH standards at concentrations of 100 and 400 μM resulted in detection variabilities of less than 2% and analytical recoveries of 98–102%. Both an internal calibration plot for NADH and a dose–response curve for digoxin in serum were constructed. Calibrator serum, patients' sera with hemolyzed, lipemic, and icteric interference factors, and other pigmented blood components (e.g., serum albumin, bilirubin, hemoglobin, uric acid, coproporphyrin, melanin, protoporphyrin IX, and uroprophyrin) demonstrated no interference in this method. The authors believed that this method is useful for analyzing digoxin in hemolyzed, lipemic, and icteric blood samples that are known to create problems in conventional EMIT assays and may be applicable to other EMIT-based assays for monitoring drugs in complex biological matrices.

Since its advent in the late 1950s,[1,2] immunoassay has become a primary analytical tool not just in clinical diagnostics but also in many other applied scientific fields such as food and environmental analyses.[3] The methodology is mainly based on the inherent chemical specificity of an immunological reaction and the exquisite sensitivity in detecting labeled antigens or labeled antibodies, which allow fast, accurate, and precise quantitation of a variety of analytes at very low concentrations in complex sample matrices.

Quantitation of an immunological reaction often uses label molecules. Immunolabels can be divided into two classes: isotopic and nonisotopic. Most early immunoassays used isotopic labels such as ^{125}I, ^{57}Co, ^{3}H, ^{14}C, and ^{32}P. Due to health and environmental concerns, nonisotopic labels have become more widely used in immunoassays.[4–6] The nonisotopic labels include enzymes, chemiluminescence and bioluminescence compounds, metal complexes, and electrochemically active molecules. In the case of enzyme immunoassay, the enzyme molecule is used as the label that converts enzyme substrate into its product at a relatively high reaction rate. As the result of enzyme amplification, a significant amount of product can be produced for final detection. Therefore, assays that use enzymes as labels usually have excellent limits of detection.

One of the assay formats used frequently in therapeutic drug monitoring is known as the homogeneous enzyme immunoassay. It requires minimum sample handling and is well suited for measuring low molecular weight molecules in a concentration range of micrograms to milligrams per liter. The principle of homogeneous enzyme immunoassay can be illustrated by the technique known as the "enzyme-multiplied immunoassay technique" (EMIT), which is based on the competition between antigen in the sample and enzyme-labeled antigen for limited antibody-binding sites. Upon binding of enzyme-labeled antigen to the antibody, enzyme activity is inhibited or altered through steric exclusion of the enzyme substrate or conformational change of enzyme molecule,[7] so the antigen concentration in the sample can be measured in terms of enzyme activity.

One of the challenges in developing homogeneous enzyme immunoassays is to detect the enzyme product in whole blood or in samples that are hemolyzed, lipemic, and icteric.[8] Previous

(1) Berson, S. A.; Yalow, R. S.; Bauman, A.; Rothschild, M. A.; Newerly, K. *J. Clin. Invest.* **1956**, *35*, 170–90.
(2) Yalow, R. S.; Berson, S. A. *Nature* **1959**, *184*, 1648–9.
(3) Van Emon, J. M.; Lopez-Avila, V. *Anal. Chem.* **1992**, *64*, 79A-88A.
(4) Petterson, K. *Clin. Chem.* **1993**, *39*, 1359–60.
(5) Kricka, L. J. *Clin. Chem.* **1994**, *40*, 347–57.
(6) Xu, Y.; Halsall, H. B.; Heineman, W. R. In *Immunochemical Assays and Biosensor Technology for the 1990s*; Nakamura, R. M., Kasahara, Y., Rechnitz, G. A., Eds.; American Society for Microbiology: Washington, DC, 1992; pp 291–309.
(7) Schuurs, A. H. W. M.; Van Weemen, B. K. *Clin. Chim. Acta* **1977**, *81*, 1–40.
(8) Thompson, S. G. In *Clinical Chemistry*; Kaplan, L. A., Pesce, A. J., Eds.; The C. V. Mosby Co.: St. Louis, MO, 1989; pp 191–206.

0003-2700/95/0367-3211$9.00/0

efforts[9,10] have been made by using chromatographic separation with amperometric detection. In spite of the achievements in circumventing the matrix effect of biological samples, the method required a switching between size exclusion and reversed-phase columns. Therefore, it complicated the routine operation.

Recent advances in capillary electrophoresis (CE)[11,12] allow the separation of both charged and neutral molecules with very high efficiencies. Several studies[13-15] have demonstrated the applicability of capillary electrophoresis for separation of antibody–antigen complexes from unbound antibodies and antigens by direct injection of reaction mixtures into the separation capillaries. With laser-induced fluorescence detection, both Schultz and Kennedy and Chen and Sternberg were able to achieve the detection limits needed for monitoring insulin[14] and digoxin[15] in the therapeutic ranges. However, the direct injection of protein mixture onto the separation capillary often caused adsorption on the inner surface of the capillary, which affects the reproducibility of the methods and seriously compromises their reliability in quantitative analysis.

The present study was aimed at coupling CE with homogeneous enzyme immunoassay for quantitative analyses of drugs or drug metabolites in hemolyzed, lipemic, or icteric serum samples. Digoxin, a widely used cardiac active drug for treatment of heart failure, atrial fibrillation, and supraventricular tachyarrhythmias was chosen as the model analyte. Because of its narrow therapeutic range (0.5–2.0 μg/L),[16] it is clinically important to precisely monitor its level in sera. In our study, an FDA-approved EMIT assay kit for digoxin was used. After the enzyme immunoassay, the product of enzymatic reaction (NADH), together with the remaining substrate (NAD^+) and an internal standard (*p*-nitrophenol, NP), was electrokinetically injected into a capillary and separated by CE. Detection was accomplished by monitoring UV absorbance at a wavelength of 260 nm. The digoxin concentration in human serum was determined by measuring the peak area ratio of NADH and NP using internal calibration. The factors that influence CE separation in both coated and uncoated capillaries were also investigated and compared. Calibrator serum, patients' sera containing hemolyzed, lipemic, and icteric interfering factors, and other blood components were tested and showed no interference in this method. The authors believe that this approach is valuable for quantitation of drug molecules in complex biological matrices.

EXPERIMENTAL SECTION

Reagents. The EMIT digoxin assay kit (Lot 6H419UL-F1) was obtained from Syva Co. (San Jose, CA), which consisted of reagent A, reagent B, serum pretreatment reagent, buffer concentrate, and digoxin calibrators. β-Nicotinamide adenine dinucleotide (NAD^+), reduced β-nicotinamide adenine dinucleotide (NADH), and calibrator serum and diluent (Catalog No. 620213) were purchased from Boehringer Mannheim Corp. (Indianapolis, IN). *p*-Nitrophenol, bovine albumin, human hemoglobin, proptoporphyrin IX, coproporphyrin, uroprophyrin, and melanin were purchased from Sigma Chemical Co. (St. Louis, MO). Hydroxypropyl methyl cellulose (HPMC) was a product of Fluka Chemical (Ronkonkoma, NY). Bilirubin was obtained from the Hartman-Leddon Co. (Philadelphia, PA). Bovine hemoglobin (Certain tHb level 2) was from Ciba-Corning Diagnostics (Medfield, MA). Uric acid was from Mallinckrodt Chemical Works (St. Louis, MO). γ-(Methacryloyloxy)propyltrimethoxysilane (bind-silane), ammonium persulfate, *N,N,N′,N′*-tetramethylethylenediamine (TEMED), and acrylamide were obtained from Pharmacia Biotech (Piscataway, NJ). All other reagents were of analytical grade or better and purchased from standard reagent suppliers.

Aqueous solutions were prepared with deionized water (Barnstead NANOpure system, Boston, MA). Phosphate run buffers (11.5 mM) with pH values between 6.5 and 8.1 were prepared by dissolving the appropriate amount of disodium hydrogen phosphate and sodium dihydrogen phosphate in deionized water. All buffers were filtered through 0.45-μm cellulose acetate membrane filters (Alltech Associates, Inc., Deerfield, IL) before use. Tris–borate buffers (200 mM) with pH values between 7.2 and 8.0 were prepared by mixing appropriate amounts of tris(hydroxymethyl)-aminomethane and boric acid in 250.00 mL of deionized water. Tris–borate/HPMC buffer was prepared by dissolving 0.2% (w/w) of hydroxypropyl methyl cellulose (0.2 g) in 100.00 mL of the Tris–borate buffer at the specified pH value. This solution was sonicated for 15 min to allow complete wetting of hydroxypropyl methyl cellulose and then stirred in an ice bath until it clarified. Filtration was performed using a 0.8 μm cellulose acetate membrane filter (Alltech Associates, Inc.). NADH, NAD^+, and NP standard solutions were prepared in 20 mM Tris-HCl buffer (pH 7.4). All buffers and solutions were stored at 4 °C until use.

Serum Samples. Hemolyzed, lipemic, and icteric serum samples used in the interference study were obtained from Metro-Health Medical Center (Cleveland, OH). Universal infectious precautions were followed during the handling of these specimens.

Analyses. The EMIT digoxin assay is a homogeneous enzyme immunoassay. The assay procedure as described by Syva Co. was followed until the conversion of NAD^+ to NADH by glucose-6-phosphate dehydrogenase (G6PDH). The reaction mixture was separated by CE after the addition of NP (1.1 mM) as internal standard. Compared to the EMIT procedure, this method used only one-fifth of the reagents and sample volumes for each analysis. The volume of reaction mixture used in the CE separation can be further reduced to one-thirtieth of that of the EMIT procedure if a pipeting device with good precision is used.

Capillary Columns. The fused-silica capillaries (360-μm o.d.) was purchased from Polymicro Technologies Inc. (Pheonix, AZ). The uncoated capillary was 57 cm in length (50 cm to detection window) with 75-μm i.d. This capillary was mounted in a P/ACE cartridge that was connected to a temperature control system. New capillaries were conditioned by rinsing sequentially with 0.1 M NaOH, deionized water, and phosphate run buffer before use.

Polyacrylamide-coated capillary was prepared from the uncoated capillary with 100-μm i.d. as described below. The inner surface of a 1-m-long capillary was first pretreated with 1 M NaOH for 30 min and then flushed with H_2O for 30 min. The pretreated capillary was rinsed with a silane solution (pH 3.5) for 3 h at room temperature. The silane solution was prepared by adding 50 μL of acetic acid (glacial) and 50 μL of γ-(methacryloyloxy)propylt-

(9) Eggers, H. M.; Halsall, H. B.; Heineman, W. R. *Clin. Chem.* **1982**, *28*, 1848–51.
(10) Wright, D. S.; Halsall, H. B.; Heineman, W. R. *Anal. Chem.* **1986**, *58*, 2995–8.
(11) Xu, Y. *Anal. Chem.* **1993**, *65*, 425R–33R.
(12) Monnig, C. A.; Kennedy, R. T. *Anal. Chem.* **1994**, *66*, 280R–314R.
(13) Nielsen, R. G.; Rickard, E. C.; Santa, P. F.; Sharknas, D. A.; Sittampalam, G. S. *J. Chromatogr.* **1991**, *539*, 177–85.
(14) Schultz, N. M.; Kennedy, R. T. *Anal. Chem.* **1993**, *65*, 3161–5.
(15) Chen, F. T. A.; Sternberg, J. C. *Electrophoresis* **1994**, *15*, 13–21.
(16) Chen, I. W. In *Clinical Chemistry*; Kaplan, L. A., Pesce, A. J., Eds.; The C. V. Mosby Co.: St. Louis, MO, 1989; pp 1088–91.

rimethoxysilane to 9.90 mL of H_2O; the resultant mixture was stirred until it clarified (~15 min). After sequentially washing with methanol and H_2O, the capillary was blown dry with N_2. A monomer solution was prepared by dissolving 0.4 g of acrylamide in 10 mL of deaerated Tris–borate buffer (200 mM), followed by addition of 100 μL of 10% freshly prepared ammonium persulfate and 10 μL of TEMED. This solution was then pushed through the silanized capillary for 1 h using a N_2-pressurized capillary wash tube (Alltech Associates, Inc.). After polymerization, the capillary was flushed with H_2O and ready for use. This procedure produces a bonded layer of linear polyacrylamide (non-cross-linked) on the inner surface. The on-column detection window was generated by either razor pilling or etching with a drop of hot (~130 °C), concentrated (96–98%) sulfuric acid to remove a small section of polyimide coating on the outside of the capillary. If sulfuric acid is used, it should be applied using the tip of a mercury thermometer as it retains heat longer.

Capillary Electrophoresis with UV Detection. A Beckman (Fullerton, CA) P/ACE 2050 system and an IBM personal computer with System Gold software were used. On-column UV detection was performed at 260 nm, and the separation temperature was maintained at 25 °C. Samples were introduced into the capillary by electrokinetic injection at 5 kV for 3 s. The optimal conditions of electrophoretic separation were 20 kV/34 μA at pH 8.0 in the phosphate run buffer using uncoated fused-silica capillary and 25 kV/27 μA at pH 7.9 in the Tris–borate/HPMC buffer using polyacrylamide-coated capillary. Between runs, the capillary was rinsed by run buffer for 2 min. If uncoated capillary was used, the cathode was placed in the outlet side of the capillary and the anode was in the inlet. If coated capillary was used, the polarity of the electrodes was reversed.

RESULTS AND DISCUSSION

NADH and NAD^+ Separation. In homogeneous enzyme immunoassay for digoxin, the active glucose-6-phosphate dehydrogenase simultaneously converts glucose 6-phosphate (the substrate) to glucono-δ-lactone 6-phosphate and NAD^+ (the coenzyme) to NADH. The amount of NADH formed is proportional to the digoxin level in the sample. Resolving of NADH from NAD^+ and other potential interferents is critical to the quantitative measurement of digoxin. Figure 1 shows the separations of NAD^+, NADH, and NP (internal standard) in both coated (A) and uncoated (B) capillaries. In both cases, NAD^+, NADH, and NP were completely resolved within 8 min. Peak identities were tentatively assigned on comparison to the electropherograms generated by single components and subsequently confirmed through stepwise addition of known components to the mixture. The small unidentified peak close to the NADH peak was probably associated with the impurity found in the NADH preparation. Due to the suppression of electroosmotic flow, only electrophoretic migration existed in the coated capillary. Accordingly, NADH (net charges of 2−) migrated toward the anode (outlet) at a faster rate relative to NAD^+ (net charge of 1−) (Figure 1A). In the uncoated capillary, the electroosmotic mobility was greater than the electrophoretic mobilities of NADH and NAD^+. As the result of combination of two opposite forces, NADH migrated slower toward the cathode (outlet) compared to NAD^+ (Figure 1B). The migration rate of the internal standard (NP) pK_a of 7.15 at 25 °C, may be modulated by adjusting the buffer pH (Figure 2).

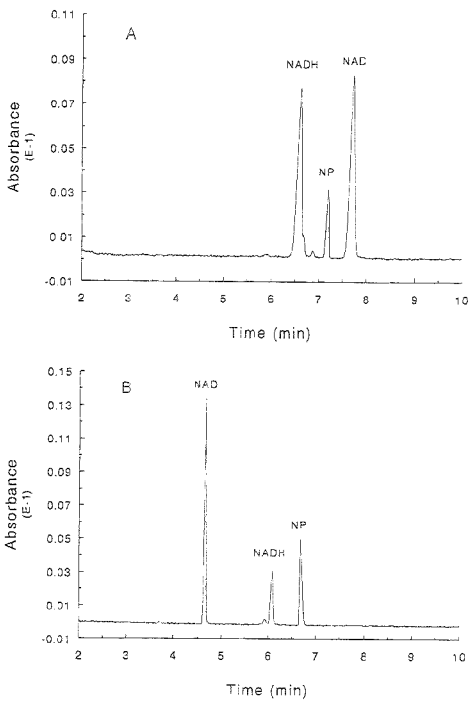

Figure 1. Electropherograms of NADH, NAD^+, and NP in both the coated (A) and uncoated (B) capillaries. Experimental conditions: (A) coated capillary, 100 μm (i.d.) × 57 cm; separation potential/current, 25 kV/27 μA; run buffer, 200 mM Tris–borate/HPMC buffer at pH 7.9; injection potential/time, 5 kV/3 s; UV filter, 260 nm; sample concentration, NADH 1.0 mM, NAD^+ 1.0 mM, and NP 1.5 mM in 20 mM tris-HCl buffer at pH 7.4; anode, outlet; cathode, inlet; temperature, 25 °C. (B) uncoated capillary, 75 μm (i.d.) × 57 cm; separation potential/current, 20 kV 34 μA; run buffer, 11.5 mM phosphate buffer at pH 8.0; anode, inlet; cathode, outlet; the other were the same as (A).

The conditions that allow complete separation of NADH and NAD^+ were best obtained between pH 6.5 and 8.5 using an uncoated capillary. At a pH higher than 8.5, the electroosmotic flow became too fast to achieve good resolution. At a pH below 6, NADH was not stable. It is also demonstrated that separation using polyacrylamide-coated capillary was best accomplished at pH 6.5–8.0. At a pH higher than 8.0, the coating becomes unstable.

NADH Quantitation. Quantitations of NADH using coated and uncoated capillaries by external and internal calibrations were investigated and compared. Peak areas were plotted against the known concentrations of NADH in external calibration (Figure 3), where it was assumed that the volume of NADH injected remained constant from run to run. Quantitation was based on the direct comparison of the peak area of NADH in the test sample with those of the NADH calibrators. However, our results indicated that the above assumption was not valid, as small deviations in timing and applied potential caused variations in the injection volumes. Between two different types of capillaries, a much improved linearity was observed in the coated capillary (Figure 3A). This marked improvement in linearity may be

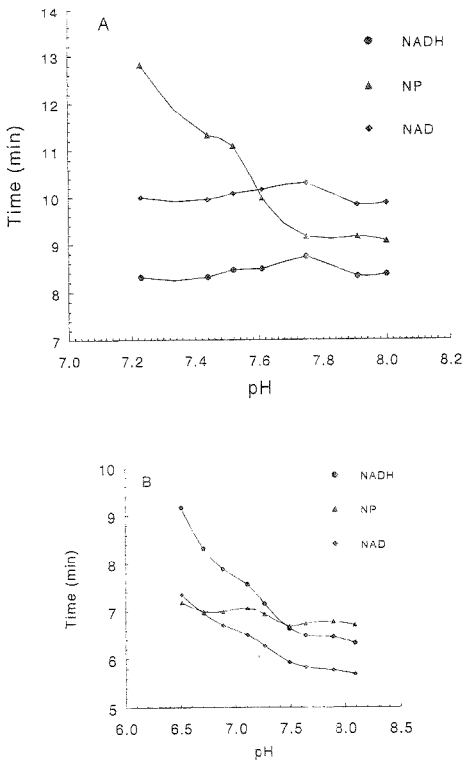

Figure 2. Influence of pH on migration times of NADH, NAD^+, and NP in coated (A) and uncoated (B) capillaries. Experimental conditions were the same as in Figure 1.

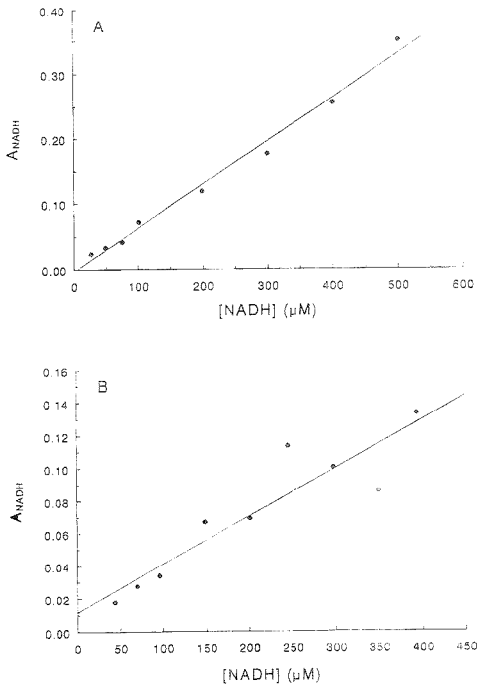

Figure 3. Calibration plots of NADH in coated (A) and uncoated (B) capillaries without internal standard. Experimental conditions were the same as in Figure 1.

attributed to the suppression of the electroosmotic flow and the creation of better surface uniformity with polyacrylamide coating.

The internal calibrations of NADH with NP are shown in Figure 4 using coated (A) and uncoated (B) capillaries. In internal calibration, a known amount of NP was added to each NADH calibrator and unknown sample prior to electrophoresis. Peak area ratios (A_{NADH}/A_{NP}) were plotted against the NADH concentrations to obtain a calibration plot. The NADH concentration in the test sample was determined in the calibration plot by knowing the area ratio of the unknown vs NP. The use of the relative area obviated the need to maintain constant injection volume and detector response during the analysis. As a result, excellent linearities of the internal calibration plots were obtained. Although the upper limit of NADH was not explored in either the coated or uncoated capillaries, the limit of detection for NADH, defined as the ratio of the triple average area of 30 baseline peaks to the area of NP (signal/noise 3), was calculated as 11.5 μM or 68.4 fmol for the coated capillary (Figure 4A) and 9.53 μM or 42.9 fmol for the uncoated capillary (Figure 4B).

Precision and Recovery Studies of NADH Detection. To evaluate the accuracy and reproducibility of NADH detection in hemolyzed, lipemic, and icteric serum samples, where common endogenous interfering substances can often create analytical problems, samples of each type of interference spiked with NADH standards at concentrations of 100 and 400 μM were analyzed and compared with NADH standards dissolved in a buffer free from such interferences (20 μM tris-HCl buffer at pH 7.4). As seen in Table 1, the interday variability was less than 2%, and the analytical recoveries ranged from 98 to 102%. These recovery values are within the range reported for most of the CE applications. The detection variability of 2% in the presence of various interfering factors is a good indicator of the analytical dependability of this method under less than ideal analytical conditions.

Capillary Electrophoretic Enzyme Immunoassay for Digoxin. Electropherograms for the separation of enzyme immunoassay mixtures using both coated and uncoated capillaries were given in Figure 5. The peaks were identified by sequentially spiking the immunoassay mixtures with NADH, NAD^+, and NP. The results were further verified by comparing the electropherograms of the assay mixture with those of each individual immunoreagent (results are not shown) for correct peak assignments. The unidentified peaks that appeared in Figures 5 were reagent constituents present in the assay kit. Since these unidentified peaks did not overlap with the NADH and NP peaks, no effort was made to reveal their identities.

Figure 6 shows the dose–response curves for digoxin, which were constructed by plotting the area ratios of NADH generated by the enzyme reaction and internal standard, NP, against the digoxin concentrations in human serum. In either coated capillary

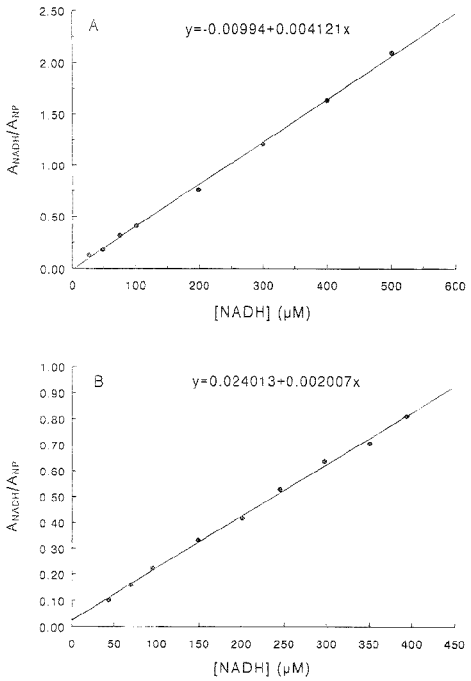

Figure 4. Calibration plots of NADH in coated (A) and uncoated (B) capillaries with internal standard. Experimental conditions were the same as in Figure 1.

Table 1. Interday Precision and Recovery of NADH[a]

NADH (μM)	sample matrix[b]	% SD ($n = 3$)	% recovery
100	Tris-HCl buffer	0.436	100
	serum 1	1.64	98.0
	serum 2	1.67	100
	serum 3	1.82	102
400	Tris-HCl buffer	0.486	100
	serum 1	1.26	101
	serum 2	1.35	99.4
	serum 3	1.26	99.3

[a] Separation conditions were the same as in Figure 1A. [b] Human sera 1–3 were known to be rich in cholesterol, hemoglobin, and bilirubin, respectively. The sample preparation procedure was the same as that in the digoxin EMIT kit.

(A) or uncoated capillary (B), a calibration of digoxin over therange of 0–6 ng/mL was obtained, which is significantly wider than the therapeutic range of 0.5–2.0 ng/mL. Apparently, the signal response was not zero at zero-dose digoxin in Figure 6, this is because the reaction solution contained both antibody and enzyme-labeled digoxin and enzyme activity was not zero. The assay had twice the sensitivity (signal per unit mass of analyte) in the coated capillary (A) compared to that in the uncoated capillary (B). This observation is also consistent with the findings in the sensitivity of NADH detection (Figures 4). The area ratio that corresponded to the lowest digoxin calibrator (0.5 ng/mL) was much higher than the detection limit of NADH (Figure 4), which implies that there is ample opportunity for

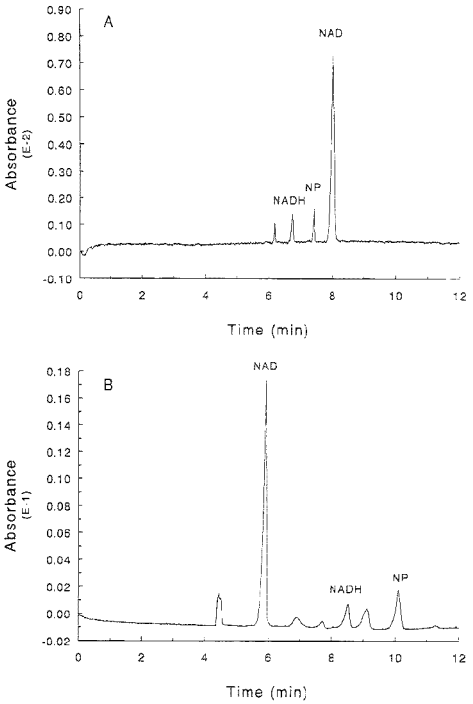

Figure 5. Electrophoretic separation of NADH from EMIT digoxin assay using coated (A) and uncoated (B) capillaries. Immunoassay: digoxin, 2.0 ng/mL in human serum; EMIT digoxin assay procedure from Syva Co. was followed until the conversion of NAD^+ to NADH and then 20 μL of 24 mM NP was added to the reaction mixture (410 μL) prior to the separation by CE. Separation conditions were the same as in Figure 1.

shortening the enzyme incubation time, or the total analysis time, with no apparent compromise in the practical usefulness of the method.

In this method, the lowest detectable digoxin concentration was 0.5 ng/mL. Due to the use of a manually attended EMIT procedure and a single-capillary CE, it is currently difficult to accommodate multiple injections per digoxin concentration within a dose–response curve. Nevertheless, the interday assay precision, which ranged from 3.12 to 10.1%, is given in Table 2. Since the detection precision of NADH by CE was consistently <2% (Table 1), the major source of error was in the manual EMIT procedure. Common sources of analytical variability when EMIT was performed manually include day-to-day temperature fluctuations, inconsistencies in reagent pipeting, uncontrolled nonspecific surface adsorption of enzyme product on reaction vessels, and variations in timing precision of reagent addition and reaction duration. Generally, switching from a manually attended EMIT procedure to an automated one can improve analytical variability at least by 5%.

Electrokinetic Injection. In electrokinetic injection, the amount of solute that is injected into the capillary depends on its apparent mobility under the injection voltage. Since different solute molecules may have different apparent mobilities during the injection, the amount of solute being injected may vary

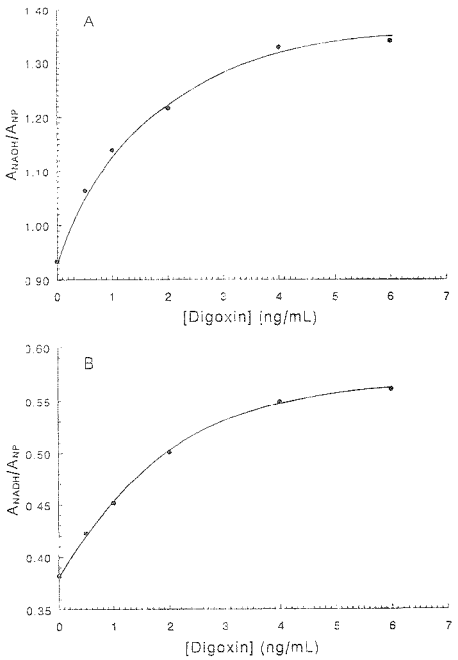

Figure 6. Dose–response curves for digoxin in human serum by capillary electrophoretic enzyme immunoassay. Experimental conditions were the same as in Figure 5: (A) coated capillary; (B) uncoated capillary.

Table 2. Interday Precision of CE–EIA Procedure[a]

digoxin (ng/mL)	0	0.5	1	2	4	6
% SD ($n = 3$)	6.87	10.1	8.64	3.15	4.32	3.12

[a] Experimental conditions were the same as in Figure 5A.

among species from the same sample. This biased nature of electrokinetic injection can be described by the bias factor (b)[17]

$$b = \frac{\mu_{ep(S)} + \mu_{eo}}{\mu_{ep(L)} + \mu_{eo}}$$

where μ_{eo} is the electroosmotic mobility, and $\mu_{ep(S)}$ and $\mu_{ep(L)}$ are the electrophoretic mobilities of the small and large analytes. In uncoated capillary, $\mu_{eo} \gg \mu_{ep(S)}$ and $\mu_{ep(L)}$; therefore, $b \approx 1$ and electrokinetic injection is free from bias. Accordingly, there were more peaks in Figure 5B (uncoated capillary) as compared to those in Figure 5A (coated capillary). In coated capillary, $\mu_{eo} = 0$ and $b > 1$, and electrokinetic injection is biased. Small analytes (e.g., NADH, NAD^+, and NP) that move quickly into the capillary will be injected to greater extents than large analytes (e.g., serum proteins) that move slowly into the capillary. Exclusion of these large protein molecules may be possible by regulating the injection potential and duration.

(17) Huang, X.; Gordon, M. J.; Zare, R. N. *Anal. Chem.* **1988**, *60*, 377–80.

Table 3. Separation Efficiency of the Capillary Columns, $N = 5.54(t_r/w_{0.5})^2$

	analytes ($\times 10^{-4}$) in Tris-HCl buffer (20 mM)[a]		analytes ($\times 10^{-1}$) in serum matrix[b]	
	coated	uncoated	coated	uncoated
NAD^+	2.59	6.56	2.48	1.70
NADH	2.77	4.68	4.29	1.79
NP	2.93	3.10	12.2	2.12

[a] The separation conditions and the concentrations of NAD^+, NADH, and NP were the same as in Figure 1. [b] The separation conditions and the concentrations of NAD^+, NADH, and NP were the same as in Figure 5.

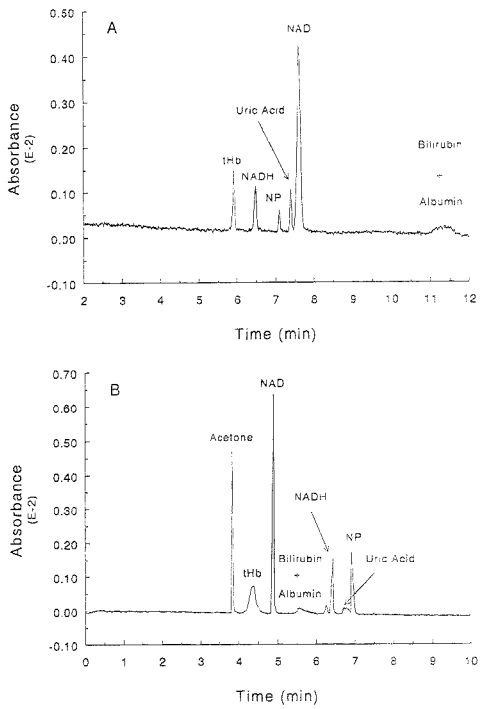

Figure 7. Electropherograms of NADH, NAD^+, and NP in the presence of potential interferents in coated (A) and uncoated (B) capillaries. Experimental conditions were the same as in Figure 1: bovine serum albumin, 3.52 mg/mL; bilirubin, 200 μg/mL; bovine hemoglobin, 20% of Certain tHb level 2 (Ciba-Corning Diagnostics); uric acid, 3.54 mg/mL.

Theoretically, the volume of electrokinetic injection can be calculated. If we assume that the conductivity of the sample was the same as that of the separation buffer, the volume of electrokinetic injection can be estimated by

$$\text{injection volume} = \frac{\pi d^2}{4} L_{inj} = \frac{\pi d^2}{4} (t_{inj} v_{app}) = \frac{\pi d^2 L_d}{4} \left(\frac{t_{inj} V_{inj}}{t_{app} V_{sep}} \right)$$

where d is the inside diameter of the capillary. L_d is the capillary length from inlet to detection window, t_{inj} is the injection time, V_{inj} is the injection potential, t_{app} is the apparent migration time of the analyte, and V_{sep} is the separation potential. If the elution of

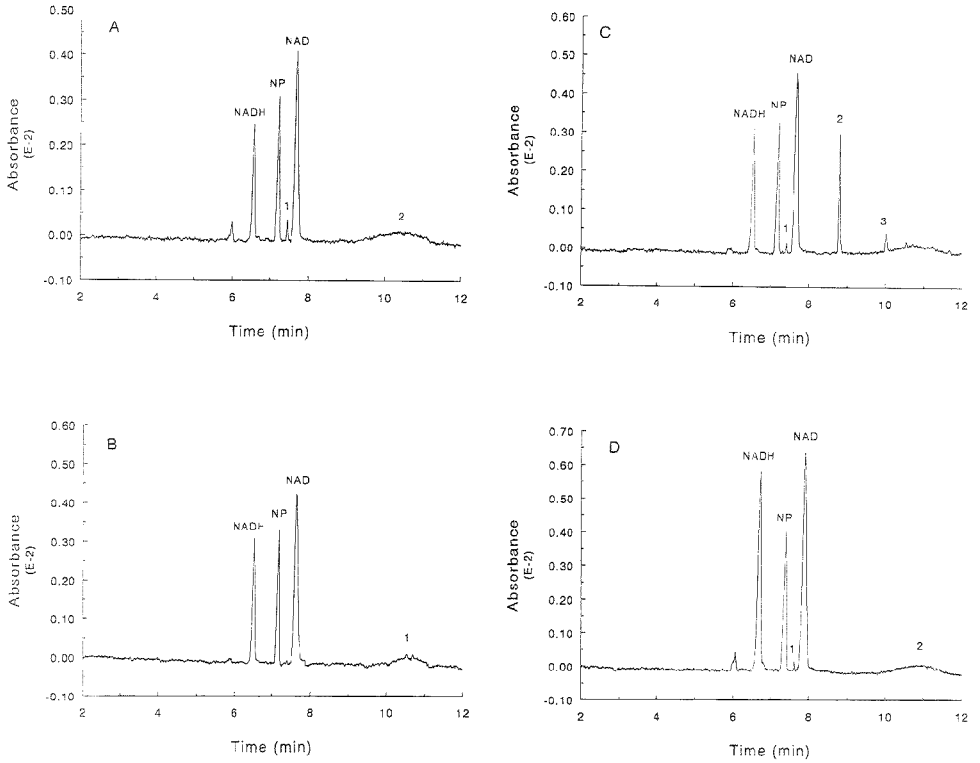

Figure 8. Electropherograms of serum samples spiked with NADH, NAD^+, and NP by coated capillary. The separation conditions and concentrations of NADH, NAD^+, and NP were the same as in Figure 1A: (A) calibrator serum (Boehringer Mannheim); (B) serum sample rich in hemoglobin; (C) serum sample rich in cholesterol; (D) serum sample rich in bilirubin. All these serum samples were diluted (1:1) with 40 mM tris buffer (pH 7.4) before use. The peaks numbered by Arabic numerals preexisted in the control sera and showed no interference to the spiked components.

NADH took 6.13 min in the uncoated capillary (75 μm × 57 cm) from buffer matrix at a separation potential of 20 kV and the same elution required 6.60 min at a separation potential of 25 kV in the coated capillary (100 μm × 57 cm), an injection potential of 5 kV for 3 s would deliver 5.95- and 4.50-nL samples to the coated and the uncoated capillaries, respectively.

Column Performance. The column efficiencies of both coated and uncoated capillaries for separating NADH, NP, and NAD^+ in either buffered or serum matrices are summarized in Table 3. If sample was in 20 mM Tris-HCl buffer (pH 7.4), the uncoated capillary displayed greater column efficiency than that of the coated capillary. This was primarily due to the focusing effect of the two opposite forces (electrophoretic and electroosmotic flows) concurrently existing inside the uncoated capillary. However, if the sample was in a serum matrix, the coated capillary had greater column efficiency than that of the uncoated capillary. As compared with the electropherogram obtained by the coated capillary (Figure 5A), there were much band broadening and skewed peak appearances when the uncoated capillary was used (Figure 5B). This may be related to the adsorbed protein on the inner surface that may interact with NADH, NAD^+, and NP and resulted in the fronting migration behavior as seen in Figure 5B. By use of polyacrylamide coating, there were no significant changes of peak symmetry in either sample matrices (Figures 1A and 5A). This implied that either less protein was injected, less protein was adsorbed onto the coated capillary, or both.

Interference Study. To determine whether the CE–EIA would be subject to the interferences in biological samples, potential interferents were introduced to the solutions containing NADH, NAD^+, and NP, and the mixtures were electrophoresed by CE. As indicated in Figures 7, bovine serum albumin (BSA), bilirubin, bovine hemoglobin, and uric acid showed no interference in separation of NADH in either coated (A) or uncoated (B) capillaries. The peak identities in these electropherograms were assigned by running an electrophoretic separation for each interferent, mixture of interferents, and mixture spiked with NADH, NAD^+, and NP standards, respectively. Similar studies were also carried out in the coated capillary using calibrator serum (Figure 8A), patients' sera with noted hemolysis (Figure 8B), lipemic (Figure 8C), or icteric factors (Figure 8D), and other pigmented blood components that might impose analytical problems on the EMIT procedure including human hemoglobin, coproporphyrin, melanin, protoporphyrin IX, and uroprophyrin (results are not shown). In all these tests, no interference was experienced.

CONCLUSION

CE–EIA, the combined use of a homogeneous enzyme immunoassay with capillary electrophoretic detection, is a useful analytical technique where maximal sensitivity, minimal biological interferences, low reagent usage, and minimal sample requirement are important consideration for the method. Quantitation in CE–EIA for digoxin in human serum was achieved by internal calibration. This approach has the potential of being applicable to most EMIT or enzyme assays where NADH is being generated as the product of a widely used enzyme (G6PDH) system. The major advantage of CE–EIA over the conventional EMIT procedure is that NADH is measured as a clean separated component from the interfering sample matrix. It is also demonstrated in this study that better separation of NADH was obtained using a polyacrylamide-coated capillary with electrokinetic injection because less serum protein would be introduced into or adsorbed onto the capillary. The performance of CE–EIA can be improved through automation of the immunoassay procedure and the advent of multicapillary CE. This awaits further instrument development.

ACKNOWLEDGMENT

A loan from Beckman Instruments, Inc. for the data acquisition unit is gratefully acknowledged.

Received for review February 23, 1995. Accepted June 23, 1995.

AC950202R

* Abstract published in *Advance ACS Abstracts*, August 1, 1995.

Anal. Chem. 1995, *67*, 3219–3222

Dynamics of DNA during Pulsed Field Electrophoresis in Entangled and Dilute Polymer Solutions

Xuelong Shi, Richard W. Hammond, and Michael D. Morris*

Department of Chemistry, The University of Michigan, Ann Arbor, Michigan 48109-1055

Using fluorescence video microscopy, DNA electrophoretic behavior under field inversion conditions has been investigated in hydroxyethyl cellulose (HEC) solutions both above and below its entanglement limit. DNA conformational fluctuation periods are found to be strongly influenced by the frequency of the applied electric field. DNA maximum extension is found to be dependent on both the frequency and the strength of the applied field. It is proposed that both above and below the HEC entanglement limit, field inversion serves to keep the average DNA conformation in a size-dependent regime intermediate between full extension and random coil. In this time-averaged geometry, efficient long-chain DNA electrophoretic separation is enabled.

The introduction of ultradilute polymer solutions for capillary electrophoretic separations of double-stranded nucleic acids by Barron and co-workers[1-3] has allowed rapid separations of fragments as long as 23×10^6 base pairs (23 kbp). At any given column length and field strength, separations are 5–10 times faster than possible in conventional entangled polymer solutions. The short times are a direct consequence of the low viscosities of the unentangled polymer solutions. We have shown that field inversion can be used to extend the range of ultradilute polymer solution electrophoresis to nucleic acids as long as 1.6×10^6 base pairs (1.6 Mbp)[4] with running times of just over 13 min. Despite these spectacular experimental results, the separation mechanism remains largely conjectural.[2,3]

Recently, we have used video microscopy of fluorescence-labeled long-chain nucleic acids to probe DNA electrophoretic motions in entangled and unentangled (ultradilute) hydroxyethyl cellulose solutions during constant field (dc) nucleic acid electrophoresis.[5] That work demonstrated that the nucleic acid motions were qualitatively similar in all polymer concentration regimes. Generally, molecules migrated in V- or U-shaped topologies, consistent with a dominant interaction at a single point or region. In concentrated polymer solutions, the interaction region moved only slowly, because it consists of cellulose strands which are part of an extended network. However, below the cellulose entanglement threshold (also called entanglement limit, C^*), the interaction region moved at almost the same velocity as the DNA center of mass, because the cellulose molecules or clusters were not retarded by entanglement with an extended network. At any time, only some of the DNA molecules were in extended topologies in dilute polymer solutions. Most of the remainder were present as random coils which appeared as compact masses under the light microscope.

In this article, we describe the extension of our fluorescence microscopy studies to pulsed field electrophoresis conditions in entangled and unentangled hydroxyethyl cellulose solutions. Fluorescence microscopy has previously been used to study nucleic acid motions in field inversion agarose gel electrophoresis[6] and in orthogonal field agarose gel electrophoresis.[7] We know of no analogous studies in linear polymer solutions, either dilute or concentrated.

EXPERIMENTAL SECTION

The microscopy system has previously been described.[5] Briefly, it consisted of an Olympus BH-2 epifluorescence microscope equipped with a Reichert 50×/1.0 NA water immersion objective and a Photometrics Star-I scientific CCD camera containing a 576 × 384 pixel chip. The excitation source was 532 nm light from a frequency-doubled CW diode-pumped Nd:YAG laser. The laser power into the microscope was about 12 mW, and the exposure time for each image frame was 0.4 s. Electrophoretic experiments were performed in a locally constructed cell consisting of two polyacrylamide-coated cover slips resting on a microscope slide, to which two electrodes were cemented with a 2.5 cm gap.[5]

The DNA samples were yeast chromosomal DNA (New England Biolabs, PFG Marker, 225 kbp–1.9 Mbp). The staining dye for visualization was ethidium homodimer I (Molecular Probes). The sieving polymer was hydroxyethyl cellulose (HEC) with M_n = 438, 800) and entanglement threshold 0.09% (w/w).[1] Samples were prepared in 0.5× TBE (Tris–borate–EDTA) buffer. To increase viscosity and thereby slow DNA motions, solutions were made 55–60% in sucrose.[5,8]

As in our previous work,[5] quantitative measurements were made of DNA center of mass velocity (v_x) and radii (R_1 and R_2), as defined by Oana et al.[9] Physically, R_1 and R_2 are the two principal axes of a DNA molecule modeled as an elliptical object. In contrast to the dc field case, a sign has been assigned to R_1 in

(1) Barron, A. E.; Soane, D. S.; Blanch, H. W. *J. Chromatogr.* **1993**, *652*, 3–16.
(2) Barron, A. E.; Blanch, H. W.; Soane, D. S. *Electrophoresis* **1994**, *15*, 597–615.
(3) Barron, A. E.; Sunada, W. M.; Blanch, H. W. *Electrophoresis* **1995**, *16*, 64–74.
(4) Kim, Y.; Morris, M. D. *Anal. Chem.* **1995**, *67*, 784–786.
(5) Shi, X.; Hammond, R. W.; Morris, M. D. *Anal. Chem.* **1995**, *67*, 1132–1138.
(6) Rampino, N. J.; Chrambach, A. *Biopolymers* **1991**, *31*, 1297–1307.
(7) Gurrieri S.; Rizzarelli, E.; Beach, D.; Bustamante, C. *Biochemistry* **1990**, *29*, 3396–3401.
(8) Perkins, T. T.; Smith, D. E.; Chu, S. *Science* **1994**, *264*, 819–822.
(9) Oana, H.; Masubuchi, Y.; Matsumoto, M.; Doi, M.; Matsuzawa, Y.; Yoshikawa, K. *Macromolecules* **1994**, *27*, 6061–6067.

0003-2700/95/0367-3219$9.00/0

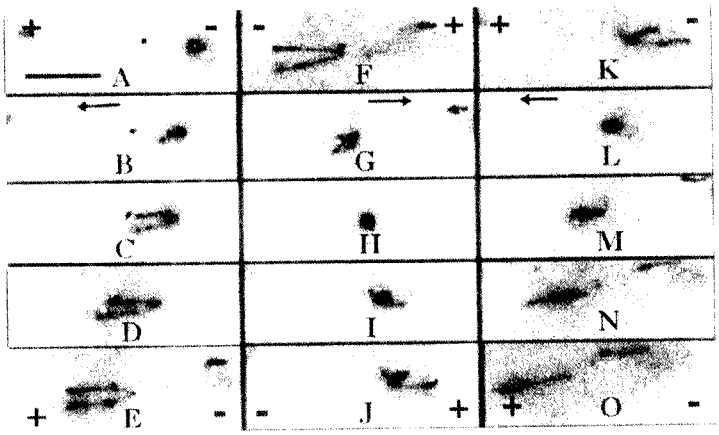

Figure 1. Time sequence of yeast chromosomal DNA motions under pulsed field electrophoresis in 0.16% HEC, 55% sucrose, and 0.5× TBE solution. Forward field was 25 V/cm, and backward field was −20 V/cm. The frames were taken at 4.0 s intervals. The field was switched every 20 s (five frames). Contrast is inverted (fluorescence regions black) for clarity. The migration direction is indicated by the arrows, and the scale bar represents 10 μm.

analysis of pulsed field data in order to define the direction of DNA orientation. The center of mass and intensity moments of the DNA were calculated using the IPLab image processing program (Signal Analytics Corp.).

RESULTS AND DISCUSSION

Figure 1 shows an example of the electrophoretic behavior of an isolated DNA molecule in a periodically reversed electric field in 0.16% HEC solution (55% sucrose, viscosity 161 cp). In order to maximize the viewing time of a given DNA, the field was chosen to impart only slight net electrophoretic motion to the nucleic acid while keeping the times in the forward and reverse directions identical. The HEC concentration was chosen to be above the entanglement threshold.

When the electric field was applied to the sample, the DNA molecule started to move toward the positive electrode, as during dc electrophoresis in the absence of electroosmosis. As expected, the polyacrylamide coatings on the coverslip surfaces served to largely or completely suppress electroosmosis. The sequence of frames A–E in Figure 1 shows collision of an initially compact DNA molecule with the HEC network and extension of DNA into a characteristic U-shaped configuration.

In repeated experiments, the exact conformation of the extended DNA molecule was found to depend on its conformation at the time of collision. Occasionally, the DNA molecule was slightly elongated along the direction normal to the electric field at the collision. When this happened, the DNA molecule became extended into a W-like shape before assuming the characteristic U- or V-shape. Predominantly, the DNA molecule formed a U- or V-shape directly after the collision with the polymer network. Both arms continuously grew during migration until the applied electric field was reversed.

The effect of field inversion (direction reversal) is shown in frames F–J of Figure 1. When the direction of the applied field was reversed, the DNA molecule started to move toward the newly defined anode. In response to the new field direction, both arms of the elongated DNA molecule began to retreat back along their stretching paths. After the DNA molecule collapsed back to a globular conformation, it would usually move some distance in this configuration before re-extending into the U- or V-shape, with arms pointing toward the anode. This process was repeated when the field direction was again reversed, as shown in frames K–O of Figure 1. Although there was alternation in the orientation of the extended DNA, the exact shapes were not repeated on successive cycles.

Consistent with our earlier observations under dc electrophoresis conditions,[5] the apex of a U-shape moved in 0.16% HEC solutions under pulsed electric field. The movement direction of the apex was always toward the anode and reversed immediately with electric field direction. This observation further confirmed that the movement of the apex was due to partial rupture of the polymer network caused by the force the DNA molecule exerted on the network.

We investigated the cause of collapse of an extended DNA into a globular form upon electric field reversal. In principle, the cause could be either the reversed electric field force or the elastic restoring (entropic) force. Experimentally, collapse due to an elastic restoring force alone can be examined by simply turning off the field instead of reversing the field. Figure 2 shows the DNA entropic collapse (relaxation) in 0.16% HEC solution under field-free conditions. Entropic collapse required more than 50 s. By contrast, collapse to globular form required only about 9 s under field inversion conditions. While an elastic restoring force may contribute to the collapse of DNA, the process is primarily field-driven.

Rapid collapse required a large velocity difference between the apex and the ends of the arms and demonstrated the large difference in the resistance forces experienced by the apex and the arm ends. The arm ends were expected to experience very little resistance during collapse because they retreated back along their stretching paths. The apex of the molecule experienced a much larger resistance force because of its direct interaction with the polymer network.

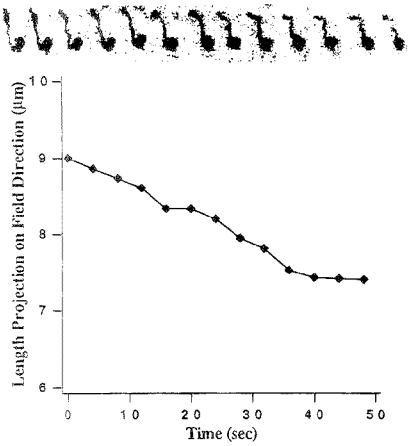

Figure 2. Relaxation of a yeast chromosomal DNA molecule in 0.16% HEC, 55% sucrose, and 0.5× TBE solution in the absence of electric field. The points on the plot correspond to the sequence of DNA images.

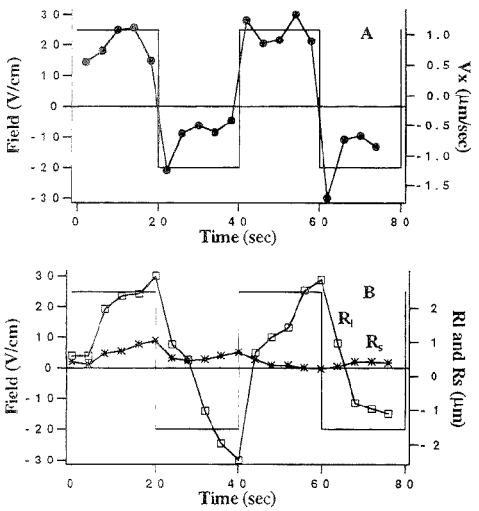

Figure 3. Time evolution of v_x, R_l, and R_s of a yeast chromosomal DNA under field inversion in 0.16% HEC, 55% sucrose, and 0.5× TBE solution. The square waves in the figures are the electric field values. The field was cycled at 1/40 Hz between 25 and −20 V/cm. (A) Response of v_x (●) to the pulsed field. (B) Response of R_l (□) and R_s (*) to the pulsed field.

Figure 3 shows the behavior of v_x, R_l, and R_s during 1/40 Hz field reversal cycles in 0.16% HEC. Within the time resolution of our measurements, the center of mass velocity of a DNA molecule responded instantaneously to the change in field direction, but the DNA conformational response to the electric field change was retarded. At a field strength of 20−25 V/cm, a DNA molecule required about 9 s to reorient. Most of the reorientation is along the field axis, as shown by the large change in R_l. Less conformational change occurred perpendicular to the field axis, as demonstrated by much smaller fluctuations in R_s.

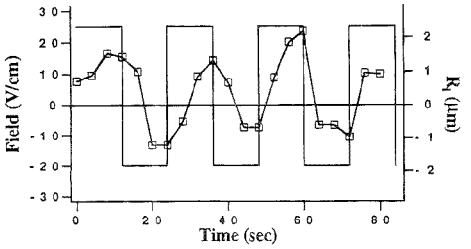

Figure 4. Time evolution of R_l of a yeast chromosomal DNA. Electric field was cycled at 1/24 Hz. Other conditions as in Figure 3.

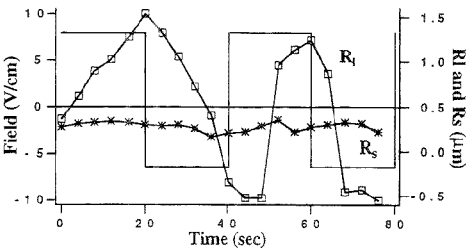

Figure 5. Time evolution of R_l (□) and R_s (*) of a yeast chromosomal DNA. The field was cycled between 8 and −6.4 V/cm. Other conditions as in Figure 3.

The ultimate extension of DNA was a strong function of both field strength and frequency. In Figure 4, the behavior of R_l at higher frequency, 1/24 Hz, is shown. On the average, the maximum extension is less than that at 1/40 Hz (Figure 3B). In Figure 5, we show the behavior of R_l and R_s at 1/40 Hz, but at lower field strength than in Figure 3B. Again, the maximum extension is less than that at higher field. Together these data demonstrate the strong effects of both field strength and field frequency on the average extension of DNA. Field inversion frequency is an important variable not present in dc electrophoresis. In the dc case, the periodicity of DNA conformational fluctuations has been shown to depend on the field strength and the separation medium for a given size DNA.[9]

It has long been known that in the limit of complete extension, frequently called strongly biased reptation, DNA mobility becomes size-independent.[10,11] The optimum geometry for size-dependent mobility is intermediate between a random coil and an extended chain. In the loosely entangled polymer solutions, field inversion serves to keep the average DNA conformation somewhere near the optimum. This optimization occurs if the field inversion takes place in less than the dc field entanglement/disentanglement time.

In 0.01% HEC polymer solution (60% sucrose, viscosity ~42 cp), which is about 1 order of magnitude lower than the 0.09% entanglement threshold, U- or V-shaped DNA molecules were still observed, but less than 10% of the nucleic acids were extended at any given time (Figure 6). The maximum extension was much smaller than that observed in 0.16% HEC under the same field conditions. Similarly, reversal of the orientation of the U- or V-shape was observed when the field direction was changed (frames F−J of Figure 6). These effects were caused by interac-

(10) Lumpkin, O. J.; Dejardin, P.; Zimm, B. H. *Biopolymers* **1985**, *24* 1573−1593.
(11) Slater, G. W.; Noolandi, J. *Biopolymers* **1986**, *25*, 431−454.

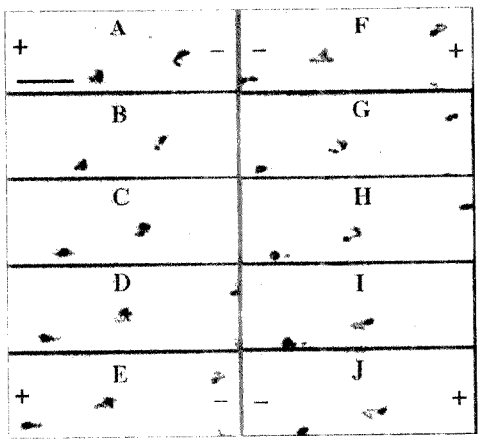

Figure 6. Time sequence of yeast chromosomal DNA motions under pulsed field electrophoresis in 0.01% HEC, 60% sucrose, and 0.5× TBE solution. Other conditions as in Figure 1.

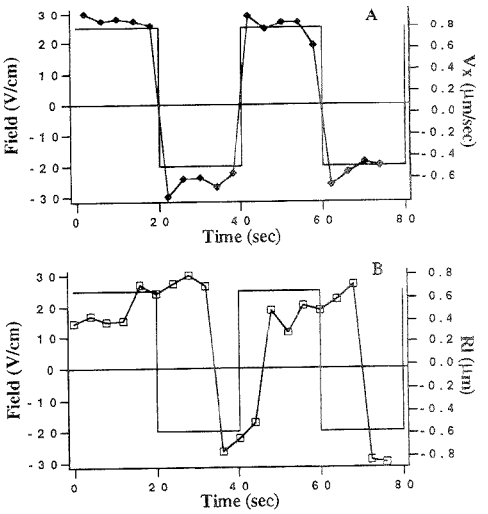

Figure 7. Time evolution of v_x and R_l of a yeast chromosomal DNA under field inversion in 0.01% HEC, 60% sucrose, and 0.5× TBE solution. Other conditions as in Figure 3.

tions between DNA and HEC molecules. No U- or V-shape with appreciable size could be observed in 0% HEC solutions.

At HEC concentrations well below the entanglement limit, the largest fraction of DNA molecules were in almost globular conformations. These globular conformations had small fluctuations and were difficult to distinguish from the DNA conformations in HEC-free solution. In the absence of HEC, DNA molecules assumed largely globular conformations during migration and had small conformational fluctuations too. Such small random conformational fluctuations were observed even in the absence of an applied electric field. They may originate from segmental random motions of DNA.

Qualitatively, the behavior of an observed U-shaped DNA molecule in 0.01% HEC solution was similar to that in 0.16% HEC solution, as suggested in Figure 7. In both cases, measurements were made on molecules of apparent radius of gyration of ~2.0 μm. As in the case of loosely engtangled HEC (Figure 3), the center of mass velocity response to the electric field was instantaneous within the time resolution of our instruments. Uncorrected for solvent (sucrose solution) viscosity, the response of R_l to the electric field, a lag of ~15 s, was more retarded than that in entangled HEC solution. However, if this number is corrected for the ratio of sucrose solution viscosities (22 cP at 55%, 40 cP at 60%), the lag time is reduced to about 8.3 s. That number is similar to the R_l lag time in 0.16% HEC, 55% sucrose, about 9 s.

The smaller size of the U-shaped DNA suggests that the difference in resistance forces experienced by the apex and the ends of a U-shaped DNA molecule is smaller in 0.01% HEC solution than in 0.16% HEC solution. This behavior is consistent with the picture of ultradilute HEC as freely floating obstacles and 0.16% HEC as a loosely entangled but extended network. As in 0.16% HEC polymer solution, the periods of the conformational fluctuations of the U- or V-shaped DNA were also strongly influenced by the field reversal intervals of the applied electric field. The low magnitudes of R_l in 0.01% HEC solution prevented us from making detailed examinations of field strength and field frequency effects on DNA conformational evolution during field reversal cycles.

CONCLUSIONS

Our observations underscore the basic qualitative similarity of DNA electrophoretic migration under field inversion conditions in entangled and unentangled polymer solutions. The differences are quantitative rather than qualitative. We propose that the pulsed field confers size-dependent mobility only on those DNA molecules which are actually entangled with HEC. Subentanglement separations of long-chain DNA can be successful because there is a size-dependent average mobility which depends upon the fraction of the time that DNA is entangled with HEC and on its average conformation during entanglement. Good separation conditions can be maintained if the field reversal interval is less than the lifetime of the transient DNA/HEC adduct.

The optimum separation conditions for field inversion electrophoresis in ultradilute solution are not yet known. Further protocol exploration is certainly needed. But this work must be complemented by more detailed imaging studies and by theoretical studies which define the optimum geometry for size-dependent mobility and the conditions for maximizing its presence.

ACKNOWLEDGMENT

We thank the National Institutes of Health for financial support through Grant GM-37006 to M.D.M.

Received for review April 20, 1995. Accepted June 30, 1995.[a]

AC950389M

[a] Abstract published in *Advance ACS Abstracts*, August 1, 1995.

Anal. Chem. 1995, *67*, 3223–3228

Enantiomeric Separation of Sulfur- and Selenium-Containing Amino Acids by Capillary Electrophoresis Using Vancomycin as a Chiral Selector

Radim Vespalec,† Hugo Corstjens,‡ Hugo A. H. Billiet,‡ Johannes Frank,*,‡ and Karel Ch. A. M. Luyben‡

Institute of Analytical Chemistry, Academy of Sciences of the Czech Republic, Brno, Czech Republic, and Kluyver Laboratory of Biotechnology, Delft University of Technology, Delft, The Netherlands

Vancomycin is a highly efficient chiral selector for the enantioseparation of methionine, ethionine, cystine, and their selenium analogues, derivatized with 6-aminoquinolyl-*N*-hydroxysuccinimidoyl carbamate. Concentrations of vancomycin as low as 0.3 mM in 20 mM MOPS/Tris buffer pH 7.0 produce differences in mobility that lead to a resolution far exceeding baseline separation, at a pH where the amino acids are fully ionized. Under these conditions, *meso*-cystine and *meso*-selenocystine are also baseline separated from the corresponding D-isomers. At these low vancomycin concentrations, the migration of the L-enantiomers is hardly decelerated. The differences in mobility observed when the concentration of vancomycin is raised to 5 mM are higher than 3.2×10^{-9} $m^2 V^{-1} s^{-1}$ for singly-charged species, such as the derivatives of methionine, selenomethionine, ethionine, and selenoethionine, and they increase to 7.6×10^{-9} and 8.5×10^{-9} $m^2 V^{-1} s^{-1}$ for cystine and selenocystine, respectively. For a capillary with an internal diameter of 50 μm, the separation efficiency is 250 000 theoretical plates/m.

Since it has been recognized that selenium is an important micronutrient for the human organism (daily requirement, 50–80 μg),[1] a variety of liquid chromatographic procedures has been developed to analyze a large number of naturally occurring selenium compounds.[2] These methods have given us more insight in the occurrence and metabolism of selenium, and, since amounts exceeding the daily requirement produce toxic effects, they are equally valuable to evaluate the utilization of selenium in nutrition.

The beneficial effect of selenium for human health is associated with its occurrence in proteins.[3] The potential of a given food to supply the daily selenium requirement or its toxicity cannot be judged from a determination of its total selenium content alone, because the efficiency of biological utilization of different seleno compounds varies or is not always known. Therefore, speciation of selenium is required, and in this respect, the analysis of selenium analogues of the sulfur-containing amino acids is particularly relevant, since these amino acids are readily incorporated into proteins. Further resolution of the different seleno amino acids into their D- and L-enantiomers is also of interest for physiological studies since it is known that, in general, D- and L-amino acids display different absorption kinetics and follow partly different metabolic pathways in the human organism.[4]

A satisfactory separation with capillary gas chromatography or HPLC of a mixture of selenocystine, selenomethionine, and selenoethionine in the presence of other commonly occurring amino acids after derivatization with phenyl isothiocyanate, 6-aminoquinolyl-*N*-hydroxysuccinimidoyl carbamate (AQC), or ethyl chloroformate has been reported recently.[5] Enantiomeric resolution of methionine and selenomethionine by reversed phase HPLC after derivatization with (+)-1-(9′-fluorenyl)ethyl chloroformate has been reported by Hansen and Poulsen.[6]

The high resolving power of capillary zone electrophoresis has been used to separate selenocystine, selenomethionine, selenite, and selenenate.[7] In addition, its potential for chiral separations has been clearly demonstrated.[8,9] We decided, therefore, to investigate the potential of this technique for the chiral separation of selenium- and sulfur-containing amino acids derivatized with AQC[10] which can be detected with a high sensitivity, either by absorbance or fluorescence spectrometry and for which the enantioseparation by HPLC has been described.[11] In the search for a proper chiral selector for this particular analytical problem, we chose vancomycin, which has been shown to have a high affinity for D-amino acid-containing peptides.[12] This member of the group of macrocyclic antibiotics has been succesfully exploited to resolve the enantiomers of several anionic compounds[13] by liquid chromatography. Our study on the chiral separation by

† Academy of Sciences of the Czech Republic.
‡ Delft University of Technology.

(1) Schwartz, K.; Foltz, C. M. *J. Am. Chem. Soc.* **1957**, *79*, 3292.
(2) Köbl, G.; Kalcher, K.; Irgolic, K. J.; Magee, R. J. *Appl. Organomet. Chem.* **1993**, *7*, 463–466.
(3) Rotruck, J. T.; Pope, A. L.; Ganther, H. E.; Swanson, A. B.; Hapeman, D. G.; Hoekstra, W. G. *Science* **1973**, *179*, 588–590.
(4) Berg, C. P. In *Protein and Amino Acid Nutrition*; Albanese, A. A., Ed.; Academic Press: New York, 1959; pp 57–96.
(5) Janák, J.; Billiet, H. A. H.; Frank, J.; Luyben, K. Ch. A. M.; Husek, P. J. *J. Chromatogr. A* **1994**, *677*, 192–196.
(6) Hansen, S. H.; Poulsen, M. N. *Acta Pharm. Nord.* **1991**, *3*, 95–97.
(7) Albert, M.; Demesmay, C.; Rocca, J. L. *Analusis* **1993**, *21*, 403–407.
(8) *Capiliary Electrophoresis, Theory and Practice*; Camelleri, P., Ed.; CRC Press: Boca Raton, FL, 1993.
(9) Bereuter, T. L. *LC-GC* **1994**, *12*, 748–766.
(10) Cohen, S. A.; Michaud D. P. *Anal. Biochem.* **1993**, *211*, 279–287.
(11) Pawlowska, M.; Chen, S.; Armstrong, D. W. *J. Chromatogr.* **1993**, *641*, 257–265.
(12) Nieto, M.; Perkins, H. R. *Biochem. J.* **1971**, *123*, 773–787.
(13) Armstrong, D. W.; Tang, Y.; Chen, S.; Zhou, Y.; Bagwill, C.; Chen, J.-R. *Anal. Chem.* **1994**, *66*, 1473–1484.

0003-2700/95/0367-3223$9.00/0

capillary electrophoresis of sulfur- and selenium-containing amino acids shows that unusually high differences in mobility for the enantiomers are realized, even with low concentrations of vancomycin, confirming the high separation potential of this antibiotic in capillary electrophoresis that was demonstrated by Armstrong and co-workers.[14]

EXPERIMENTAL SECTION

A Waters Quanta 4000E (Waters, Milford, MA), operated at 25 °C, equipped with a 370 μm o.d., 50 μm i.d. uncoated fused silica capillary of 57.8 cm total length (50.0 cm migration distance) from Chrompack (Middelburg, The Netherlands), was used for the electrophoretic experiments. The starting and home electrode compartments were laboratory-adapted for glass test tubes of small volume in order to decrease the solution volume in the electrode compartments from 17 to 1.4 and 0.9 mL, respectively. The UV detector was operated at 254 nm with a 0.3 s time constant and a sensitivity of 0.002 or 0.005 AUFS. Migration times (precision, 0.01 min) were measured with a HP 3392 A integrator (Hewlett-Packard, Avondale, PA). The hydrodynamic injection time applied was 10–30 s. A voltage of +10 kV was used in a preliminary study of the properties of vancomycin and the mobilities of the analytes. During chiral separations, a voltage of +20 kV was used with vancomycin concentrations in the background electrolyte (BGE) up to 1.0 mM; at higher vancomycin concentrations, a voltage of −20 kV was used.

Methionine (Met), selenomethionine (SeMet), ethionine (Eth), cystine (Cys2), selenocystine (SeCys2), and tryptophan (Trp) (either as racemates or as pure enantiomers), *N*-2,4-dinitrophenyl (DNP)-DL-methionine (dMet), dansylmethionine (dsMet), dansyltryptophan (dsTrp), and vancomycin hydrochloride were from Sigma (St. Louis, MO). The AQC kit for derivatization of amino acids, consisting of 0.2 M borate buffer pH 8.8, water-free pyridine, and dry AQC reagent, was from Waters. Malonic acid and mesityl oxide, serving as electroosmotic markers, were from Fluka (Buchs, Switzerland). All other chemicals were from Merck (Darmstadt, Germany).

For derivatization, cystine and selenocystine were prepared as 1 mM solutions in water adjusted to pH 9 with NaOH; the other amino acids were dissolved in water as 2 mM solutions. Twenty microliter aliquots of the amino acid solutions and a blank, containing water only, were mixed with 70 μL of borate buffer. The solution of the AQC reagent was prepared just before use by adding 1 mL of water-free pyridine to the vial with dry AQC reagent and heating its contents to 50 °C for 10 min. After that, 20 μL of the reagent solution was added to the buffered amino acid solution, and the mixture was immediately agitated for 10 s with a vortex mixer. After 1 h at room temperature, the stock solutions of derivatized amino acids were stored at 5 °C. Before injection, a 10-fold dilution was made by adding 200 μL of distilled water to a 20 μL aliquot of the amino acid solution.

For enantioselective separations, 20 mM 3-(*N*-morpholino)-propanesulfonic acid (MOPS) buffer, adjusted to pH 7.0 with solid Tris, was used as the BGE, to which varying concentrations of vancomycin chloride were added. The small shift in the pH of the 20 mM MOPS/Tris buffer caused by dissolution of vancomycin chloride (amounting to 0.15 pH units at 5 mM vancomycin chloride) was corrected by addition of solid Tris. Stock solutions of vancomycin chloride (5 and 3 mM) in 20 mM MOPS/Tris buffer were stored at 5 °C and used within 3 days for the preparation of more diluted vancomycin solutions. The composition of buffers used in preliminary experiments with vancomycin is specified in Table 1. The buffer concentrations given in this table pertain to the final concentration of the first buffer component; the second component was added to adjust the pH to the indicated value.

Table 1. pH Dependence of Vancomycin Mobility

pH	buffer composition[a]	pK_a[b]	I[c]	μ ($\times 10^{9}$ m^2 V^{-1} s^{-1})
4.5	acetic acid + Tris	4.8	1.8	7.0
5.0	acetic acid + Tris	4.8	2.5	6.5
5.5	malonic acid + Tris	5.7	3.9	4.2
5.5	MES + Tris	6.1	0.7	7.2
6.0	MES + Tris	6.1	1.5	6.9
6.5	MES + Tris	6.1	1.9	6.0
7.0	sodium phosphate	6.8	4.8	2.9
7.0	MOPS + Tris	7.2	1.4	3.9
7.5	HEPES + Tris	7.5	1.3	1.5
8.0	Tris + HEPES	8.1	0.7	−1.7
8.5	Tris + CHES	8.1	0.2	−7.5
9.0	CHES + Tris	9.3	0.9	−9.0
9.5	CHES + Tris	9.3	1.2	−11.0
10.0	CAPS + NaOH	10.4	1.3	−17.3
10.5	CAPS + NaOH	10.4	1.8	−18.7
11.0	CAPS + NaOH	10.4	2.9	−19.4

[a] Concentration of the main buffering constituent is 15 mM; the second buffer component is added to adjust the pH to the indicated value. [b] Pertaining to the first buffer constituent. [c] Current flowing through the capillary, in μA.

When BGEs containing vancomycin were used, the capillary was flushed with 0.1 M NaOH for 15 min at the end of a daily series of experiments. The next day, after a 5 min purge with 0.1 M NaOH, the capillary was washed with water for 10 min. Finally, the capillary was washed twice with BGE for 15 and 5 min, with a 10 min pause in between.

The mobility (μ) and electroosmosis data, calculated in a standard way from the voltage, the capillary dimensions, and the migration time, are reported in units of 10^{-9} m^2 V^{-1} s^{-1}. Mobilities are corrected for electroosmosis, and the mobility difference ($\Delta\mu$) data are given as absolute values. In the electropherograms, the peaks of the separated enantiomers are numbered in the order of decreasing absolute mobilities.

RESULTS AND DISCUSSION

Glycopeptide antibiotics are known to form homodimers in solution, a process that is influenced by the chemical nature and concentration of other solution constituents.[12,15] Because no information is available on the interaction of vancomycin with the various constituents of commonly employed electrophoretic buffers, Good buffers, characterized by a minimal interaction with compounds of biological origin,[16] were preferred in the present study. Low concentrations of these buffers were used initially to minimize the interference of Joule heat production with the chiral recognition potential of vancomycin for the negatively charged enantiomers.

Investigation of the Behavior of Vancomycin in Good Buffers. The relevant electrophoretic properties of vancomycin

(14) Armstrong, D. W.; Rundlett, K. L.; Chen, J. R. *Chirality* **1994**, *6*, 496–509.

(15) Groves, P.; Searle, M. S.; Mackay, J. P.; Williams, D. H. *Structure* **1994**, *2*, 747–754.

(16) Ferguson, W. J.; Braunsweiger, K. I.; Braunsweiger, W. R.; Smith, J. R.; McCormick, J. J.; Wasmann, C. C.; Jarvis, N. P.; Bell, D. H.; Good, N. E. *Anal. Biochem.* **1980**, *104*, 300–310.

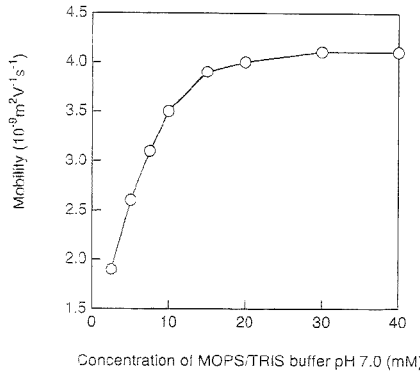

Figure 1. Dependence of the vancomycin mobility on the concentration of the MOPS/Tris buffer pH 7.0.

were investigated in Good buffers at low and approximately equal ionic strength, covering a pH range of 5.5–11.0 (Table 1). Outside the pH range covered by the available Good buffers, acetic and malonic acid were selected as buffering compounds, and a sodium phosphate buffer was included for comparison. The data listed for the vancomycin mobility are the averages of 3–7 consecutive measurements. A 0.5 mM vancomycin solution in 2.5 mM MOPS/Tris buffer pH 7.0, spiked with mesityl oxide as the electroosmosis marker, was injected in these experiments. The pH of zero vancomycin mobility at 25 °C, interpolated from the data given in Table 1, is 7.8, which is in reasonable agreement with the values that were obtained from electrochemical titrations, 7.5[17] (20 °C, ionic strength 0.02 M) and 8.3[18] (25 °C, ionic strength 0.2 M). Interestingly, a much lower value, 7.2,[14] is observed when the point of zero migration is measured in 100 mM phosphate buffer pH 7.0 (ionic strength ~0.2 M) at 22 °C, suggesting that phosphate has a specific interaction with vancomycin.

The unexpected low mobility of vancomycin at pH 5.5 in the malonic acid buffer was further investigated with buffers of varying concentration and composition. It appears that vancomycin mobility is dependent not only on the buffer pH but also on its concentration (Figure 1) and chemical composition. For example, replacing the 15 mM malonic acid divalent anions in the pH 5.5 buffer by the same concentration of zwitterionic MES, yielding roughly the same number of ions in solution, increases the vancomycin mobility from 4.2×10^{-9} to 7.2×10^{-9} m^2 V^{-1} s^{-1} (Table 1). Similarly, a 35% increase in vancomycin mobility is observed at pH 7.0 when sodium phosphate buffer containing divalent anions is replaced by the zwitterionic MOPS/Tris buffer. Replacing sodium cations in the phosphate buffer by Tris or replacing Tris in the MOPS buffer by sodium cations has no observable effect on the mobility of vancomycin and on its peak shape (data not shown). This indicates that the positive charge, located on the N atom of the Tris cation, has negligible, if any, influence on the interaction of vancomycin with the negatively charged uncoated fused silica. Hence, it seems unlikely that the zwitterionic biological buffers used here, which have a similar positive charge, will affect the adsorption of vancomycin on the capillary wall and consequently its mobility. An alternative explanation for the low mobility of vancomycin in malonic acid buffers may be that vancomycin has a specific interaction with the divalent malonate anions, resulting in a partial shielding of its effective charge. This view is supported by the fact that in sodium phosphate pH 7.0, vancomycin also has a lower mobility (Table 1) and a much lower isoelectric point (see above).

(17) Chu, Y.-H.; Whitesides, G. H. *J. Org. Chem.* **1992**, *57*, 3524–3525.
(18) Takács-Novák, K.; Noszál, B.; Tökés-Kövesdi, M.; Szász, G. *Int. J. Pharm.* **1993**, *89*, 251–263.

Table 2. Effect of the Vancomycin Concentration on the Mobility Difference, $\Delta\mu_2$, and the Mobility of the Less Retained Enantiomer, μ_1 (Both in 10^9 m^2 V^{-1} s^{-1})

		vancomycin concentration (mM)						
		0.1	0.2	0.3	0.4	2.0	3.0	5.0
Met	$\Delta\mu$DL	0.00	0.21	0.31	0.43	1.98	2.60	3.45
	μL	17.4	17.5	17.3	17.5	16.3	16.1	15.7
SeMet	$\Delta\mu$DL	0.00	0.22	0.33	0.44	2.00	2.55	3.38
	μL	17.3	17.3	17.2	17.2	16.4	15.7	14.7
Eth	$\Delta\mu$DL	0.00	0.18	0.29	0.39	1.82	2.45	3.25
	μL	17.0	17.0	16.8	16.9	16.4	15.5	14.7
Cys2	$\Delta\mu_{12}$	0.40	0.67	0.94		4.14	7.35[a]	7.60[a]
	$\Delta\mu_{23}$	0.00	0.02	0.26		2.18		
	μL	25.9	25.7	25.6		21.6	19.0	15.5
SeCys2	$\Delta\mu_{12}$	0.45	0.80	1.10		4.80	5.29	5.49
	$\Delta\mu_{23}$	0.00	0.05	0.02		2.01	2.63	3.06
	μL	25.7	25.5	25.3		21.1	18.3	15.3
Trp	$\Delta\mu$DL	0.15	0.29	0.46	0.58	2.07	2.53	2.82
	μL	16.6	16.5	16.3	15.9	14.3	12.8	10.8
dMet	$\Delta\mu$DL			0.00			0.66	1.10
	μL			20.0			18.9	17.9

[a] Mobility difference for L-enantiomer (first peak) and D-enantiomer (third peak).

A decrease in vancomycin mobility with increasing concentration of the buffer, as depicted in Figure 1, is observed not only with MOPS/Tris buffer pH 7.0 but also with sodium phosphate buffer pH 7 and acetate–Tris buffer pH 4.5. These observations imply that the interaction of vancomycin with the anionic analytes could depend, to an extent not commonly observed with the chiral selectors described so far, on the type and concentration of the buffer used.

Based on these experiments, 20 mM MOPS/Tris buffer pH 7.0 was selected for the chiral separation experiments. At this pH, the amino acids studied here are completely ionized, and vancomycin has a small positive charge, essentially independent of small deviations in the buffer concentration. The relatively low concentration of the buffer, consisting of ions with rather low mobilities, keeps the production of Joule heat below 0.11 W/m of 50 μm i.d. capillary, even at 20 kV.

The background absorption of vancomycin at 254 nm, measured in a 50 μm i.d. capillary filled with 5 mM vancomycin (the highest concentration used in this study), did not exceed 0.08 AU.

Chiral Separations. The main results of the chiral separation experiments using 0.1–5 mM vancomycin in 20 mM MOPS/Tris buffer pH 7.0 are summarized in Table 2. Data for AQC-derivatized DL-tryptophan and *N*-2,4-DNP-DL-methionine are included for comparison. The data in Table 2 demonstrate that vancomycin causes a remarkable difference in mobility of the AQC-derivatized amino acid enantiomers. Interaction with vancomycin of a concentration as low as 0.2 mM leads to a mobility difference of 0.18 mobility units for amino acid enantiomers having a single primary amine group. To achieve a comparable mobility difference with underivatized β-cyclodextrins, the concentration

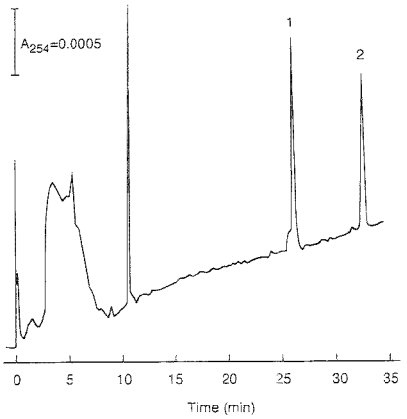

Figure 2. Separation of racemic ethionine in 2 mM vancomycin. Peak assignment: 1, L-ethionine; 2, D-ethionine; A, anionic decomposition product of the derivatization agent. Sample concentration, 2 × 10^{-5} M; injection time, 30 s; detection sensitivity, 0.005 AUFS at 254 nm.

of this chiral selector must be higher by 1 order of magnitude.[19] In practice, however, concentrations higher by 2 orders of magnitude are usually necessary.[20]

The mobility difference is roughly proportional to the vancomycin concentration up to 2 mM and attains a maximum value of about 2 mobility units. This unusually high mobility difference is accompanied by only a minimal loss of the mobility of the less retained enantiomers (amounting to 5–10%) and is characterized by a high separation efficiency (Figure 2). At vancomycin concentrations up to 0.4 mM, inducing a mobility difference of at least 0.4 mobility units (more than sufficient for baseline separation, even in the presence of a relatively strong electroosmosis, see Figure 3), the mobility decrease of the less retained enantiomer is negligible. This should be compared with separations using cyclodextrins, where the maximum attainable mobility difference (rarely higher than 0.4 mobility units) is generally accompanied by a mobility drop as high as 30–50%.[20] Furthermore, enantioseparations with cyclodextrins sometimes require that the analytes are only partially ionized, and this restricts the pH range within which separation can be realized.

The separation efficiency, calculated from several separations of AQC-derivatized amino acids and from the separation of the *N*-2,4-DNP-DL-methionine by 5 mM vancomycin (Figure 4) amounts to 250 000 theoretical plates/m of capillary, a value indicating fast kinetics of the separation process.

For cystine and selenocystine, having two negative charges and two derivatized amino groups, the mobility difference observed at low concentrations of vancomycin is 3–4 times higher than that for singly-charged derivatives. It allows baseline separation of DL-cystine with only 0.1 mM vancomycin in the BGE (Figure 5) or the separation of *meso*-selenocystine from the D- and L-enantiomers of selenocystine with only a 0.3 mM concentration of the chiral selector (Figure 6a). The separation of *meso*-cystine, present as a minor impurity in commercially available racemic

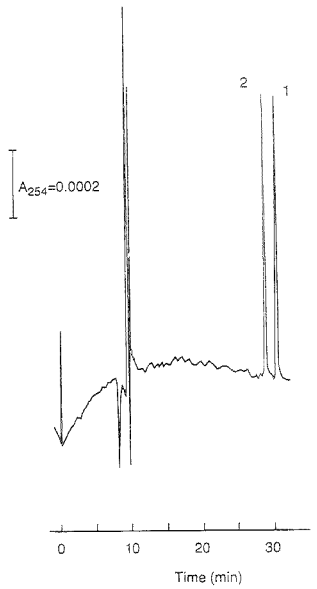

Figure 3. Separation of racemic selenomethionine in 0.4 mM vancomycin. Peak assignment, 1, L-selenomethionine; 2, D-selenomethionine. Sample concentration, 2 × 10^{-5} M; injection time, 20 s; detection sensitivity, 0.002 AUFS at 254 nm.

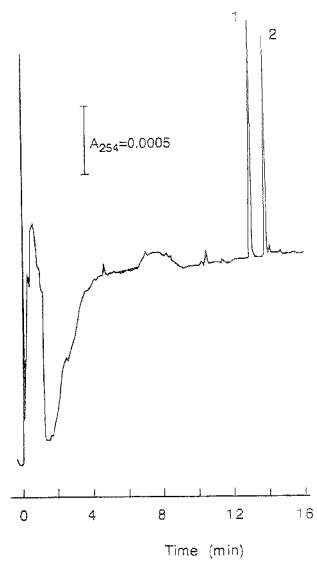

Figure 4. Separation of racemic *N*-2,4-DNP-DL-methionine in 5 mM vancomycin. Peak assignment: 1, L-enantiomer; 2, D-enantiomer. Sample concentration, 5 × 10^{-5} M; injection time, 25 s; detection sensitivity, 0.005 AUFS at 254 nm.

cystine, is also possible at this vancomycin concentration. Resolution of the critical pair of analytes is even better (Figure 6b), in spite of the fact that the mobility difference of the D- and

(19) Kuhn, Z.; Hoffstetter-Kuhn, S. *Chromatographia* **1993**, *34*, 505–512.
(20) Wren, S. A. C.; Rowe, R. C. *J. Chromatogr.* **1993**, *635*, 113–118.

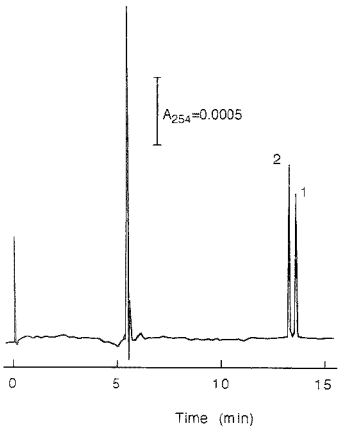

Figure 5. Separation of approximate 1:1 mixture of cystine enantiomers in 0.1 mM vancomycin. Peak identity: 1, L-cystine; 2, D-cystine. Total cystine concentration, 1×10^{-5} M; injection time, 20 s; detection sensitivity, 0.005 AUFS at 254 nm.

L-enantiomers of cystine is less than that of D- and L-selenocystine (Table 2). The same effect, a lower mobility difference of enantiomers of the sulfur analogue, was also found for methionine and selenomethionine.

From an analytical point of view, submillimolar vancomycin concentrations appear to be more advantageous for the chiral separation of sulfur- and selenium-containing AQC-derivatized amino acids. Vancomycin at 0.4 mM is able to produce mobility differences that are sufficient to separate all stereoisomers of these compounds, even in the presence of strong electroosmosis. These mobility differences are generated without loss of the separation speed resulting from deceleration of the less retained enantiomer. Low concentrations of vancomycin in the BGE have a negligible background absorption at 254 nm and therefore do not adversely affect the baseline noise or drift, resulting in a minimal, if any, decrease in detection sensitivity. With 2 mM vancomycin, the mobility differences far exceed what is needed for separation, and the mobility of the less retained enantiomer is markedly decreased, leading to unnecessary long analysis times. Moreover, baseline noise and instability increase significantly (Figure 4).

At vancomycin concentrations between 0.5 and 1.5 mM, the electroosmotic flow and the mobilities of the analytes are approximately equal, so under these conditions, no measurements can be performed. For the same reason, data for cystine and selenocystine in 0.4 mM vancomycin are absent in Table 2.

Spiking the racemates with pure L-enantiomers allowed the identification of the separated enantiomers, except for selenocystine, since its L-enantiomer is not commercially available. In all cases it was found that the L-enantiomer is less retained, which is in agreement with the data of Armstrong and co-workers.[14]

Remarkably, we observe in our study mobility differences that are 2–3 times as large as those reported by Armstrong et al.[14] (Table 3). We ascribe this to the use of different buffers. The ionic strength of 20 mM MOPS/Tris is 0.02 M, one-tenth that of the buffer used by Armstrong et al. (100 mM sodium phosphate pH 7.0, ionic strength ~0.2 M), suggesting that the affinity of vancomycin for the derivatized amino acids is at least partially

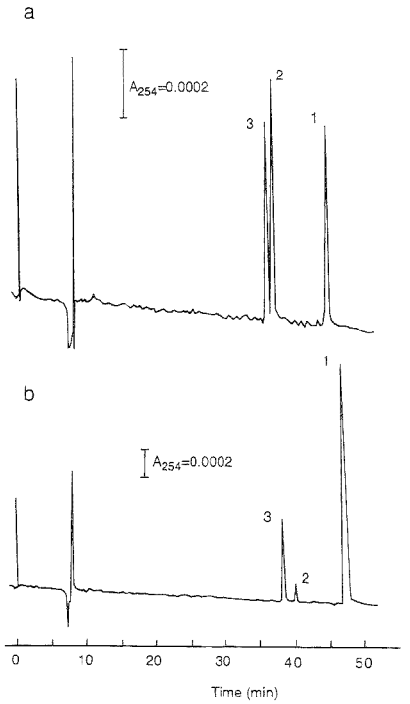

Figure 6. Separation of (a) racemic selenocystine and (b) 1:3 mixture of D- and L-cystine enantiomers in 0.3 mM vancomycin. (a) tentative peak assignment (based on analogy with Figure 6b): 1, L-selenocystine; 2, *meso*-selenocystine; 3, D-selenocystine. Sample concentration, 2×10^{-5} M; injection time, 15 s; detection sensitivity, 0.002 AUFS at 254 nm. (b) Peak assignment: 1, L-cystine; 2, *meso*-cystine; 3, D-cystine. Sample concentration, 2×10^{-5} M; injection time, 20 s; detection sensitivity, 0.002 AUFS at 254 nm.

Table 3. Comparison of the Difference in Mobility (in 10^9 m^2 V^{-1} s^{-1}) of the D- and L-Enantiomers of Derivatized Amino Acids Caused by 5 mM Vancomycin in (a) 100 mM Sodium Phosphate Buffer pH 7.0 (Taken from Ref 14), and (b) 20 mM MOPS/Tris Buffer pH 7.0

	Met[a]	Trp	Thr	dMet	dsMet	dsTrp
a	1.2 (1.6)[b]	1.2 (1.8)[b]	0.4	0.3	2.2	0.3
b	3.5	2.8	1.4	1.1	8.4	1.4

[a] Met, Trp, Thr: methionine, tryptophan, and threonine, respectively, derivatized with AQC. dMet: *N*-2,4-DNP-DL-methionine. dsMet: dansylmethionine. dsTrp: dansyltryptophan. [b] Values measured in our laboratory.

governed by electrostatic forces. The stronger interaction of phosphate with vancomycin might play a role as well. In addition to adjusting the concentration of the chiral selector, these effects can be used to fine-tune the separation selectivity of vancomycin. Unfortunately, uncoated capillaries are not very convenient for a more detailed study of buffer effects, since the cathodic electroosmotic flow depends in a complex way on the type and concentration of the buffer and on the vancomycin concentration (Figure 7), leading in some cases to very low migration rates of the analytes.

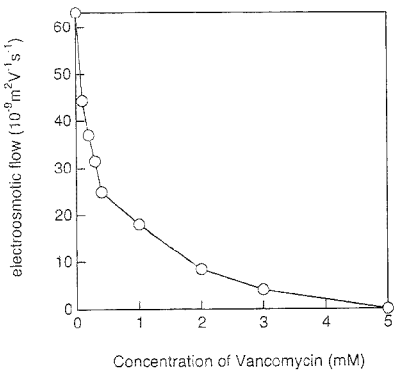

Figure 7. Dependence of the electroosmotic flow on vancomycin concentration in 20 mM MOPS/Tris buffer pH 7.0.

The reproducibility of the enantioselective separations during one day was checked by repeated (≥3) injections of the same sample, and the standard deviation of the mobility, corrected for electroosmosis, never exceeded 0.07×10^{-9} m^2 V^{-1} s^{-1}. The effect of long contact times between vancomycin and the capillary was also investigated by leaving 2 mM vancomycin in the instrument overnight at room temperature. Repeating the analysis of selenomethionine and selenocystine revealed an increase in the mobility difference between the second (*meso*-selenocystine) and the third peaks (D-selenocystine) of the selenocystine sample (Figure 6a) by 0.6 mobility units. The mobility difference between the first two peaks of DL-selenocystine and DL-selenomethionine decreased by 0.05 and 0.07 mobility units, respectively, while their mobilities increased by 0.3 mobility units. These variations are of the same order of magnitude as observed for day-to-day reproducibility using fresh vancomycin solutions and indicate that vancomycin is sufficiently stable at room temperature, even after a 16 h exposure to the capillary wall.

Since vancomycin is a charged compound, it can be expected that its concentration will have an influence on the current flowing through the capillary. Indeed, 5 mM of vancomycin almost doubles the current of 3.2 μA measured in the absence of vancomycin.

The dependence of the electroosmotic flow on the vancomycin concentration in the BGE (Figure 7) indicates that vancomycin adsorbs to the wall of the capillary. When the concentration of vancomycin in a capillary, equilibrated with 5 mM vancomycin in 20 mM MOPS/Tris buffer pH 7, is decreased to 0.05 mM in the same buffer by flushing it under reduced pressure, the baseline level, electroosmosis, and separation selectivity are completely changed in less than 5 min. The subsequent stabilization of the electroosmotic flow is, however, much slower, taking at least 60 min.

The failure to separate several randomly chosen cationic racemates (diltiazem, bupivacaine, isoprotenerol, and propanolol) and the successful separation of all the anionic racemates studied here, in addition to the enantioseparation of a large number of anionic racemates reported by Armstrong et al.,[14] clearly indicate that a negative charge of the analyte plays an essential role in the chiral discrimination by vancomycin. AQC-derivatized DL-methionine is much better resolved than the dinitrophenyl derivative, suggesting that hydrophobic and steric interactions are equally important. This is also indicated by the fact that the mobility difference of the AQC-derivatized DL-tryptophan enantiomers is systematically greater than that observed for the methionine, selenomethionine, and ethionine racemates.

Vancomycin is a good choice for the separation of all enantiomeric forms of the analytes studied here. It combines the separation selectivity of proteins (which are, however, characterized by a low separation efficiency) with the high separation efficiency typical of cyclodextrins and crown ethers. The latter compounds produce mobility differences lower by at least 1 order of magnitude compared to vancomycin. These particular properties of vancomycin should enable the design of an analysis in which the separation of all the enantiomers of each of the studied amino acids is achieved within a few minutes. Studies to achieve this goal are in progress.

ACKNOWLEDGMENT

We thank the Dutch Organisation for Scientific Research (NWO) for a grant to R.V. Waters (Etten-Leur, The Netherlands, and Milford, MA) is gratefully acknowledged for the loan of the Quanta 4000E.

Received for review February 1, 1995. Accepted June 20, 1995.[⊗]

AC9501102

[⊗] Abstract published in *Advance ACS Abstracts*, August 1, 1995.

Anal. Chem. 1995, *67*, 3229–3233

On-Line Coupling of Flow Field-Flow Fractionation and Multiangle Laser Light Scattering for the Characterization of Polystyrene Particles

Heiko Thielking, Dierk Roessner, and Werner-Michael Kulicke*

Institut für Technische und Makromolekulare Chemie, Universität Hamburg, Bundesstrasse 45, 20146 Hamburg, Germany

The on-line coupling of a flow field-flow fractionator (F^4) and a multiangle laser light scattering detector (MALLS) produces a novel analytical system for dispersed samples. Absolute distribution measurements are obtained for the molar mass and radius of gyration, which is directly related to the particle diameter. In this work, polystyrene latex standards (50, 105, and 304 nm and a mixture) dispersed in water were used to investigate the accuracy of a system with on-line coupling of F^4 and MALLS. Tests were carried out in a constant field of force and for the first time in a programmed field of force mode. The results show that it is possible to use MALLS and a decreasing cross-flow for separation and that, even with changing cross-flow and under nonideal elution conditions, coupling to MALLS gives more reliable results than those obtained with a F^4 system alone.

Flow field-flow fractionation (F^4) is probably the most universally applicable fractionation method for dissolved or dispersed particles involving polymer molecules (nonionic and ionic),[1] aggregates,[2] colloids,[3] proteins,[4] or virus samples.[5] Separation in F^4 is based on differences in diffusion coefficients. F^4 has a dynamic separation range from $\approx 10^4$ to 10^{12} in molar mass and requires only that the sample be soluble or dispersible in some carrier liquid.[6] There are no problems with adsorption, charge repulsion, or degradation, as known from other separation techniques.[1,7]

Multiangle laser light scattering (MALLS) is one of the few absolute methods available for the determination of molar mass and particle size over a broad range (between a few thousand and several million).[8] An absolute MALLS experiment yields the molar mass and the corresponding radius of gyration without any need for polymer standards. However, if MALLS is not coupled with a fractionation method, these results will only be average values.

Often there is a great demand for information on the distributions of size and mass. In technical applications for latices, these distributions are crucial in controlling the properties of the product. The production of paper or water-based paints, for example, calls for broadly distributed latices because the small particles increase the adhesive power and the larger ones are responsible for a smooth and shiny surface. On-line coupling of F^4 and MALLS makes it possible to sort particles according to their size and analyze their molar mass and dimensions one by one in order to obtain the absolutely determined distributions of molar mass and radius of gyration for broadly dispersed samples. Our very first results obtained on latices and dextran were published recently.[9]

Naturally, there are some limitations and problems associated with tandem techniques. As described in publications about the coupling of MALLS with other fractionation methods, a concentration detector (e.g., a differential refractive index detector, DRI) is needed.[8] The sensitivity of MALLS/DRI requires extremely pure solvents and samples.[10] In the case of F^4, there is a great demand for a well-poised flow and pressure balance. To improve the detectability and the separation speed of broadly dispersed samples, it is sometimes useful to work with decreasing instead of constant cross-flow. To obtain an ideal, programmable cross-flow, it is necessary to have computer control over all flows at any one time. In addition, when the flow is switched between the cross-flow pump pistons, there is no active field of force for a fraction of a second. During this period, some of the sample may be eluted and be well detected by the MALLS but not recognized by the DRI (which leads to unwanted spikes).

The aim of this work was to test the accuracy of F^4/MALLS/DRI investigations on very well-characterized (transmission electron microscopy, TEM) polystyrene latex standards using a constant cross-flow to analyze individual samples. An additional aim was to try to establish a programmable cross-flow which could improve the efficiency and detection quality of this method for very broadly dispersed samples. The programmable F^4/MALLS/DRI was tested by mixing the standards so that they could be analyzed in one run.

THEORY

Flow field-flow fractionation is probably the most generally useful of all of the FFF methods for the separation/characterization of macromolecules and particulates.[6] F^4 separates particles according to their diffusion coefficients using two streams of the same liquid flowing perpendicularly against each other. The general theory was developed by Giddings et al.[1] Simple equations relate the diffusion coefficient of a species to its retention time. The Einstein–Stokes equation gives the relation between the diameter and the diffusion coefficient for homogeneous

(1) Benincasa, M. A.; Giddings, *J. C. Anal. Chem.* **1992**, *64*, 790.
(2) Giddings, J. C.; Benincasa, M. C. *Polym. Mater. Sci. Eng.* **1991**, *65*, 21.
(3) Ratanathanawongs, S. K.; Giddings, J. C. *Polym. Mater. Sci. Eng.* **1991**, *65*, 24.
(4) Giddings, J. C.; Yang, F.; Myers, M. N. *Anal. Biochem.* **1977**, *81*, 395.
(5) Giddings, J. C.; Yang, F.; Myers, M. N. *J. Virol.* **1977**, *21*, 131.
(6) Kirkland, J. J.; Dilks, C. H.; Rementer, S. W. *Anal. Chem.* **1992**, *64*, 1295.
(7) Kulicke W.-M.; Böse N. *Colloid Polym. Sci.* **1984**, *262*, 197.
(8) Wyatt, P. J. *Anal. Chim. Acta* **1993**, *272*, 1.
(9) Roessner, D.; Kulicke W.-M. *J. Chromatogr. A* **1994**, *687*, 249.
(10) Kulicke W.-M.; Kniewske R. *Makromol. Chem.* **1980**, *1*, 719.

0003-2700/95/0367-3229$9.00/0

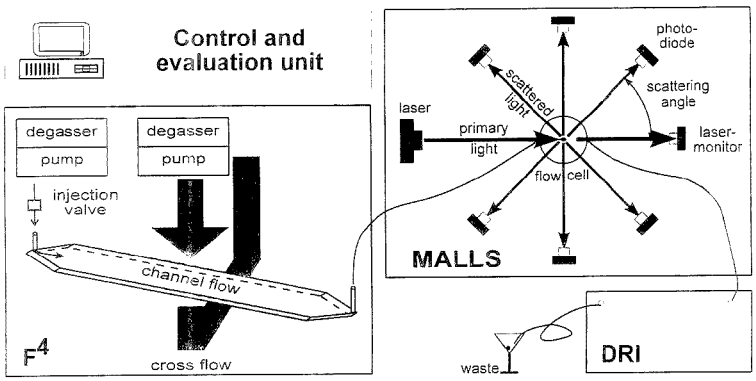

Figure 1. Schematic representation of the flow field-flow fractionator on-line coupled to the multiangle laser light scattering detector with its flow cell and the 18 photodiodes (only six to be seen) and the differential refractive index detector.

spherical particles. Equation 1 gives the Stokes diameter d_{FF} as a function of elution time t_R (approximation for $\lambda \ll 1$),[1] where $\dot{V}_x$ and $\dot{V}_z$ are the volume velocities of the two flows, w the channel thickness, and η the viscosity of the eluent.

$$d_{FF} = \frac{2kT\dot{V}_z}{\pi\eta w^2 t_R \dot{V}_x} \tag{1}$$

Multiangle Laser Light Scattering. Early formulations of the theory of light scattering were put forward by Einstein,[11] Raman,[12] Debye,[13] and Zimm[14] and can be found in any modern textbook (e.g., ref 15). Multiangle laser light scattering means measuring the intensity of the scattered light emitted by the sample particles under different scattering angles θ. With a modern MALLS photometer, it is possible to monitor continuously the scattering by means of several detectors mounted at different angles. This allows the MALLS photometer to be coupled with any fractionation method and then used to carry out absolute measurements. The values for the molar mass M_w and the radius of gyration $\langle R_G^2\rangle_z^{0.5}$ at each "slice" along the distribution can be calculated using the following equations:

$$\frac{Kc}{R_\theta} = \frac{1}{M_w P(\theta)} + 2A_2 c + \ldots \tag{2}$$

$$P(\theta) = 1 - a_1[2k \sin(\theta/2)]^2 + a_2(2k \sin(\theta/2))^4 - \ldots \tag{3}$$

where K is a light scattering constant, containing the wavelength λ_0 of the incident light, the refractive index n_0 of the pure eluent, and the refractive index increment dn/dc; c is the concentration; A_2 is the second virial coefficient; R_θ is the excess Rayleigh ratio; and $P(\theta)$ is a general form of a scattering function. For very diluted concentrations, the second and higher order terms in eq 2 can usually be neglected and R_θ becomes directly proportional to $M_w P(\theta)$. Plotting R_θ/Kc against $\sin^2(\theta/2)$ gives M_w from the intercept with the ordinate and $\langle R_G^2\rangle_z^{0.5}$ from the angular dependence of the intensity of the scattered light, which is included in a_1 and higher order terms of eq 3. The definition of the z-average square radius of gyration, in the event that a distribution of molecular size is present, is given by eq 4.

$$a_1 = {}^1/_3\langle R_G^2\rangle_z^{0.5} = \frac{1}{3M}\int r^2 \, dM \tag{4}$$

The values obtained for $\langle R_G^2\rangle_z^{0.5}$ are independent of dn/dc (assumed constant), M_w, or even c (sufficiently small) and therefore insensitive to errors.[8] When interpreting the value obtained for the molar mass, it is necessary to bear in mind that two assumptions of the light scattering theory for molecules might not have been fulfilled in the case of latices. The first assumption is that the wave front is not altered on its passage through the sample, and the second is that the refractive index difference between sample and solvent is small.

EXPERIMENTAL SECTION

Apparatus. Figure 1 is a schematic diagram of the system used in this study. The fractionator was a model F-100 from FFFractionation, Inc. (Salt Lake City, UT). The 250 μm Teflon spacer (28.5 cm tip-to-tip length, 2.0 cm width) was bound by ceramic frits with a pore size of 3–5 μm. The lower frit was covered with a cellulose membrane, type YM 10. The channel flow was delivered by an MC-1000 HPLC pump from Costa Metrics (LDC Analytical, Riviera Beach, FL) at constant rates. The cross-flow was provided by a double piston precision pump from Reichelt (Reichelt Chemietechnik GmbH & Co., Heidelberg, Germany). With inlet and outlet flow under computer control, the magnitude of the cross-flow could be varied as desired. The channel effluent was directed through a DAWN-DSP-F light scattering photometer (Wyatt Technology Corp., Santa Barbara, CA) and then into a RI SE-51 differential index detector (Showa Denko K.K., Tokyo, Japan).

Materials. The samples were narrowly distributed polystyrene latex spheres from Duke Scientific (Palo Alto, CA) with nominal diameters of 50 ± 2, 105 ± 3, and 304 ± 6 nm and were certified to as calibrated with methodology traceable to the U.S. National Institute of Standards and Technology. The carrier solution was deionized, and double-distilled water containing

(11) Einstein, A. *Ann. Phys.* **1910**, *33*, 1275.
(12) Raman C. V. *Ind. J. Phys.* **1927**, *2*, 1.
(13) Debye P. *J. Appl. Phys.* **1944**, *15*, 338.
(14) Zimm B. H. *J. Chem. Phys.* **1945**, *13*, 141.
(15) Kratochvil P. In *Light Scattering from Polymer Solutions*; Huglin, M. B., Ed.; Academic Press: London, 1981.

0.005% (w/w) sodium dodecyl sulfate was used as a dispersant and 0.02% (w/w) of sodium azide as a bactericide. The solution was purified by filtration (0.1 μm)[10] and on-line degassed (Knauer, Germany).

Procedures. The particles were dispersed by immersion in a low-power ultrasonic bath for 15–30 s. The injection volume was 50 μL, with an amount ranging from 0.08 to 1.00 mg for samples consisting of a single size of latex particles and 1.00 mg (Duke 50, 0.71 mg; Duke 105, 0.27 mg; Duke 304, 0.08 mg) for the particle mixture. Following injection, samples were allowed to relax into their equilibrium distribution under the influence of the cross-flow but with a bypassed channel flow. This stop-flow condition was maintained until ~1.5 channel volumes of cross-flow had passed across the channel.

The calibration of the DAWN was done with ultrapure toluene, and the normalization of the fixed 18 scattering angles was performed with a disperse solution of gold with known diameter. For determination of the interdetector volume, the "spider" plot method[8] was used. The signal of the DRI detector was routed to the DAWN, which was interfaced to an AT computer.

RESULTS AND DISCUSSION

To get an ideal, programmable cross-flow, we connected the frit inlet and the frit outlet of the channel with one and the same pump so as to form a closed circuit. Having this pump under computer control means that there are no unwanted changes in the flow balance. However, when a suction pump is fitted on the frit outlet side, it becomes necessary to provide as much back pressure on the channel outlet side as the membrane generates in order to prevent the system from drawing in air. The second problem of spiking was controlled by installing pulse damping and pressure restriction on both pumps.

The use of a MALLS photometer enables the radius of gyration to be calculated for each eluting slice. The calculation is independent of experimental parameters, i.e., flow rates, detector delay, calibration, concentration, the refractive index increment, interdetector volume, and band broadening. The only source of error lies in the accuracy with which the sensitivity of the 18 detectors has been normalized. For this reason, the determination of the radius of gyration is very useful in checking the quality of a fractionation method.

The scattering function gives a linear graph for small particles and a more curved one for larger particles.[15] Therefore, it is useful to use different order fits of eq 3 for different particles sizes. Figure 2 shows the angular dependence for the samples Duke 105 and 304 at the peak maxima. The plot of R_θ/Kc against $\sin^2(\theta/2)$ for the sample Duke 105 was fitted to a second-order function and that for the Duke 304 sample to a third-order function in order to give the minimized squares of the errors.

Figure 3 shows the radius of gyration calculated from the angular dependence of the three single runs. The radius for each individual fraction is plotted against the elution time. In order to gain an impression of the concentration at each point, the elution profile has been included in the background. For greater clarity, the data for the Duke 304 sample were shifted 10 min to a higher elution time in Figure 3. It can be seen that there is a gentle slope in the radius of gyration plots with higher elution volumes for all three samples. This means that even narrowly distributed standards can be fractionated with this method. The width of the elution profile is not only a result of the band broadening. Taking both pieces of information ($\langle R_G^2\rangle^{0.5}$ and c) separates

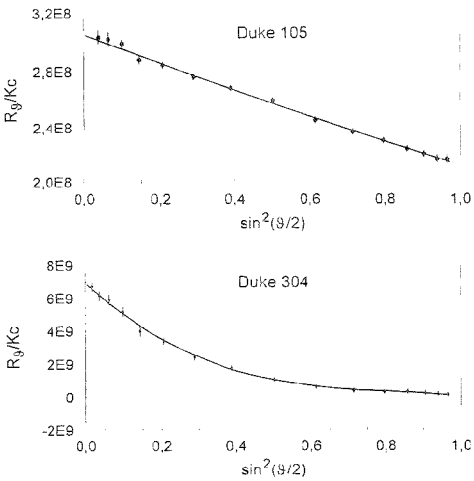

Figure 2. Representation of the angle dependence of the intensity of the scattered light for the samples Duke 105 and 304 at the peak maximum.

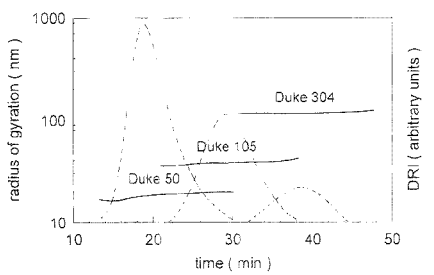

Figure 3. Radius of gyration for the samples Duke 50, 105, and 304 plotted against the elution time (the elution profiles have been plotted as dotted lines). For greater clarity, the data for the Duke 304 sample were shifted 10 min to a higher elution time ($\dot{V}_z$ = 1.08 mL/min; Duke 50, $\dot{V}_x$ = 0.75 mL/min, Duke 105, $\dot{V}_x$ = 0.42 mL/min, and Duke 304, $\dot{V}_x$ = 0.13 mL/min).

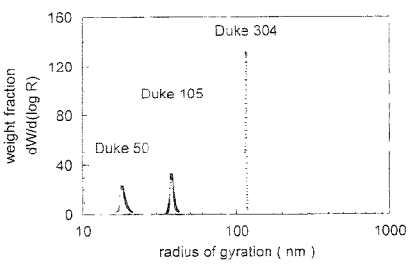

Figure 4. Differential distribution of the radii of gyration for the samples Duke 50, 105, and 304. Fractionation and detection were performed with CFF F4/MALLS/DRI (T = 298 K, in water containing 0.005% (w/w) sodium dodecyl sulfate and 0.02% (w/w) sodium azide, λ = 632.8 nm, θ = 3°–160°).

polydispersity from band broadening, because the evaluation involves adding fractions of the same size, and thus the true distribution of the radius of gyration is the result (see Figure 4).

Table 1. Calculated Mean Values of Molar Mass and Radius of Gyration for Duke Samples 50, 105, and 304 Determined by MALLS/DRI and the Stokes Diameter Calculated from the Retention Time Using F^4 Theory[a]

	Duke 50	Duke 105	Duke 304
M_n (g/mol)	3.73×10^7 (±3%)	3.20×10^8 (±2%)	8.30×10^8 (±3%)
M_w (g/mol)	3.85×10^7 (±3%)	3.22×10^8 (±2%)	8.34×10^8 (±3%)
M_w/M_n	1.03	1.01	1.00
$\langle R_G^2 \rangle_z^{0.5}$ (nm)	18.9 (±2%)	37.8 (±2%)	116.5 (±2%)
d_{TEM} (nm) – nominal	50 (±2)	105 (±3)	304 (±6)
d_{LS} (nm)	48	98	300
d_{F^4} (nm)	48	128	366

[a] The errors indicated are the percentage standard deviation of the results from five experiments.

It can be seen that the polydispersity decreases from Duke 50 to Duke 304. If F^4 theory had been employed alone, it would not have been possible to distinguish polydispersity from band broadening. This error in F^4 has been discussed by Andreev[16] among others.

Table 1 gives the numerical results (polydispersity of the molecular mass distribution and the mean values of molar mass and radius of gyration) which were obtained with CFF F^4/MALLS/DRI. The percentage error indicated gives the standard deviation for five identical runs.

Equation 5 enables the diameter to be calculated for homogeneous spherical particles by using the radius of gyration measured by light scattering (Table 1). This allows the results

$$d_{LS} = \sqrt{\frac{20}{3}\langle R_G^2 \rangle_z} \qquad (5)$$

to be compared with the nominal diameters given by TEM. In addition, the Stokes diameter of the particles can be calculated from the retention time using eq 1 (Table 1).

There is good agreement between the light scattering data and the nominal diameters for all samples. For the Duke 50 sample, there is also good agreement with the results obtained from the retention time using F^4 theory. For the larger samples, we found deviations of ~20% from the nominal diameter. This may be the result of a nonideal elution process. The best fractionation conditions chosen for the larger latices may not have been the best possible. A lot of possible errors and deviations from ideal elution theory are discussed in the literature.[16,17] However, using MALLS/DRI for detection instead of DRI or UV gives more reliable results, even if the ideal elution conditions are not known.

To discover how well F^4/MALLS/DRI analysis performs over a broad size range and to see how the MALLS/DRI detection reacts to a changing field of force in F^4, we mixed the three Duke samples in different amounts and separated them in one run using a programmed field of force. As can be seen in Figure 5, there is no problem in obtaining good baseline separation. Figure 5 shows the response of 17 MALLS detectors against the elution time. A semilogarithmic plot was chosen because of the large scattering intensity differences of the 50 the 304 nm Duke samples (see boxed figure). The different angular dependencies for small and large particles are particularly visible. The numeric results are comparable with those reported for the single runs with constant field (Table 1).

(16) Andreev V. P.; Stefanovich L. A. *Chromatographia* **1993**, *37*, 325.
(17) Litzen A.; Wahlund K.-G. *J. Chromatogr.* **1991**, *548*, 393.

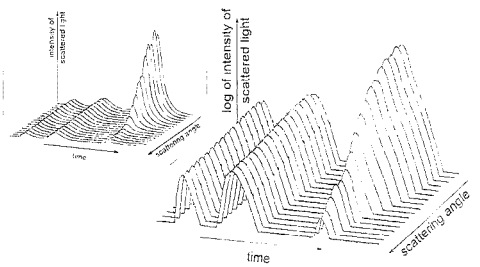

Figure 5. Scattering intensity of the MALLS detectors from 3° to 160° versus elution time for a mixture of three Duke standards. Measurement performed with PFF F^4/MALLS/DRI. The channel flow was $\dot{V}_z$ = 1.08 mL/min, and the cross-flow $\dot{V}_x$ decreased from 1.5 down to 0.07 mL/min in 140 min (T = 298 K, in water containing 0.005% (w/w) sodium dodecyl sulfate and 0.02% (w/w) sodium azide. λ = 632.8 nm).

ACKNOWLEDGMENT

This work was kindly supported by the Deutsche Forschungsgemeinschaft (DFG). This work is dedicated to Prof. Dr. J. Klein on the occasion of his 60th birthday.

GLOSSARY

A_2	second virial coefficient in the Zimm–Debye equation
a_1, a_2, ...	virial coefficiens
CFF	constant field of force
c	concentration
D	diffusion coefficient
DRI	differential refractive index
d_{F^4}	Stokes diameter obtained from F^4 theory
d_{LS}	diameter obtained from light scattering theory
dn/dc	refractive index increment
FFF	field-flow fractionation
F^4	flow FFF
K	light scattering constant, equal to $4\pi^2(dn/dc)^2 n_0^2/N_A\lambda_0^4$
k	Boltzmann constant
k	constant, equal to $2\pi n_0/\lambda_0$
M	molar mass
M_w	weight average molar mass
MALLS	multiangle laser light scattering
n_0	refractive index of pure solvent

N_A	Avogadro number
PFF	programmed field of force
$P(\theta)$	scattering function
$\langle R_G^2 \rangle^{0.5}$	radius of gyration
$\langle R_G^2 \rangle_z^{0.5}$	z-average radius of gyration
R_θ	excess Rayleigh factor
r	distance from the center of gravity
T	absolute temperature
TEM	transmission electron microscopy
t_R	retention time
V^0	void volume
$\dot{V}_x$	flow rate of cross flow
$\dot{V}_z$	flow rate of channel flow
w	channel thickness
θ	scattering angle
η	viscosity
λ	retention parameter, equal to $DV^0/\dot{V}_z w^2$
λ_0	wavelength of incident light

Received for review February 23, 1995. Accepted June 20, 1995.[⊗]

AC950201Z

[⊗] Abstract published in *Advance ACS Abstracts*, August 1, 1995.

Anal. Chem. 1995, *67*, 3234–3245

Electroosmotically Transported Baseline Perturbations in Capillary Electrophoresis

Christa L. Colyer,† Keith B. Oldham,* and Artjom V. Sokirko

Department of Chemistry, Trent University, Peterborough, Ontario K9J 7B8, Canada

Two anomalous capillary electrophoresis (CE) phenomena, referred to as the baseline shift and spontaneous-marker peak, are investigated. The baseline shift and spontaneous-marker peak have been observed in a simple CE system with no sample injection and no deliberately formed concentration boundaries, a sodium benzoate solution as the running electrolyte, and on-column UV absorbance detection. The baseline perturbations, which are believed to have physical origins at the capillary inlet, are transported along the capillary at the rate of electroosmotic flow. Baseline perturbations observed previously have been attributed to pH changes or temperature changes, and although the latter may influence our results somewhat, neither of these effects can explain the phenomena that we have observed. Instead, we believe these baseline shifts and spontaneous-marker peaks are attributable to changes in the actual concentration of the running electrolyte. Although the property of a capillary end which is responsible for the generation of baseline perturbations remains unknown, the transport of the concentration excursions and the origin of spontaneous-marker peaks are explained.

Capillary electrophoresis (CE) is now a well-established field with many unique features and valuable applications. Much effort has been devoted to the development of CE as a powerful separation tool, with attention focused on the role of migration in the transport of analyte species.[1-6] Recently, the role of electroosmosis in analyte transport in CE systems has become a topic of interest,[7-13] although for analytical purposes, electroosmosis is often intentionally controlled because of its variability.[14-20] Our present interest, however, is predominantly in the study of electroosmosis and its implications for simple CE systems. In particular, we have investigated two anomalous CE phenomena which are believed to have physical origins and whose effects are transported along the capillary column at the rate of electroosmotic flow. These phenomena, which are interrelated perturbations in the baseline UV signal, representative of disturbances in the electrolyte concentration, are referred to as the "baseline shift" and "spontaneous-marker signal". It is believed that these phenomena may exist in other CE studies but that the interests of those studies are such that the baseline perturbations discussed herein have been either discounted or obscured by other signals. Unlike most CE studies, the present work does not involve the injection of a sample onto the capillary column for subsequent analysis, nor does it concern the separation efficiency of a given CE system. Instead, the factors which affect the appearance and behavior of the baseline shift and spontaneous-marker signal are investigated.

Related work includes that of Vinther and co-workers,[21] who observed a positive shift in baseline UV absorbance occurring at the time of electroosmotic flow, which they attributed to a dependence of the absorbance on buffer pH. System peaks and baseline disturbances, occuring before the electroosmotic flow marker, were studied by Beckers[22] for a discontinous buffer system. Furthermore, temperature-induced fluctuations in the baseline UV absorbance have also been studied.[23,24] These other studies, although somewhat related to this work, are unable to provide an explanation of the origin of the baseline shift and spontaneous-marker signal described herein. Although such an explanation remains incomplete, we believe that a study of these features will provide us with a greater understanding of CE systems. Brief descriptions of these phenomena follow.

In order to provide a "marker" of electroosmotic flow in CE, it is common practice to add a neutral species to injected analyte samples. On many occasions, however, we have observed spontaneous-marker signals in a simple system with on-column UV absorbance detection, a sodium benzoate solution as the running electrolyte, and no injection whatsoever. The spontaneous markers appear to originate at the instant of field application

† Queen's-Trent Graduate Program in Chemistry; Department of Chemistry, Queen's University, Kingston, Ontario K7L 3N6, Canada.

(1) Quang, C.; Khaledi, M. G. *J. Chromatogr. A* **1994**, *659*, 459–466.
(2) Smith, S. C.; Khaledi, M. G. *Anal.Chem.* **1993**, *65*, 193–198.
(3) Lee, T. T.; Yeung, E. S. *Anal. Chem.* **1991**, *63*, 2842–2848.
(4) Compton, B. J.; O'Grady, E. A. *Anal. Chem.* **1991**, *63*, 2597–2602.
(5) Grossman, P. D.; Colburn, J. C.; Lauer, H. H. *Anal. Biochem.* **1989**, *179*, 28–33.
(6) Mikkers, F. E. P.; Everaerts, F. M.; Verheggen, P. E. M. *J. Chromatogr.* **1979**, *169*, 1–10.
(7) Andreev, V. P.; Lisin, E. E. *Chromatographia* **1993**, *37*, 202–210.
(8) Wu, C.-T.; Lopes, T.; Patel, B.; Lee, C. S. *Anal. Chem.* **1992**, *64*, 886–891.
(9) Kuhr, W. G.; Licklider, L.; Amankwa, L. *Anal. Chem.* **1993**, *65*, 277–282.
(10) Chien, R.-L.; Helmer, J. C. *Anal. Chem.* **1991**, *63*, 1354–1361.
(11) Rohlíček, V.; Deyl, Z.; Mikši, I. *J. Chromatogr. A* **1994**, *662*, 369–373.
(12) Vinther, A.; Søeberg, H. *J. Chromatogr.* **1992**, *589*, 315–319.
(13) Schützner, W.; Kenndler, E. *Anal. Chem.* **1992**, *64*, 1991–1995.
(14) Keely, C. A.; Holloway, R. R.; van de Goor, T. A. A. M.; McManigill, D. *J. Chromatogr. A* **1993**, *652*, 283–289.
(15) Bruin, G. J. M.; Chang, J. P.; Kuhlman, R. H.; Zegers, K.; Kraak, J. C.; Poppe, H. *J. Chromatogr.* **1989**, *471*, 429–436.
(16) Kaneta, T.; Tanaka, S.; Taga, M. *J. Chromatogr. A* **1993**, *653*, 313–319.
(17) Hayes, M. A.; Ewing, A. G. *Anal. Chem.* **1992**, *64*, 512–516.
(18) Chang, H.-T.; Yeung, E. S. *Anal. Chem.* **1993**, *65*, 650–652.
(19) Huang, T.-L.; Tsai, P.; Wu, C.-T.; Lee, C. S. *Anal. Chem.* **1993**, *65*, 2887–2893.
(20) Birrell, H. C.; Camilleri, P.; Okafo, G. N. *J. Chem. Soc., Chem. Commun.* **1994**, *1*, 43–44.
(21) Vinther, A.; Everaerts, F. M.; Søeberg, H. *J. High Resolut. Chromatogr.* **1990**, *13*, 639–642.
(22) Beckers, J. L. *J. Chromatogr. A* **1994**, *662*, 153–166.
(23) Bello, M. S.; de Besi, P.; Righetti, P. G. *J. Chromatogr. A* **1993**, *652*, 317–327.
(24) Gaš, B. *J. Chromatogr.* **1993**, *644*, 161–174.

0003-2700/95/0367-3234$9.00/0

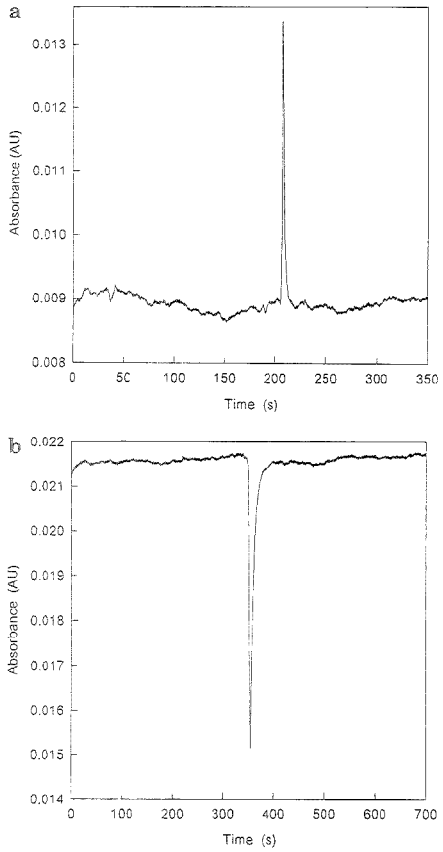

Figure 1. Capillary electropherograms showing typical spontaneous-marker peaks for a CE system with no injection. 20.0 mM NaBz original running electrolyte, 15.03 kV applied voltage, and detection at 225 nm. (a) A positive spontaneous-marker peak. Experimental conditions: column length, 57.30 cm; inlet-to-detector length, 31.20 cm; average measured current, 9.24 μA. (b) A negative spontaneous-marker peak. Experimental conditions: column length, 88.70 cm; inlet-to-detector length, 30.00 cm; average measured current, 6.39 μA.

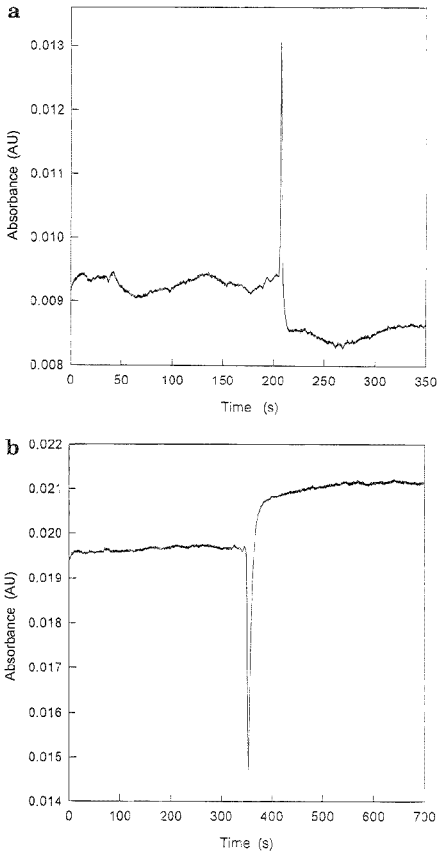

Figure 2. Capillary electropherograms showing typical spontaneous-marker peaks accompanied by baseline shifts resulting from changes in the applied field strength for a CE system with no injection. 20.0 mM NaBz original running electrolyte, 15.03 kV applied voltage, and detection at 225 nm. (a) A positive spontaneous marker accompanied by a negative baseline shift resulting from an increase (87.6 V cm^{-1}) in the applied field strength. Experimental conditions: column length, 57.30 cm; inlet-to-detector length, 31.20 cm; average measured current, 9.30 μA. (b) A negative spontaneous marker accompanied by a positive baseline shift resulting from an increase (56.7 V cm^{-1}) in the applied field strength. Experimental conditions: column length, 88.70 cm; inlet-to-detector length, 30.00 cm; average measured current, 6.36 μA.

at the column inlet, are peak-shaped, and may be either positive or negative of the baseline absorbance, depending on some presently unknown property of the capillary end. Examples of typical spontaneous-marker peaks are shown in Figure 1. We believe that spontaneous markers arise from diffusion-controlled processes at the interface between the solution in the column and that in the bulk electrolyte reservoir(s).

The spontaneous-marker signal is sometimes accompanied by a field-dependent shift in baseline absorbance. In the case of positive marker signals, increasing the applied field results in a decrease in the baseline absorbance. Conversely, in the case of negative marker signals, increasing the applied field results in an increase in the baseline absorbance. The end of a column giving rise to the former case is referred to as a "depleting end", while that giving rise to the latter case is referred to as an "enriching end". Electropherograms generated at both types of "active" ends are shown in Figure 2. The baseline shifts represent real changes in electrolyte concentration, as confirmed by independent measurements of absorbance, conductivity, and electroosmotic mobility. Thus, baseline shifts indicate the existence of electrolyte concentration boundaries, which move along the column and past the detector by way of electroosmosis only. The time at which a baseline shift occurs coincides with that at which a spontaneous marker appears, and both serve to "mark" the rate of electroosmotic flow.

It appears that the existence of field-dependent baseline shifts, coupled with spontaneous-marker signals, depends in an undetermined way on the physical geometry of the end of the capillary

column. Thus, altering the end of the column by cutting to form a "new" end with a possibly different geometry, can result in the appearance or disappearance of these phenomena. Similarly, Cohen and Grushka[25] and Schwartz et al.[26] have shown that the capillary cut can influence separation efficiency and peak shape. Only a minority of column ends or "cuts" successfully generated baseline shifts and spontaneous-marker peaks. Over the course of these studies, three capillaries were installed. The length of each of these was continually diminished throughout its lifetime by cutting small lengths of capillary from either end, thereby exposing new cross-sectional annuli of the capillary. Spontaneous-marker signals were observed for all of the columns. The majority of baseline shift studies were conducted on the second and third columns, over a period of about 4 months on each. On the second column, seven cuts were made, and only two of these (29% of all cuts) resulted in an "active" column end which gave rise to baseline shifts. On the third column, 47 cuts were made, 10 of which (21% of all cuts) produced baseline shifts. The magnitudes of the baseline perturbations vary greatly depending on the cut of the column and are often small enough to go unnoticed under the conditions normally encountered in analytical electrophoresis. When large, however, baseline shifts and spontaneous markers can cause concentration enhancements or depletions significant enough to warrant consideration if quantitative analysis is to be undertaken.

EXPERIMENTAL SECTION

Apparatus. All experiments described herein were conducted with an Isco (Lincoln, NE) Model 3850 capillary electropherograph with on-column UV absorbance detection. Although rarely employed in these studies, sample injection was by syringe using a split-flow mechanism. The high-voltage power supply of this instrument was operated in constant voltage (0–30 kV) mode, with both positive and negative applied voltages being used. The capillary compartment of the electropherograph was not thermostated, but a fan maintained good ambient circulation. In order to record CE data with great accuracy, we used the analogue current, voltage, and absorbance outputs of the instrument. These signals were monitored by a Hewlett-Packard Model HP-3497A data acquisition unit, which, in turn, was interfaced to a Hewlett-Packard Model HP-9000, series 200 computer. Computer programs, written in-house in HP Basic 3.0, enabled the computer to partially control the CE system and to collect, analyze, and store current and absorbance data.

Capillary Columns. In all experiments, we employed capillaries made of fused silica, coated with a thin layer of polyimide to improve their durability (Isco). Capillary dimensions were 50 μm i.d., 156.5 μm wall thickness, 16 μm coating thickness, and 54.95–98.75 cm length. The distance from the high-voltage end of the capillary to the detector ranged from 29.95 to 67.80 cm, while the distance from the detector to the grounded end ranged from 24.10 to 58.70 cm. Capillary columns were cut to length using a blunt, Isco ceramic capillary cutter. Cutting necessitated removal of the capillary ends from their fittings in the electropherograph. Cuts obtained in this way were not always "clean", as revealed by optical microscopy and scanning electron microscopy.

Since electroosmosis is very sensitive to the condition of the inside wall of the capillary, we subjected the column to a treatment which led to fairly reproducible electroosmotic flow rates (<1% relative standard deviation) over the course of several days. For a new capillary column, this treatment, referred to as "conditioning", consisted of filling the column with 1.0 M NaOH (BDH, Toronto, Canada) for 1 h, followed by leaving it filled with 0.10 M NaOH overnight. The column was then flushed sequentially with distilled, deionized water, 0.10 M HCl (Baxter/Canlab, Toronto, Canada), and again water. Even with this treatment, reproducible electroosmotic flow was not realized until the column had undergone about 1 month of regular use, with one column requiring 4 months of use before reproducibility was achieved. Electroosmosis increased throughout these periods of "conditioning", and soaking the column in water for extended periods of time (at least 2 days) when not in use appeared to be the most effective method of maintaining the electroosmotic flow rate at a stable value. Thus, we adopted a simple treatment which consisted of filling the capillary with water whenever it was idle, followed by refilling the column with fresh water for 1 h prior to daily experimentation. Column ends were submerged in water during storage to prevent evaporation from the column.

Solutions. Studies of the baseline shift and spontaneous-marker signal were conducted mostly in simple, uni-univalent electrolyte systems. In most instances, a 20 mM sodium benzoate (NaBz) solution was used, prepared by dissolving reagent grade NaBz (Caledon, Georgetown, Canada) in deionized and distilled water. The measured pH of this solution was 6.98 at 23 °C. Although all experiments presented herein were conducted with NaBz solutions, we determined that the existence of baseline shifts and spontaneous markers was not unique to the NaBz system by conducting similar experiments with several other running electrolytes, all prepared from analytical grade reagents, including 20.0 mM potassium benzoate (KBz; Aldrich, Milwaukee, WI), 20.0 mM sodium salicylate (NaSal; BDH), and 15.0 mM trisodium citrate (Na_3Cit; BDH). The measured pH's of these solutions were 7.01 at 20 °C, 5.85 at 24 °C, and 8.22 at 25 °C, respectively. All solutions were passed through a cellulose acetate syringe filter (pore size 0.45 μm; Nalge Co., Rochester, NY) and were degassed under vacuum by a water aspirator for ~1 h prior to use.

Procedure. Some terminology should be defined at the outset to make sure that its usage is clear and consistent. The "inlet end" of the column is not necessarily that end of the column physically located near the injection port. "Inlet" simply refers to the end through which electroosmotic flow carries solution into the capillary. Thus, during positive polarity experiments, the inlet end is indeed the high-voltage end of the capillary, located near the injection port, but during negative polarity experiments, the inlet is the low-voltage end of the capillary. Conversely, the "outlet" refers to the end through which solution exits the capillary. The solution reservoir in which the inlet end of the column is submerged is called the "supply reservoir", while the outlet end is submerged in the "receiving reservoir". The solution which fills the capillary column at the beginning of an experiment is called the "running electrolyte", and in most cases, the same solution is also used to fill the supply and receiving reservoirs. Reservoir volumes are about 10 mL. Care is taken to equalize

(25) Cohen, N.; Grushka, E. *J. Chromatogr. A* **1994**, *864*, 323–328.
(26) Schwartz, H. E.; Ulfelder, K. J.; Guttman, A. Injection Related Artifacts in Capillary Gel Electrophoresis. Poster presented at the Seventh International Symposium on High Performance Capillary Electrophoresis, Würzburg, Germany, 1995.

the solution levels in the two reservoirs to inhibit hydrodynamic flow. The solution which enters the capillary from the supply reservoir as a result of electroosmotic flow during a CE experiment is called the "replacement electrolyte," and may or may not be the same as the running electrolyte.

The majority of experiments, referred to as "uniform-electrolyte experiments", involved no sample injection and no deliberately formed concentration boundaries. The first such experiment conducted each day was referred to as the "equilibration run". After having first used a microliter syringe to fill the capillary with running electrolyte, the equilibration run served to flush the capillary by way of electroosmotic flow, to rid the capillary of any small bubbles which may have been present after conditioning, etc. Results from the equilibration run were disregarded. Uniform-electrolyte experiments were then conducted to try to determine the effect of applied field, column end conditions, and other factors on the magnitude of both the baseline shift and the spontaneous-marker signal. A single uniform-electrolyte experiment, or "run", consisted of applying a constant high voltage across the capillary for a certain length of time while recording absorbance and current data. At the end of the experimental run, the high voltage was turned off for a period of time. Typically, 2–5 min elapsed between runs with no field applied, and this period of time is referred to as the "standard interlude" in what follows. However, the period of time between runs with no field applied was as short as 5 s in some cases. The next experimental run was commenced by applying a constant high voltage which was not necessarily the same as in the previous experiment. If, in fact, the applied voltage was not the same in two successive runs, then it is said that a change in applied field strength has occurred between those runs.

RESULTS

Experiments that involved neither a deliberately formed concentration boundary nor an injected slug of analyte might be expected to produce no absorbance signals. Some such experiments, however, gave rise to absorbance signals, either positive or negative of the baseline. These spontaneous-marker signals appear to have their origin at the inlet end of the column, despite the fact that no sample was injected there or elsewhere. Accompanying these markers in some cases were field-dependent shifts in baseline absorbance. Both phenomena evidently represent concentration disturbances in the running electrolyte, and as such, are likely traveling along the column and past the detector by way of electroosmotic flow alone. Thus, the typically peak-shaped spontaneous-marker signal, reminiscent of a small injected slug of an uncharged analyte, and the plateau-shaped baseline shift, reminiscent of a concentration boundary, serve as markers of the rate of electroosmotic flow in the CE system. The discovery of these phenomena is important not only in its own right, but also because both baseline shifts and spontaneous markers may be occurring at the same time as, and thus interfering with, the results of "typical" slug-type CE experiments. Uniform-electrolyte experiments were thus conducted to try to determine the effect of applied field, column end conditions, and other factors on the magnitude of both the baseline shift and the spontaneous-marker signal.

"Depleting ends" of the capillary somehow acted to deplete the concentration of electrolyte entering the column from the supply reservoir. For such ends, an increase in the applied electric field resulted in a decrease in baseline absorbance. Positive spontaneous-marker signals accompanied the baseline shift produced by depleting ends. In contrast, "enriching ends" acted to enhance the concentration of electrolyte entering the column from the supply reservoir, and in these cases, an increase in the electric field resulted in an increase in baseline absorbance. Negative spontaneous markers accompanied the baseline shift produced by enriching ends. Although the two phenomena—baseline shift and spontaneous marker—exist concurrently and presumably have a common cause, we will first attempt to characterize the baseline shift.

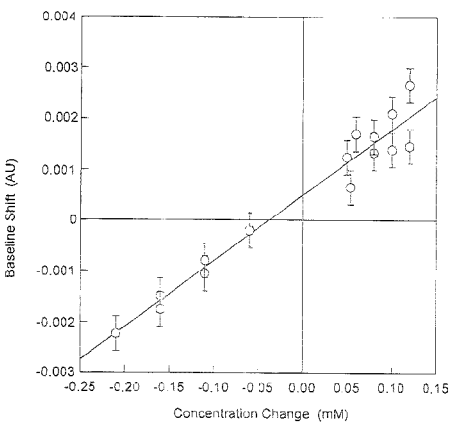

Figure 3. Calibration curve relating the magnitude of baseline shift (or change in absorbance) to the change in NaBz electrolyte concentration. Circles represent experimental data points, shown with error bars based on the standard error in the ordinate of the regression line (solid line). Slope of the regression line, 0.013 mM^{-1}; correlation coefficient, 0.95.

Baseline Shift. *Absorbance Studies.* In order to quantify baseline shifts, that is, to describe an observed change in UV absorbance in terms of the concentration difference between running and replacement electrolytes, we conducted a series of baseline shift calibration experiments. These experiments, conducted at a room temperature of 24.7 ± 0.6 °C, involved a series of successive "spikings" (beginning with the smallest and ending with the largest concentration increase) and a series of successive dilutions (beginning with the smallest and ending with the largest concentration decrease) of the 20 mM NaBz replacement electrolyte. Since most baseline shifts observed during uniform electrolyte experiments were fairly small, this calibration involved concentration increases of up to 0.12 mM and decreases of up to 0.21 mM. Figure 3 shows the resulting baseline shift calibration curve. By linear regression, the relationship between baseline shift (ΔA) and change in sodium benzoate concentration (Δc) was found to be

$$\Delta A \text{ (AU)} = (0.013 \pm 0.001)\Delta c \text{ (mM)} + (4.9 \pm 3.4) \times 10^{-4} \quad (1)$$

or equivalently

$$\Delta c \text{ (mM)} = (77 \pm 5)\Delta A \text{ (AU)} - (0.038 \pm 0.026) \quad (2)$$

with a correlation coefficient of 0.95. The fact that the regression

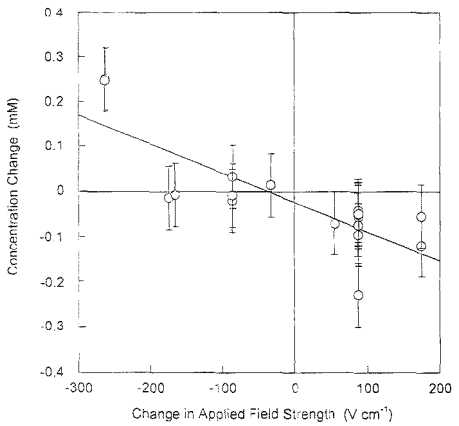

Figure 4. Effect of applied field on NaBz electrolyte concentration for cut (a). The solid line represents a linear least-squares fit of the data (slope, -0.62 μM cm V^{-1}; correlation coefficient, 0.61). Error bars are based on the standard error in the ordinate of the least-squares fit.

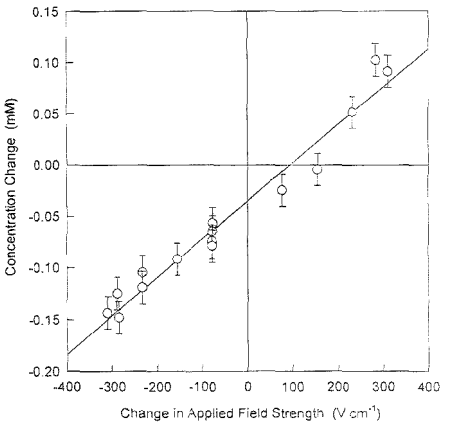

Figure 5. Effect of applied field on NaBz electrolyte concentration for cut (b). The solid line represents a linear least-squares fit of the data (slope, 0.37 μM cm V^{-1}; correlation coefficient, 0.96). Error bars are based on the standard error in the ordinate of the least-squares fit.

line does not pass through the origin, but instead has a positive intercept on the ΔA axis, indicates that a slight "drift" occurs in the baseline even when there has been no apparent change in electrolyte concentration. Possible reasons for this drift include changes in optical alignment or detector response over several hours of use or the gradual evaporation of solvent (water) from the supply reservoir, leading to a gradual increase in concentration of replacement electrolyte. Equation 2 was used to express the baseline shift resulting from an enriching or depleting column end in terms of concentration change.

The effect of applied field on baseline shift was studied in detail for several "active", that is, enriching or depleting, capillary ends. In these studies, the applied field was held constant during each run, but was changed before commencing a new run. The "standard interlude" elapsed between runs. The correlation between baseline shift, expressed as a concentration change, and change in applied field strength (ΔE) for one particular depleting end, referred to as cut a, is shown in Figure 4. Experiments were conducted at a room temperature of 22.6 $\pm$ 0.5 °C. Despite the scatter in the data, a decreasing linear relationship between concentration and applied field is evident. A regression line was calculated for these data and was found to have a slope of -0.64 $\pm$ 0.12 μM cm V^{-1} and an intercept on the Δc axis of -0.024 $\pm$ 0.070 mM. The negative slope is indicative of a depleting column end: as the magnitude of the applied electric field is increased, the concentration of solution entering the column from the supply reservoir under the influence of electroosmotic flow is decreased. That is, the column end somehow acts to deplete the concentration of NaBz entering the column from the supply reservoir, and this depleting ability is enhanced by the application of stronger electric fields. For example, if the applied field were to be increased by 150 V cm^{-1} (equivalent to increasing the voltage applied along the 57.3 cm length of the column by 8.6 kV) when conducting experiments with cut a as the inlet end, then the NaBz solution entering this column from the supply reservoir would be 0.12 $\pm$ 0.07 mM less concentrated than that already present in the column, even though the running and replacement electrolytes were initially identical 20 mM NaBz solutions.

To provide further evidence of "active" end behavior, we now characterize another capillary end, referred to as cut b. Cut b was also an "active" cut, but unlike cut a, cut b acted to enrich the concentration of solution entering the column. The correlation between baseline shift, expressed in terms of concentration change and change in applied field (ΔE) for cut b, is shown in Figure 5. Since the Δc versus ΔE data (collected at a room temperature of 24.7 $\pm$ 0.8 °C) appear to be linearly related, a linear regression of the data was carried out. The resulting slope was $+0.37$ $\pm$ 0.02 μM cm V^{-1}, while the intercept on the Δc axis was -0.035 $\pm$ 0.016 mM, and the correlation coefficient was 0.96. The positive slope is indicative of an enriching column end: as the magnitude of the applied electric field is increased, the concentration of solution entering the column from the supply reservoir under the influence of electroosmotic flow is also increased. This behavior is opposite to that of the depleting end discussed previously. Thus, it appears that cut b somehow acts to enrich the concentration of NaBz entering the column relative to that in the supply reservoir. For example, consider increasing the applied field by 150 V cm^{-1} (by increasing the applied voltage along the 64.30 cm long column by 9.6 kV) when conducting an experiment with cut b. The NaBz solution entering this column from the supply reservoir would be 0.02 $\pm$ 0.01 mM more concentrated than that already present in the column, even though the running and replacement electrolytes were initially identical 20 mM NaBz solutions.

Of even greater interest is the extreme enriching ability of a third cut, referred to as cut c. When an electric field of magnitude 280 V cm^{-1} was first applied so that solution would pass through cut c and replace the contents of the column by electroosmosis, a baseline shift of 0.097 AU occurred. Using the correlation between baseline shift and concentration change given in eq 2, it was found that solution filling the column through cut c was 7.5 $\pm$ 0.4 mM more concentrated than the original running electrolyte. This large enrichment does represent a somewhat unique case,

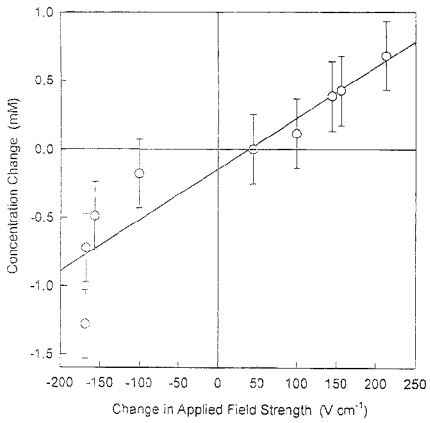

Figure 6. Effect of applied field on NaBz electrolyte concentration for cut c. The solid line represents a linear least-squares fit of the data (slope, 3.7 μM cm V^{-1}; correlation coefficient, 0.86). Error bars are based on the standard error in the ordinate of the least-squares fit.

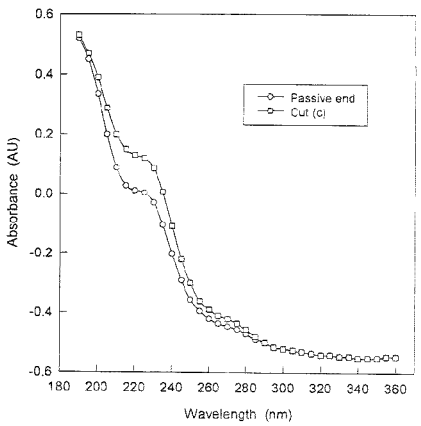

Figure 7. Absorbance spectra of NaBz solutions: solution entering the column by way of electroosmosis through the passive column end opposite cut c is indicated by circles; solution entering through cut c is indicated by squares. The zero of absorbance was set at 225 nm when the column was filled with the original 20.0 mM NaBz running electrolyte.

in that it occurred only during the first experiment, with solution entering the capillary through the end which had previously been functioning as the outlet. Thus, a change in solution flow direction and field polarity and strength had occurred. The effect of subsequently changing the applied field on concentration of electrolyte entering this particular end, at a room temperature of 22.3 ± 0.4 °C, is shown in Figure 6. Again, a linear relationship was observed, and regression of the data gave a line with slope +3.7 ± 0.6 μM cm V^{-1}, intercept −0.14 ± 0.25 mM, and correlation coefficient 0.86. This positive slope, which is 10 times greater than that for cut b, indicates that the enriching (or depleting) ability of all cuts is not equal and that cut c was extremely effective at enriching the concentration of NaBz entering the column. In fact, the concentration of NaBz entering the column through cut c would be 0.42 ± 0.26 mM greater than that already present in the column if the applied field were to be increased, as in the previous examples, by 150 V cm^{-1} (achieved by increasing the applied voltage along the 89.25 cm length of column by 13.4 kV).

To confirm that cut c was functioning as an enriching end and that the significant absorbance changes observed during these experiments were, indeed, due to real changes in the concentration of NaBz entering the column through this cut, we recorded the absorbance spectra of first the original NaBz running electrolyte, which entered into the column by way of electroosmotic flow through the "passive" column end opposite cut c, and then the solution which had entered the column by way of electroosmosis through cut c. These spectra, recorded after the electric fields which had been used to fill the column were disabled, are shown in Figure 7. Moreover, it should be noted that the absorbance spectrum of 20.0 mM NaBz was found to be independent of applied field strength during experiments with a passive column end, and so any change in the absorbance spectrum cannot be attributed to some effect of the electric field on the optics of the CE instrument. The similarity in shape between the two spectra in Figure 7 indicates that the electrolyte in the column is pure NaBz in each case, although the greater absorbance demonstrated by the solution entering through cut c indicates that this cut did, indeed, enrich the concentration of NaBz relative to the supply and receiving reservoirs.

During the experiments investigating the effect of applied field change on electrolyte concentration, cut c was positioned in the capillary electropherograph such that it was submerged in the reservoir housing the grounded rather than the high-voltage platinum electrode, and large negative voltages were applied along the length of the capillary. If, in fact, some physical feature of cut c was responsible for the enrichment of solution during these experiments, then its enriching behavior should be observable regardless of its position in the electropherograph. To verify this, the column was reversed, so that cut c was submerged in the reservoir housing the high-voltage electrode, and then large positive voltages were applied along its length at a room temperature of 25.5 ± 0.1 °C. Indeed, in its reversed position, cut c continued to act as an enriching end, as shown in Figure 8, although the effect of changing the applied electric field on the concentration of electrolyte entering the column was somewhat less dramatic than it had been in its original position. In its new position, the rate of change in concentration as a function of applied field for cut c was found to be (by way of linear regression of the data in Figure 8) +2.3 ± 0.1 μM cm V^{-1}. This means that increasing the applied field by 150 V cm^{-1} would result in an increase in concentration of NaBz entering the column through cut c of 0.33 ± 0.06 mM, as opposed to an increase of 0.42 ± 0.26 mM in its original position. The intercept on the Δc axis and the correlation coefficient for Figure 8 were −0.021 ± 0.056 mM and 0.98, respectively. It should be noted that reversal of the column subjects the exposed cut to some physical stress, in that it must be removed from and refitted through tight ferrules. This may, in some way, alter the condition of the cut, and so we cannot be sure that cut c in its reversed position was identical to cut c in its original position. Nevertheless, the degree to which a column end is able to deplete or enrich the concentration of electrolyte entering the column under the influence of electroosmotic flow appears to depend on the very nature of the end itself.

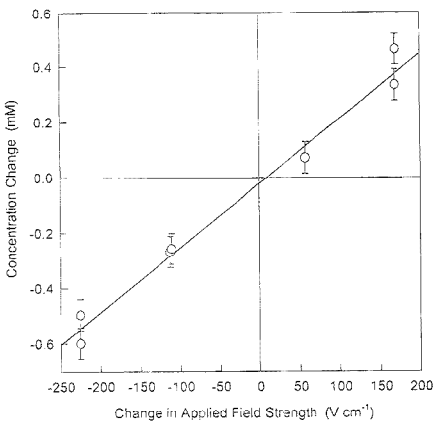

Figure 8. Effect of applied field on NaBz electrolyte concentration for cut c in its reversed position. The solid line represents a linear least-squares fit of the data (slope, 2.3 μM cm V^{-1}; correlation coefficient, 0.98). Error bars are based on the standard error in the ordinate of the least squares fit.

In an effort to determine if enriching or depleting behavior was caused by some physical or geometrical feature of the cut, scanning electron micrograph (SEM) images of several cuts, both passive and active, were recorded using a Cambridge S90 stereoscan scanning electron microscope. Samples were not conductively coated before imaging with an accelerating voltage of 25 kV. Unfortunately, there was no visible feature present in (or absent from) the images that could distinguish between an active cut and a passive cut. The exposed surface of the capillary resulting from all cuts appeared to be nonuniform, with features such as chips out of the fused silica, fused silica "overhangs", debris remaining on the cut surface, or removal of small pieces of polyimide coating (which may have occurred either during cutting or perhaps during imaging). It is unclear from the SEM images if any of these features are responsible for the enriching or depleting ability of some column ends.

Baseline Shift. *Conductivity Studies.* The changes in absorbance used to characterize the "active" behavior of some column ends are supported by conductivity (current) and electroosmotic flow rate measurements. For an enriching end, an increase in applied field strength leads to an increase in absorbance. If an increase in electrolyte concentration is indeed responsible for this increase in absorbance, then the conductivity of the solution should also increase. This increase in conductivity was observed whenever a column end appeared to be enriching the solution entering the column and so provided an additional piece of evidence for this phenomenon.

The equation relating solution conductivity κ to the concentration c of a uni-univalent electrolyte is

$$\kappa = Fc(\mu^+ + \mu^-) \tag{3}$$

where F is the faraday constant and μ^+ and μ^- are the electrophoretic mobilities of the cation and anion, respectively. This equation can be combined with that relating conductivity to current I,

$$\kappa = IL/VA \tag{4}$$

where L is the length of the column, V is the constant applied voltage, and A is the cross-sectional area of the column. An equation is thus developed which enables us to calculate the concentration c of our uni-univalent electrolyte from the measured conductivity (or current) and applied voltage:

$$c = \frac{\kappa}{F(\mu^+ + \mu^-)} = \frac{IL}{FVA(\mu^+ + \mu^-)} \tag{5}$$

This equation was used to calculate the concentrations of solutions filling the column during experiments conducted on a column into which solution flowed first from the end opposite cut c and then through cut c itself. Initially, a positive voltage (+25.03 kV) was applied, and because cut c was positioned in the grounded reservoir, solution entered the column from the supply reservoir containing 20.0 mM NaBz by way of electroosmosis through the end opposite to cut c (that is, through the high voltage end). The concentration of this replacement electrolyte, calculated from eq 5 and based on a conductivity of 0.18 ± 0.01 Ω^{-1} m^{-1} (average measured current, 10.1 ± 0.1 μA) and mobilities of 51.9 × 10^{-9} and 33.5 × 10^{-9} m^2 s^{-1} V^{-1} for Na^+ and Bz^- at 25 °C, respectively,[27] was 22 ± 2 mM. In view of factors that could have a bearing on the magnitudes of the mobilities and uncertainty in the exact value of A, this can be considered good agreement with the concentration of the running electrolyte.

The polarity was then reversed by applying −24.96 kV, and since the magnitude of the resulting field was approximately the same as in the positive polarity experiment, the Joule heating would be comparable. Under the influence of this field, solution entered the column through cut c by way of electroosmosis. The calculated concentration of this replacement electrolyte, based on a conductivity of 0.28 ± 0.02 Ω^{-1} m^{-1} (final measured current, 15.2 ± 0.2 μA), was 34 ± 2 mM. Notice that the increase in conductivity resulting from filling the capillary with sodium benzoate solution through enriching end c by electroosmosis was >50%. The enrichment of the running electrolyte predicted by these conductivity measurements (14 ± 2 mM), conducted at a room temperature of 22.6 ± 0.1 °C, was greater than that predicted by the absorbance measurements (7.5 ± 0.4 mM) discussed previously. The discrepancy between these results may, in part, be attributed to the use of mobility values at infinite dilution and 25 °C in the calculation of concentration by way of eq 5. In addition, the calibration curve relating change in absorbance to change in concentration (Figure 3) covered a range of <0.4 mM, and as such, may not have been valid for quantifying significantly larger changes in concentration, as in these examples. It is clear, however, from both absorbance and conductivity measurements that the concentration of solution entering the column through cut c was enriched.

A subsequent experiment was conducted by applying −29.00 kV, and this led to a calculated concentration of 38 ± 3 mM, based on a conductivity of 0.31 ± 0.02 Ω^{-1} m^{-1} (final measured current, 19.8 ± 0.2 μA). Thus, the conductivities measured during this

(27) Oldham, K. B.; Myland, J. C. *Fundamentals of Electrochemical Science*; Academic Press, Inc.: San Diego, 1994; p 12.

and previous experiments indicated that the concentration of electrolyte entering the column through cut c was greatly enriched compared to the original running electrolyte and that the extent of enrichment appeared to depend on the magnitude of the applied field.

Baseline Shift. *Electroosmotic Mobility Studies.* In addition to using absorbance and conductivity measurements to support the concept of an enriching column end, it is also possible to use measurements of electroosmotic mobility. In this work, the electroosmotic flow velocity was confirmed by injection of a small slug of electrolyte with the same composition as but at a slightly different concentration than the running electrolyte. The rate of mobilization (or electroosmotic velocity v^{eo}) of the baseline shift is proportional to the electroosmotic mobility μ^{eo}, which itself depends on the ζ potential of the column, according to the equation[28]

$$v^{eo} = \mu^{eo}E = (E\zeta/\eta)\epsilon \tag{6}$$

where E is the applied electric field, η is the solution viscosity, and ϵ is the permittivity of the medium. The ζ potential, in turn, depends on the surface charge density σ and double-layer thickness β:[29]

$$\zeta = \sigma\beta/\epsilon \tag{7}$$

while the double-layer thickness depends on the concentrations and charge numbers of all solute ions:[30]

$$\beta = \left(\frac{RT\epsilon}{F^2\sum_i z_i^2 c_i}\right)^{1/2} \tag{8}$$

Here, R represents the gas constant, T is the temperature of the solution, and all other symbols are as previously defined. Thus, the electroosmotic mobility is dependent on the concentration (and the temperature) of the electrolyte. Since the baseline shift is believed to represent a concentration disturbance, it should act to alter the rate of electroosmotic flow somewhat.

From eq 8 it can be seen that if the concentration of the running electrolyte is increased, the double-layer thickness will decrease. This, in turn, will decrease the ζ potential according to eq 7, and finally will decrease the electroosmotic mobility, as predicted by eq 6. Since cut c has been shown to function as an enriching end, it should, by virtue of passing more concentrated electrolyte through the column, reduce the ζ potential and hence the electroosmotic velocity. Because cut c was originally positioned in the grounded reservoir, the initial application of +25.03 kV, at a room temperature of 22.6 ± 0.1 °C, filled the column with solution through the "passive" end opposite to cut c by way of electroosmosis with $\mu^{eo} = (4.71 \pm 0.04) \times 10^{-4}$ cm^2 V^{-1} s^{-1}. Upon applying a constant voltage of −24.96 kV, the magnitude of the electric field was approximately the same as in the previous experiment but in a direction such that solution would enter the column through cut c by way of electroosmosis. The electroosmotic mobility in this case was $(4.00 \pm 0.04) \times 10^{-4}$ cm^2 V^{-1} s^{-1}, indicating that the ζ potential had, indeed, been decreased. Such a decrease could be attributed to an increase in electrolyte concentration. Of course, a change in concentration would lead to a subsequent change in the amount of Joule heating and thus in the temperature. Because of the dependence of temperature on concentration, and the dependence of electroosmotic mobility on both of these variables, the effect of increasing the concentration on the electroosmotic mobility is quite complex.

When a constant voltage of −29.00 kV was subsequently applied to allow flow through cut c, a further decrease in electroosmotic mobility was observed ($\mu^{eo} = (3.88 \pm 0.03) \times 10^{-4}$ cm^2 V^{-1} s^{-1}), indicating a further increase in concentration. Thus, measurement of electroosmotic mobility provided evidence of the enriching behavior of cut c, as did the measurement of current and absorbance.

Spontaneous-Marker Peak. Since the baseline shift did not occur in isolation, we will now discuss the concomitant phenomenon of the spontaneous-marker signal. This signal appeared only when the column end gave rise to baseline shifts. Enriching capillary ends gave rise to negative spontaneous-marker peaks, while depleting ends gave rise to positive spontaneous markers. Often, the marker peaks were skewed rather than Gaussian in shape. Whereas baseline shifts occurred only when the applied field was changed, spontaneous markers appeared whenever there was a period of time with no field applied and when the inlet end of the capillary was enriching or depleting, regardless of change in field strength. Thus, when the field strength remained unchanged between runs, the only feature in the electropherogram was a spontaneous marker, as seen in Figure 9a, but when the field was altered, a spontaneous marker was superimposed onto a baseline shift, as seen in Figure 9b. The size of these markers appeared to depend primarily on the extent of enrichment or depletion and on the length of time elapsed with no field applied between experimental runs.

When no electric field is applied along the column, as is the case between CE runs, transport of NaBz through the column by either migration or electroosmosis will cease. Thus, diffusion will become the only mechanism of ion movement. Diffusion of NaBz into or out of the column will occur if a concentration gradient exists at the interface between the solution in the column and that in the bulk reservoir.[31] Thus, it seems reasonable to assume that spontaneous-marker peaks could be formed as a result of diffusion of NaBz into or out of the column between runs, given that the observed baseline shifts represent concentration boundaries formed at the capillary end. To investigate this possibility, the effect of no-field time on spontaneous marker size was studied for cut c in its original and reversed positions. The results are presented in Figure 10. Because cut c is an enriching end, it produces negative spontaneous markers, and so the marker peaks are negative of the baseline. Using eq 2 along with peak widths at half-height, these "negative" peaks were transformed into amounts of NaBz representative of the markers. As expected, the spontaneous markers generated by cut c in its original position were larger than those generated in its reversed position at all times, due to the greater enriching ability of cut c before reversal. In both cases, however, spontaneous markers approached a maximum decrease in the amount of NaBz as the standard

(28) Laidler, K. J.; Meiser, J. H. *Physical Chemistry*; Benjamin/Cummings Publishing Co., Inc.: Menlo Park, 1982; p 841.
(29) Reference 28, p 794.
(30) Grossman, P. D. Factors Affecting the Performance of Capillary Electrophoresis Separations: Joule Heating, Electroosmosis, and Zone Dispersion. In *Capillary Electrophoresis: Theory and Practice*; Grossman, P. D., Colburn, J. C., Eds.; Academic Press, Inc.: San Diego, 1992; p 18.
(31) Dose, E. V.; Guiochon, G. *Anal. Chem.* **1992**, *64*, 123−128.

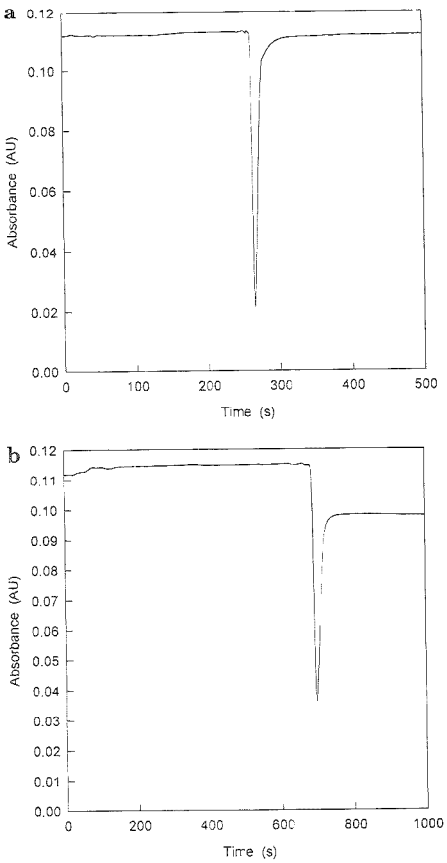

Figure 9. Capillary electropherograms showing negative spontaneous-marker peaks generated at enriching capillary end c with no injection; 20.0 mM NaBz as the original running electrolyte; column length, 88.70 cm; inlet-to-detector length, 30.00 cm; and detection at 225 nm. (a) A negative spontaneous marker with no accompanying baseline shift. Experimental conditions: applied voltage in this and in previous run, −24.99 kV; average measured current, −5.54 μA. (b) A negative spontaneous marker accompanied by a negative baseline shift. Experimental conditions: applied voltage in previous run, −24.99 kV; applied voltage in this run, −10.04 kV; average measured current, 5.87 μA.

interlude was approached. The amounts of NaBz represented by the markers approached zero as the time between runs approached zero. This implies that if the applied field were never disabled, spontaneous-marker peaks would not be generated. Experimentally, this was observed. Recall that baseline shifts occur only when the applied field is changed, while spontaneous-marker peaks occur regardless of applied field strength changes, provided there is some no-field time between runs. Thus, if the applied field is changed in the middle of a uniform electrolyte experiment, one would expect to see a baseline shift without an accompanying spontaneous-marker peak. This was indeed the case during an experiment with cut c in its reversed position, when the applied field was decreased from 282 to 110 V cm^{-1} in the middle of a run, generating a baseline shift of -3.6×10^{-3} AU

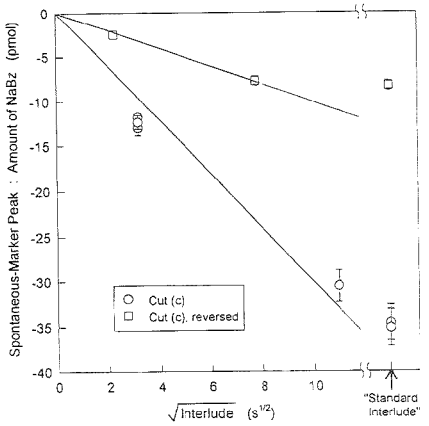

Figure 10. Spontaneous-marker peak size, represented as an amount of NaBz, as a function of the square root of the interlude (where the interlude represents the time elapsed between runs with no field applied). Solid lines represent least-squares fits of the data (excluding standard interlude data) for cut c in its original (circles) and reversed (squares) position. Propagated error in the calculated amounts of NaBz are less than the size of the data symbol or is shown as an error bar.

(equivalent to a decrease in concentration of 0.32 ± 0.03 mM) but not generating a spontaneous marker. Thus, it appears that some period of time with the field disabled is essential to the occurrence of the spontaneous-marker peak.

DISCUSSION

Baseline shifts have been observed previously. Vinther et al.[21] observed shifts attributable to pH changes, but we do not expect significant pH changes to occur in our system. The electrolysis of water would, indeed, result in the production of hydrogen ion in the supply electrolyte reservoir, thus establishing a buffer system (benzoate/benzoic acid) which would prevent significant changes in pH. Consider, for example, a series of 10 experiments conducted in 1 day, each lasting 10 min with a typical current of 10 μA flowing. The amount of hydrogen ion produced in the supply electrolyte reservoir as a result of these experiments was calculated to be about 6×10^{-7} mol, but after taking into consideration the HBz/Bz buffer system formed, this would result in only a 0.3 decrease in pH relative to the running electrolyte's original pH. This was confirmed experimentally when, after 100 min of operation with an applied voltage of 20.01 kV ($I \approx 10$ μA), the measured pH of the 20.02 mM NaBz solution in the inlet reservoir had changed from 6.75 to 6.43 (at 22 °C).

Moreover, if a significant pH change were somehow to occur, it would be a progressive effect, and so one might expect to observe a progressive change in absorbance. Experimental changes in absorbance were not progressive: they occurred in both positive and negative directions, depending upon the capillary end and the change in applied field. Furthermore, measured UV absorbances of sodium benzoate and benzoic acid solutions were found to be indistinguishable at 225 nm, and so a change in pH (or a change in the relative amounts of benzoate and benzoic acid present) would not result in any observed change in absorbance. Finally, if baseline shifts were pH induced, one would expect to

see such features during every experiment, with every capillary and with any change in field strength, since the electrolysis of water would proceed regardless of these experimental variables. Such constancy in baseline perturbations was not observed. Baseline shifts have also been linked[23,24] to temperature changes in the running solution caused by Joule heating. While such thermal effects are undoubtedly present in our experiments, they alone cannot explain the phenomena that we have observed.

We attribute the baseline shift and spontaneous marker signals to changes in the actual concentration of the sodium benzoate solution in the capillary observed at the site of spectrophotometric analysis. We did consider a number of other possible explanations of the changed absorbance, such as its being due to temperature-induced changes in the refractive index of the solution or some other artifact, induced in the detector by changes in temperature or field strength rather than by concentration changes. However, such possibilities are ruled out by the persistence of the signal even when the applied voltage is turned off during a run, which interrupts the flow, as well as both heat generation and the electric field. Moreover, the several independent pieces of experimental evidence that we report above all point to concentration excursions being responsible for both phenomena: the permanent baseline shift and the transient spontaneous-marker peaks.

Flow rate through the capillary is not a quantity that is open to direct measurement in CE as usually conducted. However, subsidiary experiments employing short slugs of analyte provided access to this quantity and demonstrate that flow through our apparatus occurred at a rate consistent with electroosmosis driven by a zeta potential of about −100 mV. Knowing the flow rate, one can calculate the delay before a concentration perturbation, initiating at the capillary inlet, would reach the spectrophotometer. In all cases, this calculated delay closely matched the experimental residence time in the column prior to the signal—baseline shift and/or spontaneous-marker peak—being observed. We regard this as very strong evidence that these phenomena, when they exist, have their origins at the mouth of the column and are propagated down the column at a velocity close to that of electroosmotic flow.

These effects are not trivial. Permanent concentration enrichments of 37% were observed in one extreme case, with more typical activity generating 1 or 2% enrichment or depletion. Nevertheless, in 75% of the cases studied, there was either no effect whatsoever, or it was at too low a level to be experimentally significant. Whether or not the concentration excursion occurred and, if it did occur, its magnitude and sign depended entirely on some still-unidentified aspect of the end of the capillary tube. Paring the end of the capillary can destroy or create activity, though we have yet to learn how to do this in other than a random fashion.

There are four important questions still to be answered: First, what property of an end causes it to be active? Second, how does that property induce and maintain a concentration excursion in the solution entering the capillary? Third, how does the concentration step move along the column, ultimately making its existence manifest as a baseline shift at the spectrophotometer? And fourth, what is the origin of marker peaks and why are they inversely related to the baseline shift? We have no convincing answer to the first question. We have some qualitative guesses as putative answers to the second question. We believe that we can satisfactorily answer the third and fourth questions.

Though it may not be the logical place to start, let us first examine the circumstances surrounding the third question: How does a concentration step propagate? Imagine a concentration junction $c_2|c_1$ of a uni-univalent electrolyte to exist between two fixed points x_2 and x_1 in the column. These points are in homogeneous regions, but the concentration is not uniform between them. In general, there will not be a sharp concentration discontinuity, but we may nevertheless associate "the boundary" between the two regions with a specific point x_b along the column, such that

$$(x_1 - x_b)c_1 + (x_b - x_2)c_2 = n/A \tag{9}$$

where A is the cross-sectional area of the capillary and n is the total amount of electrolyte between x_1 and x_2. Let us inquire about the speed with which electrophoresis causes this boundary to move.

A current I flows from left to right across the boundary, carried in part by cations moving across the boundary from left to right and in part by anions moving in the opposite direction. In a time interval Δt, the increase in the amount of cations in the boundary zone $x_2 < x < x_1$ is

$$\Delta n^+ = (E_2\mu_2^+c_2 - E_1\mu_1^+c_1)A\Delta t \tag{10}$$

where each E denotes the field strength and each μ^+ is the cation mobility ($m^2\ s^{-1}\ V^{-1}$). The corresponding increase in anion content is

$$\Delta n^- = (E_1\mu_1^-c_1 - E_2\mu_2^-c_2)A\Delta t \tag{11}$$

but, of course, electroneutrality requires that these two Δn expressions be equal. This equality is also evident from the standard expressions

$$I/AF = E_1(\mu_1^+ + \mu_1^-)c_1 = E_2(\mu_2^+ + \mu_2^-)c_2 \tag{12}$$

relating current to field strength. Combining eqs 10 and 12 leads to

$$\Delta n/\Delta t = \frac{I}{F}\left[\frac{\mu_2^-}{(\mu_2^+ + \mu_2^-)} - \frac{\mu_1^+}{(\mu_1^+ + \mu_1^-)}\right] = \frac{I}{F}(t_2^- - t_1^-) \tag{13}$$

where, in the final step, the cationic transport number t^- is introduced.

Now, all terms in eq 9 except n and x_b are constants, and therefore, $\Delta n/A = (c_2 - c_1)\Delta x_b$. Combining this result with eq 13 leads to

$$\Delta x_b/\Delta t = \frac{I}{AF}\left(\frac{t_2^- - t_1^-}{c_2 - c_1}\right) \tag{14}$$

This expression gives the electrophoretic velocity v^{ep} of the boundary. Stockmayer[32] derived this result, and it was used by Gaš[24] to estimate the speed with which disturbances propagate.

(32) Stockmayer, W. H. *Trans. N. Y. Acad. Sci.* **1951**, *13*, 266–269.

The electrophoretic velocity will be zero if, as it would be reasonable to assume, the transport numbers in the two regions are equal. There are (at least) three effects that could lead to the cation having a different mobility in the two regions. First, there is the direct effect of concentration itself. Ionic mobilities are known to decrease from their infinite dilution values as the concentration increases, for reasons that are incorporated into the Onsager theory.[33,34] Second, the electric field will be stronger in the more dilute region, and this is known to increase ion mobilities (the Wien effect[35]). Third, because the electrical conductivity will be less in the more dilute region, heat generation will be greater there, leading to a higher temperature and consequently higher mobilities. Though the third effect is likely the most important, all three of these effects conspire to make ionic mobility greater in the more dilute region. However, all three effects operate on both the cation and the anion, and we are unable to predict whether the sodium ions or the benzoate ions would be more affected. A proportionate increase, i.e., $\mu_2^+/\mu_1^+ = \mu_2^-/\mu_1^-$, would leave the transport numbers unchanged. Certainly it is hard to imagine that t_2^- would differ from t_1^- by more than 1% for a 1 mM difference between c_2 and c_1, and the discrepancy in transport number would likely be much less than this. For a current of 8 μA, which was typical of our experiments, we then estimate from eq 14 that $|v^{ep}| < 0.4$ mm s^{-1}.

This estimate of a ceiling to the electrophoretic velocity of the boundary is to be compared with the value $v^{eo} = 1.5$ mm s^{-1} which is typical of the electroosmotic velocities in our experiments. Thus, while we cannot rule out the possibility of an electrophoretic contribution (additive or subtractive), it would appear from this analysis that electroosmosis is the major factor in transporting concentration excursions from the inlet to the spectrophotometer, in agreement with the experimental evidence.

Could the factors that have been discussed above be responsible not only for the propagation of the concentration excursion but also for its creation? There is no doubt that thermal effects due to Joule heating are of paramount importance in electrophoresis and must be considered in any thorough analysis of conditions during CE. We estimate that the local temperature elevation may be as high as 30 K in some of our experiments. In the literature, the greatest attention has been directed toward an understanding of the radial distribution of temperature, because this has a bearing on the resolution of electrophoretic peaks and thereby directly affects the success of chemical analysis by CE. In our case, however, it is to the axial dimension that we must look for the most likely explanation of our effects. While recognizing that this is possibly an oversimplification, we therefore ignore radial distribution of the variables in what follows.

The axial heat flux density (W m^{-2}) is given by the sum of two terms, one representing conduction and the other convection:

$$j_h = -k\left(\frac{\partial T}{\partial x}\right) + \varrho C v T \qquad (15)$$

Here k denotes the thermal conductivity (W m^{-1} K^{-1}) of the solution, ϱ its density, and C its heat capacity (J kg^{-1} K^{-1}). T is the local temperature, and v is the (largely electroosmotic) axial velocity which, if we ignore the thermal expansion of the liquid and the capillary, we can regard as a constant.

The change in the axial heat flux density along the capillary is one of three factors that leads to the possibility of a change in the local temperature with time. Another is Joule heating, which is proportional to the square of the current density, and the third is conductive heat loss through the capillary wall. These three factors lead to the three right-hand terms in the equation

$$\varrho C\left(\frac{\partial T}{\partial t}\right) = \left(\frac{\partial j_h}{\partial x}\right) + \frac{(I/A)^2}{\kappa} - \frac{2h}{r}(T - T_0) \qquad (16)$$

In this equation, κ is the local electrical conductivity (Ω^{-1} m^{-1}) equal to $Fc(\mu^+ + \mu^-)$, r is the radius of the capillary, and A (= πr^2) is its cross-sectional area. T_0 represents the ambient temperature, and h is an overall heat transfer coefficient (W m^{-2} K^{-1}) of the capillary wall related[36,37] to the dimensions and thermal conductivities of the silica capillary and its polyimide coating. A detailed derivation of the previous two equations is described by Gaš[24] who, however, omitted the final term in eq15 because he excluded electroosmosis from consideration. The inclusion of convection could have important ramifications beyond the introduction of this term, making Gaš's conclusions inapplicable to our system.

The equations incorporated into expression 12 apply to regions in which the properties are uniform; they require augmentation when applied to regions in which electrolyte concentration c, electric field strength E, and temperature T are all functions of the axial dimension x. In a nonuniform region, we have

$$I/AF = E(\mu^+ + \mu^-)c - D^+\left[\left(\frac{\partial c}{\partial x}\right) + \sigma^+ c\left(\frac{\partial T}{\partial x}\right)\right] + D^-\left[\left(\frac{\partial c}{\partial x}\right) + \sigma^- c\left(\frac{\partial T}{\partial x}\right)\right] \qquad (17)$$

where D^+ and D^- are the diffusivities of the cation and anion, the σ^+ and σ^- terms being the corresponding Soret coefficients.[38,39]

The mathematical problem presented by eqs 15–17 is strongly nonlinear, as noted by Gaš[24] and an analytic solution is out of the question. In principle, computer modeling of the system is possible, but the main impediment is the paucity of information about the values of the various parameters—diffusivities, Soret coefficients, and mobilities—and how they depend on concentration, temperature, and field. Doubtless by choosing appropriate concentration, field, and temperature dependences of these parameters for the sodium and benzoate ions, one could model a wide variety of behaviors. One might even obtain simulations that match some of our experimental observations, but in this eventuality we would hesitate to claim that we had then "explained" the effects.

Our main reason, though, for not pursuing these approaches is the inescapable experimental evidence that the baseline shift originates in a concentration disturbance at the capillary inlet,

(33) Onsager, L. *Phys. Z.* **1927**, *28*, 277.
(34) Fuoss, R. M.; Onsager, L. *J. Phys. Chem.* **1957**, *61*, 668.
(35) Reiger, P. H. *Electrochemistry*; Prentice-Hall, Inc.: Englewood Cliffs, NJ, 1987; p 147.
(36) Gobie, W. A.; Ivory, C. F. *J. Chromatogr.* **1990**, *516*, 191–210.
(37) Bird, R. B.; Steward, W. E.; Lightfoot, E. N. *Transport Phenomena*; Wiley: New York, 1960.
(38) Haase, R. *Thermodynamics of Irreversible Processes*; Dover Publications: New York, 1990.
(39) Agar, J. N. Thermogalvanic Cells. In *Advances in Electrochemistry and Electrochemical Engineering*; Delahay, P., Ed.; Interscience: New York, 1963; Vol. 3, pp 31–121.

where the equations are inapplicable. Moreover, the magnitude and sign of the concentration excursion evidently depend on some feature of the capillary end that can be changed by recutting but which is sufficiently intimate that is it not revealed by optical or electron microscopy. Some ends are "active", some are not. This brings us to the first two of the four questions that were enumerated at the beginning of this section: What property of the capillary end makes it active, and how does that property cause activity?

Frankly, we have no idea what the special property of an end is that makes it active nor how it comes about that some active ends reproducibly induce a positive concentration excursion, while others, with equal reproducibility, cause a negative excursion. We imagine that the important feature could be a geometrical anomaly: a small notch, crack, or flute, for example. The feature is resistant to the normal, careful handling of day-to-day usage: it endures rinsing with a jet of water, for example. There is some evidence, however, that more stressful actions, such as forcing the end into a tight-fitting ferrule, do impair the activity of an active end. The positioning of each end of the column in the electrolyte reservoirs may play a role in activity, although our experiments have not shown this to be so.

Recall that the inlet is simply the cut end of the capillary dipping vertically into a small beaker of electrolyte solution. The distinctive feature of the inlet is the rapid, convergence-induced change in the values of the salient properties as one proceeds from the bulk solution toward and through the aperture. The properties that change in this unique way are the flow velocity, the field strength, and presumptively the temperature. If changes in any of these properties lead to changes in the transport number of either the cation or anion, then a change in concentration can arise. Unfortunately, knowledge of the dependence of transport numbers on such properties is very limited, and so it is difficult to predict what sort of concentration changes could be expected in different regions of the capillary. We speculate that there may be some angular dependence of the properties, arising perhaps from whatever anomaly is responsible for activity, that enhances the magnitude of the concentration excursion compared with the symmetric conditions that apply when that anomaly is absent. Possibly hydrodynamic factors are involved, but this is still speculation.

Though the origins of the baseline shift remain conjectural, once it is accepted that they represent real concentration changes developed at the capillary inlet, spontaneous-marker peaks can be explained rather simply. Recall that these peaks develop if, but only if, the field is interrupted between runs. Consider that we have an "enriching end" at the column inlet. Then, during the interlude between runs, the capillary, filled with enriched solution, is sitting in the supply reservoir which contains unenriched solution. There will be a slow diffusion of electrolyte from the capillary into the reservoir. Then, when the field is reapplied and electroosmosis resumes, there will be a renewal of the enrichment process at the inlet. But now there will be a small slug of partially depleted solution, trapped between the "old" enriched solution and the "new" enriched solution. This slug will travel at the usual electroosmotic velocity to the spectrophotometer, where it will cause a temporary negative excursion in absorbance. This is exactly what is observed with enriching ends: a negative spontaneous-marker peak observed after a delay corresponding to the electroosmotic journey from the inlet. Conversely, positive peaks are observed with depleting ends, and no peak whatsoever is found with inactive ends. If the field is changed, an active end will display both a baseline shift and a spontaneous-marker peak, but without an inter-run interlude, the baseline shift is not accompanied by a marker peak.

In summary, we believe that we understand what baseline shifts and spontaneous-marker peaks are. We can explain how baseline shifts give rise to marker peaks, but we do not understand the mechanism by which baseline shifts arise.

ACKNOWLEDGMENT

We thank Professors R. Cassidy (University of Saskatchewan) and B. Gaš (Charles University) for their very helpful comments on this work. The authors gratefully acknowledge support from the Natural Sciences and Engineering Research Council (NSERC) of Canada (C.L.C. for a 1967 Science and Engineering Scholarship; K.B.O. for a Research Grant; and A.V.S. for a NATO Science Fellowship). C.L.C. also acknowledges the Trent-Queen's Graduate Program and a doctoral scholarship from the I.O.D.E.

Received for review February 22, 1995. Accepted June 20, 1995.[⊗]

AC9501912

[⊗] Abstract published in *Advance ACS Abstracts*, August 1, 1995.

Anal. Chem. 1995, *67*, 3246–3252

Effect of Multiple Electrolyte Buffers on Peak Symmetry, Resolution, and Sensitivity in Capillary Electrophoresis

John Bullock,* Joost Strasters,† and Jeff Snider‡

Sanofi-Winthrop Pharmaceuticals, 1250 South Collegeville Road, P.O. Box 5000, Collegeville, Pennsylvania 19426

The use of multiple electrolyte buffers in capillary electrophoresis was investigated from theoretical and experimental points of view. A series of model substituted aromatic carboxylic acids was used to investigate the effect of different combinations of buffer co-anions on individual analyte peak symmetry. A theoretical model with computer simulations was used to aid in the interpretation of the observed peak dispersion phenomena. The cumulative data demonstrate that it is possible to simultaneously optimize peak symmetry for a mixture of different analytes with widely varying mobilities by judicious choice of the buffer co-ions. The value of this approach for controlling peak symmetry was demonstrated in terms of both optimization of resolution and sensitivity for mixtures involving analytes with a broad range of mobilities and samples composed of widely varying concentrations of the individual species. In addition, the utility of this technique for improving sensitivity for low-level weakly UV-absorbing impurities was demonstrated. Potential problems encountered in using multiple electrolyte buffers were discovered and their effects interpreted with the aid of the computer simulations.

Free solution capillary electrophoresis (CE) is firmly established as an efficient method for separating a wide variety of ionic species. Examples of different classes of ionic compounds analyzed by this technique include inorganic ions,[1,2] pharmaceuticals,[3] proteins/peptides,[4,5] organic acids,[6] and amino acids.[7] Advantages of CE include high selectivity for compounds of similar structure and high peak efficiencies. Some of the difficulties encountered with CE include its inherently low concentration sensitivity (using conventional UV detection) and the difficulty of analyzing mixtures involving a broad range of mobilities. These problems are exacerbated when analyzing for trace components in the presence of major analytes or when analyzing compounds with poor chromophores. In these situations, the amount of sample injected relative to the concentration of the background electrolyte is of necessity quite high. When operating in these overload conditions, electrical dispersion phenomena become significant, resulting in loss of peak symmetry and efficiency for analytes with mobilities different than that of the buffer co-ion.[8] Typically, one is faced with trying to achieve a compromise by choosing a buffer co-ion with a mobility that is in between those of the different sample components. In this situation, the peak symmetry and efficiencies of those sample components with mobilities closest to that of the buffer co-ion will be favorable, while the symmetries and efficiencies of the components with mobilities that are very different from that of the buffer co-ion will be suboptimal.

A basic understanding of the electrical dispersion processes which give rise to peak asymmetry when operating under overload conditions has been reported. Mikkers et al.[9] first described a model which accounted for dispersion effects resulting from mobility differences between the sample constituents and the carrier electrolyte. This model was able to account for the concentration distribution of the analytes, which can result in asymmetric peaks. Poppe[10] presented a mathematical treatment of overloading phenomena in CE with emphasis on indirect detection systems. A series of equations was described to account for the complex interaction and transport phenomena of all constituents in an electrophoretic system. Computer simulations were able to accurately describe migration and dispersion properties for a series of acids. Vinther and Søeberg[11] derived a mathematical model that quantitatively described the dispersion processes in free solution CE under stacking and nonstacking conditions. Dose and Guiochon[12] described a mathematical model with computer simulations of both CE and isotachophoretic separations. They were able to demonstrate the feasibility of simulating practical experiments with realistically low dispersion. Gas et al.[13] simulated the zone sharpening effect in CE and anomalous spikes in isotachophoretic systems. Ermakov et al.[14–16] developed a highly quantitative mathematical model with com-

† Present address: Nycomed Research and Development, Collegeville, PA 19426.

‡ Present address: Warner-Lambert, Morris Plains, NJ 07950.

(1) Foret, F.; Fanali, S.; Nardi, A.; Bocek, P. *Electrophoresis* **1990**, *11*, 780–783.
(2) Romano, J.; Jandik, P.; Jones, W. R.; Jackson, P. E. *J. Chromatogr.* **1991**, *546*, 411–421.
(3) Wainright, A. *J. Microcolumn Sep.* **1990**, *2*, 166–175.
(4) Grossman, P. D.; Colburn, J. C.; Lauer, H. H.; Nielson, R. G.; Riggin, R. M.; Sittampalam, G. S.; Richard, E. C. *Anal. Chem.* **1989**, *61*, 1186–1194.
(5) Lauer, H. H.; McManigill, D. *Anal. Chem.* **1986**, *58*, 166–170.
(6) Nielen, M. *J. Chromatogr.* **1991**, *542*, 173–183.
(7) Novotny, M. V.; Cobb, K. A.; Liu, J. *Electrophoresis* **1990**, *11*, 735–749.
(8) Mikkers, F. E. P.; Everaerts, F. M.; Verheggen, T. P. *J. Chromatogr.* **1979**, *169*, 11–20.
(9) Mikkers, F. E. P.; Everaerts, F. M.; Verheggen, T. P. *J. Chromatogr.* **1979**, *169*, 1–10.
(10) Poppe, H. *Anal. Chem.* **1992**, *64*, 1908–1919.
(11) Vinther, A.; Søeberg, H. *J. Chromatogr.* **1991**, *559*, 3–26.
(12) Dose, E. V.; Guiochon, G. A. *Anal. Chem.* **1991**, *63*, 1063–1072.
(13) Gas, B.; Vacik, J.; Zelensky, I. *J. Chromatogr.* **1991**, *545*, 225–237.
(14) Ermakov, S. V.; Mazhorova, O. S.; Zhukov, M. Y. *Electrophoresis* **1992**, *13*, 838–848.
(15) Ermakov, S. V.; Bello, M. S.; Righetti, P. G. *J. Chromatogr. A* **1994**, *661*, 265–278.
(16) Ermakov, S. V.; Righetti, P. G. *J. Chromatogr. A* **1994**, *667*, 257–270.

0003-2700/95/0367-3246$9.00/0

puter simulations of electrical dispersion phenomena which showed good quantitative coincidence with experimental data. Hjerten[17] developed equations to describe zone width and shape as a function of diffusion, Joule heat, adsorption, and the conductivity difference between the solute zone and the surrounding buffer. The principle and design of multibuffer systems for sample stacking at the head of the capillary were also described.

The objective of this work was to investigate approaches to control peak symmetry when analyzing samples comprised of components in high concentrations with a broad range of mobilities. A report demonstrating the utility of properly selecting the background electrolyte co-ion with respect to electromigration dispersion in monoelectrolyte buffers was described by Sustacek et al.[18] It was shown by theoretical modeling of separations and by actual experiments that it is possible to substantially reduce the electromigration dispersion by proper selection of the composition of the background electrolyte. However, if the mobilities of the analytes vary significantly, there will still be peak asymmetry for some components when this approach is used, as described above. In the present work, we investigated the use of multiple electrolyte buffers containing co-ions with different mobilities selected to coincide with the measured mobilities of the analytes, which span a broad range. A computer model was applied which was found to be useful in gaining an understanding of the resulting experimental data. The simulations obtained with this model demonstrated certain unexpected peak dispersion phenomena encountered with certain buffer combinations. The combination of the experimental data and the results from the computer simulations supports the use of multiple electrolyte buffers for controlling peak symmetry throughout the electropherogram for a mixture composed of species with widely varying mobilities. The utility of this approach was demonstrated in terms of optimizing resolution for a number of closely eluting species as well as for improving sensitivity and resolution for low-level impurities in the presence of major components.

THEORETICAL SECTION

As indicated above, extensive descriptions on the cause of peak asymmetry in free zone electrophoresis are available in the literature, starting with the work by Mikkers et al.[8,9] The basic mass balance equation can be represented by

$$\frac{\delta C_{z,t,i}}{\delta t} = -\frac{\delta F_{z,t,i}}{\delta z} + D_i \frac{\delta^2 C_{z,t,i}}{\delta z^2} \qquad (1)$$

where $C_{z,t,i}$ represents the concentration of ion i at location z in the column at time t, $F_{z,t,i}$ the migrational flux of that ion, and D_i the diffusion coefficient of ion i. For a monovalent ion and in the absence of electroosmotic flow, F can be expressed as the following function of C, ion mobility μ, and the local electric field E:

$$F_{z,t,i} = C_{z,t,i}\mu_i E_{z,t} \qquad (2)$$

Nonlinearities are introduced due to the fact that E is a function of the concentrations of all ions in the specified region. In other words, the migrational flux of an ion will depend on the concentrations of that ion and other solute and buffer ions at a given location. Thus, not all fractions of a given ionic species will travel with the same speed, and peak asymmetry will be introduced.

In the case of single electrolyte buffers, analytical solutions were described[9] showing that the asymmetry of the peaks is related to the difference in mobilities between the sample ions and the buffer electrolyte ions. When both ions have identical mobilities, the variation in the electric field does not occur, and symmetrical peaks are obtained. If the mobility of the buffer ions is larger than that of the analyte, a tailing peak is obtained, while a lower mobility of the buffer results in a fronting peak.

For a system containing multiple electrolyte buffers, the mathematical equations are in principle similar, but the analytical solutions are less apparent. This prompted us to use computer simulation to obtain a prediction of the expected peak shape for more complicated systems, as described below.

EXPERIMENTAL SECTION

Reagents. Purified water was from a Barnstead purification system (Barnstead/Thermolyne). All buffer components were reagent grade, obtained from J. T. Baker, except for 2-hydroxyisobutyric acid (HIBA, 99%) and methanesulfonic acid (99%), which were from Aldrich. The following test compounds were obtained from Aldrich: 1,2,4-benzenetricarboxylic acid (97%), 1,2,3-benzenetricarboxylic acid (98%), 1,3,5-benzenetricarboxylic acid (98%), 1,2-benzenedicarboxylic acid (phthalic acid), 4-methylphthalic acid (99%), 4-hydroxybenzoic acid, and 3-nitrophthalic acid (99%). Benzoic acid and 2-hydroxybenzoic acid (salicylic acid) were purchased from Kodak.

Apparatus. CE experiments were conducted on a P/ACE Model 2100 instrument (Beckman, Palo Alto, CA) equipped with a UV detector. Data from the instrument were collected and processed with Fisons Multichrom LAS (Danvers, MA). The separation capillary was fused silica of 50 μm i.d. with a total length of 56.5 cm, and the length to the detector was 50 cm. The capillary was initially conditioned with 1 N NaOH for 20 min and reconditioned by rinsing with 1 N NaOH for 0.5 min between each different buffer. Absorbance was measured at 200 nm. All separations were conducted at 25 kV and 30 °C. Typical currents were 30–35 μA. Samples were injected with pressure for 3 s.

Procedures. All separation buffers were prepared by making solutions of the respective anionic acids (total concentration of anionic acids, 30 mM) and adjusting the pH to 8.65 with ammonium hydroxide. These solutions were then filtered through 0.45 μm nylon membrane filters. Various samples of the test compounds were prepared in the respective separation buffers at the concentrations denoted in the text.

Computer Simulations. The main objective in the use of computer simulations to predict peak shape for the case of multiple electrolyte buffers was to confirm the principles underlying the observed phenomena. In other words, a correlation between the simulations and the experimental data would establish that the observations were (at least in part) a direct result of the principles of the electrophoretic process employed in CE.

To this end, we selected an approach described previously by Dose and Guiochon[12] that was easy to implement and could be used to simulate a number of different combinations of buffers and analytes in a relatively short amount of time. The algorithm is based on the combination of finite difference and finite element calculations to approximate eq 1. Electroneutrality is maintained

(17) Hjerten, S. *Electrophoresis* **1990**, *11*, 665–690.
(18) Sustacek, V.; Foret, F.; Bocek, P. *J. Chromatogr.* **1991**, *545*, 239–248.

by deriving the migrational flux of the counterion of the buffer electrolytes from the mobilities of the other ions.

The algorithm was implemented using Borland Pascal with Objects version 7.0 (Borland International, Scotts Valley, CA) on a 486/33 PC (Advanced Logic Research Inc., Irvine, CA). To shorten the calculation time, it was assumed that the diffusion coefficients of analytes and buffer electrolytes were 3 times the theoretical values.[12] In addition, the calculation was limited to 3 s of real-time separation, starting with a 0.012 cm sample plug at the beginning of the column at time 0. All other settings used in the simulation followed the experimental conditions given above as closely as possible.

Asymmetry was defined as the width of the leading half of the peak divided by the width of the trailing peak-half. The width of each half was found by determining the tangent through the inflection point and measuring the distance on the *x*-axis between the projection of the intersection of the two tangents and the intersection of the respective tangent and the *x*-axis.

RESULTS AND DISCUSSION

Peak Symmetry in Buffers with Different Compositions of Buffer Co-ions. The first set of experiments was performed on a mixture of benzoic acid (10 mM), 3-nitrophthalic acid (5 mM), and 1,2,4-benzenetricarboxylic acid (3.33 mM), which have −1, −2, and −3 charges, respectively, at pH 8.65. The concentration of carboxylate functionality was maintained constant for each of these three compounds at 10 mM (total, 30 mM). Electropherograms were obtained in an ammonium buffer at pH 8.65 with HIBA, methanesulfonic acid, or formic acid as the counterion. Separations were obtained in the individual buffers in addition to different combinations of the three anionic counterion buffers. The total concentration of organic anion was maintained constant at 30 mM for each buffer matrix. These three anionic counterions were chosen since they have mobilities close to those of the three analytes (3.42×10^{-4} cm^2/V·s for HIBA versus 3.37×10^{-4} for benzoic acid, 4.83×10^{-4} cm^2/V·s for methanesulfonate versus 4.90×10^{-4} for 3-nitrophthalic acid, and 5.85×10^{-4} cm^2/V·s for formate versus 6.08×10^{-4} for 1,2,4-benzenetricarboxylic acid). The experimental design used here, in which the concentration of analytes is high relative to that of the background electrolyte, typifies the situation in which compounds with weak chromophores are being analyzed or where the background electrolyte needs to be maintained at low levels, such as in indirect UV detection techniques.

Figure 1 contains electropherograms of this three-component mixture obtained with the seven different buffer combinations. The peak symmetries for the three separands obtained in the buffers containing the individual buffer co-anions (panels A, B, and C) are as would be anticipated on the basis of the known mobilities. Acceptable peak symmetry is obtained for the separand with a mobility close to that of the buffer co-anion, while the other two separands display considerably more peak asymmetry. The separations obtained in the three different binary combinations of these three anionic buffer co-ions (panels D−F) produced some interesting results. The buffer combining HIBA and methanesulfonate produces the desired peak symmetry for the first two separands, while the higher mobility 1,2,4-benzenetricarboxylic acid still displays the expected peak tailing. Combining methanesulfonate with formate produces the expected peak symmetry for the later-eluting two separands, while the slower benzoic acid displays the predicted peak fronting. The buffer containing HIBA and formate produces the anticipated peak symmetry for the first- and last-eluting separands, whose mobilities match those of these two buffer co-anions. However, 3-nitrophthalic acid, which has a mobility in between those of the two buffer co-anions, is severely distorted. In fact, this type of peak distortion was predicted by the computer simulations of this separation (see below). This type of electromigration dispersion was observed with other separands with other binary electrolytes in situations in which the mobility of the separand is in the midrange between and significantly different from that of the two buffer co-ions. Finally, the last panel (G) shows the separation obtained in a buffer containing 10 mM concentrations of each of the three buffer co-anions. In this case, acceptable peak symmetry is obtained for all three separands.

Comparison of Computer-Simulated and Experimental Data. The separations involving three components in different buffer systems shown in Figure 1 were simulated as described in the Experimental Section. The results of the simulations and a comparison with the results of the actual experiments are presented in Figure 2, which displays the peak asymmetry values obtained by computer simulation and experimentation in a log/log correlation plot.

It is clear that there is a strong correlation between the two data sets, indicating that even in the case of multiple electrolyte buffers, the general behavior with respect to peak symmetry is, at least to some extent, governed by the basic electrophoretic principles. A closer inspection shows that, although the general trend is predicted, significant differences in the degree of asymmetry were observed. These differences are due to the following:

(1) The diffusion coefficients in the simulations were estimated as 3 times the theoretical values to keep the time required for the simulations within reason. Since diffusion counteracts the effects causing the peak asymmetry, an overestimate of this coefficient will improve the predicted peak shape.

(2) The applied model is an oversimplification in that effects of pH (that is, concentration of hydronium ions and occurrence of multiple ionic species for each analyte) are neglected.

As indicated earlier, the peak asymmetry of nitrophthalic acid in the buffer system containing HIBA and formic acid is especially interesting (Figure 1F). In contrast to the experimental data, in which peak asymmetry could not be calculated due to severe peak distortion, a peak asymmetry value could be determined in the simulation, although the value was anomalously higher than any of the other values found in the simulations. This indicates that even the simplified model predicts, under certain circumstances (e.g., Figure 1F), a severely distorted peak shape for a component with a mobility between the mobilities of the two buffer components. Therefore, this phenomenon is directly linked to the electrophoretic behavior of the components involved in the separations.

To investigate this further, a number of additional simulations were performed based on the observed mobilities of HIBA and formic acid. A hypothetical component comparable to nitrophthalic acid with a mobility varying between those of the two buffer components was defined and the behavior in the system recorded. The results are shown in Figure 3 (solid lines). Initially, a decrease in the peak asymmetry is observed, similar to the response of a one buffer component system, as the difference in the mobility of the test analyte relative to that of one of the individual buffer co-ions is increased. However, for

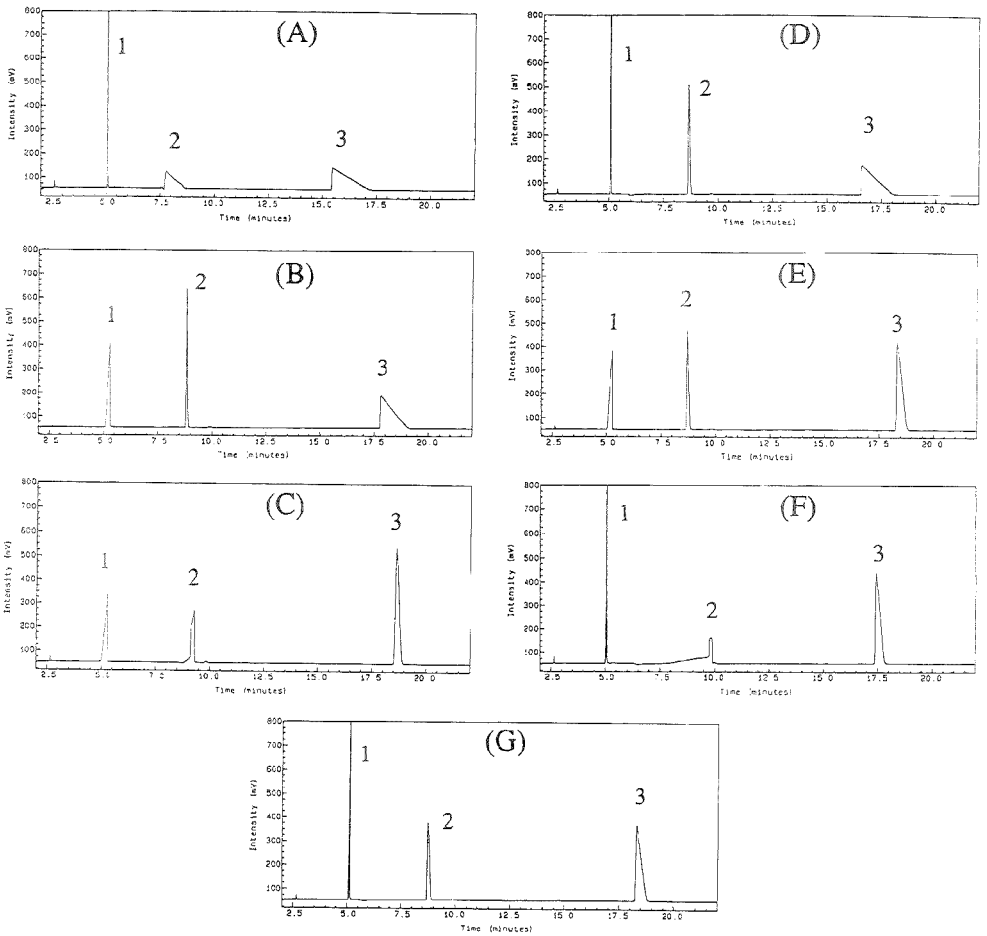

Figure 1. CZE separations of a sample containing (1) 10 mM benzoic, (2) 5 mM 3-nitrophthalic, and (3) 3.33 mM 1,2,4-benzenetricarboxylic acids. Conditions are as given in the Experimental Section, with ammonia as the buffering species and the buffer co-anion(s) being (A) 30 mM HIBA, (B) 30 mM methanesulfonic acid, (C) 30 mM formic acid, (D) 15 mM each HIBA and methanesulfonic acid, (E) 15 mM each methanesulfonic and formic acids, (F) 15 mM each HIBA and formic acid, and (G) 10 mM each HIBA, methanesulfonic acid, and formic acid.

two of the experiments (open squares), a poorly defined peak (broad without a clear maximum) was obtained, indicating that there is a range of mobilities, coinciding with the midrange of the mobilities of the two buffer co-ions, where it is not possible to obtain good electropherograms at the examined concentrations.

To determine whether this area of poorly defined peak symmetry would be removed when the mobilities of the two buffer systems were moved closer together, a last set of simulations was performed using a buffer system with mobilities of 0.00050 and 0.00035 $cm^2/V·s$ (dashed lines in Figure 3). Again, there is a range of mobility values where ill-defined peaks are obtained (open triangles), although it is narrower than the area in the previous set of simulations. In addition, it seems that the peak asymmetry drops faster as the mobility difference between analyte and closest buffer increases. A preliminary conclusion would be that inclusion of multiple buffer electrolytes can result in ill-defined peaks in certain regions of the electropherogram, a fact which will have to be taken into consideration when optimizing the CE separation of a complex mixture.

Peak Resolution in Multiple Electrolyte Buffers. The utility of multiple electrolyte buffers in terms of peak resolution is demonstrated in Figure 4. This series of separations was obtained on a mixture of nine substituted aromatic carboxylic acids (three monoacids, three diacids, and three triacids). Shown in this figure are the separations obtained with the buffers containing the individual buffer co-anions (A–C) and the mixture of the three anionic buffer co-ions (D). With each of the single anion-containing buffers, resolution and peak efficiencies are highest for the set of substituted aromatic carboxylic acids with mobilities closest to that of the buffer co-anion. In each case, the resolution and efficiencies of the remaining compounds in the mixture are poor. For the separation obtained in the mixture of the three

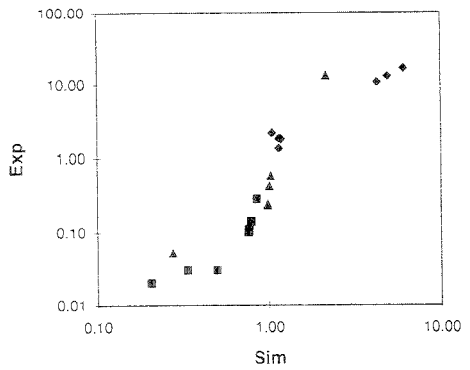

Figure 2. Correlation of the peak asymmetry (defined as the ratio of the fronting and trailing peak widths) observed in the experiments (Exp) and simulations (Sim) for benzoic acid (◆), nitrophthalic acid (▲), and 1,2,4-benzenetricarboxylic acid (■). See Figure 1 for description of the buffer systems.

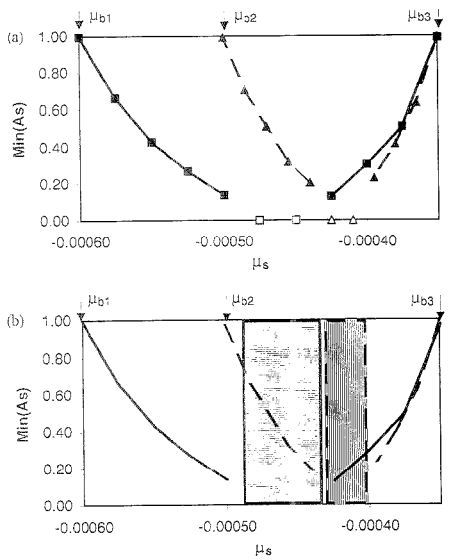

Figure 3. Resulting peak asymmetry (defined as the minimum value of the ratio of the fronting and trailing peak widths and the ratio of the trailing and fronting peak widths for a given peak, Min(As)) found for a hypothetical component with mobility μ_s in (1) a buffer system with electrolytes with mobilities of 0.000 60 and 0.000 35 $cm^2/V\cdot s$ (■, solid lines) and (2) a buffer system with electrolytes with mobilities of 0.000 50 and 0.000 35 $cm^2/V\cdot s$ (▲, dashed lines). (a) The results of the various simulations as indicated by the symbols. The open symbols refer to conditions where the peak shape was ill-defined and no value for the asymmetry could be obtained. (b) Mobility regions where it is expected that ill-defined peaks will be observed in system 1 (horizontally shaded area) and system 2 (vertically shaded area).

buffer co-anions (D), adequate resolution and peak symmetry are obtained for all nine components. It is interesting to note that the full range of peak asymmetry is displayed for each of the three sets of three substituted aromatic carboxylic acids using buffer (D). Thus, the first peak in each set displays some peak fronting,

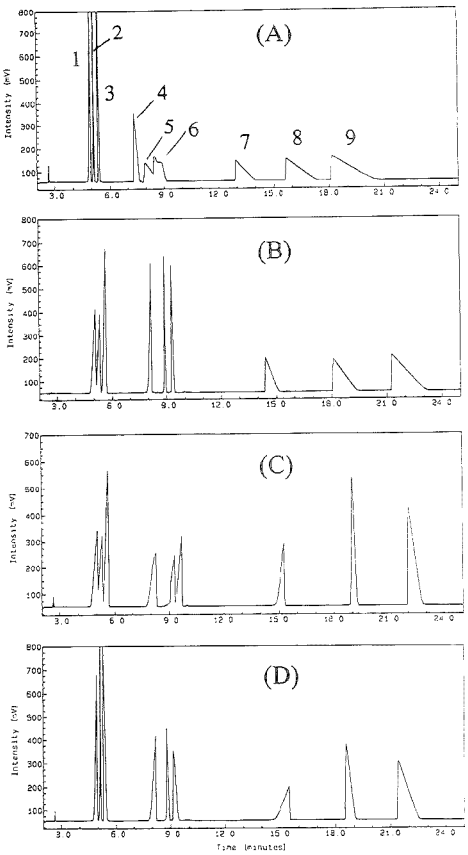

Figure 4. CZE separations of a sample containing 10 mM concentrations of (1) p-hydroxybenzoic, (2) benzoic, and (3) salicylic acids; 5 mM concentrations of (4) 4-methylphthalic, (5) 3-nitrophthalic, and (6) phthalic acids; and 3.33 mM concentrations of (7) 1,2,3-benzenetricarboxylic, (8) 1,2,4-benzenetricarboxylic, and (9) 1,3,5-benzenetricarboxylic acids. Conditions are as given in the Experimental Section, with the buffer co-anions being (A) 30 mM HIBA, (B) 30 mM methanesulfonate, (C) 30 mM formate, and (D) 10 mM each of HIBA, methanesulfonate and formate.

the middle peak is more or less symmetrical, and the last peak in each set displays tailing, as would be predicted on the basis of the mobility difference for each analyte compared to that of the buffer co-anion with a mobility closest to those components in each set (HIBA for the monoacids, methanesulfonate for the diacids, and formate for the triacids).

The data from Figure 4D provide some insight into the phenomena that minimize electrodispersion in multiple co-ion systems. It is clear from the peak shapes of the three sets of analytes that the peak symmetry for each component in the sample is dominated by the buffer co-ion whose mobility most closely matches those of the respective analytes. This is supported by the simulations of these experiments, which revealed that in multiple co-ion buffers, the individual analytes primarily displace the co-ion that has a mobility closest to that of the analyte. In

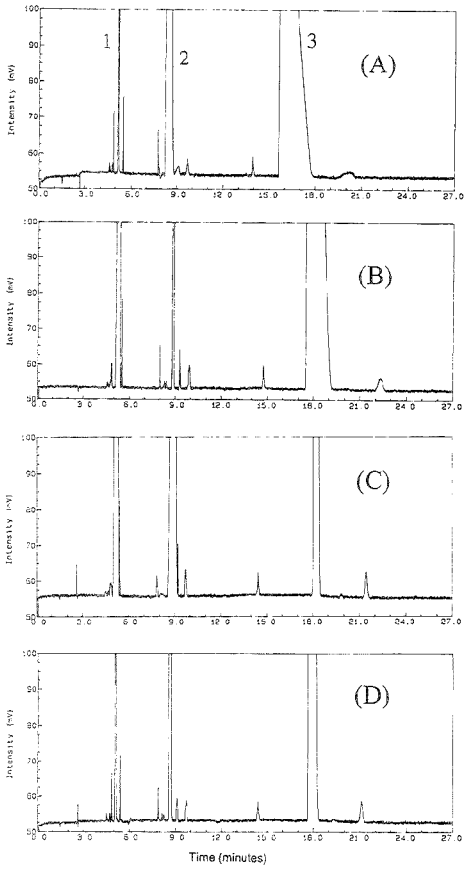

Figure 5. CZE separation of a sample containing (1) 10 mM benzoic acid with 0.5% w/w each of *p*-hydroxybenzoic and salicylic acids. (2) 5 mM 3-nitrophthalic acid with 0.5% w/w each of 4-methylphthalic and phthalic acids, and (3) 3.33 mM 1,2,4-benzenetricarboxylic acid with 0.5% w/w each of 1,2,3-benzenetricarboxylic and 1,3,5-benzenetricarboxylic acids. Conditions and buffer identities are as given in Figure 4.

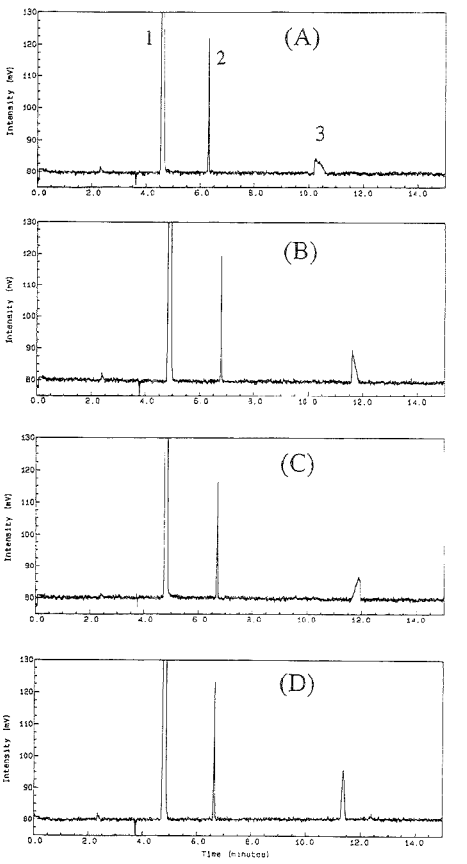

Figure 6. CZE separation of a sample of a drug intermediate (1) and its two degradation products (2) and (3). Capillary, 50 μm i.d. × 67 cm; temperature, 30 °C; wavelength, 200 nm; voltage, 25 kV; and injection time, 4 s. Sample concentration, 2.5 mg/mL. Buffers are (A) 50 mM boric acid, pH 9.2 with NaOH; (B) 35 mM boric acid and 15 mM ethyl sulfate, pH 9.2; (C) 35 mM boric acid and 15 mM NaH_2PO_4, pH 9.2; and (D) 35 mM boric acid and 15 mM methanesulfonic acid, pH 9.2.

the simulations, this is observed as a depletion zone in the the concentration profile for the co-ion which overlaps the solute zone. The magnitude (concentration) of this depletion zone is equal to the magnitude of the individual solute in the zone when the mobilities are equal. This produces a situation in which the field strength across the solute plug and bulk buffer in the capillary are equal, and therefore, peak asymmetry due to field inhomogeneity is minimized. In the case of simulations of buffer systems in which there is a mobility mismatch, the magnitude of the depletion of the co-ion in the analyte zone is not of the correct value to give equivalent field strengths across the sample plug and bulk buffer in the capillary. In this situation, peak asymmetry is introduced due to the field inhomogeneity.

Influence of Multiple Electrolyte Buffers on Resolution and Sensitivity for Low-Level Impurities. A typical application for CE is the determination of low-level impurities in the presence of major components. In this case, the level of major component injected is typically quite high. The usefulness of multiple electrolyte buffers in such applications is demonstrated in Figure 5. The separations in this figure were obtained on the same set of three aromatic carboxylic acids used in Figure 1 at the same concentrations used in Figure 1, to which was added 0.5% w/w (relative to the respective major components in each class) of the remaining aromatic acids used in Figure 4. It should be noted that the benzoic acid and 3-nitrophthalic acid contained some additional low-level impurities which were observed in these electropherograms in addition to the intentionally added impurities. The separations in panels A–C were obtained in the buffers containing individually the three different anionic co-ions (HIBA, methansulfonate, or formate). The separation in the last panel (D) was obtained in a buffer with all three anionic co-ions. Only in the buffer with all three anionic co-ions are all of the low-level

impurities clearly resolved and detectable. Two problems are encountered in the single anionic buffer compositions. The first is poor resolution of the impurities from the major component for some of the separands due to significant peak asymmetry for the major component. The second is a peak dispersion or peak broadening for the low-level impurities which results in decreased intensity (see, for instance, the impurities following 3-nitrophthalic acid and 1,2,4-benzenetricarboxylic acid in panel A and preceding benzoic acid in panel C). This is believed to be due to a dispersion or dilution of the minor component in the presence of the major component which takes place at the beginning of the analysis, before the low-level impurity is completely separated in the capillary from the major component.

Even when the low-level impurities do not elute close to the major components, there can still be an advantage to this multiple electrolyte approach to improve sensitivity. Figure 6 contains a series of electropherograms obtained on a sample of a drug intermediate (DTPA-DA) and its two degradation products. Details of this method can be found elsewhere.[19] The analysis is conducted using a borate buffer (Figure 6A), the mobility of which most closely matches that of the first-eluting of the two degradation products at about 6.5 min. These compounds are highly charged and possess weak UV chromophores. Even at the low levels found in this sample, the later-eluting degradant (which carries a −3 charge) displays significant peak asymmetry in the borate buffer, which reduces sensitivity. Several different secondary buffer co-ions were investigated having mobilities higher than that of borate and closer to that of the later-eluting degradant in an attempt to improve symmetry and sensitivity. Adding ethyl sulfate (B) or phosphate (C) improved the symmetry for the later-eluting degradation product, resulting in a 2-fold improvement in sensitivity. Using methanesulfonate (D), which has a mobility much closer to that of the later-eluting degradation product (4.82×10^{-4} versus 4.89×10^{-4} cm^2/V·s) resulted in much better peak symmetry and improved sensitivity by a factor of 3 over that obtained in the borate buffer alone. It should be noted that adding the methanesulfonate to the borate buffer had no significant effect on the peak symmetry/intensity of the other components.

CONCLUSIONS

In this work, the effects of using multiple electrolyte buffers were studied experimentally and with the aid of computer simulations. The following conclusions have been drawn:

(1) The trends in peak asymmetry in buffer systems containing multiple buffer electrolytes are governed by primary electrophoretic characteristics of analytes and buffer components.

(2) When including additional buffer electrolytes, one should be aware of potentially ill-defined peaks in regions in the electropherograms between the mobilities of the buffer system. First indications are that bringing the mobilities of the buffer electrolytes closer together would not necessarily solve this problem.

(3) By judicious choice of buffer co-ions, significant improvements in resolution and sensitivity are possible as a result of increasing peak symmetry.

It is clear that the presented simulations were intended to obtain a first impression of the phenomena that can be expected in buffer systems containing multiple electrolytes. In order for the simulations to be used for true predictions of the electrophoretic behavior, many refinements are possible, as described in the literature.[10-16] Specifically, the use of alternative ways to describe the electrophoretic process[10] might give further insight into the relationships between mobilities and peak shapes found in these more complex buffer systems.

The practical applications of using multiple electrolyte buffers were demonstrated in terms of improving resolution for sample components with very similar mobilities and for improving sensitivity and resolution for minor components in the presence of major components. Of course, one of the limitations of this approach is the need to have at one's disposal an appropriate choice of buffer co-ions with mobilities similar to those of the analytes to be separated. Ultimately, the success of this approach will depend not only on the availability of buffer co-ions with the appropriate mobilities but also the appropriate spectral properties, pK_a values (if weak electrolytes), and the desired effect on any secondary equilibria. In many real-life situations, some compromise will still be necessary. However, significant improvements over single electrolyte buffers are possible, as long as one is aware of the trade-offs.

Received for review March 9, 1995. Accepted July 3, 1995.[⊗]

AC950244F

(19) Bullock, J. A. *J. Chromatogr.*, in press.

[⊗] Abstract published in *Advance ACS Abstracts*, August 15, 1995.

Anal. Chem. 1995, *67*, 3253–3260

Single Molecule Fluorescence Burst Detection of DNA Fragments Separated by Capillary Electrophoresis

Brian B. Haab and Richard A. Mathies*

Department of Chemistry, University of California, Berkeley, California 94720

A method has been developed for detecting DNA separated by capillary gel electrophoresis (CGE) using single molecule photon burst counting. A confocal fluorescence microscope was used to observe the fluorescence bursts from single molecules of DNA multiply labeled with the thiazole orange derivative TO6 as they passed through the ~2-μm diameter focused laser beam. Amplified photoelectron pulses from the photomultiplier are grouped into bins of 360–450 μs in duration, and the resulting histogram is stored in a computer for analysis. Solutions of M13 DNA were first flowed through the capillary at various concentrations, and the resulting data were used to optimize the parameters for digital filtering using a low-pass Fourier filter, selecting a discriminator level for peak detection, and applying a peak-calling algorithm. Statistical analyses showed that (i) the number of M13 molecules counted versus concentration was linear with slope = 1, (ii) the average burst duration was consistent with the expected transit time of a single molecule through the laser beam, and (iii) the number of detected molecules was consistent with single molecule detection. The optimized single molecule counting method was then applied to an electrophoretic separation of M13 DNA and to a separation of pBR 322 DNA from pRL 277 DNA. Clusters of discreet fluorescence bursts were observed at the expected appearance time of each DNA band. The autocorrelation function of these data indicated transit times that were consistent with the observed electrophoretic velocity. These separations were easily detected when only 50–100 molecules of DNA per band traveled through the detection region. This new detection technology should lead to the routine analysis of DNA in capillary columns with an on-column sensitivity of ~100 DNA molecules/band or better.

High-sensitivity detection methods are finding increasing importance and usefulness in many fields, such as bacterial and viral diagnostics, environmental studies and health care, and basic physical and biochemical research. The ultimate in high-sensitivity detection is the detection of individual molecules. This goal has been achieved in several different formats. In the solid phase, the spectroscopic isolation of individual fluorescent impurities in low-temperature crystalline hosts[1] has been used to study molecular properties[2] and changes in local environments and spectral characteristics.[3–5] Near-field optical scanning microscopy has been used to detect single fluorescent dyes on a surface,[3,7] and this method has also been used to study properties and dynamics of individual fluorophores.[8,9] Individual dye molecules adsorbed on a surface have also been imaged using a position-sensitive photon counting apparatus.[10] Many analytical and bioanalytical applications are anticipated for single molecule detection in the liquid phase, where single molecules of both fluorescent dyes and DNA labeled with multiple fluorescent dyes have been detected in confined drops,[11] levitated microdroplets,[12] focused sheath flows,[13–15] and capillary flows.[16–18] Biological macromolecules have been observed at the single molecule level by microscopic imaging,[19] and this technique has been used to study conformational dynamics[20–22] and physical properties of DNA[23] as well as the behavior of RNA polymerase.[24] While many of these techniques have involved the analysis of DNA and other biological macromolecules, an electrophoretic or chromatographic analytical

(1) Moerner, W. E.; Kador, L. *Phys. Rev. Lett.* **1989**, *62*, 2535–2538.
(2) Orrit, M.; Bernard, J.; Brown, R.; Fleury, L.; Wrachtrup, J.; von Borczyskowski, C. *J. Lumin.* **1994**, *60*, 991–996.
(3) Basche, T.; Moerner, W. E. *Nature* **1992**, *355*, 335–337.
(4) Ambrose, W. P.; Basche, T.; Moerner, W. E. *J. Chem. Phys.* **1991**, *95*, 7150–7163.
(5) Moerner, W. E. *Science* **1994**, *265*, 46–53.
(6) Betzig, E.; Chichester, R. J. *Science* **1993**, *262*, 1422–1425.
(7) Trautman, J. K.; Macklin, J. J.; Brus, L. E.; Betzig, E. *Nature* **1994**, *369*, 40–42.
(8) Ambrose, W. P.; Goodwin, P. M.; Martin, J. C.; Keller, R. A. *Science* **1994**, *265*, 364–367.
(9) Xie, X. S.; Dunn, R. C. *Science* **1994**, *265*, 361–364.
(10) Ishikawa, M.; Hirano, K.; Hayakawa, T.; Hosoi, S.; Brenner, S. *Jpn. J. Appl. Phys.* **1994**, *33*, 1571–1576.
(11) Nie, S.; Chiu, D. T.; Zare, R. N. *Science* **1994**, *266*, 1018–1021.
(12) Whitten, W. B.; Ramsey, J. M.; Arnold, S.; Bronk, B. V. *Anal. Chem.* **1991**, *63*, 1027–1031.
(13) Nguyen, D. C.; Keller, R. A.; Jett, J. H.; Martin, J. C. *Anal. Chem.* **1987**, *59*, 2158–2161.
(14) Shera, E. B.; Seitzinger, N. K.; Davis, L. M.; Keller, R. A.; Soper, S. A. *Chem. Phys. Lett.* **1990**, *174*, 553–557.
(15) Soper, S. A.; Shera, E. B.; Martin, J. C.; Jett, J. J.; Hahn, J. H.; Nutter, H. L.; Keller, R. A. *Anal. Chem.* **1991**, *63*, 432–437.
(16) Peck, K.; Stryer, L.; Glazer, A. N.; Mathies, R. A. *Proc. Natl. Acad. Sci. U.S.A.* **1989**, *86*, 4087–4091.
(17) Lee, Y. H.; Maus, R. G.; Smith, B. W.; Winefordner, J. D. *Anal. Chem.* **1994**, *66*, 4142–4149.
(18) Wilkerson, C. W., Jr.; Goodwin, P. M.; Ambrose, W. P.; Martin, J. C.; Keller, R. A. *Appl. Phys. Lett.* **1993**, *62*, 2030–2033.
(19) Hirschfeld, T. *Appl. Opt.* **1976**, *15*, 2965–2966.
(20) Schwartz, D. C.; Koval, M. *Nature* **1989**, *338*, 520–522.
(21) Smith, S. B.; Aldridge, P. K.; Callis, J. B. *Science* **1989**, *243*, 203–206.
(22) Perkins, T. T.; Smith, D. E.; Chu, S. *Science* **1994**, *264*, 819–822.
(23) Smith, S. B.; Finzi, L.; Bustamante, C. *Science* **1992**, *258*, 1122–1126.
(24) Schafer, D. A.; Gelles, J.; Sheetz, M. P.; Landick, R. *Nature* **1991**, *352*, 444–448.

0003-2700/95/0367-3253$9.00/0

separation technique employing single molecule detection has not yet been demonstrated.

We present here the application of single molecule fluorescence burst detection to the separation of DNA in capillary gel electrophoresis (CGE). CGE is an attractive method to couple with single molecule detection since it is a widely used, reliable technique which offers high-resolution separation of DNA and other biological macromolecules.[25,26] Applications employing CGE would be further enhanced by improvements in signal-to-noise ratio and sensitivity. Single molecule detection would provide the ultimate improvement.

Optimization of the signal-to-noise ratio (S/N) is the main challenge in developing a single molecule detection system for CGE. The limiting factor for high-sensitivity detection in electrophoresis has been the background count rate caused by scattering and impurity fluorescence from the separation matrix as well as limited signal from the sample molecules. To address these issues, this work builds upon that of Zhu et al.,[27] who recently evaluated a variety of intercalation dyes for the detection of CGE separations of double-stranded DNA. The dye [(*N,N*'-tetramethylpropanediamino)propyl]thiazole orange (TO6)[28] was determined to have the best detection limits of the monointercalators, and for that reason it was chosen for use in this work. TO6 is advantageous because it has a high quantum efficiency and because its extremely high affinity for DNA permits DNA detection with very low concentrations of dye in the electrophoresis buffer. The S/N was further enhanced through the use of confocal optics, efficient spectral filtering, and a high numerical-aperture oil immersion objective to increase the light gathering efficiency and to reduce scattering caused by the air–glass interface.

The development of a digital photon counting interface for single molecule detection was also critical to this effort because it offers the potential for improved time resolution and S/N over analog detection.[29] Because a single molecule in a typical electrophoresis experiment will travel through the laser beam in only 2–10 ms, amplified photoelectron pulses must be captured in bins of 300–500 μs in duration to achieve a desired minimum of 4 or 5 bins per DNA transit time. At this high rate of counting, commercially available counting circuits typically do not have enough on-board memory to allow extended, uninterrupted data collection. We therefore constructed a computer-based counting circuit to accomplish this task efficiently.

With these technical improvements, we have successfully developed a single molecule fluorescence burst detector and method for CGE. To optimize the spectroscopic apparatus and data analysis methods, solutions of M13 DNA were first flowed through the detector and the fluorescence bursts recorded. Statistical analyses were performed off-line to confirm single molecule detection and to better understand and optimize the system. In particular, we examined whether (i) the number of single molecule events is linear with concentration, (ii) the duration of fluorescence bursts corresponds to the expected transit time of one molecule through the laser beam, and (iii) the number of molecular events corresponds to that expected for single molecule counting. In addition, these M13 data were used to optimize the noise filtration and peak-calling algorithms. Finally, M13, pBR322, and pRL 277 DNA were injected into the capillary and separated by CGE. Clusters of fluorescence bursts were observed at the expected appearance time of each DNA band. The statistical tests and single molecule counting system were applied to these data and used to confirm that the individual bursts within the clusters arose from single molecules of DNA. This work establishes the feasibility of single molecule photon burst detection of DNA in all types of capillary separations.

EXPERIMENTAL SECTION

Samples. M13 (7250 bp) and pBR 322 DNA (4631 bp) were purchased from New England Biolabs (Beverly, MA). The M13 DNA was linearized with *Bam*HI, and the pBR 322 DNA was linearized with *Eco*RI. pRL 277 DNA (6798 bp)[30] was a gift from Dr. Yuping Cai of the UC Berkeley Molecular and Cell Biology Department and was linearized with *Eco*RI. DNA samples were diluted with a 0.4 mM Tris–acetate, 0.1 mM Na_2EDTA buffer (pH 8.0) and stored at −20 °C.

Capillary Electrophoresis. Fused silica capillaries (100 μm i.d., 200 μm o.d.) were purchased from Polymicro Technologies (Phoenix, AZ) and the interior surfaces derivatized according to the protocol of Hjerten.[31] The capillary length was 50 cm, and a 2-mm observation window was burned 25 cm from the injection end. The capillary was filled with a solution of 40 mM Tris–acetate, 1 mM EDTA, pH 8.0 (1× TAE), and 0.10%–0.50% (w/v) hydroxyethyl cellulose (HEC, M_n = 438 000; Polysciences Inc., Warrington, PA). This HEC-containing buffer was first degassed under vacuum for 20–25 min and then centrifuged at 17 000 rpm for 40 min (Sorvall Superspeed RC2-B). The monomeric intercalating dye [(*N,N*'-tetramethylpropanediamino)propyl]thiazole orange (TO6)[28] was added to the solution (10 nM) before centrifuging. At this concentration, the DNA should be nearly saturated with dye, giving a labeling density of 2–4 bp/dye. The HEC buffer solution was manually injected into the capillary using a 100-μL syringe. Samples were electrokinetically injected (100–150 V/cm for 5–8 s) from a 5-μL volume in an Eppendorf tube, which was then replaced by a buffer reservoir. Electrophoresis was performed at 150–200 V/cm. At the conclusion of each experiment, the capillary was flushed with water and acetone and purged with nitrogen gas. For the experiments using flowing solutions of DNA, a syringe pump (Harvard Apparatus, Millis, MA) and a 100-μL syringe were coupled to the capillary.

Instrumentation. The experimental apparatus described in Figure 1 is similar to that presented earlier.[27] Excitation (488 nm) from a Coherent Innova 70 krypton/argon ion laser was passed into a confocal microscope (Axioskop; Carl Zeiss), reflected off a 510-nm long-pass dichroic beam splitter, and focused into the capillary by a 40×, 1.3 NA oil immersion objective (Plan Neoflor; Carl Zeiss). The capillary was placed on a microscope slide, and a drop of immersion oil (Carl Zeiss; n = 1.518) was placed between the objective and the observation window of the capillary. The laser power was optimized according to the theory described

(25) Ewing, A. G.; Wallingford, R. A.; Olefirowicz, T. M. *Anal. Chem.* **1989**, *61*, 292A–303A.
(26) Landers, J. P.; Oda, R. P.; Spelsberg, T. C.; Nolan, J. A.; Ulfelder, K. J. *Biotechniques* **1993**, *14*, 98–111.
(27) Zhu, H.; Clark, S. M.; Benson, S. C.; Rye, H. S.; Glazer, A. N.; Mathies, R. A. *Anal. Chem.* **1994**, *66*, 1941–1948.
(28) Benson, S. C.; Mathies, R. A.; Glazer, A. N. *Nucleic Acids Res.* **1993**, *21*, 5720–5726.
(29) Ingle, J. D.; Crouch, S. R. *Spectrochemical Analysis*; Prentice-Hall: Englewood Cliffs, NJ, 1988; Chapter 5.
(30) Black, T. A.; Cai, Y.; Wolk, C. P. *Mol. Biol.* **1993**, *9*, 77–84.
(31) Hjerten, S. *J. Chromatogr.* **1985**, *347*, 191–198.

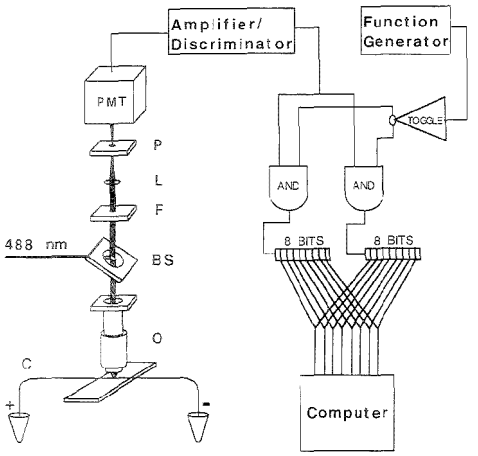

Figure 1. Schematic of the laser-excited, confocal fluorescence detection system and photon counting circuit. The 488-nm excitation light is reflected by the long-pass beam splitter (BS) and focused by the objective (O) into the capillary. Emission from the capillary is collected by the objective, passed through the beam splitter and green bandpass filter (F), and then focused by the lens (L) through pinhole (P) to the photomultiplier (PMT). The photoelectron pulses from the PMT pass through an amplifier/discriminator and are counted by the counting circuit. The circuit toggled between two 8-bit counters so that as one counter was counting, the other was being read and cleared. The capillary (C) was mounted on a microscope slide, and a drop of immersion oil ($n = 1.518$) was placed between the objective and the detection window of the capillary.

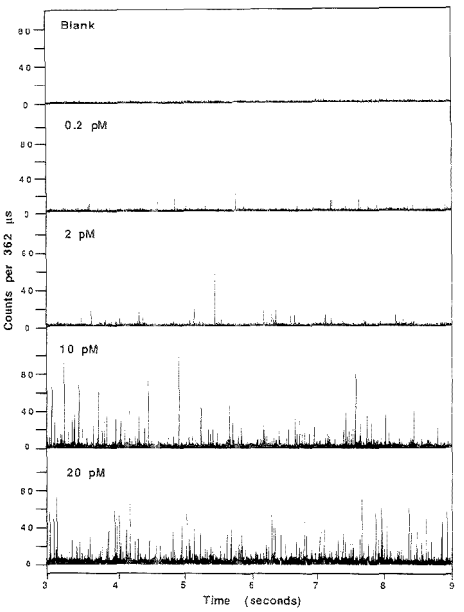

Figure 2. M13 DNA dilution series. Solutions of M13 DNA in 1× TAE stained with 10 nM TO6 were flowed through the 100-μm-i.d. capillary using a syringe pump. The trials were 108 s long (300 000 data points with a binwidth of 362 μs), and a 6-s portion of each trial is shown. The laser power at 488 nm was 0.3 mW at the sample, and the mean flow velocity was 0.044 cm/s.

earlier[32] and was set between 0.3 and 0.5 mW at the sample. Fluorescence was collected by the objective, passed through the beam splitter, filtered by a bandpass filter (530DF30, Omega, Brattleboro, VT), focused on a 50-μm pinhole, and detected with a photomultiplier (Hamamatsu R943-02) in a cooled housing (TE210RF; Products for Research, Danvers, MA). After being passed through an amplifier and discriminator (SSR 1120), the photoelectron pulses were fed to a counting circuit that was built on a "breadboard" which plugged into one of the expansion slots of a 386-based AT personal computer. This circuit toggled between two 8-bit counters (Jameco, 74F193) at a rate of between 360 and 450 μs/bin, set by a function generator. While one counter was counting, the other was being read to the computer's RAM disk and cleared, so that there was no dead-time in collecting the data.

Data Analysis. Data were first filtered to remove any anomalously large one-bin noise spikes. The spikes occurred approximately once per 100 000 points and were replaced by the average of the two adjacent points. Data were then Fourier transformed using an algorithm from ref 33, low-pass filtered in frequency space, and reverse Fourier transformed. The peak-calling algorithm searched for maxima in the data set which were above a defined discriminator level and also had immediately flanking points at a lower value.

(32) Mathies, R. A.; Peck, K.; Stryer, L. *Anal. Chem.* **1990**, *62*, 1786–1791.
(33) Press, W. H.; Vetterling, W. T.; Teukolsky, S. A.; Flannery, B. P. *Numerical Recipes in C*, 2nd ed.; Cambridge University Press: New York, 1992; Chapter 12.

RESULTS AND DISCUSSION

M13 DNA Dilution Series. To test the single molecule detection apparatus and to develop data analysis methods, solutions containing linear M13 DNA (7.25 kb) were flowed through the capillary with a syringe pump. Figure 2 presents 6-s portions of each 108-s trial in a M13 DNA dilution series. The concentrations ranged from 0 to 20 pM. When the blank solution was flowed through the capillary, no large fluorescence bursts were observed, and the average count rate was 0.38 counts/bin. When DNA solutions were introduced, discreet fluorescence bursts were seen, and the number of these bursts increased with concentration, suggesting that they were due to the passage of individual DNA molecules through the focused laser beam. If the probability of more than one DNA molecule simultaneously occupying the probe volume is extremely low, then the observed fluorescence bursts can be attributed to single molecules of DNA. An occupancy, or average number of molecules per probe volume, of ~0.01 has been shown to be an effective criterion for single molecule detection.[15] The e^{-2} probe volume in our case was approximated to be a cylinder 4.0 μm in height and 2.4 μm in diameter, giving a volume of 18 fL. The 2.4-μm diameter is our best estimate of the effective beam diameter based on the capillary electrophoresis measurements described below, and the 4.0-μm height is an estimate of the convolution of the depth of focus of the laser beam with the confocal detection efficiency.[34] For an 18-fL probe volume, the occupancies range from 0.002 to 0.2 for

(34) Wilson, T.; Carlini, A. R. *Opt. Lett.* **1987**, *12*, 227–229.

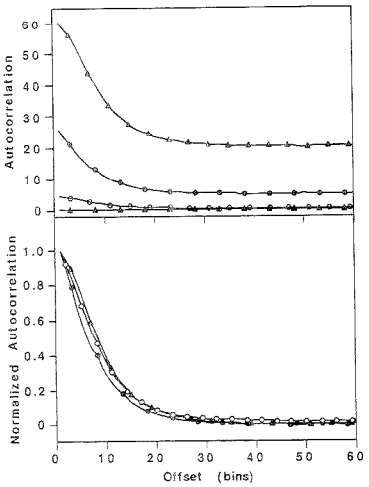

Figure 3. Autocorrelation functions calculated from the M13 DNA dilution series data. The concentrations were 20 (△), 10 (●), 2 (○), and 0 pM (▲). (top) Unnormalized autocorrelation functions. (bottom) Normalized autocorrelation functions. The noise spike at $\tau = 0$ was removed from all data, and data were normalized to have the same value at $\tau = 1$. Each offset bin is 362 μs in duration, and the formula used to calculated the autocorrelation function was $G(\tau) = (1/N)\Sigma n(t)n(t + \tau)$, where G is the autocorrelation, N is the size of the data set, $n(t)$ is the value at time t, and τ is the offset.

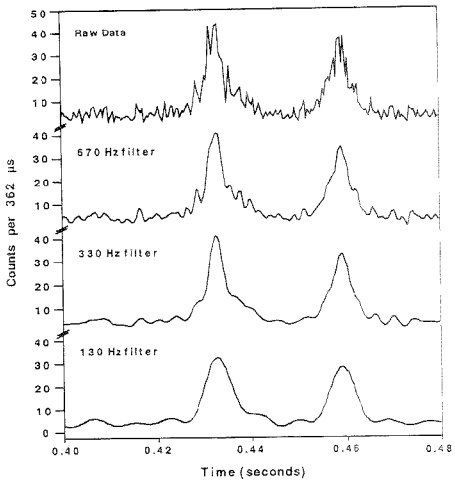

Figure 4. Data illustrating the digital filtering procedure. Representative M13 fluorescence burst data from the 20 pM run are shown, followed by the same data after applying a 670-, 330-, and 130-Hz low-pass filter. The 330-Hz filter was chosen to analyze the full data set because it provided the greatest high-frequency filtration without significantly broadening the bursts.

the 0.2–20 pM concentrations. For the 2 pM concentration, assuming a Poisson distribution, the probability of no molecules in the probe volume is 0.980, the probability of 1 molecule in the probe volume is 0.0196, and the probability of two or more molecules simultaneously in the probe volume is 1.97×10^{-4}. For the 20 pM solution, the probability of two or more molecules simultaneously in the probe volume is 0.0175, which means that even at this concentration, the majority of the observed fluorescence bursts must arise from single molecules.

The autocorrelation function has been shown to be effective in demonstrating the presence of non-Poissonian bursts due to single molecules[14,16] and in characterizing transit times and particle numbers.[15,35] Figure 3 presents the calculated autocorrelation functions from the M13 DNA dilution series data. The autocorrelations are approximately Gaussian in shape. The unnormalized autocorrelations in Figure 3 (top) show that the magnitude of the autocorrelations increases with concentration, and the normalized autocorrelations in Figure 3 (bottom) show that the shape and width of the autocorrelation functions change very little with concentration, as expected for single molecule detection. The values of the autocorrelation function at $\tau = 0$ and $\tau = \infty$ should be linear with concentration,[15] and this is observed within the uncertainties of the concentrations for these very dilute DNA samples. The transit time, defined by the e^{-2} width, can be determined by fitting a Gaussian to the autocorrelation function. The autocorrelation of a Gaussian yields a half-Gaussian with a standard deviation that is increased by a factor of $(2)^{1/2}$, so the transit time is given by $4\sigma/(2)^{1/2}$, where σ is the standard deviation of the Gaussian fit. The data fit approximately to a Gaussian with an average standard deviation of 7.1, which yields a mean transit time of 7.3 ms. The beam was focused 10–15 μm beneath the top wall of the capillary, where, based on the average linear velocity from the syringe pump of 440 μm/s and assuming a parabolic flow profile, the flow velocity was calculated to be 300 μm/s. This velocity estimate allows us to calculate an effective e^{-2} beam diameter of 0.0073 s × 300 μm/s = 2 μm. This observed beam diameter was larger than that calculated from diffraction-limited optics but agreed well with that determined in subsequent electrophoresis experiments (see below). The increased size of the beam is presumably due to defocusing of the laser by refractive index mismatches at the oil–quartz–water interfaces[36] and by the cylindrical lens formed by the capillary.

Single Molecule Counting. To count single molecules, it is first necessary to digitally filter the data to remove high-frequency noise, making the single molecule bursts easily identifiable by a peak-calling algorithm. Figure 4 demonstrates this digital filtration. As described in the Experimental Section, the data were Fourier transformed, low-pass filtered, and reverse Fourier transformed. As the frequency cutoff is lowered, the data become smoother, but after a certain point, the underlying peak shape is distorted. From the data in Figure 4, a 330-Hz cutoff was determined to be best since it removed most of the high-frequency noise without changing the underlying peak shape.

Previous workers have enhanced the S/N in single molecule burst detection by applying a weighted quadratic summing filter[14,37] or a weighted sum algorithm.[38] The weighted quadratic summing filter squares the data and then convolutes the data with a weighting function, which smoothes the data and enhances

(35) Petersen, N. O. *Biophys. J.* **1986**, *49*, 809–815.

(36) Hell, S.; Reiner, G.; Cremer, C.; Stelzer, E. H. K. *J. Microsc. (Oxford)* **1993**, *169*, 391–405.

(37) Soper, S. A.; Davis, L. M.; Shera, E. B. *J. Opt. Soc. Am. B* **1992**, *9*, 1761–1769.

(38) Castro, A.; Fairfield, F. R.; Shera, E. B. *Anal. Chem.* **1993**, *65*, 849–852.

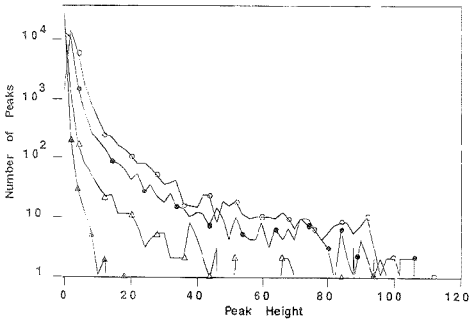

Figure 5. Distributions of fluorescence burst heights from the M13 DNA dilution series after applying a 330-Hz low-pass filter. A histogram of the number of peaks versus peak height for the blank (▲), 2 (△), 10 (●), and 20 pM (○) data is presented.

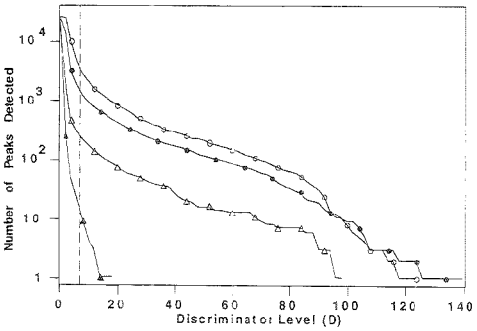

Figure 6. Plots of the number of peaks counted versus discriminator level (D) for the blank (▲), 2 (△), 10 (●), and 20 pM (○) M13 DNA dilution series data. The dashed line indicates $D = 6$.

peaks but also has the effect of greatly heightening and broadening the data plus biasing peaks toward the shape of the weighting function. We have chosen to use a Fourier filter in our applications since it maintains the height, width, and underlying shape of the peak. Information on the number of photons per peak is retained, and peaks which are close together are still resolvable after filtration, which often is not the case in our experience with the weighted quadratic summing filter.

For the use of the Fourier filter, one does need to know the approximate duration of the bursts so that a proper low-pass cutoff can be set; this information can be obtained from the autocorrelation function. It is observed empirically that the best low-pass cutoff is at a frequency 1.5–3 times that of the reciprocal burst duration. For example, if a burst lasts 8.0 ms, its reciprocal duration is 1/0.0080 s = 120 Hz, and the optimum low-pass cutoff is from 180 to 360 Hz. The application of the filter to model data showed that cutoff frequencies more than 1.5 times that of the reciprocal burst duration broaden the burst by no more than 2%, while cutoff frequencies more than 3 times that of the reciprocal burst duration leave high-frequency noise on top of a burst. We have applied this criterion in the analysis of all subsequent data sets presented here.

After filtration, peaks were identified by an algorithm which searched for maxima in the data set having immediately flanking points at a lower value. The requirement for two flanking points at a lower value was used to reject small fluctuations which may be left over after filtration, but this criterion is not so restrictive that it rejects actual peaks that are close together.

The final parameter to be set before performing single molecule counting is the discriminator level (D), which is the level above which peaks are accepted and below which they are rejected. D should be set to maximize detection of true single molecule events while minimizing false positives from random fluctuations and noise in the background. To determine the proper value for D, it is useful to plot a histogram of the number of peaks counted versus peak height. For the M13 DNA dilution series data, such a plot is presented in Figure 5. This plot shows that the blank falls as a perfect Poisson distribution about its average (0.38) until about a height of 5, where a shoulder occurs, indicating a small amount of fluorescent impurities in the blank. The distributions of the higher concentrations of M13 DNA show increasing numbers of peaks at each peak height. The wide distribution of burst heights is probably due to the fact that the spatial intensity distribution of the laser beam is nonuniform, and the burst height is then dependent on where a molecule travels through the beam.[39] From this plot, the optimum D will presumably lie between 5 and 10, the lowest discriminator setting that distinguishes a single molecule burst from fluctuations in the blank.

The effect of a change in D on the count rate can be visualized more clearly by plotting the number of peaks detected versus discriminator level. Figure 6 presents such a plot for the M13 dilution series data. In the blank, 32 molecules were detected when $D = 5$, and 15 were detected when $D = 7$, well above the numbers expected by the Poisson distribution, once again indicating the presence of some chemical noise.[40] As D is raised from 0 to 5, the counts from the DNA solutions fall rapidly but reach a semiplateau extending from level ~6 on out to about ~80. D should be set in this "single molecule counting plateau" region because the number of peaks counted is then a less sensitive function of D, just as one would select a single photon counting plateau. As a consistency check, we calculated the number of molecules expected and compared this result to the data in Figure 6. For a 2.4- × 4.0-μm cross section probe area, a flow rate of 0.030 cm/s, a collection time of 108 s, and a concentration of 2.0 pM, 370 molecules are expected if we neglect uncertainties such as wall adsorption and false positives. For the 2 pM solution, this count was found for a value of D between 5 and 6, confirming that this region at the edge of the single molecule counting plateau gives us the proper choice for D. Thus, a D value of 6 was adopted for subsequent analysis of the dilution series data.

The peak-calling algorithm was then applied to the data set using the defined discriminator level of 6. Figure 7 presents a representative portion of the filtered 10 pM dilution series data, where the circles indicate peaks counted at $D = 6$. The background fluctuations are well below this level, and nearly all of the obvious peaks have been identified, demonstrating the effectiveness of this peak selection method.

The relationship between molecules counted and concentration using various discriminator levels is examined in Figure 8. In

(39) Mets, U.; Rigler, R. *J. Fluoresc.* 1994, *4*, 259.

(40) If the average background count rate is 0.38 and the fluctuation in counts is purely random, the Poisson probability of a count of 5 or greater is 4.8×10^{-5}, or 14 times per 300 000-point data set, and the probability of a count of 7 or greater is 1.6×10^{-7}, or less than once per data set of 300 000 points.

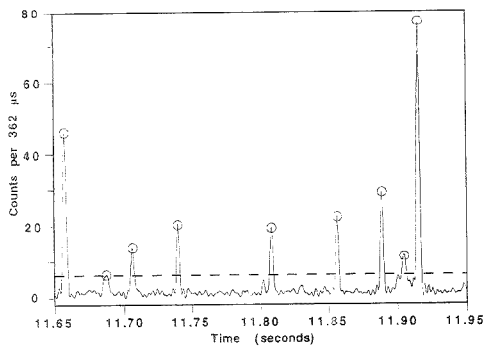

Figure 7. Representative filtered M13 fluorescence burst data from the 10 pM flow experiment. The circles indicate peaks selected by the peak counting algorithm. The algorithm searched for maxima above a defined discriminator level, set at 6 for this analysis (dashed line). Proper peaks were also required to have immediately flanking points at a lower value.

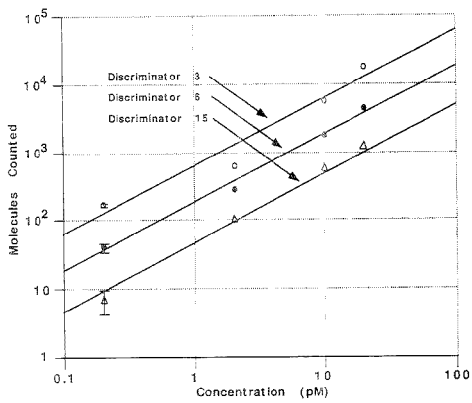

Figure 8. Examination of the linearity of the single molecule detection system at various discriminator levels. The plot displays the numbers of molecules counted versus concentration at discriminator levels of 3 (○), 6 (●), and 15 (△). The number of "molecules" counted in the blank at each discriminator level has been subtracted. The slope of the $D = 3$ least-squares fit is 0.994 with $R = 0.971$; the slope of the $D = 6$ fit is 1.01 with $R = 0.995$; and the slope of the $D = 15$ fit is 1.12 with $R = 0.999$.

single molecule counting, the number of molecules counted versus concentration should be linear with a log/log slope of 1. If, for example, the simultaneous presence of two or more molecules in the beam were the source of the observed bursts, the plots would have a slope of 2. At each discriminator level, the slope of the least-squares fit to the data is very nearly 1, with good linearity, which confirms single molecule detection and proper peak identification. The $D = 3$ data have the smallest correlation coefficient due to the large contribution of background fluctuations at this low discriminator level. In addition to background fluctuations, uncertainty in the concentration is probably the largest source of error in all the data sets. There is no systematic change in slope with discriminator level, indicating that the distribution of burst heights is nearly the same for all the concentrations.

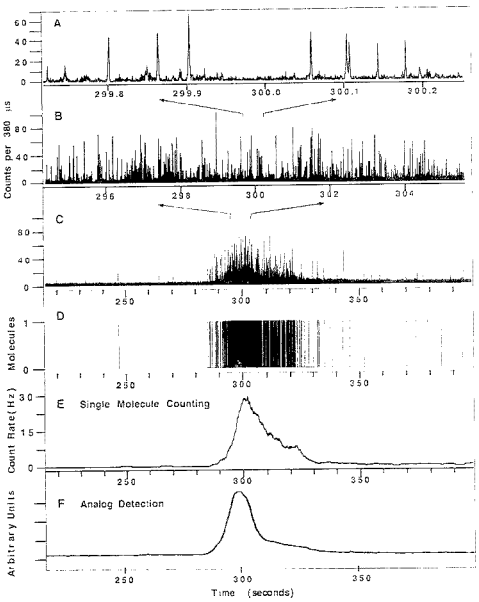

Figure 9. Capillary gel electrophoresis separation of M13 DNA detected by single molecule counting. DNA was electrophoresed at 200 V/cm in 0.10% HEC with 10 nM TO6. The injected DNA concentration was 10 pg/μL, and the bin width was 380 μs. (A) A 0.6-s region of raw data from the center of the M13 band, showing individual, well-resolved fluorescence bursts. (B) A 12-s region from the center of the same band. (C) A 200-s region of the raw data, showing the entire M13 band. (D) Single molecule counting applied to the electrophoresis data. A 500-Hz filter was applied to the data, and a discriminator level of 10 was chosen on the basis of the peak height distribution function. A value of 1 indicates a molecule counted. (E) Frequency of molecules counted versus time. Counts from the above trace were added in a sliding window of 13 000 bins, or 4.9 s. (F) Analog detection of M13 DNA (100 pg/μL) separated under the same conditions as above.

Single Molecule Detection of Capillary Gel Electrophoresis. With these methods developed and optimized, we were ready to apply the single molecule counting system to capillary gel electrophoresis. Figure 9 presents a study of the electrophoretic separation of M13 DNA. A large number of bursts appeared about 300 s after injection, as indicated in Figure 9C. Figure 9B presents an expansion of an 8-s portion of the band, and Figure 9A presents a 0.6-s region, showing that the fluorescence bursts from the middle of the band are clear and discreet. At this injected DNA concentration (10 pg/μL, or 2 pM), the calculated occupancy is only ~0.006, a strong indication that bursts arise primarily from single molecules. The autocorrelation function from this data set indicated a transit time of 2.7 ms, in close agreement with the 2.9 ms value expected for molecules having a velocity of 830 μm/s (25 cm/300 s) through a 2.4-μm beam waist. Since the velocity profile in the capillary is flat and the velocity of the DNA is precisely known, this number for the beam waist was deemed to be more accurate than that determined from the flow pump experiments, where the velocity profile is parabolic. The single molecule counting method was then applied to these data. A 500-Hz filter was used, and since the background was slightly higher

than that in the flow experiments due to the presence of HEC, D was set at 10. A digital plot indicating the counted molecules versus time is presented in Figure 9D. A total of 489 molecules were counted from 285 to 340 s. To compare this detection method with standard analog detection, the frequency of the counted molecules was calculated. The molecular counts were summed over a 4.9-s (13 000 bin) sliding window to produce a plot of count rate versus time, presented in Figure 9E. The resulting DNA band has approximately the same shape as the analog band, presented in Figure 9F, confirming that this method has successfully detected the component M13 DNA molecules after an electrophoretic separation. Interestingly, even some of the fine structure of the analog band is preserved in the single molecule frequency plot. For example, the small shoulder on the right portion of the band and the broad tail at the end appear in both. This molecular level resolution of small features in a DNA separation suggests that this technique could be used to examine the chemical origins of the differences in the migration rates of these molecules.

The true power of electrophoresis is that it can separate molecules on the basis of differing size. To demonstrate the combination of this capability with single molecule detection, the single molecule counting system was applied to the separation of pBR 322 DNA (4631 bp) from pRL 277 (6798 bp) DNA. Figure 10 presents the results of this experiment. Two distinct clusters of fluorescent bursts were observed about 790 and 810 s after injection. The top panels in Figure 10 show that the fluorescence bursts from the middle of each of these bands are discreet and well resolved. The calculated occupancy, assuming that the band has the same concentration as the injected solution, is only about 0.01. The transit times calculated from the autocorrelation function were 7.4 ms for the first band and 7.8 ms for the second band. The velocities of 320 μm/s (25 cm/790 s) for the first band and 310 μm/s (25 cm/810 s) for the second band give a 2.4-μm beam waist, in agreement with the width determined in the M13 electrophoresis experiment. Based on the relative mobilities, we assign the first band to pBR 322 and the second band to pRL 277. The single molecule counting method was applied to the data using a 400-Hz filter and a discriminator level of 12, and two separate clusters of molecular counts were observed. Fifty-two molecules were counted in the pBR 322 band, and 106 molecules were counted in the pRL 277 band. When the digital count rate is converted to a frequency, the frequency profiles in Figure 10D are very similar in shape to the analog bands, as expected. Also, the small features of the analog bands are again visible in the frequency plot, such as the small bump at the end of the pRL 277 band. The variation in appearance times of the bands between the analog run and the single molecule counting run is due to natural mobility differences seen after the capillary is refilled with buffer.[41]

We have demonstrated that single molecule fluorescence burst counting can be used as an ultrasensitive detection method for electrophoretic separations. This accomplishment has been based on two fundamental improvements in the detection technology. First, it was important to optimize the S/N by binding large numbers of high-quantum-yield dye molecules to the DNA and to minimize the fluorescence and scatter from the gel matrix. We have exploited the optimization of intercalation dye technology developed by Glazer and co-workers to select a thiazole orange

(41) Clark, S. M.; Mathies, R. A. *Anal. Biochem.* **1993**, *215*, 163–170.

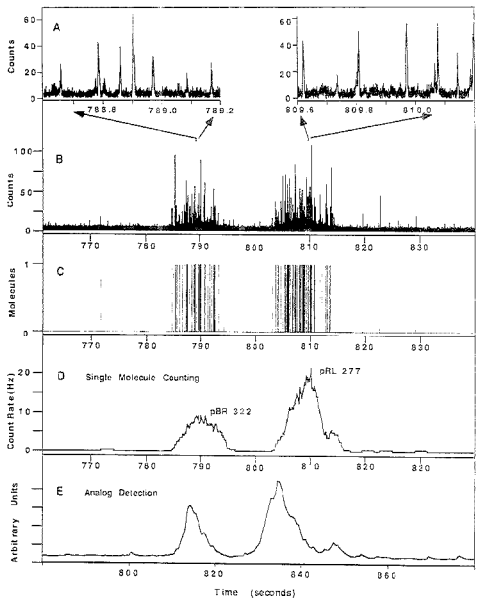

Figure 10. Capillary gel electrophoresis separation of two different kinds of DNA detected by single molecule counting. pBR 322 DNA (4.6 kbp) was separated from pRL 277 DNA (6.7 kbp) in 0.50% HEC with 10 nM TO6 at a field strength of 150 V/cm. The injected sample concentration was 50 pg/μL, and the bin width was 450 μs. (A) Expansion of a 0.6-s region of raw data from the center of each DNA band, showing individual, well-resolved fluorescence bursts. (B) An 80-s region of the raw data, showing the fluorescence bursts in both DNA bands. (C) Single molecule counting applied to the electrophoresis data, using the methods described above, with a 400-Hz filter and a discriminator level of 12. A value of 1 indicates a molecule counted. (D) Frequency of molecules counted versus time. Molecules counted were added in a sliding window of 5000 bins, or 2.25 s. (E) Analog detection of the pBR 322 and pRL 277 separation using the same conditions as above.

derivative (TO6) as the most sensitive of the mono- and bis-intercalators.[27] Second, we have constructed a 0 dead-time photon counting detector with the capability of recording the number of counts received in arbitrary length microsecond or longer bins. This has permitted full temporal resolution of the bursts and optimization of both the experiment and data analysis. Despite these excellent results, a number of experimental and technical improvements are desirable. The first issue is the efficiency of detection, or the fraction of molecules traveling through the capillary which get detected. For this discussion, the detection efficiency will be considered to be given by the fraction of the flowing stream or electrophoretic band that actually passes through the illumination beam defined by the e^{-2} intensity profile. This definition makes the implicit assumption that the molecules that pass through the beam are all counted. Our present configuration has been useful to demonstrate the feasibility of single molecule detection in capillary electrophoresis, but the detection efficiency is very low (~0.1%). This low efficiency reduces the overall on-column mass sensitivity. For a detection limit of S/N = 3, our current configuration would require a total of ~10 000 M13 molecules in a band, which is about the same as

our analog detection limits.[26] Lee et al.[17] have addressed the issue of detection efficiency by confining the sample to a 10- × 10-μm square capillary and focusing the laser over the entire inner bore of the capillary. Using this method, they achieved near unity detection efficiency of an infrared dye in flowing methanol. A similar approach could be taken in capillary electrophoresis by performing separations in micromachined channels. DNA separations have recently been demonstrated in micromachined channels by Woolley and Mathies.[42] Using our probe beam cross section of 2.4 μm × 4.0 μm and detection channels of 20 μm × 6 μm, the detection efficiency would be ~8%, and as few as 125 molecules on-column would constitute a detectable band (S/N = 3). Increased efficiency could be achieved by increasing the beam cross section and further decreasing the channel dimensions.

Further improvement in the S/N is also desired in order to allow detection of smaller DNA fragments. Many applications of interest would require detection of DNA that is 100 bp or less in length. Since the number of fluorescent dyes intercalated into the DNA is proportional to the length, the fluorescence signal strength is also proportional to the length of the DNA.[43] Keller and co-workers have used the fluorescence burst intensity as a measure of DNA size and have reached a lower size limit of about 1500 bp.[44] Based on preliminary experiments with shorter DNA samples and extrapolation of the burst height distributions reported here, the detection size limit in our current configuration is around 1000 bp, which means that an order of magnitude improvement in S/N is desirable. This improvement may be achieved through the use of heterodimeric energy-transfer intercalating dyes. Dyes such as TOTAB and its derivatives[45] have the advantage of extremely high binding affinities and excellent spectral characteristics. A high binding affinity means that less dye is required in the running buffer, thus lowering background, and a high extinction coefficient and fluorescence quantum yield mean that the signal strength from these dyes will be at least as strong as that from TO6. Another advantage of energy-transfer intercalators is that the fluorescence of these dyes can be Stokes-shifted into the red region of the spectrum, where background is much lower. We anticipate that these and other improvements will yield a substantial increase in the S/N of single DNA molecule counting in the future and a corresponding reduction in the minimum size of detectable single molecules of DNA, thereby enhancing the applicability of this new detection technique.

(42) Woolley, A. T.; Mathies, R. A. *Proc. Natl. Acad. Sci. U.S.A.* **1994**, *91*, 11348–11352.
(43) Glazer, A. N.; Peck, K.; Mathies, R. A. *Proc. Natl. Acad. Sci. U.S.A.* **1990**, *87*, 3851–3855.
(44) Goodwin, P. M.; Johnson, M. E.; Martin, J. C.; Ambrose, W. P.; Marrone, B. L.; Jett, J. H.; Keller, R. A. *Nucleic Acids Res.* **1993**, *21*, 803–806.
(45) Benson, S. C.; Singh, P.; Glazer, A. N. *Nucleic Acids Res.* **1993**, *21*, 5727–5735.

PROSPECTS

The successful application of single molecule fluorescence burst detection to capillary electrophoresis opens up new horizons in high-sensitivity DNA detection. One possible application of this technology would be the identification of an incipient cancer or trace viral or bacterial contamination when the amount of target nucleic acid is minuscule. A second application of this technique would be the quantitation of low-abundance species of mRNA. Single molecule detection and CGE would enable direct detection of a desired mRNA without the introduction of large uncertainty due to amplification. Standard assays would also benefit from this detection method. For example, the polymerase chain reaction could be performed with fewer cycle numbers of amplification, which would save time, reduce noise, and improve sensitivity.

ACKNOWLEDGMENT

We thank the members of the UC Berkeley High Sensitivity DNA Analysis Project for many valuable interactions. This research was supported by the Director, Office of Energy Research, Office of Health and Environmental Research of the U.S. Department of Energy under Contract DE-FG-91ER61125. This work is dedicated to the memory of our friend and colleague Dr. Huiping Zhu (1959–1995).

Received for review June 5, 1995. Accepted July 7, 1995.[⊗]

AC950542C

[⊗] Abstract published in *Advance ACS Abstracts*, August 15, 1995.

Anal. Chem. 1995, *67*, 3261–3264

Determination of Subnanomolar Concentrations of Nitrite in Natural Waters

Robert J. Kieber* and Pamela J. Seaton†

Department of Chemistry and Marine Science Program, University of North Carolina at Wilmington, Wilmington, North Carolina 28403

Dissolved nitrite in natural waters was determined at subnanomolar levels by derivitization with 2,4-dinitrophenylhydrazine (2,4-DNPH) followed by liquid chromatography. The analysis is rapid, involves minimal sample preparation, and requires fairly standard laboratory equipment. The method has undetectable blanks and a detection limit of 0.1 nM with an average precision of 4% RSD at ambient natural water concentrations. The azide formed upon reaction of NO_2^- with 2,4-DNPH at levels typically found in coastal seawater is stable for at least 4 weeks when kept cold in the dark. The stability of the nitrite derivative is extremely useful because it allows for large numbers of samples to be collected and derivatized in relatively short time periods for later chromatographic analysis. Analytical results were verified by intercomparison with a standard, completely independent, colorometric technique in several natural water types. Applications to fresh, estuarine, and marine samples are also presented.

The marine nitrogen cycle plays a crucial role in the chemistry and biology of the sea. Because nitrate is a critical limiting factor to primary productivity in the oceans, the dynamics of nitrogen cycling have been studied extensively.[1,2] Nitrate is assimilated by phytoplankton, and "new" nitrate is recycled back to the euphotic zone from the deep ocean through bacterial nitrification of dissolved and particulate organic nitrogen in the water column and sediments. Nitrite is an obligatory and stable intermediate in both of these processes and is therefore a general indicator of biogeochemical processes that drive the nitrogen cycle. Trace amounts of nitrite in environmental samples can also indicate the extent of pollution and eutrophication of natural waters.[3]

Despite the significance of nitrite in the marine nitrogen cycle, outside of the primary and secondary nitrite maxima, little is known about the distribution of nitrite throughout the rest of the water column. Examination of spatial and temporal variations of nitrite in the ocean has been limited primarily by the inadequacy of existing analytical methods. Nitrite, and in many cases nitrate, cannot be detected at the low concentrations at which critical processes take place. Nitrite has been measured by colorimetry,[4,5] chemiluminescence,[6] fluorometry,[7] or Raman spectroscopy.[3] Two predominant methods for analysis of nitrite in seawater, the colorometric and chemiluminescent techniques, do not provide sensitivities required for critical evaluation of subnanomolar levels of nitrite.

The standard colorometric technique,[4] which is based on formation of a diazo dye from the reaction of nitrite with *N*-(1-naphthyl)ethylenediamine and sulfanilamide, has a detection limit of 30–50 nM, although 100 nM is considered to be a more realistic detection limit for shipboard determination of nitrite.[5] This method is not sensitive enough to detect nitrite levels in over 99% of the ocean. An optimized version of the colorometric method involves preconcentration of larger samples and allows for a detection limit of 1–2 nM.[8] However, this method is extremely susceptible to atmospheric contamination and is not suitable for rapid determination of nitrite.

The chemiluminescent technique for determination of nitrite in seawater has detection limits to the subnanomolar range (0.1–0.2 nM). This method, developed by Garside[6] and modified by Zafiriou and co-workers,[1] is quite sensitive; however, it is plagued by several limitations. The method is difficult and time consuming and requires fairly sophisticated equipment. Erratic air contamination during sample collection is such a large source of error that zero blanks cannot be obtained and reproducibility is compromised. Because of these limitations, large sample sizes are necessary with subsequently lengthy analysis times. This is of particular concern in biologically active samples where there is a rapid turnover of nitrite by the biota.

We have developed a simple and extremely sensitive method for rapid analysis of nitrite in natural waters. The analysis is based on the known reaction[9,10] of nitrite with 2,4-dinitrophenylhydrazine to form an azide, which is separated from interfering substances and quantified by HPLC. Other attempts at using HPLC for the quantification of fluorometric or colorometric derivatives of nitrite are unsuitable for natural waters because their detection limits are too high.[5,7] The method presented here is extremely desirable for natural samples because it very rapid and simple, has undetectable blanks, and has the lowest detection limit reported. In addition, it is well suited for shipboard and field analyses because samples can be analyzed in real time or stored for later laboratory analysis.

* Correspondence should be addressed to this author. FAX: (910) 395-3013. E-mail: KIEBERR@VXC.UNCWIL.EDU.
E-mail: SEATON@VXC.UNCWILEDU.

(1) Zafiriou, O. C.; Ball, L. A.; Hanley, Q. *Deep Sea Res.* **1992**, *39* 1329–1347.
(2) Carpenter, E. J., Capone, D. G., Eds. *Nitrogen in the marine environment*; Academic Press: New York, 1983.
(3) Kang, X.; Sharma, S. K.; Taylor, G. T.; Muenow, D. W. *Appl. Spectrosc.* **1992**, *46*, 819–826.
(4) Clesceri, L. S., Greenberg, A. E., Trussell, R. R., Eds. *Standard Methods for the Examination of Water and Wastewater*; Port City Press: Baltimore, 1989.
(5) Verma, K. K.; Verma A. *Anal. Lett.* **1992**, *25*, 2083–2093.
(6) Garcide, C. *Mar. Chem.* **1982**, *11*, 159–167.
(7) Zhou, J. Y.; Progner, P.; Dauphin, C.; Hamon, M. *HPLC Fluorescence Chromatogr.* **1993**, *3/5*, 57–60.
(8) Wada, E.; Hattori, A. *Anal. Chim. Acta* **1971**, *56*, 233–240.

0003-2700/95/0367-3261$9.00/0

EXPERIMENTAL SECTION

Reagents and Standards. All chemicals were obtained from Fisher Scientific (Fair Lawn, NJ) and were reagent grade or HPLC grade, unless otherwise noted. 2,4-Dinitrophenylhydrazine (2,4-DNPH; Aldrich, Milwaukee, WI) was recrystallized twice from a 70:30 mixture of acetonitrile/water (v/v) followed by a final recrystallization from pure acetonitrile. The reagent was dried under vacuum and stored in the dark in airtight 30-mL Teflon vials. The derivatizing reagent was prepared in a 30-mL Teflon vial by dissolving 15 mg of recrystallized 2,4-DNPH in a 15-mL solution of concentrated HCl (~12 M), water, and acetonitrile in a ratio of 2:5:1 (v/v/v). Just prior to use, nitrite contamination contained within the 2,4-DNPH reagent solution was removed with successive extractions with carbon tetrachloride (Mallinckrodt Inc., Paris, KT). CCl_4 (5 mL) was added to the reagent solution and shaken on a wrist-action shaker (Model 75, Burrell Corp., Pittsburgh, PA) for 5 min. The mixture was centrifuged at 2000 rpm (Model PR-6 centrifuge, International Equipment Co., Needham, MA) for 5 min in order to separate the phases. The organic layer was removed via a 5-mL pipet, and reagent solution was reextracted as described above. The purified reagent was prepared immediately prior to use.

HPLC Instrumentation. The HPLC system consisted of an E-Lab Model 2020 gradient programmer and data acquisition system (OMS Tech, Miami, FL) installed in an IBM-compatible PC. An Eldex model A-60-S pump (Eldex Laboratories, San Carlos, CA), with an inert solenoid valve placed on its low-pressure side, was used to generate the mobile phase. A two-solvent mobile phase was employed: (A) 10% acetonitrile in water and (B) 100% acetonitrile. Derivatized samples were injected into a Valco six-port injector (Valco Instruments, Houston, TX) with a 2000-μL sample loop. The 2,4-dinitrophenylazide was separated isocratically (60% A, 2 mL/min) on a radial compression module with an 8 mm i.d. × 10 cm C18 reversed-phase Radial-pak cartridge (Type 8NVC184, Millipore Corp., Waters Chromatography Division, Milford, MA) and detected by an Isco V4 variable-wavelength absorbance detector (Isco, Lincoln, NE) at 307 nm. The signal was stored and processed by the E-Lab data system. The column was at ambient temperatures.

Standard Colorometric Determination of Nitrite. Nitrite was analyzed in natural samples by the standard colorometric test described in ref 4. The color reagent was prepared by dissolving 10.0 g of sulfanilamide in 800 mL of deionized water plus 100 mL of 85% phosphoric acid. N-(1-Naphthyl)ethylenediamine hydrochloride (1.0 g) was added to the above solution, and the volume was brought to 1 L with deionized water. The reagent was stored at 4 °C in the dark. Filtered natural water samples or nitrite standard solutions (5 mL) were treated with the reagent (0.2 mL) in cuvette tubes. The color developed for 15 min, and the absorbance at 543 nm was recorded with a Spectronic 20.

RESULTS

Confirmation of Azide Structure. Nitrite reacts with 2,4-DNPH to form 2,4-dinitrophenyl azide under acidic conditions. The azide has been extracted and purified from 2,4-DNPH-treated natural seawater samples and has been synthesized through the reaction of an aqueous solution of sodium nitrite with 2,4-DNPH in sulfuric acid. The infrared spectra of both isolated and synthesized products are identical and show a very intense band at 2136 cm^{-1}, characteristic of the azide functionality. The proton and carbon NMR spectra of the azide show only aromatic proton and carbon signals. The UV maximum of the azide in acetonitrile is at 307 nm. All spectra were identical to spectral data reported in the literature.[9,10] Extracted and synthetic 2,4-dinitrophenyl azide analyzed by HPLC coeluted with the nitrite derivative formed upon 2,4-DNPH treatment of natural water samples.

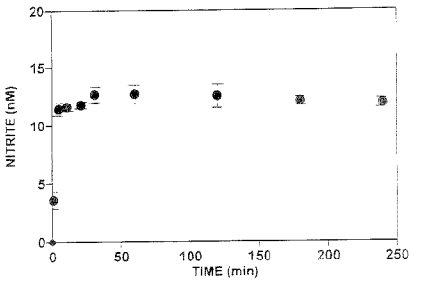

Figure 1. Formation of the azide derivative as a function of time in coastal seawater. Each data point represents the average of four samples. Errors bars represent one standard deviation based on $n = 4$.

Derivatization Reaction. The time required for complete derivitization of nitrite by 2,4-DNPH was evaluated by following the derivitization to the azide as a function of time in coastal seawater collected from Wrightsville Beach, NC. One liter of the seawater was gravity filtered through a 47-mm glass fiber filter (type GF/F, Whatman International Ltd., Maidstone England) and four, 5-mL aliquots per sampling time were withdrawn and derivatized by adding 50 mL of 2,4-DNPH reagent in a 7-mL Teflon vial. The vial was shaken and the derivatization reaction allowed to proceed at ambient temperatures for varying time periods. A 2-mL aliquot was removed from each vial and analyzed by HPLC. The results presented in Figure 1 indicate the formation of the azide through reaction of nitrite by 2,4-DNPH is rapid, with complete derivitization after only 5 min at ambient temperatures.

Blanks and Detection Limit. Nitrite is undetectable in blanks prepared in deionized water. A typical blank chromatogram is presented in Figure 2A. The detector and integrator for this chromatogram were set to their most sensitive setting, and no peaks in the blank were observed in the area where the nitrite derivative elutes. Similar undetectable blanks have been obtained for samples taken on a variety of days and locations. The chromatogram obtained for a typical coastal seawater sample is presented in Figure 2B (20 nM nitrite) for comparison. Formaldehyde, present in many natural water samples, elutes ~1 min after the nitrite azide derivative. The undetectably low background signal is an important component of this analysis because it allows for determination of extremely low levels of nitrite in natural waters. A conservative detection limit based on a signal-to-noise ratio of 3 is 0.1 nM (0.0046 mg of NO_2^-/L) nitrite.

Storage of Derivatized Nitrite Samples. In order to test for stability of the nitrite derivative, a 500-mL sample of coastal seawater was collected and filtered and 5-mL aliquots were placed in 80 Teflon vials. 2,4-DNPH (50 μL) was added to each; the samples were shaken and placed in storage in the dark at 4 °C. Four vials were subsequently removed per sampling day and

(9) Dyall, L. K. *Aust. J. Chem.* **1986**, *39*, 89–101.
(10) Gromping, A. H. J.; Karst, U.; Cammann, K. *J. Chromatogr. A* **1993**, *653*, 341–347.

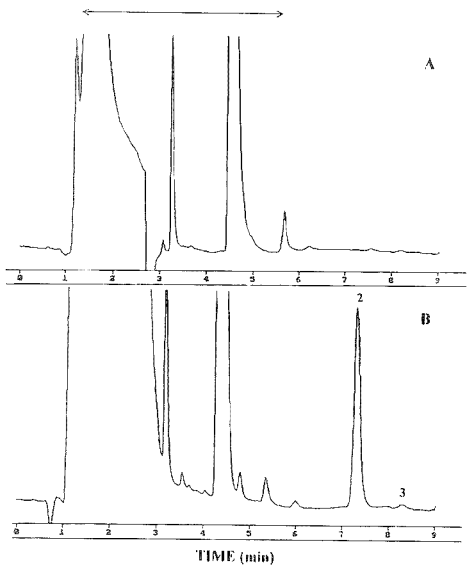

Figure 2. HPLC chromatograms. (A) System blank prepared by adding 50 mL of purified 2,4-DNPH to 5 mL of deionized water with 2 mL injected into the HPLC system. (B) Direct injection of 2 mL of derivatized coastal seawater. The nitrite–2,4-DNPH derivative elutes at 7.2 min (1); reagent; (2) azide derivative; (3) formaldehyde.

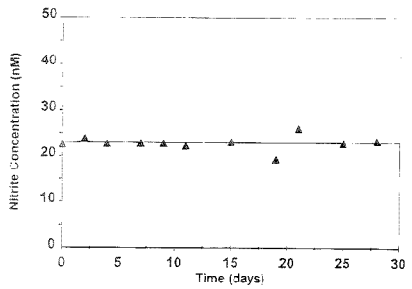

Figure 3. Test of storage procedure. Eighty coastal seawater samples were added to Teflon vials and derivatized with 50 mL of 2,4-DNPH. Each time point represents the average concentration of nitrite observed in four samples on a given day.

analyzed. This procedure was repeated at various time intervals throughout a 4-week period. The results are presented in Figure 3. The derivatized nitrite is stable over the 4-week period within analytical uncertainty ($\pm 1\sigma$) of the method. In addition, the nitrite derivative in four samples placed in the dark in a freezer over the 4-week period was also stable.

Linearity and Precision. The response of the detector is linear over the concentration range of 0.5–1000 nM, which covers the range of nitrite typically found in most natural waters. The correlation coefficient over the entire range was 0.999 ($n = 7$), which is typical of our routinely run calibration curves. The precision of the method was determined, at ambient levels by performing multiple injections ($n = 4$) of samples run for each water sample tested. In some instances, as is the case for coastal

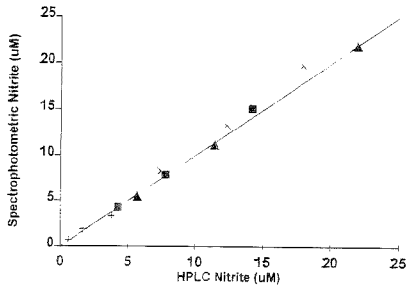

Figure 4. Intercomparison between the standard colorometric method[4] and the chromatographic determination of nitrite in a variety of natural waters. The line represents perfect agreement between results, not a statistical fit to the data: (+) Sargasso seawater, (×) Cape Fear Estuary, (▲) Greenfield Lake, and (■) coastal seawater.

seawater, this procedure was repeated many times. The average relative standard deviation of the analysis was 4%.

Intercalibration and Spike Recovery. In order to verify the analytical results obtained by the HPLC analysis of nitrite reported here, an intercomparison study was performed. Samples from a variety of natural waters (including fresh, estuarine, coastal seawater, and oligotrophic seawater) were collected, filtered, spiked with NO_2^-, and analyzed for nitrite chromatographically and by a completely independent, standard colorometric analysis.[4] The detection limit of the latter technique is ~100 nM; therefore, to have sufficient NO_2^- several of the samples were spiked with a nitrite standard. The results of this study are presented in Figure 4. In all cases, the disparity between the chromatographic and colorometric analyses was less than a few percent, which is well within analytical uncertainty. The recovery of the nitrite in spiked samples by the HPLC analysis was 100%.

DISCUSSION

We have developed an extremely sensitive and relatively simple analysis for the determination of subnanomolar concentrations of nitrite in natural waters. The analytical results have been verified by intercalibration with a completely independent, standard, colorometric technique.[4] Nitrite concentrations determined by both analyses from a wide array of natural water types agreed within a few percent, well within analytical uncertainty. The HPLC analysis is not subject to any known interferences and has excellent precision with a relative standard deviation of 4% at concentrations of nitrite typically found in natural waters.

When the derivatizing agent is properly purified, nitrite is not detectable in blanks. Background contamination is one of the limiting factors reported by Zafariou et al.[1] in their chemiluminescent analysis of nitrite in seawater. An undetectable blank is also important because it ultimately dictates the limit of detection, which for the method reported here is 0.1 nM, the lowest reported for routine determination of nitrite in seawater . This detection limit is sufficiently low to determine nitrite even in the most oligatrophic open oceans.[1,11,12]

One of the greatest utilities of the nitrite analysis discussed in this paper is its ease of operation. A relatively inexpensive

(11) Holligan, P. M.; Balch, W. M.; Yentsch C. M. *J. Mar. Res.* **1984**, *42*, 1051–1073.

(12) Bonilla, J.; Senior, W.; Bugden J. *Geophys. J. Res.* **1993**, *98*, 2245–2257.

Table 1. Concentration of Nitrite (nM) in a Variety of Natural Waters[a]

water type	salinity (ppt)	av nitrite concn (nM)
Greenfield Lake	0.00	231 ($n = 4$)
Cape Fear Estuary	10.00	331 ($n = 4$)
coastal seawater	35	17.5 ($n = 12$)

[a] Sampling sites were located near Wilmington, NC.

isocratic HPLC system can be outfitted for use in the field or aboard ship. The chemiluminescent technique requires more elaborate hardware and is more cumbersome in its operation.[1,6] Our HPLC analysis of nitrite is rapid, approximately eight samples per hour can easily be analyzed. Another valuable aspect of our method is that the derivatization process is rapid, resulting in negligible air contamination and correspondingly undetectable nitrite blanks. The derivatized nitrite at levels typically found in coastal seawater is also stable for several hours at ambient temperatures and up to 4 weeks when kept cold in the dark. The ability to store samples allows for collection of greater numbers of samples, as many as 100/h for later HPLC analysis. An entire 12-bottle CTD cast from a shipboard collection system has been collected and derivatized with replicates in under 1 h.[13] This rapid processing of samples will greatly lessen alterations in nitrite concentrations which may occur during the time between analyses.

We have used the HPLC analysis of nitrite by derivatization with 2,4-DNPH to study nitrite distributions in natural waters collected near Wilmington, N C. The concentrations observed are reported in Table 1. Coastal seawater always contained the lowest NO_2^- concentrations, and estuarine samples collected from the Cape Fear River Estuary contained the highest levels. This agrees with nitrite levels reported in the literature.[11,12]

ACKNOWLEDGMENT

Financial assistance was provided by the Center for Marine Science Research Center at UNCW, Contribution 106, and by a Charles L. Cahill Award for faculty research and development. Shiptime on the RV *Cape Hatteras* was provided by NSF as a Duke—UNC Consortium cruise.

Received for review February 20, 1995. Accepted June 21, 1995.[⊗]

AC950184D

[⊗] Abstract published in *Advance ACS Abstracts*, August 1, 1995.

(13) Nuccio, J. Masters Thesis, University of North Carolina at Wilmington, 1994.

Anal. Chem. 1995, *67*, 3265–3274

Sample Introduction Approaches for Solid Phase Microextraction/Rapid GC

Tadeusz Górecki† and Janusz Pawliszyn*

Department of Chemistry and Waterloo Centre for Groundwater Research, University of Waterloo, Waterloo, Ontario, Canada, N2L 3G1

Solid phase microextraction was used as the sample introduction technique for high-speed GC. The design of the dedicated injector was modified, and its operating conditions were optimized. Separation of BTEX was achieved in 8.4 s. The system was then used for separation of volatile organic compounds listed in EPA method 624. Short, narrow-bore Vocol and SPB-1 columns were used. Ion trap MS and FID were examined as detectors for high-speed separations. Separation of all 28 compounds detected by ITMS was achieved in less than 150 s. The possibility of using internally heated SPME fibers was then studied. Heating was achieved by passing an electric current directly through a wire used in place of the fiber or by using a hollow fiber equipped with an internal microheater. The results indicate that internally heated fibers are a viable alternative to the dedicated injector.

Time is becoming an increasingly important factor in chemical analyses. The rapid development in the field of data processing prompted by the ever-increasing computational power and decreasing costs of desktop computers creates an impression that many analytical techniques do not keep pace with progress. One such field is definitely chromatography. Analysis times of the order of minutes are exceptions rather than rules. In the case of trace analysis, the overall analysis time is usually even much longer, as the final separation must be preceded by sample pretreatment and/or preconcentration.

The reduction of the analysis time in capillary gas chromatography has been an important research topic for years. The first studies on high-speed separations were published by Desty and Giddings in 1962.[1,2] Desty et al. pointed out that the analysis time can be shortened when narrow-bore columns are used. On the other hand, the sample capacity of such columns is relatively low.[3] Therefore, high-speed separations are performed with the use of both small and regular inner diameter short capillary columns, operated most often at unusually high carrier gas flow rates.[4] A successful separation requires that the injection band width is small in comparison with chromatographic band broadening, and all other contributions to band broadening, such as interfaces, detector volume, and electronics, are negligible.[5]

The research on high-speed separations is usually focused on sample introduction techniques producing narrow enough injection bands. They were listed in a previous paper.[6] It seems that the most practical approach is the application of some form of thermal desorption, usually preceded by cold trapping.[4,5,7–18] This, however, requires complicated instrumentation, and the sample must be delivered to the sample introduction device already in gaseous form, which often means complex sample preparation. Also, little data have been published on the quantitative aspects of these techniques.

It was demonstrated in a previous paper[5] that solid phase microextraction (SPME) is compatible with high-speed separations. The technique itself has been described elsewhere.[17–23] It utilizes a small-diameter fused-silica fiber coated with a polymeric stationary phase for sample extraction and concentration. The trapped analytes can be liberated by thermal desorption. By using a specially designed dedicated injector, the desorption process can be shortened to a fraction of a second, producing an injection band narrow enough for high-speed GC. Separation of BTEX (benzene, toluene, ethylbenzene, *o,m,p*-xylenes) in as little as 12 s was demonstrated. The repeatability of the results was very good as measured by the estimated values of their relative standard deviations. The overall analysis time (sampling and separation) was ~2.5 min.

The purpose of this work was to further investigate the possibilities of high-speed analysis using SPME as the sampling and sample introduction technique and fast capillary gas chro-

† On leave from the Faculty of Chemistry, Technical University of Gdańsk, Gdańsk, Poland.

(1) Desty, D. H.; Goldup, A.; Swanton, W. T. In *Gas Chromatography*; Brenner, N., Callen, J. E., Weiss, M. D., Eds.; Academic Press: New York, 1962.
(2) Giddings, J. C. *Anal. Chem.* **1962**, *34*, 314.
(3) Schutjes, C. P. M.; Vermeer, E. A.; Rijks, J. A.; Cramers, C. A. In *Capillary Chromatography*; Kaiser, R. E., Ed.; Huethig Buch Verlag: Heidelberg, 1981.
(4) Klemp, M. A.; Akard, M. L.; Sacks, R. D. *Anal. Chem.* **1993**, *65*, 2516.
(5) Van Es, A. J. J. *High Speed Narrow Bore Capillary Gas Chromatography*; Huethig Buch Verlag: Heidelberg, 1992.
(6) Górecki, T.; Pawliszyn, J. *High Resolut. Chromatogr.* **1995**, *18*, 161.
(7) Jacobsson, S.; Berg, S. *J. High Resolut. Chromatogr. Chromatogr. Commun.* **1982**, *5*, 236.
(8) Jacques, C. A.; Morgan, S. L. *J. Chromatogr. Sci.* **1980**, *18*, 679.
(9) Hopkins, B.; Pretorius, V. *J. Chromatogr.* **1978**, *158*, 465.
(10) Pretorius, V.; Lawson, K. *J. High Resolut. Chromatogr. Chromatogr. Commun.* **1986**, *9*, 278.
(11) Settlege, J. A.; Jennings, W. G. *J. High Resolut. Chromatogr. Chromatogr. Commun.* **1980**, *3*, 146.
(12) Burger, B. V.; Munro, Z. *J. Chromatogr.* **1986**, *370*, 449.
(13) Sacks, R.; Ewels, B. *Anal. Chem.* **1985**, *57*, 2774.
(14) Peters, A.; Sacks, R. *J. Chromatogr. Sci.* **1991**, *29*, 403.
(15) Rankin, L. R.; Sacks, R. *J. Chromatogr. Sci.* **1994**, *32*, 7.
(16) Van Es, A. J. J.; Janssen, J.; Cramers, C.; Rijks, J. A. *J. High Resolut. Chromatogr. Chromatogr. Commun.* **1988**, *11*, 852.
(17) Arthur, C. L.; Pawliszyn, J. *Anal. Chem.* **1990**, *62*, 45.
(18) Louch, D.; Motlagh, S.; Pawliszyn, J. *Anal. Chem.* **1992**, *64*, 1187.
(19) Arthur, C. L.; Chai, M.; Pawliszyn, J. *J. Microcolumn Sep.* **1993**, *5*, 1.
(20) Arthur, C. L.; Killam, L. M.; Motlagh, S.; Lim, M.; Potter, D. W.; Pawliszyn, J. *Environ. Sci. Technol.* **1992**, *26*, 979.
(21) Potter, D. W.; Pawliszyn, J. *J. Chromatogr.* **1992**, *625*, 247.
(22) Arthur, C. L.; Killam, L. M.; Bucholz, K. D.; Pawliszyn, J. *Anal. Chem.* **1992**, *64*, 1960.
(23) Zhang, Z.; Pawliszyn, J. *Anal. Chem.* **1993**, *65*, 1843.

0003-2700/95/0367-3265$9.00/0

matography for sample separation. The dedicated injector was slightly redesigned and optimized to further reduce the injection band width. The applicability of the technique for the analysis of volatile water pollutants listed in EPA method 624 was evaluated, using FID and ion trap MS as detectors. An alternative approach to rapid sample desorption, i.e., internally heated fiber, was also explored.

EXPERIMENTAL SECTION

Instrumentation. The regular SPME device has been described in detail elsewhere.[17-23] Fibers coated with poly(dimethylsiloxane), 15 μm thick (Polymicro Technologies, Tucson, AZ), were glued with a high-temperature epoxy resin (Epo-tek 353 ND, Epoxy Technology, Inc.) into a 21 cm piece of gauge 31 stainless steel tubing (Chromatographic Specialties, Inc., Brockville, ON, Canada). The whole assembly was mounted in the barrel of a Hamilton 7105 syringe (Hamilton Co., Reno, NV). The device is operated like an ordinary syringe, the fiber being exposed for extraction and desorption and withdrawn into the needle for transport from the vial to the GC injection port and for piercing the septa.

For experiments with direct capacitive discharge, the fiber was replaced by a 1 cm piece of a 0.125 mm o.d. stainless steel wire, mounted in a gauge 31 tubing. Experiments with the internally heated fiber were performed with a modified device, described in the Results and Discussion section.

A Varian 6500 Vista series and a GC-3500 gas chromatograph (Varian Associates, Sunnyvale, CA), equipped with flame ionization detectors (FID) with ceramic flame jets and a custom-made injector, were used. The MS experiments were performed using a Varian Star 3400 gas chromatograph coupled to a Varian Saturn II ion trap MS system, controlled by a computer with dedicated software. The analyses were carried out using several columns: a 4 m × 0.25 mm × 0.25 μm SPB-5 column, a 2.5 m × 0.1 mm × 0.6 μm SPB-1 column, and a 2.5 m × 0.1 mm × 0.6 μm Vocol column (all delivered by Supelco, Bellefonte, PA), using hydrogen as the carrier gas in experiments with flame ionization detection and helium in experiments with MS. The separations were performed in most cases under isothermal conditions, although temperature programming was also used for the separation of complex mixtures of volatile organic compounds. A Star chromatographic system (Varian) was used for data acquisition and processing in FID experiments. Data acquisition frequency was 40 Hz.

Figure 1 presents the design of the dedicated injector. It has been slightly modified compared to the previously reported version.[6] It is made on the basis of a slightly modified detector base (1) from a Varian 3500 series gas chromatograph. The base is machined to hold a washer (2), septum (3), and nut (4). A piece of gauge 18 stainless steel tubing (5) serves as the needle guide. A 6 cm segment of a 0.53 mm i.d. fused-silica capillary (6) is connected to the injector base using a nut (7) and ferrule (8). A heater (9) made of 0.057 mm diameter resistive wire (45% Ni, 55% Cu) is coiled along a ~20 mm fragment of the fused-silica capillary. The specific resistance of the wire is 105 Ω/m. The actual resistance of the heater is ~30 Ω. The column is inserted through a butt connector (10) into the 0.53 mm capillary (6) and positioned in such a way that its end is located directly below the heater (9). The injector is flash heated by capacitive discharge. With the switch (13) open, the capacitor (12) is charged to a preset voltage (controlled on the dc supply). Closing the switch (13) activates relay (11). This results in discharging the capacitor through the heater (9) while disconnecting the dc supply. At the same time a start signal for the data acquisition system (and the GC if necessary) is generated. The connection is not shown for clarity. The switch (13) is mounted on the injector in such a way that it is closed by the plunger of the SPME device moving downward during injection. Very low mass and heat capacity of the heated part of the injector, i.e., the segment of the 0.53 mm fused-silica capillary, enables heating rates of the order of 1000 °C/s.

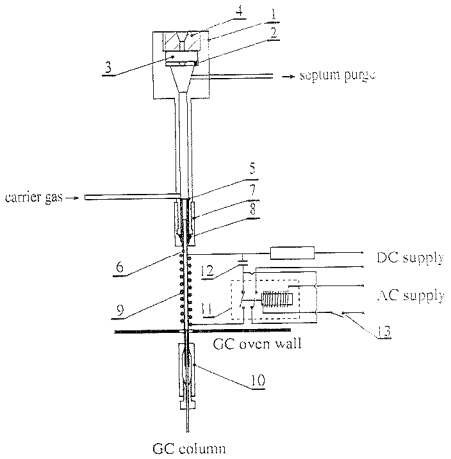

Figure 1. Schematic diagram of the injector: (1) injector body; (2) washer; (3) septum; (4) nut; (5) needle guide; (6) 0.53 mm i.d. fused-silica capillary; (7) nut; (8) ferrule; (9) heater; (10) butt conector; (11) relay; (12) capacitor; (13) switch.

The dc power supply for the injector is custom-made. It consists of an autotransformer and an ac/dc bridge. A 3500 μF/55 V capacitor is used for the capacitive discharge. The voltage to which it is actually charged is controlled by a handheld digital multimeter (DT890A, Digitek Laboratory Ltd., Hong Kong).

The changes to the previously reported design[6] include moving the carrier gas supply line down and adding the septum purge line.

MATERIALS AND METHODS

BTEX (benzene, toluene, ethylbenzene, *o,m,p*-xylenes) of 99+% purity was purchased from Aldrich Chemical Co., Inc. Fibers were exposed to standard BTEX mixtures in air. They were prepared by injecting 0.5 μL of an equivolume mixture of the BTEX components into a 0.5 L glass container equipped with two stopcocks and a septum (Supelco, Inc.). The container was hand shaken until the droplets disappeared from its walls. Small Teflon pieces were placed inside the container to facilitate mixing in the gaseous phase. Repeated analyses were performed using the same sample, as the amount extracted by the fiber was negligible compared to the amount present in the container. For experiments with optimization of the injector performance, an additional 1 μL of benzene was added to the container. The fibers were exposed to the mixture for 10 s.

Experiments with purgeables were performed on compounds listed in EPA method 624. Standard solutions (200 μg/mL each compound) were purchased from Supelco Canada. They are divided into three groups: purgeables A (trichlorofluoromethane,

1,1-dichloroethene, dichloromethane, 1,1-dichloroethane, trichloromethane, tetrachloromethane, trichloroethene, 1,2-dichloropropane, 2-chloroethyl vinyl ether, 1,1,2-trichloroethane, tetrachloroethene, dibromochloromethane, chlorobenzene), purgeables B (1,2-dichloroethene, 1,2-dichloroethane, 1,1,1-trichloroethane, benzene, bromodichloromethane, *cis*-1,3-dichloropropene, toluene, *trans*-1,3-dichloropropene, ethylbenzene, tribromomethane, 1,1,2,2-tetrachloroethane), and purgeables C (chloromethane, vinyl chloride, bromomethane, chloroethane). Standard mixtures were prepared by injecting 20 (purgeables A and B) or 50 μL (purgeables C) of the respective solution into 20 mL of water purified by a Nanopure ultrapure water system, contained in a 40 mL vial sealed with a Teflon-lined septum. For samples analyzed by FID, 1 g of NaCl was added to each vial to shift the water/headspace partition coefficients in favor of the gaseous phase. Sampling from headspace was carried out in the following way: the poly(dimethylsiloxane)-coated fiber (coating thickness 15 μm) was withdrawn into the needle, which next pierced the septum. The fiber was lowered into the headspace over the stirred sample by depressing the plunger. The equilibration time for the MS experiments was 4 min, and for the FID experiments 2 min. The fiber was then withdrawn back into the needle and removed from the vial. The device was subsequently immediately transferred to the GC injector, where the desorption process took place. After the analysis, the fiber was subject to two additional heating pulses to remove the remnants of the analytes that could possibly be left after the first desorption. The solution was changed after each analysis.

In experiments with direct capacitive discharge, the wire was dipped in an equivolume mixture of pure BTEX due to the extremely low amount of analytes trapped by steel wire. Initial experiments with internally heated fibers were performed by exposing the fibers to vapors of pure BTEX. Coated fibers were exposed to standard BTEX mixtures in air prepared in the way described above. Sampling was performed in the same way as for headspace sampling. Equilibration time was 2 min.

The coating material for the internally heated fiber was SE-30 stationary phase (Chromatographic Specialties). Coating was done by dipping the fiber in a 10% solution of the stationary phase in methylene chloride and evaporating the solvent. The fiber was then conditioned for 30 min in an oven at 100 °C. For cross-linked coatings, 1% of 2,2-azobis(2-methylpropionitrile) (Eastman Fine Chemicals, Eastman Kodak Co., Rochester, NY) was added to the SE-30 solution. The coating process was repeated twice in this case to produce a thicker coating.

RESULTS AND DISCUSSION

Optimization of the Detector. It was reported previously[6] that using the dedicated injector and a fiber with a 15 μm thick coating it is possible to separate the BTEX components in ~12 s. However, in these experiments no attempts were made to optimize the injector performance. The effect of the following factors had to be checked: the moment of firing the capacitor with respect to the position of the fiber relative to the needle, the positioning of the fiber in the heated part of the injector, and column positioning in the 0.53 mm fused-silica capillary. A series of experiments performed with the 0.25 mm i.d. SPB-5 column proved that all these factors are significant. It was established that the column should be pushed up as far as possible without touching the fiber (a safety margin of ~2 mm between the fiber tip and the column was left). The optimal position of the fiber tip in the heater was found to be ~5 mm above the lower end of the heated part of the injector. This was controlled by changing the length of the steel tubing in which the fiber was glued. Of greatest importance proved to be the moment of firing the capacitor relative to the position of the fiber. It was found that the circuit should be activated when the fiber leaves the needle. In such a case the fiber reaches the heated part of the injector at or just before the peak of the heating pulse. When the capacitor is fired earlier, the fiber is exposed to a heating pulse of a smaller magnitude. When it is fired later, the fiber is inserted into a relatively cool injector. The carrier gas flowing at a high linear rate in the injector strips a part of the analytes trapped before the peak of the heating pulse is reached, which results in injection band broadening. The studies were performed using a standard gaseous BTEX mixture. Under conditions found to be optimal, the separation of BTEX was completed in 8.4 s (retention time of the last eluting component); see Figure 2. This represents a ~30% gain compared to the previously reported result.[6]

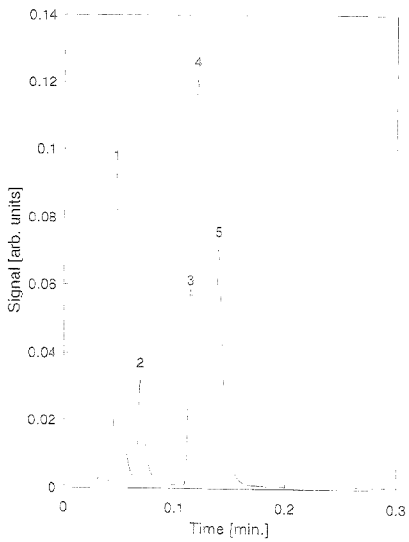

Figure 2. Separation of BTEX with optimized injector. Conditions: capacitor voltage 24 V; oven temperature 50 °C; hydrogen pressure 0.5 atm; 4 m × 0.25 mm × 0.25 μm SPB-5 column. (1) benzene, (2) toluene, (3) ethylbenzene, (4) *m,p*-xylene, and (5) *o*-xylene.

It should be emphasized that all these findings are valid for the column diameter studied and for manual injections, as the speed of depressing the plunger obviously affects the phenomena described above. Experiments with 0.1 mm columns revealed very little or no effect of the position of the switch activating the capacitive discharge on the injector performance. Most probably this is related to a much lower carrier gas linear flow rate in the injector when narrow-bore columns are used.

Fast Separation of Purgeables. To check the applicability of the method for a broader range of compounds, experiments were performed with purgeables A, B, and C, using ion trap MS for the detection. To the best of our knowledge, this is one of the first uses of a GC/ITMS system for rapid separations. Van

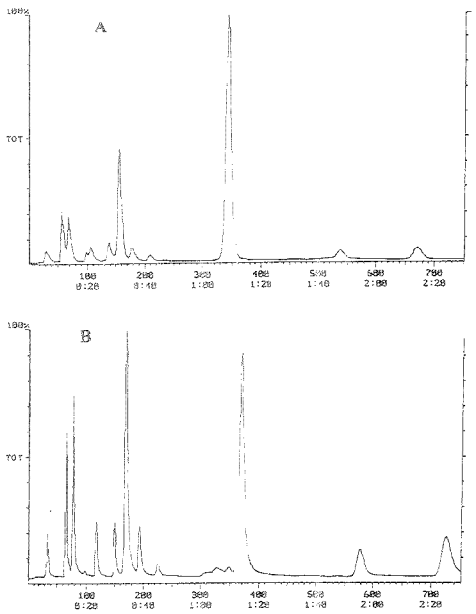

Figure 3. Comparison of the performance of the SPI injector heated to 220 °C (A) and the dedicated injector (B). Conditions: 2.5 m × 0.1 mm × 0.6 μm Vocol column; oven temperature 50 °C, helium pressure 1.4 atm. Sample, 200 ppb purgeables B, sampling from headspace.

Ysacker et al.[24] studied the applicability of ITMS for high-speed separations. However, their studies were confined to compounds of intermediate or low volatility. They used 50 μm i.d. columns and split injection. The main emphasis was put on optimization of the instrumental parameters affecting the quality of spectra obtained. No information is given on the quantitative side of separations, except the calculated values of detection limits for some compounds. Split injection used in this study is applicable only to model samples. Solid phase microextraction is unique in this respect, as it combines sample preparation and introduction into one simple step.

Experimental 0.1 mm i.d. columns, delivered by Supelco, were used in the research on fast separation of purgeables. The relatively large stationary phase film thickness of 0.6 μm made them particularly suitable for this purpose. Also, the 0.1 mm i.d. seems to be a reasonable compromise between the very high efficiency of narrower columns and the comfortable sample capacity of wider bore ones.

Mass spectrometers offer the vacuum-outlet conditions, ideal for optimum performance of the chromatographic system.[2] It seemed necessary to establish whether under such conditions the dedicated injector offers a real advantage as compared to commercially available ones. Figure 3 presents a comparison of the performance of the Varian SPI injector (considered to be the best suited for SPME) with that of the dedicated injector. Both experiments were performed using the 0.1 mm Vocol column,

(24) Van Ysacker, P. G.; Janssen, H. G.; Snijders, H. M. J.; Leclercq, P. A.; Cramers, C. A. *J. Microcolumn Sep.* **1993**, *5*, 113.

Table 1. Quantitation Masses of the Compounds Analyzed

compound	quant. mass	compound	quant. mass
1,1,1-trichloroethane	97	chloromethane	49
1,1,2,2-tetrachloroethane	83	*cis*-1,3-dichloropropene	75
1,1,2-trichloroethane	97	dibromochloromethane	129
1,1-dichloroethane	63	dichloromethane	49
1,1-dichloroethene	61	ethylbenzene	91
1,2-dichloroethane	62	tetrachloroethylene	166
1,2-dichloroethene	96	tetrachloromethane	117
1,2-dichloropropane	76	toluene	91
2-chloroethyl vinyl ether	63	*trans*-1,3-dichloropropene	75
benzene	78	tribromomethane	173
bromodichloromethane	83	trichloroethene	130
bromomethane	94	trichlorofluoromethane	101
chlorobenzene	112	trichloromethane	83
chloroethane	49	vinyl chloride	62

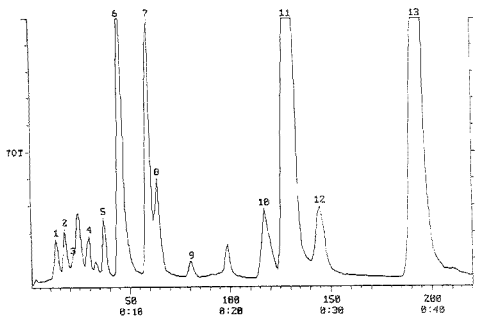

Figure 4. Separation of purgeables A on a Vocol column. Conditions: 60 °C iso, 2.1 atm, dedicated injector, capacitor voltage 24 V, MS detector, mass range 45–200. (1) trichlorofluoromethane, (2) 1,1-dichloroethene, (3) dichloromethane, (4) 1,1-dichloroethane, (5) trichloromethane, (6) tetrachloromethane, (7) trichloroethene, (8) 1,2-dichloropropane, (9) 2-chloroethyl vinyl ether, (10) 1,1,2-trichloroethane, (11) tetrachloroethylene, (12) dibromochloromethane, and (13) chlorobenzene.

oven temperature of 50 °C, 1.4 atm helium head pressure, and 200 ppb purgeables B solution sampled from headspace for 4 min. The upper chromatogram (A) was obtained with the SPI injector (temperature 220 °C), while the lower chromatogram (B) was obtained with the dedicated injector under similar conditions (pulse voltage 24.5 V). It is apparent even from visual comparison of the results that the dedicated injector produces much narrower peaks, especially for early-eluting compounds. Therefore, in further experiments, only this injector was used. Wherever possible, isothermal separations were attempted, as one of the strategic goals of this research is to apply the SPME/fast GC combination in a field-portable instrument.

Fast separations of purgeables A, B, A + B, and all three, were performed. Table 1 presents the quantitation masses used for all the components studied. Figure 4 illustrates isothermal separation of purgeables A. All the compounds were separated in 40 s at 2.1 atm carrier head pressure and 60 °C oven temperature. Dichloromethane partly coeluted with an unidentified impurity, but it could be quantified using the specific mass. In all cases presented, library searches confirmed the identity of all the components with very good matches.

The software used for data acquisition reported the retention times with only 1 s time resolution, and no differences in retention

Table 2. Mean Peak Areas (Arbitrary Units) and Relative Standard Deviations of Purgeables A–C Analyzed Separately and Together on the 2.5 m × 0.1 mm × 0.6 μm Vocol Column Using Ion Trap MS for Detection[a]

	(1)		(2)		(3)		(4)		(5)	
compound	peak area	RSD (%)	peak area	RSD (%)	peak area	RSD (%)	peak area	RSD (%)	peak area	RSD (%)
chloromethane									3 627	28.3
vinyl chloride									154 166	32.8
bromomethane									94 566	12.8
chloroethane									50 730	22.2
trichlorofluoromethane	141 290	55.0			554 644	14.4	569 776	11.8	638 988	8.3
1,1-dichloroethene	121 825	15.3			289 870	13.9	307 027	9.7	480 784	10.2
dichloromethane	46 773	9.8			71 147	10.1	57 766	2.8	108 496	9.9
1,2-dichloroethene			146 978	6.5	138 255	9.1	155 783	8.5	305 074	7.9
1,1-dichloroethane	127 864	7.3			209 697	6.5	239 303	2.6	397 452	5.5
trichloromethane	182 945	9.4			310 456	6.6	325 787	5.8	467 790	4.9
1,1,1-trichloroethane			1 180 455	9.3	1 079 990	4.6	1 050 526	1.8	1 551 559	3.4
tetrachloromethane	878 391	4.0			1 729 898	6.7	1 727 229	3.3	2 275 212	3.3
benzene			850 363	3.7	1 160 323	2.3	1 147 932	2.9	1 619 373	3.1
1,2-dichloroethane			98 476	6.7	132 762	3.7	131 970	7.8	152 316	3.0
trichloroethene	440 525	4.7			797 628	4.6	860 458	1.5	1 135 150	3.8
1,2-dichloropropane	146 827	3.1			230 986	3.1	242 858	1.8	333 758	2.1
bromodichloromethane			220 394	3.5	286 048	7.4	286 354	2.8	405 834	2.5
2-chloroethyl vinyl ether	48 439	7.1			62 002	5.0	68 867	2.0	101 375	4.0
cis-1,3-dichloropropene			344 832	4.0	382 770	4.5	390 658	1.4	575 085	2.0
toluene			3 300 791	6.8	4 124 333	5.7	4 178 290	1.0	5 575 521	2.3
trans-1,3-dichloropropene			392 291	4.2	367 093	6.8	400 157	3.9	500 351	3.1
1,1,2-trichloroethane	127 047	15.8			103 831	3.9	113 069	1.9	243 709	2.7
tetrachloroethylene	1 813 821	6.7			3 100 794	10.5	3 766 015	4.1	4 894 204	1.2
dibromochloromethane	241 213	3.6			323 208	3.3	358 074	1.7	471 348	3.9
chlorobenzene	2 775 306	2.7			4 215 906	3.5	4 537 059	1.4	6 108 729	1.1
ethylbenzene			10 723 647	2.5	12 464 228	3.2	12 439 401	1.4	16 779 873	1.1
tribromomethane			224 157	3.3	235 840	2.6	265 012	0.5	377 725	5.1
1,1,2,2-tetrachloroethane			487 070	5.4	503 814	3.9	547 270	0.8	794 701	5.5

[a] Conditions: carrier pressure 2.1 atm; dedicated injector, 24 V heating pulse. (1) Isothermal separation of purgeables A; number of analyses $n = 5$; oven temperature 60 °C, mass range 45–200. (2) Isothermal separation of purgeables B; $n = 5$; oven temperature 60 °C, mass range 45–250. (3) Isothermal separation of purgeables A and B; $n = 3$; oven temperature 35 °C, mass range 45–250. (4) Temperature-programmed separation of purgeables A and B; $n = 3$; oven temperature 35 °C at 10 °C/min, 36 °C 20 °C min, 50 °C at 30 °C/min to 70 °C, mass range 45–250. (5) Separation of purgeables A–C; $n = 3$; oven temperature 0 °C at 30 °C/min to 70 °C, mass range 45–250.

times were observed from run to run. Therefore the respective relative standard deviations were not estimated. Table 2, column (1), presents mean peak areas and precision of their determination as measured by the estimated values of relative standard deviation (RSD). For quantitative analysis, SPME requires calibration (e.g., by standard addition); hence repeatability of the results is the major factor affecting the accuracy. Except for the early eluting peaks, the precision was satisfactory. The reason for worse precision of the early eluters was the small number of data points acquired per peak. For the mass range used, one microscan took 0.2 s; thus for early eluters there were only four to five points per peak. For later eluting peaks there were more data points per peak, hence the precision was better. The two-digit RSD for 1,1,2-trichloroethane was due to secondary reactions in the ion trap, as confirmed by the observed varying ratios of the 96 and 97 mass peaks.

Carry-over of the order of up to 10% was observed when the same fiber was analyzed for the second time. As mentioned in the Results and Discussion section, the fiber was therefore cleaned by two additional heating pulses in the injector after the run was completed. It should be pointed out, however, that in SPME carry-over is not of such a big concern as in many other methods because SPME is an equilibration method. If a small percentage of an analyte is left in the coating after the desorption, it will only result in a decreased amount of this analyte actually taken from the next sample, but the equilibrium concentration in the coating will be practically unaffected. Carry-over may become a problem only when the concentration of the analyte in the following sample is so low that the equilibrium concentration in the coating is lower than the concentration due to carry-over from previous analysis, in which case some of the analyte would actually be liberated from the coating and transferred to the sample. In replicate analyses the threat does not exist. When samples of widely differing concentrations are analyzed in sequence, the fiber can be very quickly cleaned by additional heating pulses in the injector or off-line.

Figure 5 presents isothermal separation of purgeables B, under the same conditions as above, completed in ~80 s. All peaks were practically baseline resolved. Table 2, column (2), illustrates peak areas and the estimated precision of their determination for the compounds analyzed. It can be seen that the precision is satisfactory in all cases, mainly due to lack of very volatile compounds in this mix. Under the conditions applied, benzene coeluted with 1,2-dichloroethane. Apparently the experimental column used was not properly tuned.

Isothermal separation of purgeables A and B together was performed at 35 °C (Figure 6). The separation was completed in slightly above 4 min. Figure 7 presents the same separation performed with temperature programming (35 °C at 10 °C/min, 36 °C at 20 °C/min, 50 °C at 30 °C/min to 70 °C). In this case the separation was completed in ~100 s. However, it took a considerable time for the oven to cool down and equilibrate before the next analysis; hence, in these terms the two methods required comparable time. On the other hand, temperature programming yields better chromatographic conditions, which results in sharper peaks, and thus better signal-to-noise ratio for late-eluting compounds. This is also evidenced by the precision data. Column

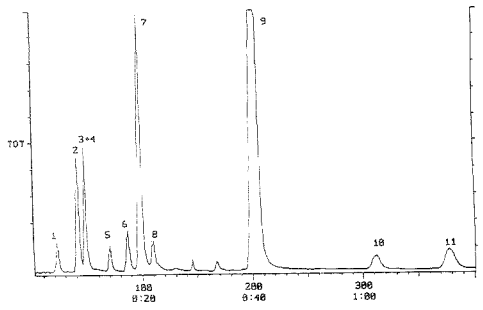

Figure 5. Separation of purgeables B on a Vocol column. Conditions: 60 °C iso, 2.1 atm, dedicated injector, capacitor voltage 24 V, MS detector, mass range 45–250. (1) 1,2-dichloroethene, (2) 1,1,1-trichloroethane, (3) benzene, (4) 1,2-dichloroethane, (5) bromodichloromethane, (6) *cis*-1,3-dichloropropene, (7) toluene, (8) *trans*-1,3-dichloropropene, (9) ethylbenzene, (10) tribromomethane, and (11) 1,1,2,2-tetrachloroethane.

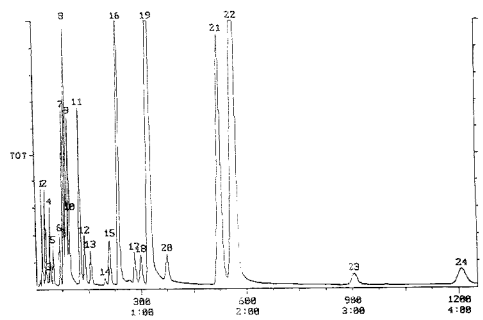

Figure 6. Isothermal separation of purgeables A and B on a Vocol column. Conditions: 35 °C iso, 2.1 atm, dedicated injector, capacitor voltage 24 V, MS detector, mass range 45–250. (1) trichlorofluoromethane, (2) 1,1-dichloroethene, (3) dichloromethane, (4) 1,2-dichloroethene, (5) 1,1-dichloroethane, (6) trichloromethane, (7) 1,1,1-trichloroethane, (8) tetrachloromethane, (9) benzene, (10) 1,2-dichloroethane, (11) trichloroethene, (12) 1,2-dichloropropane, (13) bromodichloromethane, (14) 2-chloroethyl vinyl ether, (15) *cis*-1,3-dichloropropene, (16) toluene, (17) *trans*-1,3-dichloropropene, (18) 1,1,2-trichloroethane, (19) tetrachloroethylene, (20) dibromochloromethane, (21) chlorobenzene, (22) ethylbenzene, (23) tribromomethane, and (24) 1,1,2,2-tetrachloroethane.

(3) in Table 2 presents the peak areas and precision estimation for the isothermal analysis, while column (4) presents the same for temperature programming. In general, precision seems to be better in the temperature-programmed separation. Although benzene and 1,2-dichloroethane coeluted, in both cases it was possible to quantify them separately using specific masses (peak maxima did not overlap).

Finally, Figure 8 presents the separation of all 28 components of the purgeables A–C. This separation was performed with temperature programming only (0 °C at 30 °C/min to 70 °C). Again, benzene and 1,2-dichloroethane coeluted, but could be quantified. The analysis was completed in ~2.5 min. Together with cooling down and equilibration, this time is comparable to the sampling time required (4–5 min). Column (5) in Table 2 illustrates the results obtained for all the components. Again, the RSDs are much worse for early-eluting compounds for

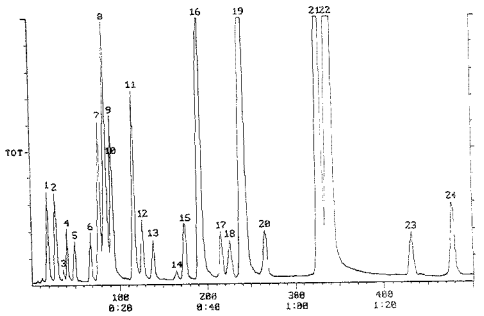

Figure 7. Temperature-programmed separation of purgeables A and B on a Vocol column. Conditions: 35 °C at 10 °C/min, 36 °C 20 °C/min, 50 °C 30 °C/min, to 70 °C; 2.1 atm, dedicated injector, capacitor voltage 24 V, MS detector, mass range 45–250. (1) trichlorofluoromethane, (2) 1,1-dichloroethene, (3) dichloromethane, (4) 1,2-cichloroethene, (5) 1,1-dichloroethane, (6) trichloromethane, (7) 1,1,1-trichloroethane, (8) tetrachloromethane, (9) benzene, (10) 1,2-dichloroethane, (11) trichloroethene, (12) 1,2-dichloropropane, (13) bromodichloromethane, (14) 2-chloroethyl vinyl ether, (15) *cis*-1,3-dichloropropene, (16) toluene, (17) *trans*-1,3-dichloropropene, (18) 1,1,2-trichloroethane, (19) tetrachloroethylene, (20) dibromochloromethane, (21) chlorobenzene, (22) ethylbenzene, (23) tribromomethane, and (24) 1,1,2,2-tetrachloroethane.

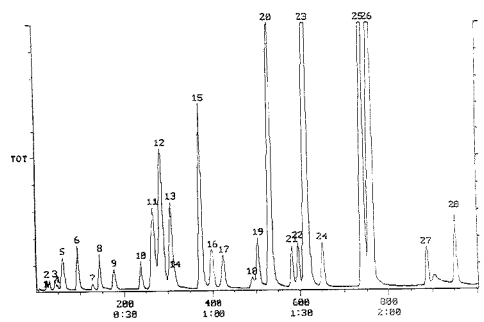

Figure 8. Separation of purgeables A–C on a Vocol column. Conditions: 0 °C at 30 °C/min to 70 °C; 2.1 atm, dedicated injector, capacitor voltage 24 V, MS detector, mass range 45–250. (1) chloromethane, (2) vinyl chloride, (3) bromomethane, (4) chloroethane, (5) trichlorofluoromethane; (6) 1,1-dichloroethene, (7) dichloromethane, (8) 1,2-dichloroethene, (9) 1,1-dichloroethane, (10) trichloromethane, (11) 1,1,1-trichloroethane, (12) tetrachloromethane, (13) benzene, (14) 1,2-dichloroethane, (15) trichloroethene, (16) 1,2-dichloropropane, (17) bromodichloromethane, (18) 2-chloroethyl vinyl ether, (19) *cis*-1,3-dichloropropene, (20) toluene, (21) *trans*-1,3-dichloropropene, (22) 1,1,2-trichloroethane, (23) tetrachloroethylene, (24) dibromochloromethane, (25) chlorobenzene, (26) ethylbenzene, (27) tribromomethane, (28) 1,1,2,2-tetrachloroethane.

the reasons described previously. Also, the first four components are gases at room temperature, and the 15 μm coating used in this study does not effectively trap them. Therefore, any variations in handling (e.g., time between the end of the sampling period and injection) can affect the results. These, however, can be eliminated by automation.

Similar experiments were performed with the 0.1 mm SPB-1 column. Due to the limited size of the paper, some figures and tables that were not crucial for the clarity of the material pertaining to this part, as well as to research on internally heated devices,

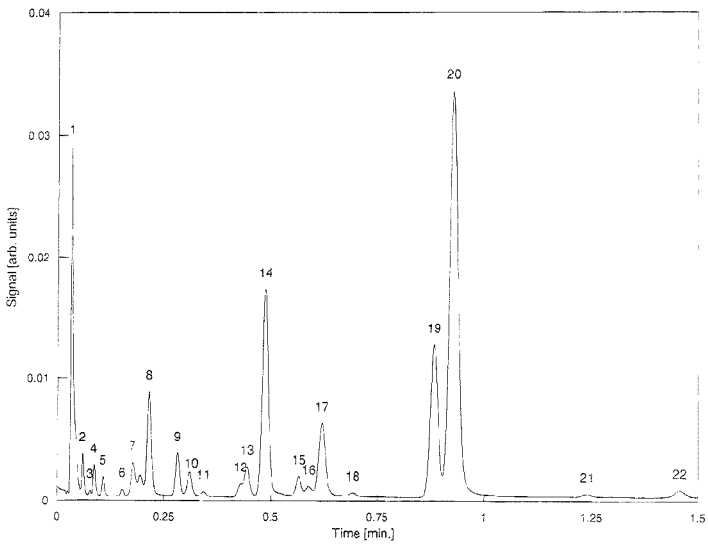

Figure 9. Temperature-programmed separation of purgeables A and B on a Vocol column. Conditions: 20 °C at 20 °C/min, 45 °C for 1 min; 2.45 atm, dedicated injector, capacitor voltage 24 V, detector: FID. (1) methanol + trichlorofluoromethane, (2) 1,1-dichloroethene, (3) dichloromethane, (4) 1,2-dichloroethene, (5) 1,1-dichloroethane, (6) trichloromethane, (7) 1,1,1-trichloroethane, (8) benzene + 1,2-dichloroethane, (9) trichloroethene, (10) 1,2-dichloropropane, (11) bromodichloromethane, (12) 2-chloroethyl vinyl ether, (13) *cis*-1,3-dichloropropene, (14) toluene, (15) *trans*-1,3-dichloropropene, (16) 1,1,2-trichloroethane, (17) tetrachloroethylene, (18) dibromochloromethane, (19) chlorobenzene, (20) ethylbenzene, (21) tribromomethane, and (22) 1,1,2,2-tetrachloroethane.

have been moved to supporting information. A narrower mass range (45–200 amu) was used in this experiment to shorten the microscan to 150 ms and thus generate more data points per peak. In general, this column yielded worse separation of the components. In the case of purgeables A, 1,1-dichloroethylene and dichloromethane coeluted under isothermal conditions. For purgeables B, ethylbenzene and tribromomethane were poorly separated. In isothermal separation of purgeables A + B, the following pairs were not separated or poorly separated: 1,1-dichloroethene and dichloromethane, bromodichloromethane and trichloroethene, ethylbenzene and tribromomethane. In temperature-programmed separation of purgeables A + B, ethylbenzene and tribromomethane were much better separated. In the separation of all purgeables (Figure 1 in supporting information), only the bromodichloromethane–trichloroethylene pair remained unresolved. In all cases quantitation was still possible owing to the use of the mass spectrometer. Precision followed in general the pattern observed for the Vocol column. Peak areas of early-eluting peaks were characterized by poorer precision than that of later eluting ones. Worse precision of the results obtained for some of the later eluting compounds in temperature-programmed runs was mainly due to secondary reactions occurring in the trap, resulting in sometimes dramatic changes of the relative abundance of peaks used for quantitation. The above discussed results are presented in Table 1 in the supporting information.

As the ultimate goal of this research is application of the technique studied in a portable instrument, the same separations were attempted with a flame ionization detector. However, most of the purgeable components are organochlorine compounds, for whom the FID response is relatively poor. To improve the sensitivity of the method, salt was added to the standard solutions to promote the transfer of the analytes from the aqueous phase to the fiber. In this way a gain in sensitivity by almost 50% was achieved for most compounds. Figure 9 presents an example of temperature-programmed separation of purgeables A and B on the Vocol column. Compared to the separation presented in Figure 7, the resolution is apparently not as good. This is most probably because the outlet of the column in the FID experiments was at atmospheric pressure, as opposed to vacuum in the MS. The FID apparently did not contribute significantly to poor resolution, as in such a case peak broadening would be observed for all peaks, while peak width at half-height for early eluters was similar to that observed in the MS experiments (~300 ms). Peak 1 in this chromatogram comes from methanol, the solvent in which the analytes are dissolved in standard solutions delivered by Supelco. Its concentration in the aqueous sample was ~0.1%; hence a large peak was observed even though the poly(dimethylsiloxane) coating has small affinity toward methanol, and so is the sensitivity of FID toward this compound. Methanol presence rendered the determination of trichlorofluoromethane and the even more volatile components of purgeables C impossible. The problem can possibly be overcome by using more concentrated standard methanolic solutions. Moreover, in real life analysis this problem can hardly occur. In the ITMS analyses, methanol did not interfere, as the mass range used started at 45 amu.

Table 3 presents the retention times and their estimated relative standard deviations for all the compounds analyzed. It follows from this table that the retention times are extremely repeatable, as the maximum RSD observed was 1.6%, and for most compounds it was below 1%. Table 4 presents the mean peak areas and estimation of precision of their determination for the GC-FID separations of purgeables A, B, A + B isothermal, and A

Table 3. Mean Retention Times and Their Relative Standard Deviations of Purgeables A and B Analyzed Separately and Together on the 2.5 m × 0.1 mm × 0.6 μm Vocol Column Using FID for Detection[a]

	(1)		(2)		(3)		(4)	
compound	RT (s)	RSD (%)	RT (s)	RSD (%)	RT (s)	RSD (%)	RT (s)	RSD (%)
trichlorofluoromethane					3.6	0.7	3.6	1.1
1,1-dichloroethene	2.7	1.4			4.6	0.5	4.6	1.3
dichloromethane	3.3	1.1			5.2	0.0	5.1	1.1
1,2-dichloroethene			3.3	0.9	6.5	0.6	6.4	1.3
1,1-dichloroethane	4.4	0.5			9.2	0.3	9.0	1.6
trichloromethane	6.0	0.4			10.8	0.0	10.5	1.4
1,1,1-trichloroethane			6.0	0.4				
tetrachloromethane					13.2	0.2	12.7	1.2
benzene + 1,2-dichloroethane			7.1	0.3	17.8	0.3	16.7	0.9
trichloroethene	11.1	0.4			20.0	0.4	18.4	0.8
1,2-dichloropropane	12.2	0.3			22.5	0.3	20.3	0.7
bromodichloromethane			11.3	0.3	30.2	0.4	25.5	0.7
2-chloroethyl vinyl ether	17.4	0.2			31.7	0.2	26.5	0.4
cis-1,3-dichloropropene			15.0	0.3	35.4	0.3	29.0	0.1
toluene			16.8	0.1	44.1	0.2	33.7	0.3
trans-1,3-dichloropropene			19.8	0.2	46.6	0.2	35.2	0.3
1,1,2-trichloroethane	26.4	0.2			49.3	0.1	37.0	0.3
tetrachloroethylene	28.3	0.2			57.8	0.5	41.4	0.3
dibromochloromethane	32.6	0.2			83.7	0.2	52.8	0.3
chlorobenzene	45.9	0.2			91.7	0.2	55.5	0.3
ethylbenzene			38.8	0.1			74.2	0.2
tribromomethane			62.0	0.1			87.3	0.2
1,1,2,2-tetrachloroethane			81.9	0.2				

[a] Dedicated injector at 24 V heating pulse; carrier gas hydrogen; number of analyses $n = 5$. (1) Isothermal separation of purgeables A; oven temperature 30 °C, carrier pressure 2.8 atm. (2) Isothermal separation of purgeables B; oven temperature 35 °C, carrier pressure 2.8 atm. (3) Isothermal separation of purgeables A and B; oven temperature 20 °C, carrier pressure 2.45 atm. (4) Temperature-programmed separation of purgeables A and B; oven program 20 °C at 20 °C/min, 45 °C 1 min, carrier pressure 2.45 atm.

Table 4. Mean Peak Areas (Arbitrary Units) and Relative Standard Deviations of Purgeables A and B Analyzed Separately and Together on the 2.5 m × 0.1 mm × 0.6 μm Vocol Column Using FID for Detection[a]

	(1)		(2)		(3)		(4)	
compound	peak area	RSD (%)	peak area	RSD (%)	peak area	RSD (%)	peak area	RSD (%)
trichlorofluoromethane	nq[b]	n/a[c]			nq	n/a	nq	n/a
1,1-dichloroethene	1837	12.2			983	8.0	1245	6.1
dichloromethane	547	11.4			139	10.9	119	10.5
1,2-dichloroethene			891	4.9	914	6.7	971	4.0
1,1-dichloroethane	879	3.6			686	7.6	719	3.0
trichloromethane	282	4.7			290	21.6	295	5.7
1,1,1-trichloroethane			1933	4.7	1862	4.2	2139	1.0
tetrachloromethane	nq	n/a			nq	n/a	nq	n/a
benzene + 1,2-dichloroethane			5799	2.2	5889	3.5	6361	0.7
trichloroethene	2525	2.3			2280	5.1	2414	1.8
1,2-dichloropropane	1922	1.6			1458	4.6	1626	1.6
bromodichloromethane			282	4.3	263	11.2	298	5.0
2-chloroethyl vinyl ether	628	3.7			428	16	550	18.5
cis-1,3-dichloropropene			1838	3.1	1868	3.7	2130	4.9
toluene			16503	0.8	15738	2.0	17185	1.6
trans-1,3-dichloropropene			1295	6.5	1319	4.1	1491	5.1
1,1,2-trichloroethane	604	8.4			524	21.1	784	4.6
tetrachloroethylene	7675	3.6			5758	2.9	6764	3.7
dibromochloromethane	193	23.1			200	20.6	313	6.7
chlorobenzene	18763	3.8			13957	2.3	15366	1.7
ethylbenzene			42796	1.6	41731	2.5	46436	3.2
tribromomethane			264	36.7	nq	n/a	369	8.4
1,1,2,2-tetrachloroethane			748	22.4	nq	n/a	1076	6.7

[a] Dedicated injector at 24 V heating pulse (carrier gas hydrogen); number of analyses $n = 5$. (1) Isothermal separation of purgeables A; oven temperature 30 °C, carrier pressure 2.8 atm. (2) Isothermal separation of purgeables B; oven temperature 35 °C, carrier pressure 2.8 atm. (3) Isothermal separation of purgeables A and B; oven temperature 20 °C, carrier pressure 2.45 atm. (4) Temperature-programmed separation of purgeables A and B; oven program 20 °C 20 °C/min, 45 °C min, carrier pressure 2.45 atm. [b] nq, not quantifiable. [c] n/a, not applicable.

+ B temperature programmed. In the case of purgeables A, trichlorofluoromethane was not determined for the reasons described above, and tetrachloromethane was not quantified due to the very poor response of the FID toward this compound. The compounds coeluting during the separation of purgeables A and B (benzene and 1,2-dichloromethane) could not be individually quantified with FID. In the isothermal separation, tribromomethane and 1,1,2,2-tetrachloroethane could not be quantified due to the poor response of the FID and significant peak broadening. In general, the pattern the results follow is different

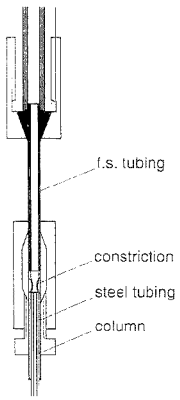

Figure 10. Modification of the injector for direct discharge through the wire.

from the case of the GC/MS analysis. For obvious reasons, precision is the worst for compounds producing peaks of a low signal-to-noise ratio. For compounds producing larger peaks, precision is very good. This indicates that the precision of the results can possibly be significantly improved by the use of a more specific detector.

The results obtained for the SPB-1 column are illustrated in Tables 2 and 3 of the supporting information. Again the retention times were very repeatable, not exceeding 0.9% RSD (<0.5% in most cases). In general, more peaks remained unresolved on this column. Precision of the results was roughly similar to that obtained for the Vocol column. Trichlorofluoromethane and tetrachloromethane were not quantified for reasons described previously.

Internally Heated Fibers. Fast desorption of the analytes from the fiber can be achieved not only by rapidly heating the injector but also by heating the fiber directly. One of the possible solutions is to pass an electric current through a conducting element. For this purpose the fiber was replaced with a segment of a 0.125 mm o.d. stainless steel wire. The amount of compounds that can be adsorbed on the wire surface is obviously too small for practical applications; however, the experiment aimed only at verifying the feasibility of this method of heating for fast separations.

The experiment required a modification of the dedicated injector design. The changes are illustrated in Figure 10. The fused-silica tubing (6 in Figure 1) is not equipped with a heater and has a smaller diameter (0.32 mm i.d.). The column is glued inside a gauge 22 stainless steel tube with a constriction in the upper part, connected to the fused-silica tubing with a butt connector. The steel tube serves only as an electric contact. The constriction in the steel tube was made by squeezing the tube with wire cutters. It is oblong in shape and narrow enough to stop the 0.125 mm o.d. wire, while not blocking the flow. The distance from the top of the column to the top of the steel tube is ~2 mm. The column is pushed all the way up to the constriction, thus practically eliminating dead volume. High-temperature epoxy was used to seal the column in the tube. The capacitive discharge supply was connected to the steel tubing and to the needle of the SPME device. For the analysis, the plunger was depressed until

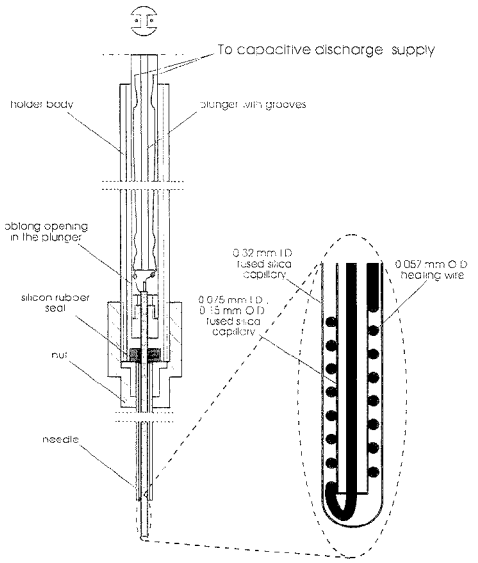

Figure 11. Schematic diagram of the Supelco SPME device modified to accomodate the internally heated fiber.

the wire mounted in the SPME device firmly contacted the steel tubing constriction, followed by closing the circuit and thus producing a capacitive discharge. As the wire had the highest resistance in the circuit, most of the heat produced by electric current evolved in the wire itself.

The experiments were performed by dipping the wire in a mixture of pure BTEX compounds and subsequent desorption of the analytes in the modified injector. The experimental conditions were as follows: 2.5 m × 0.1 mm × 0.5 μm SPB-1 column; hydrogen carrier gas, pressure 4 atm; oven temperature $T = 60$ °C, capacitor voltage $U = 42$ V. Using the narrow-bore column it was possible to complete the separation in ~10 s, which is comparable to the results obtained with the regular fiber and the heated injector.

Having demonstrated the practicability of this approach, another possibility of heating the fiber directly was studied. This time the regular coated fiber used in the previous experiments was replaced by a hollow fiber equipped with an internal microheater. To accommodate the assembly, the commercial Supelco autosampler SPME holder was used after some modifications. A schematic diagram of the device is presented in Figure 11. A 0.32 mm i.d. fused-silica capillary, flame sealed at one end, was used as the fiber. The microheater, made of a 0.057 mm o.d. NiCu wire, was coiled around another fused-silica microcapillary (0.075 mm i.d., 0.15 mm o.d.). One end of the heating wire was passed inside the microcapillary, while the other was placed outside, which yielded excellent electrical insulation between the two leads. The entire heating assembly was inserted inside the 0.32 mm capillary. The needle of the holder was replaced by a custom-made, larger diameter one. The sealed capillary/heater set was mounted in place of the fiber assembly. The plastic plunger was machined to accommodate the leads, as well as to enable mounting the internally heated device. This was accomplished by producing an oblong opening above the threaded

Table 5. Repeatability of Peak Areas for Coated Internally Heated Fiber[a]

	benzene	toluene	ethylbenzene	*m,p*-xylene	*o*-xylene
			Peak Area		
	1755	13 877	29 502	148 841	96 845
	1525	11 683	26 275	125 368	77 722
	1653	12 191	25 358	119 481	72 595
	1094	10 385	22 608	112 211	71 172
mean	1507	12 035	25 936	126 475	79 584
STD	252	1 251	2 462	13 728	10 259
RSD (%)	16.7	10.4	9.5	10.9	12.9

[a] Conditions: T = 42 °C, p = 0.49 atm, U = 23 V, 0.17 μL/L each BTEX in air.

part of the plunger. The leads were glued inside machined grooves and soldered to the heater wires. A spring wire (not shown) was fastened to the upper part of the plunger, protruding from the metal body. The wire activated a microswitch, which in turn started the capacitive discharge. In this way the discharge was synchronized with plunger movement.

Initial experiments were performed with polyimide-coated capillaries and BTEX. Although the results were encouraging, the amount of analytes trapped was extremely small. Therefore the fiber was coated with SE-30 stationary phase. This was done by dipping it in a 10% solution of the said stationary phase in methylene chloride and evaporating the solvent. Using a fiber prepared in such a way, separation of BTEX sampled from gas was achieved in 12.6 s. Unfortunately, the SE-30 coating proved to be unstable, as it tended to fall off the fiber and clog the injector. Therefore an attempt was made to induce cross-linking of the stationary phase by adding ~1% of 2,2-azobis(2-methylpropionitrile)—a free-radical initiator—to the 10% solution of SE-30 in methylene chloride. The coating produced in such a way proved to be more stable during prolonged usage.

To shorten the heating pulse duration, new heaters made of 0.05 mm silver wire were prepared. The resistance of the heater was ~3 Ω, compared to ~27 Ω for the NiCu wire heaters. The capacitor was charged to 23 V; thus the initial instantaneous current passing through the heater was very high, resulting in very sharp pulses. However, the actual temperature profile of the fiber surface was not determined due to lack of proper instrumentation.

It was observed that the polyimide coating on a fused-silica capillary significantly contributed to peak tailing, especially when the coating was exposed to very high temperatures. A significant improvement in separation was observed when the polyimide was stripped before coating the capillary with initiator-containing SE-30.

Using the fiber prepared in such a way (bare fused-silica covered with polymerised SE-30, silver wire heater), a series of experiments were performed aiming at determining the repeatability of the separations. The conditions were the following: 4 m × 0.25 mm × 0.25 μm SPB-5 column, hydrogen pressure 0.49 atm, oven temperature 42 °C, capacitor voltage 23 V, 0.17 μL/L each BTEX in air. The repeatability of retention times was determined based on 14 experiments. Relative standard deviations ranged from 0.92% for benzene (retention time 0.054 min) to 0.55% for toluene (retention time 0.086 min). The repeatability of peak areas was also determined. The results for n = 4 determinations are listed in Table 5. Compared to the results obtained for a regular fiber on a much lower concentration level,[6] the repeatability of peak areas is significantly worse. This is most probably due to inferior properties of the custom-made coating. On the other hand, it should be emphasized that there was practically no carry-over when the internally heated fiber coated with SE-30 was used, even when the fiber was withdrawn back to the needle immediately after the discharge. Certain carry-over was observed in all the experiments with the regular fiber and rapid desorption.

A series of experiments to determine the shortest possible separation time was then performed. At 48°C and 0.49 atm, all the components were separated and the retention time of the last one was 0.154 min (Figure 2 of the supporting information). Similar results were obtained when the temperature was kept constant at 40 °C and the pressure was changed. This time the best result was 0.152 min, at p = 0.62 atm.

CONCLUSIONS

Solid phase microextraction proved to be a very useful tool in fast analysis of volatile organic compounds. Application of the technique enables shortening the analysis time (including sample preparation) from hours to minutes. Use of an ion trap mass spectrometer in conjunction with fast separation significantly improves sensitivity for most compounds and adds an additional dimension to the results—analyte identity. As SPME uses no solvents, and the fiber traps practically no water when sampling is carried out in headspace, the entire GC/MS system is protected against many adverse effects. On the other hand, very narrow peaks eluting early from small-diameter columns require even faster mass scan rates to produce more repeatable results. Nevertheless, the technique can readily be used for rapid screening of water samples.

Internally heated fibers are an interesting alternative to the dedicated injector. They can produce fast separations with very simple on-column type injectors. An ideal case would be to use such a fiber with an autosampler. Both dedicated injector and internally heated fiber can be used for field analysis, especially since the power requirements of both types of devices are minimal. The capacitor can be charged from small batteries using a device similar to that used in photographic flash lights. The internally heated fiber requires further research with a coating of better properties to fully examine the potential of this approach.

ACKNOWLEDGMENT

The authors thank Supelco Canada, Varian Inc., Dow Chemical Canada Inc., and the Natural Sciences and Engineering Research Council of Canada for financial support. Presented in part at the 1995 Pittsburgh Conference and the 78th Canadian Society for Chemistry Conference and Exhibition (Guelph, ON, Canada).

SUPPORTING INFORMATION AVAILABLE

Figures showing the separation of purgeables A–C and a BTEX mixture, respectively, and tables listing mean peak areas and mean peak retention times (6 pages). Ordering information is available on any current masthead page.

Received for review March 9, 1995. Accepted June 21, 1995.[⊗]

AC9502413

[⊗] Abstract published in *Advance ACS Abstracts*, August 1, 1995.

Anal. Chem. 1995, *67*, 3275–3283

Separation of Nanoliter Samples of Biological Amines by a Comprehensive Two-Dimensional Microcolumn Liquid Chromatography System

L. A. Holland and J. W. Jorgenson*

Department of Chemistry, The University of North Carolina at Chapel Hill, Chapel Hill, North Carolina 27599-3290

A two-dimensional liquid chromatography system based on the combination of a charge separation mechanism, provided by anion exchange chromatography, with a hydrophobic separation mechanism, provided by reversed phase chromatography, is presented. A 90 cm long anion exchange microcolumn is coupled to a 3 cm long reversed phase microcolumn. Both microcolumns are interfaced by two electronically controlled valves. Effluent from the anion exchange microcolumn is collected in a sample loop and then concentrated onto the head of the reversed phase microcolumn. Analyte peaks consisting of tagged amines elute from the second column and are detected by laser-induced fluorescence. The entire operation is controlled by a personal computer. The resolving power of this system is demonstrated with a two-dimensional chromatogram of the peptides obtained from a tryptic digest of porcine thyroglobulin. The sensitivity of the system is demonstrated with a two-dimensional chromatogram of the contents of a single bovine chromaffin cell.

Davis and Giddings estimated that, due to inhomogeneities in peak density, no more than 18% of the full peak capacity of a system can be used to generate adequate resolution of discrete analyte peaks.[1] This estimate reveals the importance of a large peak capacity in a separation system designed for analyses of complex samples. The combination of individual separation techniques to form a multidimensional separation system is one means of attaining a separation technique of high peak capacity. This is because the total peak capacity in a multidimensional system is determined by multiplying the peak capacities for each separation dimension.[2] Therefore, a system consisting of two coupled separation dimensions each of a high peak capacity can greatly increase the separation power over single-dimension systems. This improvement in peak capacity is the driving force behind the two-dimensional anion exchange microcolumn chromatography and reversed phase microcolumn chromatography system described here.

Multidimensional separations have been defined by Giddings as having only two criteria. The first criterion of a multidimensional system is that sample components must be displaced by two or more separation techniques based on different separating mechanisms. The second criterion is that components that are separated by any single separation dimension must not be recombined in any further separation dimension.[2] The first of Giddings' requirements of a multidimensional system is easily satisfied through prudent selection of the separation techniques to be coupled. The second requirement, however, is more difficult to fulfill in that it necessitates efficient transfer of sample from one separation dimension to the next.

The key feature of a comprehensive multidimensional system is that it should be based upon the eventual transfer of all, or a representative portion of all, analytes composing the initially injected sample to all further separation modes. In a comprehensive multidimensional system, discrete fractions of mobile phase eluted from any one separation dimension are transported, on regular intervals, to the next separation dimension throughout the entire multidimensional chromatographic run. The interval in which a fraction is to be transferred from one separation dimension to the next is determined according to the width of the peaks eluting from the earlier separation dimension. It is imperative that any peak eluting from a separation dimension is sampled a minimum of three times by the next separation dimension. This permits most of the resolution of the first dimension to be retained.

Many coupled separation systems have been developed that are not comprehensive, but are interfaced by a heart cutting method. These coupled systems are designed to isolate one or only a few analytes of interest from a complex matrix.[3-12] In heart cutting, only a small number of fractions containing the analyte of interest are transferred from one separation mode to the next. This elution fraction of the analyte of interest is determined for each separation mode by running a standard of that analyte on each individual uncoupled separation method. A system of this type has a peak capacity typical of a single-dimension system.

Recent comprehensive multidimensional techniques designed for the analysis of biological samples have focused on various separation combinations. The capabilities of coupled liquid

(1) Davis, J. M.; Giddings, J. C. *Anal. Chem.* **1983**, *55*, 418–424.
(2) Conves, H. J., Ed. *Multidimensional Chromatography Techniques and Applications*; Marcel Dekker, Inc.: New York, 1990; Chapter 1.
(3) Posluszny, J. V.; Weinberger, R. *Anal. Chem.* **1988**, *60*, 1953–1958.
(4) Posluszny, J. V.; Weinberger, R.; Woolf, E. *J. Chromatogr.* **1990**, *507*, 267–276.
(5) Szuna, A. J.; Mulligan, T. E.; Mico, B. A.; Blain, R. W. *J. Chromatogr.* **1993**, *616*, 297–303.
(6) Szuna, A. J.; Blain, R. W. *J. Chromatogr.* **1993**, *620*, 211–216.
(7) Mulligan, T. E.; Blain, R. W.; Oldfield, N. F.; Mico, B. A. *J. Liq. Chromatogr.* **1994**, *17*(1), 133–150.
(8) Puhlmann, A.; Dülffer, T.; Kobold, U. *J. Chromatogr.* **1992**, *581*, 129–133.
(9) Mader, R. M.; Rizovski, B.; Steger, G. G.; Rainer, H.; Proprentner, R.; Kotz, R. *J. Chromatogr.* **1993**, *613*, 311–316.
(10) Agbaria, R.; Ford, H., Jr.; Kelley, J. A.; Xie, F.; Politi, P.; Grem, J. L.; Cooney, D. A.; Marquez, V. E.; Allegra, C. J.; Johns, D. G. *Anal. Biochem.* **1993**, *213*, 90–96.
(11) Mifune, M.; Krehbiel, D. K.; Stobaugh, J. F.; Riley, C. M. *J. Chromatogr.* **1989**, *496*, 55–70.
(12) Brown-Thomas, J. M.; Moustafa, A. A.; Wise, S. A.; May, W. E. *Anal. Chem.* **1988**, *60*, 1929–1933.

0003-2700/95/0367-3275$9.00/0

chromatography (LC)/capillary zone electrophoresis (CZE) systems for the analysis of proteins and of peptides have been presented by Lemmo and Jorgenson[13,14] and by Larmann et al.[15] A gel electrophoresis/LC multidimensional system was designed by Rose and Opiteck for protein separations.[16] A cation exchange, fast size exclusion system operated continuously with a valve, loop interface was developed by Bushey and Jorgenson for the separation of protein standards and serum proteins.[17] Takahashi and others have developed a tandem anion exchange, reversed phase system operated by stopping the flow in one column while the second column is running.[18-23] The system utilizes conventional chromatographic columns for the separation of proteins or peptides which are typically collected and sequenced after separation.

The two-dimensional LC/LC system to be described here fulfills both of Giddings' requirements of a multidimensional system. First, it combines anion exchange chromatography, a separation mechanism based on charge, with reversed phase chromatography, a separation mechanism based on hydrophobicity. Second, components that are separated by the first dimension remain separated in the second dimension by careful control of sampling frequency of the first dimension.

EXPERIMENTAL SECTION

Instrumentation. (a) Liquid Chromatography. The microcolumns were first fritted according to a previously described procedure[24] and were then packed as outlined by Kennedy and Jorgenson.[25] The first dimension is a 90 cm long, 100 μm internal diameter microcolumn packed with 5 μm diameter strong anion exchanger particles with a permanently bonded quaternary amine, of 300 Å pore. The second dimension is a 3 cm long, 100 μm internal diameter microcolumn packed with 5 μm reversed phase octadecylsilyl particles of 300 Å pore. Both the anion exchange and reversed phase stationary phases have a pore size of 300 Å to allow diffusion of the peptides in the pores. The anion exchange microcolumn is operated at a flow rate of 33 nL/min and has a dead time of 180 min, while the reversed phase microcolumn is operated at a flow rate of 6 μL/min and has a dead time of 1.2 s.

The mobile phase for the anion exchange chromatography is always buffered with 5 mM 3-(*N*-morpholino)propanesulfonic acid (MOPS) at pH 7.9, in 50% water/50% acetonitrile. The mobile phase contains 50% acetonitrile in order to minimize the reversed phase characteristics introduced by the carbon content of the anion exchange stationary phase. This allows the first dimension to be based mainly on charge separation, rather than on a mixed-mode charge/hydrophobicity separation. This is important in fulfilling Giddings' first requirement that the separation mechanisms of each separation mode be orthogonal. A salt gradient is generated by linearly increasing the concentration of guanidine thiocyanate as the chromatographic run progresses. Guanidine thiocyanate is used as the eluting salt because it provides a strong negative charge and is soluble in 50% acetonitrile. The salt gradient is achieved by changing the percentage of the following four different eluents: eluent A is an aqueous 5 mM MOPS solution buffered at pH 7.9 in 50% acetonitrile, eluent B is an aqueous 5 mM MOPS/12.5 mM guanidine thiocyanate solution buffered at pH 7.9 in 50% acetonitrile, eluent C is an aqueous 5 mM MOPS/50 mM guanidine thiocyanate solution buffered at pH 7.9 in 50% acetonitrile, and eluent D is an aqueous 5 mM MOPS/200 mM guanidine thiocyanate solution buffered at pH 7.9 in 50% acetonitrile. The concentration change in guanidine thiocyanate is shown in Table 1.

Table 1. Guanidine Thiocyanate Concentration Change of the Anion Exchange Gradient

time (h)	guanidine thiocyanate (mM)
0.0	2.5
15.0	17.5
22.5	50.0
35.0	125.0
37.5	170.0
40.0	170.0

Table 2. Acetonitrile Composition of the Reversed Phase Gradient

time (min)	acetonitrile (% vol)
0.00	24
0.10	28
1.60	50
1.70	100
2.10	100
2.15	15
2.95	15
3.00	24

An organic gradient is achieved for the reversed phase microcolumn by linearly increasing the percent of acetonitrile as the chromatographic run progresses. This is accomplished by changing the percentage of the following two eluents: eluent A is an aqueous 0.1% trifluoroacetic solution at pH 2, containing 15% acetonitrile, and eluent B is a 0.1% trifluoroacetic dissolved in 100% acetonitrile. The change in the acetonitrile content, as well as the percent composition of eluent A and eluent B, are shown in Table 2.

(b) Detection. A schematic of the detection system is contained in Figure 1. Peaks eluting from the second column are detected by the laser-induced fluorescence of tagged amines. The fluorescent group, tetramethylrhodamine, is excited with the green line from a 0.75 mW HeNe laser (Edmund Scientific, Barrington, NJ) at 543.5 nm and emits with a band centered at 570 nm. Light provided by the green HeNe laser passes through a 546 nm bandpass filter of 10 nm bandwidth (546DF10, Omega Optical, Inc., Brattleboro, VT) and is reflected off of a dichroic filter (565DRLP, Omega Optical) to a 60× microscope objective

(13) Lemmo, A. V.; Jorgenson, J. W. *J. Chromatogr.* **1993**, *633*, 213–220.
(14) Lemmo, A. V.; Jorgenson, J. W. *Anal. Chem.* **1993**, *65*, 1576–1581.
(15) Larmann, J. P., Jr.; Lemmo, A. V.; Moore, A. W., Jr.; Jorgenson, J. W. *Electrophoresis* **1993**, *14*, 439–447.
(16) Rose, D. J.; Opiteck, G. J. *Anal. Chem.* **1994**, *66*, 2529–2536.
(17) Bushey, M. M.; Jorgenson, J. W. *Anal. Chem.* **1990**, *62*, 161–167.
(18) Mant, C. T., Hodges, R. S., Eds. *High-Performance Liquid Chromatography of Peptides and Proteins: Separation, Analysis, and Conformation*; CRC Press: Boca Raton, FL, 1991; Section XIII.
(19) Matsuoka, K.; Taoka, M.; Isobe, T.; Okuyama, T; Kato, Y *J. Chromatogr.* **1990**, *515*, 313–320.
(20) Isobe, T.; Uchida, K.; Taoka, M.; Shinkai, F.; Manabe, T.; Okuyama, T *J. Chromatogr.* **1991**, *588*, 115–123.
(21) Takahashi, N.; Takahashi, Y.; Putnam, F. W. *J. Chromatogr.* **1983**, *266*, 511–522.
(22) Takahashi, N.; Ishioka, N.; Takahashi, Y.; Putnam, F. W. *J. Chromatogr.* **1985**, *326*, 407–418.
(23) Takahashi, N.; Takahashi, Y.; Ishioka, N.; Blumberg, B. S.; Putnam, F. W. *J. Chromatogr.* **1986**, *359*, 181–191.
(24) Hoyt, A. M., Jr.; Beale, S. C.; Larmann, J. P., Jr.; Jorgenson, J. W. *J. Microcolumn Sep.* **1993**, *5*, 325–330.
(25) Kennedy, R. T.; Jorgenson, J. W. *J. Microcolumn Sep.* **1990**, *2*, 120–126.

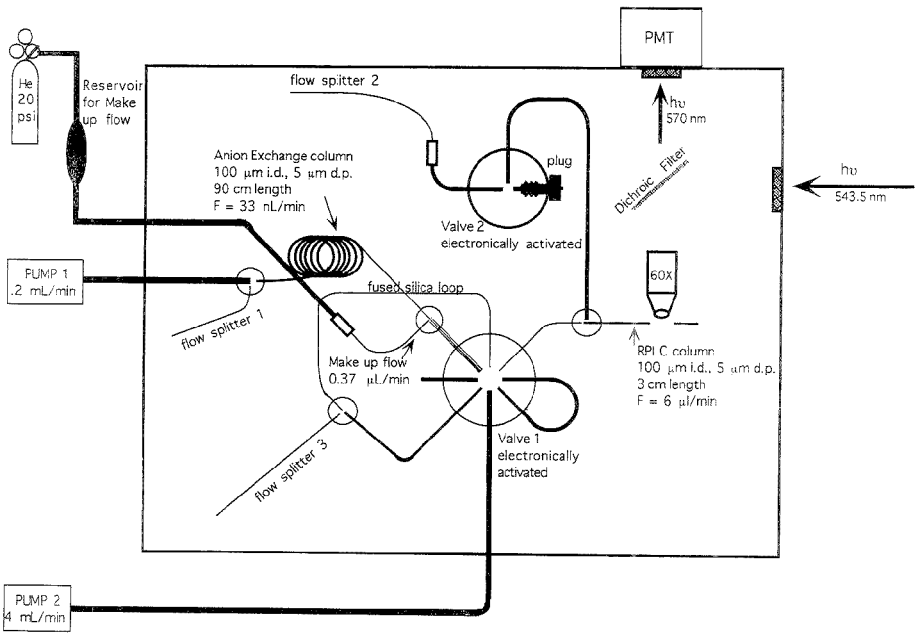

Figure 1. General schematic of the experimental setup.

lens (Edmund Scientific) which focuses the light just beyond the fritted end of the second-dimension column. Emitted fluorescent light is collected with the same 60× microscope objective lens. It is transmitted through the dichroic filter, passes through a 590 nm bandpass filter of 35 nm bandwidth (590DF35, Omega Optical), and is thus directed to the detector. This collected fluorescent light is converted to an electrical signal by a photomultiplier tube (R1477, Hamamatsu Corp., Bridgewater, NJ), and the current is converted to a voltage by an amplifier (427, Keithley Instruments, Cleveland, OH) with a gain of 10^6 and a rise time of 100 ms. The entire optical system is mounted on an optical breadboard (Technical Manufacturing Corp., Atlanta, GA) and is covered with an aluminum housing custom-built in-house. The breadboard provides stability as well as some vibration isolation, while the aluminum housing prevents interference from stray room light.

(c) Valve Interface. The anion exchange microcolumn is coupled to the reversed phase microcolumn by means of two electronically actuated valves, as shown in Figure 2. Mobile phase pumped at 0.2 mL/min by pump 1 (600E, Waters Associates, Milford, MA) is split at flow splitter 1, such that mobile phase flows through the anion exchange column at a rate of 33 nL/min. When valve 1 (EC8W, Valco Instruments Co. Inc., Houston, TX) and valve 2 (E8UW, Valco Instruments Co. Inc.) are positioned in the configuration denoted by position 2, mobile phase eluted from the anion exchange column is directed onto the fused silica sample loop. The mobile phase eluting from the anion exchange microcolumn is diluted with a makeup flow, making the total sample volume collected over 150 s in the fused silica loop 1 μL. At the same time mobile phase pumped at a rate of 4 mL/min by pump 2 (HP1050, Hewlett-Packard, Palo Alto, CA) is split at flow splitter 2. The rate of solvent delivery of pump 2 is maintained at 4 mL/min to minimize the dwell time required for the eluent to travel from the head of the pump to the head of the microcolumn. Flow splitter 2 is positioned after the tee connected to the reversed phase microcolumn to further minimize this dwell time. Flow through the reversed phase microcolumn is 6 μL/min. During the 150 s run time, the reversed phase microcolumn is subjected to an organic gradient in order to elute peaks injected onto the column. Immediately after the run, valves 1 and 2 are actuated so that they are in the configuration denoted by position 1. In this configuration, mobile phase pumped at 4 mL/min from pump 2 is split at flow splitter 3 and flushes the sample in the fused silica sample loop onto the reversed phase microcolumn at a flow rate of 6 μL/min. The valve port of valve 2, which is connected to the reversed phase flow, is plugged so that all flow split at flow splitter 3 is loaded onto column 2. A sample volume of 3 μL is loaded onto the reversed phase column in 30 s. During this 30 s sample loading, effluent from the anion exchange microcolumn is diverted to waste. After 30 s the valves are actuated such that they are in the configuration denoted by position 2, and the cycle is repeated. The entire system is operated under computer control to ensure that the valve actuation, gradient initiation, and data collection are synchronously timed. The exact timing of the two-dimensional system is displayed in Table 3.

(d) Data Collection and Graphical Representation. Control of valve actuation, the initiation of the reversed phase gradient, and data collection are achieved with a multifunction data acquisition board (Scientific Solutions Inc., Solon, OH) and a HP386 Vectra computer (Hewlett-Packard). A computer program written in-house in Quickbasic version 4.5 (Microsoft Corp.,

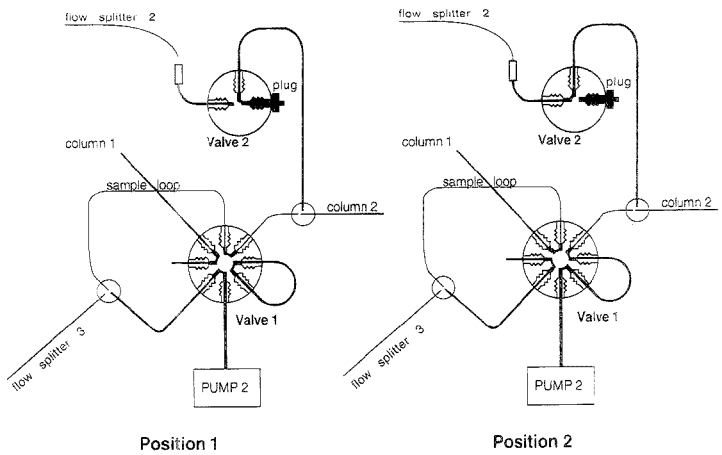

Figure 2. Detailed diagram of valve configuration showing the flow paths in each actuated position.

Table 3. Timing of the Two-Dimensional System

	time (min)		
	0	0.5	3.0
anion exchange microcolumn	eluted mobile phase diverted to waste	eluted mobile phase diverted to loop	eluted mobile phase diverted to loop
reversed phase microcolumn	load loop contents onto RPLC microcolumn	run sample loaded onto RPLC microcolumn	run sample loaded onto RPLC microcolumn
data collection	off	on	on

Redmond, WA) is used to execute commands to the data acquisition board. Data for the chromatograms of the porcine thyroglobulin are processed with a background subtraction involving a median filter written in-house in Quickbasic version 4.5. A similar background subtraction technique written in Labview was described previously.[26] Two-dimensional data are graphically represented with the aid of Spyglass Transform version 3.01 (Spyglass Inc., Savoy, IL) and Spyglass Format version 1.12 (Spyglass Inc.).

Sample Preparation. (a) Tagging of Samples. Samples are reacted with excess tetramethylrhodamine 5-isothiocyanate (TRITC). a 1 mg sample of TRITC is dissolved in 100 μL of dimethyl sulfoxide (DMSO). Samples are first diluted with 0.15 M boric acid at pH 8.5 and then combined with the DMSO containing TRITC in a volume ratio of 3:1 (0.1 M boric acid/DMSO containing TRITC). The tagging reaction proceeds for 4 h in the dark at room temperature. A blank run revealed that the TRITC tags a significant amount of amine contaminants if special precautions are not taken. As a result, plastic is eliminated from all sample preparation procedures with the exception of procedures involved in the culturing of the bovine chromaffin cells, as no alternative exists. All glass vials, microvials, volumetric flasks, round-bottom flasks, and calibrated and uncalibrated pipets and micropipets used in the procedures are first cleaned with chromic acid and then rinsed with distilled deionized water. Measured quantities of solid sodium hydroxide are added to solutions requiring pH adjustment. Measurements of pH are made from aliquots removed from these solutions to determine that the proper amount of base has been added. These pH measurements are made on aliquots removed from the bulk solution to prevent contamination of the solution by the pH electrode.

(b) Preparation of Porcine Thyroglobulin. Porcine thyroglobulin is reduced with slight modification to the procedure of Canfield.[27] Fifteen milligrams of porcine thyroglobulin is added to 1.5 mL of 10 M urea/0.1 M boric acid, with the pH adjusted to 8.5 with solid sodium hydroxide. β-mercaptoethanol (30 μL) is added, and if necessary, the pH is again adjusted with sodium hydroxide to 8.5. Helium is sparged through the solution briefly to remove dissolved oxygen, and the solution is then held at 37 °C for 4 h to aid in the dissociation of the native disulfide bonds of the protein by β-mercaptoethanol. A 10.5 mL volume of 2% HCl in ethanol (v/v) is added to quench the disulfide exchange via protonation of the thiol groups, as well as to precipitate the protein out of solution. The sample is centrifuged, and the supernatant is drawn off. A sealed ampule of iodoacetic acid is then opened, and 75 mg is weighed out and added to the protein along with 1.5 mL of 8 M urea/0.1 M boric acid adjusted with sodium hydroxide to pH 8.5. Upon addition of iodoacetic acid, the free thiols of the protein undergo alkylation which blocks the reformation of the disulfide bonds. The sample is vortexed, and if necessary, the pH is adjusted with sodium hydroxide to approximately 8.5. The alkylation is allowed to proceed for 10 min, after which time the reaction is quenched by the addition of 375 μL of β-mercaptoethanol. Approximately 10.5 mL of absolute ethanol is added, and the solution is centrifuged. After centrifuga-

(26) Moore, A. W.; Jorgenson, J. W. *Anal. Chem.* **1993**, *65*, 188–191.

(27) Canfield, R. E.; Anfinsen, C. A. *J. Biol. Chem.* **1963**, *238*, 2684–2690.

tion the ethanol is drawn off. The protein is washed by adding absolute ethanol, mixing the sample by vortexing it, centrifuging the sample, and then drawing off the ethanol. The wash is repeated one more time. The protein is then suspended in absolute ethanol and transferred to a round-bottom flask. The ethanol is removed with a rotary evaporator. The round-bottom flask is frozen in dry ice, and the protein is lyophilized over a period of 24 h. Recovery from this procedure is 38%.

The porcine thyroglobulin is digested with trypsin at a mass ratio of 30:1 (porcine thyroglobulin:trypsin) in 1 mL of 0.1 M boric acid at pH 8.5. The digestion proceeds at 37 °C for 24 h. A 150 μL aliquot of the digested porcine thyroglobulin is then tagged with 50 μL of 10 mg/mL TRITC. The tagging reaction proceeds in the dark, at room temperature, for 4 h. The sample is then diluted 5-fold in the mobile phase used in the initial conditions of the anion exchange separation and injected onto the anion exchange column for 15 s at 67 bars of pressure.

(c) Preparation of Bovine Chromaffin Cells. Bovine adrenal glands are obtained and processed according to the procedures of Wilson and Viveros,[28] with minor exceptions. Modifications are as follows: the glands are manually perfused, a balanced salt solution of 14.5 mM NaCl, 5.4 mM KCl, 1.12 mM glucose, 1.5 mM *N*-(2-hydroxyethyl)piperazine-*N*'-2-ethanesulfonic acid (HEPES), and 0.1 mM NaH_2PO_4 adjusted to pH 7.4 is used instead of Locke's solution, and glands are only incised to remove chromaffin cells. Cells dissociated from the glands are purified with a Renografin gradient as described by Wilson and Kirshner[29] with the exceptions that the gradient is carried out at 26 °C and the Locke's solution is replaced with a balanced salt solution similar to the solution described previously, except that 1.8 mM calcium and 0.797 mM magnesium are added. The cells are plated as described by Leszczyszyn et al.[30] Furthermore, all solutions and supplies used for the cell preparation are obtained as described by Leszczyszyn et al.[30] The cells are used after the third day of incubation, but not after the seventh day of incubation.

Cells are removed from the cell plate with the use of a hydraulic microsyringe. Briefly, the syringe consists of a micropipet connected to polypropylene tubing by means of Teflon heat shrink tubing. The opposite end of the polypropylene tubing is connected to a 1 mL glass syringe filled with clean mercury. Sample is drawn into and expelled from the glass micropipet by applying positive or negative force on the mercury in the syringe.

A solution of 14.5 mM NaCl, 0.54 mM KCl, 1.12 mM glucose, and 1.5 mM HEPES is adjusted to pH 7.4 with solid sodium hydroxide. The solution is made immediately before cell isolation and removal. A cell plate is removed from the incubator. The growth medium is drained, and approximately 2 mL of the above salt solution is added to the plate. This procedure is repeated five times. With the aid of a stereoscope, the hydraulic microsyringe is then used to remove a single cell from the cell plate. Once the cell is in the microsyringe, it is transferred to a 0.25 μL glass vial. The vial is then covered with a plastic film and immediately placed in dry ice. The microsyringe is then used to collect a small sample of the solution in the cell plate, approximately 10–30 nL, which is placed in another 0.25 μL glass vial which is also covered and placed on dry ice. This sample of solution is used as a blank and will undergo the same procedures used on the cell. After a cell and a cell blank have been removed from a plate, both the plate and glass micropipet are discarded.

Once the cell is isolated, it is lysed. This is accomplished by allowing the vial to undergo a 30 s freeze followed by a 3 min thaw. This freeze/thaw sequence is repeated three times. After the cell is lysed, it is tagged. Approximately 1 mg of TRITC is dissolved in 5 μL of DMSO. Once the TRITC is dissolved, 15 μL of 0.15 M boric acid adjusted to pH 8.5 is added and the solution is mixed. The reaction solution is drawn into a pneumatically controlled glass micropipet. The pneumatic controller has been described previously.[31] A reproducible droplet of the reaction solution is then expelled first into the vial containing the cell blank and then a second droplet is expelled into the vial containing the lysed cell.

After the reaction solution has been dispensed, the micropipet is calibrated by dispensing a drop of the same solution into a dish of mineral oil. This calibration must be made after the micropipet has been used in order to prevent contamination of the micropipet by immersing it into mineral oil and thus prevent contamination of the sample. The diameter of the dispensed droplet is measured with a calibrated retical in a light microscope. Measurements are taken as the droplet sinks in the oil, but not after the droplet rests on the bottom of the dish. The diameter measurement of the droplet is converted into a volume. If the solution volume is found to be greater than 30 nL, the vials are centrifuged at 12000*g* for 4 min and allowed to react in the dark for 4 h. If the reaction droplet volume added to the vials is less than 30 nL, a new glass micropipet is made and the procedure is repeated to ensure that an adequate concentration of TRITC is added to the sample.

After a single cell sample or blank is reacted for 4 h, the sample is immediately injected onto the two-dimensional system, or stored at −20 °C for up to 1 week. For injection onto the two-dimensional system the sample is drawn into a pneumatically controlled glass micropipet. The injection end of the anion exchange microcolumn is then removed from the system and held in place on an aluminum block. The glass micropipet is then inserted into the microcolumn with the aid of a light microscope. The sample is injected onto the microcolumn by expelling the pipet contents by means of the pneumatic controller. The anion exchange microcolumn is then placed back into the two-dimensional system and the chromatographic run is started.

Reagents. β-Mercaptoethanol, boric acid, glucose, guanidine thiocyanate, HEPES, iodoacetic acid, MOPS, and trifluoroacetic acid were obtained from Sigma (St. Louis, MO). Sodium chloride and potassium chloride were obtained from Mallinckrodt (Paris, KY). Acetonitrile (Optima grade) was obtained from Fisher Scientific (Raleigh, NC). TRITC was obtained from Molecular Probes (Eugene, OR). Sodium hydroxide was obtained from EM Science (Gibbstown, NJ). Ethanol was obtained from AAPER Alcohol and Chemical Co. (Shelbyville, KY). All aqueous solutions were made with deionized water obtained from a Barnstead Nanopure System (Boston, MA).

RESULTS

The high peak capacity of a multidimensional system is demonstrated in the two-dimensional chromatogram of porcine thyroglobulin shown in Figure 3. The total number of peaks counted in this chromatogram is roughly 150. The two-dimensional plot reveals that the reversed phase microcolumn is

(28) Wilson, S. P.; Viveros, H. *Exp. Cell Res.* **1981**, *133*, 159–169.
(29) Wilson, S. P.; Kirshner, N. *Methods Enzymol.* **1983**, *103*, 305–312.
(30) Leszczyszyn, D. J.; Jankowski, J. A.; Viveros, H. O.; Diliberto, E. J., Jr.; Near, J. A.; Wightman, R. M. *J. Neurochem.* **1991**, *56*, 1855–1863.
(31) Kennedy, R. T.; Jorgenson, J. W. *Anal. Chem.* **1988**, *60*, 1521–1524.

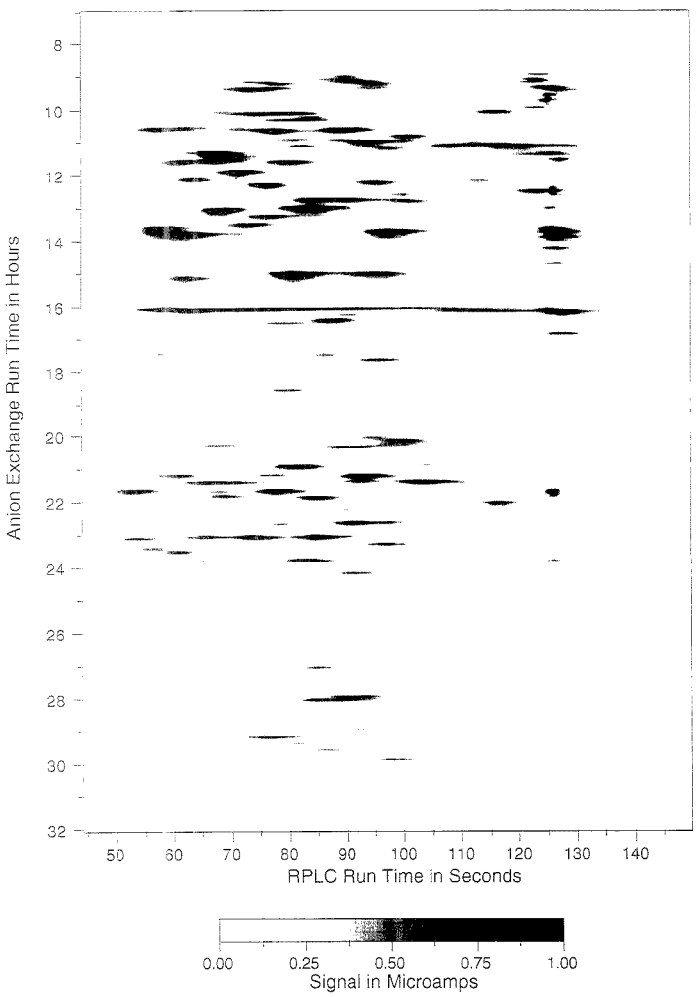

Figure 3. Two-dimensional separation of peptides obtained from a tryptic digest of reduced porcine thyroglobulin.

separating peaks that overlap in the anion exchange dimension. This observation is demonstrated more clearly by comparison of the two-dimensional separation of porcine thyroglobulin in Figure 3 with the reconstructed one-dimensional separations shown in Figures 4 and 5. The reconstructed one-dimensional anion exchange liquid chromatography run shown in Figure 4 is the sum of the total fluorescent signal for each reversed phase run. The reconstructed one-dimensional reversed phase liquid chromatography run shown in Figure 5 is the sum of the fluorescent signal recorded at the same data point for all reversed phase runs. Examination of the reconstructed anion exchange chromatogram shows that the typical anion exchange peak width is 9 min and the retention window in which a majority of the peaks is separated is 30 h. Using these numbers, the peak capacity of this separation is estimated to be 200. Examination of the reconstructed reversed phase chromatogram indicates a typical reversed phase peak width of 13.5 s and a retention window of 95 s. From these numbers the peak capacity of the reversed phase separation is estimated to be 7. Given a peak capacity of 200 for the first dimension and a peak capacity of 7 for the second dimension, the total peak capacity of the two-dimensional system is estimated at 1400 peaks. As the primary sequence of porcine thyroglobulin is not known, the primary sequence of bovine thyroglobulin already reported in the literature[32] was used to determine the number of fragments produced from a tryptic digest of the protein. The number of peptides that should be produced from a tryptic digest of bovine thyroglobulin was arrived at by counting the number of lysine and arginine residues that are not bonded to a proline residue on the carboxyl side, as trypsin will not cleave the carboxyl bond of a lysine or arginine residue adjacent to proline. The digest yields multiple fragments of both a single lysine residue and a single arginine residue. Identical fragments produced by the tryptic

(32) Mercken, L.; Simons, M.; Swillens, S.; Massaer, M.; Vassart, G. *Nature* **1985**, *316*, 647–651.

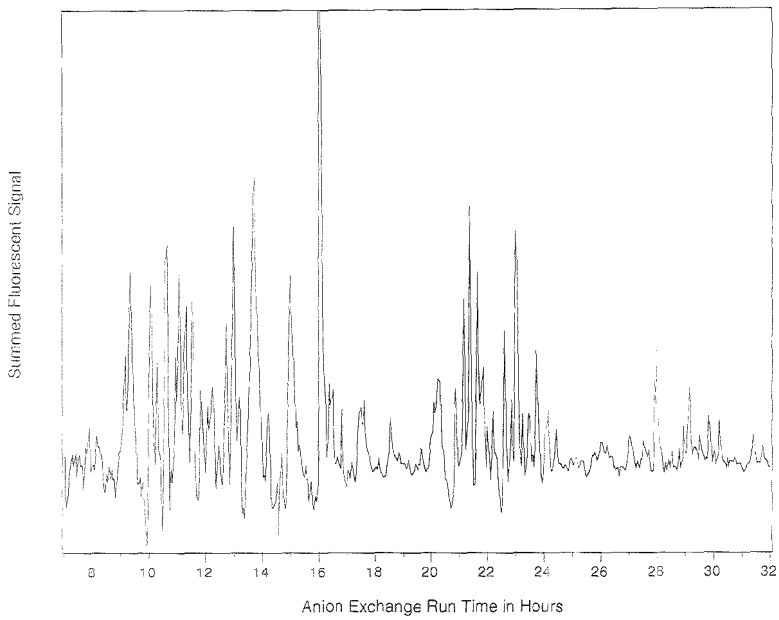

Figure 4. Reconstructed one-dimensional anion exchange liquid chromatography separation of the porcine thyroglobulin separation in Figure 3 obtained by summing the total fluorescent signal for each reversed phase run.

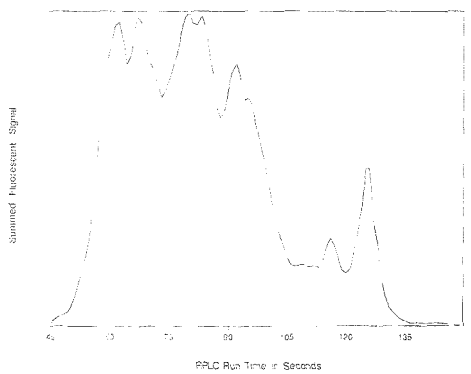

Figure 5. Reconstructed one-dimensional reversed phase liquid chromatography separation of the porcine thyroglobulin separation in Figure 3 obtained by summing the fluorescent signal at the same data point for all reversed phase runs.

digest, such as lysine residues and arginine residues, are not counted more than once. Porcine thyroglobulin, when reduced and fragmented by a tryptic digest, should yield approximately 211 unique peptides per protein dimer.

The two-dimensional chromatogram of porcine thyroglobulin shown in Figure 3 also reveals the high sensitivity of this two-dimensional LC/LC system. The concentration of each fluorescently tagged peptide of porcine thyroglobulin is 4×10^{-4} M. The volume of sample injected onto the anion exchange microcolumn at 67 bar of pressure for 15 s is 4×10^{-8} L. Given these values, the estimated quantity of a single resolved peptide in the two-dimensional chromatogram shown in Figure 3 is 16 pmol. The two-dimensional chromatogram of the tryptic digest of porcine thyroglobulin contains roughly the same number of peaks, 150, as that expected after the digest, 211. The peaks resolved in the chromatogram are most likely single peaks. The peaks shown in Figure 3 do not appear to be uniform in concentration, as depicted by the gray scale imaging. These differences in peak intensity can be attributed to differences in the fluorescent quantum yield of the tagged peptides. They can also be attributed improper cleavages in the tryptic digest.

The usefulness of this two-dimensional LC/LC system for the analysis of samples of limited volume is demonstrated with the two-dimensional chromatogram of a single bovine chromaffin cell shown in Figure 6. The volume of a bovine chromaffin cell is in the order of a few picoliters. Despite this low sample volume, there are several peaks in the chromatogram in Figure 6 that are not attributed to background peaks. Peaks present in the background run are labeled as "B" in the chromatogram in Figure 6. The catecholamine content of single bovine chromaffin cells has been studied previously and determined to be 150 fmol total in epinephrine and norepinephrine.[33] The concentration of most amines present in a bovine chromaffin cell is unknown. The peaks in this chromatogram have not been identified as yet. Standard solutions of epinephrine and norepinephrine separated on this two-dimensional system were found to elute in the dead time of the anion exchange separation dimension due to the lack of a net negative charge on either of these analytes. Because both of these chatecholamines are eluted in the dead time with other positively charged amines they are not resolved adequately for qualitative analysis.

(33) Cooper, B. R.; Jankowski, J. D.; Leszczyszyn, D. J.; Wightman, R. M.; Jorgenson, J. W. *Anal. Chem.* **1992**, *64*, 691–693.

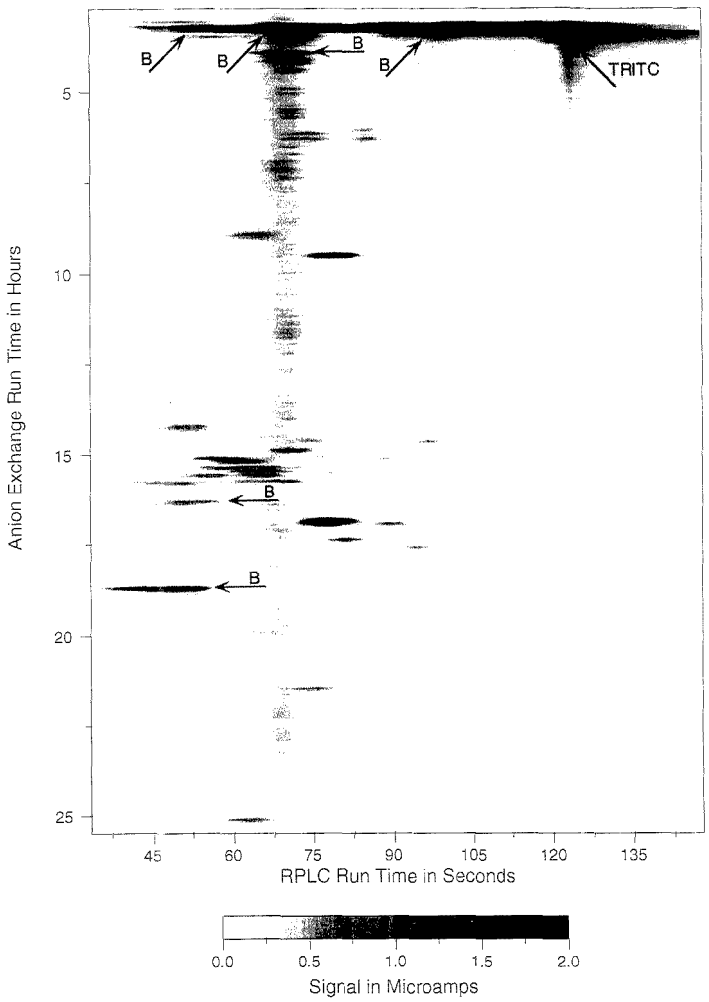

Figure 6. Two-dimensional chromatogram of the amine content of a single bovine chromaffin cell. Peaks labeled with a "B" are present in the background run.

DISCUSSION

The individual separation modes have been improved through the implementation of microcolumns. The length of a chromatography column is important because theoretical plate count increases with column length. Microcolumns on the order of 1 m in length, unlike conventional columns, can be easily fabricated and operated without appreciable band broadening. Microcolumns are also better suited than conventional sized columns for analysis of small sample volumes. This is due to the low mobile phase volume of a microcolumn compared to that of a conventional sized column of similar length. This low mobile phase volume allows small sample volumes to be loaded and run on a microcolumn without diluting the contents of the injected sample so much that it is difficult to detect. Furthermore, the flow of mobile phase through both microcolumns has been manipulated such that the system will operate without interruption of flow. This is beneficial over systems based on stopped-flow methods because interruption in the flow of mobile phase in a chromatographic column will increase longitudinal band broadening, thus decreasing the resolution of the system.

The interfacing of the individual separation modes has focused on the physical transfer of sample and mobile phase from the first separation dimension to the second and on the timing of this sample transfer. The most important aspect of the physical transfer of sample is that all of the analytes eluted from the anion exchange microcolumn are transferred to the reversed phase microcolumn, thus improving sensitivity. The tagged fragments that are eluted from the anion exchange column are diluted in a makeup flow before being injected onto the second column. This dilution serves two purposes. First, it increases the volume of

sample transferred from 82.5 nL to 1 μL, making the direct coupling of the first and second columns more feasible with commercially available electrically actuated valves. This coupling is more feasible with the transfer of a 1 μL loop because valve 1 used in this work requires a minimum transfer of a volume of 0.5 μL. This volume results from valve ports and the rotor slots that turn within the valve, thereby changing the valve port paths. The second advantage of the introduction of the makeup flow is that it dilutes the high organic content of the anion exchange effluent from 50 to 15% acetonitrile. This decrease in the percent acetonitrile contained in the fused silica sample loop, coupled with the increased hydrophobicity introduced to each tagged amine by the presence of the TRITC moiety, allows the sample to be concentrated at the head of the reversed phase. This concentration enables a 3 μL volume to be loaded onto a column that has a total mobile phase volume of 0.1 μL.

The timing of the sample transfer from the first separation dimension to the second separation dimension is critical to the operation of the system. The flow rate of mobile phase through the reversed phase microcolumn is controlled by two factors. The first factor is the minimum sample volume of 1 μL required by the commercial valves. This loop volume of 1 μL as well as an appropriate volume of liquid to flush residual sample from the loop must be loaded onto the reversed phase microcolumn. A minimum flush volume of 2 μL is required by this system to prevent sample carry-over, so that a total volume of 3 μL must be loaded onto the reversed phase microcolumn. In addition, the system is designed so that while the sample is loaded onto the reversed phase column, mobile phase from the anion exchange column is diverted to waste. This loss of sample from the anion exchange column must be kept small relative to the width of any peaks that elute from the column. This means that the loading time of the reversed phase column must be short. A load time of 30 s allows adequate time for loop transfer to the reversed phase column without excessive loss of information from the anion exchange separation. This requirement for 3 μL to be loaded within 30 s dictates the need for a reversed phase mobile phase flow rate of 6 μL/min.

The second factor that determines the flow rate of the mobile phase through the reversed phase column is the maximum pressure the HPLC pump can supply. That is, typical HPLC pumps are not operated above a pressure of 200 bar. The 3 cm long, 100 μm internal diameter microcolumn packed with 5 μm diameter packing material has a back pressure of 167 bar at the flow rate of 6 μL/min. Thus, a mobile phase flow rate of 6 μL/min is near the maximum flow rate the second column can be operated at.

The flow rate of mobile phase through the anion exchange microcolumn is determined according to the required flow rate of mobile phase through the reversed phase microcolumn. This is because the flow rate of the mobile phase in the anion exchange microcolumn must be maintained such that the peaks eluted from this microcolumn are wide enough to be sampled three times by the reversed phase separation. When operated at a flow rate of 6 μL/min, the reversed phase dimension requires a minimum of 150 s for an adequate gradient separation of biological amines. This required 150 s run time when added to the required 30 second load time for each reversed phase run dictates that peaks eluted from the anion exchange dimension must be at least 9 min wide in order to be sampled three times by the reversed phase dimension. The anion exchange dimension must be run over 40 h in order to elute peaks of approximately 9 min peak widths.

The small injection volume of this system coupled with the ability of this system to separate complex samples should allow for practical applications. This has been illustrated in the two-dimensional chromatograms of porcine thyroglobulin and of the contents of a single bovine chromaffin cell. These chromatograms contain a multitude of resolved biological amines. While the amines are well separated, their identity is unknown. It would be advantageous to employ a method of detection that could be used to identify all peaks eluting from the reversed phase separation dimension in real time. This could be accomplished by coupling the two-dimensional system to a mass spectrometer. Mass spectral detection could provide the molecular weight of each separated analyte. Molecular weight information would be useful in the identification of fragments of a protein where the primary sequence is known. The identification of biological amines found in a single bovine chromaffin cell such as dopamine, tyrosine, and other amino acids and enkephalins and other small peptides would be enhanced by mass spectral information.

ACKNOWLEDGMENT

Funding for this research is provided by Grant GM39515 from the National Institutes of Health. The computer and the pump used for the second dimension were donated by Hewlett Packard. The pump used for the first dimension was donated by Waters Associates. The anion exchange and reversed phase packing materials were donated by Rockland Technologies Inc. We thank Showchien Hsieh, Paula Cahill, and Jennifer Finnegan for guidance in the preparation of the bovine chromaffin cells.

Received for review January 27, 1995. Accepted June 21, 1995.[⊗]

AC9501001

[⊗] Abstract published in *Advance ACS Abstracts,* August 1, 1995.

Anal. Chem. 1995, *67*, 3284–3292

Influence of Stationary Phase Chemistry on Shape Recognition in Liquid Chromatography

Lane C. Sander* and Stephen A. Wise

Chemical Science and Technology Laboratory, Analytical Chemistry Division, National Institute of Standards and Technology, Gaithersburg, Maryland 20899-0001

Molecular shape recognition is examined for a series of C_{18} columns prepared using a variety of synthetic approaches. Mono-, di-, and trifunctional silanes are used to prepare stationary phases through monomeric and polymeric surface modification procedures, including an approach employing self-assembled monolayer technology. Shape discrimination properties of the columns were investigated with various nonplanar, planar, and linear polycyclic aromatic hydrocarbon solute probes. Chromatographic retention behavior is examined in the context of recently proposed statistical mechanical "interphase" retention models.

Retention behavior in liquid chromatography is influenced by a wide variety of physical and chemical properties of both the chromatographic system and the solute. The development of retention models reflects an effort to describe the interaction processes between the solute and the stationary and mobile phases which are responsible for retention.[1-4] Differences in separations that are commonly observed among supposedly similar columns have been attributed to differences in silanol activity,[5] carbon loading,[5] substrate composition, stationary phase morphology, and bonding chemistry.[6]

For isomers and other solute classes with similar physical and chemical properties, molecular shape can sometimes provide a basis for separation. Parameters affecting shape selectivity have been studied in some detail by our research group and others,[2-4,7-11] and reviews of shape selectivity have been presented.[12,13] A few trends can be summarized. Shape selectivity is enhanced by increased phase loading, longer chain length bonded phase ligands, reduced column temperature, increased organic modifier composition in the mobile phase, and the use of polymeric phases. The use of mobile phase additives such as cholesterol can also influence shape recognition.[14] However, shape selectivity differences are most strongly influenced by the type of surface modification chemistry employed.

It has been recognized that certain C_{18} columns provide enhanced separations of structural isomers.[15,16] An early example is provided in Environmental Protection Agency (EPA) method 610, for the determination of priority pollutant polycyclic aromatic hydrocarbons (PAHs) from aqueous effluents.[17] This method specifies the use of a specific C_{18} column. Although not recognized at the time, the unique properties of this column were the result of the polymeric surface modification procedure used in the synthesis of the bonded phase, since C_{18} columns prepared using monomeric surface modification chemistry do not exhibit the required selectivity characteristics and are unable to resolve all of the components in the priority pollutant PAH mixture. In general, better separations of PAH isomers can usually be achieved by use of polymeric C_{18} columns than with monomeric C_{18} columns.

The unique chromatographic properties of polymeric C_{18} columns have received surprisingly little attention in the literature, although procedures for the synthesis of polymeric stationary phases were reported over ten years ago[6,18,19] and the columns have been available commercially even longer. However, the advantages offered by polymeric C_{18} columns toward isomer separations are widely recognized by analysts involved in environmental measurement of PAHs,[20,21] as well as the separation of carotenoid isomers.[22-24] Polymeric C_{18} columns have been largely ignored outside of these specialties, perhaps because differences in retention behavior are less dramatic for other classes of compounds, compared with monomeric C_{18} columns. Compounds not constrained to rigid conformations (i.e., with free rotation about single bonds) often exhibit similar retention behavior on monomeric and polymeric C_{18} columns. For example, methylene unit selectivity for alkylbenzene homologs is comparable on monomeric and polymeric column types.[25]

(1) Martire, D. E.; Boehm, R. E. *J. Phys. Chem.* **1983**, *87*, 1045–1062.
(2) Yan, C.; Martire, D. E. *J. Phys. Chem.* **1992**, *96*, 3489–3504.
(3) Yan, C.; Martire, D. E. *Anal. Chem.* **1992**, *64*, 1246–1253.
(4) Dill, K. A. *J. Phys. Chem.* **1987**, *91*, 1980–1988.
(5) Walters, M. J. *J. Assoc. Off. Anal. Chem.* **1987**, *70*, 465–469.
(6) Sander, L. C.; Wise, S. A. *Anal. Chem.* **1984**, *56*, 504–510.
(7) Sander, L. C.; Wise, S. A. *LC-GC* **1990**, *8*, 378–390.
(8) Sander, L. C.; Wise, S. A. *Anal. Chem.* **1989**, *61*, 1749–1754.
(9) Wise, S. A.; Bonnett, W. J.; Guenther, F. R.; May, W. E. *J. Chromatogr. Sci.* **1981**, *19*, 457–465.
(10) Cole, S. R.; Dorsey, J. G. *J. Chromatogr.* **1993**, *635*, 177–186.
(11) Sentell, K. B.; Dorsey, J. G. *J. Chromatogr.* **1989**, *461*, 193–207.
(12) Sander, L. C.; Wise, S. A. *J. Chromatogr.* **1993**, *656*, 335–351.
(13) Dorsey, J. G.; Cooper, W. T. *Anal. Chem.* **1994**, *66*, 857A–867A.
(14) Cole, S. R.; Dorsey, J. G. *44th Pittsburgh Conference on Analytical Chemistry and Applied Spectroscopy*, Atlanta, GA, 1994; Abstr. 1002.
(15) Ogan, K. L.; Katz, E. D. *J. Chromatogr.* **1980**, *188*, 115–127.
(16) Amos, R. *J. Chromatogr.* **1981**, *204*, 469–478.
(17) EPA Test Method, Polynuclear Aromatic Hydrocarbons—Method 610, U.S. Environmental Protection Agency, Environmental Monitoring and Support Laboratory: Cincinnati, OH, 1982.
(18) Majors, R. E.; Hopper, M. J. *J. Chromatogr. Sci.* **1974**, *12*, 767–778.
(19) Verzele, M.; Mussche, P. *J. Chromatogr.* **1983**, *254*, 117–122.
(20) Dong, M. W.; DiCesare, J. L. *J. Chromatogr. Sci.* **1982**, *20*, 517–522.
(21) Fetzer, J. C.; Biggs, W. R.; Jinno, K. *Chromatographia* **1986**, *21*, 439–442.
(22) Matus, Z.; Ohmacht, R. *Chromatographia* **1990**, *30*, 318–322.
(23) Epler, K. S.; Sander, L. C.; Ziegler, R. G.; Wise, S. A.; Craft, N. E. *J. Chromatogr.* **1992**, *595*, 89–101.
(24) Leseliier, E.; Tchapla, A.; Krstulovic, A. M. *J. Chromatogr.* **1993**, *645*, 29–39.
(25) Sander, L. C.; Wise, S. A. *14th International Symposium on Column Liquid Chromatography* Boston, MA, 1990; Abstr. P109.

Table 1. Reaction Conditions and Properties of Stationary Phases

no.	designation	silane functionality	silica (g)	silane	solvent, vol (mL)	reaction time (h)	conditions	% carbon	coverage (μmol/m^2)	$\alpha_{TEN/BaP}$	plates (N)	comments
M-1	monomeric[49]	monochloro	3.50	10.22 g	xylene, 100	23	reflux	12.45	3.51	1.82	9473	2 mL of 2,6-lutidine added
M-2	monomeric	monochloro	3.56	10.35 g	heptane, 100	22	ambient	11.88	3.32	1.78	8812	humidified silica
M-3	monomeric	trichloro	6.94	10 mL	heptane, 110	24	ambient	7.77	2.03	1.43	6694	anhydrous
M-4	monomeric (end cappec)[6]	HMDS	3.55	10 mL	xylene, 100	2	reflux	9.20		1.82	6024	M-3 end capped
P-1	solution polymerized[6]	trichloro	3.5	10 mL	xylene, 100	4	reflux	17.07	5.26	0.73	12258	0.5 mL of H_2O added
P-2	solution polymerized	dichloro	3.15	10 mL	xylene, 100	2	reflux	15.10	4.48	1.48	9940	0.5 mL of H_2O added
S-1	surface polymerized[27,28]	trichloro	3.61	10 mL	heptane, 100	22	ambient	19.84	6.45	0.31	6009	humidified silica
								19.90	6.48			
S-2	surface polymerized[27,28]	trichloro	3.1	10 mL	heptane, 100	16	ambient	19.54	6.32	0.34		humidified silica, replicate of S-1
S-3	surface polymerized	dichloro	3.55	10 mL	heptane, 100	17	ambient	17.31	5.34	1.05	10360	humidified silica
								17.37	5.37			
S-4	surface polymerized	dichloro	3.1	10.3 g	heptane, 100	16	ambient	17.67	5.49	1.04		humidified silica, replicate of S-3
S-5	surface polymerized	trichloro	3.0	10 mL	heptane, 100	7 days	ambient	21.90	7.44	0.35	3423	72 μL of H_2O added
S-6	surface polymerized	trichloro	3.0	10 mL	heptane, 100	7 days	ambient	38.09	19.76			630 μL of H_2O added

Recently Wirth and Fatunmbi reported a procedure for the preparation of mixed alkyl ligand stationary phases with enhanced hydrolytic stability.[26,27] The synthetic approach is based on the self-assembled monolayer research of Maoz and Sagiv[28] and Wasserman et al.[29] These research groups described the reaction of humidified silica with octadecyltrichlorosilane (termed "horizonal polymerization") to yield surfaces with properties comparable to Langmuir–Blodgett films. The surfaces were characterized by ellipsometry and X-ray reflection, and they were found to have a thickness of 22.6–27.6 Å[30] and a surface density of 21 ± 3 Å^2/chain.[29] Wirth and Fatunmbi viewed these surfaces as "much too dense for chromatographic applications", and prepared instead mixed-ligand stationary phases using propyl- and octadecyltrichlorosilane with the intention of increasing the space between individual C_{18} chains.[26,27] NMR studies confirmed the spacing, and chromatographic performance (i.e., efficiency and selectivity) was comparable to monomeric C_{18} columns. Although Wirth and Fatunmbi predicted that horizonal polymerization of octadecyltrichlorosilane would result in surfaces that could not be used in liquid chromatography, we have utilized this approach for the preparation of *homogeneous* self-assembled monolayer phases for comparison to alternative bonding schemes. We have also utilized difunctional silane reagents with both polymeric and self-assembled monolayer modification approaches. Since cross-linking is not possible with difunctional silanes, the type and extent of surface modification can be expected to differ from polymeric phases prepared with trifunctional silanes.

This work describes the preparation of C_{18} stationary phases by a variety of procedures utilizing mono-, di-, and trichlorosilane reagents. A procedure utilizing homogeneous self-assembled monolayer technology will be compared with more conventional monomeric and polymeric syntheses. Selectivity characteristics for each phase will be examined by use of shape-relevant PAH probes, and retention behavior is discussed in light of recently proposed retention models.

(26) Wirth, M. J.; Fatunmbi, H. O. *Anal. Chem.* **1992**, *64*, 2783–2788.
(27) Wirth, M. J.; Fatunmbi, H. O. *Anal. Chem.* **1993**, *65*, 822–826.
(28) Maoz, R.; Sagiv, J. *J. Colloid Interface Sci.* **1984**, *100*, 465.
(29) Wasserman, S. R.; Whitesides, G. M.; Tidswell, I. M.; Ocko, B. M.; Pershan, P. S.; Axe, J. D. *J. Am. Chem. Soc.* **1989**, 5852.
(30) Wasserman, S. R.; Tao, Y. T.; Whitesides, G. M. *Langmuir* **1989**, *5*, 1074.

EXPERIMENTAL SECTION

Materials and instrumentation. Reagents were obtained from the following sources: dimethyloctadecylchlorosilane, methyloctadecyldichlorosilane, and octadecyltrichlorosilane from United Chemical Technologies, Inc. (formerly Hüls America, Bristol, PA); 2,6-lutidine, biphenyl, 1,6-diphenylhexatriene, triphenylene, tetraphenylmethane, and triptycene from Aldrich Chemical Co. Inc. (Milwaukee, WI); pyrene and 1,3,5-triphenylbenzene from Fluka Chemical Co. (Ronkonkoma, NY); *o*-terphenyl from Analabs, Inc. (New Haven, CT); and *p*-terphenyl from Eastman Organic Chemicals (Rochester, NY). PAH isomers having a molecular weight of 278 are from sources previously identified.[31] Standard Reference Material (SRM) 869, "Column Selectivity Test Mixture for Liquid Chromatography", was obtained from the Standard Reference Materials Program (NIST, Gaithersburg, MD). HPLC grade solvents were used in the chromatographic separations. All reagents were used as received without further purification.

Silica used in the preparation of stationary phases was from a single lot of YMC SIL-200-S3 spherical silica (YMC, Inc., Wilmington, NC). This silica has a nominal particle size of 3 μm, a pore diameter of 200 Å, and a surface area of 200 m^2/g. Pore diameter and surface area values determined by the manufacturer for this lot of silica are 174 Å and 200 m^2/g, respectively. Surface coverage values were calculated from carbon determinations, which were carried out by Galbraith Laboratories, Inc. (Knoxville, TN). Commercial C_{18} columns were obtained from the following sources: Zorbax C_{18} from MacMod Analytical Inc. (Chadds Ford, PA), μBondapak C_{18} from Waters (Milford, MA), Cosmosil 5C18-P from Nacalai Tesque (Kyoto, Japan), Phenomenex ODS (20) from Phenomenex, Inc. (Torrance, CA), Beckman ODS from Beckman Instruments (San Ramon, CA), YMC S-5 60Å ODS from YMC, Inc., and Adsorbosphere HS C18 from Alltech Associates, Inc. (Deerfield, IL). Separations were carried out using a liquid chromatograph consisting of a reciprocating piston pump, autosampler, and variable-wavelength ultraviolet absorbance detector.

Bonded Phase Synthesis. A variety of approaches were utilized to prepare C_{18} columns with different characteristics. A summary of these stationary phases and their physical characteristics is presented in Table 1. Monomeric and polymeric

(31) Wise, S. A.; Sander, L. C. *HRC CC, J. High Resolut. Chromatogr. Chromatogr. Commun.* **1985**, *8*, 248–255.

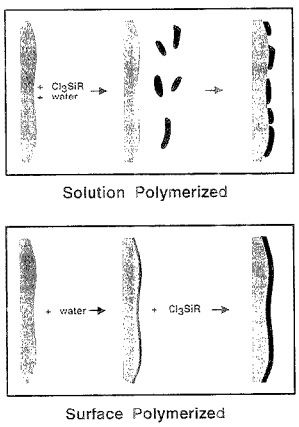

Figure 1. Diagram distinguishing two approaches to the synthesis of polymeric stationary phases. Silane polymerization occurs in solution or at the silica surface, depending on the order of addition of reagents.

syntheses were carried out using procedures similar to those previously described.[6] For all syntheses, silica was dried at 150 °C for 4 h under reduced pressure prior to use. At the completion of each synthetic procedure, the modified silica was filtered and washed with several portions each (~50 mL) of nonpolar and polar solvents. A typical washing sequence was as follows: heptane or xylene, acetone, methanol, water, methanol, and pentane. Columns were slurry packed at 62 MPa (9000 psi) using pentane.

Monomeric synthesis M-1 was carried out by adding silica to a solution of xylene containing the silane. 2,6-Lutidine was added, and the mixture refluxed for 23 h. Monomeric synthesis M-2 was prepared in a similar fashion, except that prior to reaction, the silica was equilibrated with humid air so that a layer of water was adsorbed (termed "humidified silica"). To accomplish this, the silica was placed in a sintered glass frit funnel and aspirated for ~3 h. Using more sophisticated apparatus, Wirth and Fatunmbi[27] demonstrated that a steady state for the surface adsorbed water is achieved within 2 h of exposure (see discussion below). No reaction catalyst was used, and the reaction was carried out under ambient conditions. Monomeric synthesis M-3 was carried out using octadecyltrichlorosilane under anhydrous condition. Sufficient silica was used so that at the completion of the reaction, half of the material could be end capped for comparison (synthesis M-4). The end capping reaction was carried out with hexamethyldisilazane.

The procedures developed for polymeric phase syntheses summarized in Table 1 have been classified as "solution polymerized" and "surface polymerized" to distinguish how water is introduced to initiate polymerization (see Figure 1). For solution polymerization, water is added to a slurry of the silica containing the di- or trichlorosilane. Polymerization occurs in solution, with subsequent deposition onto the silica. Surface polymerization describes a synthetic procedure in which water is added to dry silica either through exposure to humid air or by direct addition, with the "wet" silica introduced into a solution containing the silane. Both procedures have appeared in the literature,[6,19,32] and are used by commercial column manufacturers. Recently, Wirth and Fatunmbi described a procedure for adsorbing a monolayer of water onto dry silica, followed by reaction with a mixture of short and long chain length trichlorosilanes.[26,27] We have used a variation of this procedure to coat silica with water (syntheses S-1–S-4), as well as a different procedure for direct addition of measured quantities of water to silica (syntheses S-5 and S-6).

Synthesis P-1 was carried out by "solution polymerization".[6] The order of addition of reagents and application of reflux influences the reaction, and the procedure is as follows. Dry silica is dispersed in xylene and octadecyltrichlorosilane is added. Water is added and the slurry mixed. Polymerization is allowed to proceed at room temperature for 5 min. Finally, the slurry is heated to reflux for 4 h. At the completion of the reaction, the slurry is filtered while hot so that unbonded silane polymer remains dissolved and can be removed by filtration and washing. Synthesis P-2 was carried out in an identical manner, except methyloctadecyldichlorosilane was used instead of octadecyltrichlorosilane.

Syntheses S-1 and S-2 (replicate) were performed by "surface polymerization". Silica hydrated with an adsorbed monolayer of water was dispersed in heptane, to which octadecyltrichlorosilane was subsequently added. The slurry was allowed to react at ambient temperature, with occasional resuspension. Syntheses S-3 and S-4 (replicate) were carried out under identical conditions, except methyloctadecyldichlorosilane was used instead of the trifunctional silane. Syntheses S-5 and S-6 are surface polymerization reactions in which an excess quantity of water (compared to the amount required for monolayer coverage) was equilibrated with the silica. A weighed quantity of dry silica was equilibrated with humid air to achieve monolayer water adsorption. The silica was again weighed and the mass of adsorbed water determined. This mass was used as the basis for the addition of water in larger amounts. For synthesis S-5, silica was equilibrated with a mass of water equivalent to 2 times a monolayer coverage, and for synthesis S-6, 10 times this mass of water was used. Water was added to the silica with mixing and sealed in a container for 24 h prior to reaction.

RESULTS AND DISCUSSION

We have reported two approaches for the synthesis of polymeric C_{18} bonded phases, distinguished by the order of addition of water to the reaction mixture.[6,33,34] In the first method (solution polymerization), water is added to a solution containing silica and a trichlorosilane, and the slurry refluxed.[6] In the second method (surface polymerization), water is added directly to the silica and equilibrated prior to reaction. This "wet" silica is added to a solution containing the trichlorosilane and the reaction refluxed.[6,34] Columns prepared by this process exhibited poor peak shape and low efficiency, whereas columns prepared by solution polymerization exhibited performance comparable to columns with monomeric bonding. We have observed that surface coverage values in excess of ~6.5 μmol/m^2 are difficult to achieve by solution polymerization, even with the addition of relatively large quantities of water during synthesis.[6] By contrast, surface coverage values can exceed theoretical limits for monolayers with surface polymerization reactions (see reaction S-6, Table 1) and thus suggests the formation of multiple layers.

(32) Sander, L. C.; Wise, S. A. *Crit. Rev. Anal. Chem.* **1987**, *18*, 299–415.
(33) Sander, L. C.; Wise, S. A. *J. Chromatogr.* **1984**, *316*, 163–181.
(34) Sander, L. C.; Wise, S. A. *Advances in Chromatography*; Giddings, J. C., Grushka, E., Cazes, J., Brown, P. R., Eds.; Marcel Dekker: New York, 1986; Vol. 25, pp 139–218.

Surface coverage values for each of the stationary phases are listed in Table 1 and range from 2.0 to 7.4 μmol/m^2. An upper limit to bonded phase density is given by the space requirement for alkyl chains in normal paraffin crystals. This value has been estimated by Nyburg and Lüth to be 20.6 Å^2 (8.08 μmol/m^2), which is also approximately the spacing of silanols at the silica surface.[35] The bonding density for phases S-1 (6.45 μmol/m^2) and S-2 (6.32 μmol/m^2) are somewhat lower than the predicted values; however, the excellent reproducibility of these syntheses suggest that surface hydration was uniform and complete. This discrepancy may be the result of the curvature of the silica within the pores. A similar proposal was made by Berendsen et al. in a description of the effect of surface curvature on bonding density, as a function of alkyl phase length.[36] Berendsen and co-workers observed that the bonding density for monochlorosilanes decreased with increasing ligand length and attributed this trend to the increased space requirement for extended chains bonded to a curved surface. This effect should be most pronounced for narrow-pore substrates and less important with increasing pore size. The surface coverage for synthesis S-6 (carried out with added water in excess of monolayer coverage) was greater than is possible for monolayer coverage. To achieve this level of loading, portions of the stationary phase must consist of bulk-polymerized silane (i.e., silane polymer extending away from the silica surface).

In previous work, the influence of bonding chemistry on retention behavior was demonstrated in some detail for two classes of stationary phases: monomeric and polymeric C_{18} phases. These differences are most apparent for solutes with rigid molecular shapes, such as PAHs. For other classes of molecules (e.g., alkyl hydrocarbons), these differences are less significant. Meaningful evaluation of shape selectivity depends on the selection of appropriate solute probes. Standard Reference Material (SRM) 869 "Column Selectivity Test Mixture for Liquid Chromatography" has been developed for this purpose.[37,38] This mixture consists of three PAHs: benzo[*a*]pyrene (B*a*P; planar shape), phenanthro[3,4-*c*]phenanthrene (PhPh; nonplanar shape), and tetrabenzonaphthalene (TBN; nonplanar shape). The elution order of these compounds has been shown to correlate with stationary phase shape recognition performance and permits classification of phases into monomeric and polymeric categories.[7,37,38] The selectivity coefficient $\alpha_{TBN/BaP}$ is defined as the ratio k'_{TBN}/k'_{BaP} and has been used as a numerical descriptor of shape selectivity. Values of $\alpha_{TBN/BaP}$ typically range from 0.3 to 2.2. For polymeric C_{18} columns, which exhibit a high degree of shape recognition, $\alpha_{TBN/BaP} < 1$, and for monomeric C_{18} columns (low shape recognition), $\alpha_{TBN/BaP} > 1.7$. Selectivity coefficients ($\alpha_{TBN/BaP}$) are listed in Table 1 and will be described below. To supplement the study of retention behavior, additional probes were selected (see Figure 2). These compounds were selected on the basis of differences in retention behavior that are expected to occur for planar and nonplanar, linear and nonlinear, rigid and nonrigid, and square and narrow molecules.

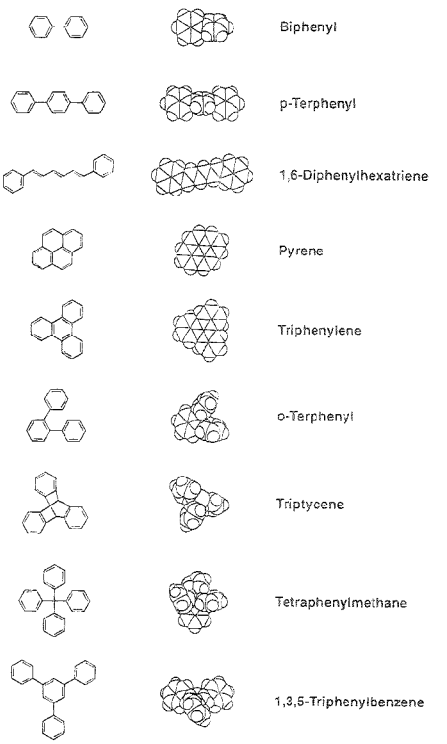

Figure 2. Structures of solute probes utilized in the evaluation of column shape selectivity.

It is instructive to compare the separation of the compounds in Figure 2 for several commercial C_{18} columns (Figure 3). Separations were carried out under the same mobile phase conditions; however, the figure is presented so that retention is normalized to the last component, 1,3,5-triphenylbenzene (time scales remain correct). Even though absolute retention varies by as much as a factor of 4 among the various columns, selectivity for the probes remains remarkably constant. Separation of *o*-terphenyl and pyrene is achieved with only three of the columns, so differences do exist, but overall selectivity is best characterized as similar rather than dissimilar.

Separations of the nine-component mixture are presented in Figure 4 for several of the columns listed in Table 1. The chromatograms are ordered by increasing $\alpha_{TBN/BaP}$ values (top to bottom). The values range from 0.31 to 1.82, indicating changes in elution order of TBN and B*a*P with phase density. The separation for column M-1, monomeric C_{18}, is very similar to the commercial columns shown in Figure 3. It is not surprising that these columns have all been characterized as monomeric in nature in previous studies (selectivity coefficient $\alpha_{TBN/BaP}$ values range from 1.8 to 2.1).[7,37,38] Significant changes in selectivity are apparent among the columns represented in Figure 4. The elution behavior of the last four components is of particular interest. A trend can be observed if the retention of the bulky solutes [tetraphenylmethane (TPM) and 1,3,5-triphenylbenzene (TPB)] is compared with the retention of the extended solutes [*p*-terphenyl and 1,6-

(35) Nyburg, S. C.; Lüth, H. *Acta Crystallogr.* **1972**, *B28*, 2992–2995.
(36) Berendsen, G. E.; Pikaart, K. A.; de Galan, L. *J. Liq. Chromatogr.* **1980**, *3*, 1437–1464.
(37) Sander, L. C.; Wise, S. A. Certificate of Analysis, SRM 869, Standard Reference Materials Program, NIST, Gaithersburg, MD, 1990.
(38) Sander, L. C.; Wise, S. A. *HRC CC, J. High Resolut. Chromatogr. Chromatogr. Commun.* **1988**, *11*, 383–387.

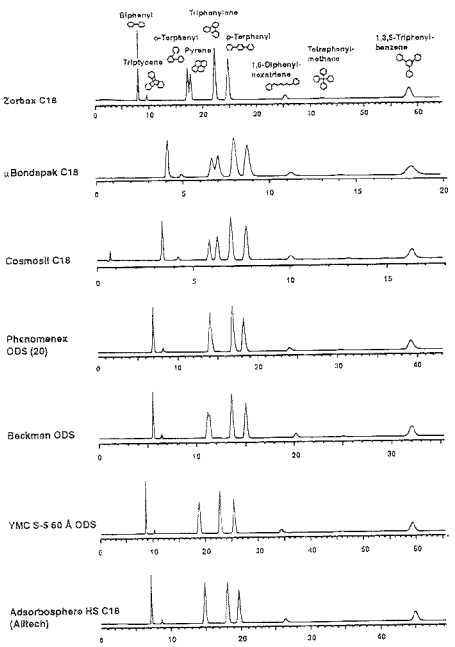

Figure 3. Separation of the nine-component shape selectivity mixture on commercial C_{18} columns. Mobile phase composition, 60: 40 acetonitrile/water.

diphenylhexatriene (DPHT)]. Retention of TPM and TPB decreases relative to *p*-terphenyl and DPHT, with decreasing values of $\alpha_{TBN/BaP}$ (increasing shape selectivity). Similarly, the absolute retention of *p*-terphenyl and DPHT is observed to increase with decreasing $\alpha_{TBN/BaP}$. This change in retention is continuous, and at various intermediate points (e.g., columns P-2, S-3 and P-1), the elution order of these four compounds changes. Pyrene and *o*-terphenyl are separated on all columns except the monomeric column, and the elution of biphenyl and triptycene is unchanged on all of the columns.

The retention behavior observed for the columns in Figure 4 can be discussed in terms of recently advanced models of retention. Martire and co-workers described a model of solute retention based on statistical thermodynamics.[1-3] This model is intended to describe the retention of rigid "blocklike" molecules such as PAHs on ordered stationary phases. Retention depends on repulsive and attractive contributions of the stationary and mobile phase species with the solute molecules and can be expressed in terms of state variables and molecular parameters. Solute parameters include the effective contact area, the van der Waals volume, and the minimum cross-sectional area. This theory predicts that in liquid chromatography shape selectivity should increase with increases in stationary phase order (i.e., chain straightening and lengthening). The following order for shape descrimination among solutes is predicted: rods > plates > flexible chains. An empirical "slot model" of retention was advanced by Wise and Sander based on the retention behavior of planar and nonplanar PAHs.[31] In this model, the stationary phase is represented as consisting of a number of slots into which solute molecules penetrate during retention. For slots of finite size, planar solutes penetrate more slots and will be retained in preference to nonplanar solutes, which are excluded from the slots. By similar reasoning, long narrow molecules with large length to breadth ratios (L/B) will be retained in preference to square molecules.

Both the rigorous treatment of Martire et al.[1-3] and the empirical model of Wise and Sander[31] are descriptive of the trends observed in Figure 4. For the solutes utilized in the test mixture, DPHT has the largest L/B ratio (2.6), and unlike biphenyl and *p*-terphenyl, DPHT is planar. DPHT elutes last for the most densely loaded columns (S-1, P-1), but elutes earlier on the less densely loaded monomeric column (M-1), as might be expected on the basis of its molecular weight. TPM elutes relatively early on the densely loaded columns, which is in accord with its overall "globular" shape. Apparently greater interaction of TPM with the stationary phase results from wider interchain spacing, as with columns M-1 and P-2, and TPM has increased retention. It is interesting to note that the bulky and rigid solute triptycene elutes early with all of the columns, perhaps indicating poor interaction with even relatively widely spaced alkyl chains of the monomeric column M-1. The models of Martire et al. and of Wise and Sander provide logical explanations of the observed trends: bulky solutes elute before planar species, and long, narrow solutes elute after square-shaped species.

Several columns not included in Figure 4 deserve comment. Separation of the nine-component test mixture for the end-capped column M-4 was nearly identical to the monomeric column M-1. We have observed that end capping has little effect on shape recognition for nonpolar solutes.[12] Two of the syntheses were repeated to give an indication of the reproducibility of the procedures. Also, the carbon values for S-1 and S-3 represent duplicate measurements of the same sample, submitted for analysis over a 2-month interval. As indicated in Table 1, columns S-1 and S-2 and columns S-3 and S-4 have nearly identical percent carbon loadings and $\alpha_{TBN/BaP}$ values. This is a good indication that the silica "hydration" step is not a critical parameter (or at least is not difficult to reproduce) in the surface polymerization reactions.

Column S-5, prepared by surface polymerization with silica equilibrated with a 2-fold excess of water (compared to monolayer coverage), exhibited very poor chromatographic performance. Peak tailing was severe for each of the nine solutes, and absolute retention for all of the compounds was significantly reduced. A column could not be prepared from the bonded silica from synthesis S-6 due to complete blockage (i.e., loss of flow) during packing. In general, peak shape appears to be degraded for the most heavily loaded stationary phases (S-1, S-5) and is most severe for strongly retained solutes, particularly with large L/B values. The origin of this effect needs further study; however, the trend would appear to indicate reduced mass transfer and/or overloading of extended solutes within densely loaded stationary phases. NMR and neutron scattering studies have indicated that the mobility of segments of immobilized alkyl chains increases with the distance from the silica surface[39,40] and with decreasing bonded phase density.[41-43] Diffusion within high-density bonded phases may be reduced compared with more conventional stationary

(39) Sindorf, D. W.; Maciel, G. E. *J. Am. Chem. Soc.* **1983**, *105*, 1848–1851.
(40) Beaufils, J. P.; Hennion, M. C.; Rosset, R. *Anal. Chem.* **1985**, *57*, 2593–1596.
(41) Gangoda, M. E.; Gilpin, R. K. *J. Magn. Reson.* **1983**, *53*, 140–143.

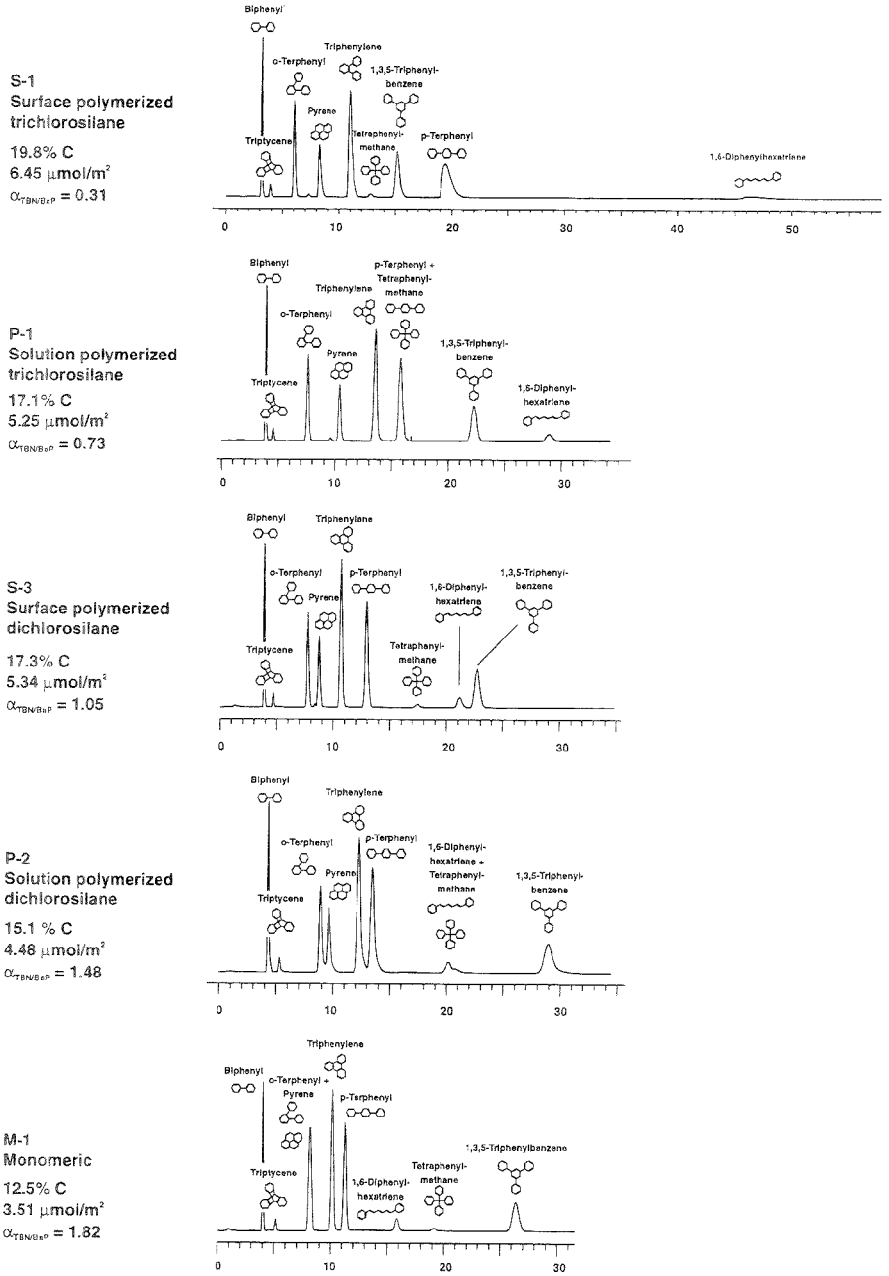

Figure 4. Separation of the nine-component shape selectivity mixture on selected columns listed in Table 1. Mobile phase composition, 60:40 acetonitrile/water.

phases, resulting in peak tailing for highly retained solutes. The efficiency of monomeric (M-1, $N = 9473$) and polymeric (P-1, $N = 12258$) C_{18} columns are comparable (N is the number of theoretical plates, determined from the peak width at half-height for triphenylene). These columns are similar in performance to conventional monomeric and polymeric C_{18} columns from com-

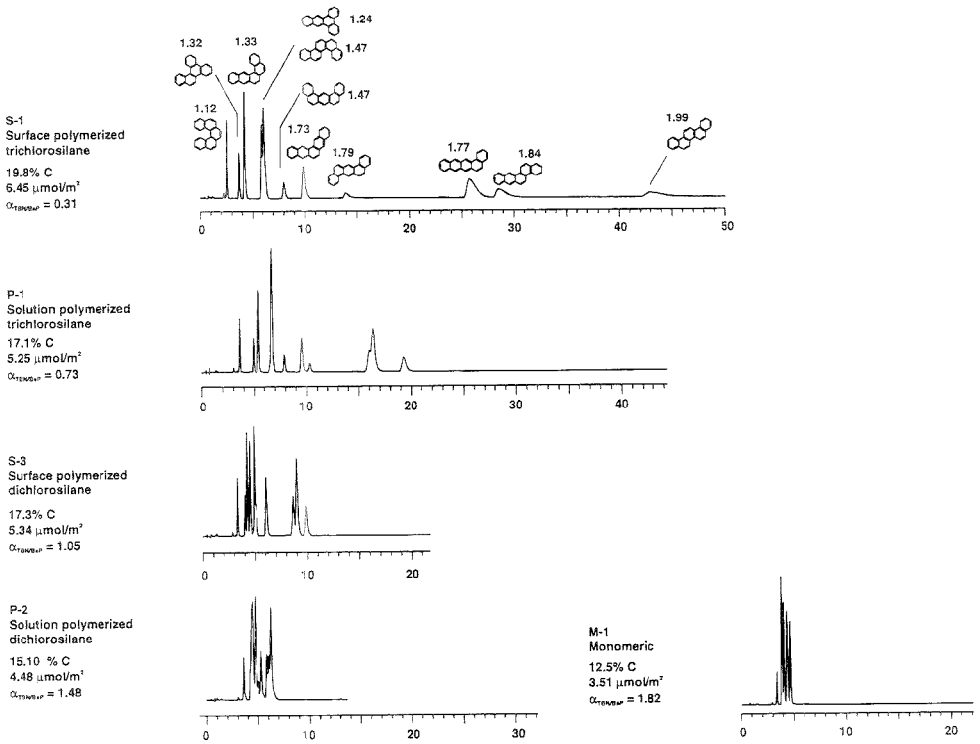

Figure 5. Separation of MW 278 PAH isomers on selected columns. Mobile phase composition, 85:15 acetonitrile/water.

mercial sources. This is contrary to numerous arguments that have been advanced against polymeric C_{18} columns, i.e., that polymeric C_{18} columns are inefficient due to poor mass transfer characteristics of the polymeric stationary phase. These arguments are widely professed *without the support of data*. Since the thickness of typical polymeric C_{18} stationary phases is comparable to monomeric C_{18} stationary phases, mass transfer should not be appreciably different between the two stationary phase types based on differences in stationary phase thickness. The differences in chain mobility determined through NMR experiments for these two phase types[43] do not appear to be sufficient to significantly affect column efficiency. A similar NMR experiment for homogeneous octadecyl self-assembled monolayers would provide additional insight.

An additional comparison of differences in column selectivity is shown in Figures 5 and 6 for the separation of PAH isomers having a molecular weight of 278. PAH isomer mixtures are commonly utilized to illustrate differences in shape discrimination since better separations are usually possible with shape-selective columns.[44,45] The separations in Figure 5 were all carried out under the same conditions, while for Figure 6, mobile phase strength was varied to increase retention on columns with a reduced carbon loading. Significant differences in absolute retention are apparent among the columns, and little separation of the isomer mixture is possible for the monomeric C_{18} column (M-1). Better separations are possible for columns with increasing surface coverage (and decreasing selectivity coefficient $\alpha_{TBN/BaP}$). The use of weaker mobile phase compositions (Figure 6) did not appreciably affect column shape selectivity toward the isomer mixture.

It is interesting to compare columns P-1 (solution polymerized, trichlorosilane, 17.1% carbon) and S-3 (surface polymerized, dichlorosilane, 17.3% carbon). The separations in Figures 5 and 6 for these columns are quite different, yet the carbon loadings and resulting surface coverage values are very similar. Even if the stationary phase loading difference of 0.2% carbon is significant, the trend is opposite that expected, namely, increasing shape recognition and decreasing $\alpha_{TBN/BaP}$ with increasing phase loading. The fact that columns S-3 and P-1 have nearly identical carbon loading but exhibit significantly different chromatographic retention behavior suggests different alkyl chain organization exists between the columns. Two stationary phases with the same carbon loading might exhibit different selectivity if the alkyl chains are spaced differently. A uniform ligand distribution would result in larger interchain spacing than for isolated clusters of ligands.[46] This idea was first proposed by Lochmüller and Wilder, who

(42) Albert, K.; Evers, B.; Bayer, E. *J. Magn. Reson.* **1985**, *62*, 428–436.
(43) Fatunmbi, H. O.; Bruch, M. D.; Wirth, M. J. *Anal. Chem.* **1993**, *65*, 2048–2054.
(44) Wise, S. A.; Sander, L. C.; Lapouyade, R.; Garrigues, P. *J. Chromatogr.* **1990**, *514*, 111–122.
(45) Wise, S. A.; Sander, L. C.; Chang, H.; Markides, K. E.; Lee, M. L. *Chromatographia* **1988**, *25*, 473–480.

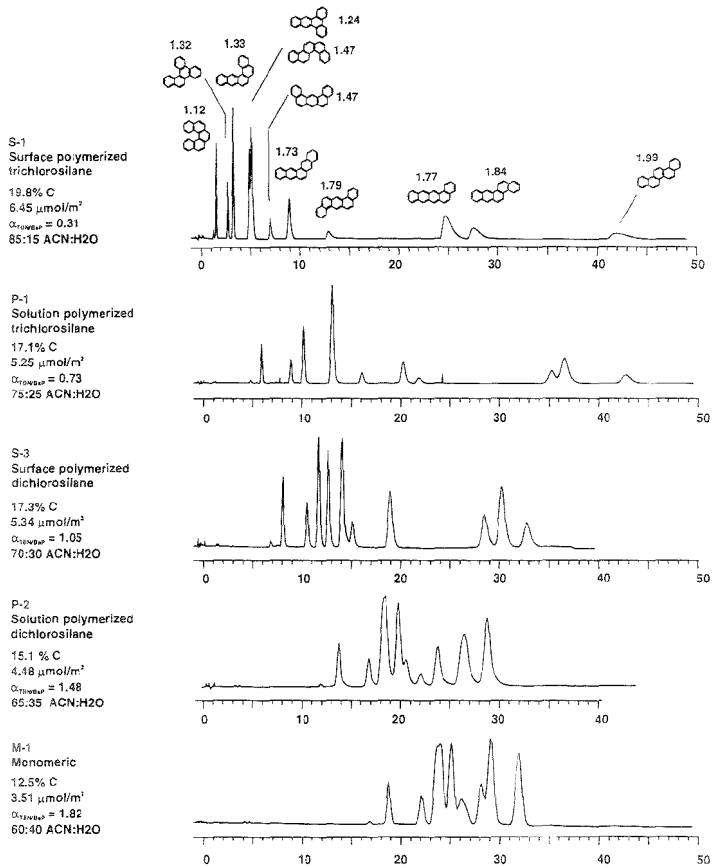

Figure 6. Separation of MW 278 PAH isomers on selected columns. Mobile phase composition has been adjusted to increase retention for columns with lower stationary phase loadings.

described the isolated clusters as liquid droplets.[47] This model is not unreasonable for solution polymerization, for which silane polymers form in solution and are deposited on (and ultimately bonded to) the silica surface (see Figure 1). The distribution of ligands for surface polymerization reactions may be more uniform due to the initial monolayer of water on the silica surface.

A comparison of the absolute retention for various solutes on the different columns provides further insight into solute retention mechanisms. The retention model of Dill[4] predicts that solute retention will increase with stationary phase ligand density to a point, and then at higher ligand densities, retention will decrease as the "energetic cost" of creating a cavity for the solute in the stationary phase becomes large. This retention behavior was observed experimentally by Sentell and Dorsey[48] for a series of monomeric C_{18} phases with stationary phase loadings of 1.6–4.1 μmol/m^2. Surface coverages of monomeric and polymeric columns in Table 1 span a wider range, namely, 2.03–7.44 μmol/m^2. Plots of k' vs surface coverage are shown in Figure 7 for solutes listed in Figure 2. This plot is not directly comparable to the research of Sentell and Dorsey since k' is plotted rather than the partition coefficient K (determination of K requires knowledge of the phase ratio, which is controversial for polymeric stationary phases). In spite of this difference, the fact that a maximum in k' is observed supports the retention model of Dill and is in agreement with the findings of Sentell and Dorsey.[48] It is perhaps more interesting to examine trends in retention suggested by these data. If the curves in Figure 7 are examined carefully, it is apparent that maximum retention occurs at different surface coverage values for different solutes. Several solutes exhibit maximum retention at or near 4 μmol/m^2, whereas other solutes exhibit a maximum at much higher phase loadings. Bulky solutes such as TPB, TPM and *o*-terphenyl are examples of solutes for which maximum retention is observed at lower surface coverages. Extended solutes such as DPHT and *p*-terphenyl exhibit maximum retention at much higher phase loadings approaching 7 μmol/

(46) Lochmüller, C. H.; Colborn, A. S.; Hunnicutt, M. L.; Harris, J. M. *Anal. Chem.* **1983**, *55*, 1344–1348.
(47) Lochmüller, C. H.; Wilder, D. R. *J. Chromatogr. Sci.* **1979**, *17*, 574–579.
(48) Sentell, K. B.; Dorsey, J. G. *Anal. Chem.* **1989**, *61*, 930–934.
(49) Sentell, K. B.; Barnes, K. W.; Dorsey, J. G. *J. Chromatogr.* **1988**, *455*, 95–104.

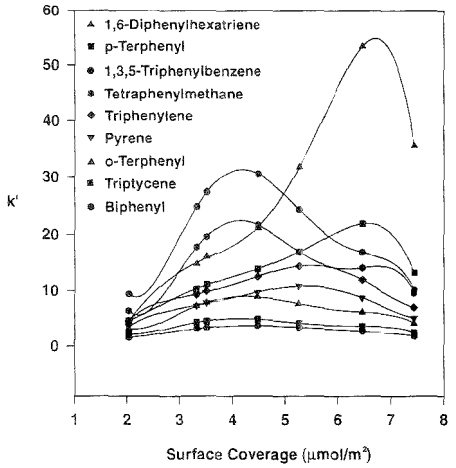

Figure 7. Plot of retention as a function of surface coverage for various C_{18} columns (Table 1) and selectivity probes (Figure 2).

m^2. This retention behavior might be expected on the basis of interchain distances. Bulky solutes should require larger interchain spacing for partitioning within the stationary phase compared with planar or linear solutes.[4] The retention of bulky molecules is reduced for stationary phases with high surface coverages due to the higher energetic cost of cavity creation compared with planar or linear molecules. As the space between bonded alkyl chains decreases, solute/stationary phase interactions are favored for extended and linear solutes.

ACKNOWLEDGMENT

The authors thank Robert Cooley (YMC Inc., Wilmington, NC) for gifts of YMC SIL200 silica. Certain commercial equipment, instruments, or materials are identified in this report to specify adequately the experimental procedure. Such identification does not imply recommendation or endorsement by the National Institute of Standards and Technology, nor does it imply that the materials or equipment identified are necessarily the best available for the purpose.

Received for review April 6, 1995. Accepted June 21, 1995.[*]

AC950345D

[*] Abstract published in *Advance ACS Abstracts*, August 1, 1995.

Anal. Chem. 1995, *67*, 3293–3299

Kinetic Detection of Overlapped Amino Acids in Thin-Layer Chromatography with a Direct Trilinear Decomposition Method

Min Gui and Sarah C. Rutan*

Department of Chemistry, Virginia Commonwealth University, Richmond, Virginia 23284-2006

Armel Agbodjan

Department of Chemistry, North Carolina State University, P.O. Box 8204, Raleigh, North Carolina 27695

Kinetic fluorescence detection (KFD) was employed to determine the concentrations of two overlapped components after a thin-layer chromatographic (TLC) separation. Two amino acids, glycine and glutamine, were used as model analytes. These species exhibited very similar retardation factors (R_f) under our experimental conditions. A reaction that produced a fluorescent product was performed subsequent to the separation. The reaction can be described by the following scheme: amino acid + OPA → fluorescent product → nonfluorescent product. Here OPA stands for *o*-phthalaldehyde. The kinetic profile of the reaction was monitored with a charge-coupled device camera by taking sequential images of the separation medium after the reaction starts. A direct trilinear decomposition (TLD) method was used to analyze the resulting third-order data that consist of fluorescence intensities as a function of elution distance, reaction time, and sample number. This approach was used to determine the initial concentrations of the two overlapped components based on the different kinetics and retention exhibited by these species. This paper discusses the kinetic approach and the applicability and limitations of the direct trilinear decomposition (TLD) method using both synthetic and experimental data. Efforts to optimize the experimental conditions are also reported. The major focus of this work is to explore the application of this novel kinetic fluorescence detection method for TLC separations (TLC-KFD) combined with the TLD data analysis method.

Hyphenated instruments have seen increasing applications in analytical chemistry laboratories in the past few years. These instruments, such as liquid chromatography-UV diode array detection (LC-DAD), gas chromatography/mass spectrometry (GC/MS), and excitation/emission fluorescence have been used for many important analyses. A two-dimensional matrix can be obtained for each sample from these hyphenated or second-order techniques. Based on the two-dimensional data, calibration in the presence of unknown interferents can be performed, which is impossible for zero- or first-order methods. This is the so-called "second-order advantage".[1] Chemometric methods, such as the generalized rank annihilation method (GRAM) and the direct trilinear decomposition (TLD) method,[2] have been developed to extract useful information from the data obtained from second-order instruments. These chemometric methods allow taking the second-order advantage, and they have been utilized to solve several practical problems.[3-8] The present work was dedicated to the evaluation of a novel second-order technique combined with a chemometric method and the application to a chemical problem, in which uncharacterized interferents or background components contribute to the measured response.

Kinetic fluorescence detection subsequent to thin-layer chromatographic separation (TLC-KFD) provides a second-order analytical method.[9] A two-dimensional data array, which is represented as fluorescence intensities as a function of elution distance and reaction time, is obtained for each sample. Combination of the data matrices from several samples constitutes a third-order data array. The TLD method can be used to analyze the third-order data and provide estimates for the real physical factors that underlie the data. In the case of TLC-KFD, the real physical factors are the retention, kinetics, and composition for each component. This approach allows the determination of overlapped species after TLC separation in the presence of unknown interferents.

To test the feasibility of this general analytical approach, two amino acids, glycine and glutamine, were chosen as model compounds. These two species demonstrate similar retardation factors in TLC under our separation conditions. After TLC separation, the species on the separation medium undergo an in situ reaction with *o*-phthalaldehyde (OPA). The reaction scheme is

amino acid + OPA → fluorescent product →
nonfluorescent product

(1) Booksh, K. S.; Kowalski, B. R. *Anal. Chem.* **1994**, *66*, 782A–791A.

(2) Sanchez, E.; Kowalski, B. R. *J. Chemom.* **1990**, *4*, 29–45.

(3) Josefson, M.; Tekenbergs-Hjelte, L. *J. Pharm., Biomed. Anal.* **1991**, *9*, 643–654.

(4) Gemperline, P. J.; Miller, K. H.; West, T. L.; Weinstein, J. E.; Hamilton, J. C.; Bray, J. T. *Anal. Chem.* **1992**, *64*, 523A–531A.

(5) Lin, Z.; Booksh, K. S.; Burgess, L. W.; Kowalski, B. R. *Anal. Chem.* **1994**, *66*, 2552–2560.

(6) Booksh, K. S.; Lin, Z.; Wang, Z.; Kowalski, B. R. *Anal. Chem.* **1994**, *66*, 2561–2569.

(7) Henshaw, J. M.; Burgess, W.; Booksh, K. S.; Kowalski, B. R. *Anal. Chem.* **1994**, *66*, 3328–3336.

(8) Smilde, A. K.; Tauler, R.; Henshaw, J. M.; Burgess, L. W.; Kowalski, B. R. *Anal. Chem.* **1994**, *66*, 3345–3351.

(9) Corcoran, C. A.; Rutan, S. C. *Anal. Chim. Acta* **1989**, *224*, 315–328.

0003-2700/95/0367-3293$09.00/0

The mechanism of this reaction as it occurs in solution has been investigated by several workers[10,11] and can be approximately described by a consecutive first-order reaction model. The formation and decay of the intermediate fluorescent product (λ_{ex} = 366 nm, λ_{em} = 440 nm) was monitored with a charged-coupled device (CCD) camera by taking sequential images of the TLC plate. A third-order data array for this experiment was obtained by stacking the sequential chromatograms of all the samples along the reaction time coordinate. Therefore, the three-way data consisted of the fluorescence intensities as a function of elution distance, reaction time, and sample number.

Both GRAM and TLD methods are useful for analyzing data matrices obtained from hyphenated instrumentation. However, GRAM is restricted to the use of only one standard and one mixture sample at a time. TLD can be used to process a third-order data array which consists of two-dimensional data matrices for several samples (standards and unknowns) simultaneously. Therefore, more precise solutions can be obtained by the signal averaging of multiple calibration standards that occurs when TLD is used. In order to use TLD, the three-way data should obey the trilinear model described in the equation[2]

$$R_{ijk} = \sum_{r=1}^{N} X_{ir} Y_{jr} Z_{kr} + E_{ijk} \qquad (1)$$

where R_{ijk} represent the elements of a third-order data array, which are the fluorescence intensities as a function of retention, reaction time, and sample number, and E_{ijk} indicates the error contribution. In our case, the **X**, **Y**, and **Z** are matrices describing the retention, kinetic, and relative sample composition behavior for each pure component, and each represents a real physical or chemical factor. It has been found that a unique factor analysis decomposition, i.e., a unique solution to **X**, **Y**, and **Z**, can be achieved, given the array R, when the following assumptions are valid: the physical or chemical factors are linearly independent in at least two orders (e.g., **X** and **Y**) and not identical in the third order.[2]

EXPERIMENTAL SECTION

Nine 500 nL samples containing the amino acids glycine and glutamine (Sigma Chemical Co., St. Louis, MO) in the concentration range of 2.5−10 mM were applied to a nonfluorescent, scored, silica gel TLC plate (Catalog No. 4805-411; Whatman International Ltd., Clifton, NJ) using a 2.0 μL syringe (Hamilton Co., Reno, NV) and a TLC spotter Model PS01 (Desaga, Heidelberg, Germany). The plate was dried at 100 °C in an oven, and was subsequently developed using a mobile phase of 1-butanol (Sigma)/acetone (Sigma)/acetic acid (J. T. Baker Inc., Phillipsburg, NJ)/deionized water (7:7:2:4). The development was carried out in a "sandwich"-type chamber. After development for 15 min, the plate was air-dried in the hood for 5 min, followed by oven drying at 100 °C for 10 min. The plate was then dipped in a 0.05% (w/v) solution of *o*-phthalaldehyde (Calbiochem Co., La Jolla, CA) in methanol (EM Science, Gibbstown, NJ), which contained 0.2% (v/v) 2-mercaptoethanol (J. T. Baker Inc.) and 0.09% (w/v) Brij-35 (Eastman Kodak Co., Rochester, NY),[12] and the plate was immediately removed and placed on the imaging stand (Camag, Muttenz, Switzerland) and illuminated with 366 nm light. The CCD camera was a Star I camera system (Photometrics, Tucson, AZ). Images were obtained at 2 min intervals, with integration performed for 30 s. The pixels spanning the complete width of each lane (usually 38 pixels/lane) were summed, and the data were represented as the total fluorescence intensities as a function of elution distance. Hampton and Rutan described this experimental setup in more detail, as it applies to the detection of fluorescent products produced by enzymatic action, after separation of enzymes via gel electrophoresis.[13] Data were obtained for 9 different sample lanes, and for 40 time intervals during the reaction, providing an 87 (pixels, elution distance) × 40 (images, reaction time) × 9 (sample number) third-order array of intensity values. These original experimental data were corrected to eliminate the effects of dark current, uneven illumination, and variation in sensitivities among the pixels, using a dark image and a flat field image. The flat field image was generated by imaging a TLC plate doped with a green fluorophor and illuminated at 254 nm. This procedure has been explained in detail by Hampton and Rutan.[13]

The corrected data array (R) was input into a program written in MATLAB (The MathWorks Inc., Natick, MA), based on the TLD method described by Kowalski.[2] The resulting **X**, **Y**, and **Z** data matrices describe the retention and kinetic behavior, as well as the relative composition, in each sample for each individual pure component.

In the background study, reflectance spectra were obtained using a UV/visible spectrophotometer (Shimadzu Model UV 265).

RESULTS AND DISCUSSION

In the preliminary experiments, the images were taken without a bandpass filter in front of the CCD camera. It was found that the background varied with time during imaging and that the measured signals were dominated by the background. This phenomenon has been observed with TLC plates from different sources. Therefore, the kinetic differences between the two amino acids were overwhelmed by the large, varying background signals and could not be adequately resolved from the experimental data. This led to a careful examination of the background factors, which led to the development of the optimal detection conditions.

Background Study. The purpose of this study was to evaluate the different parameters controlling the background contribution to the overall signal. Factors considered included the use of a bandpass filter (centered at 450 nm with fwhm = 25 nm, S25-450-R-H840; Corion, Holliston, MA), the effects of the wetting degree of the TLC plates, interferences due to the diffuse reflection of the silica surface and the glass stage underneath the TLC plate, and fluorescence due to the glass substrate supporting the silica gel layer. The major contribution comes from the diffuse reflection due to the silica gel. A TLC plate was divided into six regions, as illustrated in Figure 1. Black paper was placed underneath the right half of the TLC plate, and the bottom half of the TLC plate was dipped into methanol before imaging. Regions 3 and 4 were the bare glass substrate without silica gel. Forty images were taken of the TLC plate with an integration time of 17 s, and at an interval of 2 min. The experiment was done

(10) Yoshimura, T.; Kamataki, T.; Miura, T. *Anal. Biochem.* **1990**, *188*, 132–135.
(11) Yoshimura, T.; Kaneuchi, T.; Miura, T.; Kimura, M. *Anal. Biochem.* **1987**, *164*, 132–137.
(12) Schiltz, E.; Schnackerz, K. D.; Gracy, R. W. *Anal. Biochem.* **1977**, *79*, 33–41.
(13) Hampton, R. S.; Rutan, S. C. *Anal. Chem.* **1993**, *65*, 894–899.

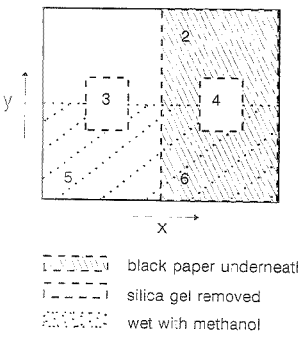

Figure 1. Six regions of the TLC plate evaluated in the background study.

Table 1. Signals from Different Regions in the Background Study

region no.[a]	mean signal without filter	mean signal with filter
1	1.04×10^5	108
2_b	1.01×10^5	29
3_{ns}	6.18×10^4	267
$4_{b,ns}$	1.79×10^4	26
5_w	1.07×10^5	130
$6_{b,w}$	9.40×10^4	70

[a] b, black paper underneath this region; w, wet with methanol before imaging; ns, no silica.

twice, one with the bandpass filter in front of the CCD camera, and one without it. All the images were corrected in the same manner as the actual experimental data using a dark image and a flat field image. The digital signals were summed across 38 pixels over the width of a sample spot and then a mean value and a standard deviation were calculated for each region using 30 pixels along the y direction.

The mean signals of the background from the different regions at the end of the imaging process are summarized in Table 1. It is observed that the bandpass filter reduces the detected signals by more than 99.9% in all cases. This value is consistent with the transmittance of the bandpass filter at 366 nm. On the other hand, the signals listed in Table 1 were obtained when the wet regions were almost dry. Therefore, it is concluded that the detected signal is mainly from the diffuse reflection of the incident illumination (366 nm) from the silica gel and that the bandpass filter suppresses this reflected light significantly. The diffuse reflection from the silica gel dominates the detected signal when no bandpass filter is placed in front of the CCD camera.

Regions 3 and 4 had no silica gel on the glass substrate. Therefore, the difference between the signals from regions 3 and 4 should be due to the effect of the glass stage on which the TLC plate stays during imaging. It is seen that region 4 (where black paper prevents the excitation light from reaching the glass stage) showed significantly lower intensities than region 3 (70% reduction in signal intensity without the filter; 90% reduction in signal intensity with the filter). That means that the glass stage contributes significantly to the background intensity, and the black paper underneath the TLC plate eliminates this factor effectively. However, the signal intensity of region 3 relative to that of region 4 for with filter is higher than that without the filter. The possible explanation is that the glass stage has two effects: reflection of the exciting radiation at 366 nm and fluorescence at a higher wavelength that is closer to 450 nm. Comparing regions 1 and 2 and 5 and 6 leads to the same conclusion. Under conditions when the filter is not present, the intensities from regions 2 and 6 are just slightly lower than those of regions 1 and 5, respectively. The reason is that, without the filter, the diffuse reflection due to the silica gel dominates the detected signals. The effects of the glass stage were not detected. However, with the filter, the fluorescence contribution from the glass stage becomes significant, since most of the reflected light contribution is effectively removed. This can be seen by comparing regions 1 and 2, and 5 and 6 with the filter present.

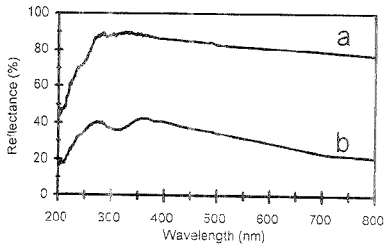

Figure 2. Diffuse reflectance spectra of the TLC plate under (a) dry and (b) wet conditions.

The effects of wetting the silica gel with methanol (the solvent used to introduce the OPA reagent) can be observed by comparing regions 2 and 6 under both filter conditions. Regions 2 and 6 had black paper underneath, and the contribution of the glass stage to the background signal was removed. When the filter was not used, region 6 gave lower intensities than region 2. This is because diffuse reflection is the major background contributor in this case, and wetting the silica gel decreases the diffuse reflection. However, in the case with the filter, region 6 showed a significantly higher signal than region 2. A plausible explanation is that the wet region 6 fluoresces at a wavelength close to 450 nm. Therefore, it is concluded that wetting the TLC plate has two effects. First, the diffuse reflection due to the silica gel is reduced, and hence, the transmittance of the incident light is increased (366 nm). This explanation was confirmed by measuring the diffuse reflection due to the silica gel under dry and wet conditions. Figure 2 shows the reflectance vs wavelength for a TLC plate under dry and wet conditions. It can be seen that the reflectance is lower under wet conditions as compared with dry conditions overall. Second, the transmitted light induces fluorescence of the glass, and the wet silica gel also allows this fluorescence emission to be transmitted and detected by the CCD camera. The TLD results shown in the subsequent section support this interpretation.

One of the goals of this study was to optimize the detection system in order to minimize the background contribution. Based on the above discussion, the black paper underneath the TLC plate and the bandpass filter successfully eliminated the effects of the glass stage and minimized the diffuse reflection due to the silica gel. In fact, regions 2 and 6 represent the signals obtained under the optimal conditions. Note that the intensities listed in Table 1 represent the sum of intensities from 38 pixels. Therefore, under

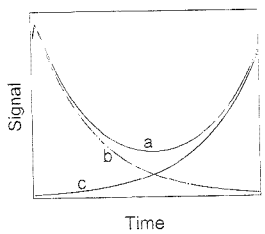

Figure 3. Background factors: (a) total background signal; (b) glass fluorescence signal; and (c) diffuse reflection due to the silica gel.

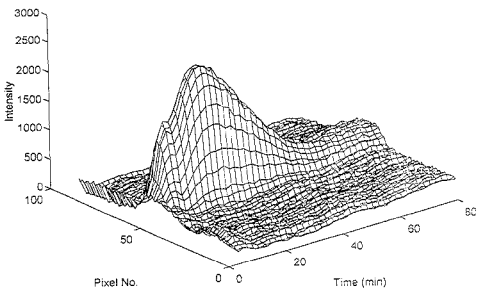

Figure 4. Experimental data for a representative mixture sample.

optimal conditions, the mean background signal detected by each pixel is only a few counts.

This study was also aimed at understanding the time-dependent background variations observed in the preliminary experiments. Curve a in Figure 3 represents the kinetic curve for a wet region under optimal conditions (black paper on the glass stage, and bandpass filter). Note that the extent of wetting of the silica gel changes with time due to evaporation. It appears that this kinetic curve can be decomposed into two factors, represented by curves b and c. A plausible model is that curve b is caused by changes in detected fluorescence due to evaporation of methanol, and curve c is the diffuse reflection due to the silica gel. The diffuse reflection increases as the wetting degree of a TLC plate decreases. During imaging, the wetting degree decreases because of evaporation. Therefore, curve c is assumed to represent this changing factor. As discussed above, the fluorescence from the glass substrate can not be removed since this background fluorescence wavelength is close to the emission maximum (440 nm) of the products monitored during the reaction between amino acids and OPA. Moreover, this fluorescence intensity varies with the degree of wetting. When the TLC plate becomes completely dry, no fluorescence is seen. Therefore, curve b represents this factor. This fluorescence is therefore not a serious interference. Although other fluorogenic derivatization reagents could be used to shift the detected signal away from this interference, the OPA derivatives used here provide us with the best chance of observing the different reaction rates required for kinetic resolution of overlapped zones.[10-12] Note that the variations in both background factors discussed above are related to wetting. They cannot be removed since the reaction between amino acids and OPA has to be carried out under wet conditions on the TLC plates. This requirement has been confirmed experimentally. On the other hand, evaporation during imaging is unavoidable. The evaporation process is hard to control and may vary from one experiment to another. Therefore, the background kinetics may exhibit slightly different profiles from Figure 3, but the overall kinetic trend for the background is always similar to curve a in Figure 3. However, this variable background does not prevent us from applying the TLC-KFD method to this specific system, since the chemometric method, TLD, has the capability of resolving the varying background factors from the analyte signal as long as the background factors are relatively consistent in behavior in all the sample lanes for one experiment. Mathematically, the TLD algorithm treats the changing background factors as additional components. An understanding of the background factors is very helpful in interpreting the output from the TLD algorithm.

Experiments with Amino Acids. The experimental procedures were as described in the Experimental Section, but the detection system was optimized as described in the previous section with the bandpass filter in front of the CCD camera and the glass stage covered with black paper. Figure 4 shows a representative data matrix from a TLC-KFD experiment obtained for a single sample, expressed as fluorescence intensity as a function of elution distance (pixel number) and reaction time (min). For each experiment, nine samples were applied to the TLC plate. Therefore, a three-way data array can be constructed from these nine data matrices. Analysis of the three-way data array using the TLD algorithm yields three two-dimensional matrices, **X**, **Y**, and **Z**, as shown in Figure 5. These profiles describe the chromatographic behavior, kinetics, and relative contribution of each physical component, respectively. For our experimental data, it was found that the best results (i.e., the most chemically reasonable) were obtained when four components were assumed to be present. These components were identified as being due to the two background components, and the products of the glycine–OPA, and glutamine–OPA reactions, respectively. This interpretation was based on our understanding of the background factors and observation of the kinetic and elution behavior of the pure samples. Both glycine and glutamine were observed to react with OPA to form an intermediate fluorescent product, followed by a decay process. Glycine demonstrated faster reaction kinetics than glutamine. On the other hand, glycine was retained more than glutamine on the TLC plate under our separation conditions. The retardation factors (R_f) for glycine and glutamine are 0.33 and 0.35, respectively.

Calibration was performed using the two-dimensional matrix depicted in Figure 5C. Both the actual (standard) concentration and predicted concentration (from a linear least squares fit) for each sample are listed in Table 2. Small concentrations for glutamine in samples 1–3, and glycine in samples 4–6 were "predicted", when actually their concentrations should be zero. That is attributed to the experimental noise and the similarity of the kinetic and elution behaviors between glycine and glutamine. A summary of the calibration results from three different experiments is shown in Table 3. Experiments 1a and 1b were performed on the same day, and experiment 2 was done on a different day. It can be seen that the reproducibility of this experiment is adequate, but the accuracy and precision of the concentration prediction are only moderate. The reason may be that the two amino acids have relatively similar kinetic profiles and their elution distances are extremely close. In fact, their elution distances differ by only 5 pixels (0.7 mm on the TLC plate).

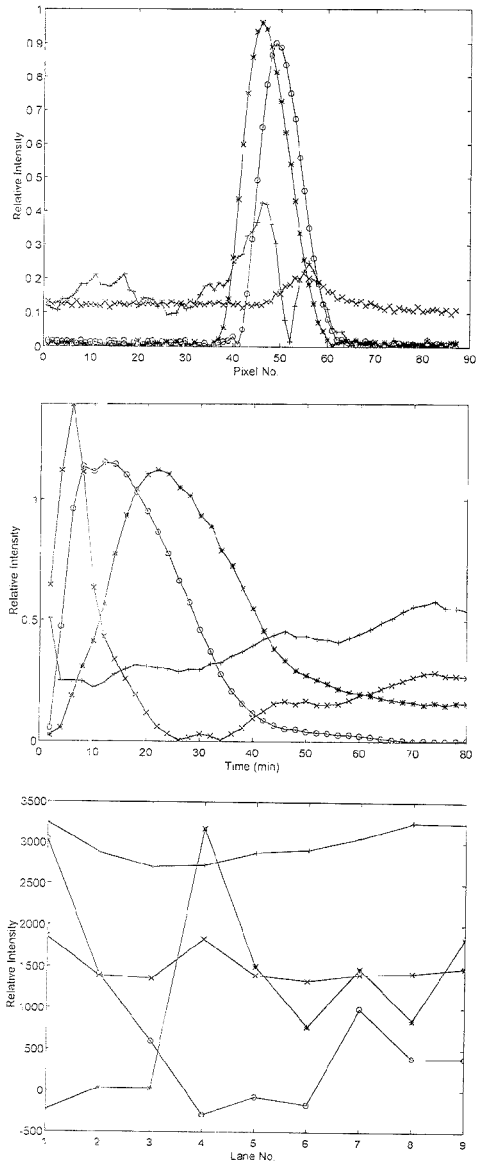

Figure 5. TLD output: TLD estimates for (A, top) pure component chromatograms, (B, center) pure component kinetic profiles, and (C, bottom) relative contributions from each component. (O): glycine; (*) glutamine; (+) and (×) background factors.

The resolution of the TLC chromatographic separation can be seen by comparing the chromatograms shown in Figure 6A–C. Generally, the prediction for the glutamine concentration is more accurate than for glycine. This may be due to the kinetic similarity of glycine with one of the background factors. Another reason may be that the reaction kinetics for glutamine are slower than those for glycine. Therefore, the kinetic data for glutamine span a longer time period and provide more information than the kinetic data for glycine.

Table 2. Calibration of Glycine and Glutamine Concentrations Using TLD

	glycine (mm)		glutamine (mm)	
sample no.	actual	predicted	actual	predicted
1	10.0	11.9	0	0.8
2	5.0	5.4	0	0.1
3	2.5	2.3	0	0.0
4	0	1.1	10.0	10.2
5	0	0.3	5.0	4.8
6	0	0.6	2.5	2.5
7	5.0	3.8	5.0	4.8
8	2.5	1.5	2.5	2.7
9	4.0	1.5	6.0	5.9

Table 3. Relative Standard Deviation (RSD) of the Slopes of the Calibration Curves for Glycine and Glutamine

	% RSD	
expt no.	glycine	glutamine
1a	9.7	2.2
1b	11	12.8
2	11	7.1

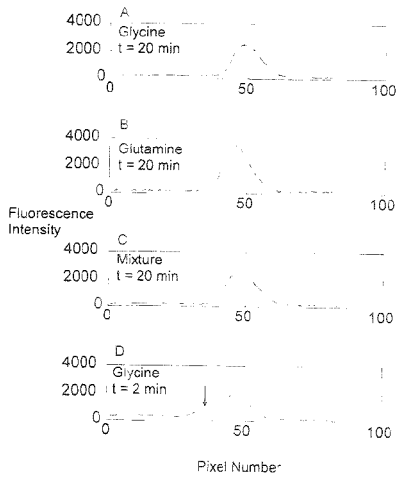

Figure 6. Chromatograms of (A) glycine at $t = 20$ min, (B) glutamine at $t = 20$ min, (C) glycine/glutamine mixture at $t = 20$ min, and (D) glycine at $t = 2$ min, where the arrow indicates the impurity.

Another problem with these experiments was that each sample spot had an extra spot appearing on the plate directly above the main spot. These extra spots exhibit relatively low fluorescence intensities and disappear within 10 min after the reaction starts. The chromatogram shown in Figure 6D is a chromatogram of glycine after only 2 min of reaction time, where the arrow points out the impurity. This may be another reason for poor accuracy in concentration prediction. Efforts have been put into identifying the source of these extra spots. Originally, these extra peaks were thought to be caused by the dipping process. Dipping was

performed along the mobile phase elution direction. This may cause migration of the sample spots on the TLC plate during the dipping process via a mechanism similar to the development of a TLC plate. Therefore, dipping the plates perpendicular to the mobile phase direction and dipping horizontally were also tried. The extra peaks showed up as before in these two experiments, so that the dipping method does not account for these spots. Other potential causes, such as the impurity of reagents, the presence of the preabsorbent band on TLC plates, and the type of development vessel have also been evaluated. Freshly purchased amino acids from Lancaster, as well as recrystallized samples, were tested. Application of the samples above the preabsorbent band, and the use of a full-sized development tank instead of the "sandwich" type development chamber (which was used in our experiments generally), have also been tried. It was found that the extra bands showed up in all of the above experiments. The source of these bands remains an unresolved problem.

The TLC-KFD experiment was also performed with one pure sample of glycine and glutamine, and seven mixtures, as well as two pure samples of glycine and glutamine, plus five mixtures. It was found that when only one pure sample of each kind was present, the TLD results were very poor, but when two pure samples of each were applied, the TLD results were comparable to the results obtained for the experiment with three pure samples of each analyte (shown in Table 2). Since the kinetic and chromatographic behaviors of the two analytes, glycine and glutamine, are very similar, one pure sample of each analyte may not provide enough information for the TLD algorithm to resolve the two different species.

Computer Simulations. Computer simulations were performed in order to better understand the reasons for the results discussed above. First, we wanted to see whether the number of pure samples of each analyte included in the experimental design affected the capability of the TLD algorithm. The plots in Figure 5A,B and the concentration profiles for the two background components in Figure 5C were used to generate the synthetic data. Note that panels A–C of Figure 5 were obtained from the output of the TLD algorithm for real experimental data. The concentration profiles for the two analytes were varied to mimic different experimental designs for the calibration standards. It was found that when no noise was added to the simulated data, the TLD algorithm could reconstruct these data even for the case when no pure samples were present, as long as the concentration profiles for the two analytes were linearly independent. However, when Gaussian-distributed noise with a standard deviation of 80 (the standard deviation for experimental data) was added to the synthetic data (S/N = 51), the output from the TLD program was not consistent with the profiles used to construct the data. Therefore, it was concluded that noise is one of the factors that affects the capability of TLD program. However, at the same noise level, the TLD algorithm reconstructed the synthetic data with one pure sample of each analyte very well. As mentioned before, the TLD program did not provide good calibration curves for the real experimental data that had only one pure sample of each component. The reason may be that, in the actual experiments, migration and spreading of the sample spots during imaging might occur, and the interaction between the two analytes might affect the kinetic and chromatographic behavior of each analyte. These factors were not included in the simulated experiment. This is probably also the reason that the calibration curves for the experimental data with three pure samples were not significantly better than the results obtained when two pure analyte spots were present. On the basis of the above computer simulations and evaluation of the experimental data, it is recommended that improving the S/N ratio, minimizing migration and spreading of sample spots during imaging, and application of as many pure samples of each analyte as possible on each TLC plate would improve the quality of the calibration obtained using the TLD algorithm.

The TLD method requires that physical factors be linearly independent in at least two of the three directions. These two directions are considered to be more informative than the third one (referred to as the z direction). We would like to know how this requirement affects our experimental design. Our TLD program was designed to allow us to assign the least informative direction for our experimental data. Therefore, there are three ways to analyze our experimental data using TLD, since any one of the three directions can be assigned as the least informative direction. In the following computer simulations, the synthetic data sets were analyzed using all the three methods. For this TLC-KFD approach, the real physical factors are the kinetic, chromatographic, and concentration variations of glycine, glutamine, and the background factors. For this next set of computer simulations, the data were generated the same way as described above, including noise, unless stated differently. Through our computer simulations, we found that the TLD could not reconstruct the profiles used to generate the data for the following three cases: (1) when the concentration profiles for the two analytes used to synthesize the data were linearly dependent on each other, but the kinetic and chromatographic curves for the two analytes were different, (2) and (3) when either the kinetic or the chromatographic profiles for the two analytes were the same, but the concentration profiles were linearly independent. When the chromatographic and kinetic matrices resulting from the TLD algorithm match the original curves used to generate the synthetic data, and a linear calibration curve is obtained, the TLD is considered to reconstruct the original data. From cases 2 and 3, it is seen that the concentration composition direction is generally the least informative under our experimental conditions. This is due to the fact that, along the concentration composition direction, there are the fewest data points (only nine data points). For the glycine and glutamine experiment, the kinetic and chromatographic behaviors of the two analytes are not the same. Therefore, the restriction imposed by the TLD algorithm on our experiment design is that the concentrations of glycine and glutamine should not be linearly dependent with one another in the nine samples. This can be avoided in our experimental design, at least for known calibration samples.

CONCLUSIONS

It has been demonstrated that the TLC-KFD method combined with the TLD algorithm is suitable for the determination of two overlapped amino acids, glycine and glutamine. The capabilities and limitations of the TLD algorithm in this application have been analyzed with computer simulations. The glycine/glutamine two-component model mixture represents the case of highly overlapped chromatographic peaks and high similarity in kinetic behavior. On the basis of our experimental results for glycine/glutamine mixtures, and the computer simulations, it can be concluded that, for other unresolved amino acid–OPA derivative combinations, if the differences in chromatographic separation and

reaction kinetics are enhanced compared with our test mixture system, and the S/N ratio could be maintained, the reliability of the established method should be improved upon. Our computer simulation results provide guidelines not only for the glycine/glutamine model system but also for separation of other classes of unresolved analytes using a similar approach.

It is worth mentioning that quantitative analysis with the TLD method can be achieved without making a priori assumptions about the specific characteristics of the resulting kinetic and chromatographic profiles for each individual component. This is a great advantage in the determination of two overlapped species using TLC-KFD approach, since in these experiments the background exhibits kinetics and the kinetic behavior of the background and the analytes may not be reproduced exactly from one experiment to another. Establishing a kinetic model for the different components mathematically or experimentally is almost impossible. Considering these difficulties with the TLC-KFD method, the TLD algorithm is nearly a perfect data analysis method for our experiment. Compared with "hard modeling" approaches, the TLD method imposes many fewer restrictions on experimental conditions, but requires data from multiple sample lanes for analysis. Calibration can be achieved through evaluation of the output from the TLD program directly. Compared with hard modeling methods, TLD takes much less time for data analysis.[14] It takes about 2 min for TLD to analyze one set of experimental data of nine samples vs about 45 min for a hard modeling method.[14] Generally, this TLD method is applicable to any multidimensional chromatographic technique where the signals combine in a linear fashion.

(14) Gel, M.; Rutan, S. C. *Anal. Chem.* 1994, *66*, 1513−1519.

ACKNOWLEDGMENT

We thank Dr. P. J. Gemperline for his help in the development of the TLD program and acknowledge financial support from the Department of Chemistry at Virginia Commonwealth University and the U.S. Department of Energy.

Received for review April 3, 1995. Accepted June 21, 1995.[⊗]

AC9503320

[⊗] Abstract published in *Advance ACS Abstracts*, August 1, 1995.

Anal. Chem. **1995**, *67*, 3300–3304

Determination of Partition Coefficients and Quantitation of Headspace Volatile Compounds

Alain Chaintreau,* Andrea Grade, and Rafael Muñoz-Box

Nestle Research Centre, NESTEC Ltd., P.O. Box 44, Vers-Chez-les-Blancs, 1000 Lausanne 26, Switzerland

A survey of partition coefficient values reported in the literature showed numerous discrepancies. These could be attributed to technical problems encountered during headspace measurements. Consequently, a novel method based on a combination of static headspace sampling and dynamic headspace traps was developed. The new method also includes determination of partition coefficients independently of the concentration of the reference. Once the partition coefficient is known, a simple calibration of the gas phase constituents can be performed. This headspace quantification method does not require addition of a standard. Estimation of variance showed the method to be accurate (0.5–15%, depending on component and matrix). A model mixture of flavors was investigated by the new method. Varying the concentration of one compound had no effect on the rest of the aroma profile. Small differences in the aroma profile due to changes in the matrix were investigated as exemplified by alterations in flavor retention observed when water, lipids, or emulsions were used as the solvent.

The aroma of the gas phase in equilibrium with a food or a beverage is a key parameter that influences the choice of a consumer who opens a package. Similarly, the flavor released by the food when preparing a meal or when chewing will also determine consumer preference. Both require quantitation of the aroma components in the gas phase, as well as measurement of the partition coefficients between air and the matrix. However, if we consider the literature, quantitation in the gas phase appears to be a hard task.

During the last decade many improvements have been made in headspace (HS) sampling, and automated HS injectors are now commercially available. HS is generally classified into two categories: static headspace (S-HS), in which the vapor phase is directly injected in a gas chromatograph, and enriched (or dynamic) headspace (E-HS), which requires trapping of the volatiles onto an adsorbant prior to GC injection. The HS analysis of plants and flowers has been reviewed by Bicchi and Joulain[1] while Seto recently described the biological applications.[2]

Quantification. While E-HS offers a better sensitivity than S-HS, it is generally not suitable for quantitation of headspace components as release of the volatiles in the gas phase is strongly dependent on their interaction with the matrix. In other terms, the headspace composition is related to the air-to-matrix partition coefficients of each compound.

Among the different quantitation methods that have been proposed, the most appropriate seems to be multiple headspace extraction (MHE) using S-HS sampling.[3–8] Kolb[4] proposed two MHE calibration methods, using an internal or an external standard:

External Standard. The calibration mixture must be contained in a vial as a gas phase only without any solvent. This limits the calibration to very volatile compounds, and it requires the measurement of very small volumes which cannot be accurate.

Internal Standard. The GC response coefficients must be determined separately in the same matrix. If matrices differ, partition of the flavorings and of the standard in both phases will change. Stable isotope-labeled standards appear to be the only alternative since their behavior will be similar to that of the nonlabeled molecules.

In conclusion, calibration for headspace quantitation remains either tedious (labeled standards) or inaccurate (external standards or nonlabeled internal standards).

Errors in Partition Coefficient Measurements. Great discrepancies appear between the values measured by different authors (Table 1). Drawbacks were found in all methods proposed if they had to be applied to the low-concentration range found in the headspace above foods.

Dynamic Methods. Burnett[9] used a stripping gas to extract the volatiles from the solution. The partition coefficient is mathematically deduced from a dynamic process rather than from a system at equilibrium. Efficiency of the stripping step should be previously ascertained.

Pressurized Vials. Kolb et al.[10] pressurized the headspace of the sample vial prior to injection. This can modify the partition of the solute between phases, and values are higher than in systems operating at atmospheric pressure (Table 1). However, other important parameters are probably responsible for the great difference of hexane values (1400%), since all authors used different operating conditions.

Glass Syringes. Wall adsorptions and leaks occur when operating with syringes.[11,12] They may seriously alter the results (up to 80% nonanal absorbed[9]) when operating in the usual ppm range of flavors in a food matrix, which corresponds to the ppb range in the gas phase.

(1) Bicchi, C.; Joulain, D. *Flavour Fragrance J.* **1990**, *5*, 131–145.
(2) Seto, Y. *J. Chromatogr.* **1994**, *674*, 25–62.
(3) Milana, M. R.; Maggio, A.; Denaro, M.; Feliciani, R.; Gramiccioni, L. *J. Chromatogr.* **1991**, *552*, 205–211.
(4) Kolb, B. *Chromatographia* **1982**, *15*, 587–594.
(5) Hagman, A.; Jacobsson, S. *HRC CC, J. High Resolut. Chromatogr. Chromatogr. Commun.* **1988**, *11*, 830–836.
(6) Bosset, J. O.; Gauch, R. *J. Chromatogr.* **1988**, *456*, 417–420.
(7) Uhler, A. D.; Miller, L. J. *J. Agric. Food Chem.* **1994**, *36*, 772–775.
(8) Maggio, A.; Milana, M. R.; Denaro, M.; Feliciani, R.; Gramiccioni, L. *HRC CC, J. High Resolut. Chromatogr. Chromatogr. Commun.* **1991**, *14*, 618–620.
(9) Burnett, M. G. *Anal. Chem.* **1963**, *35*, 1567–1570.
(10) Kolb, B.; Welter, C.; Bichler, C. *Chromatographia* **1992**, *34*, 235–240.
(11) Vitenberg, A. G.; Ioffe, B. V.; Dimitrova, Z. St.; Butaeva, I. L. *J. chromatogr.* **1975**, *112*, 319–327.
(12) Guitart, R.; Puigdemont, A.; Airboix, M. *J. Chromatogr.* **1989**, *491*, 271–280.

0003-2700/95/0367-3300$9.00/0

Table 1. Air-to-Water Partition Coefficients from Literature Data

	k	temp (°C)	ref	method
2-butanone	1.9×10^{-3}	25	13	gas loop/atm pres
	3.9×10^{-3}	30	10	pressurized vial
	2.3×10^{-3}	25	11	syringe/atm pres
1-butanol	8.5×10^{-4}	30	10	pressurized vial
	2.95×10^{-4}	25	9	stripping/atm pres
	3.6×10^{-4}	25	13	gas loop/atm pres
ethyl acetate	1.6×10^{-2}	40	10	pressurized vial
	0.9×10^{-2}	40	12	syringe/atm pres
n-hexane	7.14	40	10	pressurized vial
	58	40	12	syringe/atm pres

Calibration. All methods are faced with this difficulty already mentioned above. Most calibrate the gas phase by fully vaporizing a small amount of the pure compound in an empty vial.[10,11,13,14] Accurate measurement of small volumes is difficult, and full vaporization is limited to highly volatile components. Direct injection of the standards in a solvent is sometimes used.[9,15] It assumes that the GC response factors must be identical when a vapor phase or a solution is injected.

Theoretical Calculations. Rohrschneider starts from a calculated partition value.[16] Unfortunately, Voilley et al. have shown discrepancies of 23–60% between experimental data and calculated coefficients.[17] In addition, thermodynamic models do not apply when the solutes are highly water soluble, which often happens with flavors.

Dilution. In spite of the good linearity of the calibration curves, Eztweiler's apparatus, used by Graf,[18] did not seem suitable because sampling large volumes would lead to a dilution of the gas phase by air entering the system.

EXPERIMENTAL SECTION

Sampling Cell. The sampling cell (Figure 1) is formed of a 5 cm × 15 cm glass tube (d) (Omnifit, Cambridge, U.K.). The bottom end piece (e) and the end of the piston (f) were made in-house with Teflon and Viton seals. A removable glass receptor (g) was inserted into (e), to receive up to 2 mL of the solution to be equilibrated with the headspace.

Before use, all glass pieces of the modified syringe were silanized with Sylon CT (5% dimethylchlorosilane in toluene) (Supelco, Bellefonte, PA) to avoid any adsorption effects on the glass walls.

The volume has been calibrated by filling the cell with water, pressing the piston down, and weighing the expelled water. There was almost no dead volume when the piston was at the bottom.

To verify that no significant gas diffusion occurred through the tube (h), a Tenax trap was connected, and the cell was equilibrated for 30 min with a 22 ppm solution of 2-butanone in the receptor. The trap was then disconnected without pressing the piston and desorbed into the GC. No peak was detected.

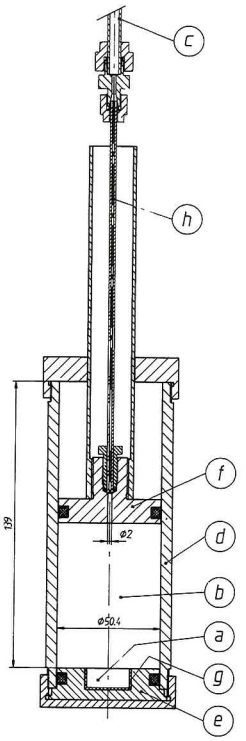

Figure 1. Headspace cell.

All solutions were prepared at concentrations between 2 and 150 ppm. For the measurement of the influence of increasing one compound, the concentration of this compound was chosen to be 5000 ppm. The solvents used were deionized water, medium chain triglycerides (MCT), soja oil, or milk as an oil in water emulsion. The milk contained 2.8 g of milk fat in 1 dL and was partially skimmed.

Headspace Sampling. At the beginning of each experiment, a blank of the sampling cell was made. After that 1 or 2 mL of the prepared solutions was added. (The dead volume in the receptor was negligible, 0.4% error, when 1 mL of solution was used.) The sampling cell was then closed with the piston at the top and equilibrated for exactly 30 min in a water bath at 30 °C. After this time, the gas phase was trapped by pressing down the piston at a constant flow of 50 mL/min into a stainless steel tube containing 60–80 mesh Tenax as adsorbent. The amount of Tenax in the different traps was between 160 and 170 mg, and the traps were cleaned for 24 h at 350 °C before use.

The loaded traps were desorbed by an ATD 400 (Perkin Elmer, Beaconsfield, U.K.) desorption unit and analyzed by gas chromatography.

The desorbed traps were cleaned by a special program of the ATD 400. The sampling cell was washed with EtOH and dried in a vacuum oven for at least 1 h at 60 °C.

To determine reproducibility of cell sampling, measurements were repeated three times at each concentration level under the same conditions.

(13) Buttery, R.; Ling, L. C.; Guadagni, D. G. *J. Agric. Food Chem.* **1969**, *17*, 385–389.
(14) Nelson, P. E.; Hoff, J. E. *J. Food Sci.* **1968**, *33*, 479–482.
(15) Le Tanh, M.; Pham Thi, S. T.; Voilley, A. *Sci. Aliments* **1992**, *12*, 587–592.
(16) Rohrschneider, L. *Anal. Chem.* **1973**, *45*, 1241–1247.
(17) Le Tanh, M.; Lamer, T.; Voilley, A.; Jose, J. *J. Chim. Pys.-Chim. Biol.* **1993**, *90*, 545–560.
(18) Graf, E.; de Roos, K. B. In *Thermally Generated Flavors*; Parliment, T. H., Morello, M. J., McGorrin, R. J., Eds.; American Chemical Society: Washington, DC, 1994; pp 437–448.

Instrument Conditions. A Perkin-Elmer adsorption thermal desorption system (ATD 400) coupled on line with a Hewlett-Packard 5890 gas chromatograph (Palo Alto, CA) was used. The GC was equipped with a flame ionization detector (FID) and an apolar widebore CPSIL 5 CB fused silica capillary column (50 m × 0.53 mm, 1.0 μm film thickness; Chrompack, Middleburg, The Netherlands). Helium was used as the carrier gas at 10 mL/min. Operating parameters for the two instruments were as follows:

ATD 400. The traps were desorbed at 300 °C for 15 min. The volatiles were focused in a cold Tenax trap at −30 °C and then desorbed at 280 °C for 3 min. There was no split between the traps and the GC column, and the transfer line was maintained at 150 °C. After each injection the traps were cleaned at 350 °C for 30 min.

GC. The column temperature was held at 50 °C for 2 min and programmed at 4 °C/min to 200 °C. The detector was maintained at 300 °C.

Curve Fitting. The parametric equations were adjusted to the experimental data using a regression software, TableCurve 2D for Windows (Jandel Scientific, Erkrath, Germany).

DISCUSSION

Sampling Cell. From the analysis of the literature, a suitable headspace cell should fit the following requirements: (1) sampling of the vapor phase at equilibrium, (2) no pressure change during sampling or separation of the liquid and the gas phase, (3) no dilution while sampling.

In addition, measurement of low partition values and low headspace concentrations implies sampling of large volumes which cannot be directly injected onto a gas chromatograph. Therefore a method combining static headspace and purge and trap technique was chosen (Figure 1). The volatiles equilibrate between the sample cell (a) and the headspace chamber (b). Pressing the piston pushes the gas through the Tenax cartridge (c) in which the flavors are trapped.

To detect a possible breakthrough, the headspace sampling was performed using two traps in series. Flows exceeding 100 mL/min through the cartridge gave insufficient adsorptions in the first trap. Therefore a 50−80 mL/min flow was chosen for the other experiments. In addition, a higher sampling flow rate would give cause a pressure variation in the cell, which could alter the phase equilibrium. A typical 30 min equilibration time was used as longer times did not increase the GC peak area.

Peak Area Linearity and Accuracy. (All symbols used are listed in Table 2.) Defining the partition coefficient as $k_v = C_g/C_l$ with C_g and C_l the concentrations of the solute in the headspace and in the liquid, respectively, and V_g and V_l the headspace and the liquid volumes. Since the initial mass, m_o, is distributed between both phases: $m_o = m_g + m_l$, the concentration in the vapor phase is

$$C_g = k_v \frac{m_o - C_g V_g}{V_l} \tag{1}$$

$$C_g = \frac{k_v m_o}{V_l + k_v V_g} \tag{2}$$

Or, using the initial concentration in the solution $C_l^o = m_o/V_l$

Table 2. Symbols Used

symbol	definition
V_g	volume of the gas phase
V_l	volume of the liquid phase
m_g	mass of the flavor in the gas phase at equilibrium
m_l	mass of the flavor in solution at equilibrium
m_o	initial mass of flavor in the solution
C_g	flavor concentration in the gas phase at equilibrium
C_l	flavor concentration in the liquid phase at equilibrium
C_l^o	initial flavor concentration in the liquid phase
k_v	air-to-solution partition coefficient
A	area of the GC peak corresponding to a flavor in the headspace
λ	response factor of the GC detector
p	slope of the GC area curve as a function of the initial concentration in the solution
q	slope ratio for two different amounts of the same solution in the headspace cell

$$C_g = \frac{k_v C_l^o}{1 + k_v V_g/V_l} \tag{3}$$

For a given volume, V_g, of injected vapor phase, the area A of the GC peak is proportional to the concentration C_g in the headspace:

$$A = \lambda C_g \qquad \lambda \text{ being the GC response factor} \tag{4}$$

from (3) and (4):

$$A = \frac{\lambda k_v C_l^o}{1 + k_v V_g/V_l} \tag{5}$$

Equation 5 shows a linear relationship between the GC area and the initial concentration C_l^o in the solution. The experimental data using a solution of 2-butanone in water fit well this relationship (Figure 2). From 0 to 83 mg/L a least-squares fitting gave the following results: (1) coefficient of determination 0.996; (2) standard error of the slope 1.1%. No residual (in absolute value) exceeded 10% of the corresponding estimated value. As replicate experiments were included in the regression procedure, a lack-of-fit test was performed giving a p-value of 0.55, which confirms the adequacy of the linear model.

As the regression line was based on 15 experiments, more than 1 week was required to achieve the injections, and possible variations of the GC detector could not be excluded. However, the repeatability of the vapor phase sampling appeared satisfactory (Table 3).

Determination of Partition Coefficients. Ideally, the determination of partition coefficients should avoid previous headspace calibration, since the use of standards has been shown to be tedious. We present hereafter a regression method. Equation 3 is a straight line calibration function: $A = pC_l^o$ with $p = \lambda k_v/(1 + k_v V_g/V_l)$. Starting from two different sample volumes V_{l1} and V_{l2} having the same initial concentration C_l^o, two slopes p_1 and p_2 can be obtained. If the volume of the headspace V_g and the response coefficient λ are considered to be constant, the ratio of the slopes is

$$\frac{p_1}{p_2} = \frac{1 + k_v V_g/V_{l2}}{1 + k_v V_g/V_{l1}} \tag{6}$$

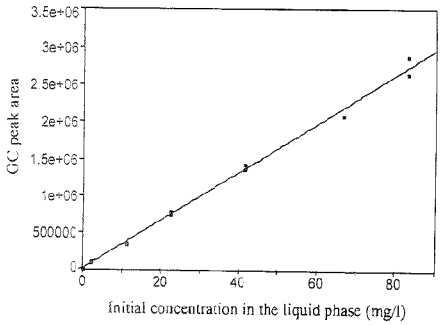

Figure 2. GC peak area as a function of the initial concentration of 2-butanone.

Table 3. Sampling Repeatability[a] from an Aqueous Solution of a Model Mixture

	concn (mg/L)	RSD (%)
2-butanone	41.6	0.9
1-butanol	35.4	1.0
pyridine	30.2	1.6
3-methylpyridine	23.6	5.6
2,6-dimethylpyrazine	23.6	2.8

[a] Repeatability of the GC peak area, three injections.

Defining ϱ as $\varrho = p_1/p_2$, the partition coefficient is independent of the concentration in the solution:

$$k_v = \frac{(1 - \varrho)V_{l1}V_{l2}}{(\varrho V_{l2} - V_{l1})V_g} \tag{7}$$

Variance of k_v can be estimated by the standard formula from the variances that are given for p_1 and p_2 by the fitting program, if other parameters are considered to be constant:

$$\mathrm{var}(k_v) = \left(\frac{\mathrm{d}k_v}{\mathrm{d}p_1}\right)^2 \mathrm{var}(p_1) + \left(\frac{\mathrm{d}k_v}{\mathrm{d}p_2}\right)^2 \mathrm{var}(p_2) \tag{8}$$

Applied to (7), it becomes

$$\mathrm{var}(k_v) = \left(\frac{p_2 V_{l1} V_{l2}(V_{l1} - V_{l2})}{V_g(p_1 V_{l2} - p_2 V_{l1})^2}\right)^2 \mathrm{var}(p_1) + \left(\frac{p_1 V_{l1} V_{l2}(V_{l2} - V_{l1})}{V_g(p_1 V_{l2} - p_2 V_{l1})^2}\right)^2 \mathrm{var}(p_2) \tag{9}$$

Consequently, increasing the gas volume of the cell will decrease the variance when p_1 and p_2 are close together (low k_v values). Numerical application to the headspace cell depicted in Figure 1 using 1 and 2 mL of solution is given in Table 4. Slopes (Figure 3) were determined for the two sample volumes (1 and 2 mL) of 2-butanone in water. For each of them, three different concentration levels were used in addition to the blank.

An adjustment by least-squares fitting from these four headspace injections gave less than 0.6% standard error of the slope in each case (Table 4). As residuals were much lower than in Figure 2 with this small number of injections, it seems to confirm the possible influence of the detector stability over time as previously mentioned. The k_v value for 2-butanone in water listed in Table 4 is in good agreement with that of authors who did not apply a pressure to the headspace before sampling (Table 1). The relative standard deviation was estimated to be 4.5%. Under the same operating conditions, the partition coefficient of pure 1-butanol in water was found to be 2.8×10^{-3} with a 1.2% relative standard deviation. It is higher than the literature values (Table 1), which vary widely.

Table 4. Slopes and Partition Coefficient of 2-Butanone in Water

	value	std error	coeff of determination	residuals
slope (1 mL)	30840	122	0.9998	<1%
slope (2 mL)	37115	176	0.9998	<2%
k_v	2.1×10^{-3}	9.5×10^{-5}		

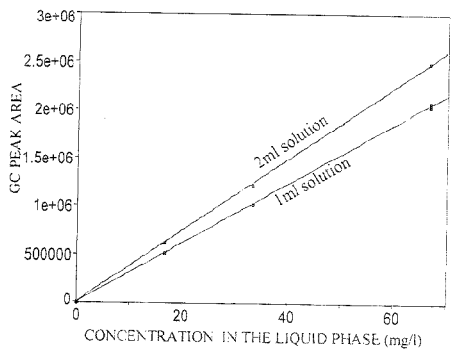

Figure 3. Slope determination for two sample volumes of a 2-butanone solution in water.

Quantitation in Headspace. From the preceeding paragraph, a new calibration method can be proposed. Since the air-to-water partition coefficients can be accurately determined without previously calibrating the solute concentration in the gas phase, it becomes possible to calculate their corresponding headspace concentrations. The partition coefficient value may be used in eq 3 to replace in Figure 2 the initial concentration in the liquid phase by the corresponding concentration in the vapor phase.

$$C_g = \frac{k_v}{p(1 + k_v V_g/V_l)}A \tag{10}$$

If C_g, k_v, and A are considered to be independent, the variance of C_g can be estimated as

$$\mathrm{var}(C_g) = \left(\frac{\mathrm{d}C_g}{\mathrm{d}p}\right)^2 \mathrm{var}(p) + \left(\frac{\mathrm{d}C_g}{\mathrm{d}k_v}\right)^2 \mathrm{var}(k_v) + \left(\frac{\mathrm{d}C_g}{\mathrm{d}A}\right)^2 \mathrm{var}(A) \tag{11}$$

Using the headspace sampling cell (Figure 1) with 1 mL of 2-butanone solution, the corresponding slope in Figure 2, and the standard deviation of the area measurement (less than 3.4% in Figure 2), the standard deviation can be evaluated:

$$\sigma(C_g) = (4.5 \times 10^{-10})A \qquad (12)$$

Dividing eq 12 by the numeric form of eq 10 gives the relative standard deviation as 3.4%. This value shows the method to be a very accurate quantification technique of the vapor phase constituents, compared to the use of internal or external standards. It must be pointed out that, when a complex matrix is used, only the concentration in the gas phase is thus obtained. However, applying the MHE technique allows deduction of the concentration of the volatile in the matrix.

Influence of the Volatile Mixture Composition. In a recent paper, Baltes[19] mentioned the influence of other volatiles in a model flavoring mixture on the individual component concentrations in the gas phase. Since such an observation could be an explanation to the "synergy" between flavorings, which is often claimed by flavorists, the phenomenon required a quantitative verification. The Baltes' assumption would mean that the partition coefficient of a given component is modified by the addition of another. Therefore, a mixture containing several compounds used by Baltes was formulated. The 2-butanone and the 1-butanol coefficients remained unchanged (Table 5).

Similarly to Baltes' experiment, we increased the 2-butanone concentration of the mixture. The concentrations of the other volatiles were unchanged, as shown by the GC area of the other peaks in spite of the large excess of the ketone (up to a 0.5% concentration) (Table 6). All values fell within a deviation of less than 10% above or below the average. Even 1-butanol, 3-methylpyridine, and 2,6-dimethylpyrazine, which are said to be strongly decreased by adding an excess of another volatile molecule, were not affected. It can be concluded that composition of the mixture has very little influence on the partition of its constituents as stated by Guitart.[12]

When the solutions exhibit amphiphilic properties, formation of aggregates may alter their concentration in the headspace above a critical concentration in the solution.[20] Since none of the ingredients used in our model flavor mixture or in Baltes' mixture was amphiphilic, this phenomenon did not occur, and according to our findings, the vapor phase concentrations are expected to follow Raoult's law.

Matrix Effect. To exemplify the matrix influence on flavor release, the system was tested using MCT and soja oil as fat examples and milk as an emulsion model (Table 7). When 2-butanone was dissolved in soja oil, the partition coefficient was found to be similar to that in Nelson's experiments[14] (1.9×10^{-3}) for safflower oil. The limited number of experiments performed did not lead to a conclusion concerning the role of lipid composition, and further systematic investigations would be useful.

CONCLUSIONS

A new method based on a combination of static headspace sampling and dynamic headspace traps was developed. It has the following advantages: determination of the partition coefficients does not require calibration, quantification is achieved without adding a standard, according to estimation of variance the method is accurate, combination of static headspace with traps allows components with low vapor phase concentrations to be analyzed, and small changes in the aroma profile due to nonvolatile constituents can be investigated.

It was also found that the concentration of one of the flavor components in a cocktail has no influence on the partition of the other ingredients. Consequently, using this method, it is possible to measure individual partition coefficients in a mixture of flavorings.

Table 5. Partition Coefficient Determination of an Aqueous Solution of a Model Mixture

	k_v	RSD (%)
2-butanone	2.1×10^{-3}	0.57
1-butanol	2.9×10^{-3}	1.5
pyridine	7.4×10^{-4}	2.2
3-methylpyridine	9.7×10^{-4}	2.4
2,6-dimethylpyrazine	4.1×10^{-4}	15

Table 6. Influence of an Addition on the Vapor Phase Concentration of the Other Components (GC Area Counts and Deviations from the Average)

	concn (mg/L) 2-butanone					RSD
	41.6	741.6	1481	5161	av	(%)
1-butanol	254 631 (−5.8%)	261 048 (−3.4%)	295 048 (+9.2%)	*a*	270 242	8.0
pyridine	257 672 (+7.8%)	226 852 (−5.1%)	245 186 (+2.6%)	226 198 (−5.3%)	238 977	6.3
3-methyl-pyridine	141 833 (+13%)	115 283 (−8.4%)	124 324 (−1.3%)	122 173 (−3.0%)	125 903	9.0
2,6-dimethyl-pyrazine	31 256 (+5.8%)	27 770 (−6.0%)	30 198 (+2.2%)	28 913 (−2.1%)	29 534	5.1

[a] Not measurable because of the overlap of the GC peak with that of the 2-butanone.

Table 7. Influence of the Matrix on the Partition Coefficient of 2-Butanone

matrix	$10^3 k_v$	std error (%)
water	2.1	0.37
MCT	1.4	5.4
soja oil	2.6	1.7
milk	2.3	0.6

ACKNOWLEDGMENT

We gratefully acknowledge Mr. H. Berthout for making the many prototypes of the headspace cell and for his useful suggestions, Dr. E. Prior for English revision, and Mr. J. Stefaniuk for drawing Figure 1.

Received for review February 2, 1995. Accepted June 21, 1995.[⊗]

AC9501194

[⊗] Abstract published in *Advance ACS Abstracts*, August 1, 1995.

(19) Bohnenstengel, F.; Soltani, N.; Baltes, W. *J. Chromatogr.* **1993**, *655*, 249–255.

(20) Conner, J. M.; Paterson, A.; Piggott, J. R. *J. Sci. Food Agric.* **1994**, *66*, 45–53.

Anal. Chem. 1995, *67*, 3305–3318

Pulsed Flame Photometer Detector for Gas Chromatography

Aviv Amirav* and Hongwu Jing

School of Chemistry, Sackler Faculty of Exact Sciences, Tel-Aviv University, Tel-Aviv 69978, Israel

A new pulsed flame photometer detector (PFPD) design is described with improved performance. Detection limits of 180 fg/s (sulfur), 7 fg/s (phosphorus), and 2 pg/s (nitrogen) are demonstrated when 2 rms noise is considered as the detection limit. The minimum detected amount of sulfur was further reduced with a sulfur doping method to about 30 fg/s. The factors affecting the selectivity are analyzed in terms of operating the PFPD as a specific detector without any hydrocarbon interferences. The effect of the pulsed nature of the PFPD on the chromatographic peak area and height reproducibility is modeled and analyzed. It is shown that above 3 Hz, the standard deviation of peak area is 2%, which is dominated by nondetector effects. The detector temperature effect was studied and is presented. The difference between light guide and lens optics is discussed. The column operation with hydrogen as a carrier gas is compared to that with helium, and the injection of chlorinated and fluorinated solvents is shown and discussed. New ways of obtaining additional information by using the added dimension of time are analyzed. It is shown how the simultaneous use of dual gates can provide unambiguous heteroatom identification. It is also described how a dual gate subtraction method results in a considerable enhancement of the interheteroatom selectivity, especially for phosphorus versus sulfur. The dual gate approach also provides up to an order of magnitude increase in the measurement dynamic range. Practical utilization of the PFPD is illustrated with the analysis of real-world samples, including thiophene in benzene, pesticides in a broccoli extract, and a sulfur-containing drug in human serum.

The flame photometer detector (FPD) is a known and established detector for gas chromatography.[1,2] Recently, we introduced a new concept for the operation of FPD based on a pulsed flame instead of a continuous flame for the generation of flame chemiluminescence.[3–5] This pulsed FPD (PFPD) was also coupled with a pulsed flame ionization detector (PFID) to form a combined pulsed flame photometric ionization detector (PFPID).[6]

The PFPD is characterized by the additional dimension of a light emission time and the ability to separate in time the emission of carbon species from that of sulfur and phosphorus, resulting in a considerable enhancement in the detection selectivity. In addition, the detection sensitivity is markedly improved thanks to (a) reduced flame background noise, which is filtered in time, (b) increased signal due to higher brightness of the pulsed flame, stemming from a small combustion cell volume and low combustible gas flow rate, and (c) the use of broad-band color glass filters instead of interference filters. Moreover, the hydrogen and air gas consumption is greatly reduced, and the increased selectivity and sensitivity allow for the selective detection of nitrogen compounds via their HNO^* flame chemiluminescence.[5]

In this paper we report on the results of our continued effort to improve the PFPD hardware, further characterize its behavior, and explore the various possibilities for enhancing its performance through added time domain information. The PFPD is now available from Varian, and we hope this paper will help analysts to effectively use the commercial detector as well.

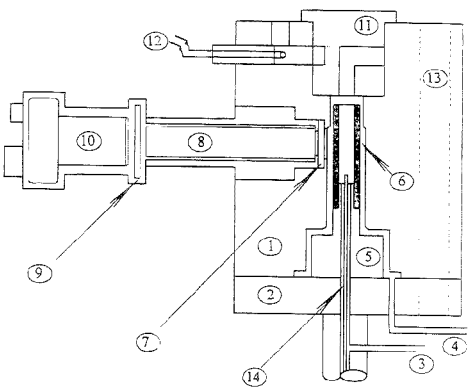

Figure 1. Schematic diagram of the new PFPD design. (1) PFPD body; (2) GC-heated detector base; (3) central hydrogen-rich H_2/air mixture tube leading to the combustor; (4) outer bypass H_2/air mixture tube; (5) combustor holder (6) quartz combustor tube; (7) sapphire window; (8) light guide; (9) colored glass filter; (10) photomultiplier; (11) spiral igniter light shield; (12) heated wire igniter; (13) assembly guiding rod in a guiding hole; (14) column.

THE NEW PFPD DESIGN

A schematic diagram of the new PFPD is shown in Figure 1. The PFPD main body (1) is mounted on a GC detector base (2) provided by Varian (for the Varian PFPD) and clamped with two screws (not shown). A Varian 3600 GC was used for all the experiments described in this paper. Two hydrogen/air gas mixtures, for which flow and composition are separately con-

(1) Dressler, M. *Selective Gas Chromatographic Detectors*; Elsevier: Amsterdam, 1986.
(2) Farwell, S. O.; Barinaga, C. J. *J. Chromatogr. Sci.* **1986**, *24*, 483.
(3) Amirav, A. Pulsed Flame Detector Method and Apparatus. U.S. Patent 5153673; Israel Patent 95617; European and Japan Patent Applications.
(4) Atar, E.; Cheskis, S.; Amirav, A. *Anal. Chem.* **1991**, *63*, 2061.
(5) Cheskis, S.; Atar, E.; Amirav, A. *Anal. Chem.* **1993**, *65*, 539.
(6) Tzanani, N.; Amirav, A. *Anal. Chem.* **1995**, *67*, 167.

0003-2700/95/0367-3305$9.00/0

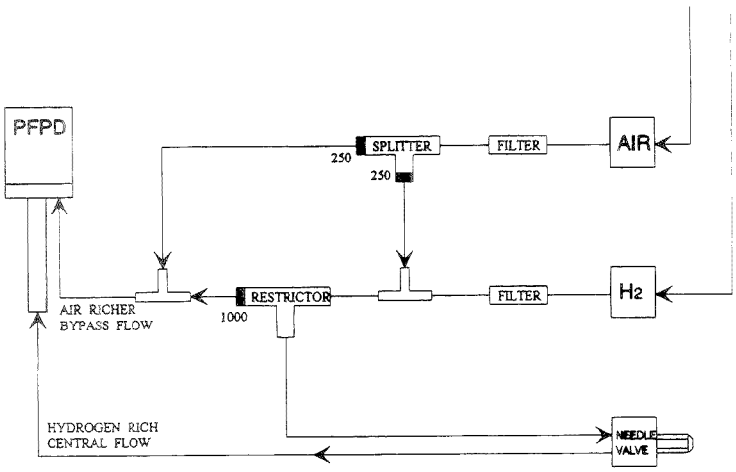

Figure 2. Schematic diagram of the PFPD pneumatics including H_2 and air Porter flow controllers followed by a pencil gas filter, a needle valve, and four Swagelock tees with or without Mott flow restrictors as indicated (can be unified into a single structure).

trolled, are fed from gas tubes (3 and 4). The central hydrogen-rich combustible gas mixture flows through the combustor holder (5) directly into an open quartz tube combustor (6), where the flame chemiluminescence occurs. The flame emission is viewed through a sapphire window (7), a quartz light guide rod (8), and a colored glass filter (9) and detected by a photomultiplier (10). While the combustor is filled with the gases eluting from the column and the combustible gas mixture (3), a separate air-richer combustible gas mixture (4) bypasses the combustor around it, mixes with the combusted gases from the previous pulse, and fills the volume of the igniter light shield element (11). The pulsed flame is ignited by a heated wire igniter (12), propagates through the igniter light shield (11), passes through the combustor (6), and self-terminates on the combustor holder (5). The combustor holder has a 0.9 mm hole which prevents further flame propagation. The following are new aspects in the design of this detector which make it different from the previous design:[3]

(1) The detector is fed with externally mixed air/H_2 gas mixtures, instead of utilizing dynamic gas mixing inside the detector.

(2) No screw valve is used, and all the pneumatics are external to the detector. The layout of the new pneumatics is shown in Figure 2. It is based on a pneumatics module provided by Varian and modified by us as shown in Figure 2. The air and hydrogen supply is flow controlled by Porter flow controllers.

(3) The air flow is split with a Swagelock tee equipped with two Mott flow restrictors (250 mL/min each). One portion of the air is mixed with hydrogen and flows in the external flow tubes (4 in Figure 1), where it is further mixed with the second portion of air after passing an isolation frit flow restrictor (1000 mL/min). Parallel to this flow and prior to the 1000 mL/min flow restrictor, there is a needle valve which controls the amount of hydrogen-rich gas mixture that flows into the combustor through tube 3 of Figure 1. This needle valve adjusts the ratio of total flow inside and outside the combustor so that soon after the bypass flow purges the previously combusted igniter chamber gases, the combustor is also refilled by the central flow (3) to ensure maximum signal brightness. Thus, practically all the eluting compounds are combusted inside the combustor with near zero dead volume. Note that in our previous design, there was a small dead volume above the combustor and below the screw valve which was too rich with hydrogen and thus harmful to the triggering, especially under massive hydrocarbon elution.

(4) The combustor is now made of simple quartz tubes, 4 mm o.d., 2 or 3 mm i.d., instead of the previously used nozzled combustors. Straight tubes are easier to produce and clean. Cleaning is achieved by dipping them in 40% HF for 1–3 min, followed by ultrasonic rinsing with methanol and flame annealing below melting temperatures. This flame annealing is performed on a homemade combustor holder made of quartz mounted on a slowly spinning hand drill and using a Little Torch purchased from Cole Parmer with an oxygen/propane flame. Proper combustor cleaning and flame annealing is very important for optimized performance, and once it is achieved, there is no apparent deterioration of performance if the detector body is kept clean.

(5) The detector body includes two holes, 5 mm in diameter, and the detector base has two rods of 4.6 mm diameter (13). The detector is mounted on its base through these guiding rods, which provide a smooth guide without touching the combustor or its holder.

(6) The combustor entrance in the body has a small guiding alignment counterbore with an upper bore of 4.3 mm i.d. to ensure proper flame extinction of the flame in the bypass flow. The central body bore diameter is 4.8 mm up to the upper portion of the light guide window. Above the light observation window, the central bore diameter is reduced to 4.3 mm to prevent flashbacks outside the combustor. The increased diameter is intended to reduce the outer gas flow impedance in order to reduce the risk of its leakage into the combustor.

(7) The main body is made of stainless steel 316. Hastalloy C278 and Inconnel 625 were also tried and found to be slightly superior in their cleaning and probably in their long-term stability under chlorinated solvent injections, but SS-316 is easier to machine. All the stainless steel parts were degreased after

machining and then descaled by immersion in a 1% HF/10% HNO_3 solution for 1 h at room temperature, followed by 1 h of immersion in 65% HNO_3 for final passivation. After being rinsed in distilled water, all stainless steel parts were baked in an oven at 450 °C for several hours. The descaling step was found to be very desirable and effective in reducing phosphorus background, probably through the elimination of machine shop oil buried under scales.

(8) No external heater was used, and heating was provided through contact with the detector base. The overall height was kept short (42 mm) to reduce the temperature gradient. With a 250 °C detector base temperature, the actual main body temperature was 170 °C. In order to reduce the temperature gradient, a 50 mm o.d., 54 mm long glass cover was used (a stainless steel cover was also tested). With this cover, the temperature gradient was reduced by 50% and at 250 °C base temperature, the body was 210 °C, while at 400 °C base temperature, the body was ~300 °C. A base temperature of 300 °C was chosen for phosphorus pesticide analysis, while for sulfur analysis, a base temperature of 200 °C was employed.

(9) A new type of spiral channel igniter light shield was used (11). Several pieces were tried, and a good shield was achieved with a 270° channel followed by an internal M-3 tapped central down-going hole. This new design allows effective prior cleaning of this element and provides the best light shielding per volume ratio. We used a 2.5 mm wide spiral channel with a depth of 1.4 mm, and the central bore was equipped with M-3 threads acting as a further light baffle. After cleaning, this element was placed in an oven at 450 °C for several hours to provide it with a brown matte finish.

(10) The igniter is placed directly inside the main structure, and no electrical feed-through is mounted on the main body. The exit gas channel is short, and the red color of the igniter can be viewed from the top of the detector.

(11) The ratio of the volume of the igniter light shield chamber to that of the combustor volume is important for determining the air split ratio in the pneumatics. This volume ratio was 4:1 with a 16 mm long, 2 mm i.d. sulfur combustor having 12 mm open internal length. At this volume ratio, the combustor was typically fed with 4 mL/min air and 4 mL/min hydrogen, while the bypass was fed with 6 mL/min hydrogen and 16 mL/min air. Total flows are therefore 10 mL/min H_2 and 20 mL/min air. Note that under these flow rates and including the 8 mL/min of combusted gases from the previous pulse in the combustor, the gas volume ratio was 30/8 = 3.75. Use of the 3 mm i.d. combustor required the combustor flow rate to be higher.

(12) Triggering for the gated amplifier was achieved from the light spike generated by the impact of the pulsed flame at near stoichiometric gas mixture composition on the upper combustor wall. The height of the combustor entrance above the center of the light optics was adjusted to be 5.3 mm to minimize the time difference between the trigger light spike and pulsed flame background emission. This helps to reduce the time difference between the trigger spike and the main pulsed flame background and decrease the variability of this time by the elution of large amounts of hydrocarbon compounds.

We note that the figures and studies described in this paper were achieved only in part with this new design; some were achieved with other PFPD designs intended to improve our previously described design[5] (Figures 7 and 9–11) or with the Varian PFPD (Figures 19 and 20). However, we found that the design shown in Figures 1 and 2 is our best in terms of overall engineering quality, ease of use, and (slightly) performance.

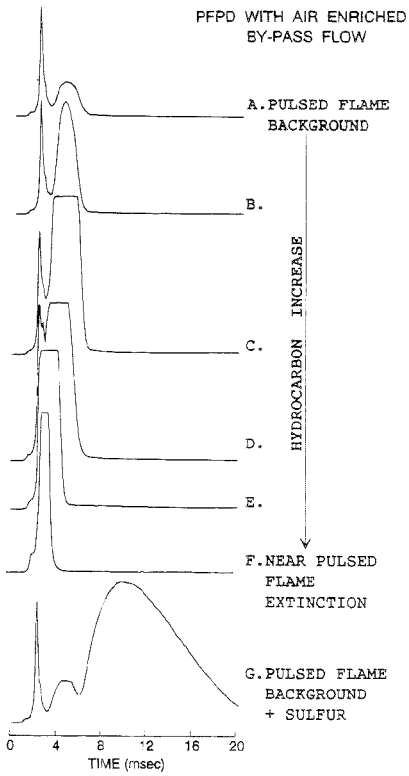

Figure 3. PFPD light emission time dependence on the elution of hydrocarbon and sulfur compounds.

DETECTION SELECTIVITY AGAINST HYDROCARBONS AND SENSITIVITY

The enhanced selectivity of the PFPD is based on time separation of hydrocarbon emission from that of sulfur or phosphorus, the relative weakness of carbon flame emission, and the use of an optical filter. In the PFPD, a colored glass, broadband optical filter is used to enhance the sensitivity on the basis of increased selectivity through the collection of a broader spectral band width. We have tested the effect of replacement of an interference filter with colored glass BG12 or GG495 Schott filters and found that the detected light emitted by sulfur and phosphorus was increased by over an order of magnitude, while the light emitted by carbon was increased by twice as much. This finding is in full agreement with the FPD literature.[7]

In Figure 3, we show the emission time dependence of the PFPD. Trace A shows the pulsed flame background. The first light spike peak near zero time is attributed to the flame hitting the top of the combustor in an air-richer environment. The second light peak at ~3 ms later is due to the pulsed flame background

(7) Aue, W. A.; Hastings, C. R. *J. Chromatogr.* **1973**, *87*, 232.

as it passes by the light collection window. In traces B–F, we show the PFPD response to a series of increasing amounts of hydrocarbon molecules (cyclohexane), where trace B corresponds to about 50 ng of carbon/s. We note that in this improved design with an air-richer bypass gas mixture, the time separation between the early light spike used for triggering and the main pulsed flame background remains unchanged and eventually is reduced under all the conditions of traces E and F, up to about 10 μg of carbon/s. Above this hydrocarbon elution rate, the pulsed flame cannot propagate through the too-fuel-rich gas mixture in the combustor. Trace G shows the PFPD response to a sulfur compound, tetrahydrothiophene, in which the sulfur emission is markedly delayed and can easily be separated *in time* by the use of a gated amplifier. Note that under these conditions, the PFPD is a sulfur-specific detector, and no carbon-related positive chromatographic peaks are observed, even at the noise level. Initially in traces B and C, no change is observed in the baseline, while at higher carbon flux, a small negative peak appears, due to the quenching of chemical background noise. In Figure 3, a combustor with 2 mm i.d. was used. When a 3 mm i.d. combustor is used, the time separation of the pulsed flame background and its trigger is initially slightly increased, which may induce a slight carbon-related chromatographic peak. However, if the gate is separated by 3 ms from the center of the pulsed flame background, a P- or S-specific response can be achieved as well. The pulsed flame emission time behavior under hydrocarbon elution is affected by the reduced flame velocity inside the combustor when a hydrocarbon molecule is eluted at a high flux, which may induce "invasion" into the gate. This reduced flame velocity is counteracted by the opposite process of flame arrestation near the column exit, which reduces this invasion and is the dominant factor under the conditions of Figure 3. As is evident from Figure 3 and has been demonstrated before,[7] the PFPD can be an element-specific detector.

The detection sensitivity has been only marginally improved in this new design of the PFPD. However, it is easier to achieve this sensitivity over a broader range of conditions, such as temperature, column flow rate, carrier gas (He, N_2, H_2), frequency, combustor size, etc. In both the older design and this design, the column output was integrated in the combustor volume and the detection luminosity was similar, while the improved detector cleaning procedures (using acid pickling and a straight flame annealed combustor) resulted in the detection sensitivity shown in Figure 4. A standard MX5 pesticide mixture was used containing 10 ng/μL each of diazinon, methyl parathion, parathion, methyl trithion, and ethion. A 0.1 μL aliquot was injected and split 100:1, so that 10 pg of each analyte was eluted with about 1–1.1 pg of phosphorus and sulfur in the first three compounds. The obtained signal to rms noise ratio is 64 in the sulfur mode and 300 in the phosphorus mode for diazinon. Considering a chromatographic peak width of 1–1.1 s, the quadratically extrapolated minimum detected amount (MDA) for sulfur is 180 fg/s with 2 rms noise, or 300 fg/s when twice the peak to peak noise is considered. In the phosphorus mode, the MDA for phosphorus is 7 fg/s or 20 fg/s for 2 rms and twice the peak to peak noise levels, respectively. These values are close to the values reported by Varian, obtained on their PFPD.[8] We note that at an elution rate of 1 pg of sulfur or phosphorus/s as in Figure 4, there are

(8) Robinson, J., Varian Chromatography System, Walnut Creek, CA, private communications.

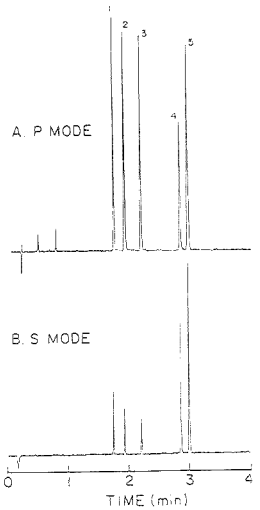

Figure 4. Sensitivity evaluation in the detection of five pesticides, 10 pg each, in the phosphorus mode (A) and the sulfur mode (B). A 3.7 m narrow bore column (J&W DB-1, 0.25 μm film thickness) was used with injection at 100 °C and a column temperature programmed after 6 s to 220 °C at 50 °C/min. MX5 pesticide mixture, 0.1 μL, was injected with a split ratio of 100:1. (1) Diazinon; (2) methyl parathion; (3) parathion; (4) methyl trithion; (5) ethion.

no interheteroatom interferences at a given detection mode, and the optical filter provides sufficient interheteroatom selectivity. The major remaining question is whether these are the absolute lowest MDAs of the PFPD. Clearly, one can change the design for a specific purpose, and with a smaller combustor length whose entire volume is viewed by the light guide, the MDA can be further reduced at the price of a reduced emission time delay and a higher dependence on the column flow rate. Currently, the signal luminosity for sulfur at 2.7 Hz using a 2 mm i.d. combustor is about 600 detected photons pulse^{-1} (pg of S/s)$^{-2}$, and for phosphorus it is 7 photons pulse^{-1} (fg of P/s)$^{-1}$ (using a 3 mm i.d. combustor). Thus, in the phosphorus mode, the MDA of 7 fg/s implies 2 rms noise of ~50 photons, which under statistical noise conditions emerge from 625 photons/pulse background chemical noise. Similarly, the MDA in the sulfur mode indicates a 100 photons/pulse background of chemical noise in the sulfur mode. Clearly, these values are much higher than that for the dark current, which is only 1–2 photons/pulse with a photon counting photomultiplier such as the R647P from Hamamatsu. Further detector body cleaning and background reduction can help to achieve better records; however, the above-mentioned values can be achieved under normal careful PFPD operation.

It should be emphasized, however, that the quadratic behavior of the sulfur signal provides an alternative method for improving the MDA through the provision of a constant background of sulfur molecules. The addition of a constant flow of sulfur dopant to the flame in a FPD was studied in the past and is well documented for the "linearization" of the sulfur response as well as for lowering its detection limits.[9–11] In Figure 5, we demonstrate the sulfur doping method applied to the PFPD in the detection of 1 pg each

(9) Aue, W. A.; Flinn, C. G. *J. Chromatogr.* **1978**, *158*, 161.

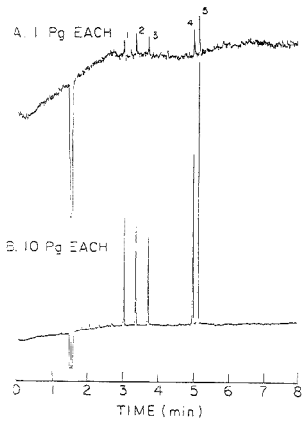

Figure 5. Sensitivity evaluation in the detection of five pesticides, 1 pg (A) or 10 pg each (B), using the sulfur doping method in the sulfur mode. A 30 m narrow bore column was used with injection of the MX5 pesticide mixture after a 10-fold dilution; 0.1 μL was injected with a split ratio of 100:1. Injection was at 100 °C with column temperature programmed at 45 °C/min to 250 °C from the injection. (1) Diazinon; (2) methyl parathion; (3) parathion; (4) methyl trithion; (5) ethion.

of the MX5 pesticides in the sulfur mode. The linearly extrapolated MDA for sulfur is about 30 fg/s, which is similar to that reported for the flameless sulfur chemiluminescence detector.[12]

The figure of merit in terms of lowered MDA can be quantitatively accounted for and can even be predicted. Let us assume that the PFPD possesses a luminosity L in units of detected photons pulse^{-1} (pg of S/s)$^{-2}$. The MDA is then determined by the noise level of N detected photons/pulse under the gate (without averaging), and thus the 2 rms noise magnitude is $2\bar{N}^{1/2}$ (with units of detected photons/pulse). Using these definitions, the MDA is given by

$$(\mathrm{MDA})^2 L = 2\bar{N}^{1/2} \rightarrow \mathrm{MDA} = \sqrt{2\bar{N}^{1/2}/\mathrm{L}} \qquad (1)$$

Thus the MDA is improved with the square root of the light collection efficiency and is reduced by the fourth root of the chemical background noise. If a constant sulfur background C (pg/s) is introduced, then the total signal (in photons/pulse) is given by

$$S = L(C + E)^2 \qquad (2)$$

where E is the flux of eluting sulfur compound in units of picograms of sulfur per second. S can be written as

$$S = LC^2 + 2LCE + LE^2 \qquad (3)$$

Under normal conditions, C will be much larger than E near the MDA, and thus LE^2 can be neglected, while LC^2 is a constant background that contributes to the noise alone. At the MDA (when E = MDA), we have

$$(\mathrm{MDA})\ 2LC = 2\sqrt{N + LC^2} \qquad (4)$$

We may further assume that $LC^2 \gg N$, so that the noise is dominated by the sulfur background contribution, and thus we obtain

$$\mathrm{MDA} = \sqrt{1/L} \qquad (5)$$

The emerging conclusion is that with the sulfur doping method, the MDA is lower by a factor of $(2N^{1/2})^{1/2}$ than that without the background. An additional conclusion is that the absolute value of the background C is relatively unimportant as long as it is stable enough that the noise is statistical and not a constant fraction of the background. Realistically, the range of 0.5–2 pg of S/pulse is optimal, and in our case this was achieved with benzothiophene fed through an external seeding device. A better way should be through the use of a SO_2 permeation tube at a rate of 0.3–1.2 ng/min connected to the air supply, assuming 3 Hz operation and 20% air flowing in the combustor while 80% is flowing in the igniter chamber.

We note that in our PFPD, N was determined to be 100, and thus the net gain in reduced MDA is a factor of 4.5, which is in rough agreement with the measurement shown in Figure 5. We also note that under these conditions, the sulfur concentration dependence is linear at low concentration and becomes quadratic through intermediate values, as is shown in trace B of Figure 5 at higher levels.[9–11] The final conclusion is that the sulfur doping method can reduce the MDA by a factor of 4, and the improvement is greater with dirtier detectors having a large chemical background.

Recently, Hamamatsu introduced a new, red-sensitive photomultiplier, Model R5070. This photomultiplier is claimed to be about 5 times more sensitive at 760 nm in its quantum yield than our previously used R1463P. Thus we reexamined our detection sensitivity in the nitrogen selective detection mode using this R5070 photomultiplier in combination with a RG9 Schott high-pass filter. In Figure 6, we show a nitrogen selective detection chromatogram of several organonitrogen compounds introduced into the column at a level of 2 ng each. The extrapolated MDA for nitrogen from the GC peak of the nitrobenzene is 1.6 pg/s assuming 2 rms noise as the detection limit. This value is 3 times better than our previously reported value,[5] due mostly to the use of the R5070 photomultiplier, which provides a 2.5 times lower MDA. It is mentioned here that in the nitrogen mode, the elimination of the light emitted by the igniter is very important, and the spiral igniter light shield (11 in Figure 1) is very effective in achieving this. In this light shielding element, the pulsed flame propagates in a 270° round channel before entering the central axis of the detector. The igniter light is scattered several times from the stainless steel walls and thus is practically eliminated. The nitrogen mode is optimized using combustor tubes of 3 mm i.d. and is relatively insensitive to the air/H_2 gas composition under hydrogen-rich conditions. The PFPD body temperature can be in the range of 200–250 °C. While the PFPD nitrogen selective detection mode is less sensitive than the nitrogen–phosphorus detector (NPD), it has a uniform nitrogen response, unlike the NPD, whose response is greatly affected by molecular and

(10) Crider, W. L.; Slater, R. W. *Anal. Chem.* **1969**, *41*, 531.
(11) Zehner, J. M.; Semonaitis, R. A. *J. Chromatogr. Sci.* **1976**, *14*, 348.
(12) Shearer, R. L. *Anal. Chem.* **1992**, *64*, 2192.

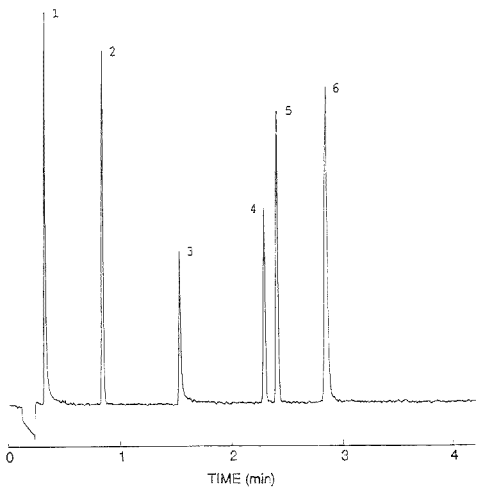

Figure 6. Nitrogen selective detection of (1) acetamide, (2) nitrobenzene, (3) nicotine, (4) azobenzene, (5) trinitrotoluene, and (6) caffeine in order of their elution, each at the level of 2 ng. The sample also contained 20 ng each of hexadecane and eicosane. A 4 m narrow bore column was used with injection at 60 °C for 0.2 min and then programmed at 50 °C/min to 190 °C.

structural effects.[13] A slight response enhancement was observed with nitro and nitroso compounds, as the chemiluminescence species is HNO*, but under only slightly hydrogen-rich conditions, the nitrogen response is quantitative and can be used for total nitrogen content measurements. In figure 6, we demonstrate the detection of acetamide with a sensitivity similar to that of azobenzene. We have also detected urea, and we believe that the PFPD can also detect inorganic nitrogen compounds except N_2. The selectivity N/C is limited to about 10^4 due to the short time delay of HNO* emission. The optimal gate delay is close to that of the carbon emission, and during elution rates of over 20 ng of carbon/s, the carbon emission time is slightly broadened and may partly overlap the nitrogen gate in a nonlinear manner. This nonlinear response is limited to a narrow hydrocarbon elution rate, above which the carbon emission is reduced in time, as shown in Figure 3 for a combustor tube of 2 mm i.d. With some sacrifice in sensitivity (<1.5), the nitrogen mode can be specific with no carbon interferences by delaying the gate by 1 msec more than the optimal gate delay for sensitivity.

It should be mentioned that two combustor sizes were used, 2 and 3 mm i.d. The 2 mm i.d. combustor is optimal for achieving the lowest sulfur detection level, while the 3 mm i.d. combustor is superior with phosphorus and nitrogen selective detection and is also relatively good with sulfur when a high column flow rate is used. Thus, the combustor with 3 mm i.d. is preferred for universal PFPD operation. The differences between the two combustors are usually small, with less than a factor of 2 difference in the MDAs.

PEAK AREA REPRODUCIBILITY AND PULSE FREQUENCY RESPONSE

One question concerning the PFPD in comparison with FPD is its possibly higher peak area irreproducibility due to the pulsed nature of the detector. The PFPD is adjusted to work with over 95% of the eluted compounds being integrated in the combustor through separate optimization of the igniter chamber gas flow rate at conditions known as near "tic-tac". When the flow rate of the combustible gas to the igniter is further increased, the pulsed flame enters the combustor only every other pulse, since under these conditions the combustor gas flow rate is too low to push away the combusted gases from the previous pulse by the time the flame is ignited and is ready to enter the combustor. For optimal performance, the relative gas flow rates of the PFPD are adjusted to just below this critical flow rate ratio. Thus, the PFPD integrates the GC-eluted compound, and although the elution time is not synchronized with the PFPD, no peak area irreproducibility is expected. However, while the GC-eluted compound is filling the combustor, a portion of the combustion can be out of the view of the light collection system, in spite of the dynamic gas mixing anticipated by the propagating pulsed flame.

This pulsed signal feature is also shared by GC/MS for similar reasons, although in GC/MS the fraction of the dead time is much larger. This aspect was closely evaluated and studied. Let us assume that the chromatographic peak has an impuse shape with a peak width W. We denote the dead time fraction as d, the active viewing fraction as a ($a = 1 - d$), and the PFPD frequency as f. We assume that the GC-eluted compound is fully viewed while eluting during the active time, and this active time is followed by a dead time, during which eluted molecules are lost and are undetected. It is assumed that the maximum and minimum of the signal are obtained either when the active time fraction coincides symmetrically at the center of the elution time or while the dead time fraction coincides with the center of the peak. From simple geometrical considerations, one can derive that the maximum difference in the active area of the GC peak for random active area location is d/faw, and assuming random time distribution, we obtain for the standard deviation

$$\sigma_a = d/2.8faw \tag{6}$$

For a triangular shaped GC peak, the calculation is more involved, and assuming $d < a$, we get

$$\sigma_a = d/2.8f^2w \tag{7}$$

When considering nondetector contributions σ_r, such as from the injection, we get

$$\sigma_a^2 = (d/2.8f^2w)^2 + \sigma_r^2 \tag{8}$$

In Figure 7, we show our experimental results for the measured peak area reproducibility and its frequency dependence. Each point is the result of a set of several measurements averaged to one point. The dashed line is a two parameter line fitted to eq 8, where σ_r was assumed to be the high-frequency value of σ and d was fitted as 0.22. The good fit observed supports our approch and suggests that the triangle approximation is sufficient for simulating the real GC peak shape for this purpose, even though typical peak shapes are closer to Gaussian.

We note that with the triangular peak shape, a quadratic frequency dependence is derived and experimentally confirmed; thus, the above equation can be used to assess various situations.

(13) Baker, J. K. *Anal. Chem.* **1977**, *49*, 906.

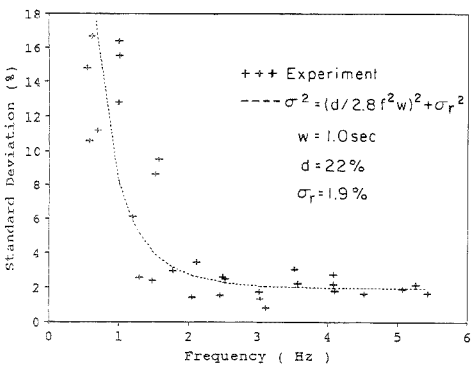

Figure 7. Peak area reproducibility dependence on the PFPD frequency. Both experimental results and model calculation are shown for a chromatographic peak width of 1.0 s. Dimethyl methylphosphonate was used as a test compound.

It is clearly observed that above 2.7–3 Hz, the standard deviation of the peak area is close to 2% and is dominated by the nondetector contribution of 1.9%, while the pulsed nature of the PFPD contributes less than 1% to the standard deviation of the peak area. Therefore, the PFPD reproducibility can be considered unaffected by its pulsed nature in terms of peak area measurement accuracy, and at 2.7–3 Hz standard operation, GC peaks of 1 s fwhm can be accurately measured. The situation is somewhat worse when peak height is considered, as the compound time integration in the combustor is irrelevant for this aspect. Using the same model of triangular GC peaks, we obtain

$$\sigma_h = d/5.6fw \qquad (9)$$

Using $d = 0.22$, $f = 3.1$ Hz, and $W = 0.8$ s, we find $\sigma_h \cong 1.6\%$.

In Figure 8, we show the result of 10 consecutive injections of a mixture of dimethyl methylphosphonate (DMMP) and diisopropyl methylphosphonate (DIMP) using a 4 m narrow bore column. In this mixture, the DIMP serves as an internal standard for the DMMP, whose standard deviation of peak height was 2.2% (peak area standard deviation, 1.8%). The measured standard deviation of the relative peak height was 3.1%, and assuming an equal standard deviation for the heights of each compound gives a 2.2% standard deviation when the injection irreproducibility is neglected. This number is slightly higher than expected, and perhaps second-order injection irreproducibility effects are not totally eliminated through the use of DIMP as an internal standard, giving us a measurement of 2.2% instead of the anticipated value of 1.6%.

In conclusion, the PFPD is capable of measuring narrow chromatographic peaks with good peak area and peak height reproducibility. In Figure 9, the fast GC of sulfur and phosphorus compounds is shown using a 3.5 m narrow bore column and a 1.3 mL/min He flow. The resulting peak widths are 0.3 (S) and 0.5 s (P), with a total chromatography time of 12 s. The PFPD frequency was 6.2 Hz.

EXPERIMENTAL PARAMETERS AFFECTING THE PFPD

Temperature is an important parameter which affects all the GC detectors including the PFPD. In Figure 10, we show the

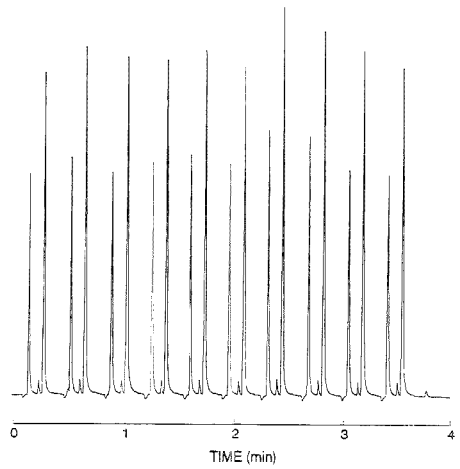

Figure 8. Chromatogram of 10 repetitive injections of a mixture of DMMP and DIMP obtained for the study of peak height reproducibility. A 4 m narrow bore column was used at 100 °C isothermally with a 1.5 mL/min helium column flow rate. $W = 0.8$ s; $F = 3.1$ Hz; $\sigma_A = 1.8\%$; $\sigma_H = 2.2\%$.

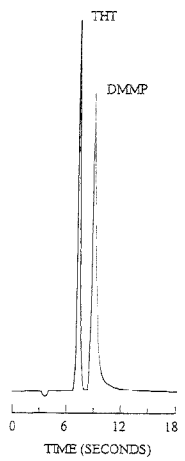

Figure 9. Fast GC of tetrahydrothiophene and dimethyl methylphosphonate. A 3.5 m column was used, and the PFPD was in the sulfur plus phosphorus mode with a WG345 high-pass filter.

PFPD body temperature effect on the detection of both MX1 and MX5 pesticide mixtures in the phosphorus mode. The indicated temperatures here are the actual body temperatures at the combustor zone when the detector used was internally heated, unlike the new design, which is heated only by heat flow from the heated GC detector base. At low detector temperatures, the detection sensitivity is reduced and becomes species-dependent as well. For example, diazinon response is greatly reduced at 140 °C, while that of methyl parathion is reduced to a much smaller extent. In addition, response to the less volatile compounds is generally further reduced at lower temperatures, as expected. Probably the major reason for this behavior is adsorp-

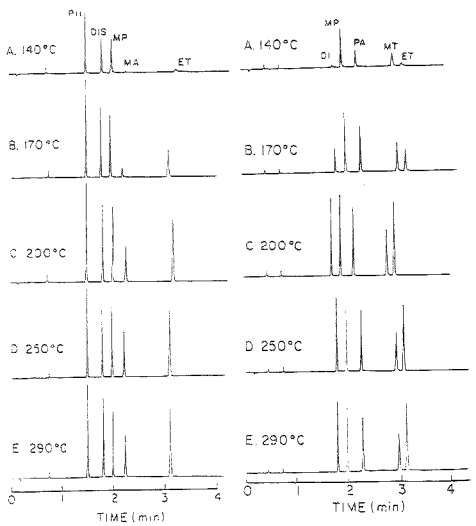

Figure 10. PFPD body temperature effect at the indicated temperatures in the phosphorus detection mode. At the left side, MX1 pesticide mixture was used with 40 pg each of phorate, disulfoton, methyl parathion, malathion, and ethion. On the right side, an MX5 pesticide mixture was used with 40 pg each of diazinon, methyl parathion, parathion, methyl trithion, and ethion in the order of their elution. The fluctuation in the retention times was due to the use of a 50 °C/min temperature programming rate, which is beyond the GC capability.

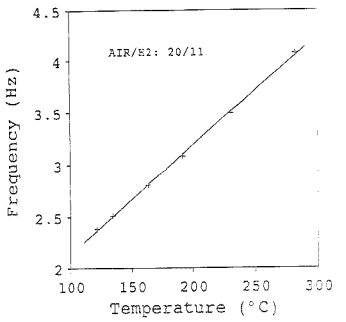

Figure 11. PFPD frequency dependence on the body temperature. The air flow rate was 20 mL/min, while the hydrogen flow rate was 11 mL/min.

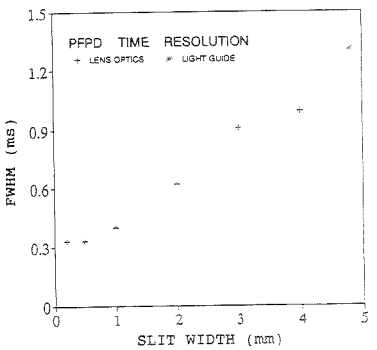

Figure 12. Time resolution of the pulsed flame background (OH^*) emission dependence on the slit width in front of the combustor.

tion on the combustor walls, which can also be selective to certain compounds. Above 200–220 °C, the entire temperature effect is practically eliminated, and at 220–250 °C, the PFPD response is dependent only on the phosphorus content with no molecular effects. Peak area measurements of eight different phosphorus-containing pesticides showed equal response with no molecular effects, so the peak area relates only to the amount phosphorus atoms within an upper limit of ±8%. Even these ±8% can partially be attributed to decomposition in the solvent prior to GC-PFPD analysis, as is evident from the two small peaks near the solvent. This observation[7] is also supported in Figure 10 by the relative area of the various pesticides. It should be noted that with a dirty detector, certain impurities may increase the molecular speciation effects and require higher temperatures. However, the PFPD is usually self-cleaned in a few days. We have studied the temperature effect on the sulfur compounds analysis in gasoline and found no temperature effects even at 140 °C for all the sulfur compounds in gasoline, which are more volatile than the MX5 and MX1 pesticides. In fact, the reduction of the PFPD temperature from 200 °C to 100 °C resulted in an increased sulfur response by a factor of 2.0 and a reduction in noise by a factor of 1.5. Thus, the record MDA achieved for sulfur could be as low as 100 fg/s at 100 °C and 2.4 Hz.

In Figure 11, the PFPD frequency dependence on the body temperature under constant gas flow conditions is illustrated. A pure linear dependence is observed as expected on the basis of a simple gas expansion with increased temperature. The slope of this temperature dependence is about 1.2, and a possible explanation for this is that the flame ignition is easier at higher body temperature and can occur with a combustible gas mixture leaner in fuel which contains a larger fraction of previously combusted gases.

We also tested several designs for the detection optics and found that the use of a quartz rod as a light guide is superior to lens optics in terms of light collection efficiency. Clearly, the small diameter of the light guide provides the best temperature insulation for the photomultiplier from the heated PFPD body, and a body temperature of 500 °C was tested without any noticeable rise in the photomultiplier temperature. Lens optics has one advantage over the light guide in that it provides better imaging of the pulsed flame light, and with the aid of a reduced slit width in front of the combustor, improved emission time resolution could be obtained. In Figure 12, the OH^* pulsed flame background emission time width is plotted against the imaging slit width. An approximate linear dependence is observed with saturation at 0.3 ms. The observed background peak width of the pulsed flame emerges from the time of travel of the pulsed flame in front of the observation window. Probably, even 0.3 ms is not the true emission time of OH and is due to the pulsed flame front having a meniscus due to the colder flame at the combustor walls. On the other hand, the sulfur emission time was independent of the slit width and can be attributed to postflame chemical processes only. The ability to achieve better time resolution may be important in the future for organometallic detection, as atomic emission exhibits only a 0.5–1 ms delay. For conventional

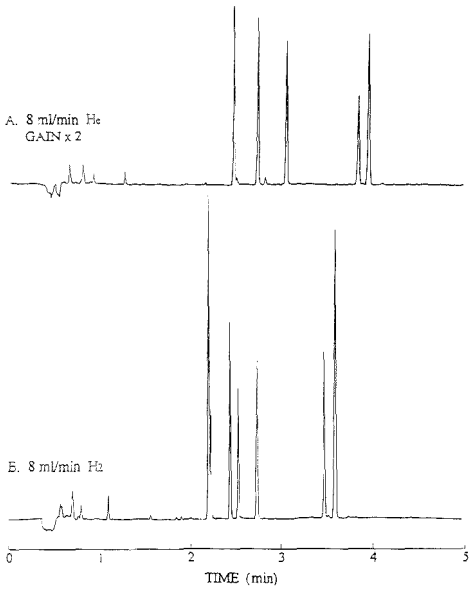

Figure 13. Comparison of pesticide analysis in the phosphorus mode using helium (A) and hydrogen (B) as carrier gases. The carrier gas flow rate was 8 mL/min, and the pesticides were (in the order of elution) diazinon, methyl parathion, parathion, methyl trithion, and ethion, each at 100 pg in the column; 25 m of 0.32 mm i.d. wide bore column was used with HP-1 film.

analysis of sulfur and phosphorus, the light guide optics is preferred, and a time resolution of 1.3 ms is sufficient.

In Figure 13, we compare the use of helium and hydrogen as carrier gases. We note that as the carrier gas flow rate is increased, the detection limits are reduced due to sample dilution, and above 6–8 mL/min, the emission time also begins to be reduced due to an extended intracombustor mixing zone above the column. The use of hydrogen as a carrier gas reduces the dilution effects and thus provides the best sensitivity at a high carrier gas flow rate. It can be seen from Figure 13 that the peak heights are more than 3 times higher with 8 mL/min hydrogen than with an 8 mL/min helium flow rate. In addition, the chromatographic analysis time is shorter and has narrower peak widths. However, hydrogen may promote catalytic dissociation in the injector, probably due to the reduction of metal oxides in the glass injector liner. This dissociation is assumed to be eliminated with on-column injection, but in Figure 13, we show a partial injector-induced dissociation of methyl parathion and parathion in the split–splitless injector. The replacement of H_2 by He eliminates this problem, but about 1 h is required for this. Such hydrogen-induced dissociation through the activation of catalytic sites in the glass injector liner is known for chlorinated pesticides,[14] and a similar explanation is provided.[14]

The use of hydrogen as a carrier gas is very appealing for field applications. Trace B was achieved with a column flow rate of 8 mL/min hydrogen, and no detector hydrogen was added; thus, the column flow serves also as the PFPD detector hydrogen. The use of hydrogen as a carrier gas allows PFPD operation with up to 40–50 mL/min hydrogen column flow. The detector sensitivity is about constant up to a 8–10 mL/min column flow rate and then decreases in a linear manner. The emerging conclusion is that with hydrogen as a carrier gas, even a packed column flow can be effectively coupled to the PFPD.

(14) Wells, G. *J. High Resolut. Chromatogr. Chromatogr. Commun.* **1983**, *6*, 651.

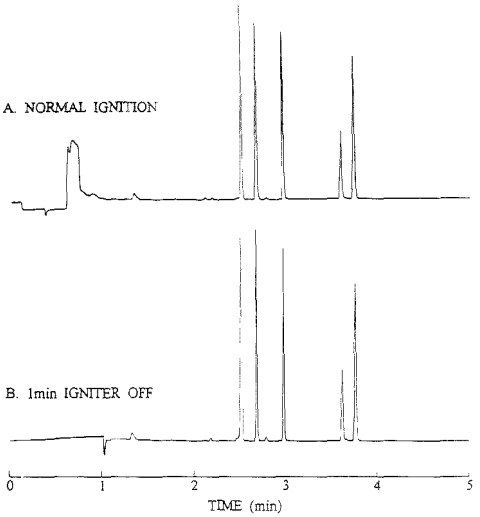

Figure 14. Injection of chlorinated, fluorinated solvent into the PFPD in the phosphorus mode. $C_2F_3Cl_3$ was injected splitless as a solvent (1.2 μL) with the pesticide mixture MX5 as in Figure 13 (120 pg of each component). In trace A, normal ignition was employed, while in trace B the igniter was off and turned on 1 min after injection.

One of the many requirements of modern GC detectors is compatibility with chlorinated and fluorinated solvents. Upon combustion, these solvents form a very chemically aggressive environment of HF and HCl with water vapor at high temperatures. This environment is highly corrosive to conventional stainless steel such as 304 or 316. In the PFPD, the majority of the solvent flows out uncombusted, as the flame cannot be ignited in the solvent elution time. Only at the solvent tail is the pulsed flame ignited, and some minor corrosion can occur, but it is greatly reduced relative to the corrosion observed with a continuous flame FPD. In Figure 14, trace A, we show the MX5 pesticide mixture analysis using 1.2 μL splitless injection of this mixture in a $C_2F_3Cl_3$ ("algofren") solvent. The pulsed flame is automatically turned off at the 30 s solvent elution and reignited only at its diluted tail. The existence of HCl and HF in the flame creates some background, probably due to impurities removed from the stainless steel body which are brought back to the combustor in the cooling decompression cycle. This background is gradually removed, and the PFPD can be used periodically, although the MDA is somewhat increased due to higher chemical noise. An alternative approach is to shut off the igniter for 1 min until the entire solvent tail has eluted from the PFPD. In this way, as shown in Figure 14, trace B, no chemical background is formed, and the PFPD can be used indefinitely without any further consideration of the chlorinated/fluorinated solvent used, as no solvent combustion occurs. Finally, although not tested, it is reasonable to assume that production of the combustor holder

and spiral igniter chamber shown in Figure 1 from Hastalloy C-276 or Inconel 625 could also reduce long-term effects, as these alloys are not attacked by halogen acids, and the PFPD has been found to work effectively with these alloys.

THE ADDED DIMENSION OF TIME AND THE DUAL GATE APPROACH

The major feature of importance of the PFPD is that it adds a new dimension of time dependence which can be used to enhance the level of information provided. In the simple description used so far, a gated amplifier was used[5] to separate the flame background and hydrocarbon emission from that of sulfur and phosphorus compounds and thereby improve both the detection sensitivity and selectivity. In this section, we shall explore further usages of this time domain information. As was previously shown,[5] each element C, S, P, and N has its own unique emission time dependence. Since hydrocarbon combustion to CO, CO_2, and H_2O is very exothermic, it is fully completed during the flame passage by the viewing window. On the other hand, the chemiluminescence reactions of heteroatoms involve the formation of molecules and radicals such as S_2, HPO, and HNO, which have weaker bonds, and thus these reactions occur in the cooler postflame reactive conditions. While the emission of hydrocarbons can be isolated and separated in time, each of the above elements (and also As, Sn, Se, Ge, Sb, etc., as will be described in a future publication) exhibits its own unique emission time dependence, with sulfur showing the longest emission time delay and nitrogen the shortest.

While each of these elements can be easily identified through its emission as observed on the oscilloscope, here we advance a new method for automatic heteroatom identification, entitled gate response ratio (GRR).

In Figure 15, we show the PFPD chromatogram of a mixture of three compounds containing either N or S or P, in order of their elution. A high-pass WG345 filter was employed with a R1463P red-sensitive PMT. In trace A, a normal gate with a short delay was used to avoid carbon emission. In trace B, the gate delay was increased by 4 ms, and the gate gain was slightly increased so that the sulfur response remained the same. It is clearly observed that in comparison with the sulfur unit GRR, the GRR of phosphorus was 0.22, while that of nitrogen was 0.09. While the actual emission time depends on the PFPD temperature and relative H_2 and air flow rates, under given detector conditions, the GRR is an element-specific feature, independent of the concentration throughout its linear dynamic range. Thus the GRR is a feature unique to each element, and by a single calibration with a solution as used in Figure 15, it can be used for unambiguous element identification. In Figure 15, a dual-gated amplifier was used with a Spectra Physics integrator having two channels and a memory, so Figure 15 was obtained with a single injection for the two traces. We have recently developed software that allows this analysis to be made with a single injection through postrun data analysis of the PC-stored PFPD emission traces.[15]

One of the more important challenges of flame photometry is the analysis of organophosphorus pesticides/insecticides in fruit and vegetable extracts.[15] While low detection limits of 10 ppb are required, a high selectivity is required against both hydrocarbon and sulfur compounds, which in certain cases makes this analysis difficult or precludes it altogether.[16] Usually, the sulfur emission is separated from that of phosphorus with the help of an optical interference filter. However, sulfur also emits at the emission wavelength of phosphorus, and its emission intensity at 526 nm is about 4% of that at 394 nm.[5,17] This problem is further exacerbated by the quadratic dependence of the sulfur emission, which is very strong at large sulfur amounts.

This problem is shared by the PFPD and FPD with some minor differences. In the PFPD, the sulfur response is enhanced slightly more than that of phosphorus, even with combustors having 3 mm i.d., and the use of a wide-band WG495 high-pass filter for phosphorus detection further reduces the P/S selectivity by a factor of 2.0 (experimentally verified). On the other hand, the use of a relatively narrow gate at a PFPD temperature of 250 °C improves the P/S selectivity by a factor of 4. Thus, it is believed that under these conditions, the PFPD is equivalent to or slightly better than the FPD in its reduced sulfur interferences. However,

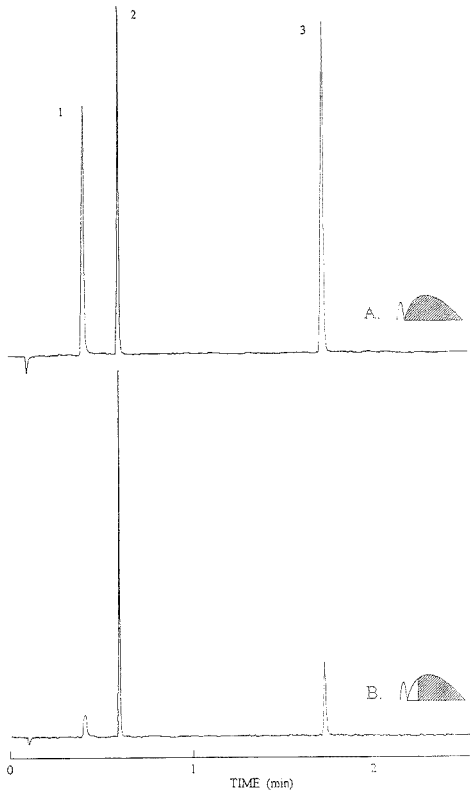

Figure 15. Gate response ratio (GRR) (dual-gated PFPD) for elemental identification. Chromatograms A and B were simultaneously achieved with different gate positions as indicated. See text for explanation. A 0.34 μL solution of 1% nitrobenzene (1, 34 ng), 3 $\times$ 10^{-5} benzothiophene (2, 100 pg), and 3 $\times$ 10^{-5} tributyl phosphate (3, 100 pg) was injected with a split ratio of 100:1 into a 4 m narrow bore column. A WG345 high-pass filter was used.

(15) PFPD software demonstration diskette is available upon request from the authors.

(16) Lee, S. M.; Wylie, P. L. *J. Agric. Food. Chem.* **1991**, *39*, 2192.

(17) Aue, S. M.; Sun, X. Y. *J. Chromatogr.* **1993**, *633*, 151.

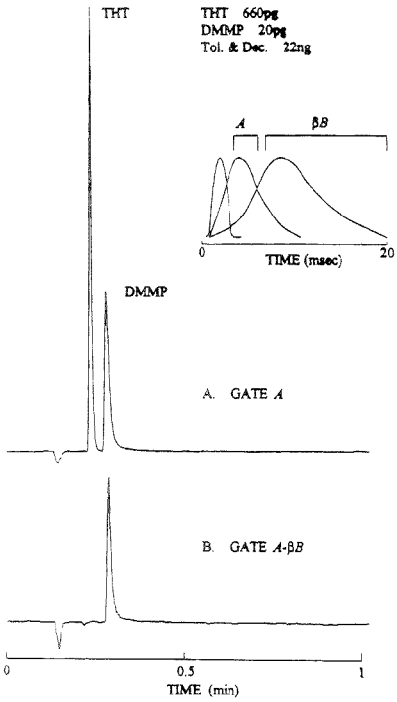

Figure 16. Dual gate subtraction method to enhance P/S interheteroatom selectivity. A 0.22 μL methanol solution of 3×10^{-4} tetrahydrothiophene, 9×10^{-6} dimethyl methylphosphonate, and 1% toluene and decane was injected using a split ratio of 100:1. A 4 m narrow bore column was used at 80 °C. A GG495 high-pass filter was used.

the different emission time dependence can be used for an almost complete elimination of sulfur interferences.

Referring to Figure 16, a dual-gated amplifier approach can be used. In the inset drawing in Figure 16, the carbon, phosphorus, and sulfur emission time dependencies are shown. Gate A can be positioned on the phosphorus emission as shown, with no time overlap with the carbon emission and with a small and unavoidable overlap with the sulfur emission. Gate B is further delayed to collect the majority of the sulfur emission and relatively little of the phosphorus emission. We can now choose a variable gain β so that $A - \beta B$ is zero for sulfur (A and B are the gate response of gates A and B, respectively). Since β is small, the phosphorus response presented by $A - \beta B$ will be only slightly reduced. This idea was experimentally tested as shown in Figure 16. Trace A is dominated by the high tetrahydrothiophene (THT) peak emerging from 660 pg of THT. In trace B, a dual-gated amplifier was used, and β was adjusted so that the sulfur response became zero and was buried in the noise. It is important to note that all the points across the THT peak are zero since the sulfur emission time shape does not depend on its concentration within its linear dynamic range. Only at sulfur levels over 300 pg/s (several nanograms of sulfur compounds) is the sulfur emission time gradually changed, and this $A - \beta B$ dual gate approach becomes less effective as the sulfur compounds manifest their

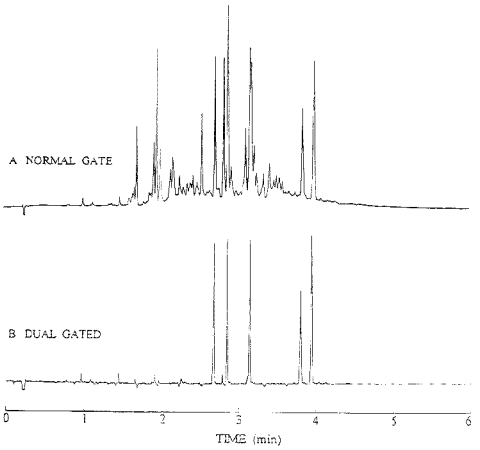

Figure 17. PFPD analysis of MX5 pesticides (50 pg of each component) in a diesel fuel (5 μg) in the phosphorus mode. Trace A was obtained using the normal phosphorus gate. Trace B was obtained using the dual gate subtraction method, and only the MX5 pesticides as identified in Figure 13 are shown.

presence in derivative-shaped GC peaks. Trace B also contains a solvent and two hydrocarbon compounds at large excess which are undetected. Thus, trace B demonstrates a greatly improved P/S interheteroatom selectivity, by more than a factor of 300, without sacrificing the specificity against carbon emission, accomplished with only a marginal reduction of the phosphorus detection sensitivity. In Figure 17, this enhanced P/S selectivity is demonstrated with the analysis of MX5 pesticide mixture spiked into an Israeli diesel fuel. Diesel fuel is known to contain several thousands parts per million of total sulfur in a large variety of compounds. In trace A, the chromatogram of the spiked diesel fuel under the normal P mode conditions is shown. Although a few of the pesticides can be observed, their quantitative analysis is hampered by the presence of many sulfur compounds, each in a large amount. Trace B shows the results of the dual gate $A - \beta B$ approach. We note that traces A and B were simultaneously obtained with the dual-gated amplifier. A dramatic improvement of P/S selectivity is observed, and the pesticides can be effectively and quantitatively analyzed. The minor dips observed are due to minor AC coupling problems that resulted in minor dips at the elution of large amounts of hydrocarbons (out of gate emission). The two small peaks at 1.0 and 1.4 min are due to pesticide impurities (P molecules). Thus, it is concluded that the dual gate approach can be used under complex mixture analysis conditions.

An additional limitation of FPD is found in its limited mesaurement dynamic range. In normal GC detection electronics, the amplifier noise is about 10 μV, which is 1% of the attenuation range 1, while the maximum signal is 1.024 V. Thus, the measurement dynamic range is limited to 5 orders of magnitude. Since the sulfur response is quadratic with the sulfur concentration, the measurement range is only 2.5 orders of magnitude at most.

In addition, the sulfur response shows saturation due to self-absorption[5] soon after this limitation is reached. With the PFPD, the emission time domain can be used to relax these limitations. Consider the simultaneous use of two gates. The first is gate A, which is the normally encountered gate for sulfur response. The

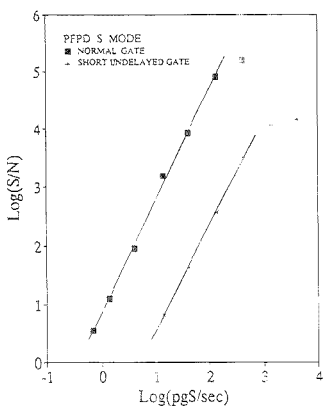

Figure 18. Dual gate approach for extended measurement dynamic range. The calibration curve with solid squares was obtained with a normal gate in the sulfur mode. The curve with asterisks was achieved with a 2 ms undelayed gate.

second gate is a short (i.e., 2 ms), undelayed gate positioned on the flame background. While the normal gate is saturated, the short, undelayed gate B is far from saturation, as the sulfur response in it is only about 1% of that of gate A. The electronics saturation is thus expected to be at a sulfur concentration which is an order of magnitude higher, while sulfur self-absorption affects the sulfur-delayed emission only.[5] In Figure 18, we show the dual gate response approach in the dual simultaneous calibration curve. It is clearly observed that the standard goal of over 3 orders of magnitude measurement dynamic range is now achievable at the small price of using two gates simultaneously. Figure 18 was achieved with an analog dual-gated amplifier, but based on our experience with our new software, it is estimated that the measurement dynamic range could be increased to 4 orders of magnitude.

Another major problem of FPD is response quenching by the coelution of a large amount of hydrocarbons.[1,2] This problem can be identified through its effect on the reduction of the sulfur emission time delay, and with the help of the GRR, it can also be corrected. Alternatively, combustible gas mixtures richer in air can be employed together with a narrow gate for the practical elimination of quenching. The subject of quenching, its origin, identification, correction, and elimination is described in detail elsewhere.[18]

It should be emphasized that the dual gate response ratio method described is similar in its concept to the dual photomultiplier channel response approach developed by Aue and coworkers.[19–21] In this elegant series of publications, it was described how a FPD having two photomultipliers with different optical filters can be used for heteroatom identification and for the increase of interheteroatom selectivity. In this dual channel approach, the response ratio of the two optical channels provides unambiguous elemental identification, and the subtraction of $A - \beta B$, where A and B are the detection channels, provides "infinite selectivity" within the linear dynamic range.

(18) Kalontarov, L.; Jing, H.; Amirav, A.; Cheskis, S. *J. Chromatogr. A* **1995**, *696*, 245.
(19) Aue, W. A.; Millier, B.; Sun, X. Y. *Anal. Chem.* **1991**, *63*, 2951.
(20) Aue, W. A.; Sun, X. Y.; Millier, B. *J. Chromatogr.* **1992**, *606*, 73.
(21) Millier, B.; Sun, X. Y.; Aue, W. A. *Anal. Chem.* **1993**, *65*, 104.

We believe that for practical applications the dual gate approach is superior to the dual optical channel approach for to the following reasons:

(1) A photomultiplier and its associated optics and electronics are far more expensive (and bulkier) than an additional electronic gate.

(2) The PFPD is more sensitive than the FPD, and its gas consumption is lower.

(3) Both the dual channel and dual gate approaches can provide improved selectivity against one additional heteroatom. In the PFPD this is generally enough, as the specificity against hydrocarbon molecules is automatically obtained through the delay of the two gates. Thus, the PFPD can be specific in the P mode against both carbon and sulfur interferences, while in the dual optical channel FPD approach, the selectivity against only one element (either C or S) can be improved. The specificity against hydrocarbons is important, as it allows the use of the dual gate approach in real-world hydrocarbon-rich mixtures, such as the diesel fuel demonstrated in Figure 17.

PRACTICAL EXAMPLES—THIOPHENE IN BENZENE, PESTICIDES IN A BROCCOLI EXTRACT, AND A SULFUR DRUG IN SERUM

The final test of any analytical instrument is in its ability to solve real-world problems. We have tested our PFPD and a PFPD provided to us by Varian (first version before its commercial availability).

We have been approached by Gadiv Petrochemistry, Haifa, Israel, with the problem of thiophene analysis in benzene solvent, and similarly methylthiophene in toluene. These compounds possess a boiling point near that of the solvent and thus require a special catalyst for their removal. The presence of thiophene in benzene is regulated to be lower than 1 ppm. Currently, a total sulfur analyzer is used, but GC-PFPD seems to be a better way, as it also provides molecular information which reflects on the operation of the catalyst. The desired goal was a detection limit of 100 ppb, which is an order of magnitude lower than the regulated level. We used the method published in the literature[22] for this analysis and employed a 30 m megabore column from J&W with a polar DB-Wax of 1.0 μm film thickness. A Varian 3600 GC was used with its split–splitless injector closed for 0.5 min and then opened to a split ratio of 8. The injection was at 50 °C, with a wait period of 1 min, programmed at 20 °C/min to 150 °C. Hydrogen was used as a carrier gas at a 7 mL/min flow rate, and 1–2.5 μL samples were injected. In Figure 19, we show our results using a Varian PFPD in the analysis of a 100 ppb thiophene in benzene sample. The sample was provided by Gadiv Petrochemistry and was determined by a total sulfur analyzer to contain 96 ppb thiophene. It is demonstrated that 100 ppb thiophene can easily be analyzed with pen-limited baseline noise. This analysis can be compared with the report of Shearer et al.,[22] who performed the same analysis (shown in their Figure 4) using the Sievers flame sulfur chemiluminescence detector (SCD). We note that the PFPD demonstrates better sensitivity and a smaller solvent effect with a much faster solvent recovery time, as well as an improved chromatographic peak shape. It should be pointed out that while the PFPD and the flame SCD may have a similar reported MDA,[5,22] the quadratic response of the PFPD results in

(22) Shearer, R. L.; O'Neal, D. L.; Rios, R.; Baker, M. D. *J. Chromatogr. Sci.* **1990**, *28*, 24.

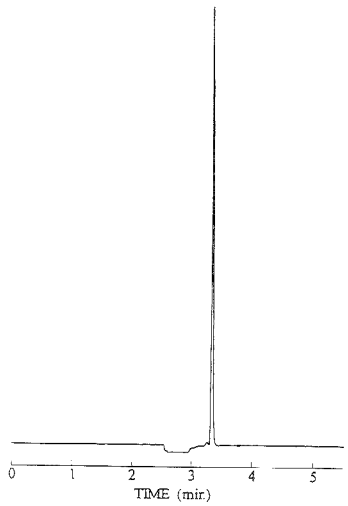

Figure 19. Analysis of 100 ppb thiophene in benzene using the Varian PFPD. See text for conditions.

a much better signal to noise ratio at a given low level of sulfur above the MDA, as shown in Figure 19. The quadratic behavior limits the measurement dynamic range, but on the other hand, it also allows quantitative measurements to be performed at levels very close to the MDA.

In Figure 20, we demonstrate the analysis of pesticides in a broccoli extract. The broccoli extract was provided to us by John Robinson of Varian Chromatography Systems and was spiked with 1% MX5 pesticide mixture, resulting in 100 ppb each of diazinon, methyl parathion, parathion, methyl trithion, and ethion (in the order of their elution time). A 4 m narrow bore (0.25 mm i.d.) column from J&W with DB-1 of 0.25 μm film thickness was used with a Varian 3600 GC. Several 1.0 μL samples were injected splitless using the split–splitless injector, and a helium carrier gas was used at a 2.6 mL/min flow rate, measured at 60 °C. The GC column was at 60 °C during the injection for 1 min and then programmed at 50 °C/min to 220 °C. The Varian PFPD was used in the P mode at a detector base temperature of 250 °C. The PFPD electronics was our homemade dual-gated amplifier.

In Figure 20, we show the results obtained using the dual gate approach. Trace A shows the chromatogram obtained using a typical phosphorus gate of 6 ms, while gate B was 12 ms long and further delayed by 4 ms. Trace A shows signals for the five phosphorus-containing pesticides, together with a multitude of weak sulfur interfering compound peaks and two very strong sulfur peaks of molecules naturally present in the broccoli extract. It is shown that the comparison of traces A and B, which were simultaneously obtained, allows the immediate identification of the five pesticides using the gate response ratio method as explained before and demonstrated in Figure 15. We have used the $A - \beta B$ gate subtraction method as shown in Figures 16 and 17, but the two very strong sulfur peaks could not be eliminated due to saturation effects, although they were the only remaining perturbation. In trace C, we show the results of the gate subtraction method achieved with the injection of 0.2 μL. In trace C, all the sulfur interferences were totally removed, and only the

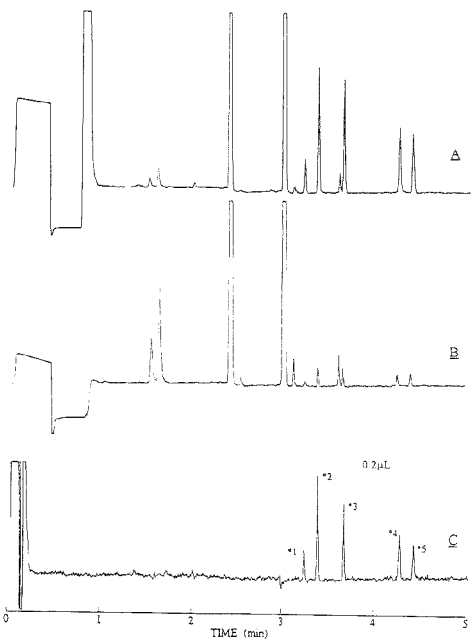

Figure 20. Analysis of pesticides in a broccoli extract spiked with 1% MX5 pesticide mixture. Trace A was achieved with the normal phosphorus gate, while in trace B the gate was delayed 4 ms. In trace C, the dual gate subtraction method was employed, and only 0.2 μL was injected. (1) Diazinon; (2) methyl parathion; (3) parathion; (4) methyl trithion; (5) ethion.

five pesticides are shown. The actual PFPD body temperature was only 160 °C during this experiment, so some molecular effects are observed, and a higher GC detector base temperature should have been used.

Figure 20 demonstrates the ability of the PFPD to analyze phosphorus pesticides at the required 10 ppb level of minimum detected concentration without any hydrocarbon interferences and with largely reduced sulfur perturbations. The elimination of these interferences allows the use of a much shorter column, with a resulting reduction in the analysis time to 5 min, as shown in Figure 20. We note that according to ref 16, FPD is considered to perform poorly in the analysis of phosphorus pesticides in broccoli extract, which is now possible with the PFPD.

Another demanding application was the analysis of a new anti-Alzheimer drug developed at the Israel Biological Institute in human serum. The goal was to analyze the drug at the 10 ppb–2 ppm concentration range. The drug, identified as AF102, contains both sulfur and nitrogen heteroatoms. A nitrogen–phosphorus detector was tried, but the result was a highly congested and unresolved chromatogram due to the presence of large amounts of nitrogen compounds in the human serum. Thus, it was decided to try the PFPD. We received a blank extract sample and a spiked extract. The serum was extracted with chloroform and then dried and rediluted with toluene. A 1 μL aliquot was injected splitless using a 4 m narrow bore column (J&W DB-1, 0.25 μm film thickness). Our PFPD was used on a Varian 3600 GC, and the results are shown in Figure 21. Three GC peaks are added in

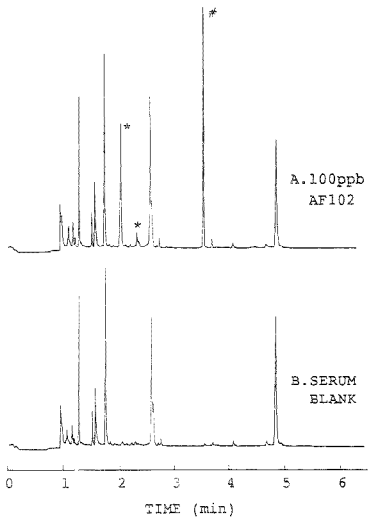

Figure 21. Analysis of an anti-Alzheimer drug in a human serum extract. The PFPD was used in the sulfur mode with a BG12 filter. The injector was at 150 °C, and a 4 m narrow bore column was used with 2.1 mL/min helium carrier gas flow rate. Splitless injection of 1 μL was performed at 80 °C initial column temperature for 1 min, followed by programming to 250 °C at 40 °C/min.

the chromatogram in comparison to that of the blank. The pronounced peak at 3.5 min marked with a # was identified as a sulfur impurity in the toluene solvent used to prepare the spiked extract and should be ignored. We have found that AF102 is a thermally labile compound which dissociates in the injector and on the column, although it is relatively volatile. The small peak with an asterisk at 2.3 min is that of the drug itself, while the higher peak at 2 min marked with an asterisk is that of a thermal dissociation product of the drug. We found that the monitoring of this dissociation product is more sensitive and reproducible than that of the drug itself, although frequent periodic recalibration will be required. Thus, the drug can be analyzed at levels close to those required. However, the major universal conclusion emerging is that sulfur drugs can be analyzed at low parts-per-billion levels in human serum, and the chemical noise and interference is much lower than with the nitrogen–phosphorus detector. Actually, all the background peaks in the blank are of 100 ppb and lower molecular concentration, and large time gaps appear even with a 4 m long column, so with the appropriate choice of column, development of a drug analysis method should be relatively simple.

(23) Jing, H.; Amirav, A. To be published.

CONCLUSIONS

Pulsed flame is a new concept in the operation of flame-based detectors. It was applied first in the development of the PFPD which is now commercially available from Varian. The main feature that characterizes the PFPD is the added dimension of time in the analysis of flame emission. As a result, the PFPD is considerably more sensitive than the FPD and incorporates dramatic improvements in its selectivity against hydrocarbons and other interfering heteroatoms. These two major features enable the selective detection of nitrogen compounds as well as several other heteroatoms.[23] With minimal hardware modifications, the PFPD can be combined with a pulsed flame ionization detector to provide a simultaneous PFPD–PFID operation.[5] On the other hand, a limited carbon channel exists in the PFPD itself through the reversed use of time separation of carbon emission from the heteroatom emission,[5] which can be used without modification. These advantages, combined with a considerably reduced gas consumption (H_2, air), make it a viable addition to the family of GC detectors. Our goal is to make the PFPD a universal, tunable, selective GC detector that provides the information content of FPD, FID, NPD, and AED in one easy-to-operate detector, with several advantages over each of the detectors mentioned above for practical applications.

ACKNOWLEDGMENT

This research was supported by a grant from the Israel Science Foundation, Administered by the Israel Academy of Sciences and Humanities. The collaboration and contributions of Richard Simon (currently of O.I. Analytical), John Robinson, and Sue Ann Scheppers of Varian Chromatography Systems are greatly appreciated.

Received from review March 2, 1995. Accepted June 21, 1995.[⊗]

AC950222T

[⊗] Abstract published in *Advance ACS Abstracts,* August 1, 1995.

Anal. Chem. 1995, *67*, 3319–3323

Enantiomer Discrimination by Continuous Precipitation

Evaristo Ballesteros, Mercedes Gallego, Miguel Valcárcel, and Felix Grases*

Department of Analytical Chemistry, Faculty of Sciences, E-14004 Cordoba, Spain

A continuous turbidimetric method for the discrimination of enantiomers (L- and D-lysine) by the inhibitory action of L-lysine on the crystallization of L-glutamic acid is proposed. A multidetection flow system including an open–closed loop and a single detector permits the determination of kinetic parameters for the crystallization of L-glutamic acid in the presence of 2-propanol. L-Lysine can thus be determined in the presence of a 20 times higher D-lysine concentration. The proposed method was applied to the determination of L-lysine in pharmaceutical preparations with good results.

Some organic substances act as crystallization inhibitors for organic molecules with similar chemical structures (or a slightly different bulk component of the molecular crystal).[1,2] The inhibitory effect can be assigned to selective interactions with the foreign molecule at specific points in the crystallizing substance which induce marked changes in the crystallization rate at very low inhibitor concentrations. These processes have found application in analytical chemistry[3] (e.g., in the determination of amino acids using batch procedures).[4,5]

The flow injection (FI) technique is a major alternative to manual methods of analysis.[6,7] Amino acids have been determined by FI using a liquid chromatograph and chemiluminiscence[8] or electrochemical detection.[9,10] Pohlmann et al.[11] reported a method for the continuous determination of L-lysine using L-lysine α-oxidase and spectrophotometric detection; the peroxide produced in the reaction was reacted with phenol and 4-aminoantipyrine in the presence of peroxidase to obtain a quinone imine dye that was monitored at 500 nm. Various FI systems have been used in conjunction with turbidimetric measurements for the determination of diphenhydramine[12] and, more frequently, sulfate.[13] Continuous precipitation systems integrated in an FI manifold including an atomic absorption detector have frequently been employed for the preconcentration of metal traces[14] and the indirect determination of organic compounds.[15] Rios et al. developed an unsegmented flow system for multidetection using a single detector where the sample plug was confined for repeated passage through the detector; the kinetic curve thus obtained afforded calculation of partial reaction orders and rate constants.[16]

This paper reports an FI system for the discrimination of L-lysine enantiomers by multidetection with a single detector. The use of an open–closed system permits the derivation of the kinetic parameters that influence the crystallization of L-glutamic acid. The presence of L-lysine in the sample inhibits crystallization of the acid. The proposed method permits the selective determination of L-lysine in the presence of D-lysine and other amino acids with no need for a prior separation.

EXPERIMENTAL SECTION

Reagents. L-Glutamic acid, L-lysine, and the other amino acids used were purchased from Sigma (St. Louis, MO). The solvents (2-propanol, ethanol, methanol, and acetonitrile), sodium hydroxide, and hydrochloric acid were obtained from Merk (Darmstadt, Germany). Glass beads (Sigma), 425–600 μm in size, were used to construct a single bead string reactor (SBSR).

L-Lysine (2 g/L) and L-glutamic acid (4 g/L) solutions were prepared in Milli-Q water and remained stable for at least a week.

Apparatus. A Unicam 8625 UV/vis spectrophotometer connected to a Radiometer REC-80 Servograph recorder and furnished with a Hellma flow-through cell (10 mm light path, 1 mm i.d., 18 μL inner volume) was used. The instrument was set at 550 nm for turbidimetric measurements.

The continuous flow system used comprised two Gilson Minipuls-2 peristaltic pumps, two Rheodyne 5041 injection valves, and PTFE tubing of 0.5 mm i.d. for coils. Poly(vinyl chloride) and Solvaflex pumping tubes were used for aqueous and organic solutions, respectively.

Pharmaceutical Preparations. A volume of 1 mL of liquid sample [drinking ampule (Acticinco; Pierre Fabre S.A.E., Barcelona, Spain), oral drops (Crecibaby; Sociedad Española de Especialidades Fármaco-Terapéuticas S.A., Barcelona, Spain), and

* Author to whom correspondence should be addressed. Present address: Department of Chemistry, University of the Balearic Islands, E-07071 Palma de Mallorca, Spain.

(1) Addadi, L.; Weinstein, S.; Gati, E.; Weissbuch, I.; Lahav, M. *J. Am. Chem. Soc.* **1982**, *104*, 4610–4617.
(2) Addadi, L.; Berkovitch-Yellin, Z.; Weissbuch, I.; Mil, J.; Shimon, L. J. W.; Lahav, M.; Leiserowitz, L. *Angew. Chem., Int. Ed. Engl.* **1985**, *24*, 466–485.
(3) Grases, F.; March, J. G. *Trends Anal. Chem.* **1991**, *10*, 190–195.
(4) Grases, F.; Genestar, C. *Talanta* **1993**, *40*, 1589–1593.
(5) Grases, F.; Costa Bauzá, A.; Forteza, R.; March, J. G. *Anal. Lett.* **1994**, *27*, 2781–2787.
(6) Ruzicka, J.; Hansen, E. H. *Flow Injection Analysis*, 2nd ed.; Wiley: New York, 1988.
(7) Valcarcel, M.; Luque de Castro, M. D. *Flow Injection Analysis. Principles and Applications*; Ellis Horwood, Chichester, 1987.
(8) Hanaoka, N.; Tanaka, H.; Nakamoto, A.; Takada, M. *Anal. Chem.* **1991**, *63*, 2680–2685.
(9) Luo, P.; Zhang, F.; Baldwin, R. P. *Anal. Chem.* **1991**, *63*, 1702–1707.
(10) Tsai, H.; Weber, S. G. *J. Chromatogr.* **1991**, *542*, 343–350.
(11) Pohlmann, A.; Stamm, W. W.; Kusakabe, H.; Kula, M. R. *Anal. Chim. Acta* **1990**, *235*, 329–335.
(12) Martínez-Calatayud, J.; Sánchez-Sampedro, A.; Navasquillo-Sarrión, S. *Analyst* **1990**, *115*, 855–858.
(13) Filha, M. M. S.; Reis, E. F.; Krug, F. J.; Collins, C. H.; Barcan, N. *Talanta* **1993**, *40*, 1529–1534.
(14) Santelli, R. E.; Gallego, M.; Valcárcel, M. *Anal. Chem.* **1989**, *61*, 1427–1430.
(15) Eisman, M.; Gallego, M.; Valcárcel, M. *Anal. Chem* **1992**, *64*, 1509–1512.
(16) Rios, A.; Luque de Castro, M. D.; Valcárcel, M. *Anal. Chem.* **1985**, *57*, 1803–1809.

0003-2700/95/0367-3319$9.00/0

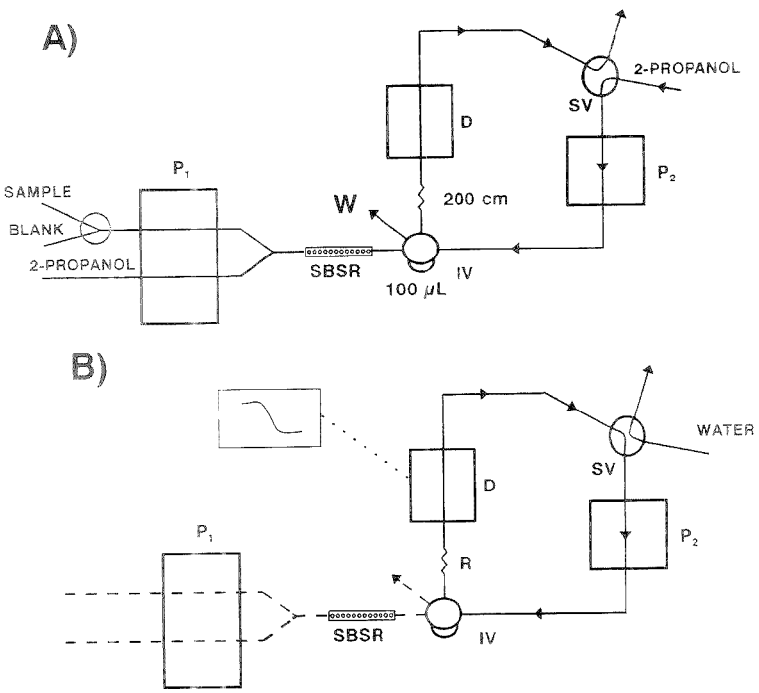

Figure 1. Schematic diagram of the setup used for the continuous determination of L-lysine: (A) introduction of sample or blank and 2-propanol and (B) multidetection of signal. P, pump; SBSR, single bead string reactor; IV, injection valve; W, waste; R, reactor; D, detector; SV, switching valve.

syrup (Trimetabol; J. Uriach & Cia S.A., Barcelona, Spain)] was disolved in 50 mL of Milli-Q water. For tablet formulations (Aminoácidos Esenciales; Nutri Sport S.A., Barcelona, Spain), 10 tablets were ground in a mortar to a fine mesh, and a portion of ~1 g of the resulting powder was accurately weighed. The powder was transferred into a 100 mL vessel, diluted to 50 mL with Milli-Q water, and stirred magnetically for 1 h. The solution was filtered and the residue washed with Milli-Q water, and then the filtrate was diluted to volume with water in a 250 mL calibrated flask. An amount of 3 g of protein–vitamin supplement powder (Gevral Proteína; Cyanamid Ibérica S.A., Madrid, Spain) was mixed with 50 mL of water in a 100 mL vessel, and the mixture was stirred magnetically for 1 h; subsequently, the procedure was continued as for the tablet formulations. For continuous flow analysis, aliquots of 50–250 μL of these solutions (containing about 100 μg of L-lysine) were placed in 10 mL calibrated flasks containing 2.6 g/L L-glutamic acid and diluted to the mark.

Procedure. The manifold used for enantiomer discrimination is depicted in Figure 1. In the first step (Figure 1A), the pharmaceutical sample or standard solution, containing 0.5–20 mg/L L-lysine and 2.6 g/L L-glutamic acid, was continuously introduced into the flow system at 0.3 mL/min and merged with a stream of 2-propanol circulated at 1.5 mL/min. Mixing of both phases was boosted by the SBSR reactor used (30 cm long, 0.8 mm i.d.). The mixture was continuously circulated through the loop of the injection valve (IV). Simultaneously, the open–closed flow loop was filled with carrier (2-propanol) via valve SV. In the second step (Figure 1B), the sample–2-propanol mixture was injected via IV into the 2-propanol carrier at 0.9 mL/min, and SV was switched in order to close the loop. Changes in the reaction mixture were monitored at 550 nm until physical and chemical equilibrium of the system was reached. After the kinetic curve was recorded, SV was switched again, and the open–closed system was flushed with water instead of 2-propanol.

RESULTS AND DISCUSSION

Signal Profile: Measurement Modes. Figure 2 shows two typical signals obtained by using the manifold of Figure 1 in the presence (sample) and absence (blank) of L-lysine. The initial portion of the signal ($0–t_1$) in Figure 2A corresponds to the homogenization of the closed loop. Signal changes arose from changes in the refractive index from pure 2-propanol to the 5:1 2-propanol–water mixture. Crystallization of L-glutamic acid started at t_2. The induction period (t_3) was calculated graphically as shown in Figure 2A. In the abscence of L-lysine (Figure 2B), crystallization started before the loop contents were fully homogeneous, so t_2 was shorter than in Figure 2A. For this reason, t_1 and t_2 were indistinguishable in the blank signal.

There were three ways of drawing analytical information from the signals. The starting crystallization time (t_2) could not be used for this purpose because, at low concentrations of L-lysine, signal changes were the result of two processes (homogenization and precipitation) and hence led to poor precision. Also, the slope of the rising portion of the spanning signal crystallization at variable concentrations of L-lysine provided inadequate differences for implementation of the analytical method. The best choice was

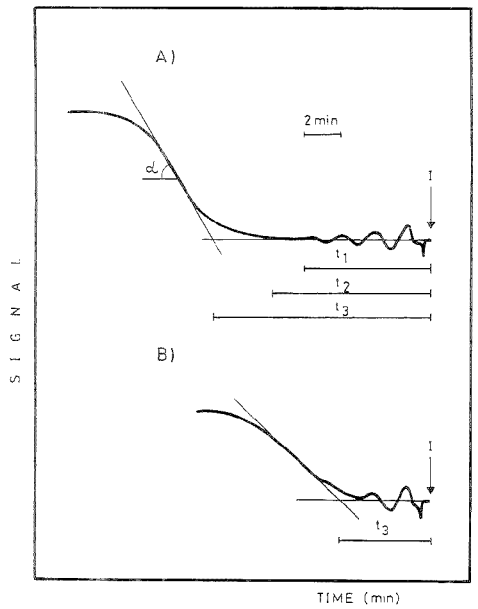

Figure 2. Typical signals for L-glutamic acid crystallization in the presence (sample) and absence (blank) of L-lysine. The sample solution (A) contained 2.6 g/L L-glutamic acid plus 7.0 mg/L L-lysine, while the blank (B) contained 2.6 g/L L-glutamic acid only. t_1, homogenization time; t_2, starting crystallization time; t_3, induction period.

thus the induction period, which was calculated in the presence and absence of L-lysine.

Chemical Variables. The effects of chemical variables were studied by using a continuous flow system similar to that depicted in Figure 1. Two aqueous solutions containing 3 g/L L-glutamic acid (blank) or 3 g/L L-glutamic acid plus 10 mg/L L-lysine (sample) were employed.

Supersaturated solutions of L-glutamic acid were prepared by altering the solvent composition. Thus, addition of an organic solvent to aqueous solutions of this amino acid allowed us to prepare unstable supersaturated solutions. For this purpose, various organic solvents [methanol, ethanol, 7:3 (v/v) ethanol–acetonitrile, and 2-propanol] were continuously mixed with an aqueous solution of L-glutamic acid to induce crystallization of the amino acid. Crystallization in methanol and ethanol was rather slow (about 40 and 15 min, respectively). On the other hand, crystallization in the 7:3 ethanol–acetonitrile mixture or 2-propanol took only 5 min. Simultaneous experiments with L-glutamic acid solutions containing L-lysine (sample) revealed that L-glutamic acid crystallization proceeded similarly in mixtures with the organic solvents tested and in the absence of L-lysine; methanol and ethanol were discarded owing to the long time required for the crystallization of L-glutamic acid. 2-Propanol was thus the optimal choice because Solvaflex pumping tubes are more resistant to it than they are to the ethanol–acetonitrile mixture. 2-Propanol was also selected as the carrier for the open–closed system as it furnished a suitable medium for crystallizing L-glutamic acid.

The L-glutamic acid concentration was optimized by running several calibration graphs for L-lysine at variable concentrations

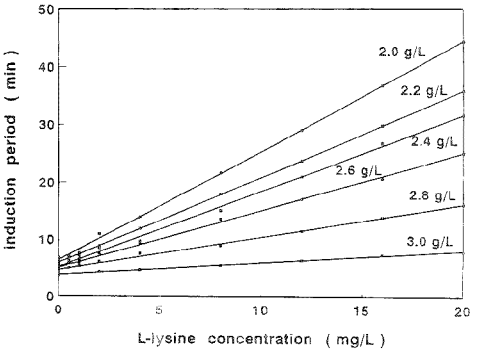

Figure 3. Calibration graphs for L-lysine at variable concentrations of L-glutamic acid.

of L-glutamic acid between 2 and 3 g/L. As can be seen in Figure 3, the length of the induction period increased with decreasing L-glutamic acid concentration; at low L-glutamic concentrations, the crystallization time for the amino acid increased more markedly in the presence of L-lysine than in its absence, which resulted in greater sensitivity. A compromise between sensitivity and sample throughput was made by choosing an L-glutamic acid concentration of 2.6 g/L for further experiments. The sensitivity of the method increased with use of a lower L-glutamic acid concentration. However, this was unnecessary because the L-lysine concentrations in the pharmaceutical preparations studied were at the gram-per-liter level, so the proposed FI system was also appropriate for sample dilution (the sample was diluted 6-fold in 2-propanol before injection into the closed loop).

In aqueous solutions, amino acids are present as cations, zwitterions, or anions depending on the pH. We therefore studied the effect of pH between 2 and 5 (adjusted with 0.1 mol/L HCl or 0.1 mol/L NaOH) on the crystallization of L-glutamic acid. The optimal pH was estimated to be from 3 to 4; outside this range, crystal growth of L-glutamic acid was significantly delayed (the pK_1 and pK_2 values for L-glutamic acid are 2.19 and 4.25, respectively); pH 3.4, obtained by dilution of the blank and sample with water, was finally selected.

Optimization of the Flow Discrimination System. The flow variables influencing the performance of the proposed continuous flow system were optimized by introducing an aqueous solution containing 2.6 g/L L-glutamic acid (blank) or 2.6 g/L L-glutamic acid plus 10 mg/L L-lysine. The sample was merged with a 2-propanol stream and the mixture passed through an SBSR for homogenization.[17]

The sample flow rate was kept at 0.3 mL/min, while that of 2-propanol was varied between 0.3 and 2.0 mL/min. Increasing the 2-propanol flow rate had two opposing effects, viz., diluting the sample (which delayed crystallization of L-glutamic acid) and increasing the proportion of 2-propanol (which boosted crystallization of the amino acid). Because the induction period increased with increasing flow rate, the diluting effect prevailed over the concentrating effect. Below 1 mL/min, throughput and reproducibility were both lower. A 2-propanol flow rate of 1.5 mL/min was thus selected as a compromise between adequate

(17) Reijn, J. M.; Poppe, H.; van der Linden, W. E. *Anal. Chem.* **1984**, *56*, 943–948.

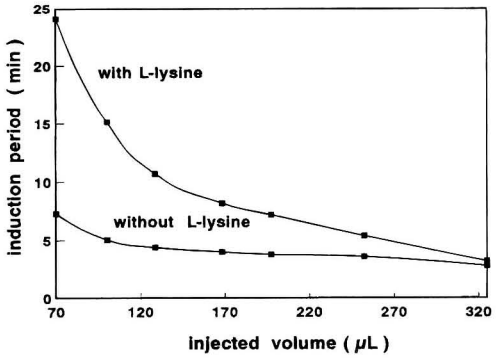

Figure 4. Effect of the injected volume on the crystal growth of L-glutamic acid. Sample, 10 mg/L L-lysine and 2.6 g/L L-glutamic acid; blank 2.6 g/L L-glutamic acid.

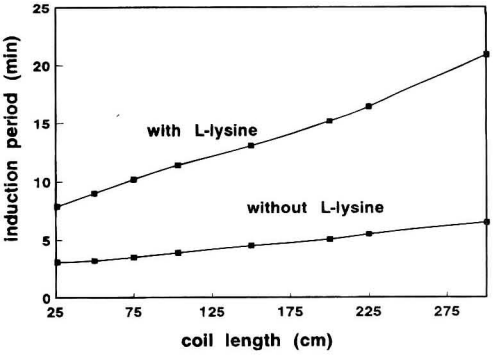

Figure 5. Influence of the coil length (R) on the crystallization of L-glutamic acid. The sample and blank concentrations were the same as in Figure 4.

reproducibility, sensitivity, and throughput. The influence of the length of the SBSR reactor on the homogeneity of the sample–2-propanol mixture was studied over the range 10–50 cm. Above 25 cm, homogenization was complete because the induction period obtained in several determinations of the same sample was quite reproducible. An SBSR reactor of 30 cm was thus selected. The injection valve (IV) could, in principle, be placed at three different positions in the open–closed system (Figure 1): before the SV valve for introduction of 2-propanol; between the switching valve (SV) and pump 2; and between pump 2 and the detector. The best results were obtained by placing the IV between pump 2 and the detector (see Figure 1), because the flow rate of 2-propanol was more uniform after the peristaltic pump and unloading of the loop contents and the subsequent operations were more reproducible. The effect of the flow rate of carrier (2-propanol) in the open–closed system was studied over the range 0.7–1.1 mL/min. At low flow rates, the induction period in the crystal growth of L-glutamic acid was somewhat shorter because of the increased sample dispersion in the system. Above 0.85 mL/min, the signal remained virtually constant in the presence and absence of L-lysine because the dispersion was insignificant. A carrier flow rate of 0.9 mL/min was thus chosen. The effect of the injected volume of the sample–2-propanol mixture on L-glutamic acid crystallization at a constant flow rate of carrier (0.9 mL/min) was studied between 70 and 325 μL. As can be seen in Figure 4, the induction period decreased with increasing injected volume through an increase in the amount of L-glutamic injected. The difference in crystal growth of L-glutamic acid in the presence and absence of L-lysine was higher at low injected volumes, which resulted in increased sensitivity. An injected volume of 100 μL was thus chosen as a compromise between adequate sensitivity and throughput. The influence of the length of the coil located before the detector (R in Figure 1) on L-glutamic acid crystallization was studied between 25 and 300 cm. As can be seen in Figure 5, increasing coil lengths increased the volume of the closed system and hence dilution, which delayed crystallization of L-glutamic acid; the effect was more marked in the presence of L-lysine than in its absence. A coil length of 200 cm was thus chosen for further experiments.

The effect of temperature on the crystallization process was studied over the range 10–40 °C by immersing coil R in a water bath. The induction period for L-glutamic acid crystallization remained constant above 15 °C in the presence and absence of L-lysine, so the open–closed system was maintained at 25 °C.

Table 1. Tolerated Limits for Amino Acids in the Determination of L-Lysine (5 mg/L)

amino acids	maximum tolerated amount (mg/L)
L-Leu, L-Gln, L-Asp, L-Phe, L-Thr, L-Ser, L-Ile, L-Met, L-Val, L-Asn, L-Cys, L-Ala, L-Tyr	>100
D-Lys	100
L-His	15
L-Orn	4

Determination of L-Lysine. Under the selected chemical and flow conditions, the manifold depicted in Figure 1 was used to run a calibration graph for the determination of L-lysine. The graph was constructed by introducing solutions containing 2.6 g/L L-glutamic acid and variable concentrations of L-lysine between 0.5 and 20 mg/L in Milli-Q water. The equation for the standard curve was $Y = 5.05 + 1.01X$ (Y, induction period, in min; X, L-lysine concentration, in mg/L), the intercept representing the induction period in the crystallization of the L-glutamic acid solution used as blank. The correlation coefficient ($n = 8$) was 0.998. The detection limit, calculated as 3 times the standard deviation of the induction period obtained in 10 determinations of the same blank (with 2.6 g/L L-glutamic acid), was 0.3 mg/L. The precision, calculated from 11 samples containing 10 mg/L L-lysine, was 2.5% as relative standard deviation.

Interferences. The effect of other amino acids on the crystallization of L-glutamic acid was studied. The amino acids selected for this purpose were those commonly accompanying L-lysine in pharmaceutical products. The tolerated limits for the amino acids in the determination of 5 mg/L of L-lysine are listed in Table 1. None was found to interfere, except for diaminocarboxylic acids similar to L-lysine (L-histidine and L-ornithine), which were tolerated at concentrations only 3 and 0.8 times the L-lysine concentration. The tolerated concentration of D-lysine was 20-fold that of L-lysine. Synthetic samples containing 5 mg/L L-lysine and variable D-lysine concentrations (25, 50, 75, and 100 mg/L) were used for the determination of L-lysine in the presence of D-lysine. The recovery obtained was almost 100% in all cases.

Analysis of Pharmaceutical Products. The proposed method was applied to the determination of L-lysine in commercially

Table 2. Determination of L-Lysine in Pharmaceutical Products

sample[a]	found[b] (g/L)	nominal contents stated by the manufacturer (g/L)
drinking ampule	39.1 ± 1.1	40.0
oral drops	98.8 ± 3.0	100.0
syrup	51.6 ± 1.8	50.0
tablets	11.8 ± 0.3[c]	11.03[c]
powder supplement	3.2 ± 0.1[c]	3.33[c]

[a] Manufacturer samples are described under Pharmaceutical Preparations. [b] Mean ± standard deviation (n = 5). [c] As % w/w.

available pharmaceutical products by using the manifold depicted in Figure 1. We analyzed five pharmaceutical products in various forms: drinking ampules, oral drops, syrup, tablets, and nutritional supplement powder. Variable volumes of the previously prepared samples (see Experimental Section) were placed in 10 mL calibrated flasks containing 2.6 g/L L-glutamic acid and diluted to the mark. Table 2 lists the results obtained in five individual determinations of L-lysine and their standard deviations. All values were consistent with the nominal contents.

Recoveries were calculated by adding variable amounts of L-lysine to each pharmaceutical product prior to preparation in such a way that the final L-lysine concentration was 2.5 or 5.0 mg/L. The recoveries thus obtained (Table 3) ranged from 96.6 to 102.7%.

CONCLUSIONS

This is the first reported example of the use of adsorption during crystalline growth for analytical purposes in the FI technique. The main advantages of this technique over manual methods, viz., ease of automation and handling, are clearly reflected in the proposed application, which is also more sensitive than its manual counterpart[4] and similarly selective. This can be ascribed to the fact that the crystallization rate of a substance is controlled by a combination of structurally related factors and other, external factors, such as the solvent, temperature, supersaturation, and stirring rate. In order to avoid exceedingly long substrate crystallization times in the proposed FI method, we used 2-propanol rather than the ethanol employed as solvent in the manual method.

Table 3. Recovery of L-Lysine Added to Pharmaceutical Products

sample	content[a] mg/L	added (mg/L)	found[a] (mg/L)	recovery (%)
drinking ampule	4.9 ± 0.1	2.5	7.3 ± 0.2	98.6
	4.9 ± 0.1	5.0	10.0 ± 0.3	101.0
	9.8 ± 0.3	2.5	12.0 ± 0.4	97.6
	9.8 ± 0.3	5.0	14.8 ± 0.4	100.0
oral drops	4.8 ± 0.1	2.5	7.4 ± 0.2	101.4
	4.8 ± 0.1	5.0	9.8 ± 0.2	100.0
	9.4 ± 0.3	2.5	11.5 ± 0.3	96.6
	9.4 ± 0.3	5.0	14.5 ± 0.4	100.7
syrup	5.1 ± 0.1	2.5	7.5 ± 0.2	98.7
	5.1 ± 0.1	5.0	10.2 ± 0.3	101.0
	10.3 ± 0.4	2.5	12.6 ± 0.3	98.4
	10.3 ± 0.4	5.0	15.7 ± 0.4	102.6
tablets	5.5 ± 0.2	2.5	7.9 ± 0.2	98.8
	5.5 ± 0.2	5.0	10.6 ± 0.3	100.9
	11.0 ± 0.3	2.5	13.2 ± 0.4	97.8
	11.0 ± 0.3	5.0	16.3 ± 0.4	101.9
powder supplement	4.8 ± 0.1	2.5	7.5 ± 0.2	102.7
	4.8 ± 0.1	5.0	9.8 ± 0.3	100.0
	9.7 ± 0.2	2.5	12.4 ± 0.3	101.6
	9.7 ± 0.2	5.0	14.3 ± 0.4	97.3

[a] Mean ± standard deviation (n = 3).

ACKNOWLEDGMENT

The Spanish CICyT is acknowledged for financial support awarded for the realization of this work (Grant PB94-0450).

Received for review March 13, 1995. Accepted June 21, 1995.[*]

AC950254G

[*] Abstract published in *Advance ACS Abstracts*, August 1, 1995.

Anal. Chem. **1995**, *67*, 3324–3335

Influence of Compressional Wave Generation on Thickness–Shear Mode Resonator Response in a Fluid

Thomas W. Schneider* and Stephen J. Martin

Microsensor Research and Development Department, Sandia National Laboratories, Albuquerque, New Mexico 87185

Acoustic interferometry was performed with thickness–shear mode (TSM) resonators to investigate the effect of compressional wave generation on the response (resonant frequency and damping). Resonator response was measured while the spacing between the resonator and adjacent solid was filled with fluid and the spacing was varied. A characteristic resonance response was observed whenever the spacing reached a multiple of $\lambda_c/2$, where λ_c is the compressional wavelength in the fluid. Compressional wave generation arises from a gradient in the in-plane surface displacement. A model is proposed to predict the resonator response that arises from combined shear wave and compressional wave generation. Experimental data fit to this model determine device coupling to shear and compressional waves. The model also relates resonator response to the surface displacement profile. By measuring this displacement profile, compressional wave generation can be estimated. The effect of surface roughness and device geometry on shear and compressional wave coupling is examined. The results indicate that even in a semiinfinite fluid, compressional wave generation contributes significantly to device damping (motional resistance) but not to the frequency shift.

A quartz resonator typically consists of a thin disk of quartz with metal film electrodes patterned on opposing surfaces. The electric field generated by applying a voltage between the electrodes creates a mechanical strain in the piezoelectric quartz. The quartz crystal resonates at a frequency determined by the crystal thickness and the acoustic mode that is excited. In X-cut quartz, for example, longitudinal modes are excited, in which the crystal thickness is modulated.[1] In Y-cut quartz, shear modes are excited, in which planes parallel to the crystal faces undergo relative in-plane displacements.[2] Since shear displacement varies across the thickness of the device, these devices are commonly called thickness–shear mode (TSM) resonators. The AT-cut of quartz, commonly used in constructing TSM resonators, is a particular Y-cut that has a low temperature coefficient of frequency around room temperature.

When longitudinal mode resonators are operated in gases or liquids, they generate compressional (sound) waves. Radiation of these compressional waves into a semiinfinite contacting fluid results in severe damping of the crystal. Thus, these devices are not well suited for general liquid-phase sensing applications. However, these devices do function as efficient compressional wave transducers. Due to the low attenuation of compressional waves, they have been used in acoustic interferometry experiments to determine gas and liquid sound velocities.[3–6] By varying the spacing h between the resonator and a parallel reflecting boundary, the compressional wave generated at the resonator surface interferes with that reflected back from the boundary. Acoustic interferometry is performed by measuring the resonator response as a function of h. Constructive interference, and an enhanced response, occurs when $h = n\lambda_c/2$, where λ_c is the compressional wavelength in the fluid and n is an integer. Since $\lambda_c = v_c/f$, where v_c is the compressional sound velocity in the medium and f is the operating frequency, the interval Δh between resonances determines the sound velocity:[7] $\Delta h = v_c/(2f)$.

Thickness–shear mode resonators have been widely used as liquid-phase sensors.[1,8] These devices are less severely damped by fluid coupling than are compressional wave devices; they can be conveniently operated as the frequency control element of an oscillator circuit. The mass sensitivity and low liquid damping of the device enable it to be used as a general purpose gravimetric detector or "microbalance".[9,10] In addition, the device sensitivity to the contacting fluid enables it to be used to measure fluid properties.[11–14]

If the shear displacement is uniform across the surface of the TSM resonator, then only plane-parallel laminar flow is generated in a contacting fluid. The mechanical coupling between the resonator and the fluid perturbs the crystal's resonant frequency and damping (as reflected in the motional resistance)[11] in proportion to $(\varrho\eta)^{1/2}$, where ϱ and η are liquid density and shear viscosity, respectively. The in-plane oscillation of the resonators surface causes a critically damped shear wave to be radiated into the contacting fluid. Since the decay length[11,14] for this shear wave

(1) Mecea, V. M. *Sens. Actuators A* **1994**, *40*, 1–27.
(2) Tiersten, H. *Linear Piezoelectric Plate Vibrations*; Plenum: New York, 1969.
(3) Hubbard, J. C.; Loomis, A. L. *Phil. Magn.* **1928**, *5* (33), 1177–1190.
(4) Pielemeier, W. H. *Phys. Rev.* **1929**, *34*, 1184–1202.
(5) Klein, E.; Hershberger, W. D. *Phys. Rev.* **1931**, *37*, 760–774.
(6) Hubbard, J. C. *Phys. Rev.* **1931**, *38*, 1011–1019.
(7) Martin, B. A.; Hager, H. E. *J. Appl. Phys.* **1989**, *65* (7), 2627–2629.
(8) (a) Buttry, D. A.; Ward, M. D. *Chem. Rev.* **1992**, *92*, 1355–1379. (b) McCallum, J. J. *Analyst* **1989**, *114*, 1173–1189. (c) Schumacher, R. *Angew. Chem., Int. Ed. Engl.* **1990**, *29*, 329–343. (d) Ebersole, R. C.; Ward, M. D. *J. Am. Chem. Soc.* **1988**, *110*, 8623–8628. (e) Roederer, J. E.; Bastiaans, G. J. *Anal. Chem.* **1983**, *55*, 2333–2336. (f) Muramatsu, H.; Dicks, J. M.; Tamiya, E.; Karube, I. *Anal. Chem.* **1987**, *59*, 2760–2765.
(9) Konash, P. L.; Bastiaans, G. J. *Anal. Chem.* **1980**, *52*, 1929.
(10) Nomura, T. *Anal. Chim. Acta* **1981**, *124*, 81.
(11) Kanazawa, K. K.; Gordon, J. G., II *Anal. Chem.* **1985**, *57*, 1770–1771.
(12) Josse, F.; Shana, Z. A.; Radtke, D. E.; Haworth, D. T. *IEEE Trans. Ultrason. Ferroelect. Freq. Contr.* **1990**, *37* (5), 359–368.
(13) Martin, S. J.; Frye, G. C.; Wessendorf, K. O. *Sens. Actuators A* **1994**, *44*, 209–218.
(14) (a) Martin, S. J.; Granstaff, V. E.; Frye, G. C. *Anal. Chem.* **1991**, *63*, 2272–2281. (b) Granstaff, V. E.; Martin, S. J. U.S. Patent 5,201,215, 1993.

0003-2700/95/0367-3324$9.00/0

is much smaller than the spacing that can be controlled between the resonator and a reflecting boundary, interferometric effects cannot be readily observed for the shear wave.

Several researchers have shown[7,15,16] that despite the extremely short decay length for shear waves, acoustic interferometry with TSM resonators *does* result in periodic variations in response for fluid thicknesses out to several hundred micrometers. Moreover, the periodicity of this response does not coincide with the shear wavelength but occurs at half-integral multiples of the compressional wavelength. The dependence of the TSM resonator response on the compressional wavelength indicates that compressional waves are somehow generated by the device, despite the purely in-plane polarization generated in Y-cut quartz.[2]

A plausible explanation for compressional wave generation by the TSM resonator has been proposed by Martin and Hager.[7] They invoked continuity arguments to show that compressional waves are generated in the contracting fluid when the magnitude of surface displacement varies in the displacement direction along the resonator surface. From conservation of mass, variation of in-plane flow leads to surface-normal flow. Displacement variation arises due to the finite lateral extent of the resonator electrodes and the manner in which the edge of the crystal is clamped. Transverse modes are generated that satisfy the boundary condition at the edge of the crystal and determine the displacement variation across the crystal surface.

Various techniques have been employed to map the surface displacement across the crystal: (1) Martin and Hager[17] measured the frequency perturbation as a stylus contacting the device surface was scanned across the surface; (2) Hillier and Ward[18] measured the radial dependence of mass sensitivity using a scanning microelectrode to create localized mass deposits on the resonator surface. These responses can be used to infer the relative surface displacement as a function of position.

The connection between the in-plane displacement profile and compressional wave generation has been made qualitatively but not quantitatively. Lin and Ward[16] have examined the effect of crystal contour on compressional wave generation. A more pronounced interference response was observed with plano-convex crystals than with plano-plano crystals. This was attributed to the greater confinement of acoustic energy near the crystal center (the energy trapping effect) that arises with the plano-convex contour. This result suggests that the in-plane displacement profile significantly influences compressional wave generation, as proposed by Martin and Hager.[7] In addition, Lin and Ward[16] measured the in-plane spatial distribution of the interference response, which indicated that compressional wave generation was maximum at a radial distance of ~1.8 mm from the center of the crystal and a minimum at the center and edges. This suggests that compressional wave generation is dependent upon the gradient of the displacement profile, also consistent with the mechanism proposed by Martin and Hager.

Progress is beginning to be made in establishing a quantitative relation between compressional wave generation and device response. Tessier et al.[15] have described the surface mechanical impedance arising from a fluid layer and an adjacent solid. Measurements made versus fluid temperature generated an interference response that closely resembled the predicted variation in surface mechanical impedance versus fluid temperature. However, a quantitative connection between surface mechanical impedance and device response was not made. The difficulty lies in determining the magnitude of the compressional wave generated by the TSM resonator.

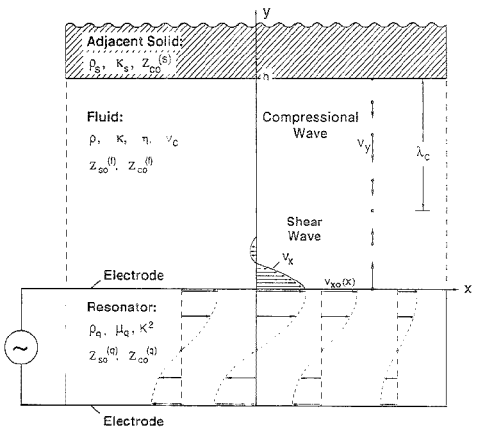

Figure 1. Cross-sectional view of the thickness–shear mode (TSM) resonator with a fluid layer confined between the resonator surface and an adjacent solid.

In this paper, a perturbational analysis is used to calculate the response arising from the combination of shear and compressional waves generated by a TSM resonator. The shear wave is generated, as previously shown,[11] from the in-plane surface displacement. To determine the strength of coupling to compressional waves, continuity arguments of Martin and Hager[7] are invoked. This new contribution to response depends on the in-plane displacement profile. Considering a resonator coupled to a fluid layer confined between the resonator and an adjacent solid provides the interferometric response that will be compared with experimental results. By fitting the calculated response to interference data, the magnitude of the compressional wave generation is determined. Examining devices with various surface roughnesses and device geometries, we determine the influence of these parameters on compressional wave generation. In addition, compressional wave generation and its influence on device response are explicitly related to the in-plane displacement profile. Following Martin and Hager,[17] we use a stylus technique to infer the displacement profile. From this profile, the amount of compressional wave generation expected from a TSM resonator is calculated and compared with experimental results.

THEORY

Liquid Velocity Field. In this section we consider the velocity fields generated by a TSM resonator in a fluid layer between the resonator and an adjacent solid, as shown in Figure 1. For experimental purposes, we assume that the thickness h of this fluid layer is between a few micrometers and a few hundred micrometers. The practical consequence of selecting this thickness range is that, for waves generated at the oscillating resonator surface ($y = 0$), (1) shear waves are highly attenuated upon reaching the upper solid surface (i.e., the liquid layer is acousti-

(15) Tessier, L.; Patat, F.; Schmitt, N.; Feuillard, G.; Thompson, M. *Anal. Chem.* **1994**, *66*, 3569–3574.
(16) Lin, Z.; Ward, M. D. *Anal. Chem.* **1995**, *67*, 685–693.
(17) Martin, B. A.; Hager, H. E. *J. Appl. Phys.* **1989**, *65* (7), 2630–2635.
(18) Hillier, A. C.; Ward, M. D. *Anal. Chem.* **1992**, *64*, 2539–2554.

cally thick for shear waves) and (2) compressional waves are only slightly attenuated over this distance. Thus, the liquid film behaves as infinitely thick for shear waves (an acoustic sink) while forming a low-loss acoustic cavity for compressional waves. In this section, we seek to (1) identify a mechanism for compressional wave generation, (2) determine the surface mechanical impedances associated with generating shear and compressional waves, and (3) relate the sensor response to these impedances.

With the TSM resonator oriented as shown in Figure 1, with displacement in the x-direction and surface-normal in the y-direction, the Navier–Stokes equations that describes fluid velocity components under sinusoidal, steady-state excitation are[19]

$$\eta\frac{\partial^2 v_x}{\partial y^2} - \varrho\dot{v}_x = \eta\frac{\partial^2 v_y}{\partial y\,\partial x} \tag{1a}$$

$$\kappa\frac{\partial^2 v_y}{\partial y^2} - \varrho\dot{v}_y = -\eta\frac{\partial^2 \dot{v}_x}{\partial y\,\partial x} \tag{1b}$$

where ϱ, κ, and η are the density, bulk compressibility, and shear viscosity, respectively, of the fluid; v_x is the liquid velocity parallel to the resonator surface; v_y is the liquid velocity in the surface-normal direction; a dot denotes a time derivative. Equations 1a,b describe waves propagating in the surface-normal direction of the fluid: v_x is a shear wave, while v_y is a compressional wave. Equations 1a,b indicate that these waves are coupled when the velocity fields vary in the x-direction: the term on the right-hand side of each equation involves a derivative of the alternate velocity component.

The source for all liquid motion is the in-plane oscillation of the upper resonator surface at $y = 0$. If the upper resonator surface extended indefinitely and had uniform surface shear velocity v_{x0}, then derivatives with respect to x in eqs 1a,b would be zero. Then the terms on the right-hand side of eqs 1a,b would be zero and these equations would decouple (i.e., the shear and compressional waves would propagate independently). With the boundary oscillating in a pure shear displacement, only a shear wave can be generated in the fluid.

Variations in the surface displacement in the x-direction lead to non-zero terms on the right-hand side of eqs 1a,b. This variation arises due to the finite lateral extent of the resonator, leading to the generation of transverse modes. Each mode satisfies the boundary condition at the edge of the crystal. If the edges of the resonator are clamped, for example, then mode amplitude goes to zero at these points. The superposition of these modes determines the overall displacement profile. Thus, v_{x0} is *not* constant across the device surface but varies as a function of x and z: $v_{x0} = v_{x0}(x,z)$. In this case, the shear and compressional waves are coupled. The in-plane surface displacement generates a shear wave; variation in displacement amplitude across the resonator surface leads to an in-plane variation in the shear wave amplitude generated (nonzero $\partial/\partial x$ in eqs 1a,b). As noted by Martin and Hager,[7] this variation in liquid flow in the x-direction leads to surface-normal flow. This is a consequence of mass conservation, as illustrated in Figure 2. The in-plane variation in the liquid velocity field ($\partial v_x/\partial x$) provides a *source* for compressional wave generation (v_y).

(19) In deriving these equations, the variation in the x-direction is presumed to be much smaller than that in the y-direction, so second derivatives with respect to x can be ignored.

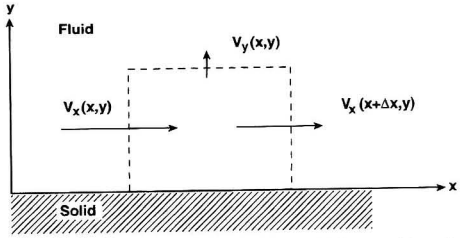

Figure 2. Infinitesimal volume of fluid near the crystal surface, illustrating generation of surface-normal fluid flow by a *gradient* in the in-plane surface displacement.

The shear wave decays rapidly with distance from the resonator surface; thus, the compressional wave originates in the near-surface region of the fluid. The compressional wave propagates largely undamped in the fluid, being reflected back to the crystal surface by an interfacial boundary. Here in-plane variation in the compressional component recouples to the shear component and influences device response. The liquid layer thus acts as a resonant cavity for the compressional wave v_y that is coupled to the shear resonator surface displacement by in-plane gradients ($v_x' = \partial v_x/\partial x$) in the shear liquid velocity field.

Since the shear wave extends only a short distance into the fluid from the resonator surface, the shear and compressional waves are uncoupled across most of the fluid layer. Moreover, if the gradient in surface displacement (v_x') is small, then the coupling terms on the right-hand side of eqs 1a,b are small. To first order, then, the velocity profiles across the fluid layer can be approximated by the uncoupled modes (i.e., solutions to eqs 1a,b when the right-hand sides are taken as zero). We begin by calculating the mode profile for the uncoupled shear wave. We then calculate the mode profile for the compressional wave, assuming coupling only at the lower boundary. We then determine the impedance associated with exciting each mode. In the next section, we use a perturbation analysis to determine device response from these impedances.

Shear Wave. The viscous nature of the fluid allows a damped shear wave to be radiated into the fluid by the in-plane displacement v_{x0} of the resonator surface. For the moment, the in-plane surface displacement v_{x0} will be considered constant; in the next section, the effect of v_{x0} varying with x and z will be considered. The uncoupled shear liquid velocity field is found by solving eq 1a with the right-hand side set to zero:[11]

$$\eta\frac{\partial^2 v_x}{\partial y^2} = \varrho\dot{v}_x \tag{2}$$

Equation 2 is solved subject to the boundary condition imposed by the in-plane oscillation of the resonator surface.

When the thickness h of the fluid layer is at least several micrometers, the solution to eq 2 consists of only a $+y$-propagating shear wave:[11]

$$v_x(y) = A\,e^{-\gamma_s y}\,e^{j\omega t} \tag{3}$$

where A is a constant; ω is the angular frequency ($\omega = 2\pi f$, where f is operating frequency); $j = (-1)^{1/2}$; and γ_s is the complex shear

wave propagation constant. The latter is found by substituting eq 3 into eq 2:[11]

$$\gamma_s = \left(\frac{\omega\varrho}{2\eta}\right)^{1/2}(1+j) = \frac{1+j}{\delta} \tag{4}$$

where $\delta = (2\eta/(\omega\varrho))^{1/2}$ is the liquid decay length.[11] For reference, $\delta = 0.25$ μm in water at 20 °C at 5 MHz. When $h \gg \delta$, satisfied when h is greater than a few micrometers, the shear wave generated at the resonator surface becomes attenuated before reaching the reflecting boundary, eliminating the need to consider a reflected wave in eq 3.

The constant A in eq 3 is determined by applying the boundary condition that particle velocity must be *continuous* across the lower solid/liquid interface: $v_x(0^-) = v_{xo}\exp(j\omega t)$. This gives $A = v_{xo}$.

The shear stress T_{xy} (force per area in the x-direction on a y-normal plane)[20] applied by the resonator to excite the shear wave (eq 3) is

$$T_{xy} = -\eta\frac{\partial v_x}{\partial y}\Big|_{y=0} = \eta\gamma_s v_{xo}\, e^{j\omega t} \tag{5}$$

The shear mechanical impedance associated with excitation of the shear wave is[21]

$$Z_s(0) = Z_{so}^{(f)} = \frac{T_{xy}}{v_x}\Big|_{y=0} = \eta\gamma_s = \left(\frac{\omega\varrho\eta}{2}\right)^{1/2}(1+j) \tag{6}$$

where $Z_{so}^{(f)}$ is the characteristic *shear* mechanical impedance of the fluid.[21]

Compressional Velocity Field. We next consider the *compressional* wave velocity field generated in the liquid cavity. The liquid film behaves as an acoustic cavity for the compressional wave. To accurately model the influence of energy storage and dissipation in this cavity on resonator response, acoustic loss mechanisms must be accounted for. There are several possible loss mechanisms: (1) propagation loss, (2) reflection loss (i.e., transmission at the liquid/solid interfaces), and (3) diffraction losses due to spreading of the acoustic beam. While the shear wave experiences severe attenuation in the fluid, compressional wave propagation is nearly lossless in most fluids. In fact, propagation loss is found to be insignificant compared to other loss mechanisms when h is less than a few hundred micrometers.

Reflection losses are found to dominate for the compressional wave. The bulk modulus of a solid does not greatly exceed that of a liquid, so the impedance mismatch is not high enough to form a highly reflecting boundary: significant compressional wave energy is transmitted across the interface—on the order of 10%. In modeling compressional wave generation in the liquid cavity (with h less than a few 100 μm), we find that transmission losses at the boundary greatly exceed attenuation losses in the liquid. We thus consider the former and neglect the latter. Diffraction losses are insignificant when the electrode diameter d is large compared with the liquid film thickness h.

The uncoupled compressional wave velocity field v_y is found by solving eq 1b, setting the right-hand side to zero:

$$\kappa\frac{\partial^2 v_y}{\partial y^2} = \varrho\ddot{v}_y \tag{7}$$

The solution to eq 7 for a lossless fluid (κ real) is

$$v_y(y) = (B\, e^{-j\beta_c y} + C\, e^{j\beta_c y})\, e^{j\omega t} \tag{8}$$

where B and C are constants and β_c is the (real) compressional wave propagation constant. Equation 8 is a superposition of compressional waves propagating in the $+y$- and $-y$-directions. Substituting the components of eq 8 into eq 7 gives $\beta_c = \omega/v_c$, where v_c is the compressional wave velocity in the fluid: $v_c = (\kappa/\varrho)^{1/2}$.

The constants B and C in eq 8 are determined from boundary conditions that apply to the compressional wave. The coupling between the shear and compressional waves occurs in a region (a few δ thick) near the resonator surface. The amplitude of the compressional wave at $y = 0$ can be estimated from the continuity condition that applies to infinitesimal volumes of the fluid, as illustrated in Figure 2. From these considerations,[7,17]

$$\frac{\partial v_y}{\partial y} = -\frac{\partial v_x}{\partial x} \tag{9}$$

This is a statement of mass conservation that indicates that a variation of flow in the x-direction generates a flow in the y-direction (Figure 2). If we approximate the shear–compressional wave coupling as occurring in an infinitesimally thin layer, then eq 9 yields a boundary condition that determines the compressional wave amplitude at the lower boundary:

$$v_y(0) = \frac{v_{xo}}{\beta_c} = (B + C)\, e^{j\omega t} \tag{10}$$

In order to allow for non-zero compressional wave transmission at the liquid/solid interface, the second boundary condition specifies the compressional impedance at the reflecting fluid boundary: $Z_c(h) = Z_{co}^{(s)} = (\kappa_s\varrho_s)^{1/2}$, where $Z_{co}^{(s)}$, κ_s, and ϱ_s are the characteristic compressional impedance, bulk compressibility, and density, respectively, of the adjacent solid. The compressional stress T_{yy} (force per area in the y-direction on a y-normal plane) corresponding to the compressional velocity field (eq 8) is[20]

$$T_{yy}(y) = Z_{co}^{(f)}(B\, e^{-j\beta_c y} - C\, e^{j\beta_c y})\, e^{j\omega t} \tag{11}$$

where $Z_{co}^{(f)}$ is the characteristic *compressional* impedance of the fluid: $Z_{co}^{(f)} = (\kappa\varrho)^{1/2} = \varrho v_c$. The compressional impedance at any position y in the fluid is then

$$Z_c(y) = \frac{T_{yy}}{v_y} = Z_{co}^{(f)}\left(\frac{B\, e^{-j\beta_c y} - C\, e^{j\beta_c y}}{B\, e^{-j\beta_c y} + C\, e^{j\beta_c y}}\right) \tag{12}$$

Applying the two boundary conditions outlined above determines B and C. The surface-normal fluid velocity is then

$$v_y(y) = \frac{v_{xo}}{\beta_c}\left(\frac{jZ_{co}^{(s)}\sin[\beta_c(h-y)] + Z_{co}^{(f)}\cos[\beta_c(h-y)]}{jZ_{co}^{(s)}\sin(\beta_c h) + Z_{co}^{(f)}\cos(\beta_c h)}\right) \tag{13}$$

for $0 \le y \le h$. Equation 13 gives the amplitude profile for the standing compressional wave in the fluid layer. This amplitude is proportional to the gradient (v_{xo}') of the shear surface displacement.

(20) Auld, B. A. *Acoustic Fields and Waves in Solids*; Wiley: New York, 1973; Chapter 8.
(21) Martin, S. J.; Frye, G. C.; Ricco, A. J.; Senturia, S. D. *Anal. Chem.* **1993**, *65*, 2910–2922.

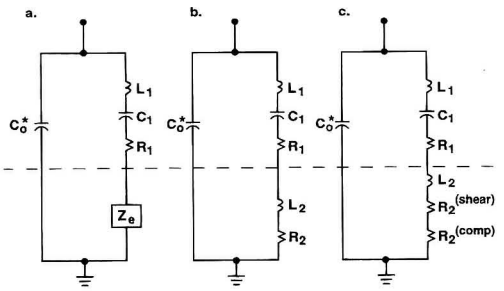

Figure 3. Equivalent-circuit model for the TSM resonator operating in contact with a fluid: (a) with complex motional impedance element Z_e, (b) with Z_e resolved into a motional inductance L_2 and resistance R_2, (c) with motional resistance R_2 separated into contributions from shear wave, $R_2^{(shear)}$, and compressional wave, $R_2^{(comp)}$, radiation (in a semi-infinite fluid).

The mechanical impedance at the resonator surface for compressional wave generation is

$$Z_c(0) = Z_{co}^{(f)}\left(\frac{Z_{co}^{(s)}\cos(\beta_c h) + jZ_{co}^{(f)}\sin(\beta_c h)}{Z_{co}^{(f)}\cos(\beta_c h) + jZ_{co}^{(s)}\sin(\beta_c h)}\right) \quad (14)$$

Equation 14 has been previously reported by Tessier et al.[15] We note from eq 14 that for $Z_{co}^{(s)} \gg Z_{co}^{(f)}$, $Z_c(0) \cong -jZ_{co}^{(f)}\cot(\beta_c h)$; $Z_c(0)$ is infinite when $\beta_c h = n\pi$, where n is an integer. This arises from compressional wave resonance in the liquid layer that occurs when $h = n\lambda_c/2$ (n = 1, 2, 3, ...), where λ_c is the compressional wavelength in the fluid: $\lambda_c = v_c/f$. This defines the fluid layer thicknesses that leads to a resonant response.[7,15,16] If the solid boundary is replaced by air, then $Z_{co}^{(s)} \ll Z_{co}^{(f)}$ and $Z_c(0) \cong jZ_{co}^{(f)}\tan(\beta_c h)$. In this case, resonance occurs when $\beta_c h = (n + 1/2)\pi$ or $h = (n + 1/2)(\lambda_c/2)$ (n = 0, 1, 2, ...).[16]

Electrical Response of Resonator. We next consider the effect that generation of shear and compressional waves in the fluid layer has on the TSM resonator response. The resonator response can be determined from the impedances associated with generating these waves. In actuality, the in-plane resonator displacement couples only to the shear wave, which, in turn, couples to the compressional wave. However, for purposes of calculating the resonator response, it is convenient to consider the device as coupling directly to both shear and compressional modes. That is, it behaves *as if* it had both an in-plane (v_{xo}) and a surface-normal (v_{yo}) displacement component.

It has been shown that the near-resonant electrical response of a resonator with an arbitrary surface perturbation can be described by the equivalent-circuit model of Figure 3. In this model, a static capacitance C_o arises between the electrodes located on opposite sides of the insulating quartz. (A parasitic capacitance C_p that is found to arise in the test fixture is included: $C_o^* = C_o + C_p$). Since the quartz is also piezoelectric, electromechanical coupling gives rise to an additional motional branch, (L_1, C_1, R_1, and Z_e), in parallel with the static capacitance. The static capacitance dominates the electrical behavior away from resonance, while the motional branch dominates near resonance. The elements C_o^*, L_1, C_1, and R_1 describe the response of the unperturbed resonator (for which $Z_e = 0$). The complex impedance element Z_e (Figure 3a) describes the change in resonator motional impedance caused by the surface perturbation[21]—the liquid layer and adjacent solid, in this case.

From perturbation theory,[20] it can be shown that the element Z_e is

$$Z_e = \frac{L_1}{2U}\sum_i [Z_i(0)\int |v_{io}|^2\, ds] \quad (15)$$

where $Z_i(0)$ is the surface mechanical impedance associated with surface displacement in the x_i direction, v_{io} is the surface particle velocity in that direction, and U is the total mechanical energy stored in the resonator. In eq 15, integration is carried out over the perturbed surface(s), over which particle velocity can be nonuniform.

To illustrate the application of eq 15, we consider the (physically unrealizable) case in which displacement is uniform across a circular resonator surface so that only a single in-plane fluid velocity component v_x is generated. The stored mechanical energy U is equal to the peak kinetic energy density integrated across the resonator thickness:

$$U = \frac{\varrho_q v_{xo}^2 A}{2}\int_0^{h_q}\cos^2(ky)\, dy = \frac{\pi\varrho_q v_{xo}^2 h_q d^2}{16} \quad (16)$$

where ϱ_q, h_q, and d are the resonator's density, thickness, and diameter, respectively; k is the shear wavenumber in the quartz ($k = n\pi/h$). The surface integral in eq 15 gives

$$\int |v_{xo}|^2\, ds = \frac{\pi d^2 v_{xo}^2}{4} \quad (17)$$

Using eqs 16 and 17 and L_1[22] in eq 15 gives the result previously reported for uniform surface displacement:[21]

$$Z_e = \frac{N\pi Z_s(0)}{4K^2\omega_s C_o Z_{so}^{(q)}} \quad (18)$$

where N is the harmonic number, K^2 is the quartz electromechanical coupling factor, $Z_s(0)$ is the surface mechanical impedance contributed by the fluid, and $Z_{so}^{(q)}$ is the quartz characteristic shear mechanical impedance ($Z_{so}^{(q)} = (\mu_q\varrho_q)^{1/2}$); μ_q and ϱ_q are the quartz shear stiffness and density, respectively.

With nonuniform surface displacement v_{xo}, the previous section showed that both shear (v_x) and compressional (v_y) waves are generated in a contacting fluid. If we consider the compressional wave as originating from a surface-normal resonator displacement, then eq 15 gives

$$Z_e = \frac{N\pi[Z_s(0) + PZ_c(0)]}{4K^2\omega_s C_o Z_{so}^{(q)}} \quad (19)$$

where $Z_c(0)$ and $Z_s(0)$ are the surface mechanical impedances associated with compressional wave (eq 14) and shear wave generation (eq 6), respectively, and the "profile factor" P is defined as

$$P \equiv \frac{\int |v_{yo}|^2\, ds}{\int |v_{xo}|^2\, ds} \cong \left(\frac{\lambda_c}{2\pi}\right)^2\frac{\int |v_{xo}'|^2\, ds}{\int |v_{xo}|^2\, ds} \quad (20)$$

in which eq 10 has been used to estimate the surface-normal particle velocity at the surface: $v_{yo} = v_{xo}'/\beta_c = \lambda_c v_{xo}'/(2\pi)$. We note that the profile factor P is a measure of the gradient in the

(22) The motional inductance L_1 of the unperturbed resonator is given by $L_1 = (N\pi)^2/(8K^2\omega_s^2 C_o)$, where ω_s is the angular series resonant frequency ($\omega_s = 2\pi f_s$).

surface displacement, normalized by the magnitude of the surface displacement. Thus, only the *relative* displacement profile is needed to determine P.

Combining eqs 19 and 20 with the expressions given previously for $Z_s(0)$, eq 6, and $Z_c(0)$, eq 14, determines the electrical motional impedance Z_e contributed by excitation of shear and compressional waves in the liquid. This result is valid for arbitrary surface profiles $v_{xo}(x,z)$. Z_e can be resolved into real and imaginary components that can be represented as a motional resistance R_2 and inductance L_2 (Figure 3b):

$$Z_e = R_2 + j\omega L_2 \tag{21}$$

where L_2 represents energy stored in the fluid, while R_2 represents power dissipation.

The electrical response of the resonator can be calculated from the equivalent-circuit model of Figure 3. The resonator electrical admittance Y, defined as the ratio of current flow to applied voltage (reciprocal of impedance), is

$$Y = j\omega C_o^* + 1/Z_m \tag{22}$$

where the motional impedance Z_m is

$$Z_m = (R_1 + R_2) + j[\omega(L_1 + L_2) - 1/\omega C_1] \tag{23}$$

The series resonant frequency f_s is defined as the frequency at which the imaginary part of Z_m vanishes:

$$f_s = 1/2\pi\sqrt{(L_1 + L_2)C_1} \tag{24}$$

Thus, the motional inductance L_2, arising from resonator loading by the fluid layer, leads to a change Δf_s in series resonant frequency:[23]

$$\Delta f_s \cong -L_2 f_s / 2L_1 \tag{25}$$

Special Case of a Gaussian Displacement Profile. While a solution of the wave equation for typical device geometries does *not* result in a Gaussian profile, this function is frequently invoked as an approximation:

$$v_{xo}(x,z) = D \exp\left(-\frac{x^2 + z^2}{R^2}\right) \tag{26}$$

where D and R are parameters that describe the peak amplitude and radial falloff, respectively, of the displacement profile.

Compressional wave generation is proportional to the gradient in the x-direction of $v_{xo}(x,z)$ (eq 10), i.e., $v_{xo}'(x,z)$. While $v_{xo}(x,z)$ is symmetric about (0,0), v_{xo}' is antisymmetric about the plane $x = 0$ (i.e., $v_{xo}'(x,z) = -v_{xo}'(-x,z)$), creating a maximum at $(x,z) = (-R/(2)^{1/2}, 0)$ and a minimum at $(R/(2)^{1/2},0)$.[16,17] While the region with $x < 0$ is generating upward liquid flow, the region with $x > 0$ is generating downward flow (and conversely). The net flow in the upward direction is zero. This does not, however, negate the effect of compressional wave generation on device response, since response is proportional to $|v_{xo}'|^2$ (eq 20).

Using the Gaussian profile of eq 26 allows the profile factor in eq 20 to the explicitly calculated:

$$P = (\lambda_c/2\pi R)^2 \tag{27}$$

From eq 27, we note that the profile factor is *independent* of the amplitude of v_{xo}, depending only on the rate of falloff of the surface displacement. As the rate of falloff increases (smaller R), P increases, indicating increased compressional wave generation.

(23) In deriving this result, the following approximation is used: $L_1 \gg L_2$.

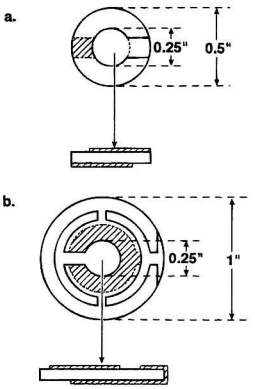

Figure 4. TSM resonator geometries used: (a) 0.5 in. diameter device and (b) 1.0 in. diameter device.

Response with a Semiinfinite Fluid. In the case of a semiinfinite liquid (no adjacent solid), the analysis for the shear wave is unchanged. The analysis for the compressional wave, however, is somewhat different due to the absence of a reflected compressional wave. The radiated compressional wave includes only the leading term, representing an upward propagating wave, in eq 8. The resulting shear and compressional surface mechanical impedances in this case are

$$Z_s(0) = (\omega\varrho\eta/2)^{1/2}(1 + j) \tag{28a}$$

$$Z_c(0) = (\kappa\varrho)^{1/2} \tag{28b}$$

Using eqs 28a,b in eq 19 determines the electrical motional impedance Z_e for operation in a semiinfinite liquid. Separating Z_e into real and imaginary parts, according to eq 21, gives

$$R_2 = \frac{N\pi}{4K^2\omega_s C_o Z_q}[(\omega\varrho\eta/2)^{1/2} + P(\kappa\varrho)^{1/2}] \tag{29a}$$

$$L_2 = \frac{N\pi}{4K^2\omega_s^2 C_o Z_q}(\omega\varrho\eta/2)^{1/2} \tag{29b}$$

for a resonator in a semiinfinite fluid. The motional resistance R_2 represents power radiated into the contacting fluid: the first term is due to shear wave radiation and has been previously reported;[14,21] the second term is due to compressional wave radiation and is a new result. For the idealized case of a uniform displacement profile, $P = 0$, and this second term vanishes; real devices, however, exhibit a nonuniform displacement profile, $P \neq 0$, that gives rise to compressional wave radiation and increased resonance damping. The motional inductance L_2 represents energy storage in the contacting fluid; this result has been previously reported[14,26] and is unchanged by compressional wave generation.

Equivalent-Circuit Model for Loading by a Semiinfinite Fluid. The equivalent-circuit model proposed[14,21] to describe the response of the TSM resonator in a semiinfinite fluid can be modified to include the effect of compressional wave radiation. Figure 3c shows a modified version in which two resistors are

used to describe the fluid contribution to motional resistance. The motional elements arising from fluid coupling are then

$$L_2 = \frac{N\pi}{4K^2\omega_s{}^2C_0Z_q}(\omega\varrho\eta/2)^{1/2} \quad (30a)$$

$$R_2^{(\text{comp})} = \frac{N\pi P(\kappa Q)^{1/2}}{4K^2\omega_s C_0 Z_q} \quad (30b)$$

$$R_2^{(\text{shear})} = \frac{N\pi}{4K^2\omega_s C_0 Z_q}(\omega\varrho\eta/2)^{1/2} \quad (30c)$$

EXPERIMENTAL SECTION

TSM Resonators. The resonators used in this study were fabricated from 0.33 mm thick AT-cut quartz wafers having a nominal fundamental ($N = 1$) resonant frequency of 5 MHz. To ascertain the effect of surface roughness on compressional wave generation, the wafers were polished to varying degrees of surface roughness before Cr/Au electrodes were vacuum evaporated onto both sides. Two different resonator geometries were used: (1) a 0.5 in. diameter quartz wafer with identical 0.25 in. diameter radio frequency (rf) and ground electrodes on opposite sides (Figure 4a) and (2) a 1.0 in. diameter quartz wafer with a 0.25 in. diameter rf electrode and a 0.5 in. diameter ground electrode (Figure 4b). In case 2, the contact for the ground electrode "wraps around" the edge of the crystal, allowing electrical contacts to both rf and ground electrodes to be made on the side with the rf electrode. The active area of the two device geometries is approximately the same since the excitation electric field is primarily confined to the area of electrode overlap.

Surface Roughness Determination. Resonator surface roughness was quantified by a measurement of average surface roughness using a Dektak Model IIA (Sloan) profilometer. The root mean square (rms) deviation of the diamond profilometer stylus about its average was measured over a surface scan length of 1 mm using a force of 1 g.

Oscillator. To measure the resonator response, the resonator was connected to an oscillator circuit. The oscillator circuit, described by Wessendorf,[24] tracks the series resonant frequency of the resonator. In addition, the circuit has an automatic level control that controls the loop gain to sustain oscillation under various crystal damping conditions. Since the feedback voltage from this level control is proportional to the motional resistance of the crystal, it is measured as an output, referred to as the "damping voltage." The oscillator circuit thus provides the series resonant frequency f_s and motional resistance ($R_1 + R_2$) of the resonator.

Instrumentation. The oscillator board requires a 5 V source that was supplied by a dc power supply (HP Model E3611A). The oscillation frequency was measured using a frequency counter (HP Model 5384A). The oscillator damping voltage, indicating R_2, was measured using a multimeter (HP Model 3478A). Data were collected via an IEEE-488 interface bus using an interface card in an IBM-compatible personal computer. Data-acquisition software was written in HP Instrument Basic for Windows.

Interference Experiment. The interference experiment consisted of measuring the resonator responses while varying the thickness of a fluid layer confined between the resonator surface and an adjacent solid surface. This adjacent solid consisted of an optically polished Si (Monsanto) wafer, 610 μm thick, connected to a digital micrometer (Oriel Corp.) that provided vertical translation. Figure 5 shows the apparatus used to vary the fluid layer thickness. The digital micrometer was mounted, along with the resonator fixture, to an optical table. The Si was cut to cover the grounded electrode area and was laid flat on the grounded resonator electrode. The post from the micrometer was carefully lowered to touch the top of the Si. Epoxi patch (Dexter Corp.) was used to glue the post to the silicon, ensuring parallelism between the resonator surface and the silicon. After the epoxy was cured, the micrometer was zeroed and the Si piece was backed away from the resonator surface. Deionized water was added to the resonator surface, and the Si boundary was lowered until liquid completely filled the region between the resonator and Si. The spacing between the resonator and Si was then decreased a few micrometers at a time while the resonator oscillation frequency and damping voltage were measured at each step.

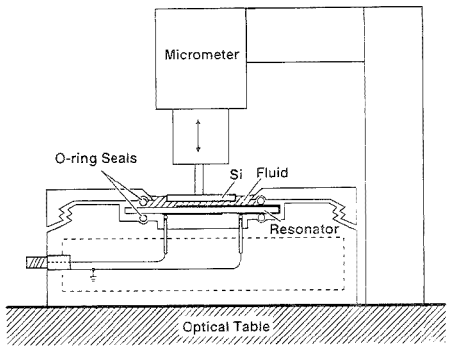

Figure 5. Apparatus used for varying the fluid layer thickness in the interference experiment.

Surface Profile Measurement. The surface profile measurement consisted of measuring the resonator responses while a probe point was moved in contact with the surface across the crystal diameter. The perturbation in resonator response is proportional to the surface particle velocity squared, $v_{z0}{}^2$, at the point of contact. As long as the probe point has uniform pressure and contact area with the surface, this response indicates relative displacement amplitude. This experiment, first reported by Martin and Hager,[17] provides a simple, elegant way of determining the surface displacement profile.

To profile the device surface, a micrometer providing translation in the horizontal direction was arranged with a stainless steel block with a sleeve for a stylus (Figure 6). A Nylatron (GS Polymer Corp.) stylus was fabricated to ride in the hole of the block. The 3.83 g weight of the stylus provided a constant tip force with a tip radius of ~0.15 mm. Data were taken as the horizontal micrometer was used to advance the stylus across the diameter of the resonator, providing a measurement of the relative displacement in air. As shown in the Theory section, only the relative displacement is needed to calculate compressional wave generation. A large difference in the surface velocity profile exists between the unperturbed (dry) and liquid-loaded cases;[18] however, the relative profile is assumed to be unchanged.

(24) Wessendorf, K. O. *IEEE Proc. Freq. Contr. Symp.* **1993**, 711–717.

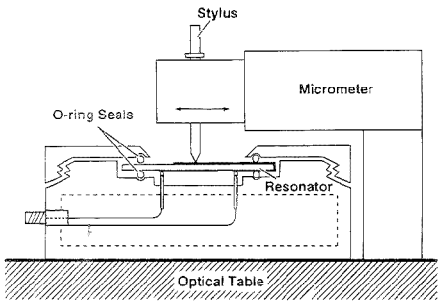

Figure 6. Apparatus used for profiling the surface displacement of a TSM resonator.

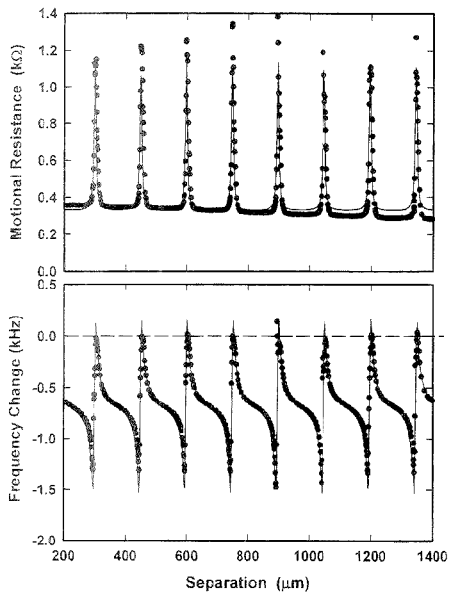

Figure 7. Change in motional resistance (upper) and resonant frequency (lower) versus the fluid layer thickness. Points are measured; solid line is calculated.

RESULTS AND DISCUSSION

Figure 7 shows the changes in motional resistance R_2 and resonant frequency Δf of a TSM resonator measured as the thickness of a water layer (h) between the resonator and an adjacent solid was varied. The motional resistance shows a "background" level of ~0.35 kΩ, with period peaks reaching 1.1–1.4 kΩ at 150 μm intervals. The resonant frequency (measured relative to the dry device) also shows a cyclical variation with the same periodicity. A rapid change in frequency coincides with the peaks in motional resistance. In the Theory section, it was noted that the in-plane motion of the TSM resonator surface generates a damped shear wave in a contacting fluid. This shear wave has a decay length δ of ~0.25 μm in water at 5 MHz. Since the fluid thickness over which the response is varying is much greater than δ, it is clear that the shear wave is *not* responsible for the variations in signal with changing h. As noted previously by Martin and

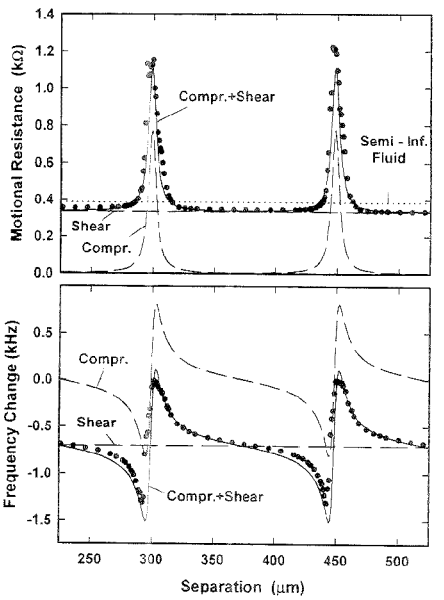

Figure 8. Components of the responses arising from shear and compressional wave coupling to the fluid layer. Dashed line (upper) represents the response in a semiinfinite fluid.

Hager,[7,17] Tessier et al.,[15] and Lin and Ward,[16] variations in the in-plane displacement amplitude, caused by transverse modes arising from the boundary condition at the edge of the crystal, lead to compressional wave generation. The liquid film behaves as a resonant cavity for compressional waves, strongly absorbing acoustic energy when $h = n\lambda_c/2$ (λ_c is the compressional wavelength in the fluid), and leading to a peak in motional resistance. The spacing between resonances, $\Delta h = 150$ μm, indicates a compressional wavelength $\lambda_c = 300$ μm and a compressional wave velocity $v_c = 1.50 \times 10^5$ cm/s. This is within 1% of the literature value[25] for the sound velocity in water at 25 °C: 1.4967×10^5 cm/s. This good agreement indicates the existence of compressional waves and shows their large influence on the response of the TSM resonator.

The solid lines in Figure 7 are calculated from the model outlined in the Theory section. The complex impedance Z_c is calculated from eq 19, using eqs 6 and 14 to calculate $Z_c(0)$ and $Z_c(0)$. Z_c is resolved into motional impedance components R_2 and L_2 using eq 21. Then Δf is calculated from L_2 using eq 25.

Shear and Compressional Contributions. The calculated response is a superposition of responses due to the shear and compressional waves interacting with the fluid layer. Figure 8 shows the individual contributions from the shear and compressional waves. Since the fluid layer thickness is much greater than the shear wave decay length δ, shear wave coupling is unaffected by changes in position of the upper fluid boundary. The shear wave contribution is thus constant, depending only on the liquid parameter $(\rho\eta)^{1/2}$. The magnitude of the shear wave response has no undetermined parameters. The compressional contribution

(25) Weast, R. C., Astle, M. J., Beyer, W. H., Eds. *CRC Handbook of Chemistry and Physics*, 65th ed.; CRC Press: Boca Raton, FL, 1984.

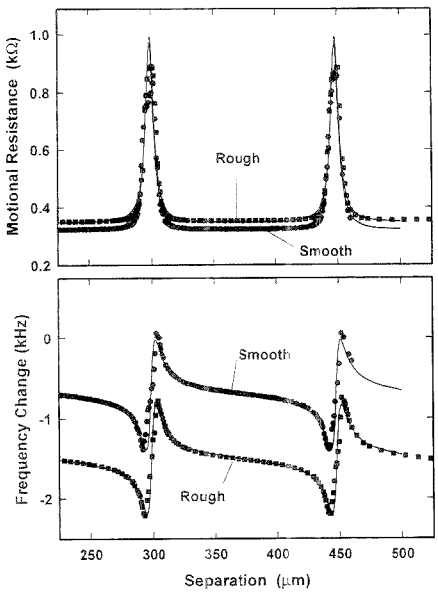

Figure 9. Responses measured versus fluid layer thickness for a smooth and rough 1.0 in. diameter TSM resonator.

shows periodic variations with h due to interference between the compressional wave generated at the lower fluid boundary and the one reflected from the adjacent solid. The magnitude of the compressional contribution depends on the profile factor P and the fluid parameter $(\varrho\kappa)^{1/2}$.

At this point, we have not considered the displacement profile for the quartz resonator necessary to calculate the profile factor P. Initially, we choose a best-fit value of P—the value that allows the shear and compressional contributions to be added (eq 19) to obtain the best fit to the total response. The contributions from shear and compressional wave coupling can thereby be determined from the data illustrated in Figure 8 obtained from an interference experiment. The fluid layer, appearing infinitely thick to the shear wave, provides constant shear wave coupling. To the compressional wave, however, the fluid layer is a low-loss (high Q) resonant cavity. It absorbs compressional wave energy strongly at resonance (i.e., when $h \cong n\lambda_c/2$), leading to a very sharp peak in motional resistance, along with a more complex excursion in frequency. The fluid cavity absorbs energy very weakly off-resonance, leading to a broad minimum between resonances. In Figure 8, the responses midway between resonances are due entirely to shear wave radiation, while the resonant response is due to a combination of shear and compressional wave effects. Thus, *the interference experiment provides a means for resolving shear and compressional wave contributions.*

Effect of Surface Roughness. It is possible that the roughness of the resonator surface might influence the generation of compressional waves. Surface asperities, it has been argued,[21] can cause in-plane surface motion to give rise to surface-normal fluid motion. Figure 9 shows a comparison of responses measured versus fluid thickness between a smooth and a rough TSM resonator (1.0 in. diameter Maxtek crystals). The smooth device has an average roughness, determined from surface profilometry, of 1.5 nm; the rough device has an average roughness of 116 nm. In Figure 9, we note an increase in the off-resonant contribution with surface roughness, with no apparent change in the resonant contribution. Fitting the data to resolve shear and compressional contributions, Table 1, confirms this. We note that for both the 0.5 and 1.0 in. resonators, the resistance offset $R_2^{(offs)}$ and frequency offset $f_s^{(offs)}$ increase with roughness. This indicates increased shear dissipation ($R_2^{(offs)}$) and energy storage ($f_s^{(offs)}$) with roughness. The additional contributions to shear wave coupling, arising from surface roughness, are denoted $R_2^{(offs)}$ and $f_s^{(offs)}$.

Table 1. Resonator Response Parameters vs Device Diameter and Surface Roughness

resonator diam (in.)	av roughness (nm)	shear wave params $R_2^{(offs)}$ (kΩ)	shear wave params $f_s^{(offs)}$ (kHz)	compressional wave param, P ($\times 10^{-4}$)
0.5	66	0.09	0.41	16
0.5	620	0.40	0.96	15
1.0	1.5	~0	0.03	4.0
1.0	120	0.01	0.80	4.0

The magnitude of the compressional wave generation is reflected in the best-fit profile factor P. For resonators of the same diameter, the profile factor P is unaffected by surface roughness. The interference experiment provides an elegant way of separating the shear and compressional wave influences on device response. From these data, the effect of surface roughness can be summarized: *surface roughness causes a significant increase in shear wave generation, with negligible effect on compressional wave generation.*

Effect of Displacement Profile. Figure 10 shows responses measured versus fluid thickness for 0.5 and 1.0 in. diameter resonators. The 0.5 in. device has an average roughness of 66 nm, while the 1.0 in. device is 1.5 nm. The smaller resonator exhibits a greater off-resonant response due to increased roughness. In addition, the smaller resonator exhibits a much greater resonant response than the larger one, indicating that resonator geometry affects compressional wave generation. The response parameters extracted from resonators of different diameter are listed in Table 1. For both the 0.5 and 1.0 in. devices, the shear parameters scale with roughness, and the effect of device geometry is obscured. The compressional parameter P, however, is clearly influenced by device geometry. The smaller diameter devices exhibit a larger P value.

In the Theory section, we noted that compressional wave generation is dependent upon the gradient (in the x-direction) of the shear displacement profile.[26] The profile factor P, defined by eq 20, is a measure of this gradient, averaged over the whole resonator surface and normalized by the displacement amplitude. Figure 11 shows the particle velocity profiles for the 0.5 and 1.0 in. diameter resonators normalized to the peak value at the center of the device, $v_{x0}(0)$. These profiles were determined by measuring the increase in motional resistance as a stylus was scanned across each device in the x-direction. The surface particle velocity is proportional to $(\Delta R)^{1/2}$, where ΔR is the change in motional resistance caused by the stylus contacting the device. The key

(26) Since particle velocity v_x is proportional to surface displacement u_x by $v_x = j\omega u_x$, the profile factor can also be defined in terms of displacement: $P = (\lambda_c/(2\pi))^2(\int|u_{x'}|^2\,ds/\int|u_{x0}|^2\,ds)$.

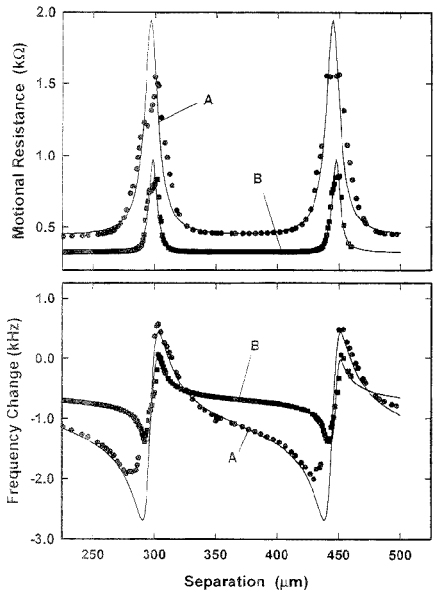

Figure 10. Responses measured versus fluid layer thickness for (A) 0.5 in. (roughness, 66 nm) and (B) 1.0 in. diameter (roughness, 1.5 nm) TSM resonators.

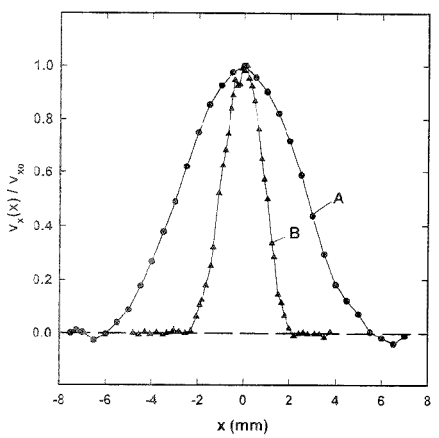

Figure 11. Relative in-plane surface particle velocity profiles measured for (A) 1.0 in. and (B) 0.5 in. diameter TSM resonators.

feature to note in Figure 11 is the more centrally localized profile for the 0.5 in. diameter device. This results in a larger gradient and profile factor P.

The profile factor P can be calculated for each device from the displacement profiles shown in Figure 11. This was done in two ways: (1) by fitting the data to a Gaussian distribution (eq 26), from which the falloff factor R is determined, and using eq 27 to calculate P and (2) by calculating the profile factor numerically without assuming the data fit any particular distribution.[27] Table 2 shows the profile factors for the two device geometries (1) determined experimentally, by fitting data from

Table 2. Profile Factors Determined Experimentally (by Fitting Interference Data) and Calculated from Surface Profiles

		calcd P ($\times 10^{-4}$)	
resonator diam (in.)	expt P ($\times 10^{-4}$)	method 1 (Gaussian fit)	method 2 (numerically)
0.5	15	13	17
1.0	4	1.9	1.7

an interference experiment to obtain a best-fit P value, and (2) calculated from the displacement profiles by the two methods outlined above. It is interesting to note that compressional wave generation is nearly 4 times larger for the 0.5 in. device than for the 1.0 in. device. Moreover, *the profile factor calculated from the displacement profiles by either method provides reasonable estimates for the magnitude of compressional wave generation.*

Semiinfinite Fluid Case. The information about compressional wave generation obtained from the interference experiments can be used to estimate the magnitude of compressional wave generation in a semiinfinite fluid. A fluid can be considered semiinfinite for compressional waves when the walls containing the fluid are positioned to prevent reflection of the wave back to the device surface. Since the compressional wave attenuation is very low, this may not be accomplished by separation alone, but also by either (1) placing an acoustic absorber in the wave path[15] or (2) obliquely reflecting or scattering the wave.[28]

The response of a resonator radiating into a semiinfinite fluid is different than that of a resonator radiating into a fluid layer, even when the thickness of the fluid layer is such that the response is midway between resonances. The fluid layer, acting as an acoustic cavity, absorbs strongly at resonance and very weakly off-resonance. In contrast, a semiinfinite fluid absorbs whatever compressional wave energy is radiated into it. The effect of this absorption is to increase the motional resistance (as predicted by eq 29a) without influencing the resonant frequency.

From the profile factors measured for the 0.5 and 1.0 in. resonators and eqs 30a–c, we can estimate the shear and compressional wave contributions to motional resistance due to radiating into a semiinfinite fluid: $R_2^{(shear)}$ is due to shear wave radiation, while $R_2^{(comp)}$ is due to compressional waves. Table 3 lists these components for water contacting 5 MHz devices. These data indicate that when operating in contact with water, compressional wave generation contributes significantly to motional resistance. The compressional contribution accounts for 13% of the total dissipation in the 1.0 in. device and 36% in the 0.5 in. device. For fluids of higher viscosity, the shear contribution increases and the relative compressional contribution becomes smaller. Previous measurements[21] of resonator motional resistance indicated an offset when results were plotted versus the

(27) The profile factor was calculated numerically from the displacement (x_i) and relative amplitude (y_i) data using $P = F/G$, where $F = \sum(y_{i-1} - y_i)^2/(x_{i-1} - x_i)$ and $G = \sum i^2(x_{i-1} - x_i)$, both summed from $i = 1$ to $M - 1$, where M is the number of data points.

(28) Both means of preventing reflection were tried. A thin layer (0.49 μm) of polystyrene coated on the adjacent solid did not serve as an effective absorber of the compressional wave. Roughening of the adjacent solid surface was also tried in an attempt to scatter the compressional wave; this too proved ineffective at eliminating interference effects. Positioning the adjacent solid surface at an angle to the resonator surface does eliminate interference effects if the reflected wave misses the active area of the resonator.

Table 3. Calculated Compressional and Shear Contributions to Motional Resistance for a 5 MHz Resonator Contacting Water (1 Side)

resonator diam (in.)	profile factor, P ($\times 10^{-4}$)	$R_2^{(shear)}$ (Ω)	$R_2^{(comp)}$ (Ω)	$R_2^{(comp)}/(R_2^{(shear)} + R_2^{(comp)})$
0.5	15	276	155	0.36
1.0	4	276	41	0.13

liquid parameter $(\rho\eta)^{1/2}$. This offset can be attributed to increased shear dissipation arising from surface roughness when roughness features are comparable to or larger than the decay length δ. However, for hydrodynamically smooth (roughness features much smaller than δ) 1.0 in. devices, the dissipation was 12% higher than that calculated for shear dissipation alone by a smooth surface. This increased dissipation is indicated by a dashed line in Figure 8 (upper). We see from Table 3 that this offset closely matches the calculated contribution (13%) arising from compressional wave radiation in a semiinfinite fluid. Thus, *compressional wave generation can account for most of the excess dissipation observed when the smoothest resonators are operated in contact with a fluid.* Alternative explanations, based on enhanced interfacial viscosities arising from liquid ordering near the solid/liquid interface,[29] are unfounded.

CONCLUSION

Electrical excitation of a TSM resonator causes, by definition, in-plane surface displacement. This in-plane motion generates a critically damped shear wave in a contacting viscous fluid. The decay length δ of this fluid is a fraction of a micrometer in water at 5 MHz. If displacement were uniform across the resonator surface, then only the shear wave would be generated. The finite lateral extent of the resonator, with edges of the device typically clamped, leads to the generation of transverse modes. This results in a variation of in-plane displacement across the device surface and a corresponding variation in the amplitude of the shear wave generated. From continuity considerations in the fluid, this variation in displacement (in the x-direction) generates surface-normal fluid flow. Thus, the shear wave couples to a compressional wave in the near-surface region where the shear wave is present.

If the fluid is bounded by an interface parallel to the resonator surface, an acoustic cavity is formed. The compressional wave resonates in this cavity when $h \cong n\lambda_c/2$. (The shear wave decays too rapidly for shear wave resonances to be observed.) Compressional wave resonances influence device response due to the coupling between shear and compressional waves. Varying the thickness of the fluid layer leads to a characteristic interference response: a peak in the motional resistance coincident with a rapid variation in resonant frequency. This response is a superposition of contributions due to shear wave and compressional wave coupling to the fluid. The off-resonant response is due to shear wave coupling alone; the resonant response is a sum of shear and compressional wave contributions. Due to these response differences with fluid thickness, the interference data can be resolved into shear wave and compressional wave contributions, indicating the magnitude of each.

Surface roughness was shown to influence shear wave generation but to have minimal effect on compressional wave generation. The device geometry, on the other hand, strongly influences compressional wave generation, with an undetermined effect on the shear wave. The response from compressional wave generation can be predicted reasonably well from the displacement profile. It is proportional to the profile factor P, a measure of the surface displacement gradient, averaged over the whole device surface and normalized by the displacement profile amplitude. The surface displacement profile can be determined by measuring device response while scanning a probe across the device surface.

The pronounced compressional wave interference effects shown in this paper indicate that care must be taken in device and fixture design to minimize these responses caused by compressional wave resonances. Otherwise, a change in fluid properties will vary the interference condition, leading to a spurious device response. There are several approaches to this problem. Compressional wave generation can be minimized by using device designs that yield displacement profiles that minimize the profile factor P. Alternatively, the fixture can be designed so that the fluid cavity thickness is chosen to detune resonances: $h = (n + 1/2)\lambda_c/2$, for $n = 0, 1, 2, \ldots$. Another alternative is to minimize the reflection of compressional waves back to the device surface. This can be done using fixture walls that are set at an oblique angle to the resonator surface; this has the adverse affect of increasing fluid volume. In theory, resonance effects can be minimized by roughening surfaces adjacent to the resonator; this results in wave scattering rather than specular reflection. To be effective, however, the scale of the roughness must be on the order of the acoustic wavelength. The long acoustic wavelength ($\lambda_c = 300$ μm in water at 5 MHz) of the compressional waves makes this difficult. Reflection could also, in principle, be prevented by interposing an absorptive material between the resonator and adjacent surfaces. Tessier et al.[15] report success using this technique. The thickness of material required for acoustic absorption must again be comparable to the acoustic wavelength.

Compressional wave radiation is a significant dissipation mechanism even for resonators operating in a semiinfinite fluid (i.e., without resonant coupling to a fluid layer). Analysis of this case has resulted in a modification to the equivalent-circuit model proposed[13,14,21] for the TSM resonator operating in a semiinfinite fluid. An extra motional resistance arises that represents power radiated as compressional waves from the device. Estimates of this contribution vary from 13% (1.0 in. diameter crystals) to 36% (0.5 in. diameter) of the total motional resistance. Measurements[21] of 12% excess dissipation are in good agreement with the compressional wave contribution estimated for hydrodynamically smooth 1.0 in. diameter devices. This casts doubt on earlier hypotheses,[29] based on enhanced interfacial viscosity arising from liquid ordering, that were advanced to explain these "excess" responses.

ACKNOWLEDGMENT

The authors are grateful to Prof. S. D. Senturia of the Massachusetts Institute of Technology and Richard Cernosek of

(29) (a) Kipling, A. L.; Thompson, M. *Anal. Chem.* **1990**, *62*, 1514–1519. (b) Rajakovic, L. V.; Cavic-Vlasak, B. A.; Ghaemmaghami, V.; Kallury, M. R. K.; Kipling, A. L.; Thompson, M. *Anal. Chem.* **1991**, *63*, 615–621. (c) Haardt, H. Ph.D. Dissertation, Universität Kiel, Kiel, Germany, 1971. (d) Thompson, M.; Arthur, C. L.; Dhaliwal, G. K. *Anal. Chem.* **1986**, *58*, 1206–1209. (e) Thompson, M.; Arthur, C. L.; Calabrese, G. S. *IEEE Trans. Ultrason. Ferroelec. Freq. Contr.* **1987**, *34*, 127. (f) Duncan-Hewitt, W. C.; Thompson, M. *Anal. Chem.* **1992**, *64*, 94–105. (g) Thompson, M.; Kipling, A.; Duncan-Hewitt, W. C.; Rajakovic, L. V.; Cavic-Vlasak, B. A. *Analyst* **1991**, *116*, 881–890.

Sandia National Laboratories for helpful discussions and to J. J. Spates of Ktech Corp. for help in constructing the resonator profiling apparatus. This work was performed at Sandia National Laboratories, supported by the U.S. Department of Energy under contract No. DE-AC04-94AL85000.

APPENDIX: SYMBOLS USED

ϱ	density of fluid
κ	bulk compressibility of fluid
η	shear viscosity of fluid
j	$(-1)^{1/2}$
f	operation frequency
ω	angular operating frequency ($2\pi f$)
v_x	shear fluid velocity
v_y	compressional fluid velocity
v_{yo}	surface normal particle velocity at resonator surface
v_{xo}	shear particle velocity at resonator surface ($y = 0$)
γ_s	complex shear wave propagation factor
A, B, C	integration constants
δ	decay length for shear wave in a Newtonian fluid
T_{xy}	shear stress in x-direction on y-normal plane
Z_s	shear mechanical impedance associated with excitation of shear wave
v_c	compressional wave velocity in fluid
T_{yy}	compressional stress (force per area in y-direction on a y-normal plane)
$Z_{co}^{(f)}$	characteristic compressional impedance of fluid
$Z_{co}^{(s)}$	characteristic compressional impedance of upper solid
$Z_c(y)$	compressional impedance at vertical position y in fluid
$Z_{so}^{(q)}$	quartz characteristic shear mechanical impedance
$Z_{so}^{(f)}$	characteristic shear mechanical impedance of the fluid
$Z_s(0)$	shear mechanical impedance at resonator surface
$Z_c(0)$	compressional mechanical impedance at resonator surface
$Z_i(0)$	surface mechanical impedance associated with surface displacement in the x_i direction
β_c	the (real) compressional wave propagation constant
κ_s	bulk compressibility of adjacent solid
ϱ_s	density of adjacent solid
λ_c	compressional wavelength in fluid
C_o	static capacitance of TSM resonator
C_o^*	static plus parasitic capacitance of TSM resonator
L_1	motional inductance of unperturbed resonator
C_1	motional capacitance of unperturbed resonator
R_1	motional resistance of unperturbed resonator
Z_c	complex change in motional impedance due to fluid layer and adjacent solid
U	total mechanical energy stored in TSM resonator
v_{io}	particle velocity in ith direction at surface of resonator
ϱ_q	quartz density
h_q	resonator thickness
d	resonator diameter
P	profile factor
Y	electrical admittance of resonator
Z_m	motional impedance of resonator
L_2	motional inductance due to the fluid
R_2	motional resistance due to the fluid
$R_2^{(comp)}$	motional resistance due to compressional wave generation in the fluid
$R_2^{(shear)}$	motional resistance due to shear wave generation in the fluid
k	shear wave number in the quartz
f_s	series resonant frequency of resonator
Δf_s	change in series resonant frequency
D	Gaussian profile parameter
R	Gaussian profile parameter
$f_s^{(offs)}$	frequency offset due to increased shear coupling by rough surface
$R_2^{(offs)}$	motional resistance offset due to increased shear coupling by rough surface

Received for review April 3, 1995. Accepted June 22, 1995.[⊗]

AC950333S

[⊗] Abstract published in *Advance ACS Abstracts*, August 1, 1995.

Anal. Chem. **1995**, *67*, 3336–3341

Direct in Situ Measurement of Phospholipid Hydration in an Aqueous Environment Using a Quartz Crystal Microbalance

Kaori Wakamatsu,* Kazuo Hosoda, Hiroshi Mitomo, and Masanao Ohya

Department of Biochemical Sciences, Faculty of Engineering, Gunma University, Kiryu, Gunma 376, Japan

Yoshio Okahata and Kouichi Yasunaga

Department of Biomolecular Engineering, Tokyo Institute of Technology, Nagatsuda, Midori-ku, Yokohama, Kanagawa 227, Japan

Hydration of phospholipid head groups is essential for stabilizing bilayer structures in an aqueous environment. Here we describe a new, easy, and rapid method that can directly and quantitatively determine phospholipid hydration in both water vapor and liquid water; i.e., a quartz crystal microbalance is employed which enables hydration to be determined in only 1 h using just 1 μg of phospholipids under various environmental conditions. Dipalmitoylphosphatidylethanolamine (DPPE) was examined with varying temperature, KCl concentration, and phase of water, where it was found that DPPE hydration in liquid water markedly increases upon raising the temperature, even when the phospholipid is in a gel phase, being maximal around its phase transition temperature (63.5 °C). Furthermore, KCl addition increased DPPE hydration in a temperature-dependent manner. The method presented is demonstrated to be capable of determining phospholipid hydration under physiological conditions; hence, it is suitable for investigating hydration phenomena involved in biological processes.

Hydration of phospholipid head groups is essential for stabilizing bilayer structures in an aqueous environment. Since hydration forces,[1–3] sometimes termed as hydration pressure, impede membrane close contact, hydration–dehydration processes are involved in the fusion and fission of biological membranes which occur during protein translocation within cells or endocytosis. The amount of phospholipid hydration in water vapor can be directly determined via a classical gravimetric method,[4,5] yet this technique cannot be applied to phospholipids suspended in liquid water. Instead, such hydration has only been quantified using somewhat time-consuming methods, e.g., X-ray diffraction (XRD),[6] differential scanning calorimetry (DSC),[7] and ^{2}H-NMR.[8,9] all of which use serial samples having increasing water/phospholipid ratios.

More recently, however, Okahata and Ebato[10] showed that the adsorption of detergents onto a dimethyldioctadecylammonium/poly(styrene-4-sulfonate) membrane in an aqueous environment can be measured by using a quartz crystal microbalance (QCM).[10] Their results showed that this adsorption was temperature dependent and reflected the membrane's phase transition. The QCM has also been successfully applied to examine the swelling behavior of Langmuir–Blodgett (LB) films,[11,12] which was found to be dependent on the film's phase.[13]

These investigations led to the present study, which employs the QCM to quantitatively measure phospholipid hydration in liquid water. Our new method is unique in that only one phospholipid sample is needed to directly determine the resultant hydration within 1 h under given conditions, e.g., temperature and ionic strength.

EXPERIMENTAL SECTION

Apparatus. Figure 1a shows a schematic diagram of the QCM apparatus, comprising a probe made of an AT-cut (angle of cut which minimizes resonance frequency temperature dependence[14]) quartz crystal disk (0.568 cm^2; Kyushu Dentsu, Nagasaki, Japan) having a 0.20-cm^2 Au electrode deposited on each side, a laboratory-built power supply, and a frequency counter (SC 7201; Iwatsu) connected to a personal computer. The probe was siliconized using dimethyldichlorosilane in toluene and blocked with methanol to avoid possible hydration of the quartz crystal or gold electrodes, though nontreated probes gave essentially the same results. In measurements taken in a KCl solution, to avoid current leakage between the two electrodes on the crystal via the ionic solution, one side of the crystal disk was covered with a plastic film. Without this shield of passivating film, the observed frequency fluctuated by >1000 Hz. The power supply applied ac voltage across the electrodes to drive the quartz at its resonance frequency (9 MHz),[13] with the vibration frequency being subsequently measured by the frequency counter. The mass change

(1) Rand, R. P. *Annu. Rev. Biophys. Bioeng.* **1981**, *10*, 277–314.
(2) McIntosh, T. J.; Simon, S. A. *Biochemistry* **1986**, *25*, 4058–4066.
(3) Cevc, G.; Marsh, D. *Biophys. J.* **1985**, *47*, 21–31.
(4) Elworthy, P. H. *J. Chem. Soc.* **1961**, 5385–5389.
(5) Jendrasiak, G. L.; Hasty, J. H. *Biochim. Biophys. Acta* **1974**, *337*, 79–91.
(6) Ruocco, M. J.; Shipley, G. G. *Biochim. Biophys. Acta* **1982**, *691*, 309–320.
(7) Chapman, D. *Forms and Function of Phospholipids*; Elsevier Scientific: Amsterdam, 1973; pp 1:7–142.
(8) Finer, E. G.; Darke, A. *Chem. Phys. Lipids* **1974**, *12*, 1–16.
(9) Borle, F.; Seelig, J. *Biochim. Biophys. Acta* **1983**, *735*, 131–136.
(10) Okahata, Y.; Ebato, H. *Anal. Chem.* **1991**, *63*, 203–207.
(11) Okahata, Y.; Ariga, K. *Thin Solid Films* **1989**, *178*, 465–471.
(12) Ariga, K.; Okahata, Y. *Langmuir* **1994**, *10*, 2272–2276.
(13) Okahata, Y.; Kimura, K.; Ariga, K. *J. Am. Chem. Soc.* **1989**, *111*, 9190–9194.

0003-2700/95/0367-3336$9.00/0

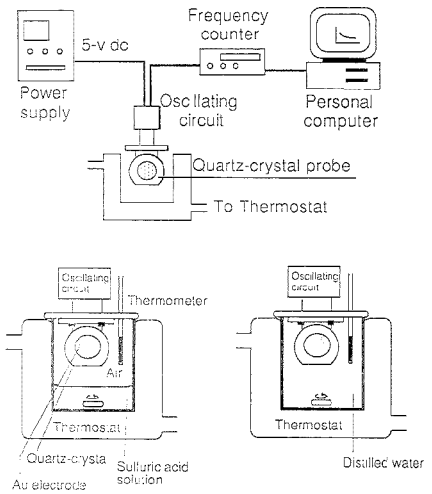

Figure 1. Schematic of experimental QCM apparatus showing the overall system and probe setup for vapor and liquid phase measurements.

Δm (g) can be calculated from the observed frequency shift ΔF (Hz) of an AT-cut, shear-mode QCM using[14,15]

$$\Delta m = \frac{-A(\varrho_q \mu_q)^{0.5}}{2F_0^2}\Delta F = -1.07 \times 10^{-9}\,\Delta F \qquad (1)$$

where F_0 is the parent frequency of the quartz crystal (9 MHz), A the electrode area (0.20 cm^2), ϱ_q the density of quartz (2.65 g cm^{-3}), and μ_q its shear modulus (2.95×10^{11} dyn cm^{-2}). In agreement with eq 1, QCM calibrations using palmitic acid indicated that a decrease in frequency (ΔF) of 1 Hz corresponds to an increase in electrode mass (Δm) of 1.05 ± 0.01 ng. This ratio ($\Delta m/\Delta F$) was subsequently employed to calculate Δm. In preliminary experiments, the employed QCM and one made of a highly polished quartz crystal gave the same results, thereby eliminating the possibility that surface roughness contributed to the measured ΔF.[16]

Materials. Dipalmitoylphosphatidylethanolamine (DPPE; Avanti Polar Lipids Inc., Alabaster, AL) was used without further purification because it gives a single spot on silicic acid thin-layer chromatography. Water (H_2O) was purified by a Milli-Q system (Millipore, Tokyo, Japan). We also employed D_2O (99.9 atom % D; Isotec, Miamisburg, OH) in some control experiments, distilled prior to use, to confirm that the observed frequency change was solely due to the change in mass of the phospholipid film. Other reagents were of analytical grade (Wako, Osaka, Japan).

Hydration in Water Vapor. To deposit phospholipids on the Au electrode, a chloroform solution (<2 μL) of DPPE, cholesterol, or a mixture of the two was coated on a nonshielded electrode, after which the chloroform was removed by evaporation.

The probe was placed in an air-tight bottle (11 mL) containing 4 mL of 97% sulfuric acid (Figure 1) maintained at 20 + 1 °C. After equilibration for about 30 min, the vibration frequency was determined and used to calculate the phospholipid dry mass. The observed mass change was consistent with that determined by a phosphorus assay,[25] which indicates a dry mass yield. Next, the probe was transferred into a similar bottle containing sulfuric acid (4 mL) adjusted to a concentration from 10 to 70% in order to vary the relative humidity (rh) from 94 to 4%, respectively.[5] The amount of hydration was calculated using the frequency shift (ΔF) between this hydrated phospholipid and the dry lipid. After each hydration, 1 μL of chloroform was dropped over the dried phospholipids to destroy the bilayer structure and to ensure complete dehydration. This procedure avoids a hysteresis effect on hydration, which is encountered when the same sample is successively hydrated at different rh values without being dried between experiments.[19] Of interest, hydration in DPPE was found to occur reversibly at rh ≤ 57%, though at rh ≥ 75%, only partial dehydration took place unless the bilayer structure was destroyed with chloroform.

Hydration in Liquid Water. Phospholipids were deposited on one Au electrode, and the dry lipid mass in air was determined as previously mentioned. The probe was then immersed in temperature-controlled (20−70 °C) distilled water (DW) or a KCl solution (Figure 1), and ΔF was monitored over time. After equilibration, ΔF was determined and used to calculate the hydration amount. Resonance resistance (R), whose change may affect the resonance frequency,[16] was determined by an impedance analyzer (Model 4192A; Yokogawa Hewlett-Packard Co., Tokyo, Japan).

To confirm that the deposited lipids did not flake off the electrode, the probe was dried while suspended over 97% sulfuric acid, and then the frequency was measured. We detected no significant mass loss (<3%) following five hydration−dehydration cycles. After hydration in the KCl solution, the probe was immersed in DW for 20 min to remove all traces of KCl. DPPE was dehydrated after each measurement at every temperature using chloroform as described above.

X-ray Diffraction. The state of hydrated DPPE was analyzed[17] using a wide-angle diffractometer (RAD-B; Rigaku Corp., Tokyo, Japan). Briefly, a solution of DPPE in chloroform/ethanol (5:1) was cast on a slide glass and the solvent evaporated under vacuum. The plate was then immersed in water, equilibrated for 10 min, and subjected to XRD.

RESULTS

DPPE Hydration in Water Vapor. Figure 2a shows the resultant DPPE hydration (ΔF) over time at 100% rh and 20 °C, where ΔF reaches a constant value (±10 Hz) within about 20 min. In this case, 0.282 μg of water was bound to 1.55 μg of DPPE (i.e., 6.7 mol of water/mol of DPPE). Note that the total amount of adsorbed water (Figure 2b) is linear with respect to the phospholipid mass (0.7−4 μg) cast on the electrode. Thus, the presented QCM method can be used to determine phospholipid hydration using only 1 μg of sample, 3 orders of magnitude less than that needed by conventional methods. In addition, as shown in Figure 2c, DPPE hydration in water vapor increased as rh increased; that is, DPPE adsorbs at most 1 mol/mol of water at rh ≤ 57%, whereas the adsorption increases abruptly at rh ≈ 75%. These results show good agreement with corresponding measure-

(14) Ebersole, R.; Ward, D. M. *J. Am. Chem. Soc.* **1988**, *110*, 8623−8628.
(15) Sauerbrey, G. *Z. Phyz.* **1959**, *155*, 206−222.
(16) Buttry, D. A.; Ward, M. D. *Chem. Rev.* **1992**, *92*, 1355−1379.
(17) Torbet, J.; Wilkins, M. H. F. *J. Theor. Biol.* **1976**, *62*, 447−458.

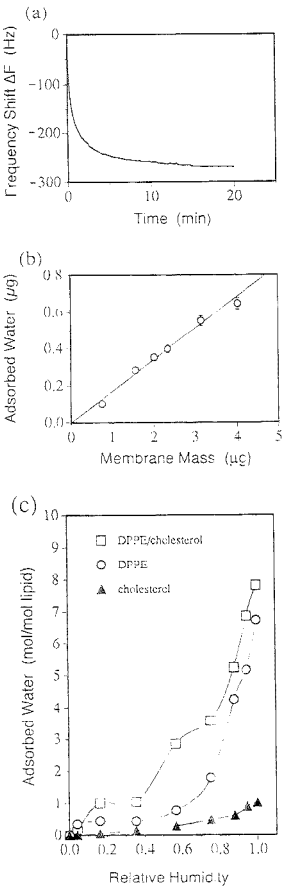

Figure 2. (a) Hydration time course of DPPE (1.55 μg) in water vapor at 100% rh and 20 °C. (b) Hydrated water amount versus phospholipid mass at 100% rh and 20 °C. Error bars show the standard error of mean (SEM) for $n = 5$. (c) Hydration of DPPE in water vapor versus relative humidity at 20 °C. DPPE/cholesterol, 1:1 mol/mol. For the mixture, the cholesterol's hydration contribution was subtracted from the total amount of water adsorbed, assuming that this hydration does not change upon the addition of phospholipids.

ments carried out using the conventional gravimetric method[18,19] (see Table 1).

Effect of Cholesterol on Hydration in Water Vapor. The addition of equimolar cholesterol to DPPE significantly enhances DPPE hydration in water vapor, though pure cholesterol adsorbs at most only one water molecule (Figure 2c). For example, the hydration at rh = 58% increases from 0.8 mol/mol for pure DPPE to 2.8 mol/mol for the DPPE/cholesterol mixture, with a shoulder appearing in the isotherm around rh = 60%. Such behavior correlates well with observations by Jendrasiak and Mendible,[19,20] indicating the QCM method effectively measures phospholipid hydration.

(18) Elworthy, P. H. *J. Chem. Soc.* **1962**, 4897–4900.
(19) Jendrasiak, G. L.; Mendible, J. C. *Biochim. Biophys. Acta* **1976**, *424*, 133–148.

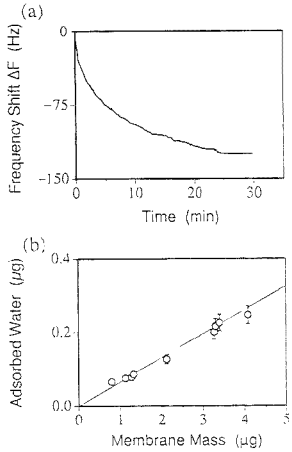

Figure 3. (a) Hydration time course of DPPE (2.12 μg) in DW at 20 °C. (b) Hydrated water amount versus DPPE mass at 20 °C. Error bars show the SEM for $n = 3$.

DPPE Hydration in Liquid Water. Figure 3a shows the hydration (ΔF) over time of DPPE in DW at 20 °C. For measurements taken in liquid water, ΔF usually shows a slight though abrupt drop just prior to reaching a steady state. Such a drop did not occur in water vapor, yet nevertheless the resultant equilibration time was comparatively similar. Also, the standard error of mean (SEM) of measurements in liquid water was only slightly larger than that in water vapor (Figures 2b and 3b). Under the conditions of Figure 3a, 2.3 mol of water is bound per mole of DPPE (Table 1), comparable to results obtained using other methods when taking into account that the amount of hydrated water is strongly dependent on temperature (discussed below). Once again, the total amount of water adsorbed onto DPPE (Figure 3b) is linear with respect to its mass (0.7–4 μg) cast on the electrode.

Note that at 20 °C, DPPE absorbs a smaller amount of water (2.3 mol/mol) than that occurring in water vapor (6.7 mol/mol) (Table 1). On the other hand, phosphatidylcholine is known to imbibe more water from liquid water than from water-saturated vapor, a phenomenon known as the vapor pressure paradox.[21,30] We therefore confirmed such behavior using the QCM; namely, at 20 °C, dipalmitoylphosphatidylcholine (DPPC) absorbed 12.7 and 10.5 mol/mol water from liquid water and from water-

(20) Jendrasiak, G. L.; Mendible, J. C. *Biochim. Biophys. Acta* **1976**, *424*, 149–158.
(21) Rand, P. P.; Parsegian, V. A. *Biochim. Biophys. Acta* **1989**, *988*, 351–376.
(22) Lis, L. J.; McAlister, M.; Fuller, N.; Rand, R. P.; Parsegian, V. A. *Biophys. J.* **1982**, *37*, 657–666.
(23) The solubility of KCl in water at 20 °C is ~5 *m*.
(24) Rydall, J. R.; Macdonald, P. M. *Biochemistry* **1992**, *31*, 1092–1099.
(25) Okahata, Y.; Ebato, H. *Anal. Chem.* **1989**, *61*, 2185–2188.
(26) Bartlett, G. R. *J. Biol. Chem.* **1959**, *234*, 466–468.
(27) McIntosh, T. J.; Simon, S. A. *Biochemistry* **1986**, *25*, 4948–4952.
(28) Janiak, M. J.; Small, D. M.; Shipley, G. G. *J. Biol. Chem.* **1979**, *254*, 6068–6078.
(29) Rand, R. P.; Fuller, N. L.; Parsegian, V. A.; Rau, D. C. *Biochemistry* **1988**, *27*, 7711–7722.
(30) Rand, R. P.; Parsegian, V. A. In *The Structure of Biological Membranes*; Yeagle, P., Ed.; CRC Press: London, 1991; Chapter 6.

Table 1. Number of Water Molecules Hydrated per Lipid Molecule

lipid	water vapor	liquid water	
		distilled water	0.15 M KCl
DPPE	6.7 (20 °C)[a]	2.3 (20 °C)[a]	10.6 (20 °C)[a]
	9.1 (22 °C)[b]	18.9 (65 °C)[a]	
	3.8 (20 °C)[c]		
DLPE		6.7 (20 °C)[d]	
		9.2 (35 °C)[e]	
POPE[f]		10.7 (30 °C)[g]	
egg PE		23.0 (25 °C)[h]	
DPPE/cholesterol (1:1 mol/mol)	7.8 (20 °C)[a]	3.7 (20 °C)[a]	
	13.5 (22 °C)[b]	25.3 (65 °C)[a]	
cholesterol	1.0 (20 °C)[a]	1.5 (20 °C)[a]	
	1.0 (22 °C)[b]	2.7 (65 °C)[a]	

[a] Present study. [b] References 14, 19. [c] Reference 13. [d] In a gel phase (T_c = 30 °C), ref 15. [e] In a liquid-crystalline phase, ref 15. [f] 1-Palmitoyl-2-oleyl-PE. [g] References 21, 29. [h] References 21, 22.

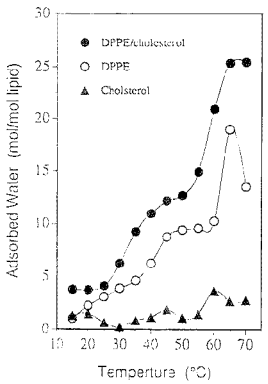

Figure 4. Hydration of DPPE in DW at various temperatures. DPPE/cholesterol, 1:1 mol/mol.

saturated vapor, respectively. Although it is not known why DPPC and DPPE show conflicting hydration behaviors, no one has thus far conclusively explained the vapor pressure paradox, either.[30] Obviously then, such anomalous behavior of DPPE should be considered in any future research directed at elucidating this paradox.

When XRD analysis was carried out on a DPPE sample that was cast and dried on a glass substrate and then swelled in water, peaks were observed up to the order 4 (data not shown), which indicates a spacing of 56 Å. This value agrees with the reported bilayer thickness of phosphatidylethanolamine (PE, 52–57 Å),[21] thereby indicating that the observed mass change reflects the hydration of DPPE in the bilayer state.

Figure 4 shows the effect of temperature on the hydration of DPPE in DW, where DPPE displays increased hydration with increasing temperature. At 65 °C, maximum hydration occurs, which probably reflects the phospholipid's phase transition, where the crystalline and liquid-crystalline phases coexist microscopically[12] (the phase transition temperature, T_c, is 63.5 °C). Such an increase in membrane hydration at T_c has also been observed for LB films of dimyristoylphosphatidylethanolamine[12] and 1,3-dioctadecyl-*rac*-glycer-2-ol,[11] being ascribed to structural defects occurring between the two phases. At 70 °C, phospholipids are in a liquid-crystalline phase, and 13 mol/mol of water is adsorbed, which is close to the values reported for dilauroylphosphatidylethanolamine (DLPE) and dioleoylphosphatidylethanolamine (DOPE) in a liquid-crystalline phase (9–11 mol/mol).[15,21,29] Thus, hydration near T_c is higher than that above T_c, where all DPPE molecules are in a single liquid-crystalline phase.

It should be noted that the amount of hydration significantly varies with temperature, even for temperatures at which the phospholipids are in a gel phase. Therefore, when hydration is described, the temperature as well as the phospholipid phase must be specified. It is known that egg yolk PE adsorbs more water (23 mol/mol at 25 °C)[21,22] than does DLPE (9.2 mol/mol at 35 °C),[13] though both are in a liquid-crystalline phase at these temperatures (T_c = 11 and 30 °C for egg yolk PE and DLPE, respectively). Such a difference in hydration is considered to be due to the two phospholipids having different flexibility in their acyl chains.

Cholesterol Effect on DPPE Hydration in Liquid Water. The addition of cholesterol enhances DPPE hydration in liquid water just as it did in water vapor (Figure 4). Of interest, the hydration peak became broad due to a broadening of the phase transition; this observation confirms our postulation that hydration is enhanced by the coexistence of two phases.

KCl Effect on DPPE Hydration in Liquid Water. To our surprise, the addition of KCl markedly enhanced ΔF upon hydration of DPPE in liquid water (Figure 5), and the corresponding increase in mass cannot be solely explained by the adsorption of KCl onto DPPE. In other words, if the amount of hydrated water did not change upon KCl addition, the KCl concentration in the hydrated water would have to be as high as 80 m[23] to account for the obtained mass increase. In addition, a comparison of ΔF in D_2O and that in H_2O indicated ΔF is primarily due to hydration (see Discussion). Moreover, binding of the chloride anion to DPPE is known to be very weak.[24] To examine whether KCl induces some structural change in the DPPE bilayer, we carried out XRD analyses on DPPE hydrated in KCl solutions for 12 h at 20 °C. In fact, the repeat period was found to be dependent on the KCl concentration: 55.7, 54.8, 55.1, and 55.4 Å at 0, 50, 100, and 150 mM KCl, respectively. In bilayers of phosphatidylethanolamine, the head groups are known to be more tightly packed than those in phosphatidylcholine,[33] suggesting that the increase in hydration may be caused by a weakened association among DPPE head groups due to increased ionic strength. Moreover, the repeat period of DLPE bilayers in a gel phase with

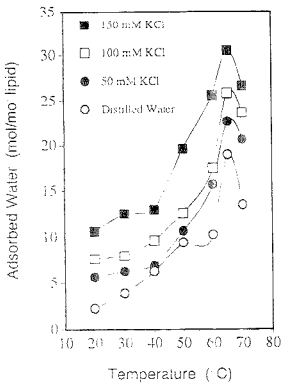

Figure 5. Effect of KCl addition on DPPE hydration in liquid water at various temperatures.

excess water is known to change upon prolonged storage, reflecting a phase change from the β_2 (acyl chains parallel to the membrane normal) to β_1 (acyl chains tilted from the normal) phase.[31] On the basis of these findings, we explain the observed decrease in the repeat period of DPPE bilayers upon the addition of 50 mM KCl (0.9 Å) as follows: The incorporation of water molecules among the head groups increases their molal area such that the molal area of acyl chains must correspondingly increase to maintain a bilayer structure: namely, the acyl chains are tilted, which decreases the repeat period. In contrast, the increase in the repeat period at higher KCl concentrations (> 50 mM) reflects an increased space between the bilayers of the tilted DPPE molecules due to increased hydration.

It is also important to realize that the extent of hydration enhancement due to KCl varies with temperature; i.e., the addition of 0.15 M KCl (physiological ionic strength) increased DPPE hydration by a factor of about 5 at 20 °C, but only a factor of 2 at 40 °C. To the best of our knowledge, salts have not been reported to affect phospholipid hydration. Because similar QCM measurements showed no change in DPPC hydration upon the addition of KCl up to 150 mM (data not shown), the dependence of hydration on ionic strength may be specific to PE; thus, the phenomenon has never been observed before.

DISCUSSION

Validation of Measurements. In addition to the mass of adsorbate on the quartz probe, other factors will also affect the QCM's resonance frequency, e.g., sample viscoelasticity, surface roughness of the quartz, and interfacial slippage.[16] However, we nevertheless consider these phospholipid hydration measurements to be accurate based on the following.

(1) The resultant amount of adsorbed water was proportional to that of the phospholipid cast on the Au electrode (Figures 2b and 3b), a behavior that must occur for the frequency change to reflect solely the mass change.[16] Such behavior also excludes the possible occurrence of slippage between phospholipid bilayers. In fact, under experimental conditions similar to those employed here, Okahata and Ebato[25] showed that no slippage occurs between bilayers of 1,3-dihexadecyl-2-glycerophosphoethanolamine, a phospholipid having a similar chemical structure.

(2) An impedance analysis of DPPE hydration in DW indicated that the resonance resistance (R) did not significantly change over the entire hydration time course (615.1 ± 6.2 Ω at 30 °C and 620.5 ± 7.9 Ω at 60 °C); thereby ruling out any possibility that viscoelastic changes in DPPE affect ΔF.

(3) It is possible to confirm that the observed frequency change is due solely to the adsorption of water molecules into a phospholipid film by comparing the frequency change in H_2O to that in D_2O and obtaining a frequency ratio of 1.1 (molecular weight ratio of D_2O and H_2O).[32] In fact, when D_2O was used instead of H_2O, ΔF due to hydration increased by a factor of 1.10 ± 0.03 (n = 3) for DW and 1.108 ± 0.003 (n = 3) for 0.15 M KCl, indicating that ΔF reflects only a change in probe mass and not a viscoelastic change in DPPE[16] (the mass of KCl does not contribute significantly to the mass ratio at 0.15 M).

(4) The amount of hydration determined in this study is consistent with those determined using other methods (Table 1); e.g., the addition of cholesterol was found to increase hydration.

(5) Measurement reproducibility is good since the SEM of hydrated water is as small as 1 mol/mol (n = 5) and 2 mol/mol (n = 3) for hydration in water vapor and liquid water, respectively.

Advantages of Using the QCM for Studying Phospholipid Hydration. Hydration of phospholipids in liquid water has been determined by XRD,[6,27,28] DSC,[7] and ^{2}H-NMR[8,9] methods, all of which require multiple measurements using serial samples with increasing water/phospholipid ratios. The amount of hydration is obtained by determining the ratio where the interbilayer distance becomes constant in XRD, where the endothermic peak appears due to thawing of (free) ice in DSC, and where a sharp resonance of free water occurs in ^{2}H-NMR. In addition to the time-consuming labor required for these techniques, DSC has another drawback in that it can determine the hydration only at 0 °C.

The presented QCM method, however, possesses many clear-cut advantages. (1) It is straightforward and monitors a frequency change that is directly proportional to the phospholipid mass change. (2) Hydration is rapidly determined (<1 h) using just a single sample under given conditions such as ionic strength and temperature. (3) Only 1 μg of phospholipids is required, which makes it possible to analyze pathological samples that may be available in only limited amounts. (4) Temperature of a sample can be easily controlled. (5) Monitoring the time course of hydration is possible at a resolution of 1 s.[12] (6) The QCM method can be applied in both gaseous and liquid environments that are close to physiological conditions.

CONCLUSIONS

The advantages of using the QCM to quantitatively measure phospholipid hydration enabled us to systematically study such hydration in liquid water under various environmental conditions, as well as to directly compare hydration in water vapor with that occurring in liquid water. Therefore, the QCM is expected to become a promising tool for studying the hydration of biological molecules under physiological conditions. In fact, our new method is believed to be generally applicable to research on the

(31) Seddon, J. M.; Harlos, K.; Marsh, D. *J. Biol. Chem.* **1983**, *258*, 3850–3854.

(32) Lasky, S. J.; Buttry, D. A. *J. Am. Chem. Soc.* **1988**, *110*, 6258–6260.

(33) Hauser, H.; Pascher, I.; Pearson, R. H.; Sundell, S. *Biochim. Biophys. Acta* **1981**, *650*, 21–51.

(34) Mason, W. P. In *Physical Acoustics: Principles and Methods, Volume I, Part A*; Mason, W. P., Ed.; Academic Press: New York, 1964; Chapter 5.

solvation of any other compound that can be fixed onto an Au electrode.

ACKNOWLEDGMENT

This work was financially supported by a Grant-in-Aid (No. 03780145) from the Ministry of Education, Science, and Culture of Japan, and by a grant from the Asahi Glass Foundation. We are grateful to Dr. Toshiaki Dobashi, Gunma University, for his valuable technical advice.

Received for review January 26, 1995. Accepted June 21, 1995.[⊗]

AC950098D

[⊗] Abstract published in *Advance ACS Abstracts,* August 1, 1995.

Anal. Chem. 1995, 67, 3342–3348

Transient Methods for in Situ NMR of Reactions on Solid Catalysts Using Temperature Jumps

David B. Ferguson and James F. Haw*

Department of Chemistry, Texas A&M University, College Station, Texas 77843-3255

Two methods for carrying out magic angle spinning (MAS) NMR experiments with temperature jumps were evaluated for their suitability for studies of rapid chemical reactions in situ. Temperature profiles, both spatial and temporal, were determined through the use of ^{207}Pb chemical shift thermometry and melting transitions. The useful range of the previously reported lead nitrate shift thermometer was extended using standard heated or cooled gas methods to 123–548 K with reasonable linearity and a slope of 0.775 ± 0.007 ppm/K. As shown previously, high temperatures and appreciable temperature jumps could be achieved by focusing 10.6-μm radiation from a CO_2 laser onto the outside of a quartz MAS rotor; however, the spatial temperature distribution observed with this method was large. The second method of achieving temperature jumps was based on radio frequency inductive heating of platinum metal coatings on quartz or zirconia MAS rotors. This method, demonstrated previously for static heating of solution samples, shows considerable potential for static heating and temperature jumps in MAS studies of solids. Our inductive heating experiments were performed using an unmodified double resonance, single coil MAS probe by injecting a continuous signal 130 kHz off-resonance from the ^1H frequency into the decoupler channel. While the spectrometer used was generally capable of performing continuous wave (CW) heating experiments with 100 W, the standard probe design limited CW heating power to ~20 W; thus, the results reported here understate the potential of the method. Since the volume of the rotor efficiently inductively heated was several times that in the laser experiment, the spatial temperature gradients were significantly smaller for the former compared to the latter. For example, with static heating at 373 K, ^{207}Pb thermometry revealed a distribution of ±8 K with inductive heating vs >±50 K with the laser heater, even though the sample size was smaller in the laser experiment. Using a combination of thermometry techniques, it was possible to establish 30–60-s heating regiments for in situ ^1H and ^{13}C NMR studies of the reactions of methanol on the acidic zeolite catalyst HZSM-5. Application of 18 W at 199.7 MHz to a 5-mm-o.d. Pt-coated zirconia rotor heated the samples from an initial value of 298 K to a final state fully equilibrated at 623 K in 30 s or less. Single-shot ^1H spectra acquired every 3 s during the dynamic part of the experiment and ^{13}C spectra acquired after quenches to 298 K were consistent with established features of the catalytic reaction mechanism.

The reactions of various absorbates on zeolites,[1–3] metal oxides,[4] and supported metal catalysts[5,6] are being studied by NMR spectroscopy in the hope of elucidating the structures of chemisorbed species formed in preequilibria or as persistent intermediates as well as the sequence of reaction steps or other mechanistic details. General considerations of reaction mechanisms would suggest that some intermediate species, stable for a few vibrations at reaction temperature or formed at vanishing steady-state concentration, will forever be out of reach of NMR studies. But typical catalytic reactors contact the reactant and catalyst bed for times ranging from tenths of seconds to hundreds of seconds; thus, significant kinetic and mechanistic information may be available by NMR measurements carried out at short but achievable reaction times.

Time scales of tens of seconds, however, are orders of magnitude shorter than those used in essentially all MAS NMR investigations of reactive adsorbates thus far. Most such experiments can be grouped into one of two classes. In the variable temperature in situ MAS approach developed in our laboratory,[7,8] the reaction is observed in progress in a sealed rotor (batch reactor) at a suitable temperature. For example, the temperature might be raised incrementally from room temperature or below to temperatures as high as 573 K (depending on the upper temperature limit of the NMR probe), and ^{13}C MAS spectra are acquired at each temperature. With this approach, the reaction time scale will typically be tens of minutes to several hours. Alternatively, sealed samples (often glass ampules) are carried between a standard laboratory oven or furnace for incremental heating periods and an MAS rotor for spectral acquisition at ambient temperature. Techniques with off-line heating then might entail total periods of hours or days, with a complicated sample temperature history. Neither the in situ nor the off-line method approaches the reaction times of flow reactors by several orders of magnitude, and the NMR studies are typically carried out at temperatures ~100 K lower than those of the corresponding flow reactions to partially compensate, although the mechanistic consequences of this compromise are not always obvious.

(1) Xu, T.; Munson, E. J.; Haw, J. F. *J. Am. Chem. Soc.* 1994, *116*, 1962–72.
(2) Xu, T.; Haw, J. F. *J. Am. Chem. Soc.* 1994, *116*, 10188–95.
(3) Anderson, M. W.; Klinowski, J. *J. Am. Chem. Soc.* 1990, *112*, 10–16.
(4) Kheir, A. A.; Howard, T.; Haw, J. F. *J. Am. Chem. Soc.* 1994, *116*, 10839–40.
(5) Chin, Y.; Ellis, P. D. *J. Am. Chem. Soc.* 1993, *115*, 204–11.
(6) Haw, J. F. In *NMR Techniques in Catalysis*; Bell, A. T., Pines, A., Eds.; Marcel Dekker: New York, 1994; pp 139–94.
(7) Haw, J. F.; Richardson, B. R.; Oshiro, I. S.; Lazo, N. D.; Speed, J. A. *J. Am. Chem. Soc.* 1989, *111*, 2052–8.
(8) Oliver, F. G.; Munson, E. J.; Haw, J. F. *J. Phys. Chem.* 1992, *96*, 8106–11.

0003-2700/95/0367-3342$9.00/0

As alternatives to approaches using long heating periods and sealed samples, one can envision a variety of NMR methods, in situ or off-line, using samples prepared with sudden changes in either the temperature or adsorbate concentration. One experiment in the literature that could be extended to achieve dynamic reaction conditions on shorter time scales is the flow reactor probe idea pioneered by Reimer and co-workers.[9] In such a probe, one might get information about short reaction time behavior by making suitable changes in the reactant stream. A second general strategy for dynamic in situ experiments would preserve the resolution advantages of magic angle sample spinning and the conservation of stable isotopes possible with sealed samples and achieve shorter reaction time scales by using temperature jumps. We have been exploring the latter possibility using two methods: use of an infrared laser to heat the MAS rotor and radio frequency inductive heating. This paper evaluates these methods for dynamic in situ experiments and is also the first report of the controlled use of inductive heating in MAS experiments.

Temperature jumps have previously been used in NMR either by using gas heating of solution NMR tubes, by Akasaka et al.[10] or by inductively heating a conductive solid sample, aluminum metal, by Guillion and Conradi.[11] Laser heating was first introduced to NMR by Taulelle and co-workers[12,13] and then was applied to MAS studies by this laboratory[14] and independently by Freude et al.[15] Laser heating was also used in a two-dimensional experiment with a temperature jump to correlate solid-state and liquid-state spectra.[16] The inductive heating of MAS rotors used in the present investigation drew from static heating of liquid sample tubes coated with a platinum film which was pioneered by Yannoni and co-workers.[17]

The use of various gas streams for sample rotation and temperature regulation makes even a standard variable temperature MAS experiment nontrivial with respect to measurements of mean temperatures and gradients across the sample volume, and these effects have been previously evaluated using chemical shift thermometry based on NMR shifts in paramagnetic solids[18-21] as well as solid–solid[22] and solid–liquid phase transitions.[8] Although early MAS probes proved to generate large temperature errors and appreciable gradients over the sample, these problems have been corrected on most recent commercial designs. The prospects of accurate temperature measurement for laser or inductive heating experiments would at first appear to be bleak even for static heating, let alone for dynamic heating in temperature jump experiments. However, careful thermometry experiments reported here show that mean temperatures and temperature gradients with respect to position and time can be reliably measured for both methods. For the laser MAS sample geometry developed by our group,[14] the spatial temperature gradient across useful sample volumes was so large as to preclude a meaningful definition of the sample temperature for comparison to standard catalysis experiments. Inductive heating of MAS rotors, however, resulted in more modest temperature gradients, and in situ NMR experiments were developed using this approach that could be conducted in as little as 30–45 s with well-characterized and reproducible time–temperature profiles and maximum temperatures identical to those of corresponding flow reactor studies. This method was demonstrated for the well-studied methanol-to-gasoline reaction on HZSM-5, and the spectroscopic results obtained were consistent with established features of the reaction mechanism. It is suggested that reasonable improvements in the continuous wave (CW) power limits of the NMR probe will permit dynamic in situ experiments with reaction time scales as short as 10 s.

EXPERIMENTAL SECTION

Methods and Materials. Lead nitrate and isophthalic acid were obtained from Aldrich and used without further purification. Lead nitrate is highly toxic and is a strong oxidizer, and care should be taken when handling it and mixing it with other compounds. Lead nitrate decomposes at 734 K. The melting point of isophthalic acid was determined to be 614–616 K.

Zeolite HZSM-5 (Union Carbide Corp., Si/Al = 18) was activated under shallow bed conditions (≤5 mm) to a final temperature of 673 K using a multistep activation procedure described elsewhere.[7] Methanol-^{13}C (99% ^{13}C) was obtained from Cambridge Isotopes and was purified via several freeze–pump–thaw cycles. During activation, the catalyst was evacuated to a pressure less than 5×10^{-5} Torr. To ensure a homogeneous adsorbate loading, all adsorptions were carried out at room temperature under shallow bed conditions. After adsorption, the sample was transferred to a glovebox, and ~100 mg fractions were loaded into Pt-plated, 5-mm zirconia MAS rotors for inductive heating experiments.

NMR Spectroscopy. 199.6-MHz ^1H, 50.2-MHz ^{13}C, and 41.6-MHz ^{207}Pb spectra were acquired on a home-built spectrometer with an Oxford 4.7 T magnet and a Tecmag Libra pulse programmer. Liquid *p*-xylene (6.9 ppm relative to TMS) and hexamethylbenzene (17.4 ppm) were used as external chemical shift standards for ^1H and ^{13}C, respectively. Lead nitrate was arbitrarily assigned a ^{207}Pb chemical shift of 0 ppm at 298 K.

All spectra shown were acquired using single pulse excitation with proton decoupling for the case of ^{13}C spectra. The 90° pulse widths were typically 3–4.5 μs. Pulse delays of 2, 4, and 10 s were used for ^1H, ^{13}C, and ^{207}Pb acquisitions, respectively. Active spin speed control (±2 Hz) was used in all experiments, and all spectra shown were acquired at spinning speeds between 4 and 5 kHz.

Standard Gas Heating. MAS experiments using hot gas heating methods were carried out with home-built, transmission line style probes fitted with MAS spinning modules similar in design to the Chemagnetics Pencil style. Variable temperature was achieved with an external heater accessory in which dry nitrogen gas was heated with a resistive element prior to being

(9) Haddix, G. W.; Reimer, J. A.; Bell, A. T. *J. Catal.* **1987**, *106*, 111–3.
(10) Akasaka, K.; Naito, A.; Nakatari, H.; Imanari, M. *Rev. Sci. Instrum.* **1990**, *61*, 66–8.
(11) (a) Guillion, T.; Conradi, M. S. *Phys. Rev. B* **1987**, *36*, 3880–3. (b) Guillion, T.; Conradi, M. S. *Phys. Rev. B* **1984**, *30*, 1133–7.
(12) Taulelle, F.; Coutures, J. P.; Massiot, D.; Rifflet, J. P. *Bull. Magn. Reson.* **1989**, *11*, 318–20.
(13) Massiot, D.; Bessada, C.; Echegut, P.; Coutures, J. P.; Taulelle, F. *Solid State Ionics* **1990**, *37*, 223–9.
(14) Ferguson, D. B.; Krawietz, T. R.; Haw, J. F. *J. Magn. Reson.* **1994**, *109*, 273–5.
(15) Ernst, H.; Freude, T.; Mildner, T. *Chem. Phys. Lett.* **1994**, *229*, 291–6.
(16) Ferguson, D. B.; Krawietz, T. R.; Haw, J. F. *Chem. Phys. Lett.* **1994**, *229*, 71–4.
(17) Maresch, G. G.; Kendrick, R. D.; Yannoni, C. S. *Rev. Sci. Instrum.* **1990**, *61*, 77–80.
(18) Haw, J. F.; Campbell, G. C.; Crosby, R. C. *Anal. Chem.* **1986**, *58*, 3172–7.
(19) Campbell, G. C.; Crosby, R. C.; Haw, J. F. *J. Magn. Reson.* **1986**, *69*, 191–5.
(20) Grey, C. P.; Dobson, C. M.; Cheetham, A. K.; Jakeman, R. J. B. *J. Am. Chem. Soc.* **1989**, *111*, 505–11.
(21) Grey, C. P.; Cheetham, A. K.; Dobson, C. M. *J. Magn. Reson., Ser. A* **1993**, *101*, 299–306.
(22) Haw, J. F.; Crook, R. A.; Crosby, R. C. *J. Magn. Reson.* **1986**, *66*, 551–4.

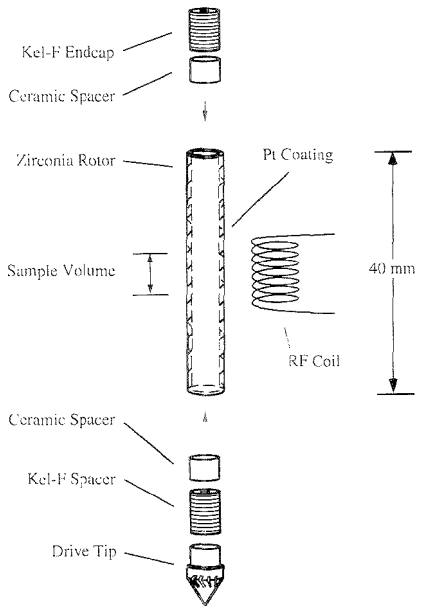

Figure 1. Experimental geometry for MAS NMR with inductive heating. The radio frequency coil that was used for transmitting and receiving NMR signals and for inductive heating is shown off-set from the platinum-plated zirconia rotor for clarity. This exploded view also illustrates the thermal bulkheads and grooved Kel-F seals used in all of the work reported here. The platinum coating was typically 25% longer than the rf coil, and the sample was limited to the center 75% of the length of the rf coil for a nominal payload of 75 μL.

directed onto the MAS rotor. The heater was top mounted in the magnet bore and mated with the top of the probe, which was bottom loading. The preheated gas was directed onto the center of the zirconia MAS rotor at a flow rate of 150 ft^3(STP)/h. A resistance temperature device (RTD) (Omega, 100W30) several centimeters upstream from the sample gave an accurate measure of the gas temperature prior to contact with the MAS rotor as determined in this and previous investigations. Primary standardization of the temperature was carried out via the observation of the solid–liquid phase transitions of hexamethylbenzene (mp = 440 K) and caffeine (mp = 508 K). Using these methods, the temperature of the gas stream, as indicated by the RTD, was identical to that of the sample to within ±3 K.

Radio Frequency Heating. The approach previously reported by Yannoni et al.[17] was adapted for use in MAS experiments. MAS rotors for radio frequency (rf) heating, illustrated in Figure 1, were prepared by coating 5-mm zirconia rotors (Chemagnetics) with a Pt suspension (Standard Ceramic Supply, S-2). The rotors were then subjected to a heat treatment in which the temperature of a glassblower's oven was slowly ramped to 923 K over an 8-h period. The final appearance of the reflective plating was a brilliant silver color. After coating or recoating each individual rotor, the calibration of sample temperature vs rf power level was verified using the melting point techniques described elsewhere in the text. After repeated use in temperature jump experiments, the coating tended to unbond; therefore, any individual rotor was used for a maximum of two in-situ runs, after which the coating was removed and the rotor replated. Similarly, 5-mm quartz rotors (Wilmad, 701-PQ-1.6) were also studied and found to plate and perform in inductive heating experiments as well as plated zirconia rotors. Plated zirconia rotors were used in all of the experiments reported here, as the greater mechanical strength simplified sealing the catalyst samples using established methods. The conductive coatings were expected to slightly reduce the rf power level reaching the sample and by reciprocity the signal intensity as well. Measurements on standards suggested that these decreases were only 30% relative to otherwise identical, uncoated rotors. The sample volume subjected to uniform inductive heating is controlled by the coil dimensions as well as those of the plating; thus, sample volumes of ~75 μL were used to constrain the sample to within the coil region. Sample payloads in the inductive heating equipment were thus very close in size to those used in hot gas experiments.

No probe modifications were needed for inductive heating experiments, but the spectrometer was modified to include a rudimentary rf channel for heating. This channel was composed of a frequency synthesizer (Programmed Test Sources, PTS-500) to generate the rf signal and a variable attenuator (Merrimac, ARC-4) to control the amplitude of the signal. The frequency for heating, 199.76 MHz, was set 130 kHz off-resonance from the ^{1}H resonance frequency to prevent saturation. A single rf power amplifier (American Microwave Technology, M3200) operating in dual CW/pulse mode was used for both ^{1}H irradiation using ~100-W pulses and rf inductive heating using lower power settings. An rf switch (MiniCircuits, ZYSW-2-50DR) under pulse programmer control directed either the CW heating signal or the normal ^{1}H transmitter channel output to the power amplifier. The heating signal was gated off only during excitation and acquisition of ^{1}H NMR signals. Acquisition lengths were intentionally kept short relative to pulse delays in order for the duty cycle of the heating to be essentially unity.

Power settings for inductive heating were measured using an oscilloscope to monitor the voltage coupled into a 50-dB extractor element contained in a $^7/_8$-in. coaxial line section. The accuracy of this method is probably not better than ~10%, and all power measurements are reported to the nearest watt. Once the power level was set, however, it was highly stable (up to ~18 W). Because of the uncertainty in power levels measured with the oscilloscope and the possibility of variable performance for different plated rotors (which was not observed), the power level was set to just fully melt isophthalic acid (>616 K) prior to repacking that rotor with the catalyst–adsorbate sample for a dynamic in situ experiment at a nominal mean temperature of 623 K.

Laser Heating. MAS laser heating experiments were carried out using a 50 W CO_2 (10.6 μm) laser (Synrad, 48-5). The laser beam was directed up the magnet bore using a custom-built reflecting–focusing assembly such that the beam passed through a gap in the rf coil and contacted the MAS rotor in the geometry suggested in Figure 2. Quartz MAS rotors (Wilmad, 701-PQ-1.6), 5 mm, were used for laser heating experiments. The home-built NMR probe was fitted with a specially designed MAS module. The laser duty cycle and amplitude were under pulse programmer control. The laser heating system, probe, and operation have previously been described in detail.[14,16] The sample size required by this geometry, as indicated in Figure 2, was such that the sample was restricted to less than the length of the rotor heated

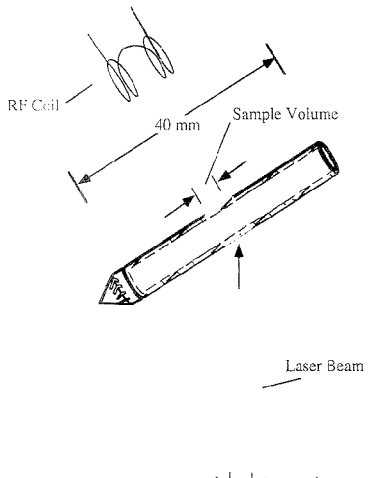

Figure 2. Experimental geometry for MAS NMR with laser heating. The split solenoid radio frequency coil with a gap to admit the laser beam is shown off-set for clarity. The beam trace on the MAS rotor is shaded. Significant temperature gradients were present even with payloads of 30 μL (see text). Quartz MAS rotors were used; these absorb the 10.6-μm radiation but conduct the heat to the sample in several seconds (see ref 14 for a more complete description of the laser experiment).

by the laser beam. Given the internal diameter of the rotors, this implied a sample volume of 30 μL for a sample 90% the length of the nominal beam profile onto the rotor. An additional factor in the signal to noise ratio of our laser heating experiments was the split solenoid geometry (see Figure 2) of the transmit/receive coil. While this coil's performance was determined to be superior to that of a coil of Helmholtz geometry, it was still inferior to a standard solenoid.

RESULTS AND DISCUSSION

Central to any variable temperature experiment is the ability to determine not only the mean sample temperature but also the existence and magnitude of spatial temperature gradients. Precise measurement of sample temperature in MAS probes is not easily carried out with an external sensor, and temperature gradients are difficult, if not impossible, to measure with this approach. These factors motivate the measurement of temperature-dependent NMR observables. While the observation of phase transitions is useful,[8,22] this approach results in discrete data points, and a continuous measurement is preferable. Several chemical shift thermometers based on paramagnetic solids have previously been reported. In the earliest reports, samarium acetate was used to measure temperature accuracy and gradients at the lower temperatures at which this thermometer is useful.[19] Samarium acetate was also used to characterize a simple temperature jump and inductive heating of a blend of graphite and the thermometer substance.[18] More recently, Grey et al. have shown that several paramagnetic stannates are excellent chemical shift thermometers.[20,21] The ^{207}Pb resonance of lead nitrate has been reported

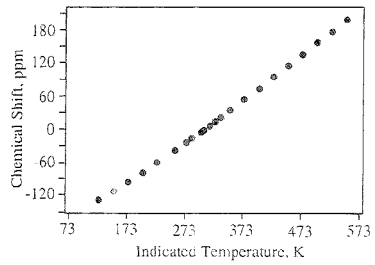

Figure 3. Calibration curve for the chemical shift thermometer based on the ^{207}Pb resonance of lead nitrate. The shift was arbitrarily assigned a value of 0 ppm at 298 K. These measurements were performed using a standard hot or cold gas probe, and melting point thermometry was carried out for primary standardization.

to be quite sensitive to temperature.[23] We chose lead nitrate for this study over the previously reported shift thermometers due to its spectral simplicity, relatively narrow line width, and excellent sensitivity; these properties are especially important for measuring gradients. Figure 3 shows our calibration curve for lead nitrate as determined from standard hot or cold gas MAS experiments. The chemical shift was determined to have acceptable linearity with a slope, obtained from a linear least-squares fit, of 0.775 ppm/K over the temperature range of 123–548 K. Primary standardization of this curve was achieved by observing the solid–liquid phase transitions of hexamethylbenzene and caffeine. The relatively narrow observed line width (≤2 ppm) allowed for the determination of small changes in sample temperature. The curvature of the extrema of the calibration curve plausibly reflects small temperature errors at the limits of the probe design, but this was not investigated further.

Figure 4 shows ^{207}Pb MAS spectra of lead nitrate from various heating schemes. Spectra a–d show representative spectra with continuous hot gas heating. Figure 4a shows a single, narrow resonance at 298 K. At temperatures of 373–523 K (Figure 4b–d), the spectra show a decrease in intensity, as predicted by the Curie law, and a slight broadening of the resonance line reflecting small gradients near the upper design temperature limit of the spinning system. Figure 4e shows the ^{207}Pb spectrum of lead nitrate under continuous 12-W laser heating using the sample geometry in Figure 2. A temperature of ~373 K was estimated for the narrow component, and a temperature distribution of at least ±50 K was estimated for the broad component. The asymmetric component of the line shape suggested a very large gradient at the ends of the sample. Figure 4f shows the ^{207}Pb spectrum of lead nitrate under continuous 7-W rf heating. A temperature distribution of approximately ±8 K was estimated on the basis of a line width (fwhm) of 12 ppm.

The relationship between sample temperature and rf power setting in the inductive heating experiment is suggested in Figure 5. Static heating with 15 W produced a ^{207}Pb chemical shift slightly outside of the calibration region from the hot gas studies, and the 18-W power setting used for the dynamic in situ

(23) Bielecki, A.; Burum, D. P. Poster Presentation at the 36th Rocky Mountain Conference on Analytical Chemistry, Denver, CO, August 1994, Abstract 305.

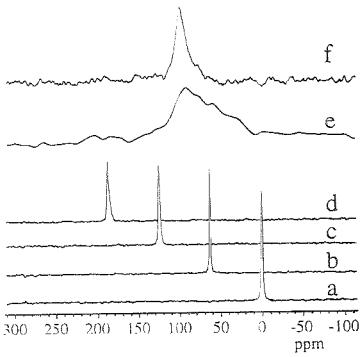

Figure 4. 41.6-MHz ^{207}Pb MAS spectra demonstrating the use of lead nitrate as a thermometer as well as an indicator of temperature gradients with various heating methods: (a) 298 K; (b) hot gas heating at 373 K; (c) hot gas heating at 448 K; (d) hot gas heating at 523 K; (e) laser heating at 12 W using the geometry in Figure 2; (f) inductive heating at 7.5 W using the geometry in Figure 1.

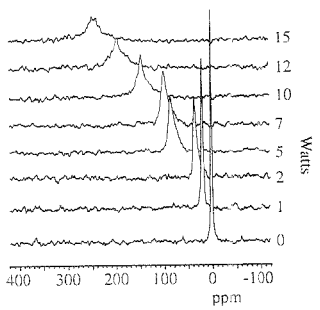

Figure 5. 41.6-MHz ^{207}Pb MAS spectra of lead nitrate in a platinum-plated zirconia rotor showing the chemical shift (and hence temperature) dependence on 199.7-MHz radio frequency heating power.

experiments was well outside the calibration range. This illustrates a practical advantage of inductive and laser heating compared to the standard hot gas approach; since gas heating affects much of the spinning system, while the other approaches limit the heating to the sample and possibly the coil, the standard method is more limited by materials constraints. We have obtained preliminary inductive heating results with power levels as high as 25 W, and melting point standards would suggest that we have achieved temperatures approaching 800 K.

The dynamics of inductive heating in temperature jumps from 298 K to higher temperatures are characterized in Figures 6 and 7. Figure 6 reports a ^{207}Pb thermometry experiment in which 3 W of inductive heating was turned on at zero time, and an equilibrium temperature of 373 K was reached after ~30 s. Signal averaging of the ^{207}Pb signal was not practical in a dynamic experiment; in order to obtain an adquate signal to noise ratio, the dynamic experiment was performed 64 times in an identical manner, and the single-shot FIDs were added appropriately to provide signal averaged spectra. Even so, 250 Hz of exponential broadening was used during data processing, so the line widths in Figure 6 overestimate the actual temperature distribution during dynamic heating.

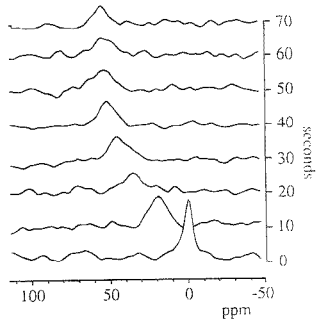

Figure 6. 41.6-MHz ^{207}Pb MAS spectra of lead nitrate acquired at 10-s intervals, beginning at 0 s, following the sudden application of a 3-W inductive heating pulse. The temperature was jumped from 298 K to a final temperature of ~373 K within 30 s. This experiment illustrates dynamic heating; see text for other details.

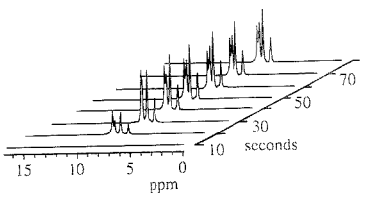

Figure 7. 199.6-MHz ^{1}H MAS spectra of isophthalic acid acquired at 10-s intervals, beginning at 10 s, during an 18-W inductive heating pulse. The entire sample volume was equilibrated at slightly greater than 616 K within 20–30 s, as indicated by completion of the melting transition. The sweep width was set so that only the narrow signals from the melt phase are evident due to undersampling of the very broad, solid phase.

The methanol-to-gasoline reaction catalyzed by zeolite HZSM-5 is performed in flow reactors at temperatures near 623 K and with contact times of seconds to minutes.[24] In order to better define dynamic heating experiments with temperature jumps to ~623 K, we made use of the melting transition of isophthalic acid, which has previously been used for temperature calibration,[8] and a representative result is shown in Figure 7. These ^{1}H spectra show that the power setting was just sufficient to melt the entire sample (mean temperature slightly greater than 616 K) after 30 s of equilibration with inductive heating at a power of 18 W, and the sample was at least 90% melted after only 20 s. In an analogous laser heating experiment using the geometry in Figure 2, isophthalic acid was partially melted after 3 s of irradiation at 40 W, but large temperature gradients were reflected by the observation that some of the sample was possibly boiling at the same time that the remainder was still melting. The conclusion from Figures 6 and 7 and other exhaustive thermometry experiments was that we were able to perform dynamic heating experiments in which inductive heating carried the bulk of the sample to very nearly 623 K in 20 s, and this temperature was fully equilibrated with modest gradients after 30 s. Based on linear extrapolation of the calibration curve and the spectra in Figure 5, a thermal distribution of ±25 K was estimated for this particular heating regiment, and that distribution was less than the difference between the inlet

(24) Chang, C. D. *Hydrocarbons From Methanol*; Marcel Dekker: New York, 1983; Chapter 6.

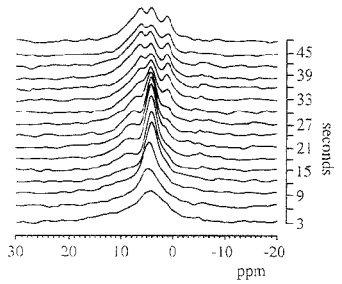

Figure 8. Single-shot 199.6-MHz ^1H MAS spectra of zeolite HZSM-5 with a 2.5 equiv (3.5 mmol/g) loading of methanol-^{13}C acquired at 3-s intervals during a 48-s, 18-W inductive heating pulse. A final mean temperature of 623 K was reached in 30–35 s; 200 Hz of exponential line broadening was applied.

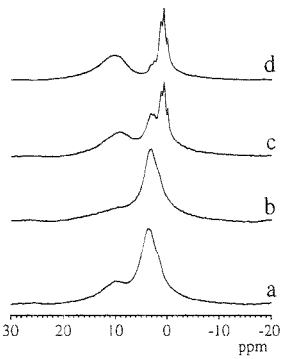

Figure 9. 199.6-MHz ^1H MAS spectra of identical samples of methanol-^{13}C on HZSM-5 acquired at 298 K (a) prior to heating and at 298 K after 18-W inductive heating pulses of (b) 32, (c) 48, and (d) 60 s. In each case a final, mean temperature of 623 K was reached in 30 s.

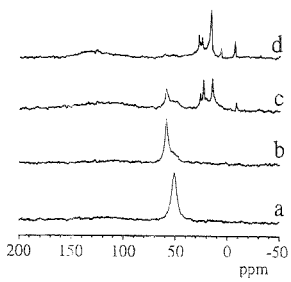

Figure 10. 50.2-MHz ^{13}C NMR spectra of identical samples of methanol-^{13}C on HZSM-5 acquired at 298 K (a) prior to heating and at 298 K after 18-W inductive heating pulses of (b) 32, (c) 48, and (d) 60 s. In each case a final, mean temperature of 623 K was reached in 30 s. The broad resonance seen in the 100–150 ppm range is background from the spinning module.

and outlet temperatures in a typical methanol-to-gasoline reactor. Furthermore, gas diffusion in a catalysis experiment might reduce temperature gradients to less than those measured for lead nitrate. Other experiments also showed that the temperature dropped appreciably in the first few seconds after discontinuing the inductive heating.

Dynamic in situ studies using inductive heating are illustrated for the case of the methanol-to-gasoline reaction catalyzed by the acidic zeolite HZSM-5. This choice was motivated by past experience with this reaction,[25,26] the low cost of methanol-^{13}C which facilitated experimentation, and the availability of an analogous study using laser heating, recently published by Freude and co-workers.[15] Several experiments were performed with total durations of between 30 and 60 s. Single-shot spectra were acquired every 3 s during the heating periods, and ^1H and ^{13}C spectra were signal averaged before the experiments and after quenching to 298 K. Figure 8 shows ^1H spectra obtained during dynamic heating to 623 K with a total experiment duration of 48 s. Signal-averaged ^1H and ^{13}C spectra collected at 298 K from identical samples subjected to various periods of inductive heating are presented in Figures 9 and 10, respectively. These results are in good agreement with previous MAS NMR studies using various approaches, including the laser experiment of Freude et al. The latter experiment involved jumps to a temperature estimated to be 523 K and a duration of 100 s. Thermometry experiments were not reported in that work, but the experimental geometry differed from that shown in Figure 2. The results in Figure 8 support the observation of Freude et al. that propane and ethane are produced before methane.[15] Briefly, the ^1H spectra in Figures 8 and 9 show that methanol adsorbed on Brønsted sites formed dimethyl ether and hydroxonium ions in exchange with additional water formed during hydrocarbon synthesis. For details of the ^1H chemical shift assignments, the reader is referred to refs 15 and 27–29. The ^{13}C spectra show that methanol (50 ppm, Figure 10a) formed dimethyl ether (60 ppm) and possibly a methoxy or some other adsorbed state at short heating times and light hydrocarbons including propane (15 ppm), ethane (5 ppm), and methane (−9 ppm) with heating times of 48–60 s.[3,25,26]

(25) Munson, E. J.; Kheir, A. A.; Lazo, N. D.; Haw, J. F. *J. Phys. Chem.* **1992**, *96*, 7740–6.
(26) Munson, E. J.; Kheir, A.; Haw, J. F. *J. Phys. Chem.* **1993**, *97*, 7321–7.
(27) Anderson, M. W.; Barrie, P. J.; Klinowski, J. *J. Phys. Chem.* **1991**, *95*, 235–9.
(28) Batamack, P.; Dorémieux-Morin, C.; Fraissard, J.; Freude, D. *J. Phys. Chem.* **1991**, *95*, 3790–6.
(29) Bosáček, V. *J. Phys. Chem.* **1993**, *97*, 10732–7.

CONCLUSIONS

Currently in our laboratory, laser heating produces faster temperature jumps to higher temperatures compared to inductive heating. This is because a 50-W laser is available, while the NMR probe works reliably only when the CW radio frequency power is less than 20 W and not all of the rf power is converted to heat. Comparison of the experimental geometries in Figures 1 and 2 suggests that larger samples will be heated more uniformly with inductive heating, and this is strongly supported by the thermometry experiments reported here. Even with power restrictions on the probe, inductive heating can be used to perform a dynamic in situ experiment with a temperature jump to 623 K in 30 s. This reaction time scale is 2 or 3 orders of magnitude shorter than that required most in situ or off-line heating methods in the literature. In the case of methanol-to-gasoline chemistry, the first-formed hydrocarbons (believed to be ethylene and/or other olefins) were not any more evident with a 48-s reaction time than they were in more conventional studies, although some details of

the secondary reactions of alkanes are visible in Figure 8 and in ref 15. The reaction time scale in Figure 8 is still 1−2 orders of magnitude longer than contact times used in flow reactors for some processes such as cracking on fluidized beds. Although reaction times of several tens of seconds may prove to be revealing even for cracking chemistry, the experimental challenge is clearly one of overcoming the limitations of laser or inductive heating so that dynamic in situ experiments can be performed in several seconds or less with reproducible and well-characterized thermal histories. In the case of laser heating, some of the strategies for this have been discussed elsewhere.[14] For inductive heating, a several-fold decrease in reaction time should be obtainable by a straightforward probe redesign to handle higher power levels.

ACKNOWLEDGMENT

Our studies of acidic zeolites and the development of the laser heater were supported by the U.S. Department of Energy (DE-FG03-93ER14354), and the spectrometer was constructed with a grant from the National Science Foundation (CHE9221406). We gratefully acknowledge Sandie Francis of IBM Almaden for advice on the preparation of platinum-coated rotors.

Received for review June 19, 1995. Accepted June 23, 1995.[⊗]

AC9506138

[⊗] Abstract published in *Advance ACS Abstracts*, August 1, 1995.

Anal. Chem. **1995**, *67*, 3349–3352

A Simple Theoretical Model for the Self-Enhancement of the Cathodic Voltammetric Waves of Weak Acids

Aleksander Jaworski and Zbigniew Stojek*

Department of Chemistry, University of Warsaw, ul. Pasteura 1, 02-093 Warsaw, Poland

Janet G. Osteryoung

Department of Chemistry, North Carolina State University, Raleigh, North Carolina 27695-8204

Weak acids dissociate negligibly, but their reduction wave heights, in the absence of supporting electrolyte, are higher by a factor of 2 compared to the excess electrolyte case. A simple theoretical model presented in this work supports the experimental findings. The model is based on solving the set of equations which include the transport equation (diffusion and migration), the Nernst–Planck equation, the electroneutrality principle, and the dissociation equilibrium of the acid under consideration. It was found that the concentration profiles of H^+ and A^- in the absence of supporting electrolyte are substantially different from those obtained for excess supporting electrolyte. Regarding the electroactive species, the gradient and the concentration of the hydrogen ion are apparently higher in the absence of supporting electrolyte and are responsible for the enhancement of the waves of weak acids by a factor of 2.

Voltammetric reduction of acids at Pt microelectrodes has gained some attention recently.[1-6] There are apparent analytical aspects behind this voltammetry, since the wave heights depend linearly, over a wide range, on the acid concentration.[1] These measurements have been found useful in probing the reaction site at a polyaniline film[3] and in polyelectrolyte solutions.[4-6] The linearity is obtained for any ratio of the concentrations of supporting electrolyte and analyte. The slopes of the calibration lines diminish with an increase in the supporting electrolyte concentration. For strong acids, the observed change agrees well with the existing theories.[7-11]

One might expect that neutral, slightly dissociated weak acids should behave like neutral molecules, and thus the heights of their voltammetric reduction waves should not depend strongly on the supporting electrolyte concentration. However, the experimental evidence is that the wave heights of acetic, ascorbic, and salicylic acids with no added electrolyte decrease exactly to half the initial value when a small amount of supporting electrolyte is added.[12] Whereas it is clear that the migration of hydrogen ion, which is the dominant counterion in the system, plays a major role in this phenomenon, the reported current ratio of 2 is not supported by a recent mathematical model.[13]

The aim of this work is to construct a simple mathematical model, amenable to numerical simulation, that describes the reduction of hydrogen ion in equilibrium with a weak acid–base pair. The work was guided by our previous observation that the ratio of the reduction currents of weak acids without and with supporting electrolyte is 2. We consider only the cases of no added electrolyte and of large excess of electrolyte.

DERIVATION

The following equations, in spherical coordinates, for transport (eq 1), current density (eq 2), and the potential gradient (eq 3) were used:

$$\frac{\partial C_k}{\partial t} = D\left[\frac{\partial^2 C_k}{\partial r^2} + \frac{2}{r}\frac{\partial C_k}{\partial r} + \frac{z_k F}{RT}\left(\frac{2C_k}{r}\frac{\partial \phi}{\partial r} + \frac{\partial C_k}{\partial r}\frac{\partial \phi}{\partial r} + C_k\frac{\partial^2 \phi}{\partial r^2}\right)\right] \quad (1)$$

$$j = \frac{i}{4\pi r^2} = -\frac{F^2}{RT}\frac{\partial \phi}{\partial r}\sum z_k^2 C_k D_k - F\sum z_k D_k \frac{\partial C_k}{\partial r} \quad (2)$$

$$\frac{\partial \phi}{\partial r} = \frac{-1}{\sum z_k^2 C_k D_k}\frac{RT}{F^2}\left(F\sum z_k D_k \frac{\partial C_k}{\partial r} + \frac{i}{4\pi r^2}\right) \quad (3)$$

Equations 2 and 3 are equivalent. The quantities C_k, D_k, and z_k are the local concentration, diffusion coefficient, and charge, respectively, of the kth species, and the other symbols have their usual meaning. We assume that the analytical concentration of the weak acid is $C^* = C_{HA} + C_{A^-} = C_{HA} + C_{H^+}$. The acid dissociates in the following way: $HA = H^+ + A^-$. The equilibrium is maintained everywhere, and the appropriate equilibrium con-

(1) Ciszkowska, M.; Stojek, Z.; Morris S. E.; Osteryoung, J. G. *Anal. Chem.* **1992**, *64*, 2372.
(2) Perdicakis, M.; Piatnicki, C.; Sadik, M.; Pasturaud, R.; Benzakour, B.; Bessiere, J. *Anal. Chim. Acta* **1993**, *273*, 81.
(3) Frank, M. H. T.; Denuault, G. *J. Electroanal. Chem.* **1994**, *379*, 399.
(4) Morris, S. E.; Osteryoung, J. G. In *Electrochemistry in Colloids and Dispersions*; MacKay, R. A., Texter, J., Eds.; VCH Publishers: New York, 1992; p 245.
(5) Morris, S. E.; Ciszkowska, M.; Osteryoung, J. G. *J. Phys. Chem.* **1993**, *96*, 10152.
(6) Ciszkowska, M.; Osteryoung, J. G. *J. Phys. Chem.* **1994**, *98*, 3194.
(7) Amatore, C.; Fosset, B.; Bartelt, J.; Deakin, M. R.; Wightman, R. M. *J. Electroanal. Chem.* **1988**, *256*, 255.
(8) Baker, D. R.; Verbrugge, M. W.; Newman, J. *J. Electroanal. Chem.* **1991**, *314*, 23.
(9) Cooper, J. B.; Bond, A. M.; Oldham, K. B. *J. Electroanal. Chem.* **1992**, *331*, 877.
(10) Oldham, K. B. *J. Electroanal. Chem.* **1992**, *337*, 91.
(11) Myland, J. C.; Oldham, K. B. *J. Electroanal. Chem.* **1993**, *347*, 49.
(12) Stojek, Z.; Ciszkowska, M.; Osteryoung, J. G. *Anal. Chem.* **1994**, *66*, 1507.
(13) Kharkats, Yu. I.; Sokirko, A. V. *J. Electroanal. Chem.* **1991**, *303*, 17.

0003-2700/95/0367-3349$9.00/0

stant is K_a. Since all three species are tied by the equilibrium, and, as we assume, the electroneutrality principle is obeyed ($C_{H^+} = C_{A^-}$), we introduce the apparent diffusion coefficient defined as $D = (1 - \alpha^*)D_{HA} + \alpha^* D_{H^+}$, where α^* is the fraction of the acid dissociated in the bulk. We also assume that the electrode reaction leads to the formation of H_2, which diffuses away from the electrode surface.

The assumption of electroneutrality is justified. As has been shown by Norton et al.,[14] the electroneutrality principle does not hold when the depletion layer is entirely included in the double layer. The depletion layer thickness can be estimated as $10r_e$ (r_e is the electrode radius), and the thickness of the double layer is $\sim 1.5\kappa^{-1}$, where κ^{-1} is the Debye–Huckel length: $\kappa^{-1} = (\epsilon\epsilon_0 kT/\sum n_i z_i^2 e_0^2)^{1/2}$, where n_i is the number of ions per volume unit and the summation covers all ions in the solution. For a 1:1 electrolyte in water, the approximate κ^{-1} values for concentrations 10^{-3}, 10^{-5}, and 10^{-7} M are 10 nm, 100 nm, and 1 μm, respectively. This thickness diminishes further when the electrode potential departs strongly from the potential of zero charge. For the most widely employed sizes of electrodes ($r_e > 1$ μm), the double layer thickness becomes insubstantial compared with the depletion layer thickness if the concentration of the electrolyte is not $<10^{-6}$ M. It is worth noting here that the latter ion concentration of 10^{-6} M is very often that of solutions without deliberately added supporting electrolyte.

The existence of a potential gradient might indicate that there is a separation of charges. However, the magnitude of this separation is so small that it does not have any significant influence on the concentration profiles. For example, under our conditions, the separation of charges corresponding to the potential gradients present is roughly 5 electrons per space increment.

The following expressions can be written for the dihydrogen, total hydrogen ion, and total anion fluxes, f, at the electrode surface, respectively:

$$f_{H_2} = 2D_{H_2}\left(\frac{\partial C_{H_2}}{\partial r}\right) = \frac{i}{4\pi r^2 F} \tag{4}$$

$$f_{H^+,HA} = D\left(\frac{\partial C_{HA}}{\partial r} + \frac{\partial C_{H^+}}{\partial r} + C_{H^+}\frac{F}{RT}\frac{\partial \phi}{\partial r}\right) = \frac{-i}{4\pi r^2 F} \tag{5}$$

$$f_{A^-,HA} = D\left(\frac{\partial C_{HA}}{\partial r} + \frac{\partial C_{A^-}}{\partial r} - C_{A^-}\frac{F}{RT}\frac{\partial \phi}{\partial r}\right) = 0 \tag{6}$$

Summing eqs 4–6 by sides and integrating the result over space gives an expression for the mass balance,

$$2D_{H_2}C_{H_2} + 2DC_{HA} + DC_{H^+} + DC_{A^-} = 2DC^* \tag{7}$$

The next assumption is that the applied potential is sufficiently negative to allow complete reduction of hydrogen ion and undissociated acid at the electrode surface. No ions other than H^+ and A^- were considered, since for a weak reducible acid, in the absence of supporting electrolyte, the concentrations of H^+ and A^- should be much larger than those of other cations and anions, respectively, and finally, the contribution of other ions to the current should be negligible. Note that in the supported case, the pH at the electrode surface becomes very high, but without added electrolyte, charge balance prevents this. The following concentrations at the electrode surface (°) and in the bulk solution (*) were used as the boundary conditions:

$$C^\circ_{HA} = 0;\quad C^\circ_{H^+} = 0;\quad C^\circ_{A^-} = 0;\quad C^\circ_{H_2} = (D/D_{H_2})C^*$$

$$C^*_{H_2} = 0;\quad C^*_{HA} = (1 - \alpha^*)C^*;\quad C^*_{H^+} = C^*_{A^-} = \alpha^* C^* \tag{8}$$

The surface concentration of H_2 can be calculated directly from eq 7 after noting that $C^\circ_{HA} = C^\circ_{H^+} = C^\circ_{A^-} = 0$. For solving the excess electrolyte problem, two more fluxes were defined:

$$f_{An} = D\left(\frac{\partial C_{An}}{\partial r} - C_{An}\frac{F}{RT}\frac{\partial \phi}{\partial r}\right) = 0 \tag{9}$$

$$f_{Ca} = D\left(\frac{\partial C_{Ca}}{\partial r} + C_{Ca}\frac{F}{RT}\frac{\partial \phi}{\partial r}\right) = 0 \tag{10}$$

where An and Ca denote the anion and the cation, respectively, of a 1:1 supporting electrolyte. The flux balance can be written now as

$$2D_{H_2}C_{H_2} + D(2C_{HA} + C_{H^+} + C_{A^-} + C_{An} + C_{Ca}) = 2D(1 + \varrho)C^* \tag{11}$$

where ϱ is the ratio of the concentrations of supporting electrolyte and the weak acid. The boundary conditions for the excess electrolyte case are given below

$$C^\circ_{HA} = 0;\quad C^\circ_{H^+} = 0;\quad C^\circ_{A^-} = C^*;\quad C^\circ_{H_2} = (D/D_{H_2})C^*;$$
$$C^\circ_{An} = \frac{2\varrho - 1}{2}C^*;\quad C^\circ_{Ca} = \frac{2\varrho + 1}{2}C^*$$

$$C^*_{H_2} = 0;\quad C^*_{HA} = (1 - \alpha^*)C^*;\quad C^*_{H^+} = C^*_{A^-} = \alpha^* C^*;$$
$$C^*_{An} = \varrho C^*;\quad C^*_{Ca} = \varrho C^* \tag{12}$$

The surface concentration of H_2 can be calculated using eq 11, after substituting $C^\circ_{HA} = C^\circ_{H^+} = 0$. The concentration profiles for the excess electrolyte case were calculated using the equations that contain the migration terms. These terms are of negligible influence when the concentration of supporting electrolyte is large, so they can but do not have to be eliminated. We have verified that both approaches give identical results.

EXPERIMENTAL SECTION

Chronoamperometry was applied with a Model 273 potentiostat (EG&G PARC) and controlled via software on a 486 microcomputer. A platinum wire counter electrode and a quasi Pt reference electrode, to eliminate a possible leak of electrolyte from a salt bridge, were used. Platinum working disk microelectrodes of 5.5 μm radius (Project Ltd., Warsaw, Poland) were initially polished to mirror finish with 1 μm alumina on a very wet pad (Buehler Ltd.). Subsequent renewals before measurements were accomplished by polishing briefly on 0.05 μm alumina on a wet pad. The electrode was rinsed of alumina with a direct stream of water from a wash bottle impinging on the electrode surface. Water was removed from the surface with a dry tissue. All reagents were of analytical reagent purity and were used as received.

(14) Norton, J. D.; White, H. S.; Feldberg, S. W. *J. Phys. Chem.* **1990**, *94*, 6772.

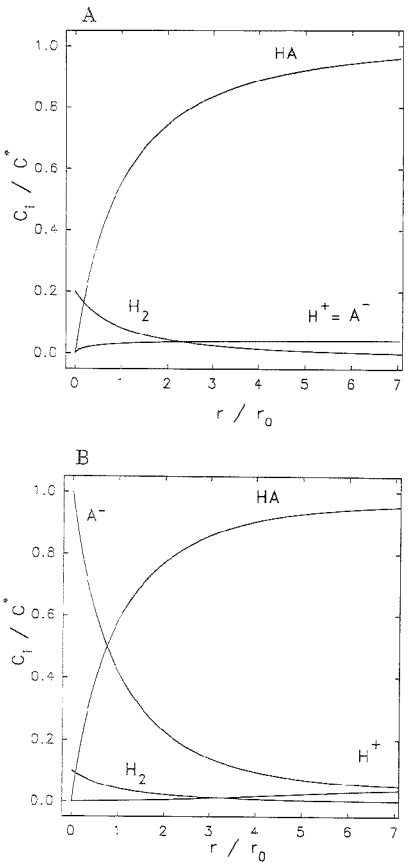

Figure 1. Calculated concentration profiles, at steady state, for chronoamperometric reduction of 10 mM acetic acid at a 5.5 μm spherical electrode. (A) without and (B) with excess supporting electrolyte.

Ultrapure water (Milli-Q, Millipore Corp.) was employed in all rinsings and preparations of solutions.

RESULTS OF CALCULATIONS

Simulations were performed by the finite difference method using unequal space intervals with $\Delta r_i = 1.01\Delta r_{i-1}$. Values used in the calculations were $D_{HA} = 9.75 \times 10^{-6}$ (for HOAc), $D_{H_2} = 5.85 \times 10^{-5}$, and $D_{H^+} = 9.3 \times 10^{-5}$, all in cm^2 s^{-1}, $r_0 = 5.5$ μm, and $K_{HOAc} = 1.8 \times 10^{-5}$ M.

Two independent ways of doing the calculations were employed. The first one involves the calculation of diffusion of H_2 only. Other concentrations then were evaluated using eq 7 (or eq 10 with excess electrolyte), the electroneutrality principle, and the K_a value.

The second way consisted of calculating independently, for each time interval, the changes in concentration of all the species involved using the transport equation, eq 1. This was followed by making corrections to the concentrations, so that the sum of their concentrations, electroneutrality, and the K_a value were preserved. The concentrations calculated independently fit well the flux conservation condition (eq 7).

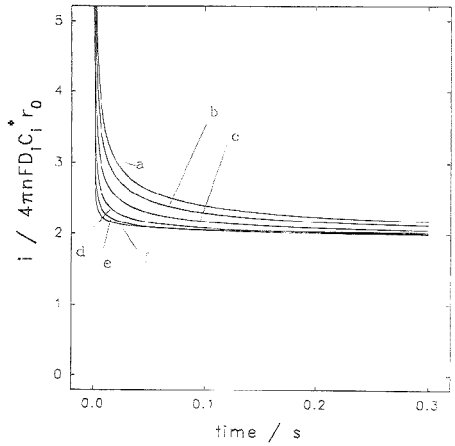

Figure 2. Calculated chronoamperometric reduction curves for 10 mM weak acid at a 5.5 μm spherical electroce. The dissociation equilibrium constants for the acid, normalized versus the K_a value for acetic acid (1.8×10^{-5}), are, from the top (a–f), 10^{-2}, 10^{-1}, 10^{0}, 10^{1}, 10^{2}, and 10^{8}.

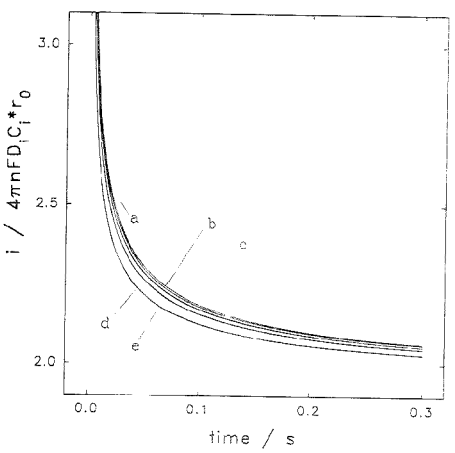

Figure 3. Calculated chronoamperograms for different diffusion coefficients of the undissociated acid, D_{HA}. From the top (a–e), the D/D_{HOAc} values are 0.2, 0.5, 1, 2, and 5. The normalized K_a value is 1. Other conditions are as in Figure 2.

The calculated currents were rendered dimensionless by dividing by the steady state current for excess electrolyte, which can be also expressed by the equation $i_{ss} = 4\pi rFDC^*$.

Each way of calculation gave the same results. A typical plot for the concentration profiles in the absence of supporting electrolyte, at steady state, is shown in Figure 1a. The profiles obtained for excess electrolyte are plotted in Figure 1b. The main difference between the plots is made by the A^- ion. Regarding the electroactive species, the gradient and the concentration of the hydrogen ion are apparently higher in the absence of supporting electrolyte and are responsible for the enhancement

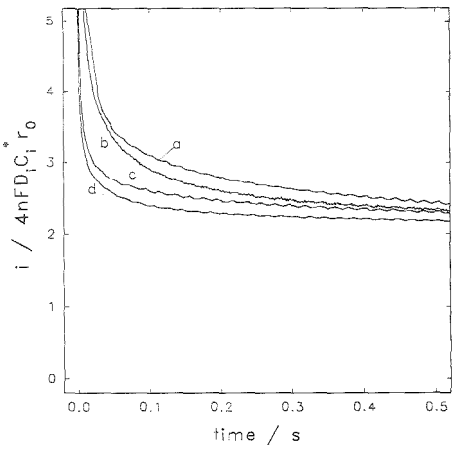

Figure 4. Experimental chronoamperograms for, from the top (a–d), CH_3COOH, $CH_2ClCOOH$, CF_3COOH, and HCl. Other conditions are as in Figure 2.

of the waves of weak acids by a factor of 2. Figure 2 presents a series of chronoamperograms, calculated for a wide range of K_a values. All calculated chronoamperometric currents decay, in time, to the steady-state value, which is just twice that expected with excess electrolyte. This agrees with our experimental results.[12] It is obvious, but we stressed it here, that the steady-state currents determined in a chronoamperometric experiment and in voltammetry are identical.

An interesting feature of Figure 2 is that the weaker acid coverges more slowly to the steady state. This is a result of lower values of apparent diffusion coefficients for weaker acids. A similar trend is seen when the diffusion coefficient of the weak acid decreases, which is portrayed in Figure 3. The trend of approaching the steady-state current shown in Figure 2 was confirmed experimentally. For four acids of decreasing strength (HCl, CF_3COOH, $CH_2ClCOOH$, and CH_3COOH), in the absence of supporting electrolyte, the sequence is as predicted theoretically (see Figure 4).

In fact, the ratio of the currents calculated for both cases is 2 for *all times*. For two reasons, we did not attempt to make a strict comparison between the theoretical and experimental chronoamperograms for short times. First, the microelectrodes are disks, not spheres, and thus the theoretical treatment is not quite accurate. Second, at short times, due to larger currents and relatively large ohmic drops, the potential at the electrode may not be sufficiently negative to yield the limiting current.

Coupling of homogeneous reactions with electron transfer reactions, for the case where migration is important, is a complicated problem, even without the introduction of kinetic considerations. The present work is somewhat ad hoc, in that the choice of boundary conditions is intuitive, and only the case without electrolyte, which is, strictly speaking, experimentally inaccessible, and the case with excess electrolyte are treated. A more general model is being developed to deal with these issues.

ACKNOWLEDGMENT

This work was supported in part by the National Science Foundation under Grants CHE9208987 and INT9112511, and by the University of Warsaw under Grant BST-475/5. The authors thank Malgorzata Ciszkowska and Peter Fedkiw for helpful discussions.

Received for review April 3, 1995. Accepted June 20, 1995.[⊗]

AC950322Z

[⊗] Abstract published in *Advance ACS Abstracts,* August 1, 1995.

Correspondence

Anal. Chem. 1995, *67*, 3353–3356

Molecular-Specific Chromatographic Detector Using Modified SERS Substrates

Keith T. Carron* and Brian J. Kennedy

Department of Chemistry, University of Wyoming, Laramie, Wyoming 82071-3838

Preliminary results for a gas chromatography detector based on surface enhanced Raman scattering (SERS) spectroscopy are described. The method described uses a SERS substrate that has been modified with a propanethiol coating that creates a hydrophobic interface to promote adsorption. The coating also prevents oxidation of the silver surface and stabilizes the SERS effect. The detector was tested with a separation of benzene, toluene, ethylbenzene, and *o,m,p*-xylenes using a capillary column. The results demonstrate that a SERS detector is able to spectrally separate the chromatographically unresolved and detect a mixture component, benzene, at the 40 ng mass detection level. The temperature dependence of the GC–SERS cell was examined, and it was shown how reversibility of the detector is related to temperature.

Separation science techniques, when coupled with a molecular-specific detector, are capable of providing detailed and often complete chemical analyses of complex mixtures. For most forms of chromatography this has been realized with mass spectroscopy (MS) and Fourier transform infrared spectroscopy (FT-IR) systems. Mass spectroscopy is the most popular method of detection for chromatography due to its sensitivity and selectivity. FT-IR also provides detailed molecular information through vibrational spectroscopy and has good sensitivity. The disadvantages of these techniques are their expense and complexity. In particular, the need to perform MS techniques in a vacuum and the problems associated with solvent interference in FT-IR chromatographies lead to complicated instrument designs.

We have shown that it is possible to qualitate and quantitate mixtures using surface-enhanced Raman scattering (SERS) spectroscopy with modified substrates.[1] The unique concept of our detection method is to fine tune the chemical potential of a SERS substrate by coating the silver or gold with a chemically bonded monolayer that matches the chemical properties of the analyte. We have demonstrated this capability with selective detection of metal ions,[1–3] pH,[4] and organics in aqueous solutions and with organics in the vapor phase.[5,6] Once the analyte has been adsorbed by the surface coating we are able to detect it with high sensitivity and selectivity using SERS.

The coatings are based on thiol chemistry and in many cases represent self-assembled monolayers. The thiols are known to strongly chemisorb to silver and gold surfaces to form monolayers that possess supramolecular properties.[7] These have been shown to drastically modify the surface energy of metals and with the addition of chemical functionalities can be tuned to provide a specific chemical property such as pH dependence, chelation with metals, or hydrophobicity.

It became apparent from our work with the detection of chlorinated ethylenes[6] and aromatics that we had developed a method of detection that mimics the interfacial processes that occur in chromatographic separations. In this paper, we will describe our first results from modified SERS substrates using gas chromatographic (GC) separation and SERS detection and identification. The mixture we have chosen for this example is benzene, toluene, ethylbenzene, and *o,m,p*-xylenes (BTEX). BTEX is of interest since it is a common environmental contaminant and can be difficult to resolve with rapid GC.[8] We will show thermodynamic relationships indicating that the results obtained with GC can be translated to other chromatographic techniques.

EXPERIMENTAL SECTION

The GC–SERS detection was made possible through recent developments in both SERS technology and fiber-optic coupling of Raman scattering. The SERS methodology for preparing substrates has been described elsewhere.[6] The coating used in this study was 1-propanethiol (99.9%, Aldrich). The SERS substrate was prepared from 0.1 mm thick silver foil (99.9%, Aldrich) etched in 30% nitric acid. The coating was applied by soaking the foil in a 1 mM ethanolic solution for several hours. Before use the foils were washed with ethanol and air dried.

Our basic Raman system has been described previously.[6] The addition of fiber optics is new and will be described here. Figure 1 shows a schematic for the system. The Kr^+ laser (Spectra

(1) Mullen, K. I.; Wang, D.; Hurley, G. L.; Carron, K. *Spectroscopy* **1992**, *7*, 24–32.
(2) Carron, K.; Mullen, K.; Lanouette, M.; Angersbach, H. *Appl. Spectrosc.* **1990**, *44*, 63–69.
(3) Crane, L. G.; Heyns, J. B. B.; Sears, L. M.; Wang, D.; Carron, K. *Anal. Chem.* **1995**, *67*, 485–490.
(4) Mullen, K.; Wang, D.; Crane, L.; Carron, K. *Anal. Chem.* **1992**, *64*, 930–936.
(5) Carron, K.; Pietersen, L.; Lewis, M. *Environ. Sci. Technol.* **1992**, *26*, 1950–1954.
(6) Mullen, K.; Carron, K. *Anal. Chem.* **1994**, *66*, 478–483.
(7) Whitesides, G.; Laibnis, P. *Langmuir* **1990**, *6*, 87–95.
(8) Xiang, Y.; Morgan, S.; Watt, B. *J. Chromatogr. Sci.* **1995**, *33*, 98–108.

0003-2700/95/0367-3353$9.00/0

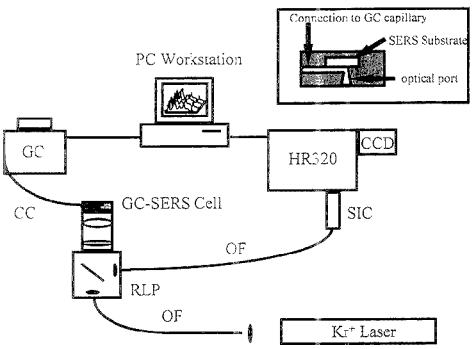

Figure 1. Schematic diagram for our GC–SERS fiber-optic coupled system. The components are described in the text.

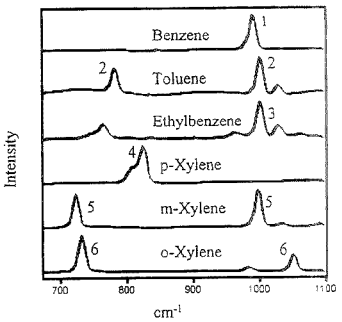

Figure 2. Raman spectra of the BTEX components in the spectral region used for the GC–SERS study. All spectra were obtained neat under the same conditions as the GC–SERS study.

Physics Model 2025S) was operated at 647 nm and was coupled into the optical fiber (OF1) with a Detection Limit Technology (DLT) laser-to-fiber coupler (LFC).[9] The laser power was adjusted to provide 40 mW of power at the sample. The laser excitation and Raman collection were coupled with a DLT remote luminescence probe (RLP).[9] The RLP was designed for use at 647 nm with a high-throughput dichroic beam splitter that acts as a highly reflective long-pass filter. Further filtering is provided with an additional long-pass filter at the output of the RLP. The laser excitation and Raman collection are made with an epiillumination design using a 50 mm, *f*/2 lens. The Raman excitation is coupled into an optical fiber (OF2) and is transferred to a spectroscopy input coupler (SIC) from DLT.[9]

The SIC *f*/# matches the fiber with the spectrograph and provides 2.36 fiber image magnification that optimizes spectral resolution and throughput. This produces optimal S/N from the CCD by minimizing the number of pixels binned in the vertical direction while optimizing the overall throughput. The Raman spectrum was dispersed with an HR320 (ISA) and detected with a Photometrics CCD 9000 system. The spectra were collected and stored with a PC workstation that also controls the interface with the gas chromatograph.

The gas chromatography was performed with a SRI 8610 B equipped with a thermal conductivity detector (TCD). The SERS detector was used both in tandem with the TCD and as a stand-alone detector when connected directly to the column. The column was a high-capacity, 1.0 μm thick methyl 50% phenyl silicone coated, 15 m, 530 μm i.d. capillary column (CC) from Quadrex Corp. The He carrier gas was set to flow at 8 mL/min and an isothermal column temperature of 75 °C chosen for this study. Total injection volumes were 3 μL. In this report we will present data for BTEX (Aldrich). Loading of the column was not observed for this injection volume.

The GC–SERS detection cell was fabricated out of aluminum. For this preliminary study, a simple cell strategy was used. Our design used to collect the data in this report had an input and exit port for capillary connections. For the data in this report we used the exit port for the effluent as an optical port (see Figure 1, inset). The optical port was large enough for us to use our epiillumination probe for excitation and collection of the SERS signal. The SERS substrate was placed in the effluent flow of the capillary column as shown in Figure 1. A temperature study was performed by cooling the cell prior to the chromatographic measurement or heating with heat tape. In all experiments the capillary line to the cell and extending from the column oven was heated to the oven temperature with heat tape.

RESULTS AND DISCUSSION

The SERS coating used in this report was 1-propanethiol. In previous reports, we have described a variety of coatings for SERS substrates. The role of the coating is twofold. It protects the silver from oxidation, and it creates a specific chemical environment at the interface to promote selective adsorption. Since silver or its oxides have very high surface energies, and therefore little affinity for hydrophobic molecules such as BTEX, a hydrophobic coating will lead to enhanced adsorption and therefore improved detection limits. Our choice of 1-propanethiol was empirically based on the decrease in SERS with increasing chain length and the increase in stability with increasing chain length. We have found that the interfacial enhancement drops off roughly as $n^{-1.28}$, where interfacial enhancement is the Raman enhancement of scattering from molecules adsorbed to the surface of the coating and n is the distance from the surface in carbon chain length units.[10]

Figure 2 shows the Raman spectra in the fingerprint region of the individual BTEX components used in this study. It can be seen that each one has characteristic vibrations that can be used to identify the adsorbate. We have found that for material physisorbed to coated SERS substrates the SERS spectra are equivalent to normal Raman spectra of the pure material, with the exception of small intensity variations. For the monosubstituted benzenes, the variation is due to the mass of the substituent and the characteristic vibrations of the substituent.[11] The disubstituted, isomeric xylenes have very different spectra due to the large variations in symmetry and ring substitution patterns.[11] The peaks that are labeled in this figure are also shown in Figure 3C to illustrate the spectral resolution of the components coming off of the column.

The SERS spectrum of 1-propanethiol, in the spectral region used in this study, contains two large Raman features that are C–C stretching vibrations at 1025 and 1084 cm^{-1}, a large Raman

(9) Schoen, C. *Laser Focus World* **1994**, *30*, 113–117.

(10) Dickey, M.; Carron, K., to be submitted to *Anal. Chem.*

(11) Schachtschneider, J.; Snyder, R. *Spectrochim. Acta* **1963**, *19*, 117–128.

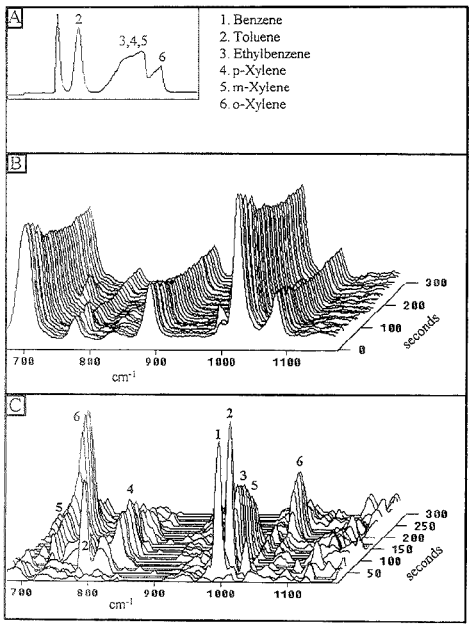

Figure 3. (A) chromatogram of BTEX obtained under the same conditions as our GC–SERS data using a thermal conductivity detector. (B) GC–SERS chromatogram of BTEX. The total acquisition time is 300 s. (C) GC–SERS chromatogram of BTEX with the coating blank subtracted. Peaks labeled correspond to BTEX peaks labeled in Figure 2.

band due to a C–S stretch of the trans configuration at 702 cm^{-1}, methyl rocking at 891 cm^{-1}, and a methylene rock at 777 cm^{-1}.[11,12] These bands can be seen in Figure 3B. They remain virtually constant in intensity throughout the separation and can be used as an internal reference for the quantitation of material adsorbed to the surface. Small variations were observed when a high coverage of benzene and toluene was present on the surface. We believe the intensity variation may be due to changes in the local index of refraction at the interface due to adsorption of material.

The chromatogram of BTEX is shown in Figure 3A. The column that we chose is not ideal for BTEX separations but illustrates the superior resolving power of a spectral technique for chromatographic detection. Benzene and toluene are chromatographically resolved while ethylbenzene, *p*-xylene, *m*-xylene, and *o*-xylene are convolved or poorly resolved.

The raw GC–SERS chromatogram is shown in Figure 3B. The experiments were repeated five times with equivalent results each time. The chromatogram is dominated by Raman features associated with the coating though one can see features that correspond to adsorbates. The effluent peaks can be seen more clearly if a spectrum of the coating is subtracted, as is shown in Figure 3C. This figure demonstrates that the equivolume (0.5 μL each) mixture of BTEX can be resolved and identified with GC–SERS. The thermodynamic relationship that best describes the surface detection process is

$$-\log P^* = \log k + ({}^i\mu_i^\circ - {}^i\mu_0)/2.3RT \qquad (1)$$

where P^* is the vapor pressure of the effluent, k is the adsorption coefficient, ${}^i\mu_i^\circ$ is the chemical potential of the adsorbate at 0.5 monolayers, ${}^i\mu_0$ is the chemical potential of the effluent in a saturated vapor, R is the gas constant, and T is the temperature in degrees kelvin. This can be derived in the same fashion as our linear free energy relationship for adsorption from solution.[6] It contains two pertinent parameters, vapor pressure and adsorption coefficient. The adsorption coefficient is inversely related to vapor pressure and in chromatography retention time is directly related to k. In other words, the lower the vapor pressure the longer the retention time. This leads to the rule of thumb that lower boiling point materials (higher vapor pressures) will elute from a column first. The intercept in eq 1 takes into account differential adsorption of material due to surface chemical potentials created by different column coating polarities. It is the intercept that allows one to predict the column coatings required for separation of different materials.

This common relationship for chromatography described above leads to an interesting result for a surface detection method like GC–SERS. The amount of material detected is ideally given by

$$\theta = kp/(1 + kp) \qquad (2)$$

where θ is the fractional coverage and p is partial pressure of the adsorbate. In chromatography, since p decreases with retention time due to band broadening, volummetric detectors have lower detectabilities for strongly retained material. The GC–SERS detector is interfacial and obeys the relationship in eq 1. Therefore, if the coating is chemically equivalent to or similar to that of

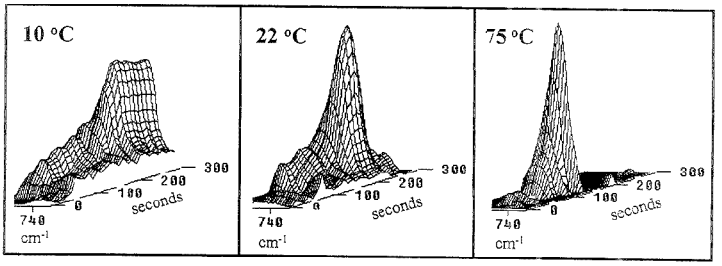

Figure 4. GC–SERS chromatogram of the 730–750 cm^{-1} region of the spectrum. This figure illustrates the temperature dependence for the detection of *o*-xylene.

(12) Bryant, M.; Pemberton, J. *J. Am. Chem. Soc.* **1991**, *113*, 3629–3637.

the column material, the detectability will stay constant throughout a separation. This is seen in Figure 3C, where the intensity of the *o*-xylene is not diminished relative to the benzene peak in comparison with the chromatogram obtained with a TCD detector shown in Figure 3A. This will make GC–SERS detection much more sensitive than current methods of detection for compounds that are highly retained.

The GC–SERS chromatogram shown in Figure 3C was formed at 22 °C. Another potentially significant advantage of GC–SERS is the ability to temperature program the detector. Programming the detector temperature from low to high during a separation could be used to produce a high coverage of material without sacrificing reversibility. The effect of temperature on the detection of *o*-xylene is shown in Figure 4. It can seen that at 10 °C the *o*-xylene is retained on the detector, at 22 °C it is showing reversibility, and at 75 °C (the column temperature) the *o*-xylene is rapidly removed from the detector and the GC–SERS chromatographic bandwidth is determined by the band broadening within the column.

A rough detection limit for benzene was determined from the 10 s integration period surrounding the benzene GC–SERS band and the point at which the signal to noise ratio is 3. We found a signal of 1185 analog-to-digital units (ADU) for the benzene peak and a noise level of 0.05 ADU, after smoothing, as determined by the standard deviation of 10 points along the background. Since our injection volume of benzene was approximately 0.5 μL, this gives a detection limit of about 50 ng.

CONCLUSION

We have demonstrated that SERS can be coupled with a chromatographic separation to provide a sensitive and selective method of molecular detection. Since the adsorption mechanism is a thermodynamically driven process, the results from GC in this report will be generally applicable to other separation science methods. For example, in GC the relevant parameter is temperature; for HPLC this would be replaced by solvent polarity, and for supercritical fluid techniques this would be replaced by fluid density. Since the surface coverage determines the detection limit and this is related to the concentration (not total mass) through the isotherm eq 2, SERS methods should have equal sensitivity for microtechniques as well as preparation-scale separations. In particular, CE–SERS will become a very important separation science method given that capillary electrophoresis uses very low masses in the separation, but high concentration due to the small volumes used. SERS methods would also be particularly advantageous for separation methods that use aqueous mobile phases since these interfer strongly with FT-IR and MS detectors.

ACKNOWLEDGMENT

The authors acknowledge the support of the NSF-EPSCoR ADP Grant EHR-9108774 for partial support of this project. We also acknowledge the support of Detection Limit Technology, LC Laramie, WY, for use of their RLP and SIC fiber-optic accessories. Finally, we acknowledge the support of the University of Wyoming for funding of patent applications.

Received for review May 22, 1995. Accepted July 18, 1995.[⊗]

AC9504880

[⊗] Abstract published in *Advance ACS Abstracts*, August 15, 1995.

Technical Notes

Anal. Chem. 1995, *67*, 3357–3362

In-Vial Derivatization and Empore Disk Elution for the Quantitative Determination of the Carboxylic Acid Metabolites of Dacthal in Groundwater

Jennifer A. Field* and Keith Monohan

Department of Agricultural Chemistry, Oregon State University, Corvallis, Oregon 97331

The monocarboxylic and dicarboxylic acid metabolites of the herbicide Dacthal were quantitatively determined in groundwater samples by concentrating the analytes onto 13 mm diameter strong anion exchange (SAX) Empore disks. The carboxylic acid metabolites were then simultaneously eluted and derivatized to their ethyl esters by placing the 13 mm SAX disk in a 2 mL autosampler vial together with 140 μL of ethyl iodide and 1 mL of acetonitrile and heating for 1 h at 100 °C. A recovery of 87.7 ± 1.0 (1.1% relative standard deviation, RSD) and 91.7 ± 0.9 (1.0% RSD) was obtained for the monocarboxylic and dicarboxylic acid metabolites from 100 mL samples of blank groundwater. Using a 100 mL sample, the detection and quantitation limits of the method are 0.02 and 0.06 μg/L, respectively. The concentrations of the monocarboxylic acid metabolite ranged from less than the detection limit (0.02 μg/L) to 1.04 μg/L in a survey of groundwater wells from eastern Oregon while the concentration of the dicarboxylic acid metabolite ranged from 0.60 to 180.70 μg/L.

Solid phase extraction is the subject of intense method development because it has the potential to replace many conventional liquid–liquid extraction methods. Compared to the cartridge format, solid phase extraction Empore disks reduce the time and cost of sample extraction because of higher sample flow rates, improved mass transfer, and complete elimination of bed channeling.[1] However, only recently has the physical flexibility of disks been exploited for additional savings in the time, cost, and number of steps associated with analyte elution from the disk.

Unlike solid phase extraction cartridges that contain loose resin, disks are pliable and can be moved from their supports, folded, and even cut into pieces. Krueger and Field[2] reported an "in-vial" elution procedure whereby small C18 disks are placed directly into a 2 mL autosampler vial where linear alkylbenzenesulfonate surfactants were eluted as their ion pairs, which were then derivatized in a high-temperature GC injection port reaction. Wu et al.[3] reported the simultaneous elution and silylation of the drug 11-nor-9-carboxy-Δ^9-tetrahydrocannabinol from a rigid glass fiber disk coated with C18-bonded phase silica by placing the disk directly in a small vial with the silylation reagent. Supercritical fluid extraction has been explored as an alternative, albeit more expensive, method for eluting solid phase extraction disks. Alzaga and Bayona[4] derivatized and eluted tributyltin compounds as their ethyl derivatives from C18 disks by supercritical fluid extraction. Hawthorne et al.[5] recovered phenols from C18 disks with the addition of an ion-pairing reagent under supercritical fluid conditions.

Strong anion exchange (SAX) solid phase extraction membranes (disks) have been used to overcome the problems of breakthrough and poor recovery often observed for water-soluble analytes on hydrophobic phases such as C8 or C18 bonded-phase silica and styrene–divinylbenzene (SDB).[6] Few reports document alternatives for directly coupling of SAX disk or cartridge elution with analyte derivatization. Tang and Ho[7] first extracted phenols onto SAX disks and then simultaneously acetylated and eluted phenols as their acetate derivatives using supercritical carbon dioxide. Chatfield et al.[8] recently demonstrated that SAX extraction media acts as a catalyst in the reaction between acids, such as 2,4-dichlorophenoxyacetic acid, and the alkylation reagent methyl iodide under liquid solvent and supercritical carbon dioxide conditions.

The herbicide Dacthal (dimethyl 2,3,5,6-tetrachloroterephthalate) is used in the United States at 1×10^6 kg/year to control annual grasses and broadleaf weeds.[9] In the Malheur River Basin of eastern Oregon, Dacthal is used for the production of onions. In the soil environment, Dacthal is hydrolyzed (Figure 1) to the corresponding monocarboxylic acid metabolite (methyl 2,3,5,6-tetrachloroterephthalic acid) and dicarboxylic acid metabolite

(1) Markell, C.; Hagen, D. F.; Bunnelle, V. A. *LC-GC* **1991**, *9*, 332.
(2) Krueger, C. J.; Field, J. A. *Anal. Chem.*, in press.
(3) Wu, A. H. B.; Liu, N.; Cho, Y. J.; Johnson, K. G.; Wong, S. S. *J. Anal. Toxicol.* **1993**, *17*, 215.
(4) Alzaga, R.; Bayona, J. M. *J. Chromatogr.* **1993**, *655*, 51.
(5) Hawthorne, S. B.; Miller, D. J.; Nivens, D. E.; White, D. C. *Anal. Chem.* **1992**, *64*, 405.
(6) Monohan, K.; Tinsley, I. J.; Shepherd, S. F.; Field, J. A. *J. Agric. Food Chem.*, in press.
(7) Tang, P. H.; Ho, J. S. *J. High Resolu. Chromatogr.* **1994**, *17*, 509.
(8) Chatfield, S. N.; Croll, M. Y.; Dange, T.; Murby, E. J.; Yu, G. Y. F.; Wells, R. J. *Anal. Chem.* **1995**, *67*, 945.
(9) Gianessi, L. P.; Puffer, C. *Herbicide Use in the United States National Summary Report*, Quality of the Environment Division, Resources for the Future, Washington, DC, 1991.

0003-2700/95/0367-3357$9.00/0

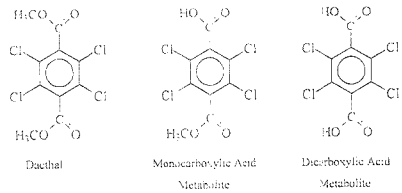

Figure 1. Dacthal and its monocarboxylic and dicarboxylic acid metabolites.

(2,3,5,6-tetrachloroterephthalic acid).[9] Estimates of the half-life of Dacthal in soil range from 11 to 295 days.[1,12] In contrast, Wettasinghe and Tinsley[13] found no degradation of the dicarboxylic metabolite of Dacthal after 300 days in batch soil experiments. The water solubility of the dicarboxylic acid metabolite (5780 mg/L) is significantly higher than that of Dacthal (0.5 mg/L);[14] consequently, the groundwater in the Malheur River Basin of eastern Oregon is contaminated with the dicarboxylic acid metabolite of Dacthal. The dicarboxylic metabolite of Dacthal was the most frequently detected pesticide residue in a recent national survey of groundwaters.[14]

Monohan et al.[6] developed a method using 47 mm SAX Empore disks for the extraction of Dacthal and its acid metabolites from groundwater. The SAX Empore disk method reduced the amount of solvent required for analysis compared to liquid–liquid extraction and the concentrations of Dacthal metabolites agreed well with those determined by liquid–liquid extraction. However, the conventional disk elution technique used by Monohan et al.,[6] which consisted of drawing the elution solvent dropwise through the disk, required excessive handling for the elution of acid metabolites and a separate step for derivatization. Similarly, Hodgeson et al.[15] found the elution of acid herbicides from strong anion exchange media cumbersome to the point that they abanadoned ion exchange for reverse phase (C18) disks.

In this paper, we describe an in-vial elution method that combines SAX disk elution with acid metabolite derivatization. The in-vial approach consists of placing the SAX disk directly in a 2 mL GC autosampler vial where the metabolites are simultaneously eluted from the SAX disk and derivatized to their alkyl esters. The use of the SAX phase as a catalyst in the alkylation reaction is adapted from the approach described in Chatfield et al.[8] Because Monohan et al.[6] detected no parent compound Dacthal above the limit of detection (0.05 μg/L) in eight samples collected from domestic groundwater wells in the Malheur region, this paper will focus on the use of the SAX extraction and in-vial derivatization and elution method for the quantitative determination of the monocarboxylic and dicarboxylic acid metabolites of Dacthal in groundwater samples collected from eastern Oregon.

EXPERIMENTAL SECTION

Samples. The groundwater samples used in this study were collected by the Soil Conservation Service, Ontario, OR, from domestic wells screened at 6–24 m below land surface from a shallow, unconfined aquifer in the Malheur River Basin in eastern Oregon. All samples were collected unfiltered from the tap nearest the well in baked glass bottles with aluminum-lined lids. The lines were flushed until the temperature stabilized at 12–14 °C, which is the average temperature of the aquifer in this region. The flushing time was typically 10 min since the wells are in constant use for domestic purposes. Unfortunately, no detailed information is available on the materials used for construction of the domestic wells sampled for this study. The groundwater samples were stored at 4 °C for a maximum of 2 weeks. A single groundwater sample that was shown to contain neither Dacthal nor its metabolites was used for matrix spike and recovery experiments. A composite groundwater sample was created to generate sufficient volume for replicate analyses for the exclusive purpose of determining the precision of the method. The composite sample was the only sample analyzed more than 2 weeks after collection; the sample was created by combining several groundwater samples analyzed by Monohan et al.[6] that had been refrigerated for 1 year.

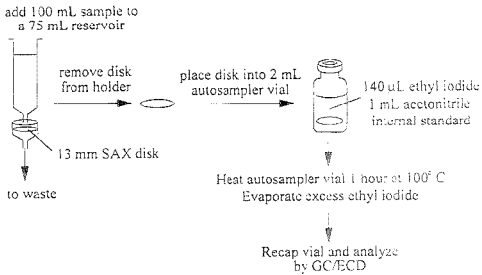

Figure 2. Procedure for in-vial Empore disk elution and Dacthal metabolite esterification.

Reagents. A standard (95% purity) of Dacthal (dimethyl 2,3,5,6-tetrachloroterephthalate) was obtained from Chem Service (West Chester, PA). A standard (100% purity) of 2,3,5,6-tetrachloroterephthalic acid, the dicarboxylic acid metabolite of Dacthal, was obtained from Ricera, Inc. (Painesville, OH). A standard (99.7% purity) of the monocarboxylic acid metabolite was obtained from the USEPA (Research Triangle Park, NC). The standards of Dacthal and its metabolites were prepared in methanol. Methyl iodide and ethyl iodide were obtained neat from Aldrich Chemical Co. (Milwaukee, WI). The dipropyl ester of the dicarboxylic acid metabolite of Dacthal was used as an internal standard in this study and was prepared using diazopropane. The acetonitrile, acetone, and methanol solvents used in this study were Burdick and Jackson GC grade (Baxter, Muskegon, MI).

Solid Phase Extraction. Small 13 mm diameter disks were cut from commercially available 47 mm diameter SAX disks (Varian, Sugarland, TX) using a cork-boring tool. The 13 mm disks were placed in 13 mm screw-together polypropylene filter assemblies (Micro Filtration Systems, Dublin, CA) and attached to a vacuum manifold (Supelco, Bellefonte, PA). A 75 mL polypropylene reservoir was attached to the disk–filter assembly (Figure 2).

The 13 mm SAX disks were preconditioned with 2 mL of acetone, allowed to soak for 30 s, and then dried thoroughly by vacuum. The disks were then prewet with 2 mL of methanol and

(10) Gershon, H.; McClure, G. W. *Contrib. Boyce Thompson Inst.* **1966**, *23*, 291–294.
(11) Ross, L. J.; Nicosia, S.; McChesney, M. M.; Heiner, K. L.; Gonzalez, D. A.; Seiber, J. N. *J. Environ. Qual.* **1990**, *19*, 715–722.
(12) Miller, J. H.; Keeley, P. E.; Thullen, R. J.; Carter, C. H. *Weed Sci.* **1978**, *26*, 20–27.
(13) Wettasinghe, A.; Tinsley, I. J. *Bull. Environ. Contam. Toxicol.* **1993**, *50*, 226–231.
(14) USEPA. *National Pesticide Survey*. Draft, 1990, October 31, pp 1–8.
(15) Hodgeson, J.; Collins, J.; Bashe, W. *J. Chromctogr.* **1994**, *659*, 395.

allowed to soak for 30 s. *Note*: The disk should not be allowed to go dry once the methanol is added to the disk. Finally, two 5 mL rinses of deionized water were added to the reservoir and drawn through the disk as the final preconditioning step. At this point, a 100 mL sample was added to the reservoir and extracted under full vacuum (25 mmHg). Once the sample had passed through the disk, the sample bottle was rinsed with 3 × 5 mL of water and added to the reservoir. The reservoir was rinsed with 2 × 3 mL of deionized water. Once all water had passed through the disk, the reservoir was removed. To initiate the process of drying the disk, 10 mL of air was pushed through the disk by attaching a small hand-held syringe to the top of the polypropylene disk holder, after which the disk was dried under full vacuum for 5 min.

To perform in-vial disk elution and derivatization, the dried disk was placed in a 2 mL autosampler vial with either 100 μL of methyl iodide or 140 μL of ethyl iodide together with 1 mL of acetonitrile and the dipropyl ester internal standard. The autosampler vial was then capped and heated for 1 h at 80 or 100 °C for methyl iodide and ethyl iodide, respectively. Even though 100 °C is above the boiling point of acetonitrile, no vials exploded; however, the vial cap septa split at temperatures of 120 °C and greater. Once the vial was allowed to cool, the cap was removed and the vial placed under a stream of nitrogen to remove excess methyl or ethyl iodide by evaporation to approximately 100 μL. Toluene was added back to approximately 1 mL, and the autosampler vial was then recapped and placed on the autosampler for analysis. For detectors other than an electron capture detector, the evaporation step can be eliminated.

Alkylation Reagent Evaluation. The optimal conditions for methylation using methyl iodide and ethylation using ethyl iodide were investigated by spiking 100 mL samples of deionized water with the dicarboxylic acid metabolite standard to give a concentration of 19 μg/L and extracting the sample with a 13 mm SAX disk. The effect of temperature on derivatization and elution was investigated by varying the temperature from 40 to 120 °C using an initial reaction time of 1 h. Subsequently, the time required for reaction was evaluated by varying the reaction time from 5 to 60 min using a temperature of 80 °C with methyl iodide and 100 °C with ethyl iodide. As the last step in optimization, the volume of methyl iodide was varied from 20 to 150 μL while the temperature was held at 80 °C and the reaction time at 1 h. In a similar manner, the volume of ethyl iodide was varied from 50 to 200 μL with a constant temperature of 100 °C and a 1 h reaction time.

Spike and Recovery. Spike and recovery experiments were initially performed with deionized water. Standards were spiked into four replicate 100 mL samples of deionized water to give concentrations of 15 μg/L for the monocarboxylic acid metabolite, 19 μg/L for the dicarboxylic acid metabolite, and 25 μg/L for Dacthal. The samples were extracted with 13 mm SAX disks, and the in-vial derivatization and elution was performed using ethyl iodide as the alkylation reagent.

Spike and recovery experiments then were performed with 100 mL blank groundwater samples. Two sets of experiments consisting of five replicate extractions each were performed by spiking the monocarboxylic and dicarboxylic acid metabolite standards into 100 mL of blank groundwater to give concentrations of 15 and 19 μg/L, respectively. In the first set of replicate extractions, a 5 mL methanol postextraction rinse was applied to the SAX disk prior to in-vial derivatization and elution. To check for metabolite elution, the methanol was collected and evaporated to near dryness. Next, the residue was dissolved in 2 mL of diethyl ether, 0.05 mL of sulfuric acid in methanol (10% v/v) was added, and the resultant mixture was derivatized with 1−2 mL of diazomethane. In this case, diazomethane was used as the derivatization reagent because the reaction is the conventional method for Dacthal metabolite derivatization and served as an independent check for the presence of Dacthal metabolites. In the second set of experiments, no methanol rinse was employed prior to in-vial derivatization and elution. In both cases, in-vial derivatization and elution was performed using ethyl iodide as the alkylation reagent.

Five replicate 100 mL samples of the composite groundwater sample were analyzed in order to determine the precision of the SAX extraction and in-vial derivatization and elution method using ethyl iodide. To determine the method detection and quantitation limits, a series of lower concentration spike and recovery experiments were performed. Single 100 mL samples of blank groundwater were spiked to give concentrations of 0.4, 2.0, and 6.0 ng/L for the dicarboxylic acid metabolite. In this set of experiments, methyl iodide was used as the alkylation reagent.

Chromatographic Analysis. All extracts were analyzed using a Hewlett Packard Model 5890 Series II gas chromatography equipped with an HP-5 column (30 m × 0.25 mm × 0.25 μm film thickness; Hewlett Packard, Wilmington, DE). The initial oven temperature was held 1 min at 130 °C and then increased at 15 °C/min to 200 °C, followed by a 4 °C/min ramp to 250 °C that was followed by a final ramp of 30 °C/min to a final temperature of 300 °C. An injection volume of 1 μL was used under splitless conditions with an injector temperature of 280 °C. The ^{63}Ni electron capture detector was operated at a temperature of 300 °C.

Quantitation. Because authentic standards of the monocarboxylic and dicarboxylic acid metabolites were not available as their ethyl esters, experiments were performed to determine whether the ethyl esters gave instrumental responses equivalent to that of their methyl esters and to Dacthal. Single 100 mL samples of deionized water were spiked with the mono- and dicarboxylic acid metabolite standards and processed through the in-vial elution method using ethyl iodide and methyl iodide as the alkylation reagents. Dacthal was used to quantitate both the methyl and ethyl ester forms of both metabolites because the methyl and ethyl esters of the monocarboxylic and dicarboxylic acid metabolites were found to give response factors equivalent to that of Dacthal. Therefore, the quantitation curves used for this study were constructed from the Dacthal standard and the dipropyl ester internal standard. Two five-point calibration curves were constructed from the Dacthal standard and internal standard to maintain optimum curve linearity and to quantitate the range of dicarboxylic acid metabolite concentrations in groundwater samples.

The concentrations reported in this study are reported as the monocarboxylic or the dicarboxylic acid metabolite and not as Dacthal. Because the formula weights of the monocarboxylic and dicarboxylic acid metabolites differ from that of Dacthal, correction factors of 0.95 (molecular weight of the monocarboxylic acid metabolite divided by that of Dacthal) and 0.91 (molecular weight of the dicarboxylic acid metabolite divided by that of Dacthal) were applied to the concentrations of the monocarboxylic and

dicarboxylic acid metabolites, respectively, that were obtained from the quantitation curves constructed from Dacthal.

RESULTS AND DISCUSSION

Solid Phase Extraction. The initial experiments in this study were aimed at reducing the volume of solvent (16 mL) and number of steps required for SAX disk elution as described by Monohan et al.[6] In order to reduce the amount of solvent required for elution, the SAX disk diameter was decreased from 47 to 13 mm. By reducing the size of the disk, the disk could be placed directly into the 2 mL autosampler vial together with the alkylation reagents, either methyl iodide or ethyl iodide, and the reaction solvent (acetonitrile).

With a reduction in SAX disk size from 47 to 13 mm, it was first necessary to determine whether the monocarboxylic and dicarboxylic acid metabolites could be quantitatively recovered from 100 mL samples. The monocarboxylic and dicarboxylic acid metabolites were both efficiently recovered at >90% from 100 mL samples of deionized water by a single 13 mm diameter SAX disk. The absence of breakthrough was confirmed by passing water that had passed through the first 13 mm SAX disk through a second SAX disk and examining the amount of analyte trapped by the second disk. Therefore, a single 13 mm SAX disk quantitatively isolates both the monocarboxylic and dicarboxylic acid metabolites from 100 mL water samples.

Alkylation Reagent Evaluation. Methyl iodide was initially selected for this work since Chatfield et al.[5] demonstrated efficient alkylation of dichlorophenoxyacetic acid from a small column of packed SAX resin. However, because Dacthal is the dimethyl ester of tetrachloroterephthalic acid, methylation of its monocarboxylic and dicarboxylic acid metabolites would lead to products that are indistinguishable from Dacthal. This outcome might be viewed favorably by analysts if conversion of all residues to a single product is desirable. However, for this study, the objective was to differentiate between the monocarboxylic and dicarboxylic acid metabolite forms in groundwater from eastern Oregon.

We investigated the optimal conditions for the alkylation of the dicarboxylic acid metabolite using both methyl iodide and ethyl iodide. It is important to note that, in the absence of a SAX disk, the reaction rate is negligible, indicating that the SAX disk acts as a catalyst in the reaction. Temperatures of 80 and 100 °C, respectively, were selected as optimal for use with 100 μL of methyl iodide and 140 μL ethyl iodide, respectively, for a 1 h reaction time (Figure 3a). Next, with an optimal temperature of 80 and 100 °C, the reaction time was varied from 5 to 60 min using 100 μL of methyl iodide and 140 μL ethyl iodide. After a 30 min reaction time, both methyl iodide and ethyl iodide yielded recoveries of >90% (Figure 3b). However, 1 h was used for subsequent experiments since coextracted organic matter or the presence of particulate matter may increase the time required for complete reaction. Finally, the optimal amount of each reagent was determined as the minimum volume that gave maximum recovery of the dicarboxylic acid metabolite. For methyl iodide at a reaction temperature of 80 °C and 1 h reaction time, 100 μL gave >96% recovery of the dicarboxylic acid metabolite (Figure 3c). A maximum recovery of 91% was obtained for the dicarboxylic acid metabolite using 140 μL of ethyl iodide with a 1 h reaction time at 100 °C (Figure 3c).

In order to determine whether the methyl and ethyl esters of the monocarboxylic and dicarboxylic acid metabolites gave similar recoveries and responses with electron capture detection, deionized water samples containing a range of monocarboxylic and dicarboxylic acid metabolite concentrations were extracted with a 13 mm SAX disk and derivatized with methyl iodide and ethyl iodide, using the optimal conditions determined above. Four samples containing from 3.8 to 38 μg/L of the dicarboxylic acid metabolite gave 98–105 and 93–97% of the expected response using methyl iodide and ethyl iodide, respectively, as the alkylation reagent (Table 1). The monocarboxylic acid metabolite gave 92–95% of the expected response when eluted and derivatized from the SAX disk with ethyl iodide as the alkylation reagent (Table 1). Because the two alkylating reagents gave similar high recoveries of the dicarboxylic acid metabolite, ethyl iodide was used for spike and recovery experiments with blank groundwater and for a survey of groundwater samples from Malheur county so that the two metabolites could be distinguished from one another.

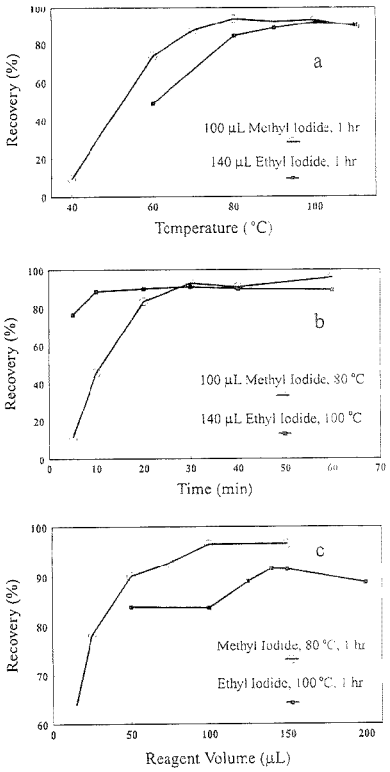

Figure 3. Effect of temperature, time, and reagent volume on the recovery of the dimethyl and diethyl esters of the dicarboxylic acid metabolite of Dacthal from a 13 mm strong anion exchange Empore disk.

Accuracy and Precision. The average recoveries of the monocarboxylic acid metabolite, dicarboxylic acid metabolite, and Dacthal were 88.6 ± 0.8 (1.0% RSD), 94.5 ± 1.3 (1.3% RSD), and 55.3 ± 1.1% (8.2% RSD), respectively, from 100 mL of deionized water (Table 2). The water that had passed through the disk was examined for Dacthal by passing it through a second 13 mm SAX disk. Approximately 30% of the Dacthal added to the original

Table 1. Recovery of the Monocarboxylic and Dicarboxylic Acid Metabolites of Dacthal as Their Methyl and Ethyl Esters over a Range of Metabolite Concentrations from 100 mL Samples of Deionized Water Using a 13 mm Strong Anion Exchange Disk[a]

analyte	concn (μg/L)	% rec rel to Dacthal std	
		methyl iodide	ethyl iodide
dicarboxylic acid metabolite	3.8	105.3	96.6
	9.5	101.8	93.3
	19.0	103.6	93.8
	38.0	98.1	94.2
monocarboxylic acid metabolite	2.9	na	95.2
	7.3	na	91.7
	14.7	na	91.9
	29.3	na	92.3

[a] Recovery of four individual samples containing 3.8, 9.5, 19, and 38 μg/L dicarboxylic acid metabolite and 2.9, 7.3, 15, and 29 μg/L monocarboxylic acid metabolite, respectively.

Table 2. Average Recovery of Monocarboxylic (15 μg/L) and Dicarboxylic Acid Metabolite (19 μg/L) from 100 mL of Deionized Water and Blank Groundwater as their Ethyl Esters Using a Single 13 mm Strong Anion Exchange Disk

sample matrix	monocarboxylic acid metabolite (%)[c]	dicarboxylic acid metabolite (%)[c]
deionized water[a,c]	88.6 ± 0.8 (1.0)	94.5 ± 1.3 (1.3)
blank groundwater[b,c] (methanol rinse)	55.1 ± 1.1 (2.0)	95.0 ± 0.9 (1.0)
blank ground water[b,d] (no methanol rinse)	87.7 ± 1.0 (1.1)	91.7 ± 0.9 (1.0)

[a] Average recovery of four replicate samples. [b] Average recovery of five replicate samples. [c] A 5 mL methanol rinse was applied to the SAX disk prior to in-vial elution and derivatization. [d] No methanol rinse applied prior to in-vial elution and derivatization. [e] The relative standard deviation (%) is given in parentheses.

solution was found on the second SAX disk, indicating that low recovery on the first disk was due to breakthrough of Dacthal. Since Dacthal interacts with the styrene–divinylbenzene matrix of the SAX resin and not through anion exchange, too little mass of sorbent is present in a 13 mm disk for quantitative isolation. As an example, Monohan et al.[6] found that a 47 mm SAX disk quantitatively isolated Dacthal from 100 mL water samples. However, because only the metabolites of Dacthal are detected in groundwater from Malheur county in eastern Oregon,[6] this study focuses exclusively on the development of an in-vial derivatization and elution method for the determination of the monocarboxylic and dicarboxylic acid metabolites in groundwater.

Spike and recovery experiments were performed using a blank groundwater sample that contained neither Dacthal nor its metabolites at concentrations above detection. Methanol was initially used for a postextraction rinse to elute any potential nonpolar interferences. Initially, the use of the postextraction methanol rinse revealed a strong matrix effect with low recovery of the monocarboxylic acid metabolite from the blank groundwater compared to higher recovery from deionized water as reported above. The recovery of the monocarboxylic acid metabolite was 55.0 ± 1.1% (2.0% RSD) from five replicate samples of a fortified blank groundwater (Table 2). In contrast, the dicarboxylic acid metabolite gave good recovery at 95.0 ± 0.9% in the same five replicate extractions of the fortified blank groundwater (Table 2). No breakthrough was detected for either metabolites by extracting

Table 3. Concentrations of the Monocarboxylic and Dicarboxylic Acid Metabolites of Dacthal in 100 mL Groundwater Samples Collected from Domestic Wells in Malheur County in Eastern Oregon[a]

groundwater sample	monocarboxylic acid metabolite (μg/L)[c]	dicarboxylic acid metabolite (μg/L)[c]
1[b]	0.66 (1.5)	109.05 (0.7)
2	<dl[e]	0.60 (1.5)
3	0.21 (4.4)	37.51 (0.3)
4	0.12 (4.0)	19.49 (0.4)
5	0.52 (0.1)	95.12 (1.2)
6	<dl[e]	1.98 (1.1)
7	0.05[d]	8.53 (0.5)
8	0.73 (6.2)	11.73 (0.9)
9	1.04 (0.5)	180.70 (1.0)

[a] Average reported from triplicate samples analyses. [b] Average reported for four replicate sample analyses of a composite groundwater sample. [c] <dl, below method detection limit (0.02 μg/L). [d] Below method quantitation limit (0.06 μg/L) but above the 0.02 μg/L detection limit. [e] The relative standard deviation (%) is given in parentheses.

the water that had passed through the SAX disk. However, the methanol used to rinse the disk prior to in-vial derivatization and elution contained 38.5% of the monocarboxylic acid metabolite and none of the dicarboxylic acid metabolite. In the second set of five replicate blank groundwater extractions, where no postextraction rinse of the SAX disk was employed, the recovery of the monocarboxylic acid metabolite increased to 87.7 ± 1.0% (1.1% RSD) and the dicarboxylic acid metabolite recovery remained high at 91.7 ± 0.9% (1.0% RSD) (Table 2). Therefore, for the remainder of the study, no methanol postextraction rinse was employed to ensure high recovery of the monocarboxylic acid metabolite. Furthermore, methanol was not needed to clean up the sample extract since no interferences were observed.

The precision of the method for a composite groundwater sample containing native monocarboxylic and dicarboxylic acid metabolites, indicated by the relative standard deviation of five replicate extractions, was 1.5 and 0.7% for the monocarboxylic and dicarboxylic acid metabolites, respectively. The concentration of the monocarboxylic acid metabolite was 0.66 ± 0.01 μg/L while the dicarboxylic acid metabolite concentration was 109.05 ± 0.79 μg/L (Table 3). The summed average concentrations of the mono- and dicarboxylic acid metabolites (109.71 μg/L) for the composite sample in this study fall within the range of concentrations reported by Monohan et al.[6] for total Dacthal metabolites in the same composite sample determined using a 47 mm disk and conventional elution (98.4 ± 3.1 μg/L) and by liquid–liquid extraction (127.8 ± 3.7 μg/L).

The detection limit of the method, defined as a signal to noise (S/N) ratio of 3, is 0.02 μg/L while the quantitation limit of the method, defined at a S/N of 10, is 0.06 μg/L.

Application to Groundwater Samples. A total of eight groundwater samples taken from domestic wells in Malheur county, Oregon, were analyzed to demonstrate the 13 mm SAX isolation and in-vial derivatization and elution method for the quantitative analysis of the monocarboxylic and dicarboxylic acid metabolites of Dacthal. This set of samples was chosen to represent a range of total Dacthal residue concentrations because the historical Dacthal (total residue) concentrations, which were determined by liquid–liquid extraction for each well, were available. A typical chromatogram of a groundwater sample containing the mono- and dicarboxylic acid metabolites is shown

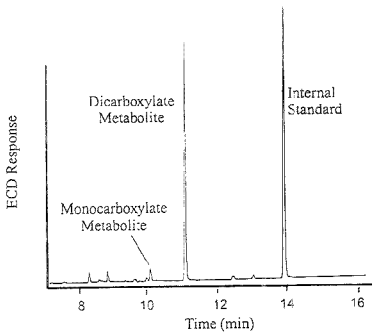

Figure 4. Typical GC-ECD chromatogram of an actual Malheur county groundwater sample containing the mono- and dicarboxylic acid metabolites of Dacthal.

in Figure 4; no Dacthal was detected in any of the samples analyzed for this study. For the eight groundwater samples analyzed in triplicate, the monocarboxylic acid metabolite concentration ranged from below detection (0.02 μg/L) to 1.04 ± 0.01 μg/L while the concentration of the dicarboxylic acid metabolite ranged from 0.66 ± 0.01 to 180.70 ± 1.81 μg/L (Table 3). The relative standard deviation was 0–6.2% for triplicate analysis of the monocarboxylic acid and 0.4–1.6% for the dicarboxylic acid metabolite. For individual wells, the concentration of the dicarboxylic acid metabolite was typically 16–200 times higher than that of the monocarboxylic acid metabolite. The higher concentrations of the dicarboxylic acid metabolite relative to the monocarboxylic acid metabolite are consistent with reports of longer half-lives for the dicarboxylic acid metabolite compared to the monocarboxylic acid metabolite.[13]

CONCLUSIONS

The 13 mm SAX disk isolation and in-vial derivatization and elution method provides significant reductions in the amount of solvent needed for the determination of the metabolites of Dacthal in groundwater. The flexible Empore disks allow the analyte derivatization and elution to take place in a 2 mL autosampler vial, thus saving solvent, time, and money. The amount of solvent consumed was reduced from the 450 mL for liquid–liquid extraction to a total of 6 mL. While ethyl iodide does require careful handling, diazomethane, a toxic and potentially explosive reagent, was successfully eliminated entirely. Besides the reduction in solvent, the method reduces the cost and amount of time required for analysis. Consequently, sample production capacity is increased from 8 samples per day for liquid–liquid extraction to 40 samples per day by SAX isolation and in-vial derivatization and elution method. The method is simple and does not require expensive materials (the disks are inexpensive at approximately 80 U.S. cents each) or specialized equipment.

ACKNOWLEDGMENT

We thank the Oregon Department of Agriculture for financial support and for providing the groundwater samples. This is Technical Report 10,716 of the Oregon Agricultural Experiment Station.

CAS Registry Numbers Provided by the Authors: Dacthal (dimethyl 2,3,5,6-tetrachloroterephthalate), 1861-32-1; tetrachloroterephthalic acid, 2136-79-0.

Received for review April 7, 1995. Accepted June 21, 1995.[⊗]

AC950347Y

[⊗] Abstract published in *Advance ACS Abstracts*, August 1, 1995.

Anal. Chem. 1995, *67*, 3363–3366

In-Vial C_{18} Empore Disk Elution Coupled with Injection Port Derivatization for the Quantitative Determination of Linear Alkylbenzenesulfonates by GC-FID

Carolyn J. Krueger† and Jennifer A. Field*,‡

Department of Chemistry and Department of Agricultural Chemistry, Oregon State University, Corvallis, Oregon 97331

An "in-vial elution" technique was developed to elute C_{18} Empore solid-phase extraction disks by placing them directly into gas chromatograph autosampler vials. Small (13 mm) C_{18} Empore disks were used to isolate linear alkylbenzenesulfonates (LAS) from samples of liquid detergent formulations and primary sewage effluent. Instead of eluting the disks in a conventional manner, the C_{18} disks were removed from their supports and transferred directly to a 2 mL autosampler vial containing 0.005 M tetrabutylammonium hydrogen sulfate in chloroform. The vials are then placed in an autosampler tray for a 40 min minimum equilibration period in which LAS is eluted from the disk as its tetrabutylammonium ion pair. Upon injection, LAS is derivatized to its butyl esters. Quantitative recovery of LAS was obtained from samples of deionized water (99 ± 2%) and primary sewage effluent (95 ± 5%). The precision of the C_{18} Empore disk extraction and in-vial elution method, indicated by the relative standard deviation, was ±5% for liquid detergent products and primary sewage effluent. The in-vial elution method is rapid and semiautomated since the autosampler and GC instrumentation manage disk elution, sample injection, and LAS derivatization.

Linear alkylbenzenesulfonates (LAS) are the highest volume anionic surfactant used in laundry detergent and household cleaning products.[1] Rapid and cost-effective analytical methods are needed for the determination of LAS in detergent products for reasons of process control and quality assurance. In addition, the analysis of environmental samples is of interest because several reports document the presence of LAS in domestic sewage influents and effluents.[2-7] While solid phase extraction disks (C_{18}) have been used for the isolation of LAS from sewage influents and effluent, the typical approach to disk elution requires multiple steps including extract collection, transfer, solvent reduction, and derivatization.[2,6]

The conventional disk elution technique consists of drawing solvents through the disk and collecting the extract. Because the disks can be removed from their supports and be folded or even cut into pieces, alternative elution techniques can be developed for further reductions in solvent use and analysis time. However, few alternative disk elution strategies have been reported. McDonnell et al.[8] eluted 47 mm diameter C_8 and C_{18} disks by soaking the disks in a beaker containing diethyl ether. Polynuclear aromatic hydrocarbons, polychlorinated biphenyls, and pesticides are recovered from disks by supercritical fluid extraction; however, specialized and expensive equipment is required.[9,10]

In this paper, we report an improved method for the determination of LAS that saves time by eliminating several preparative steps and reduces the cost and amount of solvent needed for analysis. A simple "in-vial" disk elution technique is presented whereby C_{18} disks are placed *directly into* 2 mL autosampler vials. Because LAS are eluted from the disk as their ion pairs, in-vial elution couples disk elution with derivatization, since LAS ion pairs derivatize to butyl esters upon injection. The method for C_{18} isolation and in-vial elution of LAS is then demonstrated for the determination of LAS in liquid detergent products and primary sewage effluent.

EXPERIMENTAL SECTION

Reagents. A commercial mixture of LAS (50.05% active) was obtained from Vista Chemical Co. The mixture was composed of four alkyl chain homologs including C_{10}-LAS (21.8%), C_{11}-LAS (39.1%), C_{12}-LAS (28.4%), and C_{13}-LAS (8.5%). Standards of 99% purity *n*-tetradecanesulfonic acid (C_{14}-SAS) and 99% purity 4-octylbenzenesulfonic acid (C_8-LAS) (Aldrich Chemical Co., Milwaukee, WI) were purchased from Lancaster Synthesis Ltd., (Lancaster, England). The C_8-LAS and C_{14}-SAS were selected for this study as the surrogate and internal standards, respectively, because they do not occur in commercial LAS mixtures. Reagent-grade tetrabutylammonium hydrogen sulfate (TBA; Aldrich) was prepared as a 0.005 M solution in chloroform (Burdick and Jackson, Muskegon, MI). A solution of 30 mM sodium chloride (VWR Scientific, South Plainfield, NJ) was prepared in deionized water.

† Department of Chemistry.
‡ Department of Agricultural Chemistry.

(1) Thayer, A. M. *Chem. Eng. News* **1993**, (Jan 25), 26.
(2) Field, J. A.; Field, T. M.; Poiger, T.; Giger, W. *Environ. Sci. Technol.* **1994**, *28*, 497.
(3) Berna, J. L.; Moreno, A.; Ferrer, J. *J. Chem. Tech. Biotechnol.* **1991**, *50*, 387.
(4) Marcomini, A.; Giger, W. *Tenside Surfactant Deterg.* **1988**, *25*, 226.
(5) McAvoy, D. C.; Eckhoff, W. S.; Rapaport, R. A. *Environ. Toxicol. Chem.* **1993**, *12*, 977.
(6) Borgerding, A. J.; Hites, R. A. *Environ. Sci. Technol.* **1994**, *28*, 1278.
(7) Field, J. A.; Field, T. M.; Poiger, T.; Siegrist, H. R.; Giger, W. *Water Res.* **1995**, *29*, 1301.
(8) McDonnell, T.; Rosenfeld, J.; Rais-Firouz, A. *J. Chromatogr.* **1993**, *629*, 41.
(9) Bengtsson, S.; Berglöf, T.; Granat, S.; Jonsäll, G. *Pestic. Sci.* **1994**, *41*, 55.
(10) Tang, P. H.; Ho, J. S.; Eichelberger, J. W. *J. AOAC Int.* **1993**, *76*, 72.

0003-2700/95/0367-3363$9.00/0

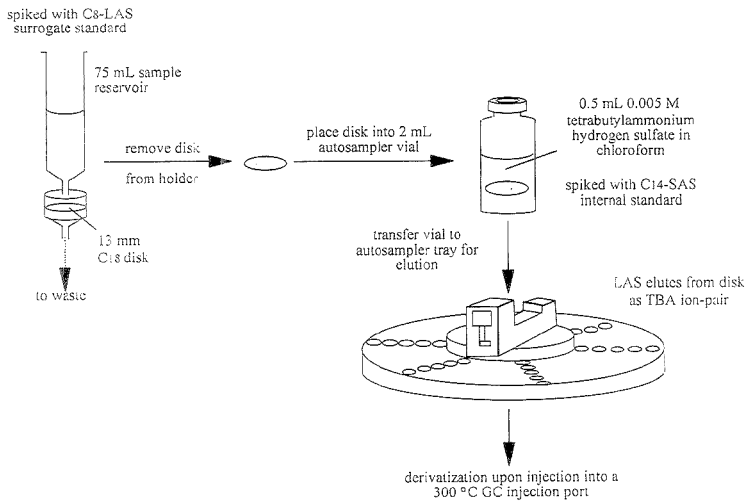

Figure 1. Schematic diagram indicating steps involved in LAS isolation, in-vial elution, and derivatization.

Table 1. Weight Percent LAS in Liquid Detergent Products[a]

product name	wt % LAS
Dermassage Dishwashing Liquid	9.7 ± 0.5
Ajax Dishwashing Liquid	13.0 ± 0.5
Dove Dishwashing Liquid	20.0 ± 0.2
Wisk Double Power Concentrated Laundry Detergent	31.9 ± 0.3
All Laundry Detergent	33.7 ± 0.8
Ivory Dishwashing Liquid	nd[b]
Tide Ultra Concentrated Laundry Detergent	nd
Palmolive Sensitive Skin Dishwashing Liquid	nd
Lemon Scent Dawn Dishwashing Detergent	nd

[a] Five replicate samples analyzed. [b] nd indicates <3.5% LAS by weight or <6 μg of LAS in a 10 mL sample of a 17 mg/L liquid detergent product solution.

Materials. For solid-phase extraction, 13 mm diameter disks were cut from commercially available, 47 mm diameter C_{18} bonded-phase silica Empore disks that were donated by the 3M Co. (Minneapolis, MN). A 13 mm diameter polypropylene filter assembly (Millipore, Bedford, MA) was used to support each 13 mm C_{18} disk. The filter assemblies were placed on a vacuum manifold (Supelco, Bellefonte, PA) and fitted with a 75 mL polypropylene reservoir (Figure 1).

Samples. Commercial liquid detergent products were purchased from a local market and are listed in Table 1. Each product was prepared as a 17 mg/L detergent solution in deionized water containing 1% (v/v) formalin. A sample of primary sewage effluent was collected from the Corvallis Sewage Treatment Plant in Corvallis, OR, and immediately preserved with 1% (v/v) formalin to prevent microbial degradation. The sample was not filtered prior to extraction.

Solid-Phase Extraction. The 13 mm C_{18} disks were preconditioned by first drawing 2 mL of ethyl acetate through each disk followed by air until the disk was dry. To wet the disk, 5 mL of methanol was then passed through the disk followed by 7 mL of deionized water. The disks were not allowed to dry once the methanol was added. Samples of standard LAS (10–200 mL), liquid detergent products (10 mL), and primary sewage effluent (15 mL) were added to the reservoirs and spiked with 10 μg of the C_8-LAS surrogate standard. Sodium chloride was added to samples to give a minimum concentration of 0.6 mM NaCl. Once the sample had passed through the disk under full vacuum, the reservoir was removed and the disk was dried in the disk assembly under full vacuum for 10 min.

For the solid-phase extraction of primary sewage effluents, 13 mm diameter circles were cut from 47 mm diameter glass fiber filters (1 μm pore diameter) (Whatman International Ltd., Maidstone, England) and placed on top of the 13 mm C_{18} disk in the filter assembly in order to minimize clogging of the C_{18} disk. The same disk preconditioning and sample extraction procedures described above were performed for the extraction of primary sewage effluent samples. However, once dry, the disk was rinsed with 2 mL of chloroform prior to elution in order to remove coisolated interferences. The chloroform was discarded, and the disk and filter were left together in the filter assembly and dried under full vacuum for 20 min.

In-Vial Elution and Derivatization. Once the disks were dry, each disk was removed from the filter assembly and transferred directly to a 2 mL autosampler vial containing 0.5 mL of 0.005 M TBA in chloroform that had been spiked with 10 μg of the C_{14}-SAS internal standard (Figure 1). For primary sewage effluent samples, the filter and the disk were placed together in the autosampler vial for elution. The vials were then capped and placed on the autosampler tray for a minimum of 40 min to allow for complete elution before initiating autoinjection. Upon injection, LAS derivatizes nearly instantaneously to its butyl esters in the 300 °C injection port.[2,11]

Gas Chromatography and Quantitation. All extracts were analyzed by a Hewlett-Packard Model 5890 Series II gas chromatograph (GC) equipped with an autosampler, an SE-54 column (30 m × 0.25 mm i.d. × 0.25 μm film thickness; Alltech, Deerfield,

(11) Field, J. A.; Miller, D. J.; Field, T. M.; Hawthorne, S. B.; Giger, W. *Anal. Chem.* **1992**, *64*, 3161.

IL), and a flame ionization detector (FID). The oven temperature program and GC conditions were similar to that described in Field et al.[2] except that the 4 mm i.d. glass inlet liner was packed with quartz wool instead of glass wool.

For quantitation, a calibration curve was constructed from the ratio of LAS to the C_8-LAS surrogate standard. The curve was linear, typically with $r^2 = 0.999$.

Spike and Recovery Procedures. Spike and recovery experiments using deionized water were performed in order to determine the accuracy and precision of the C_{18} Empore disk extraction and in-vial elution method. Three to four replicate samples ranging from 10 to 200 mL in volume and containing 50 μg of standard LAS were spiked with 10 μg of the C_8-LAS surrogate standard and NaCl.

Standard addition experiments were performed with samples of primary sewage effluent in order to determine the accuracy and precision of the method for a complex environmental sample. Prior to extraction, a known quantity of standard LAS mixture was spiked into replicate samples (n = 5) of primary sewage effluent containing 0.6 mM NaCl together with 10 μg of the C_8-LAS surrogate standard to give standard addition LAS concentrations of 1.5 and 3.1 mg/L.

RESULTS AND DISCUSSION

In-Vial Elution and Derivatization. The autosampler and GC instrumentation managed several operations in this study including disk elution, LAS derivatization, and injection. A typical GC-FID chromatogram of standard LAS extracted from deionized water is shown in Figure 2a. Commercial mixtures of LAS are composed of homologs identified by the number of carbon in the alkyl chain (C_{10}–C_{14}). Phenyl-positional isomers are identified by the position of attachment between the phenyl sulfonate group and the alkyl chain. For example, the notation 3-ϕ C_{10}-LAS indicates a C_{10}-LAS homolog with the phenyl sulfonate group attached to the third carbon of the alkyl chain. Note that under the GC conditions used not all isomers are resolved in the chromatogram given in Figure 2.

To determine the length of time required for the elution of the C_8-LAS surrogate standard and LAS to reach equilibrium (Figure 3), a 13 mm C_{18} disk containing sorbed LAS and C_8-LAS was placed in an autosampler vial together with 0.005 M TBA in chloroform. Repeated injections were performed every 20 min for 3 h. The rate of LAS homolog elution from the C_{18} disk varied with alkyl chain length (Figure 3) so that a minimum of 40 min was required to achieve greater than 95% recovery for all LAS homologs and the C_8-LAS surrogate standard. The slower elution of C_8-LAS and the shorter chain LAS from the C_{18} disk is due presumably to the decreased solubility of the TBA ion pairs of shorter alkyl chain homologs in chloroform relative to those of the longer chain homologs.

Quartz wool packing in the inlet liner reduced the carry-over between samples and improved injection precision compared to glass wool used by Field et al.[2,11] Over 400 injections were performed with the same inlet liner and column without any degradation in chromatographic quality, indicating the robust nature of injection port derivatization.

Solid-Phase Extraction. Spike and recovery experiments were performed using 100 mL of deionized water. Initially, the recovery of the C_8-LAS surrogate standard was only 23% while LAS recovery was 85%. However, in order to use the C_8-LAS as a surrogate standard, it is necessary to have nearly equivalent

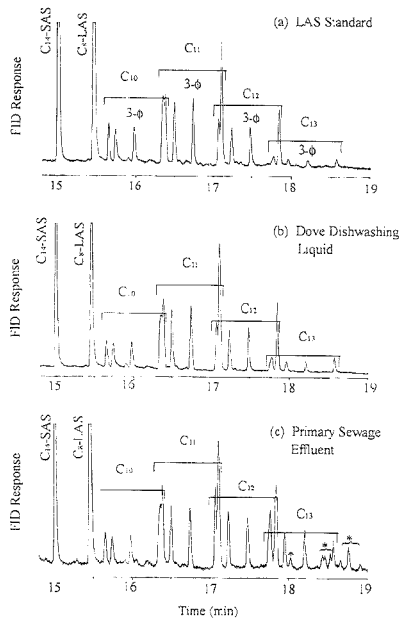

Figure 2. Gas chromatograms of (a) LAS standard isolated from deionized water, (b) Dove Dishwashing Liquid, and (c) primary sewage effluent. The isomers of each homolog are within brackets with each 3-ϕ positional isomer identified. The asterisk denotes peaks not belonging to the LAS mixture.

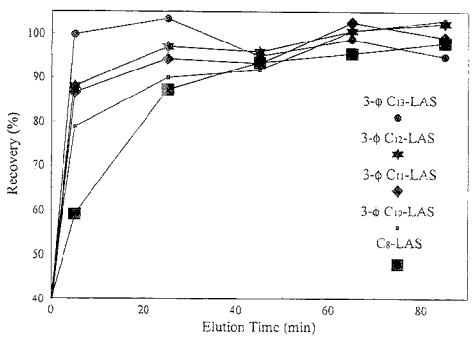

Figure 3. Recovery of the 3-ϕ isomer for each LAS homolog and the C_8-LAS surrogate standard with in-vial elution time.

recoveries of both LAS and the C_8-LAS surrogate standard. With the addition of 0.6 mM NaCl, the recovery of the C_8-LAS surrogate standard and LAS increased to 92 and 96%, respectively. Subsequently, NaCl was added to all samples to give a minimum of 0.6 mM NaCl. No LAS breakthrough was detected for 10–200 mL samples of deionized water containing 0.6 mM NaCl; the recovery of LAS ranged from 98 to 100% with an average precision of 2%.

Quantitation and Detection. The instrumental and method detection limits, defined at a signal-to-noise ratio (S/N) of 3, were identical and corresponded to 6 ng total LAS injected into the GC or 60 μg/L for a 50 mL sample. The instrumental quantitation limit and the method quantitation limit, defined at a S/N > 10,

also were equivalent at 10 ng total LAS injected into the GC or 100 μg/L LAS for a 50 mL sample. Because the detection and quantitation limits of the method are identical to those of the instrument, sensitivity is not compromised by in-vial elution even though a C_{18} disk is physically present in the autosampler vial.

Application to Liquid Detergent Products and Primary Sewage Effluent. The C_{18} Empore disk extraction and in-vial disk elution technique described in this paper was applied to samples of liquid detergent products and primary sewage effluent. Five replicate samples of each of the nine liquid detergent products were analyzed for LAS. The weight percent of LAS ranged from below detection to 33.7% (Table 1). An example of a typical chromatogram for LAS detected in liquid detergent is shown in Figure 2b. No interferences were present in any of the FID chromatograms of the detergent products and thus no sample cleanup was required even for the relatively nonspecific FID detector. The precision of detergent product analysis, indicated by the relative standard deviation (RSD), ranged from 0.9 to 5% (Table 1).

A sample of primary sewage effluent was analyzed to demonstrate the C_{18} Empore disk extraction and in-vial disk elution method for a complex environmental sample. Primary sewage effluent samples were initially extracted without the addition of the C_8-LAS surrogate standard; no interferences with the surrogate standard were detected. However, sample extracts of primary sewage effluent initially contained peaks that coeluted with LAS. For this reason, a chloroform rinse was applied as a cleanup step prior to in-vial disk elution. While chromatograms of the chloroform rinse indicated many of the interfering peaks, neither the C_8-LAS surrogate standard nor LAS were detected. Although additional peaks remained in the chromatogram after the chloroform rinse, they did not coelute with LAS (Figure 2c).

The concentration of LAS in five replicate samples of primary sewage effluent was 2.43 ± 0.06 mg/L LAS with an RSD of 2.5%. To assess the accuracy and precision of the C_{18} Empore disk extraction and isolation method for the analysis of LAS in primary sewage effluents, a series of standard additions were performed. The average recovery of the 1.5 and 3.1 mg/L LAS added to primary sewage effluent was 95 ± 6 (6% RSD) and 94 ± 5% (5% RSD), respectively, demonstrating the applicability of the method for complex environmental samples. It is important to note that the extractions of 15 mL primary sewage effluent samples were conducted with unfiltered samples and that, in addition to the 13 mm C_{18} disk, a glass fiber filter and particulate matter also were physically present in the autosampler vial.

CONCLUSIONS

The in-vial disk elution technique is an improvement over conventional methods because disk elution and injection port derivatization are managed by the GC autosampler and instrumentation, which requires no supervision by the analyst. The technique is cost-effective because each 13 mm diameter C_{18} disk costs approximately 80 U.S. cents and only relatively inexpensive equipment is required. In addition, fewer than 8 mL of solvent is required for disk preconditioning and in-vial elution. The technique is rapid with 10 min required to extract detergent product solutions and 30 min for primary sewage effluent samples so that up to 40 samples/day can be processed. Sample cleanup is not necessary for liquid detergent products although a single cleanup step is necessary in the case of primary sewage effluents.

ACKNOWLEDGMENT

This work was supported by grants from the National Geographic Society (5162W-93) and the National Science Foundation (BES-9409171). Additional financial support from the Oregon State University Research Council, Vista Chemical Co., and the Monsanto Co., is gratefully acknowledged. In addition, the authors thank Dave Miller, Craig Markell, and Sue Price for their technical assistance. This is Technical Report 10,690 of the Oregon Agricultural Experiment Station.

Received for review May 9, 1995. Accepted June 27, 1995.[⊗]

AC9504474

[⊗] Abstract published in *Advance ACS Abstracts*, August 1, 1995.

Anal. Chem. 1995, *67*, 3367–3371

Spatial-Scanning Laser Fluorescence Detection for Capillary Electrophoresis

Stephen C. Beale* and Sara Jane Sudmeier

Department of Chemistry, University of Alabama at Birmingham, Birmingham, Alabama 35294

A laser-induced fluorescence (LIF) detector using epi-illumination and confocal optical detection geometry is described. The LIF detector is designed to scan the entire length of the separation capillary. The capillary is mounted on a precision translational stage which moves the entire capillary through the probe beam. The design of the laser scanner and the results from optimization experiments are presented. The LIF scanner can be used to monitor fluorescence from fluorescein isothiocyanate-labeled proteins focused by capillary isoelectric focusing or to follow the time course of a separation. Dynamically changing the effective separation length is shown to offer a means to decrease analysis time. A method for directly measuring the diffusion coefficient is also presented.

Laser-induced fluorescence (LIF) detection offers a highly sensitive means for detecting migrating zones in capillary electrophoresis (CE). Laser fluorescence systems have provided mass detection limits at subattomole levels[1] and concentration detection limits substantially lower than those obtained by UV–vis detection. The capability to monitor the progress of the separation process or to dynamically alter the length of the separation bed by scanning the entire capillary offers several advantages over conventional instrumentation. Separation time can be optimized since the duration of the run need only be long enough to resolve the components of interest. Thus, sample throughput will be increased as the solutes do not need to migrate through the entire length of the separation bed. The ability to scan the capillary will facilitate the measurement of the solute diffusion coefficient, from which hydrodynamic radius, solvent viscosity, and expected peak variance due to diffusional band-broadening can be calculated independent of electrophoretic contributions to peak width.

Epi-illumination confocal laser fluorescence detection has recently become a popular means to achieve sensitive LIF detection.[2–7] Laser confocal fluorescence systems have been successfully used for the detection of DNA fragments separated in a capillary array[5,8] or on microfabricated chips[9] and for the detection of polycyclic aromatic hydrocarbons.[4] Since the epi-illumination confocal detection format allows the object freedom of movement throughout the focal plane, it is possible to adapt this detection geometry to scan the entire length of the capillary. The system we present is similar to the capillary array electrophoresis system described by Mathies and co-workers[5,6] for continuously monitoring the outlet ends of several capillaries in a bundle. We have adapted Mathies's geometry to scan the entire length of a single capillary.

In this paper we present the experimental details for a laser confocal fluorescence detector designed to scan the length of the separation capillary. The design of the laser scanner and present results on detection limits, minimizing separation time, and a method for measurement of solute diffusion coefficient independent of peak width contributions from the electrophoresis are reported.

EXPERIMENTAL SECTION

Instrumentation. The confocal laser fluorescence detector is shown schematically in Figure 1. The output radiation (488 nm) from an air-cooled Omnichrome Model 532-5BS argon ion laser head passes through a neutral density filter (Omega Optical, Brattleboro, VT) and is elevated to ~30 cm above the main breadboard (TMC, Inc., Atlanta, GA) surface with a Melles Griot (Irvine, CA) precision beamsteering device. Using the tube current control on the laser head and various combinations of OD 1.0 and 0.3 neutral density filters, the laser power transmitted to the capillary can be controlled over a 0.6–25 mW range. The incident beam is reflected by a dichroic beamsplitter (Omega Optical) and focused into the capillary by a Zeiss 0.42 N.A., 32× Plan Achromat long working distance infinite conjugate microscope objective. The emission signal is collected by the same objective and transmitted back through the dichroic beamsplitter. A mirror above the dichroic beamsplitter reflects the emission beam through an interference filter centered at 530 nm (Omega Optical). The emission signal is focused by a fused silica focusing lens (Melles Griot) through a 200 μm pinhole (Melles Griot) and a long pass edge filter (515 nm, Omega Optical). The entire emission train is mounted on a Melles Griot 2 in. thick breadboard mounted directly to the main optical breadboard on legs 25.4 mm high (Melles Griot). The photon signal is converted to a current by a Hamamatsu (Bridgewater, NJ) 1P28 photomultiplier tube. The current is converted to a voltage, amplified, and filtered by a Stanford Applied Research Systems low-noise SR750 current amplifier. Data are collected through a 12-bit A/D board (Keithley Metrabyte DAS 1602, Taunton, MA) and stored on an IBM PC clone using software written in-house.

The capillary, 25–100 μm i.d. × 365 μm o.d. (Polymicro Technologies, Phoenix, AZ), is mounted on an in-house constructed Plexiglas stage whose base and top were milled flat. A

(1) Cheng, Y. F.; Dovichi, N. J. *Science* **1988**, *242*, 562–564.
(2) Zhu, H.; Clark, S. M.; Benson, S. C.; Rye, H. S.; Glazer, A. N.; Mathies, R. A. *Anal. Chem.* **1994**, *66*, 1941–1948.
(3) Clark, S. M.; Mathies, R. A. *Anal. Biochem.* **1993**, *215*, 163–170.
(4) Nie, S.; Dadoo, R.; Zare, R. N. *Anal. Chem.* **1993**, *65*, 3571–3575.
(5) Huang, X. C.; Quesada, M. A.; Mathies, R. A. *Anal. Chem.* **1992**, *64*, 2149–2154.
(6) Huang, X. C.; Quesada, M. A.; Mathies, R. A. *Anal. Chem.* **1992**, *64*, 967–972.
(7) Nie, S.; Chiu, D. T.; Zare, R. N. *Science* **1994**, *266*, 1018–1021.
(8) Taylor, J. A.; Yeung, E. A. *Anal. Chem.* **1993**, *65*, 956–960.
(9) Woolley, A. T.; Mathies, R. A. *Proc. Natl. Acad. Sci. U.S.A.* **1994**, *91*, 11348–11352.

0003-2700/95/0367-3367$9.00/0

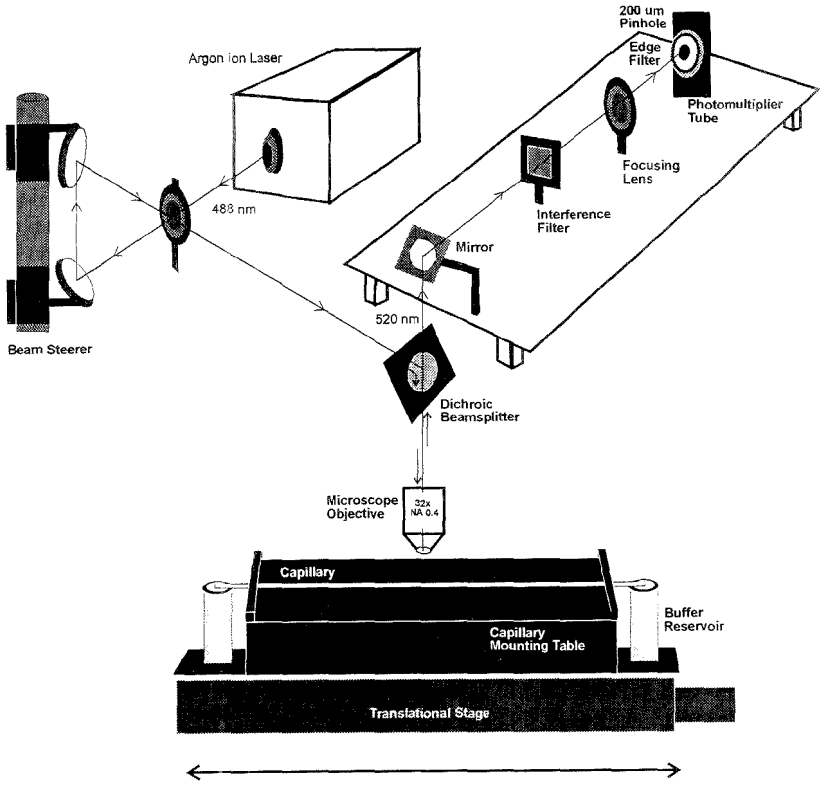

Figure 1. Diagram of the laser confocal scanner.

0.3 mm groove was milled down the center of the top to receive the capillary and maintain alignment. The sides of the stage were milled separately from the body of the stage and held in place with set screws to allow for fine adjustment of the capillary down the groove. A swagelock union is threaded into each side, concentric with the milled groove on the stage. Once the capillary is positioned in the groove, it can be locked into place with a nut and Vespel ferrule swaged to the outer end of the union. This results in a bend in the capillary on the stage. The capillary is pulled tight in the groove by backing off $\sim^1/_4$ turn on each union. Alignment of the beam down the length of the tube is achieved by filling the column with fluorescein and measuring the response at each end of the capillary. Fine adjustments of the entire stage on the positioning table are made until the response is equivalent at both ends of the capillary. The column is then scanned to ensure that the signal is uniform down the entire length of the column.

The capillaries were stripped of the polyimide coating using either a butane flame or fuming sulfuric acid and washed with water followed by methanol. We found that UV-transparent coatings tended to vary in thickness within a spool, which resulted in higher background noise levels relative to the stripped capillaries. If the polyimide-stripped capillary is handled with reasonable care, breakage during installation is rare. With the current stage design, 19 cm of a 26 cm long capillary can be scanned.

The Plexiglas stage is mounted directly to a CPS-90 precision linear positioning table (Design Components, Inc., Franklin, MA), which is anchored to an optical breadboard. The positioning table is driven by a servo motor (Design Components, Inc.), controlled by an encoder device (Design Components, Inc.) connected directly to an IBM PC clone. The software allows the operator to program motion in a stepper motor configuration (20 000 steps/in. resolution), with the encoder translating to an analog signal to the motor. The table can travel with a maximum velocity of 50 mm/s. Straight line accuracy and position location are better than 5 μm. In the scanning mode, the motor is triggered by a 5 V output from the data acquisition board to synchronize table motion with data collection.

A Spellman (Planeview, NY) CZE1000R high-voltage power supply was used to generate the electrical field across the capillary. Columns were coated with a linear polyacrylamide according to the method described by Hjerten.[10] The separation potential was always kept below 15 kV, and the current through the capillary did not exceed 45 μA. Injections were accomplished electrokinetically. No provision was made for a load resistor parallel to the capillary to minimize rise and fall time of the injection voltage.[11]

Reagents and Chemicals. Fluorescein isothiocyanate (FITC) and all buffers were purchased from Aldrich (Milwaukee, WI).

(10) Hjerten, S. *J. Chromatogr.* **1985**, *347*, 191–198.
(11) Huang, X.; Coleman, W. F.; Zare, R. N. *J. Chromatogr.* **1989**, *480*, 95–110.

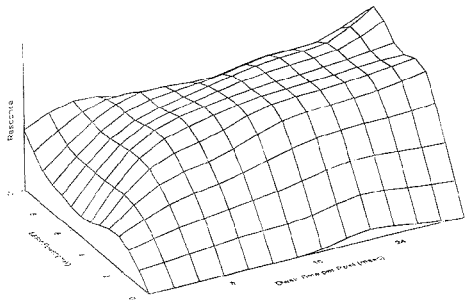

Figure 2. Plot of relative fluorescence response as a function of the laser power and dwell time per pixel.

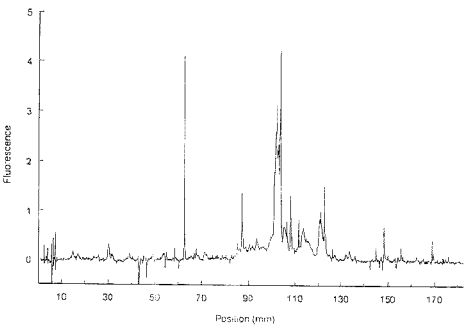

Figure 3. Capillary isoelectric focusing, without mobilization, of FITC myoglobin in pH 3–10 ampholytes. An "ampholytes-only" scan has been background subtracted from the raw data.

Amino acids and proteins were purchased from Sigma Chemical Co. (St. Louis, MO) and used without further purification. FITC-labeled insulin and lentil lectin were purchased from Sigma and used without further purification. Other proteins were labeled with FITC (limiting) in a 1:1 mole ratio, in bicarbonate buffer, pH 9.5, and dialyzed against water to remove unreacted FITC. The protein was then diluted to the appropriate concentration in the operating buffer, as indicated in the text. Glycine was derivatized under the same conditions, with FITC as the limiting reagent. Acrylamide and TEMED were purchased from Bio-Rad labs (Melville, NY) and used without further purification.

RESULTS AND DISCUSSION

In this paper, the fundamental considerations for characterization of the LIF scanner and preliminary data indicating performance are presented. One of the important experimental parameters to be investigated is detector response as a function of both laser power and dwell time per pixel.[12,13] Optimization of the signal entails balancing laser power with integration time over the pixel (dwell time per pixel) to extract as many photons as possible while minimizing photodestruction. The expected profiles should fit an exponential profile that accounts for laser intensity and the probability that a molecule will be intact after traversing the beam.[12]

Based on the model for photon emission as a function of laser power and illumination time developed by Mathies and Stryer[12] for photon counting, we tailored an experiment to our system for the optimization of laser power with dwell time per pixel (scan rate). In Figure 2 are shown the results of varying laser power over the range of 0.6–10 mW and dwell time for a 100 μm i.d. column. Two scans were made over the capillary for each data point. The first was made in a capillary filled with 10^{-8} M fluorescein (signal). The second was made on a column filled with buffer solution (blank). The plotted response is signal readout voltage divided by the square root of blank readout voltage.[12] At each power, 10 scan speeds were measured, and at each scan speed, 10 laser power levels were measured. This proved to be a sufficient number of points to reproduce the expected exponential profile. Dwell time per pixel is determined by the sampling rate, which was adjusted in concert with scan speed to keep a constant 20 μm/pixel width.

The curves follow the expected profile predicted by Mathies.[12] Long dwell times and moderate laser power, 3–6 mW, are indicated to burn high onto the response curve for good S/N performance. Our data correlate well with Mathies's theory in the high scattering background situation. Ideally, very long dwell times are indicated; however, to maintain reasonable analysis time, the dwell time was always less than 40 ms.

We investigated similar response surfaces for different capillaries with inner diameters ranging from 25 to 100 μm. The shapes of the curves were all similar, but S/N decreased with smaller diameter capillaries. We attribute this to the difficulty in maintaining a good focal point through a thick capillary wall and distortions due to inhomogeneities in the capillary surface leading to distortions of the beam profile. In light of this, we currently work with 75 or 100 μm i.d. columns. The response curves also provide a guide for selecting optimum laser power for a given migration velocity or scan rate, or vice versa.

Our initial objective in developing the laser scanner was to monitor, in situ, zones separated by capillary isoelectric focusing without mobilization. Pawliszyn and Wu[14–16] have reported the use of concentration gradient and absorbance imaging to detect focused zones without mobilization in short capillaries. We report here the detection, without mobilization, of fluorescently labeled proteins separated by isoelectric focusing. In Figure 3 is the isoelectropherogram, without mobilization, of FITC-myoglobin in pH 3–10 ampholytes with 10 mM sodium hydroxide as the catholyte and 20 mM phosphoric acid as the anolyte. The capillary was scanned at 5.08 mm/s using ~6.5 mW laser power. Data were acquired at a rate of 254 Hz, to give a pixel width of 20 μm/pixel. The background from a previously acquired "ampholytes-only" run was subtracted from the myoglobin isoelectropherogram to yield Figure 3.

Several peaks can be observed in the isoelectropherogram; this is most likely due to the fluorescent label attached at different positions and multiply labeled molecules. The concentration of FITC-myoglobin is 10^{-8} M, based on the FITC concentration. In the scanning mode, for focused peaks, detection limits are 10^{-9} M (~2.4 fmol), while detection limits in the static mode (that is, with the detection point fixed) are 10^{-12} M (~0.2 amol) for FITC-

(12) Mathies, R. A.; Peck, K.; Stryer, L. *Anal. Chem.* **1990**, *62*, 1786–1791.
(13) Art, J. J.; Goodman, M. B. In *Methods in Cell Biology*; Matsumoto, B., Ed.; Academic Press, Inc.: New York, 1993; Vol. 38, pp 47–77.
(14) Wu, J.; Pawliszyn, J. *Anal. Chim. Acta* **1995**, *299*, 337–342.
(15) Wu, J.; Pawliszyn, J. *J. Chromatogr. B* **1994**, *657*, 327–332.
(16) Wu, J.; Pawliszyn, J. *Anal. Chem.* **1994**, *66*, 867–873.

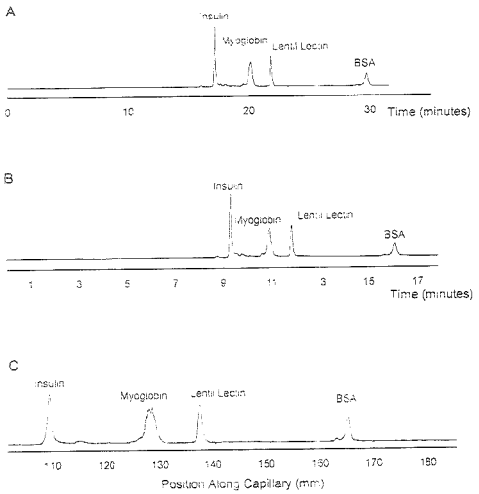

Figure 4. (A) FITC-insulin, FITC-myoglobin, FITC-lentil lectin, and FITC-BSA separated in a 6% *T* linear acrylamide gel capillary. The detection point was fixed to give an effective column length of 14 cm. (B) Detection point was fixed 8 cm from the cathode. (C) The voltage was interrupted after 10 min, and the capillary was scanned from the anodic end.

labeled glycine. The discrepancy of the detection limits in the static and scanning modes probably arises from a combination of contributions. The myoglobin signal is diluted over several different reaction products, while glycine has only a single reactive site. Scattering from inhomogeneities of the capillary wall increases the scanning background. Variations in the wall thickness along the capillary length will distort the focal point and emission beam profile. Fluid vibrations within the capillary during the scan will increase the scanning background signal. Further design improvements will be aimed at minimizing these effects through the use of square capillaries[15] and a step–scan approach. In the step–scan mode, capillary motion is ceased during the measurement period to reduce the background signal.

Scanning the entire length of the capillary gives one the power to observe the progress of the separation and also minimizes analysis time. In fact, it may not require the entire separation bed to achieve the desired resolution for the most difficult pair. Analysis time can be decreased by either positioning the detector to utilize as short an effective column length as possible while still retaining the requisite resolution[17] or scanning the column during the course of the separation. Once the desired resolution of the most difficult pair is achieved, the capillary can be flushed and prepared for the next analysis.

These concepts are illustrated in Figure 4, in which FITC-labeled insulin, myoglobin, lentil lectin, and bovine serum albumin are separated by size in a 6% *T* linear acrylamide gel. In Figure 4a, the effective column length is 14 cm (fixed detection point). Thirty minutes is required for the last component to migrate past the detection point. The same zones are completely resolved in less than 17 min with use of a 8 cm long effective capillary, as shown in Figure 4b. The resolution of all four zones is sufficient for quantitation yet requires about half the analysis time. Figure 4c depicts a capillary scan over the last 8 cm of the capillary of the same sample, at 5.08 mm/s (254 Hz sampling rate) after 10 min of applied voltage. The total analysis time was less than 11 min. The voltage was interrupted during the scan, so each zone moves through the detector window with the same velocity. The 11 min analysis time represents about a 3-fold decrease over the fixed detection point situation with use of a 14 cm long separation capillary. If, at this point, resolution between a particular pair of compounds is insufficient, the voltage could be reapplied and more of the separation bed utilized. Molecular weight can be estimated from a plot of log MW vs migration distance.

Yet another advantage to whole-column scanning is manifested in the capability to directly measure solute diffusion coefficient. The experiment is similar to the "stopped flow" experiment described by Walbraehl and Jorgenson[18] for capillary electrophoresis and originally developed by Knox and McLaren[19] for GC. The column was positioned with the beam about midway down the length of the capillary. The test solute (FITC-glycine in this case) was injected at the cathodic end of a coated capillary in which electroosmosis was eliminated. When the glycine peak migrates past the detection beam, the voltage is interupted. From this initial run, electrophoretic mobility and temporal variance can be determined. Temporal variance can be converted to spatial variance by multiplying by the square of the migration velocity. During the time the voltage is off, the zone is scanned several times. Spatial variance is measured directly since the response as a function of position within the capillary is measured. During the voltage off period, the only mechanism for increasing variance is diffusion, which can be determined from the Einstein equation:

$$\sigma^2 = 2Dt$$

Therefore, a plot of spatial variance vs time (when voltage is off) yields the diffusion coefficient from the slope. This diffusion coefficient is determined independently of any other peak variance contributions from electrophoresis. If desired, the detector can be repositioned at the anodic end of the capillary and the voltage reapplied to migrate the zone past the new detector position.[18,19] The *y*-intercept of the curve gives an indication of nondiffusional sources of band-broadening.

We made diffusion coefficient measurements of FITC-glycine in three different buffers, 25 mM Tris, pH 8.5: 4% *T* linear acrylamide, and 6% *T* linear acrylamide at a field strength of 67 V/cm and 2 h diffusion time. The diffusion coefficients were determined from 0.5 times the slope of the linear plot ($r^2 = 0.999$) of spatial variance vs time. The experimentally determined diffusion coefficients were as follows: free-solution, 6.7×10^{-6} cm^2/s, which agrees with previously reported diffusion coefficients of dansylated amino acids;[17] 4% *T* linear acrylamide, 5.1×10^{-6} cm^2/s; and 6% *T* linear acrylamide, 2.5×10^{-6} cm^2/s. It was important to operate at such a low field strength to eliminate any effects from Joule heating. The results from further investigations into capillary temperature and diffusion coefficient measurements of larger biopolymers will be the subject of another paper.

(17) Clark, B. K.; Vo-Dinh, T.; Sepaniak, M. J. *Anal. Chem.* **1995**, *67*, 680–683.

(18) Walbroehl, Y.; Jorgenson, J. W. *J. Microcolumn Sep.* **1989**, *1*, 41–45.

(19) Knox, J. H.; McLaren, L. *Anal. Chem.* **1964**, *36*, 1477–1482.

CONCLUSIONS

We have developed a laser-induced fluorescence detector for capillary electrophoresis in which the entire capillary can be scanned during the course of the electrophoretic run. The detection geometry is based on an epi-illumination format with confocal optical detection geometry. The optimization of laser power and dwell time per pixel are presented. It is apparent that there is an optimum laser intensity depending on solute transit time in the probe volume. Therefore, the capability to tune laser power is an important characteristic not only in our application but also for laser fluorescence detection in general. We have demonstrated the capabilities of the scanning detector in light of isoelectric focusing and minimization of analysis time. We have further presented a method for directly determining the diffusion coefficient. Once the diffusion coefficient is obtained, then expected peak widths can be calculated and compared with experimental peak widths.

ACKNOWLEDGMENT

We gratefully acknowledge support from the UAB Graduate School and Department of Chemistry for this work. We also acknowledge Jerry Sewell and the machine shop, operated by the Department of Physics, for construction of the capillary stage.

Received for review March 8, 1995. Accepted June 16, 1995.[⊗]

AC950236Z

[⊗] Abstract published in *Advance ACS Abstracts*, August 1, 1995.

Anal. Chem. **1995**, *67*, 3372–3375

Stabilization of Quartz Crystal Oscillators by a Conductive Adhesive

James H. Teuscher and Robin L. Garrell*

Department of Chemistry & Biochemistry, University of California, Los Angeles, California 90095-1569

Quartz crystal oscillators operating in the thickness shear mode (TSM) are widely used to detect mass and viscosity changes in thin films and to monitor adsorption from gas and liquid phases. The precision and detection limits attainable are constrained by the baseline response of the bare crystal. We show here that using a conductive adhesive (Eccobond 56C) to fix the lead electrodes to the quartz oscillator results in significant improvement in the signal-to-noise ratio in measurements of the conductance of the bare crystal and a net increase in the baseline conductance over the temperature range 5–75 °C. The baseline frequency and frequency versus temperature remain the same or change only slightly. The conductive adhesive improves the stability, precision, and reproducibility in quartz crystal microbalance (QCM, aka TSM) measurements.

Thickness shear mode (TSM) quartz crystal oscillators are widely used as mass sensors to detect adsorption from the gas phase and from solution.[1,2] More recently, TSM devices have been used to monitor changes in the viscosity of thin films and solutions[3–6] and to probe interfacial shear.[7–9] The most common type of TSM oscillator is illustrated in Figure 1a. The AT-cut crystal resonates in first order in the 3–10 MHz range and is coated with a metal keyhole-shaped electrode on each side. To these are attached the wire spring clip leads that serve to drive the oscillator and, in our experiments, to connect to the impedance analyzer by which the resonance frequency, complex conductance, and complex impedance are measured. In TSM experiments, the most commonly used instrument electronics constrain the precision in measurements of frequency to ±1 Hz, and ~10-fold better precision has been obtained in some laboratories. In practice, many factors may contribute to decreasing the precision and reproducibility of the measurements. These include poor temperature control, radiofrequency noise, frequency drift,[2] and poor electrical connections.

It is common practice to purchase unmounted crystals for TSM experiments and to mount the crystals by inserting them in spring clip holders, as illustrated in Figure 1a. One advantage to using unmounted crystals lies in avoiding the problem that the solvents used to clean the crystals and electrodes dissolve the adhesives that are normally used in commercially available mounted crystals. The disadvantage to using unmounted crystals is that laboratory vibrations and irregularities in the shape of the spring clips increase the noise in frequency and conductance measurements.

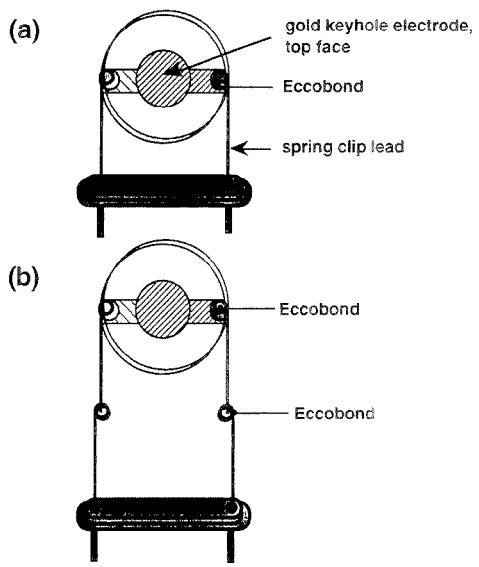

Figure 1. Typical thickness shear mode oscillator, 0.5-in. diameter, with a gold keyhole-shaped electrode on each side. (a) with standard spring clip leads, showing where Eccobond adhesive is applied, and (b) with extended leads, showing where adhesive is applied.

We show here that using a commercially available, solvent-resistant conductive adhesive to mount the quartz crystals leads to substantial improvement in the signal-to-noise ratio and stability of the baseline crystal conductance, an increase in the conductance itself, and no or only small changes in the resonance frequency. The result is improved reliability and precision in TSM (or quartz crystal microbalance, QCM) measurements, with no loss of sensitivity.

EXPERIMENTAL SECTION

Hexadecane (99%, Aldrich), octadecane (99%, Aldrich), decahydronaphthalene (reagent grade, Fisher), *n*-heptane (HPLC grade,

(1) Lu, C., Czanderna, A. W., Eds. *Applications of Piezoelectric Quartz Crystal Microbalances*; Elsevier: New York, 1984.
(2) Grate, J. W.; Martin, S. J.; White, R. M. *Anal. Chem.* **1993**, *65*, 940A.
(3) Schumacher, R. *Angew. Chem., Int. Ed. Engl.* **1990**, *29*, 329.
(4) Rajakovic, L. V.; Cavic-Vlasak, B. A.; Ghaemmaghami, V.; Kallury, K. M. R.; Kipling, A. L.; Thompson, M. *Anal. Chem.* **1991**, *63*, 615.
(5) Thompson, M.; Kipling, A. L.; Duncan-Hewitt, W. C.; Rajakovic, L. V.; Cavic-Vlasak, B. A. *Analyst* **1991**, *116*, 881.
(6) Yang, M.; Thompson, M. *Anal. Chem.* **1993**, *65*, 1158.
(7) Blake, T. D. *Colloids Surf.* **1990**, *47*, 135.
(8) Krim, J. T.; Watts, E. T.; Digel, J. *J. Vac. Sci. Technol.* **1990**, *A8*, 3417.
(9) Duncan-Hewitt, W. C.; Thompson, M. *Anal. Chem.* **1992**, *64*, 94.

0003-2700/95/0367-3372$9.00/0

Fisher), and absolute ethanol (Quantum Chemical Corp., Tuscola, IL) were used as received. Water was deionized and doubly distilled over $KMnO_4$. The 5-MHz polished, AT-cut quartz crystals were obtained from International Crystal Manufacturing Co., Inc. (Oklahoma City, OK). The metal electrodes, deposited on each side of the crystal by the manufacturer, consisted of 50-Å chromium underlayers, onto which were deposited 1000-Å-thick gold keyhole-shaped electrodes, with 0.25-in. (6.4 mm)-diameter centers, polished to a mirror finish (smooth to $<1\ \mu m$). Specifications also included a linear frequency vs temperature response over the 5–70 °C range. The crystals were cleaned by immersion in 25 mL of hexadecane at 90 °C for 1 h, followed by repeated 2–5-min immersion/emersion cycles in 25-mL solvent rinses of increasing polarity: decahydronaphthalene, *n*-heptane, ethanol (two sets of rinses), and doubly distilled deionized water (two sets of rinses). The crystals were then dried with dry nitrogen, mounted in the spring clip leads to the base, and then affixed to the spring clips with or without Eccobond adhesive, as described below and shown in Figure 1.

Eccobond solder 56C (Emerson and Cuming, Inc., Woburn, MA) was used to fix the quartz crystals in the spring clip holders. It is a silver colored, low-resistance epoxy-type polymeric adhesive whose properties are summarized in ref 10. This particular adhesive was chosen for its high conductivity and good resistance to all of the solvents we use to clean the quartz oscillator. (Similar products by other manufacturers were not evaluated.) After the precursor polymer was mixed with catalyst 9 in a ratio of 40:1,[10] the Eccobond was applied to the clip areas in contact with the plated gold. The adhesive was cured by placing the crystals in an oven for 2 h at 110 °C. The manufacturer recommends curing at temperatures ≥66 °C for maximum conductivity.[10] This is important in the present application, as we found that improper curing led to a ~50-mS *decrease* in the conductance of a 9-MHz crystal.

To measure the detection limit of the TSM device, the resonance frequency of the clean, bare oscillator was measured at 15 °C. Thin films were prepared by depositing 2 μL of an octadecane solution in ethanol and drying in air. The resonance frequency was then measured at 3-min intervals until 15 measurements had been obtained. The crystal was cleaned prior to reuse by the procedure described above, starting with decalin. Thinner films were made by depositing 2 μL of more dilute solutions.

For frequency and conductivity measurements, the quartz crystal was suspended in an electronically isolated Lauda RCS-6 thermostated bath, with a dry nitrogen stream near the crystal to keep humidity to a minimum. The temperature of the crystal was monitored by placing an iron–constantan thermocouple in close proximity to the crystal, whose temperature was measured with an AD594 integrated circuit. The thermocouple was calibrated over the complete temperature range against a thermometer in the container. The temperature was stepped in 0.5 or 1 °C increments. As each temperature step was made, 120 s was allowed for thermal equilibration. Scanning the frequency and making the other electrical measurements took an additional 120 s at each temperature. All data points are shown at the actual temperature measured at the thermocouple. The conductance, susceptance, and frequency were measured simultaneously with a Hewlett-Packard 4192A impedance analyzer. The leads to the electrode were compensated using the 4192A analyzer to decrease the effects of stray capacitance and to provide more accurate conductance measurements. A Phillips 6654C high-resolution frequency counter was also used to monitor the frequency. The frequency was typically scanned at a rate of 8 Hz/s over a 954-Hz range, with a resolution of ±1 Hz. The resolution of the conductance measurements was ±2 mS. The experiments were controlled and data collected with a personal computer.

(10) Eccobond. Emerson and Cuming Technical Bulletin 3-2-5; Emerson and Cuming, Inc.: Woburn, MA, 1987. Usable temperature range, −57 to 177 °C; lap shear strength, 56 kg/cm²; flexural strength, 857 kg/cm²; volume resistivity, 2×10^{-4} Ω-cm; thermal conductivity, 0.017 cal-cm/s-cm²-°C; coefficient of thermal expansion, 3.6×10^{-6}/°C.

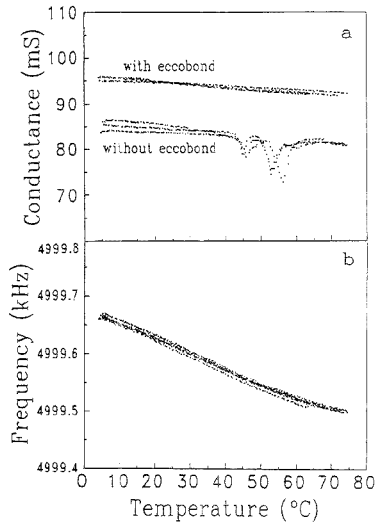

Figure 2. Temperature-dependent response for a 5-MHz oscillator, with and without Eccobond adhesive: (a) conductance vs temperature and (b) resonance frequency vs temperature.

RESULTS AND DISCUSSION

Figure 2a shows the conductance vs temperature of a 5 MHz crystal for three runs without and with Eccobond. The data improve in four ways when the adhesive is used. First, the baseline conductance increases by about 11 mS (10.9 ± 0.5). This indicates better electrical contact and can allow for measurements to be made on thicker, more viscous films than would be possible without the adhesive. Second, the irreproducible peaks observed above 40 °C without Eccobond disappear. Those artifacts are a particular problem, in that they could easily be mistaken for real features, such as phase transitions in conductance vs temperature plots for thin films[11] or adsorption and desorption of an analyte. Third, the signal-to-noise ratio improves substantially. When the data are modeled by a straight line (since the conductance vs temperature should be linear in the temperature range shown, according to the manufacturer), we find that the average correlation coefficient for the three runs without Eccobond is −0.765 ± 0.055, but improves to −0.983 ± 0.008 with Eccobond. This improved correlation coefficient reflects better precision in the conductance measurements. If only the data in the artifact-free region from 5 to 40 °C are included, the average correlation

(11) Garrell, R. L.; Chadwick, J. E. *Colloids Surf. A* **1994**, *93*, 59.

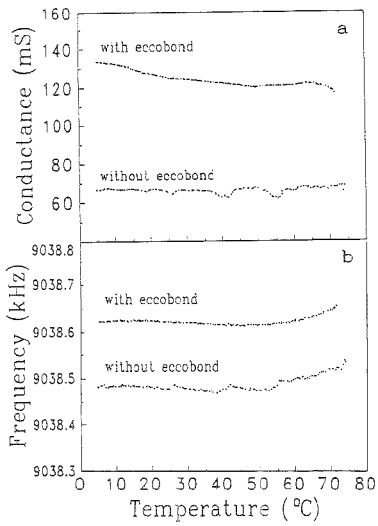

Figure 3. Temperature-dependent response of a 9-MHz oscillator, with and without Eccobond adhesive: (a) conductance vs temperature and (b) resonance frequency vs temperature.

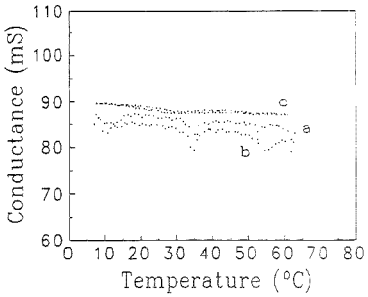

Figure 4. Temperature dependence of the conductance of a 5-MHz crystal with extended leads: (a) no adhesive, (b) with adhesive applied to the junctures between the crystal leads and the lead extensions only, and (c) with adhesive applied to both the spring clip–crystal junctures and lead–lead junctures.

coefficient still improves, from -0.953 ± 0.019 to -0.972 ± 0.027, which is statistically significant given the large number of data points included in the analysis. An alternative measure of the signal-to-noise ratio is the rms noise in conductance vs time. When fit to a horizontal line, the conductance without the adhesive averages to 79.02 ± 0.30 mS, with a correlation coefficient of 0.533, while the conductance with the adhesive is 87.20 ± 0.29, with a correlation coefficient of -0.939. Thus, while the rms noise (standard deviation from the mean value) does not change significantly, the correlation coefficient improves substantially. This is because the conductance exhibits less drift when the adhesive is used. Fourth, the precision of the conductance vs temperature measurements improves with Eccobond, as shown in Figure 2a by the coincidence of the data for the three runs with Eccobond, compared with the poor overlap observed without the adhesive.

Using the conductive adhesive has little effect on the resonance frequency of the bare oscillator, as shown in Figure 2b. The average frequency difference between crystals mounted with or without Eccobond, measured over nine runs, was -0.02 ± 0.5 Hz, which is insignificant. Similarly, the correlation coefficient for frequency vs temperature (Figure 2b) is equally good without and with Eccobond. When fit to a straight line, the average correlation coefficient for three runs with Eccobond, and also for three runs without, is -0.998 ± 0.001.

Similar results are observed for 9-MHz oscillators, as shown in Figure 3. When the conductive adhesive is used, spurious peaks disappear, the baseline conductance increases (by 59.1 mS), and the signal-to-noise ratio improves. Using a linear fit to the conductance vs temperature data, we find that the correlation coefficient improves from a pathetic 6.99×10^{-5} (!) without the adhesive to -0.915 with it. The 9-MHz crystal does behave differently than the 5-MHz crystal in one respect. The resonance frequency increases when the adhesive is used: in this particular example, an increase of 131 Hz is measured. While this phenomenon has been observed for other 9-MHz crystals in our laboratory, the reason for the shift is not clear. In our experience, it has had no adverse consequences. Because the cubic dependence of the frequency on temperature is apparent in this temperature range,[12] the data have been fit to a third-order polynomial. When data at all temperatures are included, the correlation coefficient improves from 0.965 to 0.992 with the adhesive.

For various applications, including using a TSM in a liquid cell to measure solution viscosity and characterize adsorption processes, we have found it more convenient to use TSM devices with longer electrical leads, as illustrated in Figure 1b. To test whether the conductive adhesive would be useful in these applications, we compared the frequency vs temperature and conductance vs temperature for a 5-MHz crystal mounted (a) with no Eccobond, (b) with Eccobond only at the juncture between the leads and lead extensions, and (c) with Eccobond at the lead junctures and at the electrode–spring clip junctures on the quartz oscillator (as in Figure 1b). Consistent with the results described above, the resonance frequency did not change when Eccobond was used at one or both sets of junctures, and the correlation coefficient for the linear frequency vs temperature plot remained consistently -0.998 to -0.999. The conductance vs temperature results are shown in Figure 4. Using a linear fit, we find that the correlation coefficient improves from -0.546 with no Eccobond (a), to -0.809 with adhesive at the lead extension junctures only (b), to -0.958 (average of two runs) when Eccobond was used at both sets of junctures (c).

Figure 5 shows a plot of the resonance frequency vs adsorbed mass of octadecane at 15 °C. The data are modeled by a straight line very well, with a correlation coefficient of -0.998, showing very good precision in the frequency measurements. An adsorbed mass of 6.36×10^{-9} g causes a frequency shift of -3 Hz, while an adsorbed mass of 3.18×10^{-9} g causes no detectable frequency change. (Frequency shifts were recorded to the nearest Hertz.) Thus, the limit of detection is between 3 and 6 ng, which is equivalent to 9.5–19 ng/cm^2 active electrode area. A similar detection limit is calculated when the more rigorous definition of detection limit as twice the rms noise is used. The rms noise in the frequency of the bare crystal vs time is 1.3 Hz. Twice that is

(12) Brice, J. C. *Rev. Mod. Phys.* **1985**, *57*, 105.

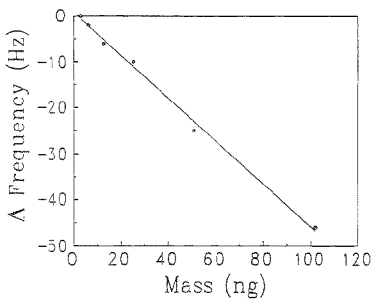

Figure 5. Frequency vs adsorbed mass of octadecane for a 5-MHz oscillator affixed with Eccobond, showing the limit of detection.

2.6 Hz, which is the frequency shift that would be measured for a 5.5-ng adsorbed mass, according to the straight line fit in Figure 5.

CONCLUSIONS

Substantial improvement in the quality of TSM (QCM) data is obtained by using a conductive adhesive to bond the electrical leads to the quartz oscillator. The signal-to-noise ratio, reproducibility, and stability in conductance measurements improve substantially, most likely because the adhesive reduces the vibrations and slip that can occur at the spring clip–quartz crystal junctures. The conductance of the TSM device also increases, which could allow measurements to be made on thicker viscous (damping) films than would otherwise be possible. The resonance frequency is not perturbed when the adhesive is used. The detection limit for the 5-MHz oscillators employed here is between 3 and 6 ng.

ACKNOWLEDGMENT

The authors gratefully acknowledge financial support of this project from the National Science Foundation (DMR-91-96138) and invaluable discussions with Dr. Janice E. Chadwick.

Received for review August 24, 1994. Accepted June 19, 1995.[⊗]

AC940847B

[⊗] Abstract published in *Advance ACS Abstracts*, August 1, 1995.

Author Index

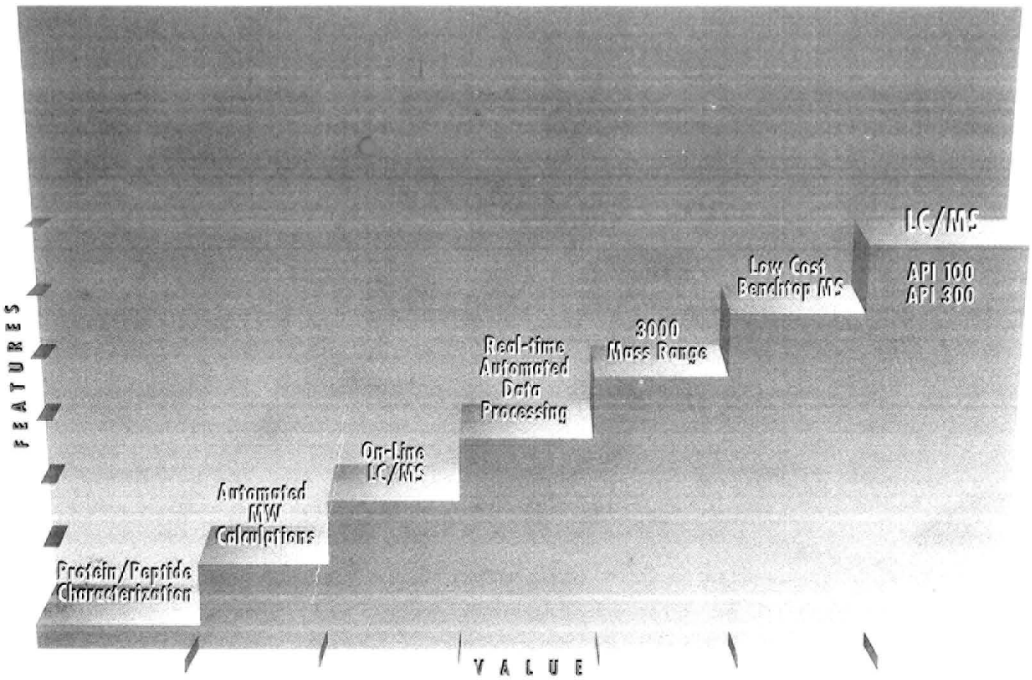

PE SCIEX takes a step up with the new benchtop API 100 and API 300 LC/MS systems.

PE SCIEX is the world leader in API LC/MS technology for both single and triple quadrupole mass spectrometers. In over 100 of the world's largest pharmaceutical and bioresearch labs, API LC/MS technology from PE SCIEX is being used to analyze a wide variety of samples—from small pharmaceutical metabolites, through peptides, to large proteins and glycoproteins.

Outselling and outperforming all other dedicated LC/MS systems, the API I and API III have been accepted worldwide as the industry standard. Our innovative IonSpray™ and TurboIonSpray™ interfaces have made LC/MS a routine and reliable technique—even for complex biological samples.

Now we've taken API technology another step up: onto the lab bench. The new API 100 and API 300 are benchtop quadrupole mass spectrometers offering a newly designed IonSpray interface with the option of µIonSpray.™ With the new µIonSpray, protein sequencing, peptide mapping, and molecular weight determinations with biomolecular characterization at femtomole levels is now possible.

Both systems offer a mass range of up to 3000, highly reliable turbomolecular pumps, and improved sensitivity. New software, fully compatible with the latest computer technology, enables the user to take advantage of the increased performance of the Apple Power Macintosh®.

Our BioToolBox™ application software is ideal for complete characterization of proteins and peptides from LC/MS, CID/MS and MS/MS data.

For more information about the new benchtop API 100 and API 300, call 1-800-345-5224 in the U.S. or contact your local Perkin-Elmer representative.

PE SCIEX

Australia Tel: 3 212 8500 Fax: 3 212 8501 **Latin America** Tel: 11 578 9600 Fax. 11 276 1864 **Italy** Tel: (039) 23831 Fax. (039) 2383490
France Tel. 1 3085 8363 Fax: 1 3085 8300 **Germany** Tel: 6150 101 0 Fax: 6150 101 101 **UK** Tel: 01494 67 6161 Fax: 01494 67 9331
Japan Tel. 45 314 8010 Fax: 45 314 8142 **Singapore** Tel: 336 0322 Fax: 338 3991

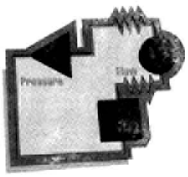

❶ *No more knobs with PPC™ programmable pneumatic control*

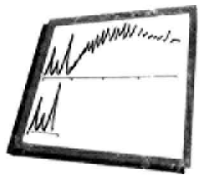

❷ *PreVent™: faster analysis, extended system life*

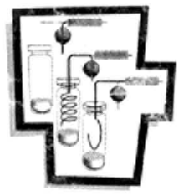

❸ *Pressure-balanced headspace sampling*

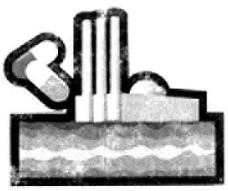

❹ *Engineered solutions for your special application*

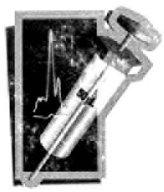

❺ *10X more sensitivity with large-volume injection*

❻ *Rapid GC/MS pumpdown*

❼ *Built-in autosampler for greater reliability*

❽ *Advanced data handling with Turbochrom™*

❾ *Two-stage thermal desorption improves results*

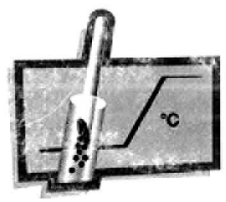

❿ *Universal capillary inlet with temperature programming*

10 reasons your next GC should be the AutoSystem XL.

Reason 2: Faster analysis and extended system life. Improve throughput as much as 10-fold with AutoSystem XL™'s unique PreVent mode. PreVent eliminates high-boiling nontarget compounds before they reach the column, reducing sample handling and extending column and detector life.

Get the full story from Perkin-Elmer. For more information about all the reasons your next GC should be the AutoSystem XL, contact Perkin-Elmer through our worldwide service and support network. In the U.S., call 1-800-762-4000. Outside the U.S., contact your Perkin-Elmer representative.

New AutoSystem XL Gas Chromatograph

PERKIN ELMER